




UNIVERSITÉ PIERRE ET MARIE CURIE

U.F.R. PHYSIQUE

ÉCOLE DOCTORALE SCIENCES DE LA TERRE ET DE L'ÉNVIRONNEMENT

THÈSE DE DOCTORAT

POUR OBTENIR LE TITRE DE

DOCTEUR EN PHYSIQUE

SPÉCIALITÉ : PHYSIQUE DE PARTICULES

PRÉSENTÉE PAR

ALVARO LOPEZ SOLIS

Contribution à la mesure d'énergie et du temps des électrons et des photons dans l'expérience ATLAS et recherche de la production de matière noire en association avec un boson de Higgs

Jury de thèse:

Karim Benakli	*Président*
Marie-Hélène Genest	*Examinatrice*
Eli Ben-Haim	*Examinateur*
Bertrand Laforge	*Directeur de thèse*
Chiara Mariotti	*Rapporteuse*
Dirk Zerwas	*Rapporteur*

Soumise aux rapporteurs le 24 Juillet 2017 à Paris, France.
Soutenue le 28 Septembre 2017 à Paris, France.

CERN-THESIS-2017-214
28/09/2017

Laboratoire de Physique Nucléaire et des Hautes Énergies (LPNHE)
4 place Jussieu, Barre 12-22, 1ère étage,
75252 Paris Cedex 05

École Doctorale 560
Sciences de la Terre et de l'environnement et Physique de l'Univers (STEPUP)
Bureau P31-32 1, rue Jussieu
75238 Paris cedex 05

Esta tesis esta dedicada a mis padres,
sin cuyo apoyo y cariño no habría podido
terminar este trabajo, y a mi hermana,
qué me alegra cada día desde hace 22 años.

Acknowledgements

During the last five years, I have been devoted to preparing myself to enter the world of particle physics, I have advanced from an elementary knowledge of particles and interactions to grasp the surface of the current searches for dark matter and, finally, give a contribution to this passionating subject. However, this could not have been possible without the help and encouragement of many people that I have met during the last years and to which I am very grateful.

First, I would like to express my deepest gratitude to my supervisor, Bertrand Laforge. I met him five years ago, when I was an Erasmus student in Paris, and since then he has guided my steps into the world of particle physics. His suggestions and guidance allowed me to understand how a scientist should think and they provided me with very important background and inspiration to develop my own ideas. I always appreciated our discussions and truly think that I could not have had a better advisor, who was fully devoted since the first moment to answer any possible question I could have.

I also want to thank all the members of my jury, who reviewed my work and asked me very interesting questions that allowed me to improve this manuscript: Chiara Mariotti, Dirk Zerwas, Marie-Hélène Genest, Karim Benakli and Eli Ben-Haim. To Eli Ben-Haim, I also want to thank all his useful lessons to teach me and all my Master 1 colleagues the basic concepts of particle physics.

I am also very grateful to the HGam group at the LPNHE: Lydia Roos, José Ocariz, Giovanni Marchiori, Sandrine Laplace, Irena Nikolic, Yee Yap, Renjie Wang and Alexander Leopold. Discussions in our meetings were always very interesting and helped me to increase my knowledge in photon reconstruction and the Higgs boson. I was very happy to work with all of them! In particular, I greatly appreciated the help from Renjie Wang, with whom I had the chance to work very closely and that became a referent to me due to his dedication and hard work during the last year. Besides, many thanks to Didier Lacour for our useful discussions on the liquid argon calorimeter and cross-talk.

Thanks to the other Ph.D students in the lab for their companionship, especially to Daniel, Rémy, Changqiao and Dilia for all the times we spent. I would also like to thank the administration team for their help with all the administrative procedures, and to Souad Rey, for her hard work to manage all the missions I engaged and her willingness to help me at any moment.

Last but not least, I want to thank all my family and friends for their constant support and love. They have encouraged and supported me, allowing me to overcome all the obstacles I found during these years and to meet my objectives. An especial thank to my parents and my sister, who have always motivated me to go on in the moments of doubt, and to Baptiste, Vagelis and Giorgos for our long discussions and support.

Contents

Introduction 1

1 Standard Model and Dark Matter 3
- 1.1 An overview of the Standard Model of particle physics . . . 4
- 1.2 Higgs phenomenology at the LHC . . . 17
- 1.3 Standard Model limitations . . . 21
- 1.4 The Dark Matter open questions . . . 24
- 1.5 Phenomenological search for DM particles at the LHC . . . 31

2 The LHC and the ATLAS experiment 45
- 2.1 The Large Hadron Collider . . . 45
- 2.2 ATLAS detector . . . 49

3 Energy and time reconstruction in electromagnetic barrel 63
- 3.1 Calorimetry . . . 64
- 3.2 Principles of electron and photon detection . . . 65
- 3.3 Liquid argon barrel readout chain and energy reconstruction . . . 69
- 3.4 Signal shape for physics signal . . . 77
- 3.5 Optimal filtering . . . 80
- 3.6 Passage from ADC to MeV . . . 81
- 3.7 Energy and time reconstruction performance . . . 84

4 Photon and electron reconstruction 89
- 4.1 Cluster and track reconstruction . . . 91
- 4.2 Electron and photon reconstruction . . . 93
- 4.3 Electron and photon identification . . . 97
- 4.4 Isolation . . . 102
- 4.5 Photon and electron calibration . . . 105

5 Cross-Talk effects in the LAr EM barrel 113
- 5.1 Types of cross-talk . . . 114
- 5.2 Test-beam and calibration cross-talk . . . 117
- 5.3 Cross-talk in physics conditions . . . 121
- 5.4 Shower shape corrections . . . 140

6 Missing transverse momentum reconstruction 145
- 6.1 Jets reconstruction and calibration . . . 146
- 6.2 Muon reconstruction and identification . . . 151
- 6.3 $E_{\mathrm{T}}^{\mathrm{miss}}$ reconstruction . . . 153
- 6.4 $E_{\mathrm{T}}^{\mathrm{miss}}$ reconstruction in $h \to \gamma\gamma$ events . . . 158

7 DM production in $h \to \gamma\gamma + E_{\mathrm{T}}^{\mathrm{miss}}$ channel 169
- 7.1 Data and simulated samples . . . 170
- 7.2 Event reconstruction and selection . . . 176
- 7.3 Categorization . . . 178

7.4 Analysis strategy . . . 188
7.5 Systematic uncertainties . . . 197
7.6 Results . . . 201
7.7 Comparison of the ATLAS $h \to \gamma\gamma + E_{\mathrm{T}}^{\mathrm{miss}}$ with other measurements . . . 215

Conclusion 225

Appendices 229

A Statistical framework 231
A.1 Hypothesis test . . . 231
A.2 Asymptotic formulae . . . 234
A.3 Confidence level formalism . . . 235

B Comparison between Z'-2HDM and Heavy Scalar model 237

C Cross-section checks between CMS and ATLAS DM models 247
C.1 Z'_B model g_q parameter . . . 247
C.2 Z'-2HDM cross-sections dependence on CP-even boson masses . . . 247

Introduction

In a very famous speech given in 1900, April 27th [1], Lord Kelvin identified two "small clouds" that physics community had to solve out before physics is completed. Indeed, at that time nobody could explain neither the black body emission spectrum based on classical mechanics nor was able to experimentally detect the ether predicted by the theory of light and electromagnetism. A third cloud came quickly after with the observation of a deviation of the Mercury perihelion precession with respect to Newtonian mechanics prediction by Urbain Le Verrier in 1859. The solution to these different issues was to abandon classical mechanics and Maxwell classical electromagnetism to give birth to quantum field theory and general relativity.

The current physical understanding of our universe faces today a major issue again: either general relativity theory is wrong or there should exist an extra matter that could allow within Einstein's theoretical framework to correctly describe the observable movement of stars in their galaxies, of galaxies in their cluster and the observable spatial correlations of cosmic microwave background temperatures in our early universe when it became transparent to photons. The main feature of this matter is the non-emission of light, which leads to different theories about its nature, such as the presence of primordial black holes or large structures non-emitting light (MACHO's). Among all these proposed theories, it is very active the search of a new type of weakly interacting of matter, made at a microscopic scale of a new type of elementary particles. This sought "Dark Matter" (DM) may explain the physics at large scales. However, this has currently no known counterpart at the microscopic scale.

The inclusion of a new type of matter requires the extension of the current model of particle physics, also called the Standard Model of Particle Physics (SM), the theory of fundamental interactions that describes the components of matter and their interactions between them. Several experiments have confirmed the validity of the Standard Model over a large range of energies, completed by the discovery of the Higgs boson (h) in 2012 by ATLAS and CMS experiments at LHC, the last missing particle in its spectrum. This boson is the phenomenological manifestation of an underlying field allowing mass terms for massive particles.

When the work explained in this thesis started, ATLAS and CMS collaborations were searching for signals of dark matter production in association with other SM particles, also called mono-X searches. Several theories encouraged searches of Higgs bosons produced in association to dark matter particles, the latter leaving a large missing transverse momentum signature in the ATLAS data. This final state probes the Higgs boson coupling with the dark sector. Among all possible channels, my work focused in the decays of the Higgs boson into two photons.

The aim of this thesis is to explain the search for a Dark Matter candidates in association to a Higgs boson in the ATLAS high energy proton-proton collision data. The Higgs boson is sought in its diphoton decay channel due to the relatively low signal-background ratio in this channel and the good photon energy resolution in the ATLAS detector. Importantly, this search is driven by performances. Missing transverse momentum can be faked by many sources in ATLAS while the dark matter production is expected to present a relatively low cross-section. Then, the correct missing transverse momentum reconstruction and the photon identification and calibration performances are critical items of this analysis which strongly benefit of any improvement in that field. In this context, this thesis also describes my contributions to the performance of the ATLAS liquid argon barrel calorimeter, aiming to to improve the measurement of energy and arrival time of the photons, the photon identification, and the recon-

struction of the missing transverse momentum quantity in events presenting a Higgs decaying into two photons. The document is organized as follows.

A brief review of the Standard Model and the Dark Matter problem are presented in Chapter 1. The text describes, in a nutshell, the history of the SM, its main predictions and its experimental successes, the Higgs boson mechanism and finally present the main SM problems. A description of the dark matter production at early times considering the theory of freeze-out and its detection strategies are also discussed. Finally, the theories used in the analysis presented in this thesis are exposed.

Chapter 2 describes the Large Hadron Collider (LHC) and the ATLAS detector. ATLAS sub-detectors are also described, with a particular emphasis on the ATLAS electromagnetic barrel and trigger system.

The principles of detection of the ATLAS electromagnetic calorimeter are summarized in Chapter 3. Calorimetry, electromagnetic showers development in the detector and energy reconstruction are presented. In addition, the ATLAS energy calibration technique is discussed together with the current performance in energy and time reconstruction. Electrons and photons reconstruction, identification, isolation and energy calibration techniques are reviewed in Chapter 4. Unfortunately, these techniques are biased by several effects concerning the passive material simulation and the cell-to-cell electronic cross-talk effect. A part of my work during the last three years consisted to revisit our knowledge of the cross-talk effect in order to improve the energy and time measurements of electrons and photons and the photon identification. Up to now, the cross-talk effect has been evaluated using calibration signals. Although it allowed reducing its impact on photon measurements, an update using signal shapes close to the data-taking ones is desired to increase the accuracy. This work is described in Chapter 5 together with the implications on shower shapes reconstruction.

The missing transverse momentum ($E_{\mathrm{T}}^{\mathrm{miss}}$) is a key quantity in the analysis presented in this thesis since it is the signature left by at least one stable dark matter particle (most probably two if one assumes fermion number conservation) in the detector. This quantity is the result of an imbalance in the final transverse momentum distribution and is estimated using a common algorithm for all final states inside ATLAS. However, some of the features of this calculation are not adapted to correctly reconstruct $E_{\mathrm{T}}^{\mathrm{miss}}$ in topologies with a Higgs boson decaying into two photons. My work has focused on the update of these features to correctly reconstruct $E_{\mathrm{T}}^{\mathrm{miss}}$ in $h \to \gamma\gamma$ topologies, as it is discussed in Chapter 6.

The search for Dark Matter candidates is reviewed in Chapter 7. No signal over the SM expected background is observed and limits on the different models considered are set. This analysis is compared with the ATLAS analysis considering the Higgs boson decay into a bottom-antibottom pair and the same CMS analysis. My contributions to the analysis cover the signal samples simulation and validation, the optimization of one of the categories (Mono-Higgs category), the evaluation of theoretical and experimental systematics and the limit setting for two of the used models (Z'_B and Z'-2HDM models).

References

[1] Lord Kelvin. *Nineteenth-Century Clouds over the Dynamical Theory of Heat and Light*. URL: https://archive.org/details/londonedinburgh621901lond.

Standard Model and Dark Matter

Contents

1.1 An overview of the Standard Model of particle physics . . . 4
1.1.1 Experimental ingredients to be included in a model of particle physics . . . 4
1.1.2 Gauge theories . . . 7
1.1.3 Quantum electrodynamics (QED) . . . 8
1.1.4 Renormalization . . . 8
1.1.5 The Higgs mechanism . . . 9
1.1.6 Electroweak unification of Glashow, Salam and Weinberg . . . 10
1.1.7 Quantum chromodynamics (QCD) . . . 13
1.1.8 The Standard Model . . . 15
1.2 Higgs phenomenology at the LHC . . . 17
1.2.1 Production and decay modes of the SM Higgs boson at LHC Run II . . . 18
1.3 Standard Model limitations . . . 21
1.4 The Dark Matter open questions . . . 24
1.4.1 Dark matter evidences . . . 24
1.4.2 An overview of the Universe evolution . . . 26
1.4.3 Boltzmann equation and Dark Matter freeze-out . . . 27
1.4.4 Dark matter detection experiments . . . 29
1.5 Phenomenological search for DM particles at the LHC . . . 31
1.5.1 Effective field theories vs simplified models . . . 31
1.5.2 Mono-Higgs theories . . . 33

The search for dark matter (DM) is presently one of the most active topics in particle physics. Since the first formulation of dark matter as a possible explanation for the ratio of the average mass/luminosity in galaxies of the Coma cluster in the 30's, the last 90 years of research in astrophysics and cosmology have introduced strong evidence supporting the existence of a non-electromagnetically interacting new type of matter. These new components of the universe are predicted to be deeply involved in the dynamics of diverse systems in cosmology and astrophysics, from low distance phenomena such as the motion of stars around the galactic center to the structure formation and our universe global evolution. However, despite the strong evidences of its existence at large scales, its microscopic nature discovery is still to be made and its possible properties and interactions with visible matter remain unknown.

A search for dark matter elementary particle candidates is also theoretically motivated by several open questions that the present Standard Model (SM) of particle physics cannot answer. The possible existence of new weakly interacting particles is indeed forecast in many extensions of the SM. The related new physics sector may especially have interactions with the Higgs sector, the less known part of the SM.

In this chapter, after a presentation of the SM and of its weaknesses, a review of the experimental constraints on possible DM particle candidate is presented. In the last section, the different models of DM used to design the analysis presented in this thesis and to interpret the results are introduced.

1.1 An overview of the Standard Model of particle physics

The Standard Model of particle physics is the theory that describes the elementary[1] particles and their associated interactions currently known in Nature. Elementary particles are the fundamental constituents of matter which, through their interactions, account for the observable phenomena at microscopic scale. Four fundamental interactions are currently known, among which the Standard Model successfully describes three of them, namely the electromagnetic, weak and strong interactions. Gravitation, whose quantum field formulation is not still fully implemented, requires an extended theoretical framework to be quantized and embedded with other interactions in a single theoretical framework: this is the goal of string theories being currently developed. The Standard Model describes these three interactions using a unique theoretical framework based on so-called *gauge theories*. As presented in this chapter, the change of the underlying gauge group allows to build: quantum electrodynamics to describe the electromagnetic interaction; the Glashow-Salam-Weinberg (GWS) electroweak unification theory to model the weak interaction and the electromagnetic force; and the quantum chromodynamics (QCD) to account for the strong interaction. In the case of the electroweak theory, which requires having massive mediators, an extra mechanism is needed to completely describe the weak interaction: the Higgs mechanism.

The research program that leads to the Standard Model of particle physics was carried out along the 20^{th} century following both experimental discoveries and incorporating theoretical breakthroughs. The main experimental ingredients motivating this theory are exposed in Section 1.1.1; gauge theory principles are presented in Section 1.1.2; QED, GWS and QCD theories are detailed in sections 1.1.3, 1.1.6 and 1.1.7 respectively in addition to the renormalization procedure in Section 1.1.4, which is a key ingredient of the great predictive power of these theories. The Higgs mechanism is presented in Section 1.1.5 and, finally, the Standard Model and its main predictions are presented in Section 1.1.8.

1.1.1 Experimental ingredients to be included in a model of particle physics

Matter composition

After the success of the atomic model at the end of the 19^{th} century, the discovery of the electron in 1897 [1] by Lord Thomson opened a century of experimental discovery of a completely ignored microscopic world exhibiting a surprising zoology of particles. Preservation of energy conservation in the measured energy spectrum of electrons from nuclear β decay led Pauli to introduce a new weakly interacting particle, the neutrino, whose existence was indeed experimentally demonstrated later on in 1956 by Reines and Cowan [2, 3]. With the positron discovery by Anderson in 1932 [4] also came the fact that two particles can annihilate into pure energy that can convert to new particles. This discovery leads to introduce the concept of antiparticle in the interpretation of the Dirac theory which aimed at including special relativity in the theory. The invention of particle accelerator speeded up the process and provided a rich collection of strongly interacting particles (the hadrons) and a new particle, the tau, similar to the electron and the muon which was discovered in the cosmic rays by Carl D. Anderson and S. Neddermeyer at Caltech in 1936 [5]. These particles are called generically leptons. Together with these leptons, Pauli introduced the neutrino, a low mass particle interacting very weakly with matter, in an attempt to explain the energy distribution of the electron issued from β decays while preserving energy conservation.

Quarks were introduced by Gell-Mann [6] as theoretical components of the hadrons, a series of composite particles interacting through the strong interaction. The first experiment showing the existence of quarks was performed at SLAC [7] by colliding high energy electrons on a proton target. Such experiments, called Deep Inelastic Scattering (DIS), put in evidence an inner structure of the hadrons and furthermore, that hadrons are bound states of more fundamental particles: quarks and gluons that are also generically called partons. The leading order Feynman diagram of the DIS collision is presented in Figure 1.1.

Further experiments have studied in more detail the structure of the hadrons, in particular of protons.

[1] Elementary particle here means particles considered as fundamental fields of the theory.

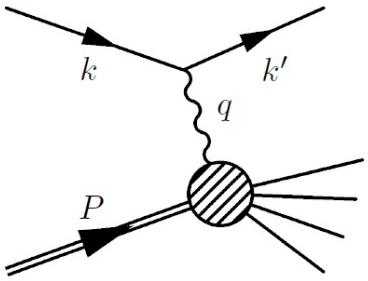


Figure 1.1: Feynman diagram of the Deep Inelastic Scattering process. An electron interacts with a quark inside the proton. The scattered electron energy and angular distributions provide information about the structure inside the proton.

These experiments showed that hadron composition depends on the energy scale Q at which they are probed and that a large fraction of the momenta of the proton is carried by the gluons. Partons carry a variable fraction x of the total momentum of the hadron whose distribution is changing with Q^2. These parton density functions (PDF's) must be determined experimentally but have the advantage that they are universal, in the sense that a unique set of those PDF's describes every hadron of a given type regardless of the high energy collision in which it is involved. In addition, the evolution of the PDF's with the interaction energy is described by the DGLAP equation [8].

Experimental facts about natural forces in Nature

At the end of the 19$^{\text{th}}$ century, the successful description of the black-body spectrum leads to the introduction of energy quantization as a major component of the theory. The introduction of the wave-particle duality by de Broglie, the introduction of the Schrödinger wave equation (for electrons) and the matrix formulation of quantum mechanics by Born, Heisenberg, Jordan and Pauli [9] constitute giant steps in the description of non-relativistic quantum mechanics. On the other hand, the Michelson-Morley experiment demonstrated that the speed of light is a constant regardless of the reference frame in which it is measured. This result pushed to reconsider our conceptual point of view of space and time and introduced the necessity to describe interactions in such a way that no interaction can propagate faster than light. Since then, physicists have tried to explain the electromagnetic interaction through a relativistic quantum field theory, aiming to explain the finer effects observed in on the energy spectra of hydrogen atoms. The fully quantized theory of the electromagnetic field was not completed until the formulation of quantum electrodynamics by Feynman, Schwinger and Tomonaga in the 1950's, being particularly successful in explaining the electron anomalous momenta and the Lamb shift, observed in 1947 [10] between the levels $2S_{1/2}$ and the $2P_{1/2}$ of the hydrogen atom [11].

The quantization of the fields blurs the distinction between particles and waves. Punctual (or point-like) particles become fuzzy and the fields (for example the electromagnetic), classically represented as a continuum, become mediated by particle-like entities (the photon for the electromagnetic field). Then, interactions become a consequence of the exchange of field quanta between particles charged under the mentioned field. This point of view can be extended to other interactions and constitutes the basis of the Standard Model description of interactions.

Indeed, while the quantum electrodynamics was being developed, new experimental facts exhibit new kinds of forces. In the early 20$^{\text{th}}$ century, the discovery of the nucleus of atoms, composed of positively charged particles, required to introduce a stronger interaction to explain how these repulsing electrical charges could be bound together. The description of the strong interaction began with Yukawa's theory [12]. In contrast to electromagnetism, he proposed a quantized field with massive mediators, the pions π, due to the short range of the interaction (it binds protons and neutrons inside the nuclei). However, this theory failed to explain the proton-neutron force at high energies and the interaction of pions among themselves. Development of particle accelerators provided the experimental proof that strong interacting particles (hadrons) are numerous and thus raised the question about their fundamental na-

ture. Hadron properties classification provided another hint on the nature of the strong interaction. Gell-Mann's hadronic model consisted on classifying hadrons according to the quantum numbers of new theoretical constituents, the quarks, which in that epoch were limited to the up (u), down (d) and strange (s) quarks. Quarks u and d are the main constituents of the proton and neutron and carry a quantum number called isospin. The s quark instead carries a strangeness quantum number and no isospin, which allows the combination of these three quarks to classify the observed hadron zoology at the time depending on their spin, strangeness and isospin. The observation of the baryon Δ^{++} forced the introduction of the color quantum number by Oliver Greenberg in 1964 [13], which reconciled the Gell-Mann's model predictions (three up quarks in the same state of spin and isospin) with the conservation of the Pauli exclusion principle. In addition, a mechanism proposed by Glashow, Iliopoulos and Maiani (GIM mechanism [14]) required the introduction of the c-quark in order to suppress flavour-changing neutral currents (FCNCs) and explain the $\Delta S = 2$ transitions in weak theory. This mechanism then pushed to extend the number of quarks in Gell-Mann's theory. In addition, the studies on the CP-violation of the weak interaction by M.Kobayashi and T.Maskawa [15] motivated the extension of quark spectra to a third flavour family, composed of the b-quark and the top quark, thus completing the particle picture in the theory.

As the electromagnetic interaction, strong interaction involves the existence of a charge, that is identified with this color charge. The mediators of the strong interaction are massless vector fields while the interaction has an effective spatial limited range. This is not contradictory since the strong force has a potential energy which is highly increased when two color charges are separated from each other so that when the distance is large enough this energy can be materialized into a new quark-antiquark pair that decouples the primary charges one from the other. Studies of the proton structure showed that quarks can only account for a fraction of the total energy of the proton. The missing fraction was postulated to belong to gluons, which are the mediators of the strong interaction. Their existence was confirmed by the discovery of 3 jet events in the Petra experiment [16] in 1979.

Another important phenomenon was also discovered studying radioactive properties of matter and gave a very strong motivation to include a new interaction between particles: the radiative $\beta-$decay. This reaction takes place only inside the nucleus of atoms, i.e at a short range of $\mathcal{O}(10^{-15}m)$. This fact implies that the mediators of the weak interaction must be massive, which present important consequences in the SM phenomenology as we will see in the next sections. Indeed, while a massless photon emitted by an electrical charge can propagate to very long distances without breaking the Heisenberg inequality $\Delta E.\Delta t \sim \hbar$ as soon it has a low enough energy, a massive interaction mediator of masse M cannot go beyond a distance $d = c\Delta t \geq \frac{c\hbar}{Mc^2}$. There is one exception to this rule concerning the strong interaction, whose mediators are massless but the interaction is short range. This is due to the structure of the interaction, as it will be explained in Section 1.1.7. A summary of the different interaction strengths and ranges is presented in Table 1.1.

Furthermore, experiments studying weak interaction showed an additional difference with other interactions with respect to the invariance properties that it respects. Parity, charge conjugation and time reversal are discrete symmetries that are conserved by the electromagnetic and strong forces. Instead, the experiments on the $\beta-$decay of Co^{60} nuclei by C.S. Wu and al. [17] and on the decay of neutral kaons by J.H. Christenson et al. [18], showed that parity symmetry (P), charge conjugation symmetry (C) and combined CP symmetries are observed to be violated by the weak force.

These discrete symmetries can be summarized as:

- **Parity (P):** a discrete symmetry transformation that changes the dynamical variables of the fields to their mirror images:
$$x = (x^0, \mathbf{x}) \rightarrow x = (x^0, -\mathbf{x}) \tag{1.1}$$
- **Time reversal (T):** Time reversal consists on the inversion of the time.
$$x = (x^0, \mathbf{x}) \rightarrow x = (-x^0, \mathbf{x}) \tag{1.2}$$
- **Charge conjugation (C):** Charge conjugation is a discrete symmetry operation where all charges of a given particle are flipped keeping however the same mass and the same spin. This is the symmetry that relates the particles in the Standard Model to their antiparticles.

Interaction	Coupling	Relative strength	Δx (m)
Strong	g_S	10^{38}	10^{-15}
Electromagnetic	e	10^{36}	∞
Weak	g_W	10^{25}	10^{-18}
Gravitational	G	1	∞

Table 1.1: Fundamental interactions and relative strength together with their range of action in meters. This table summarizes the current knowledge of these interactions and it is the subject of ongoing searches.

1.1.2 Gauge theories

Gauge theory is the framework in which all three interactions are embedded in the Standard Model. The interest of gauge theories is that they allow implementing the conservation of a quantum number in the theory. They also provide a unique way of building an interaction between particles carrying such a quantum number. Invariance of the Lagrangian of the theory under local transformations implies the conservation of a current according to Noether's theorem [19] and allows the introduction of a vector field to restore the local invariance of the Lagrangian under a gauge transformation. This quantum number is called a charge in reference to the electric charge whose conservation is ensured using a gauge theory in the building of QED. The interaction is mediated by a new type of particles, the force carriers, called gauge bosons. Their propagation through space allows a limited speed of the interaction as expected from relativity theory. Let's consider a free-motion Lagrangian for a spin-0 boson $\phi(x)$

$$\mathcal{L}_{\text{scalar}} = \partial_\mu \phi^\dagger(x)\, \partial^\mu \phi(x) - m^2 \phi^\dagger(x)\, \phi(x) \tag{1.3}$$

and consider a global $U(1)$ symmetry transformation:

$$\phi(x) \to \phi(x)' = e^{i\omega}\phi(x) \tag{1.4}$$

where ω is a global parameter independent of the spacetime point x. Under this phase rotation, the Lagrangian is invariant as shown in Eq. 1.5:

$$\begin{aligned} \mathcal{L}'_{\text{scalar}} &= \partial_\mu \phi^\dagger(x)' \, \partial^\mu \phi(x)' - m^2 \phi^\dagger(x)' \, \phi(x)' \to \\ \mathcal{L}'_{\text{scalar}} &= \partial_\mu \phi^\dagger(x) \left(e^{-i\omega}\right) \partial^\mu \left(e^{i\omega}\right) \phi(x) - m^2 \phi^\dagger(x)' \left(e^{-i\omega}\right) \left(e^{i\omega}\right) \phi(x)' \to \\ \mathcal{L}'_{\text{scalar}} &= \partial_\mu \phi^\dagger(x)\, \partial^\mu \phi(x) - m^2 \phi^\dagger(x)\, \phi(x) = \mathcal{L}_{\text{scalar}} \end{aligned} \tag{1.5}$$

In the case where local symmetries are considered (Eq. 1.6), this Lagrangian is no longer invariant under the symmetry transformation since additional terms appear:

$$\phi(x) \to \phi(x)' = e^{i\omega(x)}\phi(x) \tag{1.6}$$

$$\begin{aligned} \mathcal{L}'_{\text{scalar}} &= \partial_\mu \phi^\dagger(x)' \, \partial^\mu \phi(x)' - m^2 \phi^\dagger(x)' \, \phi(x)' \to \\ \mathcal{L}'_{\text{scalar}} &= \partial_\mu \phi^\dagger(x) \left(e^{-i\omega}\right) \partial^\mu \left(e^{i\omega}\right) \phi(x) - m^2 \phi^\dagger(x)' \left(e^{-i\omega}\right) \left(e^{i\omega}\right) \phi(x)' \to \\ \mathcal{L}'_{\text{scalar}} &= \mathcal{L}_{scalar} + (\partial^\mu \omega(x))^2 \phi^\dagger(x)\, \phi(x) + i\partial_\mu \omega(x)[\phi(x)\, \partial^\mu \phi^\dagger(x) - \phi^\dagger(x)\, \partial^\mu \phi(x)] \end{aligned} \tag{1.7}$$

These additional terms come from the derivative part of the Lagrangian. Gauge invariance can be restored if a spin-1 boson, called gauge boson, is introduced in the derivative term:

$$\partial_\mu \to D_\mu = \partial_\mu - iA_\mu(x) \tag{1.8}$$

$$\mathcal{L}_{scalar} = D_\mu \phi^\dagger(x)\, D^\mu \phi(x) - m^2 \phi^\dagger(x)\, \phi(x) \tag{1.9}$$

where D_μ is called covariant derivative of the gauge theory. This gauge boson also transforms under local rotation (Eq. 1.10) and compensate the non-invariant terms such as the ones shown in Eq. 1.7.

$$A_\mu(x) \to A'_\mu(x) = A_\mu(x) + \partial_\mu \omega(x) \tag{1.10}$$

These transformations are rotations that form a Lie group $U(1)$. The generalization to higher dimension Lie groups may be done by considering tensorial phase transformations acting on a vector of fields. Thus, considering one rotation $U(x)$ contained in the $D-$dimensional representation of the non-Abelian (non-commutative) gauge group $SU(N)$ and the N-plet Φ of dimension D, the local transformation may be written as:

$$\Phi \rightarrow \Phi' = U(x)\Phi, \quad U = e^{ig\omega(\vec{x})\vec{\tau}} \tag{1.11}$$

where τ are the generators of the $SU(N)$ group and $\vec{\omega}(x) \in \mathbb{R}^{\mathrm{N}}$. Then, the corresponding covariant derivative and the gauge field transformation become:

$$\partial_\mu \rightarrow D_\mu = \partial_\mu - ig\vec{\tau}\vec{A}_\mu(x) \tag{1.12}$$

$$\vec{A}_\mu(x) \rightarrow \vec{A}'_\mu(x) = U(x)\vec{A}_\mu(x)U^{-1}(x) + \partial_\mu\vec{\omega}(x) \tag{1.13}$$

For both, non-Abelian and Abelian Lie gauge groups, one may highlight two important features:

- Gauge theories introduce a new gauge boson per generator of the symmetry group.
- Gauge invariance forbids mass terms $\mathcal{L} \propto \frac{m^2}{2}A^\mu A_\mu$ for the gauge bosons.

1.1.3 Quantum electrodynamics (QED)

Quantum electrodynamics has been developed to explain the interaction of electrically charged fermions and constitutes the prototype of gauge theory used to model particle interaction using a simple gauge transformation group $U(1)_Q$. This gauge symmetry introduce a new gauge boson A_μ so that its Lagrangian is:

$$\mathcal{L}_{\mathrm{QED}} = \overline{\psi}(x)\, i\gamma^\mu D_\mu \psi(x) - m^2\overline{\psi}(x)\,\psi(x) - \frac{1}{4}F^{\mu\nu}F_{\mu\nu} \quad ; \quad D_\mu = \partial_\mu - ieA_\mu(x) \tag{1.14}$$

where e is the coupling strength of the interaction, which can be identified as the raw electric charge associated with the fermion $\psi(x)^i$, and $-\frac{1}{4}F^{\mu\nu}F_{\mu\nu}$ is the kinetic term of the photon with:

$$F_{\mu\nu} = \partial_\mu A_\nu - \partial_\nu A_\mu \tag{1.15}$$

being the electromagnetic force antisymmetric tensor. The Euler-Lagrange equations of this Lagrangian become the inhomogeneous Maxwell equations and the interacting Dirac equations (Eqs. 1.16 and 1.17), allowing to identify A_μ with the photon:

$$\partial_\mu F^{\mu\nu} = -e\overline{\psi}(x)\,\gamma^\nu\psi(x) \tag{1.16}$$

$$(i\gamma_\mu\partial^\mu - m)\psi(x) = -e\gamma_\mu A^\mu\psi(x) \tag{1.17}$$

This identification between the gauge boson and the mediators of the interacting particle is generalized to all gauge symmetries. Then, in analogy to QED, gauge bosons issued from QCD and GWS models are identified with the corresponding interaction mediators of the strong and electroweak interaction respectively.

1.1.4 Renormalization

When interacting with a charge at a given energy, an incoming particle is only sensitive to the *screened* charge because of the possible fluctuations of the charge through pair creation in the volume of interaction whose typical size is given by de Broglie wavelength. This suggests that interaction intensity is

energy dependent which reflects at the theoretical level by the Renormalisation Group Equations that provide the energy dependence of the coupling (the visible charge). The fact that the quantization of the QED theory introduces divergent terms in the calculations is a general feature of gauge theories. Observables such as the cross-section for a given process are estimated in the framework of quantum field theories and depend on the square of the probability amplitude of an interaction $\mathcal{M}^2$. In perturbation theory, this probability amplitude is estimated by adding up all possible configurations in which the interaction may take place. For example, in the case of an electron-muon scattering through the electromagnetic field, the lowest order contribution is the exchange of a photon between the electron and the muon. However, other configurations need to be taken into account, for instance, the virtual creation of a pair fermion-antifermion and their re-annihilation into a photon, which represents one of the next-to-leading order contributions to the scattering cross-section. The momentum of this fermion-

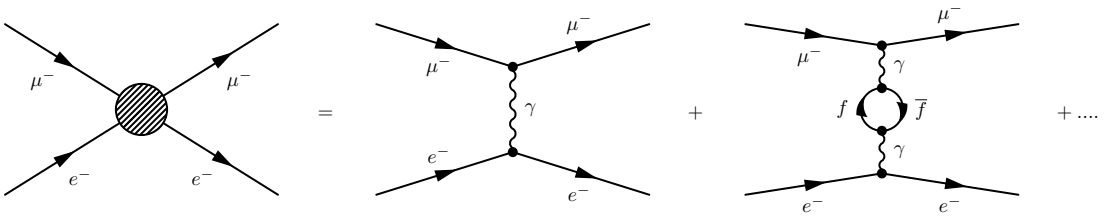


Figure 1.2: Feynman diagrams representing the leading order contributions to the interaction between an initial electron and a muon in the t-channel. The tree-level diagram corresponds to the exchange of a photon between the electron and the muon. In addition, the leading order loop correction to the electron-muon interaction is also shown.

antifermion loop is not constrained and integrals summarizing this correction are computed over all possible momenta configurations. This leads to divergences in the final observable calculation. However, divergences can be absorbed in a redefinition of the couplings of the theory, in a process called *renormalization* [20] which introduces a dependence of the coupling with a dummy mass scale μ. Renormalized theories must finally produce physics predictions that are independent of the renormalization scale μ. This dependence is encoded in the β function:

$$\mu \frac{dg(\mu)}{d\mu} = \beta(g(\mu)) \tag{1.18}$$

where μ here is the energy at which the coupling is studied. It is particularly interesting to acknowledge the behaviour of this function at high energies and low energies, where critical effects may appear.

The ensemble of equations predicting the coupling strength at different energies form what is called the renormalization group equations of the theory and in the following, couplings dependent on energy will be named running couplings. As an example, the fine structure ($\alpha_s = e^2/4\hbar c\pi\epsilon_0$ or $\alpha_s = e^2/4\pi\epsilon_0$ in units where $\hbar = c = 1$) constant equals $1/137$ when $\mu \to 0$ and $1/128$ when μ equals the mass of the Z boson. Renormalization is not only restricted to the couplings between different particles in the Lagrangian but also to kinetic terms and to the masses of the particles.

1.1.5 The Higgs mechanism

As presented in Section 1.1.2, mass terms for the gauge boson coupling are forbidden by gauge invariance while the short range of the weak interaction (Tab. 1.1) imposes that its mediators are massive. Thus, an alternative technique is needed for allowing the existence of massive vector boson together with a gauge invariant Lagrangian. The solution is the so-called Brout-Englert-Higgs (BEH) mechanism [21, 22, 23], which introduces a doublet of complex fields (Eq 1.19), called Higgs fields, and a potential term (Eq. 1.21) to the Lagrangian. Assuming $\mu > 0$ and $\lambda > 0$, this potential is represented in Fig. 1.3. It can be observed an unstable equilibrium at $\phi(x) = 0$ with degenerated ground energy states.

$$\phi(x) = \begin{pmatrix} \phi^+ \\ \phi^0 \end{pmatrix}; \quad \phi^+ = \phi_1 + i\phi_2; \quad \phi^0 = \phi_3 + i\phi_4; \tag{1.19}$$

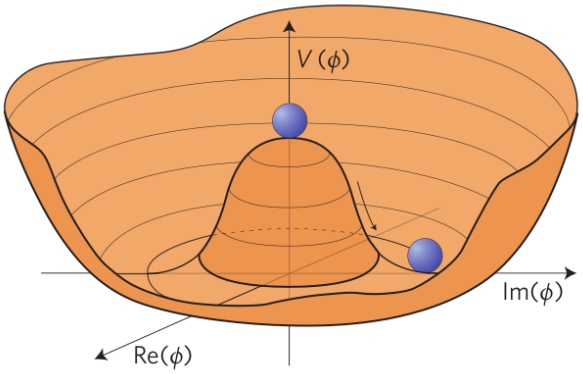


Figure 1.3: Higgs potential form represented in a 3D plot as a function of the imaginary and real part of the Higgs field. Ground state degeneracy is observed.

$$\mathcal{L}_{\mathrm{BEH}} = D_\mu \phi^\dagger (x)\, D^\mu \phi (x) + \mu^2 \phi^\dagger (x)\, \phi (x) - \lambda (\phi^\dagger (x)\, \phi (x))^2 \tag{1.20}$$

$$V(\phi) = -\mu^2 \phi^\dagger (x)\, \phi (x) + \lambda (\phi^\dagger (x)\, \phi (x))^2 \tag{1.21}$$

Under the action of this potential, a spontaneous symmetry breaking of the gauge invariance occurs when the Higgs field spontaneously collapses towards one of its ground states, which can be written as:

$$\phi_0 = \frac{1}{\sqrt{2}} \begin{pmatrix} 0 \\ v + h(x) \end{pmatrix} \tag{1.22}$$

where $v =< 0|\phi|0 >= \sqrt{\frac{\mu^2}{\lambda}}$ is the vacuum expectation value of the ground state and $h(x)$ are non-zero energy excitations of the Higgs field around the ground state, corresponding to a new particle called the Higgs boson. The ground state is no longer gauge invariant despite that the Lagrangian is. Developing the previous Lagrangian around the Higgs field ground state, the BEH mechanism generates masses for the gauge boson A^μ (Eq 1.24).

$$\begin{aligned} \mathcal{L}^{\mathrm{SSB}}_{\mathrm{BEH}} &= \frac{1}{2}\partial_\mu (h(x)^\dagger) \partial^\mu (h(x)) \\ + \frac{1}{\sqrt{2}} ie A_\mu [(v + h(x)^\dagger) \partial^\mu h(x) &- (v + h(x)) \partial^\mu h(x)^\dagger] \\ -e^2 \frac{v^2}{2} A_\mu A^\mu &+ V([v + h(x)]) \end{aligned} \tag{1.23}$$

$$\mathcal{L}_{\mathrm{mass}} = -e^2 \frac{v^2}{2} A_\mu A^\mu \tag{1.24}$$

1.1.6 Electroweak unification of Glashow, Salam and Weinberg

In the 1960's, Glashow, Salam and Weinberg developed a theory [24, 25, 26] unifying the weak and electromagnetic interactions in a single interaction gauge theory, called electroweak (EW) or Glashow-Salam-Weinberg (GWS) theory. Two charges are conserved by the electroweak interaction, the isospin and the hypercharge. The associated gauge group is $SU(2)_L \times U(1)_Y$.

The $SU(2)_L$ part of the gauge group corresponds to rotations of the isospin (I) number. The observed CP violation presented in Section 1.1.1 implies that the weak interaction only acts on the left-handed chiral components of the fermions, described in the Weyl representation as:

$$\psi (x) = \begin{pmatrix} \psi_{\mathrm{L}} \\ \psi_{\mathrm{R}} \end{pmatrix}; \quad \psi_L = \frac{1 - \gamma_5}{2} \psi; \quad \psi_R = \frac{1 + \gamma_5}{2} \psi; \tag{1.25}$$

Family	1^{nd}	2^{nd}	3^{rd}	Electric charge (Q)	Isospin (I_3)	Hypercharge (Y)
Quarks	$(u,d)_L$	$(c,s)_L$	$(t,b)_L$	(2/3, -1/3)	(1/2, -1/2)	(1/3, 1/3)
	u_R, d_R	c_R, s_R	t_R, b_R	2/3, -1/3	0, 0	4/3, -2/3
Leptons	$(v_e, e^-)_L$	$(v_\mu, \mu^-)_L$	$(v_\tau, \tau^-)_L$	(0, -1)	(1/2, -1/2)	(-1, -1)
	e_R^-	μ_R^-	τ_R^-	-1	0	-2

Table 1.2: Quark and lepton families as seen by the electroweak interaction. Fermions grouped in parentheses are elements of a doublet under the isospin symmetry. Main quantum numbers corresponding to the electroweak symmetries are shown for each weak interaction doublet ($I_3 = \pm\frac{1}{2}$) and singlets ($I_3 = 0$). Indexes L and R show the chirality of the considered particles.

$$\gamma^0 = \begin{pmatrix} 0 & 1 \\ -1 & 0 \end{pmatrix} \quad ; \quad \gamma^i = \begin{pmatrix} 0 & \sigma^i \\ -\sigma^i & 0 \end{pmatrix} \quad ; \quad \gamma^5 = i\gamma^0\gamma^1\gamma^2\gamma^3 = \begin{pmatrix} -1 & 0 \\ 0 & 1 \end{pmatrix} \tag{1.26}$$

where ψ is a spinor with two Lorentz invariant components ψ_{L} and ψ_{R}, γ^i are the Dirac γ- matrices and the symbols L and R stand for left-handed and right-handed fermion chiral components. The Standard Model presents left-handed and right-handed partners for all fermions except neutrinos. However, more recent experiments showed that right-handed neutrinos must exist, as will be explained in Section 1.1.8.

In two dimensions, $SU(2)_L$ is generated by three independent generators, the Pauli matrices σ_i, each introducing a new gauge boson: W_1, W_2 and W_3. The weak isospin has three components: I_1, I_2 and I_3. In analogy to the spin, its third component is used to describe the properties of the fermions under the weak interaction, being assembled in doublets ($I_3 = \pm 1/2$) if they are charged or in singlets ($I_3 = 0$) if they are not. The corresponding symmetry transformation for the left-handed and right-handed components is:

$$\psi_L \rightarrow \psi'_L = e^{i\frac{1}{2}g_I\vec{\omega}(x)\cdot\vec{\sigma}}\psi_L \tag{1.27}$$

$$\psi_R \rightarrow \psi'_R = \psi_R \tag{1.28}$$

with ψ_L and ψ_R representing:

$$\psi_L = \begin{pmatrix} u \\ d \end{pmatrix}_L, \begin{pmatrix} c \\ s \end{pmatrix}_L, \begin{pmatrix} t \\ b \end{pmatrix}_L, \begin{pmatrix} \nu_e \\ e \end{pmatrix}_L, \begin{pmatrix} \nu_\mu \\ \mu \end{pmatrix}_L, \begin{pmatrix} \nu_\tau \\ \tau \end{pmatrix}_L \tag{1.29}$$

$$\psi_R = \left(u_R, d_R, c_R, s_R, t_R, b_R, e_R, \mu_R, \tau_R\right) \tag{1.30}$$

where g_I represents the coupling strength of the weak interaction. On the other hand, the hypercharge conservation corresponds to the $U(1)_Y$ part of the symmetry group and introduces the B gauge boson with the new quantum number Y (hypercharge) and a coupling strength g_Y. All fermions are charged under the hypercharge group, being the corresponding gauge transformation:

$$\psi_{L,R} \rightarrow \psi'_{L,R} = e^{-iYg_Y\omega(x)}\psi_{L,R} \tag{1.31}$$

Table 1.2 summarizes the main quantum numbers for quarks and leptons as well as their chirality, as seen by the electro-weak interaction.

The total Lagrangian of the theory is:

$$\mathcal{L}_{\mathrm{GWS}} = \mathcal{L}_{\mathrm{Int}} + \mathcal{L}_{\mathrm{gauge}} + \mathcal{L}_{\mathrm{Higgs}} + \mathcal{L}_{\mathrm{Yukawa}} \tag{1.32}$$

where $\mathcal{L}_{\text{Int}}$ (Eq. 1.33) corresponds to the interaction and kinetic term of the fermions with the gauge bosons and $\mathcal{L}_{\text{gauge}}$ (Eq. 1.34) corresponds to the kinetic term of the gauge bosons.

$$\mathcal{L}_{\text{Int}} = \overline{\psi_L} i\gamma^\mu D_\mu \psi_L + \overline{\psi_R} i\gamma^\mu D_\mu \psi_R \tag{1.33}$$

$$\mathcal{L}_{\text{gauge}} = -\frac{1}{4} F_A^{\mu\nu} F_{\mu\nu}^A - \frac{1}{4} B^{\mu\nu} B_{\mu\nu}. \tag{1.34}$$

The corresponding covariant derivatives are:

$$D_\mu \psi_L = (\partial_\mu - i g_I \frac{\vec{\sigma}}{2} \vec{W}_\mu - i \frac{g_Y}{2} B_\mu) \psi_L \tag{1.35}$$

$$D_\mu \psi_R = (\partial_\mu - i \frac{g_Y}{2} B_\mu) \psi_R \tag{1.36}$$

and:

$$F_{\mu\nu}^A = -\frac{1}{i g_I} [D_\mu^A, D_\nu^A] = \partial_\mu W_\nu^A - \partial_\nu W_\mu^A - g_I C_{ABC} W_\mu^B W_\nu^C \tag{1.37}$$

$$B_{\mu\nu} = \partial_\mu B_\nu - \partial_\nu B_\mu \tag{1.38}$$

are the field strength tensors of the electroweak interaction where $A = 1, 2, 3$ and C_{ABC} correspond to structure constants of the gauge group defined by:

$$[t^A, t^B] = i C_{ABC} t^C \tag{1.39}$$

where t^i are the generators of the symmetry group. In the case of a $SU(2)$ group, $C_{ABC} = \epsilon_{ABC}$.

$\mathcal{L}_{\text{Higgs}}$ stands for a Higgs Lagrangian term like in Eq. 1.20. The Higgs field ground state breaks the $SU(2)_L \times U(1)_Y$ symmetry through the BEH mechanism and allows massive terms for the gauge bosons.

Finally, the Higgs field is also used to generate mass terms for fermions. A Yukawa term $\mathcal{L}_{\text{Yukawa}}$ is added, which introduces interactions between the fermions and the Higgs field. The addition of this last term is *ad hoc* but allows to introduce mass terms for fermions since mass terms for fermions of the form $-m\Psi_L\Psi_R$ are forbidden by $SU(2)_L$ gauge symmetry (Ψ_L changes while Ψ_R is unaffected by an $SU(2)_L$ transformation).

$$\mathcal{L}_{\text{Yukawa}} = -g_\psi \overline{\psi}_R \phi(x) \psi_L + h.c \tag{1.40}$$

After spontaneous symmetry breaking, the symmetry group of the Lagrangian reduces from the $SU(2)_L \times U(1)_Y$ group to the $U(1)_Q$ QED gauge group, since the remaining symmetry is the conservation of the electromagnetic charge. For a given particle, the relation between its electric charge Q and its isospin (I_3) and hypercharge Y is:

$$Q = I_3 + \frac{Y}{2} \tag{1.41}$$

In the $\mathcal{L}_{\text{Higgs}}$ sector, interaction terms of the Higgs field with the gauge boson leads to non-diagonal mass matrix for the W^3 and B bosons:

$$\mathcal{L}_{\text{Higgs}} \supset (D^\mu \phi^\dagger)(\partial^\mu \phi) = \frac{1}{2}(D^\mu h(x)^\dagger)(\partial^\mu h(x)) - \frac{v^2}{8} \begin{pmatrix} W_\mu^1 \\ W_\mu^2 \\ W_\mu^3 \\ B_\mu \end{pmatrix} \begin{pmatrix} g_I^2 & 0 & 0 & 0 \\ 0 & g_I^2 & 0 & 0 \\ 0 & 0 & g_I^2 & -g_I g_Y \\ 0 & 0 & -g_I g_Y & g_Y^2 \end{pmatrix} \begin{pmatrix} W^{1,\mu} \\ W^{2,\mu} \\ W^{3,\mu} \\ B^\mu \end{pmatrix} + \mathcal{L}_{\text{h-couplings}} \tag{1.42}$$

This matrix can be diagonalized separately for W_μ^3 and B_μ sector using the Weinberg angle θ_W (Eq 1.43), so that the mass matrix neutral eigenstates are the Z and A bosons (Eq 1.44), the latter being identified with the photon since its corresponding eigenvalue from the mass matrix is expected to be zero (Eq 1.45).

$$\tan\theta_W = \frac{g_Y}{g_I} \tag{1.43}$$

$$\begin{aligned} Z_\mu &= \cos\theta_W W_\mu^3 - \sin\theta_W B_\mu \\ A_\mu &= \sin\theta_W W_\mu^3 + \cos\theta_W B_\mu \end{aligned} \tag{1.44}$$

so that the bare masses (eigenvalues of the mass matrix) are:

$$m_Z = \frac{v}{2}\sqrt{g_I^2 + g_Y^2}, \qquad m_\gamma = 0 \tag{1.45}$$

In addition, the W^1 and W^2 can be reorganized as shown in Eq. 1.46, giving rise to the W^+ and W^- bosons:

$$W_\mu^\pm = \sqrt{\frac{1}{2}}\left(W_\mu^1 \mp iW_\mu^2\right) \tag{1.46}$$

with a corresponding mass of:

$$m_W = \frac{v}{2}g_I \tag{1.47}$$

The term $\mathcal{L}_{\mathrm{h-couplings}}$ in Eq. 1.42 includes the interaction terms between the Higgs boson h and the weak gauge bosons. After mass matrix diagonalization, it can be written as:

$$\mathcal{L}_{\mathrm{h-couplings}} = -\underbrace{2\frac{m_W^2}{v}}_{g_{hWW}} h(x)W_\mu^+W^{-,\mu} - \underbrace{\frac{m_Z^2}{v}}_{g_{hZZ}} h(x)Z_\mu Z^\mu - \underbrace{\frac{m_W^2}{v^2}}_{g_{hhWW}} (h(x))^2 - \underbrace{\frac{m_Z^2}{2v^2}}_{g_{hhZZ}} (h(x))^2 Z_\mu Z^\mu \tag{1.48}$$

so that the couplings of the Higgs boson to the gauge bosons $W^\pm$ and Z are [27]:

$$g_{hWW} = 2\frac{m_W^2}{v}; \qquad g_{hZZ} = \frac{m_Z^2}{v}; \qquad g_{hhWW} = \frac{m_W^2}{v^2}; \qquad g_{hhZZ} = \frac{m_Z^2}{2v^2} \tag{1.49}$$

Finally, the symmetry breaking in the Yukawa sector introduces mass terms for the fermions and interactions with the Higgs field:

$$\mathcal{L}_{\mathrm{Yukawa}} = -\frac{g_\psi v}{\sqrt{2}}[\overline{\psi_R}\psi_L] - \frac{g_\psi}{\sqrt{2}}[\overline{\psi_R}h(x)\psi_L] + h.c \tag{1.50}$$

Note that the GWS theory predicts that the fermion masses depend on their coupling to the Higgs field:

$$g_{hf\overline{f}} = \frac{g_\psi}{\sqrt{2}} = \frac{m_f}{v} \tag{1.51}$$

The stronger is the coupling, the larger is the mass of the corresponding fermion. This prediction, which is not suggested by any experiment, has important implications in the phenomenology of the Higgs boson and its production at colliders, which is studied in Section 1.2 for the LHC.

Another remarkable consequence of the GWS theory is that interaction and mass eigenstates are not the same. If one redefines the given states in the theory so that mass matrices are diagonal, a unitary matrix emerges inside the interaction term. In the case of the quark sector, this matrix is the Cabibbo-Kobayashi-Maskawa (CKM) matrix:

$$V_{\mathrm{CKM}} = \begin{pmatrix} V_{ud} & V_{us} & V_{ub} \\ V_{cd} & V_{cs} & V_{cb} \\ V_{td} & V_{ts} & V_{tb} \end{pmatrix} \tag{1.52}$$

This fact has profound consequences in the EW phenomenology, being remarkable the possibility of transitions between different quark families when charged bosons $W^\pm$ are involved, leading to flavour changing currents. On the other hand, observed CP violation in the weak sector is parametrized by adding a complex phase in the V_{td} and V_{ub} components (according to Wolfenstein parametrization [28]).

1.1.7 Quantum chromodynamics (QCD)

Quantum chromodynamics is the gauge theory explaining the processes mediated by the strong interaction between colored particles. It was formulated after the introduction of the color number [13] and is represented by a non-Abelian $SU(3)_c$ gauge group. Gauge transformations of this group involve at

most 8 independent generators called gluons, each one associated with a different gauge boson in the theory. The QCD Lagrangian is:

$$\mathcal{L}_{\mathrm{QCD}} = \overline{\psi}\left(x\right)^{c} i\gamma^{\mu} D_{\mu}\psi\left(x\right)_{c} - \frac{1}{4} G_{\mathrm{A}}^{\mu\nu} G_{\mu\nu}^{\mathrm{A}} \quad ; \quad D_{\mu}\psi\left(x\right)_{c} = (\partial_{\mu} - ig_{s}\frac{\vec{\tau}}{2}\vec{A}_{\mu})\psi\left(x\right)_{c} \tag{1.53}$$

where g_s is the strong coupling and

$$G_{\mu\nu}^{A} = -\frac{1}{ig_{s}}[D_{\mu}^{A}, D_{\nu}^{A}] = \partial_{\mu}A_{\nu}^{A} - \partial_{\nu}A_{\mu}^{A} - g_{s}C_{ABC}A_{\mu}^{B}A_{\nu}^{C} \tag{1.54}$$

$\psi\left(x\right)_{c}$ describes all quark fields with their color indices, τ_A are the generators of the $SU(3)_c$ group, represented by the Gell-Mann matrices [29], and A_{μ}^{A} are the eight gluons in the theory. In contrast with electroweak interaction, there are three color charges denoted as red, green and blue. Quarks carry a single charge of color while gluons have two color numbers, which has phenomenological consequences in jet physics. The combination of these three colors give rise to neutral particles under the gauge group as well as the combination of one colored particle with its antiparticle.

The renormalization of the g_s coupling leads to the effects of asymptotic freedom and confinement. The former implies that at low interaction energies, g_s increases, while at higher energies the coupling tends to zero. The increasing magnitude of g_s at low energy has important experimental implications. Two colored particles moving away one from each other cause the increase of the potential energy stored in the color field between them until it is large enough to be relaxed in a new pair of quark-antiquark. Pair creation process is repeated until the final state is composed of a bunch of color singlet particles, the hadrons, resulting from the binding of the initial partons and the created pairs (Fig. 1.4). This leads to the confinement of partons inside the hadron, which implies that no isolated colored charge particles (quarks or gluons) but only colored singlet particles can be observed [8].

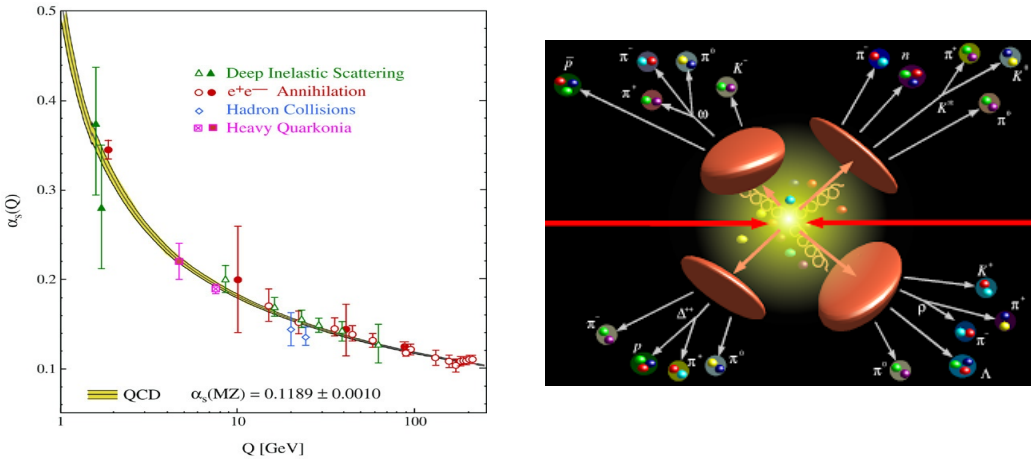


Figure 1.4: Running coupling α_s as a function of the interaction energy ($\alpha_s = g_s^2/4\pi$) and representation of the confinement effect after the emission of quarks or gluons issued from an interaction. It can be observed how quarks and gluons scatter out of the collision point. As partons move away, g_s running coupling increases and at one point, quark-antiquark pairs are created from the vacuum and combine with the outcoming partons to form hadrons.

The confinement implies that partons inside the hadron interact at very low energy. The large running coupling g_s in these interactions is then reduced by the continuous quark pair creation and soft-radiation of gluons inside the hadrons. These processes explain the structure of the proton presented in Section 1.1.1. These effects could be problematic if there was no possible separation between the QCD perturbative and non-perturbative effects. For example, the interaction of a photon against a quark in a proton would, in that case, become completely unpredictable due to the possible dependence of the cross-section of the photon-quark process with the quark distribution inside the hadron.

However, non-perturbative effects may be efficiently separated in the calculations from perturbative ones, as stated by the factorization theorem [29]. The observables, such as the cross-section of a particle-

hadron interaction, can be factorized into a perturbative (colliding particle-hadron interaction cross-section) and a non-pertubative (PDFs) part at a given scale, represented by μ_F. In the particular case of an hadron-hadron collision, the predicted cross-section can be written:

$$\sigma^{tot} = \sum_{AB} \int dx_1 dx_2 p_A(x_1, \mu_F) p_B(x_2, \mu_F) \sigma_{AB}(x_1 x_2 s, \frac{\mu_F}{s}, \mu_R) \tag{1.55}$$

where A and B denote sum over all partons inside the hadrons A and B, x_1 and x_2 represent the colliding partons energy fraction over their corresponding hadron total energy, μ_R is the renormalization scale and s is the center-of-mass energy of the collision. μ_F represents the energy scale at which perturbative QCD can no longer be applied while non-perturbative effects become important. Perturbative calculations only contain hard emissions above μ_F. There is some arbitrariness in the choice of μ_F and it will become one of the most important theoretical uncertainties in the analysis when doing signal an background cross-sections calculation (Section 7.5).

1.1.8 The Standard Model

The Standard Model combines the QCD, GWS and QED theories into a single global gauge theory based on the $SU(3)_c \times SU(2)_L \times U(1)_Y$ group. So far, six quarks and six leptons are currently known and can be grouped into three generations. The description of the fermions include the determination of their isospin, electric charge and hypercharge. As any other gauge theory, the Standard Model includes anti-particles, which are the charge-conjugate of each fermion. In the bosonic sector, the SM particle spectrum includes the three weak bosons $W^{\pm}$ and Z, the eight QCD gluons and the photon, together with the Higgs boson. A summary of this spectrum is presented in Figure 1.5.

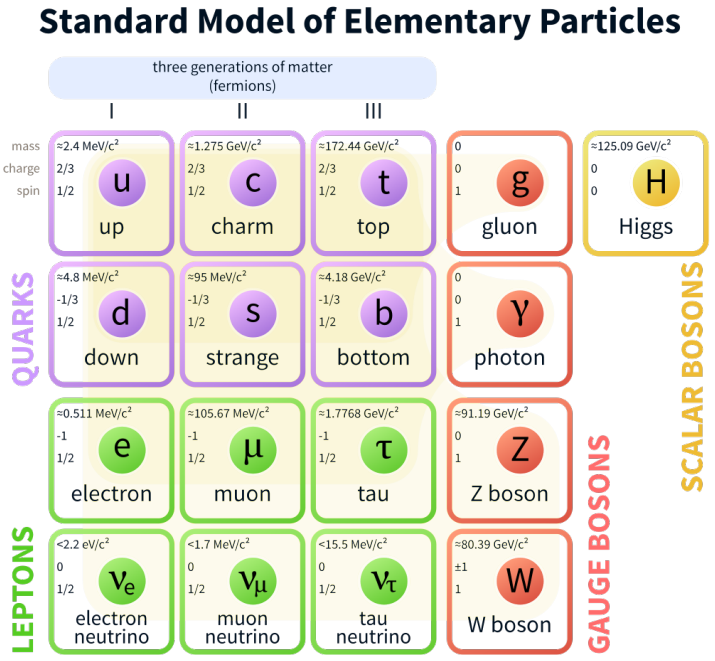


Figure 1.5: General picture of elementary particles and force carriers included in the Standard Model [30].

Originally, the formulation of the Standard Model did not include the right-handed chiral component of the neutrinos. This induced no mixing flavour matrix in the lepton sector since mass eigenstates could be rotated into the weak interaction eigenstates, as stated in Section 1.1.6. However, more recent

experiments (Super-Kamiokande [31, 32, 33], SNO [34]) on atmospheric and solar neutrinos observed flavour changing currents in the neutrino sector. As neutrino oscillations depend on the mass difference between different neutrino species, a mass term must then exists for the neutrinos. This involves a mixing matrix for the leptons, similar than the CKM matrix for quarks.

$$U_{\mathrm{PMNS}} = \begin{pmatrix} U_{e1} & U_{e2} & U_{e3} \\ U_{\mu 1} & U_{\mu 2} & U_{\mu 3} \\ U_{\tau 1} & U_{\tau 2} & U_{\tau 3} \end{pmatrix} \tag{1.56}$$

This matrix is called Pontecorvo-Maki-Nakagawa-Sakata matrix (PMNS) and can be parametrized using 3 angles θ and 1 complex phase for CP violation, like the CKM matrix.

Experimental successes

One of the most important test of the SM is its prediction of the $\rho_0 = M_W^2/M_Z^2 cos^2(\theta_W) \sim 1$ parameter, equal at leading order to 1, while experimental value is $\rho_0 = 1.00037 \pm 0.00023$ [35]. One should also notice that the SM was solid enough to incorporate unexpected effects in a natural way such as the third generation discovery in the 1970's with the τ-lepton and b-quark discovery [36, 37] or more recently with the discovery of neutrino oscillations. Its internal consistency and the GIM mechanism allowed to predict the existence of the top quark and the τ-neutrino. Six of the main predictions of the Standard Model are then the $W^{\pm}$, Z and Higgs bosons and the charm and top quarks and the τ-neutrino.

The most important implication of the possible existence of the Z boson was that it would be possible to observe the scattering of particles through weak interaction without any charge exchange (neutral current interaction). This prediction was tested and confirmed by the Gargamelle experiment at CERN in 1973 [38]. In this experiment, a neutrino beam collides against a bubble chamber filled with CF_3Br. The observation of hadrons recoiling against no visible source and no muon nor electron in the final state implies that an interaction of type $\nu_\ell/\bar{\nu}_\ell + N \rightarrow \nu_\ell/\bar{\nu}_\ell + \mathrm{hadrons}$ occurred (neutral current). In addition, interactions of type $\nu_\ell/\bar{\nu}_\ell + N \rightarrow \ell^{\pm} + \mathrm{hadrons}$ presenting a muon or electron in the final state plus hadrons were also observed (charged currents). The ratio of the observed number of events allowed to determine that neutral currents were due to an electrically neutral mediating particle (instead of a charged current process at higher orders) but charged under the weak interaction, opening the road for a discovery of the Z particle. After the indirect discovery of the neutral current interactions, $W^{\pm}$ and Z were discovered at CERN in 1983 by the UA1 and UA2 [39, 40] experiments using the Super Proton Synchrotron (SPS).This discovery was done under the scientific impulse of C. Rubbia and thanks to a technical breakthrough from S. Van der Meer, who invented the stochastic cooling of anti-proton beams that allowed to collide protons and anti-protons in the SPS and to reach the luminosity needed for the discovery.

On the fermion side, the charm quark was revealed by the observation of the J/ψ meson, discovered at SLAC [41] and BNL [42], and the b-quark, by the observation of the Υ meson, observed at Fermilab in 1977 [37]. Later, the top quark was discovered at Tevatron [43, 44] in 1995 and the τ-neutrino was observed by the DONUT collaboration in 2000 [45]. The last prediction of the Standard Model is the Higgs boson, which was discovered in 2012 by the ATLAS and CMS experiments [46, 47] at a mass of about 125 GeV. This mass measurement allows to determine all the parameters of the SM Lagrangian, especially the λ parameter of the Higgs potential, and to compute any prediction of the Standard Model. Interestingly, the measured Higgs boson mass is compatible with internal consistency test of the Standard Model based on its predictions of different electroweak observables which are dependent on the top quark and W boson masses [48] as shown on Fig. 1.6(left) and with direct constraints from Higgs search from the Tevatron Run II (Fig. 1.6-right). As the Higgs boson is a key piece of the search presented in this thesis, a precise description of its known properties is presented in Section 1.2. In addition, the SM model presents some limitations which are discussed in Section 1.3.

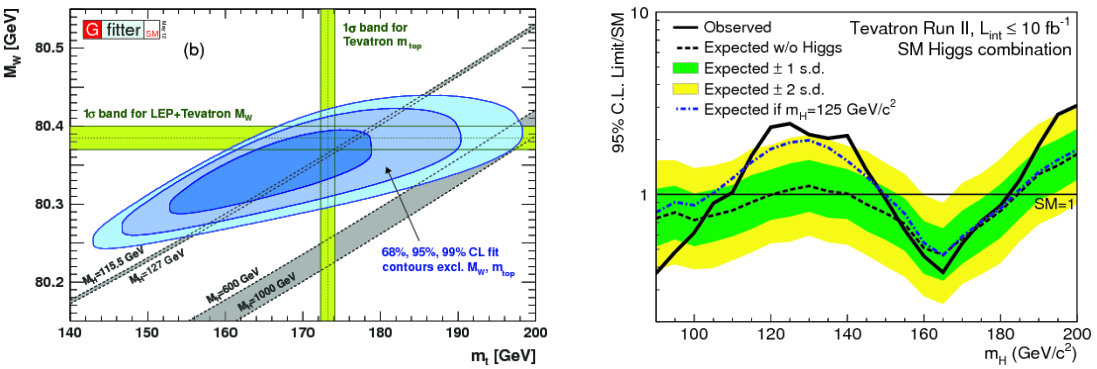


Figure 1.6: Prediction of the mass of the Higgs boson by comparing the measured masses of the top and the W boson and measured 95 % CL limits on the Higgs production cross-section at Tevatron with 10 fb^{-1} integrated luminosity [48, 49].

1.2 Higgs phenomenology at the LHC

After the discovery of a neutral heavy boson in 2012, the ATLAS and CMS experiments could start to check to which extent this boson was likely to be the Higgs boson. In order to determine the properties of this new resonance, several studies were performed focusing on its mass, spin, couplings and production modes. Spin studies confirmed that the new resonance corresponds to a spin-0 particle [50, 51, 52] with even parity as expected by the Standard Model Higgs boson. Combined measurements from both experiments on $h \to \gamma\gamma$ and $h \to 4\ell$ decays showed that the best-fit mass of the new scalar particle (Fig. 1.7) is $m_h = 125.09 \pm 0.24$ GeV [53].

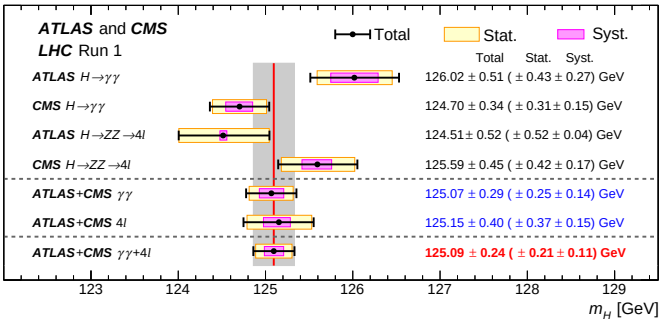


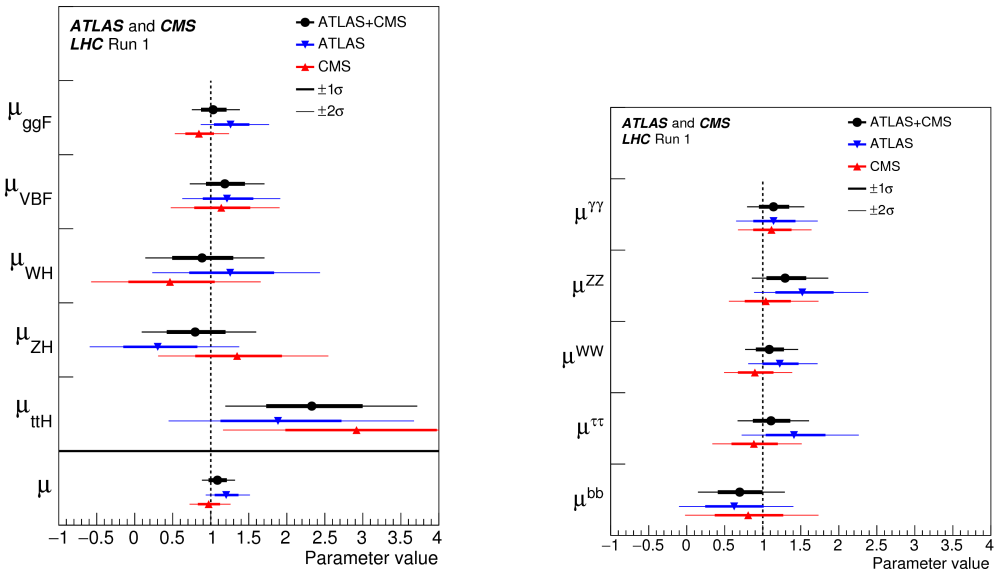
Figure 1.7: Individual and combined values of the SM Higgs-like resonance using 2011-2012 ATLAS+CMS data at $\sqrt{s} = 7$ and 8 TeV [54]. $h \to \gamma\gamma$ and $h \to 4\ell$ are used because they offer the best mass resolution. Mass measurements are performed allowing strength parameters for selected production and decay modes to vary in the fit. It is done in order to obtain a mass measurement as independent as possible of SM assumptions. The red vertical line and the gray shaded column indicate the central value and the total uncertainty of the combined measurement.

In addition, production cross-sections (σ_{prod}) and decay branching fractions (Γ_{decay}) [55] of the resonance are measured and compared with the Higgs SM predictions. For these comparison, strength parameters for each production mode and decay mode are defined, named respectively μ_{prod} and μ_{decay}:

$$\mu_{\text{prod}} = \frac{\sigma_{\text{prod}}^{\text{exp}}}{\sigma_{\text{prod}}^{\text{theo}}} \quad ; \quad \mu_{\text{decay}} = \frac{\frac{\Gamma_{\text{decay}}^{\text{exp}}}{\Gamma_{\text{tot}}^{\text{exp}}}}{\frac{\Gamma_{\text{decay}}^{\text{SM}}}{\Gamma_{\text{tot}}^{\text{SM}}}} \tag{1.57}$$

Measured strength parameters, presented in Figures 1.8, are compatible with 1 within their respective uncertainties, which indicates a good agreement between measurements and Standard Model predictions. All these measurements allow concluding that the discovered resonance is very likely to be the

predicted SM Higgs boson, thus every reference to this resonance is quoted in the following as the Higgs boson denoted as h. However, measurements are not yet precise enough to determine if the new particle respect the SM full Lagrangian or if some new physics beyond the Standard Model is about to show up.



(a) (b)

Figure 1.8: Combined measurements of the SM Higgs-like resonance production and decay couplings using 2011-2012 ATLAS+CMS data from LHC Run I at $\sqrt{s} = 7$ and 8 TeV [55]. All production modes are considered while only $b\bar{b}$, $\gamma\gamma$, $\tau^+\tau^-$, $W^\pm W^\mp$ and ZZ final state branching cross-section $\times$ branching ratios are extracted in units of the SM predictions.

1.2.1 Production and decay modes of the SM Higgs boson at LHC Run II

Searches for the Higgs boson could be performed by exploiting the features of certain production and decay modes. Certain production modes consider the emission of other particles in addition to the Higgs boson that can be used to tag the interaction, for instance, as it is done in invisible decay modes of the Higgs. In addition, the discovery of the Higgs boson was achieved by searching Higgs decays presenting a high significance as low SM background was expected, e.g. in final states with two photons or four leptons. In this section, the main production and decay modes of the Higgs boson as predicted by the Standard Model are presented.

The five processes with the largest production cross-sections are:

- Gluon-gluon fusion (ggF): $gg \to h$

  A quark loop mediates the Higgs boson creation (Fig. 1.9.a), so that the production becomes proportional to $g_{hf\bar{f}}$ (Eq. 1.51). As it has been discussed, these fermions with larger masses couple more strongly to the Higgs boson, so that the largest coupling of this type is the one between top quarks and the Higgs. Moreover, this coupling is the strongest coupling in the Standard Model of the Higgs boson thus ggF production mode is dominated by a top loop for all energies. Furthermore, gluon-gluon fusion dominates the production of the Higgs boson at the observed mass of 125.09 GeV.

- Vector-boson fusion (VBF): $qq \to qqh$

  In this case, the Higgs boson is produced by the fusion of two weak bosons (W^+W^- or ZZ) emitted by two colliding quarks (Fig. 1.9.b). The coupling allowing this interaction corresponds to the g_{hVV} coupling shown in Eq. 1.49.

- Associated production (Vh): $qq \to Vh$

  Two colliding quarks produce an intermediate excited state that can be either a weak boson (W or Z) or a Higgs boson and that later radiates either a Higgs boson or a weak boson, respectively(Fig. 1.9.c). The cross-section of this process is proportional to g_{hVV} and g_{hhV} couplings.

- $t\bar{t}$ fusion (tth): $gg \to t\bar{t}h$

  Two gluons create two top-antitop pairs so that the top from one couple and the antitop of the other collide to create a Higgs (Fig. 1.9.d).

- $b\bar{b}$ fusion (bbh): $gg \to b\bar{b}h$

  This process is similar to tth, but with gluons creating a pair bottom-antibottom (Fig. 1.9.e).

The lowest-order Feynman diagrams for those processes as well as their corresponding cross-sections at $\sqrt{s} = 13$ TeV and $\sqrt{s} = 14$ TeV are shown in Figure 1.10. Production of the Higgs boson is dominated

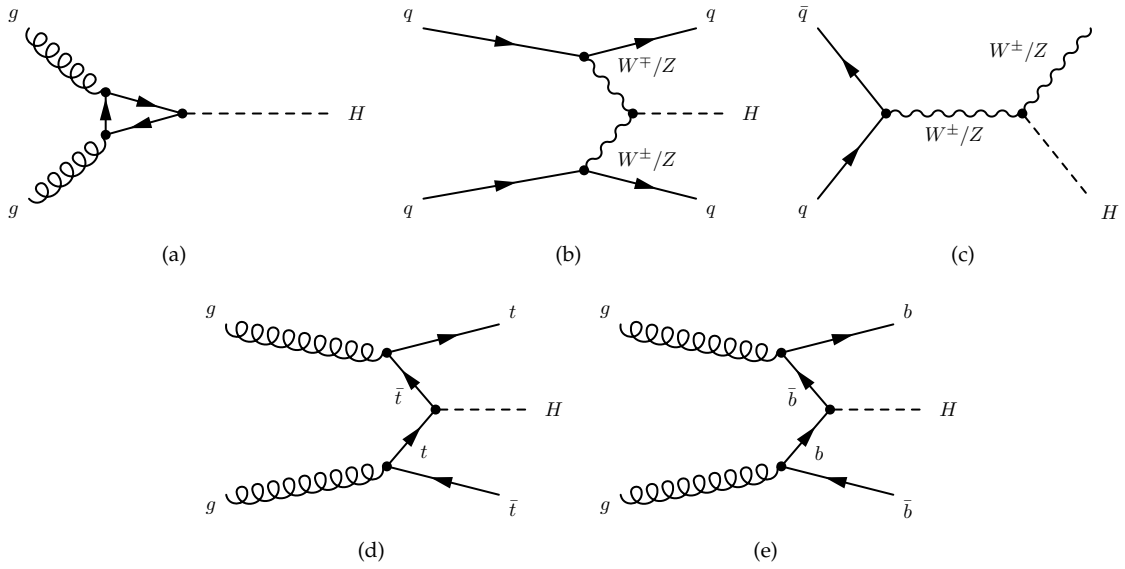


Figure 1.9: Example of the leading order Feynman diagrams for Higgs production at LHC: gluon fusion production (a), vector-boson fusion (b), associated production (c) and $t\bar{t}H$ (d) and $b\bar{b}H$ (e).

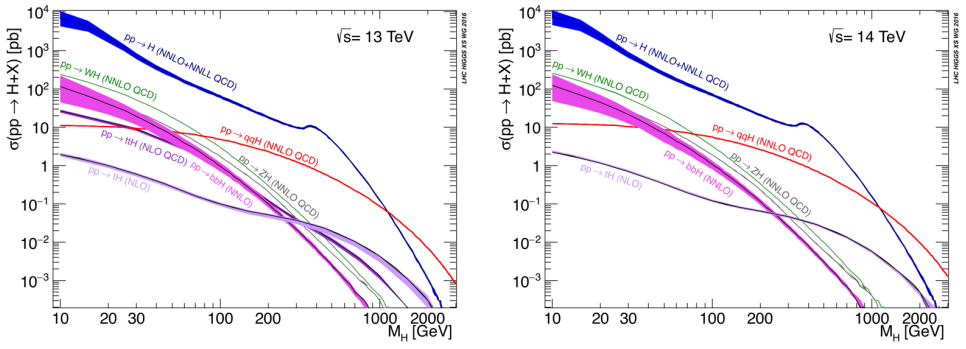


Figure 1.10: Higgs production cross-section for leading production modes. The left plot shows production the cross-section at $\sqrt{s} = 13$ TeV while the right plot at $\sqrt{s} = 14$ TeV. Bolded regions correspond to the Higgs cross-section uncertainties.

by the gluon-gluon fusion process, which represents around an 87 % of the total production of a SM Higgs boson with a mass of 125.09 GeV. The vector-boson fusion and the associated production are

Process	σ_i (pb)	$\frac{\sigma_i}{\sigma_{tot}}$ (%)
ggF	$48.52\ ^{+2.23}_{-3.25}$	87.2
VBF	$3.78\ \pm 0.08$	6.8
ZH	$0.88\ ^{+0.04}_{-0.03}$	1.6
WH	$1.37\ \pm 0.03$	2.5
ttH	$0.51\ ^{+0.03}_{-0.05}$	0.9
bbH	$0.49\ ^{+0.10}_{-0.12}$	0.9

Table 1.3: Production cross-sections of the Standard Model Higgs boson at the LHC for $\sqrt{s} = 13$ TeV [56].

subdominant processes but they represent two very interesting production modes of the Higgs boson. The reconstruction of their associated particles allows to tag the Higgs boson production process and to assign unambiguously the production mechanism.

A summary of all production mode cross-sections is presented in Table 1.3 for $\sqrt{s} = 13$ TeV and $m_h = 125.09$ GeV, taken from [56]. Gluon fusion cross-section is calculated in QCD up to next-to-next-to-next-to-leading order in α_s implementing next-to-next-to-leading logarithm resummation (N^{3}LO+NNLL). Other SM Higgs production cross-sections are calculated up to next-to-next-to-leading order (NNLO) in QCD and NLO in electroweak coupling constant.

On the other side, the Standard Model Higgs boson can decay into different modes, some of them mediated by the direct coupling of the Higgs with the final state particles or through virtual loops of particles. In the first category, one may find the Higgs decay into fermions such as quarks or leptons whose decay width at leading order can be written as:

$$\Gamma(h \to f\bar{f}) = g_{hff}^2 N_C \frac{m_h}{8\pi} \left(1 - 4\frac{m_f^2}{m_h^2}\right)^{3/2} \tag{1.58}$$

where N_C is the color factor ($N_C = 3$ for quarks and $N_C = 1$ for leptons). The dominant decay width for a Higgs mass of $m_h = 125.09$ GeV is the $h \to b\bar{b}$ channel, with a branching ratio of 58%. However, despite being the dominant decay mode, the large QCD background with two jets produced in the final state strongly reduces the Higgs observation power in this channel. It can also be observed that the large mass of the top quark suppresses the decay width of the Higgs to a top-antitop pair, thus just allowing off-shell contributions.

Decays of the Higgs into two gauge bosons are also allowed by the direct couplings g_{hVV}. The same constraint on the mass applies to $h \to W^+W^-, ZZ$, where one of the vector-bosons must be produced off-shell. However, the fact that the mass of a single W or Z boson is lower than the measured mass of the Higgs boson permits that this decay channel is not completely suppressed, yielding an expression for the width as:

$$\Gamma(h \to VV^*) = \delta_V \left(\frac{m_h}{v^2}\right)^2 \frac{m_h}{32\pi} \left(1 - 4\frac{m_V^2}{m_h}\right)^{1/2} \left(1 - 4\frac{m_V^2}{m_h^2} + 12\left(\frac{m_V^2}{m_h^2}\right)^2\right) \tag{1.59}$$

where $\delta_W = 2$ and $\delta_Z = 1$. Moreover, in contrast to $h \to b\bar{b}$, these two decays are important in LHC searches due to the low backgrounds expected for W and Z leptonic decays.

On the decay channels mediated by loops, the most important channel is the decay to $\gamma\gamma$. No direct coupling exists in the SM Lagrangian to allow a tree diagram contribution for this decay. The dominant loop contribution is the W^+W^- due to the large mass of the top quark and the small g_{hff} coupling to other fermions. The leading order width can be expressed as [57]:

$$\Gamma(h \to \gamma\gamma) = |F|^2 \left(\frac{\alpha}{4\pi}\right)^2 \frac{G_F m_h^3}{8\pi\sqrt{2}} \tag{1.60}$$

with F:

$$F = F_W(\beta_W) + \sum_f N_C Q_f^2 F_f(\beta_f) \tag{1.61}$$

$$F_W(\beta_W) = 2 + 3\beta_W + 3\beta_W(2-\beta_W)f(\beta_W); \quad F_f(\beta_f) = -2\beta_f[1+(1-\beta_f)]f(\beta_f); \tag{1.62}$$

$$\beta_W = \frac{4m_W^2}{m_h^2}; \quad \beta_f = \frac{4m_f^2}{m_h^2} \tag{1.63}$$

where:

$$f(\beta) = \begin{cases} \arcsin^2(\beta^{-1/2}) & ,\beta \geq 1 \\ -\frac{1}{4}\left[ln\frac{1+\sqrt{1-\beta}}{1-\sqrt{1-\beta}} - i\pi\right]^2 & ,\beta < 1 \end{cases} \tag{1.64}$$

Despite their low branching ratio, the excellent photon and lepton resolution and the limited expected background promote the $\gamma\gamma$ and the WW/ZZ decay channels as the leading probes of Higgs boson physics at the LHC. Table 1.4 gives the branching ratios of the dominant Higgs boson decays and the SM Higgs boson total width prediction. Figures 1.11 show the dominant Feynman diagrams for the Higgs decays and Figures 1.12 present the evolution of the Higgs boson decay branching ratios as a function of the Higgs boson mass in the Standard Model.

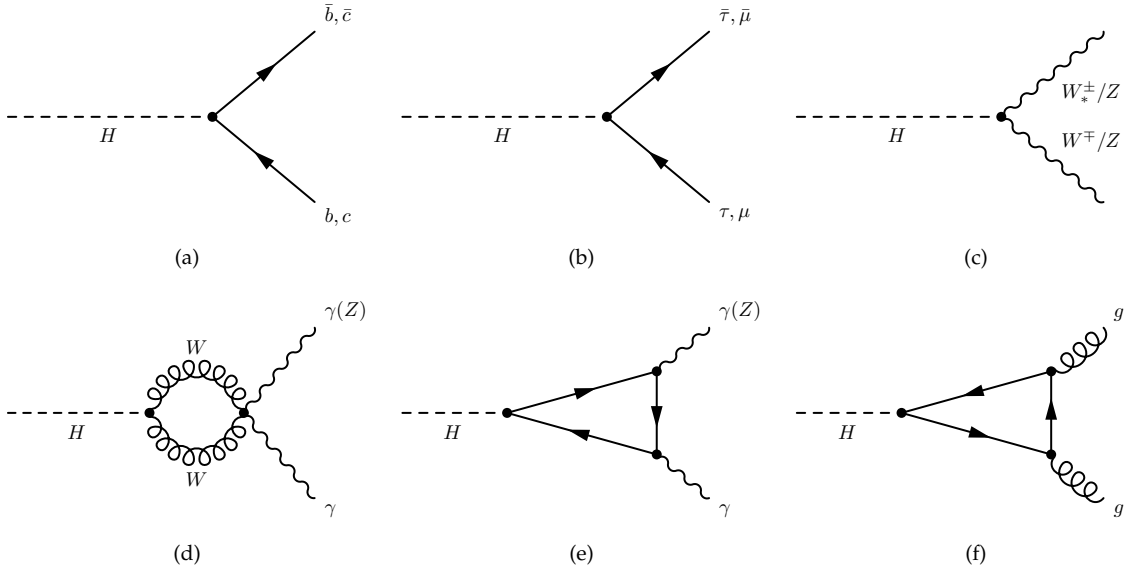


Figure 1.11: Leading-order Feynman diagrams for main Higgs boson decay modes at $m_h = 125.09\text{GeV}$: Higgs boson decay to $b\bar{b}$ and $c\bar{c}$ (a); $\tau^+\tau^-$ and $\mu^+\mu^-$ (b); decay into two vector bosons, one off-shell and other on-shell (c); decay to two photons $\gamma\gamma$ (d); to $Z\gamma$ and to two gluons (e).

1.3 Standard Model limitations

So far, the Standard Model has made proof of a large predictive power and a remarkable success in describing the current phenomena known in Nature. However, several limitations prevent the Standard Model to be a complete theory:

- **Parameters of the Standard Model**

  The fact that the Standard Model has 25 free parameters indicates that it is a very good descriptive model at low energies but it also indicates that SM could be an incomplete theory. SM could be indeed the effective low energy manifestation of a more fundamental theory, which hopefully could be formulated with a lower number of independent parameters.

Process	Branching ratio (%)	Relative Uncertainty (%)
bb	58.09	$\pm$ 1.24
$c\bar{c}$	2.88	$^{+5.55}_{-1.98}$
$\tau^+\tau^-$	6.26	$\pm$ 1.65
$\mu^+\mu^-$	0.02	$\pm$ 1.69
W^+W^-	21.52	$\pm$ 1.53
ZZ	2.64	$\pm$ 1.53
$\gamma\gamma$	0.23	$\pm$ 2.09
$Z\gamma$	0.15	$\pm$ 5.81
gg	8.18	$\pm$ 5.14
Total Width	(4.100 $\pm$ 0.056) MeV	

Table 1.4: Branching ratios of the Standard Model Higgs through all channels in Figures 1.11 at $m_h = 125.09$ GeV for $\sqrt{s} = 13$ TeV [56].

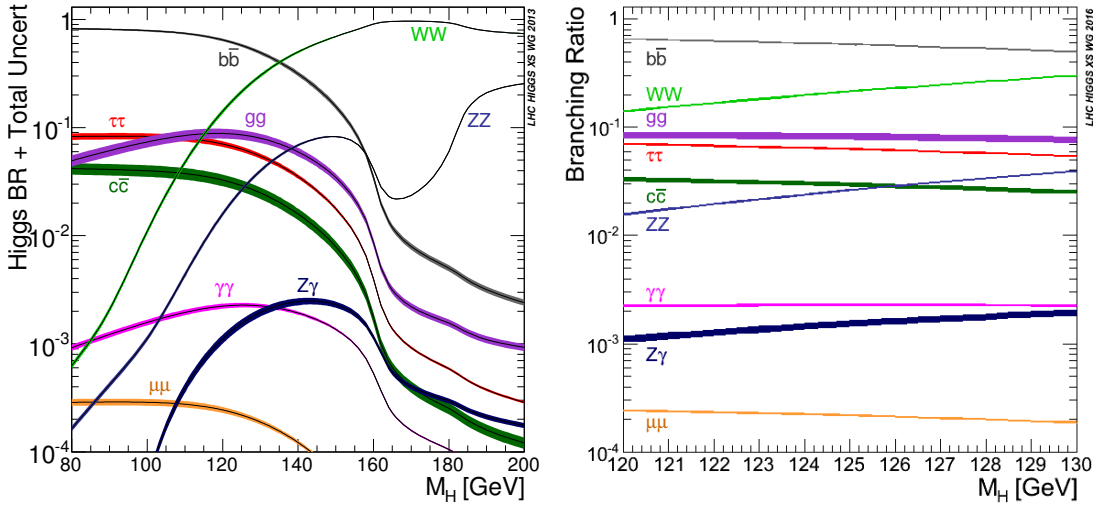


Figure 1.12: Branching ratios of the Standard Model Higgs boson decay modes as a function of the Higgs mass. Left plot shows the mass dependence of the branching ratio inside a region of $m_h \in [80, 200]$GeV and right plot shows this dependence around the combined ATLAS+CMS 2011-2012 Higgs-like resonance mass $m_h \approx 125.09$ GeV [56].

- **Hierarchy of particle masses**

  Experimental data show a clear hierarchy of the lepton and quark masses that are distributed in three families, whose properties with respect to interactions seem universal. Why are their masses so different? How to understand the effective Yukawa couplings in the theory whose magnitudes are unpredicted? The reason is expected to be found in a more fundamental theory.

- **Hierarchy (or naturalness) problem**

  The fermion loop correction to the Higgs mass shown in Fig. 1.13 presents a contribution increasing with the square of the energy (Eq. 1.65) inside the SM, which could be the unification scale $\Lambda_{\rm GUT} \approx 10^{16}$GeV or the Planck scale $\Lambda_{\rm Planck} \approx 10^{19}$GeV, where gravitation effects are expected to become important:

$$\delta m_h \propto \frac{g_f^2}{16\pi^2}(-2\Lambda^2 + 6m_f^2 \log\frac{\Lambda}{m_f} + ...) \tag{1.65}$$

  The measured mass of the Higgs is determined as the sum of the bare Higgs mass $m_h^0 = \sqrt{2\mu^2}$ (mass of the Higgs in the Lagrangian) plus a δm_h correction ($m_h = m_h^0 + \delta m_h$). In case that no new physics is found before these high energies, m_h^0 should present large values so that $m_h \sim 125$ GeV. This fine-tuning of the Higgs mass, which needs large corrections, leads to the hierarchy problem

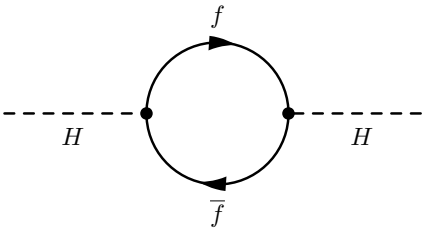


Figure 1.13: Fermion loop corrections to the Higgs self-interaction term. The dominant contribution corresponds to the top loop, due to the large $t-h$ coupling.

of the SM. Beyond Standard Model theories have been proposed to deal with this effect, such as supersymmetry. This theory predicts the existence of complementary particles to the ones forming the Standard Model, each boson has a partner fermion and vice-versa. These super-particles correct the Higgs mass by adding loop contributions equal to the SM particle ones but with opposite sign, which remove those divergences. Supersymmetry is being searched at LHC, although no sign of new physics has been observed yet.

- **Unification of couplings**

  The unification of electromagnetic and weak forces at low energies is a great success of the Standard Model. However, at high energies ($E >>$ TeV), the couplings of the weak, electromagnetic and strong interactions do not converge to the same value within the SM framework, as shown on Fig. 1.14 left. However, some supersymmetric theories such as the MSSM predict a unification of the couplings at energies of $\Lambda \approx 10^{16}$GeV. This encourages the searches for a theory unifying all interactions under a single given interaction (Grand Unification Theories) at $\Lambda_{\mathrm{GUT}} \approx 10^{16}$GeV.

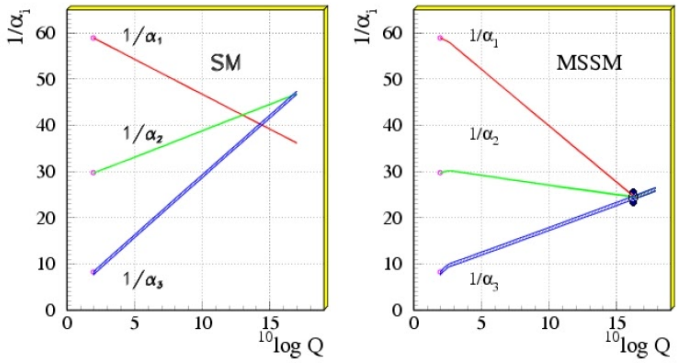


Figure 1.14: Standard Model and Minimal Supersymmetric Standard Model electromagnetic, weak and strong running couplings. Coupling unification in MSSM (plot taken from [58]).

- **Stability of the Higgs potential**

  Apart from inducing large corrections to the Higgs mass, radiative corrections due to top loops with $m_t \approx 173$ GeV drive the Higgs self-coupling λ to negative values at the Planck scale for small masses of the Higgs. This implies that $V(\phi)$ has no longer the shape in Fig. 1.3 and $\phi = v/\sqrt{2}$ becomes a metastable minimum of the theory. This problem can be observed in Figure 1.15 as a function of the Higgs and the top quark masses. Instability bound corresponds to undesired situation where no stable minima is found in the Higgs potential and $\phi = v/\sqrt{2}$ is an unstable equilibrium of $V(\phi)$. Stability corresponds to the current situation, where $\phi = \frac{e^{i\omega(x)}}{\sqrt{2}} \begin{pmatrix} 0 \\ v \end{pmatrix}$ is a stable minimum of $V(\phi)$. Non-perturbativity region means that the Higgs self-coupling (λ) becomes so high at large scales that, like in QCD, predictions could not be performed anymore using perturbation theory.

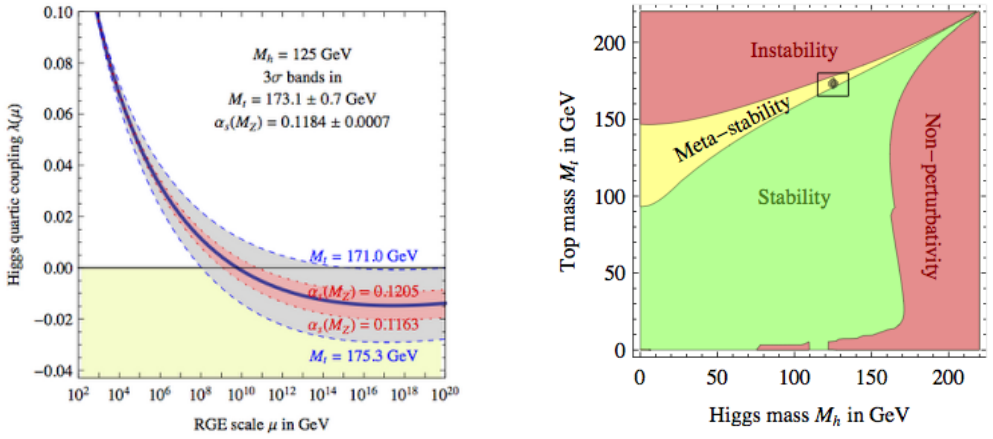


Figure 1.15: Stability of the Higgs potential extrapolated to the Planck scale from [59].

- **Matter-antimatter asymmetry**

  According to the Standard Model of cosmology, matter and antimatter should have been produced in equal abundance at Big Bang because SM interactions are producing new particles in pairs of matter-antimatter. However, the current Universe is clearly dominated by matter and therefore, in order to explain the current structure of the Universe, it is necessary to suppose that a matter-antimatter asymmetry exists and acted in the Universe evolution. Most recent measurements on the baryon asymmetry are provided by WMAP [60, 61] experiment and show a ratio of $\eta_b = (n_b - n_{\bar{b}})/n_\gamma = 6.19 \times 10^{-10}$. This ratio cannot be explained by the weak force CP violation inside the quark sector within the SM.

- **Gravity**

  Gravitational force is the only interaction which is not included in the Standard Model description. The main reason is that combination of the quantum mechanical formalism with general relativity generates infinities which cannot be absorbed by any renormalization process. In other words, the current SM framework based theories of gravitational forces are ill-defined. The corresponding mediating particle of this interaction is the so-called graviton, which is a spin-2 boson.

- **Dark matter**

  Dark matter is the general name given to a set of particles, not discovered yet, that do not interact with light and that are spread all over the Universe. They are an essential part of the Standard Model of Cosmology (ΛCDM). In this model, evolution of the Universe is explained by the existence of Dark Matter which interacted with the visible matter at primordial plasma and that at one point, decoupled from this thermal bath. No candidate of dark matter particle is available in the Standard Model and therefore, an extension of the particle spectrum, and possibly of the gauge group, are needed to explain the nature of the dark matter particle and its interactions with visible matter. Other theories propose that dark matter are large compact objects made of visible matter but emitting little or no radiation which include from primordial black holes [62] to neutron stars (e.g. MACHO [63]). However, the treatment of these theories is beyond the purpose of this work and are not further treated.

1.4 The Dark Matter open questions

1.4.1 Dark matter evidences

The first person that talked about Dark Matter was the french physicist and mathematician Henri Poincaré [64] in 1906. Lord Kelvin had proposed in 1906 [65] that the Milky Way could be described by a gas of

particles acting under the influence of gravity, from what one may derive the mass and size of the galaxy by simply measuring the dispersion velocity. In his article, Poincaré developed Kelvin's idea and explicitly mentioned that apart from visible stars, there could be some "obscure stars" which do not radiate and that therefore could remain long time unknown. The application of this model to the dispersion velocity of the Milky Way implied that the number of dark stars should be of the same or lower order than the number of visible stars. As we will see in this section, the ratio of dark matter/visible matter is actually larger than this result, but the possible existence of dark matter was already stated.

Dark matter first evidence was provided by Fritz Zwicky between 1933 and 1937 [66, 67]. Measurements of mean nebulae velocities in the Coma cluster had already been provided by Francis G. Pease [68]. Using this data, the application of the virial theorem [69] to the Coma cluster motion allowed to derive the average mass of any nebula in the cluster. Ultimately, this allowed the measurement of mass-to-luminosity ratio of nebulae in this cluster assuming a luminosity per nebula corresponding to 8.5 $\times 10^7$ that of the Sun. This implies a mass-to-luminosity ratio γ of around 500 while local Kapteyn stellar system [70] mass-to-luminosity ratio is of the order of $\gamma^{\text{Kapteyn}} \approx 3$. These results could not be explained unless a large invisible mass not interacting with light is present. Similar results were found by Sinclair Smith in 1936 [71] on the Virgo cluster.

Later on, in 1939, Horace Babcock [72] used the Doppler shift on emission and absorption lines of the Andromeda galaxy to study its rotation. Large mass-to-luminosity ratios were found together with unexpectedly large rotation velocities across the galactic plane. This behaviour is not predicted by Newton's (nor Einstein's) gravitation law, which states that the rotation velocity of the stars should decrease with the square root of the distance to the galactic center, where most of the galaxy mass is concentrated.

$$v_{\text{rot}} = \sqrt{\frac{GM_{\text{center}}}{r}} \tag{1.66}$$

However, this hint was not confirmed until the experiment performed by Vera Rubin and Kent Ford in the Andromeda galaxy using the Hα emission line (Fig. 1.16) in 1970 [73]. This result together with other experiments in other galaxies put in evidence the possible existence of dark matter and its possible concentration in the halo[2] of galaxies.

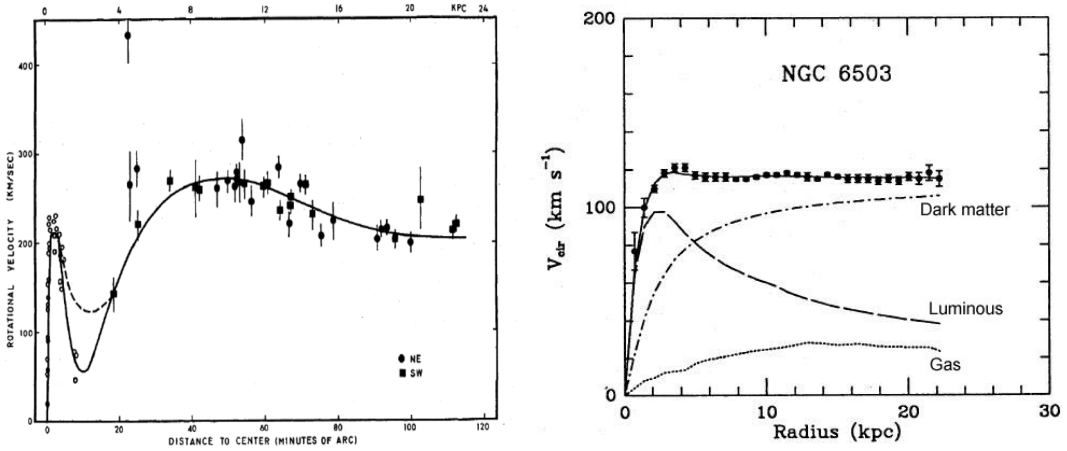


Figure 1.16: Rotational curves for (a) Andromeda galaxy, presented by Vera Rubin and Kent Ford in their article [73]; and (b) of the galaxy NGC 6503 [75]. Both galaxies are spiral.

A global analysis of the composition of the Universe based on Planck telescope data [60, 76] shows that dark matter would represent around 85% of all the matter available in the Universe and around 27% of all the energy in the Universe [60, 76] with a measured relic abundance of $\Omega_X h^2 = 0.1199 \pm 0.0022$, where $h = 67.31 \pm 0.96$ km s^{-1}Mpc^{-1} is the Hubble constant today. In addition, the observation of the bullet cluster clearly supports the idea of a collisionless Dark Matter, which would interact very

[2]The existence of dark matter is not yet demonstrated. Experiments shown in this chapter present strong evidence of its existence, but they are not conclusive in what concerns the dark matter particle existence, since other explanations, e.g. a corrected gravitational law (MOND's) [74], could also induce similar effects. However, some of these alternatives are not supported by data.

weakly with the visible matter and itself. This observation, presented in Figure 1.17, shows the result of gravitational lensing around the collision rests of two galactic clusters. A central bulk emitting X-rays (red color) concentrates hot visible matter, which interacted during the collision and whose velocity was then reduced. On the other hand, two clouds of matter observed from gravitational lensing of the background radiation (blue color) correspond to masses of the galaxy that didn't interact. The current hypothesis is that those two mass regions are mainly composed of dark matter whose initial velocity was not affected due to the lack of interactions and therefore is moving away from the collision in each direction.



Figure 1.17: Bullet cluster image, taken from the NASA measured by the Chandra X-ray observatory [77].

As it can be observed, current evidence supports the existence of dark matter just come from gravitational lensing and perturbations on star and galaxy motion. No evidence for its production nor annihilation could be determined until today, raising then the question on how dark matter could have been produced. The lack of evidence of DM from other sources suggests that, at some point of the Universe evolution, DM annihilations and production stopped so that its abundance remained stable.

1.4.2 An overview of the Universe evolution

According to our current understanding, the structure of the Universe is determined by a phenomena that occurred minutes after the Big Bang. The first elementary particles formed the primordial plasma and the high temperature after the Big Bang implies that all forces were unified. Immediately after the Big Bang, the Universe entered a process of fast expansion called inflation. Around 10^{-5} second after the Big Bang [79], the decoupling of the strong interaction took place allowing the formation of the fundamental particles. When the temperature descended to few billions of degrees, the strong interaction coupling ran large enough to allow the formation of protons and neutrons and then of the first stable nuclei as hydrogen, helium and lithium. Around 20 minutes after the Big Bang, the temperature reduced so much that nuclear fusion could not hold, giving birth to a Universe formed of a hot plasma composed of leptons, light nuclei, dark matter and photons. The high density and still high temperature of this plasma allow a large rate of interactions between photons and electrons or nuclei, so that neutral atoms cannot be produced. Furthermore, interaction rate amongst electrons, nuclei and dark matter imposed a Universe on which the relative abundance of the different components was in equilibrium. However, the continuous expansion of the Universe reduced the thermal energy and the density of the different

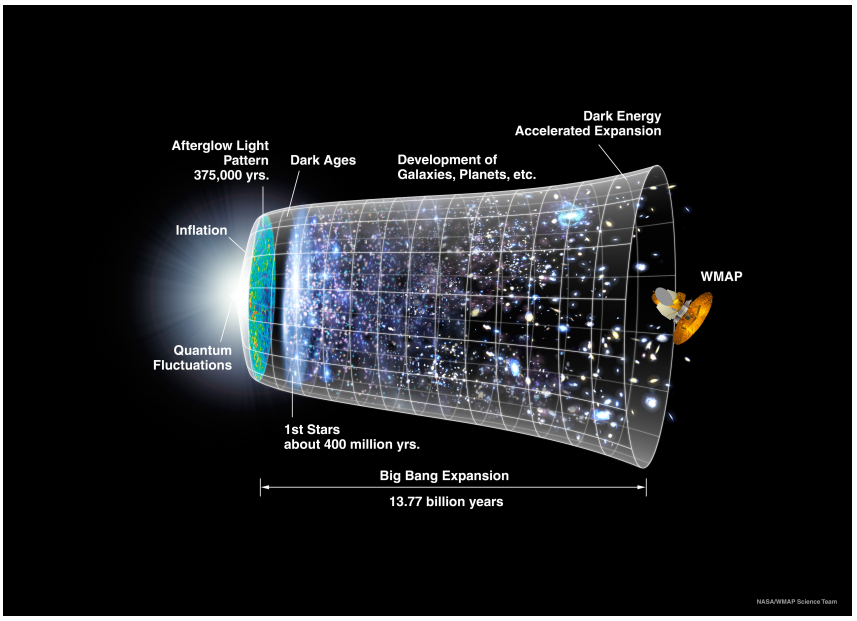


Figure 1.18: Schema of the Universe evolution since from Big Bang until today [78].

constituents. Around 375.000 years after the Big Bang, the Universe cooled down, permitting that electrons and nuclei combined and formed the first stable atoms. In parallel, the energy and density of the photons were reduced by Universe expansion, dropping the probability of interaction with the atomic electrons. Then, the interaction mean path of photons suddenly became infinite and, in consequence, they were able to travel freely. In other words, the Universe became transparent to photons. This event is called recombination, and photons that decoupled from the plasma at that moment composed the cosmic microwave background (CMB), currently studied by the Planck telescope. A widespread hypothesis suggests that dark matter also decoupled from the primordial plasma following a similar process, called freeze-out. This decoupling is explained in the next subsection and, although it is not the only theory that explains dark matter current abundance, it is the hypothesis considered along this thesis. After this recombination process, the Universe was mainly composed of hydrogen and helium with few traces of other nuclei as lithium. Around 150 million of years later, first gravitational collapses formed the first quasars, whose high energy radiation allowed the reionization of the Universe after photons decoupling. Onwards, stars and galaxies began to form. After freeze-out, dark matter abundance remained constant until today, playing an important role in the gravitational collapse allowing galaxies formation in this period.

1.4.3 Boltzmann equation and Dark Matter freeze-out

This section is based on Chapter 3 of [80]. The freeze-out theory considers that dark matter was once in equilibrium with the components of the early Universe. The production and annihilation of the dark matter with the primordial plasma and its abundance nowadays are deeply related to the nature and magnitude of the dark matter interaction with other Universe constituents. The equation describing the rate of change in the abundance of a given particle is the Boltzmann equation. Considering interactions between four species so that $1 + 2 \leftrightarrow 3 + 4$, the Boltzmann equation for the abundance of species 1 is:

$$\begin{aligned} a^{-3}\frac{d(n_1 a^3)}{dt} = \int \frac{d^3p_1}{(2\pi)^3 2E_1}\int \frac{d^3p_2}{(2\pi)^3 2E_2}\int \frac{d^3p_3}{(2\pi)^3 2E_3}\int \frac{d^3p_4}{(2\pi)^3 2E_4} \\ \times(2\pi)^4\delta^3(p_1+p_2-p_3-p_4)\delta(E_1+E_2-E_3-E_4)|\mathcal{M}|^2 \\ \times f_3 f_4[1\pm f_1][1\pm f_2] - f_1 f_2[1\pm f_3][1\pm f_4] \end{aligned} \tag{1.67}$$

$$f_i = \frac{1}{e^{\frac{E_i-\mu_i}{k_B T}} \mp 1} \tag{1.68}$$

where factors f_i correspond to the occupation number of the species i, $\mathcal{M}$ is the probability amplitude of the interaction to occur and the $\pm$ sign in $[1 \pm f_i]$ is + for bosons and - for fermions (Bose-Einstein or Fermi statistics). The factor $a(t)$ corresponds to the time-dependent scale present in the metric $ds^2 = c^2dt^2 - a^2(t)(dx^2 + dy^2 + dz^2)$ so that the Hubble constant is $H(t) = \frac{1}{a(t)}\frac{da(t)}{dt}$. The equilibrium of the abundance of species requires that the annihilation of species $1+2$ is compensated by the inverse process given by the annihilation of species $3+4$, imposing the equality of chemical potentials $\mu_1+\mu_2 = \mu_3+\mu_4$. Since typically we will be interested in systems such that the factor $(E-\mu)/k_BT >> 1$, the Boltzmann equation is then reduced to:

$$a^{-3}\frac{d(n_1a^3)}{dt} = n_1^{(0)}n_2^{(0)}\langle\sigma v\rangle\left(\frac{n_3n_4}{n_3^{(0)}n_4^{(0)}} - \frac{n_1n_2}{n_1^{(0)}n_2^{(0)}}\right) \tag{1.69}$$

$\langle\sigma v\rangle$ is the thermally averaged cross-section of the creation–annihilation process and $n_i^{(0)}$ stands for the equilibrium density [80], given by:

$$n_i^0 = \begin{cases} g_i\left(\frac{m_iT}{2\pi}\right)^{3/2}e^{-m_i/T} & , m_i >> T \\ g_i\left(\frac{T^3}{\pi^2}\right) & , m_i << T \end{cases} \tag{1.70}$$

In a generic scenario with high-mass dark matter, two dark matter particles X may annihilate producing two light particles i, which are considered very tightly coupled to the cosmic plasma so that $n_i = n_i^{(0)}$. The unknown of the equation is then the abundance of the dark matter n_X. Equation 1.69 may be rewritten:

$$a^{-3}\frac{d(n_Xa^3)}{dt} = \langle\sigma v\rangle\left(n_X^{(0)} - n_X^2\right) \tag{1.71}$$

To go further, recalling that the primordial plasma temperature scales as $T \propto a^{-1}$ permits to rewrite this equation:

$$\frac{dY}{dt} = T^3\langle\sigma v\rangle\left(Y_{eq}^2 - Y^2\right) \quad ; \quad Y = \frac{n_X}{T^3}; \quad Y_{\rm EQ} = \frac{n_X^{(0)}}{T^3}; x = \frac{m_X}{T} \tag{1.72}$$

Very high temperature corresponds to $x << 1$ (i.e. $m_{\rm DM} << T$), in which case reactions happen very rapidly and the $Y \approx Y_{\rm EQ}$. This condition is fulfilled at initial times. Since particles are relativistic at these times, this implies that $Y \approx \mathcal{O}(1)$ according to Eq. 1.70. However, as the Universe expands and cools down, x values would become larger, which implies a suppression of Y_{EQ}, evolving as e^{-x} according to Eq. 1.70. Equation. 1.72 still holds, thus Y, and in consequence n_X, are reduced. However, this fact together with the Universe expansion drop the DM density until the DM annihilations became a rare process, breaking the equilibrium. At the same time, other species collide with lower energy and dark matter production is suppressed. The immediate consequence is that DM abundance would become constant, with a density scaling with the Universe expansion. This is the freeze-out and the precise moment at which it happened depends on the thermal cross-section $\langle\sigma v\rangle$ of DM production and annihilation.

The theory of freeze-out hides an interesting effect, also called WIMP miracle. Supposing that current dark matter abundance comes completely from the freeze-out epoch, the relic density can be expressed as [82, 83]:

$$\Omega_Xh^2 = 0.3\left(\frac{x_f}{10}\right)\left(\frac{g_*(m)}{100}\right)^{1/2}\left(\frac{10^{-39}\ \mathrm{cm}^2}{\langle\sigma v\rangle}\right) \tag{1.73}$$

where x_f is the ratio $x_f = m_{dm}/T_f$ at the freeze-out and g_* represents the degrees of freedom of the primordial thermal bath. Using the value $\Omega_Xh^2 = 0.1199$ reported in [76], the average thermal cross-section of DM annihilations is approximately $3 \times 10^{-26}\mathrm{cm}^3\mathrm{s}^{-1}$, which corresponds in the Fermi weak theory to the cross-section of a 100 GeV particle interacting through the weak force. This fact supports the idea that dark matter could be composed of massive particles interacting very weakly, also called Weakly-Interacting-Massive-Particles (WIMP) [82].

$$\langle\sigma v\rangle \approx \sigma_{\rm Fermi} \propto \frac{g_X^4}{m_X^2} \quad ; \quad g_X \sim g_W \sim 0.6 \quad ; \quad m_X \sim m_W \sim 80\mathrm{GeV} \tag{1.74}$$

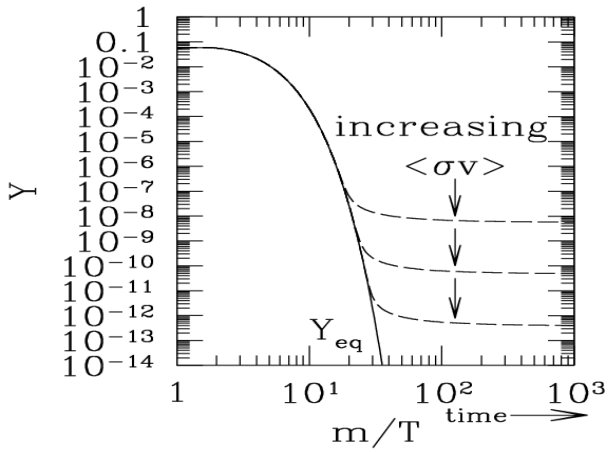


Figure 1.19: Evolution of the dark matter abundance before and at the moment of freeze-out. It can be observed that at one moment the dark matter decoupled from the interaction with the rest of the plasma species and for that time onward, its relic density remained constant [81].

1.4.4 Dark matter detection experiments

The global dark matter density has fallen after the freeze-out. However, the galactic rotation curves indicate that there must be a non-negligible concentration of dark matter at the galactic halo. In addition, DM could be present in regions with large visible mass, attracted by gravitation. In these regions, DM annihilations could be occurring at a detectable rate. Different strategies are followed for exploiting these possibilities. In this section, a state of the art on dark matter detection is presented, mentioning the most recent available results:

- **Direct detection**

  These searches aim to record the recoiling energy of visible matter nuclei from a collision with dark matter. They exploit the possibility that dark matter is present in the galactic halo and that it could be spread over our Solar System. The Earth rotation around the Sun and the rotation of the Solar System around the galactic center would then induce a relative velocity between land-based experiments and the dark matter in the halo which could allow the collision of DM against the active medium of the detector. These collisions could leave a trace of a recoiling particle from the active medium or the product of a de-excitation of the particle that, if recorded, could represent an evidence for dark matter. The large number of background sources that could imitate a DM signal together with the low interaction rate between dark matter and visible matter implies that these experiments must present a strong shielding to reduce the environmental background with a careful study of the remaining background sources and large exposure times. The detection medium is based on very stable material and experiments are usually built underground, to further reduce the background coming from cosmic rays and solar activity.

  Many of these detectors are based on two-phase configurations (liquid and gas) of an active material composed of very stable nuclei, such as argon or xenon, further purified in order to reduce the possible radiative isotopes. This is the case for the current experiments Xenon1T [84], DarkSide-50 [85], LUX [86] and PandaX-II [87]. Others are based on semiconductor detectors such as DAMIC [88] (CDDs), EDELWEISS [89], CDMS-II [90] (Ge and Si crystals) or on bubble chambers as PICO [91]. Most recent 90% CL limits on WIMP-nucleon cross-section are presented in Fig. 1.20. Most stringent limits are currently those from Xenon1T experiment for the spin-independent cross-section limits.

- **Indirect detection**

  Indirect detection consists in detecting a possible source of high energy particles in the cosmic rays that could not be explained by the currently known sources of radiation and that could then come from DM annihilation. In this category, the most important hints of dark matter were provided

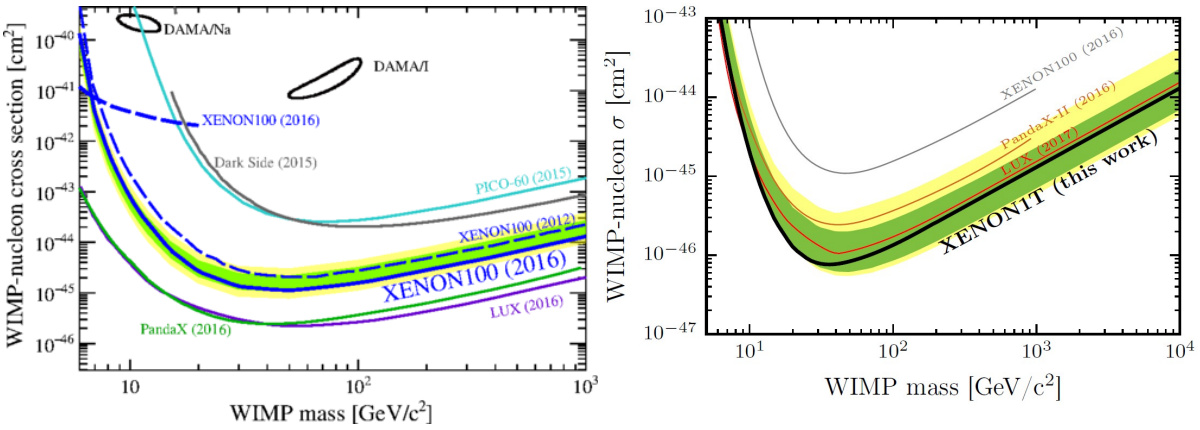


Figure 1.20: 90 % CL limits on WIMP-nucleon spin-independent cross-section are presented. Left: comparisons between most recent results for Xenon100 [92], DarkSide-50 [85], LUX [86] and PandaX-II [87] are presented. The plot is taken from [92]. Right: latest results from Xenon1T [84] experiment and comparison with LUX [86], Xenon100 [92] and PandaX-II [87] results.

by PAMELA, FERMI-LAT telescope and AMS-02. Concerning FERMI-LAT results, observations of high energy γ-ray are measured inside the Milky Way galactic center (GC). In the FERMI-LAT paper [93], interstellar emission models (IEM's) are developed to determine the galactic background γ-ray emissions, together with all possible point sources. The interstellar background comes from the interaction of cosmic rays with the interstellar gas and radiation fields. These cosmic-ray sources are mainly composed of pulsars and OB-stars (stars of spectral type O or early-type B [94]), whose spatial distribution across the galactic plane and halo is not known with high precision. Several models are built, scaled to data in the control regions and compared with data in the signal region, 15°×15°around the GC. It is found that including a dark matter model following the Navarro-Frenk-White [95] (NFW) profile distribution (Figures 1.21), the data/model agreement increases although the residual distribution between data and the background only model is dependent on the assumed IEM's. The results of this experiment [93] constitute a possible hint of dark matter indirect detection. However, H.E.S.S experiment recently investigated more in detail this γ-ray excess by directly measuring the background in regions where the DM annihilations are expected to be very reduced (OFF regions) and extrapolating the result to the signal region (ON regions: 0.3° to 0.9° annular rings of 0.1° size about the GC). No excess was found [96] using this technique, allowing to derive limits on the WIMP annihilation cross-section depending on the DM mass (Fig. 1.22). Limits depend on the DM spatial distribution and the considered annihilation product. On the other hand, PAMELA experiment observed a possible excess of positrons that could have been produced by dark matter annihilations [98]. These results, confirmed by more accurate measurements with AMS-02 [99] and Fermi-LAT present an excess of positron production for energies up to 100 GeV (Figures 1.23). By now, there is no conclusive explanation of this excess in the framework of the SM while astrophysics explanations do not seem to fill the gap either [100].

- **Collider searches**

  Collider searches aim to produce dark matter particles through high-energy collisions of visible matter particles. Currently, the most active collider measurements are performed at the LHC by the ATLAS and CMS detectors. These searches are based on general models allowing DM production in association to a detectable particle. These so-called mono-X models predict a single object X (jet, γ, W, Z or h) produced in association to DM particles. Many models are available which introduce connections between the visible matter (SM) and the dark sector, which predict signals at collider searches. The interpretation of results for all this plethora of models reveals to be arduous. Therefore, two simplified approaches are adopted instead, depending on the type of interactions which are probed: effective field theories and simplified models. Occasionally, in the case of simplified models the SM group $SU(3)_c \times SU(2)_L \times U(1)_Y$ is also extended and a new interaction is introduced in order to connect the SM sector with the dark sector. Simplified models are explained

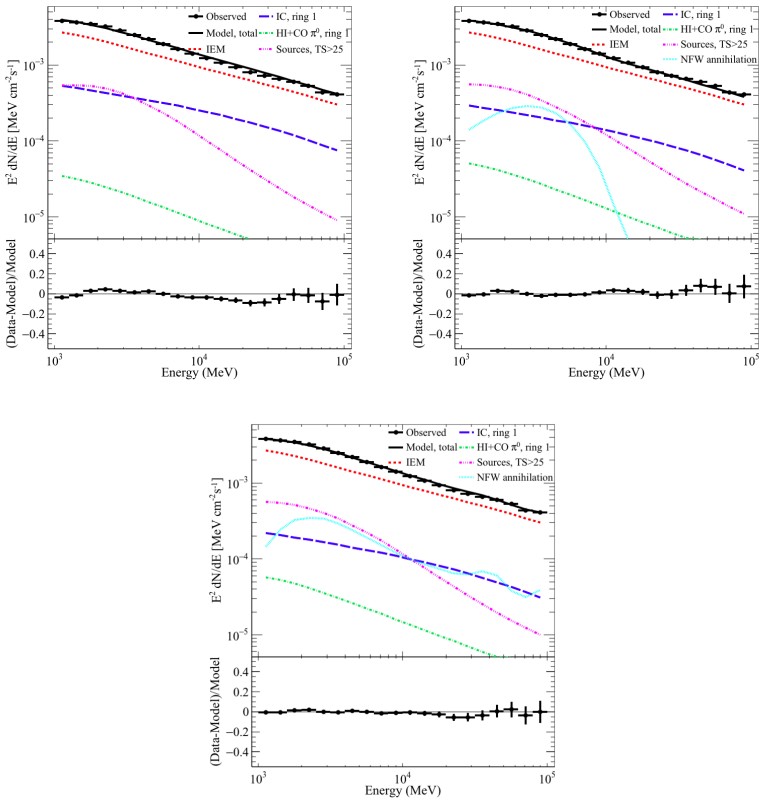


Figure 1.21: γ-ray data measured by Fermi-LAT in a region of size 15°×15°around the galactic center. It is found that model fits better the γ-ray spectra when including a contribution of WIMP dark matter annihilation distributed at the galactic center following a Navarro-Frenk-White profile distribution. Two possible distributions are considered, being shown on the center plot results using the standard NFW distribution and, on the right plot, a NFW distribution corrected with a power law [93]. In this pictures, one of the four IEM's is presented.

in more detail in Section 1.5 with a particular focus on models predicting mono-Higgs signals.

1.5 Phenomenological search for DM particles at the LHC

Dark matter has been searched in the LHC since the beginning of data taking. However, the strategy to provide useful results for the wide variety of DM theories predicting DM at LHC has varied between the Run I and Run II. This variation is due to the convenience of using effective field theories or simplified models.

1.5.1 Effective field theories vs simplified models

In Run I, effective field theories (EFT) were used to interpret results. An EFT is a very powerful way of describing physical processes at a given scale. The main advantage of these theories is that there is no need to make assumptions about the type of interaction that connects known physics sector, for example, the SM sector, with the unknown new physics degrees of freedom. Therefore the results are interpreted in a way that is model-independent to a large extent. However, despite that they provide very strong limits which can be used to constraint DM models and production phase space, their predictions are only valid within a given range of energies.

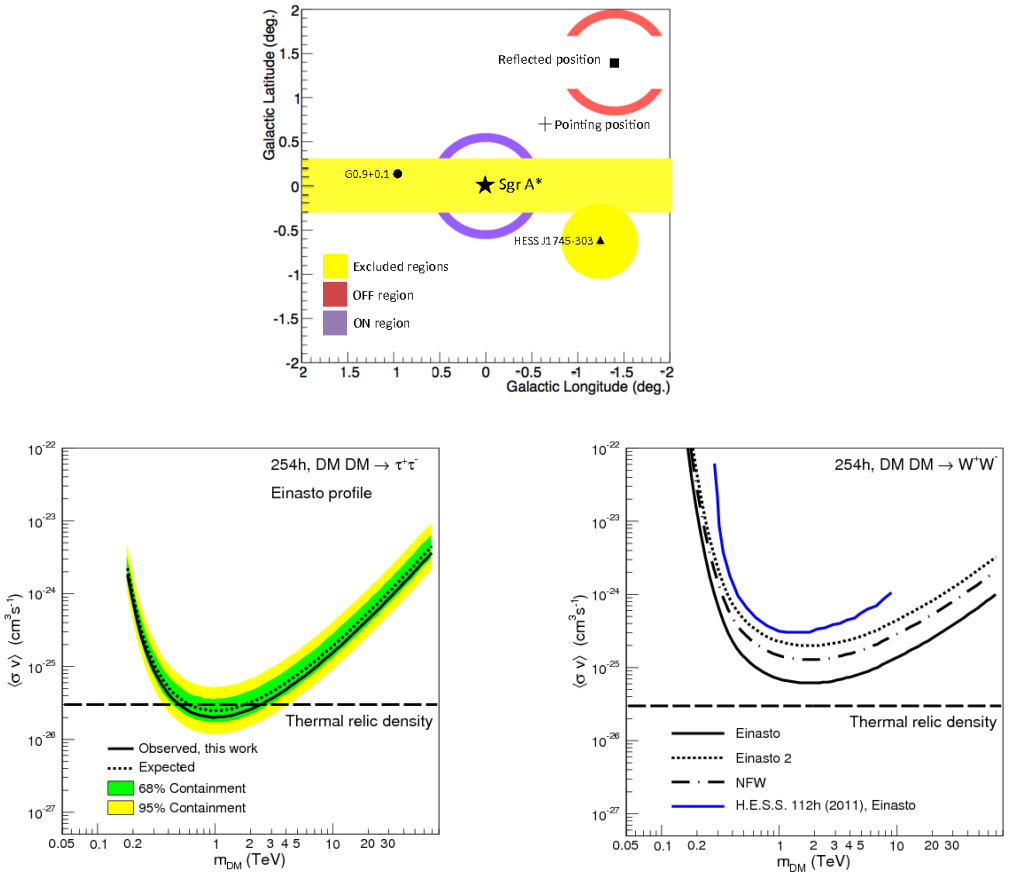


Figure 1.22: Summary of H.E.S.S. 10-year observation and results on the GC γ-ray spectrum. The top plot presents the signal (ON) and background (OFF) regions observed to study the galactic background. The bottom left plot presents the limits on WIMP thermal averaged cross-section $\langle\sigma v\rangle$ depending on the DM particle mass using the Einasto [97] profile distribution. The bottom right plot presents the dependence of H.E.S.S. limits on the DM spatial distribution model. All plots are taken from [96].

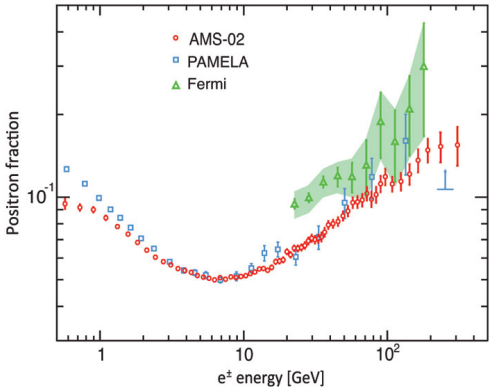


Figure 1.23: Positron excess observed by PAMELA, Fermi-LAT and AMS-02 [101].

EFT interactions are parametrized by a given scale (Λ), representative of the energy beyond which the mass of BSM particles is expected to be or, in other words, the energy up to which no new physics is expected to be found. This implies that all particles with masses beyond that scale are integrated-out from the theory and no particles with smaller masses, except DM and SM particles, are present in the theory. The validity of these theories is discussed in [102, 103, 104]. As an example, let's consider a UV-complete field theory introducing a scalar mediator of mass M, which connects the SM and DM sector.

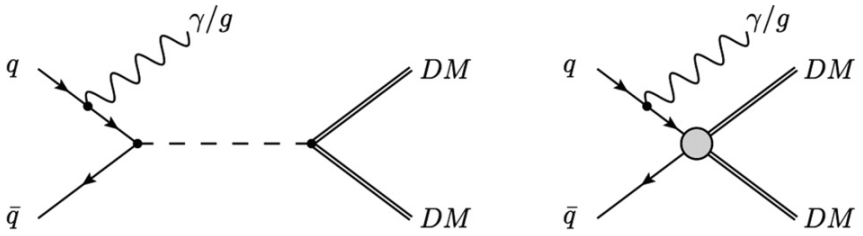


Figure 1.24: Feynman diagrams from a simplified model (left) and an effective field theory (right).

The dominant process allowing for dark matter detection (Fig. 1.24.a) then includes a SM particle radiated as initial state radiation and two dark matter particles produced via the scalar mediator produced in the s-channel. The corresponding EFT (Fig. 1.24.b) for energies lower than $\Lambda \sim M$ only presents the degrees of freedom lighter than M (SM and DM) and therefore, no additional BSM particle affecting dark matter production is present in [m_t,Λ]. The corresponding matrix-element of the interaction is then proportional to Eq. 1.75:

$$\frac{g_q g_\chi}{Q_{tr}^2 - M^2} \approx -\frac{g_q g_\chi}{M^2}(1 + \frac{Q_{tr}^2}{M^2} + \mathcal{O}(\frac{Q_{tr}^4}{M^4})...) \tag{1.75}$$

where g_q and g_χ are the couplings of the s-channel particle with the quarks and the dark sector. Further simplifications can be made (Eq. 1.76), allowing to make a connection between a simplified model lagrangian and the interaction term of an EFT:

$$\frac{g_q g_\chi}{Q_{tr}^2 - M^2} \approx -\frac{g_q g_\chi}{M^2} \equiv -\frac{1}{\Lambda^2} \tag{1.76}$$

$$\mathcal{L} \supset g_q \bar{q} S q + g_\chi \bar{\chi} S \chi \quad \rightarrow \quad \mathcal{L} \supset \frac{1}{\Lambda^2} \bar{q} q \bar{\chi} \chi. \tag{1.77}$$

As long as the assumption $M^2 \gg Q_{tr}^2$ can be made, EFT use is justified. For doing so, the exchange interaction energy (Q_{tr}) must be negligible compared to Λ. Otherwise, resonant effects become dominant and equality in Eq. 1.76 is no longer applicable, thus predictions from the EFT are no longer valid. A cut-off can be defined (Eq. 1.78) to test EFT predictions validity [102, 103, 104]:

$$R_\Lambda = \frac{\frac{d\sigma_{\text{eff}}}{dp_T d\eta}|_{Q_{tr}<\Lambda}}{\frac{d\sigma_{\text{eff}}}{dp_T d\eta}} \tag{1.78}$$

R_Λ represents the fraction of the events for a given EFT theory that are created following the condition $Q_{tr} \ll \Lambda$. Large values of this parameter mean that this process is describing events with sufficient low momentum transfer, so the use of an EFT is justified. Otherwise, EFT is no longer trustworthy and predictions such as the cross-section would present significant errors. A study is presented in [102] about EFT validity using as a benchmark model an EFT predicting mono-jet signals. In this study, Figure 1.25 shows that large values of Λ (> 2.5 TeV) are necessary to justify the use of a EFT. In the case of searches predicting s-channel dark matter production, which could be reinterpreted as an intermediate-mass resonance, effective theories are substituted by simplified models. Simplified models are UV-complete theories which represent a large number of DM theories with a similar topology. However, their predictions are model dependent and results must be interpreted for each model separately.

1.5.2 Mono-Higgs theories

Mono-X theories introduce intermediate states which interact with the dark sector and the SM sector. Usually, these intermediate particles, also called mediators, are coming from additional symmetries extending the Standard Model symmetry group $SU(3)_c \times SU(2)_L \times U(1)_Y$. These theories predict a single object X (jet, γ, W or Z) produced in association to detectable DM particles. The DM particles are not indeed expected to interact within the detector fiducial volume, thus predicted signatures include a large missing transverse momentum recoiling against one of these X particles. Detectable particles

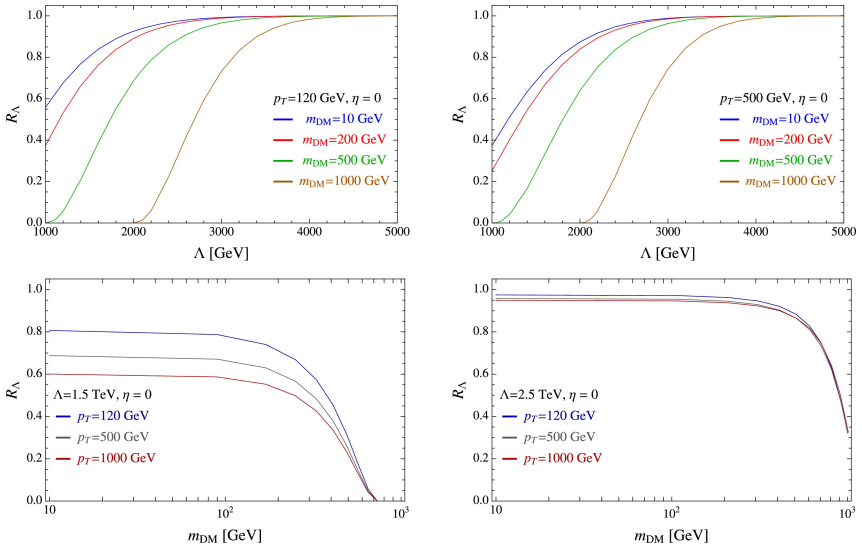


Figure 1.25: The ratio R_Λ for $\sqrt{s} = 8$ TeV at $|\eta| = 0$ from [102]. A mono-jet EFT is used. These plots show the validity of the EFT depending on the hard-jet p_{T} and/or m_χ. It can be observed that EFT is valid only considering large values of Λ. For lower values, a part of the generated events presents interactions with $Q_{tr} > \Lambda$, where predictions are no longer valid.

are either expected to be radiated as an initial state radiation or to be produced as a final state of a hard process[3]. The production of these final states depend on the coupling between the radiated object and the colliding particles. This fact motivates the search of mono-Higgs signals since, oppositely to jet, γ, W or Z, Higgs does not couple to gluons and its couplings to quarks are Yukawa suppressed. Then, the Standard Model does not predict a large contribution to these mono-Higgs final states and any deviation from SM predictions would be a direct probe of a coupling between the Higgs and a new BSM sector. On the other hand, mono-Higgs searches constitute a complementary set of measurements to direct coupling searches of the Higgs boson to invisible particles [105, 106], given that these final states are not sensitive for DM particles with masses $m_\chi > m_h/2$.

Three benchmark models are considered in the analysis presented in this thesis: two simplified models recommended by the Dark Matter Forum (DMF) [107] and a heavy-scalar model [108]. Each model introduces an intermediate resonant state produced in the s-channel that connects the dark and the Standard Model sectors. The nature of this resonance depends on the model: Z'_B model has a vector boson mediator that directly couples with the dark matter and the Higgs boson; the Z'-2HDM also uses a vector boson mediator, also called Z', that couples to the Higgs boson and a pseudo-scalar A^0 which subsequently couples to dark matter; the heavy-scalar presents a scalar mediator coupling through an effective interaction between the Higgs boson and dark matter.

Vector mediator model (Z'_B)

In this model [109], the Standard Model baryonic symmetry is explicitly imposed through a new $U(1)_B$ gauge symmetry with gauge coupling g_B. The vector mediator of this baryonic gauge symmetry is called Z'_B and its mass is generated by introducing a new "baryonic" Higgs (h_B) which induces a spontaneous breaking of $U(1)_B$ symmetry. The coupling of the Z'_B boson with the SM Higgs comes from the mixing between the baryonic Higgs and SM Higgs boson. This combination is parametrized by a missing angle θ, allowing the final state h to be radiated by the Z'_B boson.

The dark sector is composed of a single-flavour dark matter particle (χ), considered to be a Dirac fermion, singlet under the SM symmetry group and charged under $U(1)_B$ with charge B_χ. The cou-

[3] Initial state radiation (ISR) are objects produced as soft-radiation by colliding particles such as quarks or gluons. In contrast, final state radiation (FSR) are soft-radiation objects produced in association to resulting particles from the collision. A typical example of the latter is the production of soft photons by leptons issued from $pp \to Z \to \ell^-\ell^+$ process. In that case, photons from initial state radiation can be present, coming from quarks producing the Z intermediate boson.

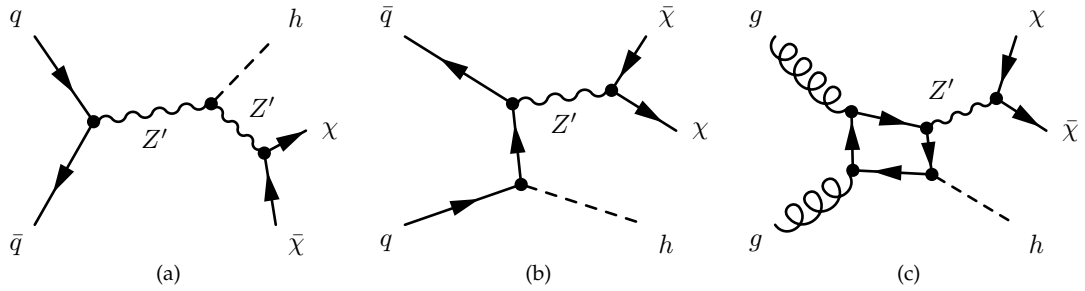


Figure 1.26: Feynman diagrams of the production of DM (χ) in association with a SM-like Higgs boson (h) arising from Z'_B models: born process (a); t-channel production of the Z'_B (b); and leading NLO box diagram producing mono-Higgs signals in the final state (c). The latter diagram is not simulated since signal events are produced at leading-order in QCD, as explained in Section 7.1.

pling of dark matter particles to Z'_B is proportional to B_χ as $g_\chi = B_\chi g_B$. Quarks are also charged, coupling to the Z'_B through $g_q = g_B/3$. In contrast, no coupling between leptons and Z'_B (leptophobic) is considered in order to avoid constraints from ATLAS and CMS lepton searches.

The corresponding Lagrangian terms after $U(1)_B$ symmetry breaking is presented in Eq. 1.79, where v_b is the vacuum expectation value of the baryonic Higgs field:

$$\mathcal{L} \supset g_q q\gamma^\mu q Z'_{B,\mu} + g_\chi \bar{\chi}\gamma^\mu \chi Z'_{B,\mu} + \frac{1}{2} m^2_{Z'_B}\left(1 + \frac{h_B}{v_B}\right) Z'_{B,\mu} Z'^{\mu}_{B} \tag{1.79}$$

The mixing between h_B and h induces an interaction of the form:

$$\mathcal{L} \supset g_{hZ'Z'} h Z'_{B,\mu} Z'^{\mu}_{B} \tag{1.80}$$

where $g_{hZ'Z'} = m^2_{Z'_B} \sin\theta / v_B$. The remaining model parameters are $\sin\theta$, g_q, g_χ, $g_{hZ'Z'}$, m_χ and $m_{Z'_B}$. Previous studies performed inside the DMF group [107] show that Z'_B-model kinematic variables do not depend on $\sin\theta$, g_q, g_χ, $g_{hZ'Z'}$ (Figs. 1.27) and their values are then fixed to 0.3,1/3, 1 and $m_{Z'_B}$, respectively. The condition $g_{hZ'Z'} = m_{Z'_B}$ is chosen because it maximizes the total cross-section. Feynman diagrams corresponding to the dominant processes are presented in Fig. 1.26. Among them, the Born process accounts for most of the final cross-section. No constraints on the masses of the Z'_B nor χ are imposed and therefore on-shell and off-shell processes are investigated.

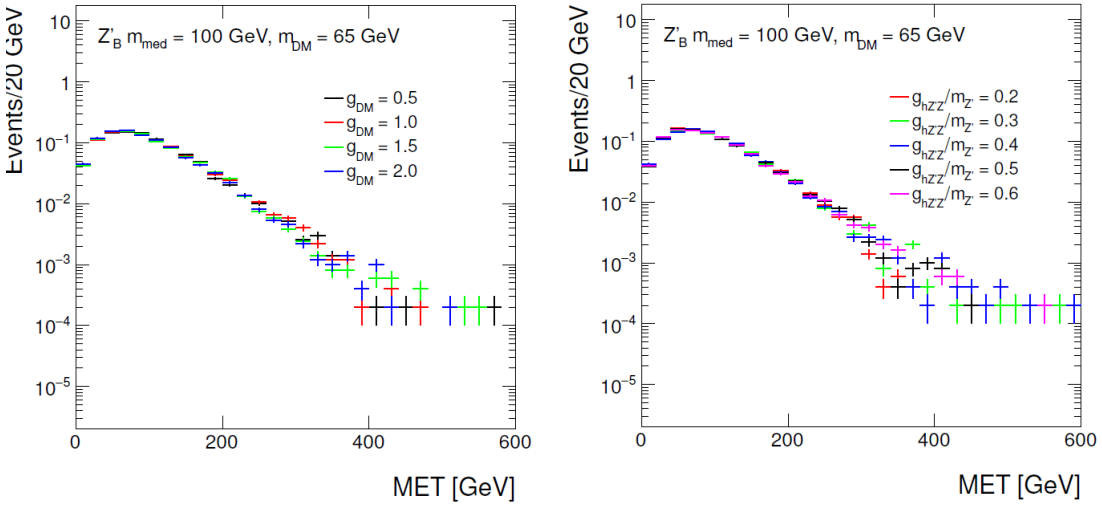


Figure 1.27: Z'_B kinematics dependence on g_χ (left) and $g_{hZ'Z'}$ (right) parameters [107].

Vector mediator model+2HDM sector (Z'-2HDM)

An alternative model is considered introducing a new $U(1)_{Z'}$ symmetry whose gauge vector is called Z'. An additional SM singlet ϕ is introduced to break spontaneously this new symmetry and allow Z' to be a massive vector boson. In this case, no mixing of ϕ with the Higgs sector is allowed and only right-handed quarks are charged under $U(1)_{Z'}$. This model [110] is called in the following Z'-2HDM since the Higgs sector is extended with a second doublet so that the Higgs sector corresponds to a type-II Two Higgs Doublet Model [111]. The doublets are charged under SM group with $Y = 1/2$ and the new $U(1)_{Z'}$ symmetry with respective charges z_u and z_d. The peculiarity of type-II of models is that one doublet couples to up-type quarks ($Q = 2/3$) and the other doublet, with down-type quarks ($Q = -1/3$) and leptons. After symmetry breaking and in unitary gauge, doublets can be parametrized following Eqs. 1.81 and 1.82, where h, H^0 are CP-even scalars and A^0 is a CP-odd scalar, α is the mixing angle that diagonalizes the $h - H^0$ mass squared matrix and $\tan\beta = \frac{v_u}{v_d}$. The main Lagrangian terms to be added to the SM from the 2HDM side are expressed in Eq 1.83:

$$\Phi_{\mathrm{u}} = \frac{1}{\sqrt{2}} \begin{pmatrix} \cos\beta H^+ \\ v_u + \cos\alpha h + \sin\alpha H^0 + i\cos\beta A^0 \end{pmatrix} \tag{1.81}$$

$$\Phi_{\mathrm{d}} = \frac{1}{\sqrt{2}} \begin{pmatrix} -\sin\beta H^+ \\ v_d - \sin\alpha h + \cos\alpha H^0 - i\sin\beta A^0 \end{pmatrix} \tag{1.82}$$

$$\mathcal{L} \supset y_u Q \tilde{\Phi}_u \bar{u} + y_d Q \tilde{\Phi}_d \bar{d} + y_e L \tilde{\Phi}_d \bar{e} + \mathrm{h.c.} \tag{1.83}$$

Leptons are considered to be neutral under the $U(1)_{Z'}$ symmetry. The Higgs vacuum expectation values

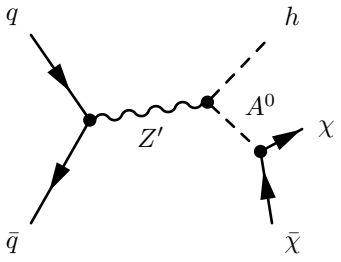


Figure 1.28: Feynman diagrams of the production of DM (χ) in association with a SM-like Higgs boson (h) arising from Z'-2HDM model.

produce a small mixing between Z and Z'. This mixing changes the mass of the Z boson with a mixing parameter ϵ:

$$M_Z^2 \approx (M_Z^0)^2 - \epsilon^2[(M_{Z'}^0)^2 - (M_Z^0)^2] \tag{1.84}$$

$$M_{Z'}^2 \approx (M_{Z'}^0)^2 + \epsilon^2[(M_{Z'}^0)^2 - (M_Z^0)^2] \tag{1.85}$$

where $M_Z^0 = g^2(v_d^2 + v_u^2)/(4\cos\theta_w)$, $M_{Z'}^0 = g_z^2(z_d^2 v_d^2 + z_u^2 v_u^2 + z_\phi^2 v_\phi^2)$ and g_z, the coupling between the Z' and the Higgs doublets.

This model imposes Z' resonant production and A^0 boson is required to decay into two DM particles on-shell. Therefore, only $m_{A^0} \geq 2m_\chi$ working points are allowed. The main Feynman diagram producing mono-Higgs signals is shown in Fig. 1.28. Concerning the other free parameters of the model, as it can be observed in Figs. 1.29, $\tan\beta$ parameter is constrained by the perturbativity of the Yukawa coupling, where $\tan\beta < 0.3$ is excluded. In addition, dijet searches [110] also impose $\tan\beta \geq 0.6$. Beyond this value, kinematic distributions do not depend on $\tan\beta$. In addition, kinematics do not either depend on g_z nor on m_χ, the latter in case that $m_{A^0} \geq 2m_\chi$. In consequence, $\tan\beta$, g_z and m_χ are fixed [107] to 1.0, 0.8 and 100 GeV, respectively. Finally, $m_H = m_{H^\pm} = 300GeV$ due to constraints on type II 2HDM models from $b \to s\gamma$ searches. Other possible configurations of these four parameters can be studied by rescaling the model cross-section.

Heavy scalar model (H)

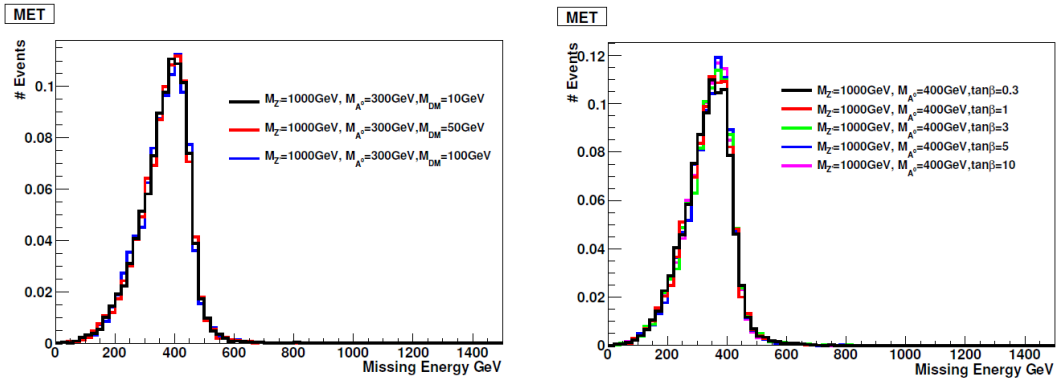


Figure 1.29: Z'-2HDM kinematics dependence on m_χ (left) and $\tan\beta$ (right) parameters [107].

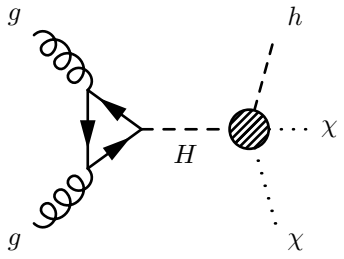


Figure 1.30: Feynman diagrams of the production of DM (χ) in association with a SM-like Higgs boson (h) arising from the heavy-scalar model.

Alongside those simplified models recommended in [107], a third model, referred to as the heavy scalar model [108], introduces a heavy-scalar boson H. The different interaction terms of this heavy-scalar are divided into:

$$\mathcal{L} \supset \mathcal{L}_H + \mathcal{L}_Y + \mathcal{L}_Q + \mathcal{L}_T \tag{1.86}$$

given that

$$\mathcal{L}_H = -\frac{1}{4}\beta_g \kappa^{SM}_{hgg} G_{\mu\nu} G^{\mu\nu} \mathrm{H} + \beta_V \kappa^{SM}_{hVV} \mathrm{H} V_\mu V^\mu \tag{1.87}$$

$$\mathcal{L}_Y = -\frac{1}{\sqrt{2}}[g_{\mathrm{H}t\bar{t}} \mathrm{H}t\bar{t} + g_{\mathrm{H}b\bar{b}} \mathrm{H}b\bar{b}] \tag{1.88}$$

$$\mathcal{L}_T = -\frac{1}{\sqrt{2}} v[\lambda_{\mathrm{H}hh} \mathrm{H}hh + \lambda_{h\chi\chi} h\chi\chi + \lambda_{\mathrm{H}\chi\chi} \mathrm{H}\chi\chi] \tag{1.89}$$

$$\mathcal{L}_Q = -\frac{1}{2}\lambda_{\mathrm{H}h\chi\chi} \mathrm{H}h\chi\chi - \frac{1}{4}[\lambda_{\mathrm{HH}\chi\chi} \mathrm{HH}\chi\chi + \lambda_{hh\chi\chi} hh\chi\chi + \lambda_{\mathrm{HH}hh} \mathrm{HH}hh] \tag{1.90}$$

where κ^{SM}_{hVV} and κ^{SM}_{hgg} are the respective effective couplings of the Higgs boson to the electroweak vector bosson and the gluons, scaled by a $\beta_{V,b}$ parameter allowing a difference between the SM Higgs and the heavy-scalar boson coupling couplings to these particles. In addition, the different g and λ parameters correspond to the different couplings of the heavy-scalar to the SM Higgs boson and the dark matter particles. In this model, dark matter particles are considered to be scalars.

The new boson is produced primarily via gluon-gluon fusion (ggF) with an effective coupling similar to the SM Higgs boson scaled by β_g^2, as explained above. An upper bound on m_H is introduced to avoid a large branching ratio of $\mathrm{H} \to \mathrm{t\bar{t}}$, which would saturate the entire H width leading to a $\mathrm{H} \to h\chi\chi$ branching ratio close to zero. In addition, a lower bound on m_H is more than twice of m_h to ensure the SM Higgs boson is produced on-shell. In summary, samples are simulated for the mass range

$2m_{\mathrm{h}} < m_{\mathrm{H}} < 2m_{\mathrm{top}}$, where m_{h} and m_{top} represent the masses of the SM Higgs boson and top quark, respectively.

While no assumptions are made here as to the nature of H, it can be viewed as a part of a 2HDM+χ scenario where H may be considered as the CP-even heavy scalar boson [108]. An effective quartic coupling between h, H, and χ is considered, where the DM χ is assumed to be a scalar. The decay branching fraction of H to h and two χ particles is assumed to be 100% for this model, for ease of further interpretations. The DM mass (m_{χ}) is taken to be roughly half of the SM Higgs boson mass to ensure on-shell decay of H $\rightarrow h\chi\chi$, and to suppress invisible decay modes of h, as described in Ref. [112].

References

[1] J.J.Thomson. "XL. Cathode Rays". In: *Philosophical Magazine* 44.269 (1897), pp. 293–316. DOI: 10.1080/14786449708621070. URL: http://dx.doi.org/10.1080/14786449708621070.

[2] C. L. Cowan and F. Reines. "The neutrino". In: *Nature* 178 (1956), pp. 446–449. DOI: 10.1038/178446a0.

[3] C. L. Cowan et al. "Detection of the free neutrino: A Confirmation". In: *Science* 124 (1956), pp. 103–104. DOI: 10.1126/science.124.3212.103.

[4] Carl D. Anderson. "The Positive Electron". In: *Phys. Rev.* 43 (6 Mar. 1933), pp. 491–494. DOI: 10.1103/PhysRev.43.491. URL: https://link.aps.org/doi/10.1103/PhysRev.43.491.

[5] S. H. Neddermeyer and C. D. Anderson. "Note on the Nature of Cosmic Ray Particles". In: *Phys. Rev.* 51 (1937), pp. 884–886. DOI: 10.1103/PhysRev.51.884.

[6] M. Gell-Mann. "A schematic model of baryons and mesons". In: *Physics Letters* 8.3 (1964), pp. 214–215. ISSN: 0031-9163. DOI: http://dx.doi.org/10.1016/S0031-9163(64)92001-3. URL: http://www.sciencedirect.com/science/article/pii/S0031916364920013.

[7] M. Breidenbach et al. "Observed Behavior of Highly Inelastic Electron-Proton Scattering". In: *Phys. Rev. Lett.* 23 (16 Oct. 1969), pp. 935–939. DOI: 10.1103/PhysRevLett.23.935. URL: https://link.aps.org/doi/10.1103/PhysRevLett.23.935.

[8] Guido Altarelli. "A QCD primer". In: *AIP Conf. Proc.* 631 (2002), pp. 70–111. DOI: 10.1063/1.1513677. arXiv: hep-ph/0204179 [hep-ph].

[9] Steven Weinberg. *The quantum theory of fields, Vol. I*. Cambridge University Press. ISBN: 0521550017.

[10] Willis E. Lamb and Robert C. Retherford. "Fine Structure of the Hydrogen Atom by a Microwave Method". In: *Phys. Rev.* 72 (3 Aug. 1947), pp. 241–243. DOI: 10.1103/PhysRev.72.241. URL: https://link.aps.org/doi/10.1103/PhysRev.72.241.

[11] Tristan Hübsch. *Advanced concepts in particle and field theory*. Cambridge University Press, pp. 135–136.

[12] Hideki YUKAWA. "On the Interaction of Elementary Particles. I". In: *Proceedings of the Physico-Mathematical Society of Japan. 3rd Series* 17 (1935), pp. 48–57. DOI: 10.11429/ppmsj1919.17.0_48.

[13] O. W. Greenberg. "Spin and Unitary-Spin Independence in a Paraquark Model of Baryons and Mesons". In: *Phys. Rev. Lett.* 13 (20 Nov. 1964), pp. 598–602. DOI: 10.1103/PhysRevLett.13.598. URL: https://link.aps.org/doi/10.1103/PhysRevLett.13.598.

[14] S. L. Glashow, J. Iliopoulos, and L. Maiani. "Weak Interactions with Lepton-Hadron Symmetry". In: *Phys. Rev. D* 2 (7 Oct. 1970), pp. 1285–1292. DOI: 10.1103/PhysRevD.2.1285. URL: https://link.aps.org/doi/10.1103/PhysRevD.2.1285.

[15] Makoto Kobayashi and Toshihide Maskawa. "CP Violation in the Renormalizable Theory of Weak Interaction". In: *Prog. Theor. Phys.* 49 (1973), pp. 652–657. DOI: 10.1143/PTP.49.652.

[16] D. P. Barber et al. "Discovery of Three-Jet Events and a Test of Quantum Chromodynamics at PETRA". In: *Phys. Rev. Lett.* 43 (12 Sept. 1979), pp. 830–833. DOI: 10.1103/PhysRevLett.43.830. URL: https://link.aps.org/doi/10.1103/PhysRevLett.43.830.

[17] C. S. Wu et al. “Experimental Test of Parity Conservation in Beta Decay”. In: *Phys. Rev.* 105 (4 Feb. 1957), pp. 1413–1415. DOI: 10.1103/PhysRev.105.1413. URL: https://link.aps.org/doi/10.1103/PhysRev.105.1413.

[18] J. H. Christenson et al. “Evidence for the 2π Decay of the K_2^0 Meson”. In: *Phys. Rev. Lett.* 13 (4 July 1964), pp. 138–140. DOI: 10.1103/PhysRevLett.13.138. URL: https://link.aps.org/doi/10.1103/PhysRevLett.13.138.

[19] Emmy Noether. “Invariant variation problems”. In: *Transport Theory and Statistical Physics* 1.3 (1971), pp. 186–207. DOI: 10.1080/00411457108231446. eprint: http://dx.doi.org/10.1080/00411457108231446. URL: http://dx.doi.org/10.1080/00411457108231446.

[20] Lewis H. Ryder. *Quantum Field Theory, Second Edition*. Cambridge University Press, Chapter 9.

[21] F. Englert and R. Brout. “Broken Symmetry and the Mass of Gauge Vector Mesons”. In: *Phys. Rev. Lett.* 13 (9 Aug. 1964), pp. 321–323. DOI: 10.1103/PhysRevLett.13.321. URL: https://link.aps.org/doi/10.1103/PhysRevLett.13.321.

[22] Peter W. Higgs. “Broken Symmetries and the Masses of Gauge Bosons”. In: *Phys. Rev. Lett.* 13 (16 Oct. 1964), pp. 508–509. DOI: 10.1103/PhysRevLett.13.508. URL: https://link.aps.org/doi/10.1103/PhysRevLett.13.508.

[23] G. S. Guralnik, C. R. Hagen, and T. W. B. Kibble. “Global Conservation Laws and Massless Particles”. In: *Phys. Rev. Lett.* 13 (20 Nov. 1964), pp. 585–587. DOI: 10.1103/PhysRevLett.13.585. URL: https://link.aps.org/doi/10.1103/PhysRevLett.13.585.

[24] Steven Weinberg. “A Model of Leptons”. In: *Phys. Rev. Lett.* 19 (21 Nov. 1967), pp. 1264–1266. DOI: 10.1103/PhysRevLett.19.1264. URL: https://link.aps.org/doi/10.1103/PhysRevLett.19.1264.

[25] S. L. Glashow. “Partial Symmetries of Weak Interactions”. In: *Nucl. Phys.* 22 (1961), pp. 579–588. DOI: 10.1016/0029-5582(61)90469-2.

[26] Abdus Salam. “Weak and Electromagnetic Interactions”. In: *Conf. Proc.* C680519 (1968), pp. 367–377.

[27] Alessandro De Angelis and Mario Joao Martins Pimenta. *Introduction to particle and astroparticle physics*. Springer.

[28] Lincoln Wolfenstein. “Parametrization of the Kobayashi-Maskawa Matrix”. In: *Phys. Rev. Lett.* 51 (1983), p. 1945. DOI: 10.1103/PhysRevLett.51.1945.

[29] Peter Skands. “Introduction to QCD”. In: *Proceedings, Theoretical Advanced Study Institute in Elementary Particle Physics: Searching for New Physics at Small and Large Scales (TASI 2012): Boulder, Colorado, June 4-29, 2012*. 2013, pp. 341–420. DOI: 10.1142/9789814525220_0008. arXiv: 1207.2389 [hep-ph]. URL: https://inspirehep.net/record/1121892/files/arXiv:1207.2389.pdf.

[30] Wikipedia. *The Standard Model of particle physics*. URL: https://en.wikipedia.org/wiki/Standard_Model.

[31] Y. Fukuda et al. “Evidence for oscillation of atmospheric neutrinos”. In: *Phys. Rev. Lett.* 81 (1998), pp. 1562–1567. DOI: 10.1103/PhysRevLett.81.1562. arXiv: hep-ex/9807003 [hep-ex].

[32] Y. Fukuda et al. “Measurement of a small atmospheric muon-neutrino / electron-neutrino ratio”. In: *Phys. Lett.* B433 (1998), pp. 9–18. DOI: 10.1016/S0370-2693(98)00476-6. arXiv: hep-ex/9803006 [hep-ex].

[33] Y. Fukuda et al. “Study of the atmospheric neutrino flux in the multi-GeV energy range”. In: *Phys. Lett.* B436 (1998), pp. 33–41. DOI: 10.1016/S0370-2693(98)00876-4. arXiv: hep-ex/9805006 [hep-ex].

[34] SNO Collaboration. “Measurement of the Rate of $\nu_e + d \rightarrow p + p + e^-$ Interactions Produced by ^8B Solar Neutrinos at the Sudbury Neutrino Observatory”. In: *Phys. Rev. Lett.* 87 (7 July 2001), p. 071301. DOI: 10.1103/PhysRevLett.87.071301. URL: https://link.aps.org/doi/10.1103/PhysRevLett.87.071301.

[35] C. Patrignani et al. “Review of Particle Physics”. In: *Chin. Phys.* C40.10 (2016), Chap. 10. DOI: 10.1088/1674-1137/40/10/100001.

[36] M. L. Perl et al. "Evidence for Anomalous Lepton Production in $e^+ - e^-$ Annihilation". In: *Phys. Rev. Lett.* 35 (22 Dec. 1975), pp. 1489–1492. DOI: 10.1103/PhysRevLett.35.1489. URL: https://link.aps.org/doi/10.1103/PhysRevLett.35.1489.

[37] S. W. Herb et al. "Observation of a Dimuon Resonance at 9.5-GeV in 400-GeV Proton-Nucleus Collisions". In: *Phys. Rev. Lett.* 39 (1977), pp. 252–255. DOI: 10.1103/PhysRevLett.39.252.

[38] F. J. Hasert et al. "Observation of Neutrino Like Interactions Without Muon Or Electron in the Gargamelle Neutrino Experiment". In: *Phys. Lett.* 46B (1973), pp. 138–140. DOI: 10.1016/0370-2693(73)90499-1.

[39] G. Arnison et al. "Experimental observation of isolated large transverse energy electrons with associated missing energy at $\sqrt{s}$=540 GeV". In: *Physics Letters B* 122.1 (1983), pp. 103–116. ISSN: 0370-2693. DOI: http://dx.doi.org/10.1016/0370-2693(83)91177-2. URL: http://www.sciencedirect.com/science/article/pii/0370269383911772.

[40] M. Banner et al. "Observation of single isolated electrons of high transverse momentum in events with missing transverse energy at the CERN pp collider". In: *Physics Letters B* 122.5 (1983), pp. 476–485. ISSN: 0370-2693. DOI: http://dx.doi.org/10.1016/0370-2693(83)91605-2. URL: http://www.sciencedirect.com/science/article/pii/0370269383916052.

[41] J. -E. Augustin et al. "Discovery of a Narrow Resonance in e^+e^- Annihilation". In: *Phys. Rev. Lett.* 33 (23 Dec. 1974), pp. 1406–1408. DOI: 10.1103/PhysRevLett.33.1406. URL: https://link.aps.org/doi/10.1103/PhysRevLett.33.1406.

[42] J. J. Aubert et al. "Experimental Observation of a Heavy Particle J". In: *Phys. Rev. Lett.* 33 (23 Dec. 1974), pp. 1404–1406. DOI: 10.1103/PhysRevLett.33.1404. URL: https://link.aps.org/doi/10.1103/PhysRevLett.33.1404.

[43] CDF Collaboration. "Observation of Top Quark Production in $\overline{p}p$ Collisions with the Collider Detector at Fermilab". In: *Phys. Rev. Lett.* 74 (14 Apr. 1995), pp. 2626–2631. DOI: 10.1103/PhysRevLett.74.2626. URL: https://link.aps.org/doi/10.1103/PhysRevLett.74.2626.

[44] D0 Collaboration. "Observation of the Top Quark". In: *Phys. Rev. Lett.* 74 (14 Apr. 1995), pp. 2632–2637. DOI: 10.1103/PhysRevLett.74.2632. URL: https://link.aps.org/doi/10.1103/PhysRevLett.74.2632.

[45] K. Kodama et al. "Observation of tau neutrino interactions". In: *Phys. Lett.* B504 (2001), pp. 218–224. DOI: 10.1016/S0370-2693(01)00307-0. arXiv: hep-ex/0012035 [hep-ex].

[46] ATLAS Collaboration. "Observation of a new particle in the search for the Standard Model Higgs boson with the ATLAS detector at the LHC". In: *Phys. Lett. B* 716 (2012), pp. 1–29. DOI: 10.1016/j.physletb.2012.08.020. arXiv: 1207.7214 [hep-ex].

[47] CMS Collaboration. "Observation of a new boson at a mass of 125 GeV with the CMS experiment at the LHC". In: *Phys. Lett. B* 716 (2012), pp. 30–61. DOI: 10.1016/j.physletb.2012.08.021. arXiv: 1207.7235 [hep-ex].

[48] T. Aaltonen et al. "Combination of the top-quark mass measurements from the Tevatron collider". In: *Phys. Rev.* D86 (2012), p. 092003. DOI: 10.1103/PhysRevD.86.092003. arXiv: 1207.1069 [hep-ex].

[49] T. Aaltonen et al. "Higgs Boson Studies at the Tevatron". In: *Phys. Rev.* D88.5 (2013), p. 052014. DOI: 10.1103/PhysRevD.88.052014. arXiv: 1303.6346 [hep-ex].

[50] Georges Aad et al. "Evidence for the spin-0 nature of the Higgs boson using ATLAS data". In: *Phys. Lett.* B726 (2013), pp. 120–144. DOI: 10.1016/j.physletb.2013.08.026. arXiv: 1307.1432 [hep-ex].

[51] *Properties of the Higgs-like boson in the decay H to ZZ to 4l in pp collisions at sqrt s =7 and 8 TeV*. Tech. rep. CMS-PAS-HIG-13-002. Geneva: CERN, 2013. URL: http://cds.cern.ch/record/1523767.

[52] *Evidence for a particle decaying to W+W- in the fully leptonic final state in a standard model Higgs boson search in pp collisions at the LHC*. Tech. rep. CMS-PAS-HIG-13-003. Geneva: CERN, 2013. URL: http://cds.cern.ch/record/1523673.

[53] Georges Aad et al. "Measurement of the Higgs boson mass from the $H \to \gamma\gamma$ and $H \to ZZ^* \to 4\ell$ channels with the ATLAS detector using 25 fb^{-1} of pp collision data". In: *Phys. Rev.* D90.5 (2014), p. 052004. DOI: 10.1103/PhysRevD.90.052004. arXiv: 1406.3827 [hep-ex].

[54] Georges Aad et al. "Combined Measurement of the Higgs Boson Mass in pp Collisions at $\sqrt{s} = 7$ and 8 TeV with the ATLAS and CMS Experiments". In: *Phys. Rev. Lett.* 114 (2015), p. 191803. DOI: 10.1103/PhysRevLett.114.191803. arXiv: 1503.07589 [hep-ex].

[55] Georges Aad et al. "Measurements of the Higgs boson production and decay rates and constraints on its couplings from a combined ATLAS and CMS analysis of the LHC pp collision data at $\sqrt{s} = 7$ and 8 TeV". In: *JHEP* 08 (2016), p. 045. DOI: 10.1007/JHEP08(2016)045. arXiv: 1606.02266 [hep-ex].

[56] D. de Florian et al. "Handbook of LHC Higgs Cross Sections: 4. Deciphering the Nature of the Higgs Sector". In: (2016). arXiv: 1610.07922 [hep-ph].

[57] William J. Marciano, Cen Zhang, and Scott Willenbrock. "Higgs Decay to Two Photons". In: *Phys. Rev.* D85 (2012), p. 013002. DOI: 10.1103/PhysRevD.85.013002. arXiv: 1109.5304 [hep-ph].

[58] D. I. Kazakov. "Beyond the standard model: In search of supersymmetry". In: *2000 European School of high-energy physics, Caramulo, Portugal, 20 Aug-2 Sep 2000: Proceedings*. 2000, pp. 125–199. arXiv: hep-ph/0012288 [hep-ph]. URL: http://alice.cern.ch/format/showfull?sysnb=2235897.

[59] Giuseppe Degrassi et al. "Higgs mass and vacuum stability in the Standard Model at NNLO". In: *JHEP* 08 (2012), p. 098. DOI: 10.1007/JHEP08(2012)098. arXiv: 1205.6497 [hep-ph].

[60] G. Hinshaw et al. "Nine-year Wilkinson Microwave Anisotropy Probe (WMAP) Observations: Cosmological Parameter Results". In: *The Astrophysical Journal Supplement Series* 208.2 (2013), p. 19. URL: http://stacks.iop.org/0067-0049/208/i=2/a=19.

[61] C. L. Bennett and al. "Nine-year Wilkinson Microwave Anisotropy Probe (WMAP) Observations: Final Maps and Results". In: 208, 20 (Oct. 2013), p. 20. DOI: 10.1088/0067-0049/208/2/20. eprint: 1212.5225.

[62] Juan GarcÃa-Bellido. "Massive Primordial Black Holes as Dark Matter and their detection with Gravitational Waves". In: *J. Phys. Conf. Ser.* 840.1 (2017), p. 012032. DOI: 10.1088/1742-6596/840/1/012032. arXiv: 1702.08275 [astro-ph.CO].

[63] Wikipedia. *Massive compact halo object*. URL: https://en.wikipedia.org/wiki/Massive_compact_halo_object.

[64] H. Poincare. "The Milky Way and the Theory of Gases". In: *Popular Astronomy* 14 (Oct. 1906), pp. 475–488.

[65] Lord Kelvin. *Baltimore lectures on molecular dynamics and the wave theory of light*. URL: https://archive.org/details/baltimorelecture00kelvia.

[66] F. Zwicky. "Die Rotverschiebung von extragalaktischen Nebeln". In: *Helv. Phys. Acta* 6 (1933). [Gen. Rel. Grav.41,207(2009)], pp. 110–127. DOI: 10.1007/s10714-008-0707-4.

[67] F. Zwicky. "On the Masses of Nebulae and of Clusters of Nebulae". In: *Astrophys. J.* 86 (1937), pp. 217–246. DOI: 10.1086/143864.

[68] Francis G. Pease. "The Rotation and Radial Velocity of the Spiral Nebula N. G. C. 4594". In: *Proceedings of the National Academy of Sciences of the United States of America* 2.9 (1916), pp. 517–521. ISSN: 00278424. URL: http://www.jstor.org/stable/83806.

[69] Wikipedia. *Virial theorem*. URL: https://en.wikipedia.org/wiki/Virial_theorem.

[70] Wikipedia. *Kapteyn system*. URL: https://en.wikipedia.org/wiki/Kapteyn%5C%27s_Star.

[71] Sinclair Smith. "The mass of the Virgo cluster". In: *Astrophysical Journal* 83 (Jan. 1936), p. 23. DOI: 10.1086/143697. URL: http://adsabs.harvard.edu/abs/1936ApJ....83...23S.

[72] Horace W. Babcock. "Rotation of the Andromeda Nebula". In: *Lick Observatory bulletin* 498 (1939). DOI: 10.5479/ADS/bib/1939LicOB.19.41B.

[73] Vera C. Rubin and W. Kent Ford Jr. "Rotation of the Andromeda Nebula from a Spectroscopic Survey of Emission Regions". In: *Astrophys. J.* 159 (1970), pp. 379–403. DOI: 10.1086/150317.

[74] Wikipedia. *Modified Newtonian dynamics*. URL: https://en.wikipedia.org/wiki/Modified_Newtonian_dynamics.

[75] Katherine Freese. "Review of Observational Evidence for Dark Matter in the Universe and in upcoming searches for Dark Stars". In: *EAS Publ. Ser.* 36 (2009), pp. 113–126. DOI: 10.1051/eas/0936016. arXiv: 0812.4005 [astro-ph].

[76] P. A. R. Ade et al. "Planck 2015 results. XIII. Cosmological parameters". In: *Astron. Astrophys.* 594 (2016), A13. DOI: 10.1051/0004-6361/201525830. arXiv: 1502.01589 [astro-ph.CO].

[77] NASA. *Bullet cluster*. URL: https://www.nasa.gov/vision/universe/starsgalaxies/dark_matter_proven.html.

[78] NASA. *Evolution of the Universe*. URL: https://www.nasa.gov/centers/goddard/news/features/2010/universe-first-moments.html.

[79] Edward W. Kolb and Michael S. Turner. *The Early Universe*. Addison-Wesley, pp. 72–74. ISBN: 0-201-62674-8.

[80] Scott Dodelson. *Modern cosmology*. Elsevier.

[81] Graciela Gelmini and Paolo Gondolo. "DM Production Mechanisms". In: (2010). arXiv: 1009.3690 [astro-ph.CO].

[82] Giorgio Arcadi et al. "The Waning of the WIMP? A Review of Models, Searches, and Constraints". In: (2017). arXiv: 1703.07364 [hep-ph].

[83] Paolo Gondolo and Graciela Gelmini. "Cosmic abundances of stable particles: Improved analysis". In: *Nucl. Phys.* B360 (1991), pp. 145–179. DOI: 10.1016/0550-3213(91)90438-4.

[84] E. Aprile et al. "First Dark Matter Search Results from the XENON1T Experiment". In: (2017). arXiv: 1705.06655 [astro-ph.CO].

[85] P. Agnes et al. "Results from the first use of low radioactivity argon in a dark matter search". In: *Phys. Rev.* D93.8 (2016). [Addendum: Phys. Rev.D95,no.6,069901(2017)], p. 081101. DOI: 10.1103/PhysRevD.93.081101, 10.1103/PhysRevD.95.069901. arXiv: 1510.00702 [astro-ph.CO].

[86] D. S. Akerib et al. "Results from a search for dark matter in the complete LUX exposure". In: *Phys. Rev. Lett.* 118.2 (2017), p. 021303. DOI: 10.1103/PhysRevLett.118.021303. arXiv: 1608.07648 [astro-ph.CO].

[87] Andi Tan et al. "Dark Matter Results from First 98.7 Days of Data from the PandaX-II Experiment". In: *Phys. Rev. Lett.* 117.12 (2016), p. 121303. DOI: 10.1103/PhysRevLett.117.121303. arXiv: 1607.07400 [hep-ex].

[88] J. R. T. de Mello Neto et al. "The DAMIC dark matter experiment". In: *PoS* ICRC2015 (2016), p. 1221. arXiv: 1510.02126 [physics.ins-det].

[89] E. Armengaud et al. "Constraints on low-mass WIMPs from the EDELWEISS-III dark matter search". In: *JCAP* 1605.05 (2016), p. 019. DOI: 10.1088/1475-7516/2016/05/019. arXiv: 1603.05120 [astro-ph.CO].

[90] SuperCDMS Collaboration. "New Results from the Search for Low-Mass Weakly Interacting Massive Particles with the CDMS Low Ionization Threshold Experiment". In: *Phys. Rev. Lett.* 116.7 (2016), p. 071301. DOI: 10.1103/PhysRevLett.116.071301. arXiv: 1509.02448 [astro-ph.CO].

[91] C. Amole et al. "Dark Matter Search Results from the PICO-60 C_3F_8 Bubble Chamber". In: (2017). arXiv: 1702.07666 [astro-ph.CO].

[92] E. Aprile et al. "XENON100 Dark Matter Results from a Combination of 477 Live Days". In: *Phys. Rev.* D94.12 (2016), p. 122001. DOI: 10.1103/PhysRevD.94.122001. arXiv: 1609.06154 [astro-ph.CO].

[93] M. Ajello et al. "Fermi-LAT Observations of High-Energy γ-Ray Emission Toward the Galactic Center". In: *Astrophys. J.* 819.1 (2016), p. 44. DOI: 10.3847/0004-637X/819/1/44. arXiv: 1511.02938 [astro-ph.HE].

[94] Wikipedia. *Stellar kinematics*. URL: https://en.wikipedia.org/wiki/Stellar_kinematics.

[95] Julio F. Navarro, Carlos S. Frenk, and Simon D. M. White. "A Universal density profile from hierarchical clustering". In: *Astrophys. J.* 490 (1997), pp. 493–508. DOI: 10.1086/304888. arXiv: astro-ph/9611107 [astro-ph].

[96] H. Abdallah et al. "Search for dark matter annihilations towards the inner Galactic halo from 10 years of observations with H.E.S.S". In: *Phys. Rev. Lett.* 117.11 (2016), p. 111301. DOI: 10.1103/PhysRevLett.117.111301. arXiv: 1607.08142 [astro-ph.HE].

[97] Volker Springel et al. "A blueprint for detecting supersymmetric dark matter in the Galactic halo". In: (2008). arXiv: 0809.0894 [astro-ph].

[98] PAMELA collaboration. "A statistical procedure for the identification of positrons in the PAMELA experiment". In: *Astroparticle Physics* 34 (Aug. 2010), 1–11. DOI: {10.1016/j.astropartphys.2010.04.007}. arXiv: 1001.3522 [astro-ph.HE].

[99] AMS Collaboration. "Electron and Positron Fluxes in Primary Cosmic Rays Measured with the Alpha Magnetic Spectrometer on the International Space Station". In: *Phys. Rev. Lett.* 113 (12 Sept. 2014), p. 121102. DOI: 10.1103/PhysRevLett.113.121102. URL: https://link.aps.org/doi/10.1103/PhysRevLett.113.121102.

[100] Maxim Laletin. *Can Dark Matter Annihilations Explain the AMS-02 Positron Data?* Mar. 2017. URL: http://moriond.in2p3.fr/VHEPU/2017/transparencies/3_tuesday/2_afternoon/3_laletin.pdf.

[101] AMS Collaboration. "First Result from the Alpha Magnetic Spectrometer on the International Space Station: Precision Measurement of the Positron Fraction in Primary Cosmic Rays of 0.5-350 GeV". In: *Phys. Rev. Lett.* 110 (14 Apr. 2013), p. 141102. DOI: 10.1103/PhysRevLett.110.141102. URL: https://link.aps.org/doi/10.1103/PhysRevLett.110.141102.

[102] Giorgio Busoni et al. "On the Validity of the Effective Field Theory for Dark Matter Searches at the LHC". In: *Phys. Lett.* B728 (2014), pp. 412–421. DOI: 10.1016/j.physletb.2013.11.069. arXiv: 1307.2253 [hep-ph].

[103] Giorgio Busoni et al. "On the Validity of the Effective Field Theory for Dark Matter Searches at the LHC, Part II: Complete Analysis for the s-channel". In: *JCAP* 1406 (2014), p. 060. DOI: 10.1088/1475-7516/2014/06/060. arXiv: 1402.1275 [hep-ph].

[104] Giorgio Busoni et al. "On the Validity of the Effective Field Theory for Dark Matter Searches at the LHC Part III: Analysis for the t-channel". In: *JCAP* 1409 (2014), p. 022. DOI: 10.1088/1475-7516/2014/09/022. arXiv: 1405.3101 [hep-ph].

[105] Georges Aad et al. "Constraints on new phenomena via Higgs boson couplings and invisible decays with the ATLAS detector". In: *JHEP* 11 (2015), p. 206. DOI: 10.1007/JHEP11(2015)206. arXiv: 1509.00672 [hep-ex].

[106] Vardan Khachatryan et al. "Searches for invisible decays of the Higgs boson in pp collisions at sqrt(s) = 7, 8, and 13 TeV". In: *JHEP* 02 (2017), p. 135. DOI: 10.1007/JHEP02(2017)135. arXiv: 1610.09218 [hep-ex].

[107] Daniel Abercrombie et al. "Dark Matter Benchmark Models for Early LHC Run-2 Searches: Report of the ATLAS/CMS Dark Matter Forum". In: (2015). arXiv: 1507.00966 [hep-ex].

[108] Stefan von Buddenbrock et al. "Phenomenological signatures of additional scalar bosons at the LHC". In: *Eur. Phys. J. C* 76.10 (2016), p. 580. DOI: 10.1140/epjc/s10052-016-4435-8. arXiv: 1606.01674 [hep-ph].

[109] Linda Carpenter et al. "Mono-Higgs-boson: A new collider probe of dark matter". In: *Phys. Rev. D* 89.7 (2014), p. 075017. DOI: 10.1103/PhysRevD.89.075017. arXiv: 1312.2592 [hep-ph].

[110] Asher Berlin, Tongyan Lin, and Lian-Tao Wang. "Mono-Higgs detection of dark matter at the LHC". In: *JHEP* 06 (2014), p. 078. DOI: 10.1007/JHEP06(2014)078. arXiv: 1402.7074 [hep-ph].

[111] G. C. Branco et al. "Theory and phenomenology of two-Higgs-doublet models". In: *Phys. Rept.* 516 (2012), pp. 1–102. DOI: 10.1016/j.physrep.2012.02.002. arXiv: 1106.0034 [hep-ph].

[112] Wan-Lei Guo and Yue-Liang Wu. "The real singlet scalar dark matter model". In: *JHEP* 10 (2010), p. 083. DOI: 10.1007/JHEP10(2010)083. arXiv: 1006.2518 [hep-ph].

The LHC and the ATLAS experiment

Contents

2.1 The Large Hadron Collider . . . 45
2.1.1 Beam injection complex . . . 47
2.1.2 Luminosity . . . 47
2.1.3 Expected number of interactions and pileup . . . 49
2.2 ATLAS detector . . . 49
2.2.1 Magnets system . . . 52
2.2.2 Inner detector . . . 53
2.2.3 Calorimetric system . . . 54
2.2.4 Muon spectrometer . . . 57
2.2.5 Trigger . . . 58

2.1 The Large Hadron Collider

The Large Hadron Collider (LHC) [1] is a two-ring-superconducting-hadron accelerator installed in a 26.7 km tunnel originally constructed for the Large Electron-Positron collider (LEP) at CERN. It is designed to collide proton beams at a maximum center-of-mass energy of 14 TeV with a nominal instantaneous luminosity of $10^{34}\mathrm{cm}^{-2}\mathrm{s}^{-1}$. Additionally, ion beams are also accelerated by the LHC at energies up to 2.8 TeV and a maximum instantaneous luminosity of $\approx 10^{27}\mathrm{cm}^{-2}\mathrm{s}^{-1}$. The tunnel is composed of eight straight sections and eight arcs and lies between 45 m and 170 m below the surface on a geological plane inclined at 1.4% towards the Léman lake. It provides data for two large experiments searching for general new high energy phenomena, ATLAS [2] and CMS [3]. Two other large detectors benefit from LHC beams to test more specific physics: LHCb [4] to study physics of the bottom quark via the decays of the $B-$mesons; and ALICE [5] to investigate quarks and gluons behaviour at temperatures five order of magnitude larger than the one at the Sun core (quark-gluon plasma). Three smaller experiments are installed at the LHC:

- The TOTEM experiment [6] is devoted to measuring precisely the total proton-proton interaction cross-section as well as diffractive proton-proton physics.It is placed on both sides of the CMS interaction point.
- The LHCf experiment [7] devoted to studying large energy cosmic-rays physics. Particles emitted in the forward region of the proton beam are used to simulate such cosmic particles. It is placed on both sides of the ATLAS interaction point, 140 meters away.
- The MoEDAL experiment [8] is devoted to the search for significant signals of magnetic monopoles.

From the LEP era, two underground and surface experimental halls were available (Point 2 and 8) where the ALICE and LHCb experiments have been installed, respectively. In addition, two more access points were added (Point 1 and 5) in order to accommodate detector and services for the ATLAS and CMS

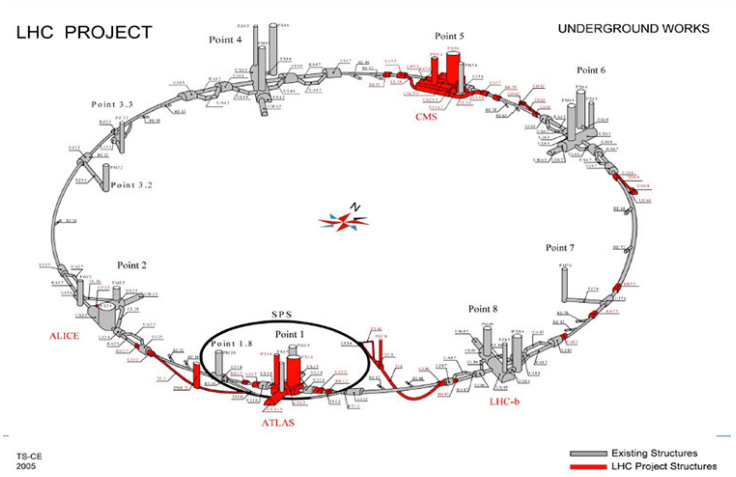


Figure 2.1: LHC layout with the positioning of the four experiments and the structure of the SPS+LHC acceleration system.

experiments. Other four access points are available, although they are not equipped in order to prevent unnecessary disruption of the beams. However, they can be used to accomplish technical maintenance of the LHC ring.

The synchrotron radiation is not important in a proton machine such as the LHC, which would ideally have longer arcs and shorter straight sections for the same circumference. However, the current configuration was accepted to reduce the LHC costs by reusing the LEP tunnel. In the LHC, beams are accelerated in a structure of two concentric rings, each beam rotating in opposite directions. This feature is required for particle-particle colliders, unlike particle-antiparticle colliders that can have both beams sharing the same phase space in a single ring. However, the tunnel arcs have an internal diameter of 3.7 m, which makes it extremely difficult to install two completely separate proton rings. This lead to the adoption of super-conducting magnets with double boring.

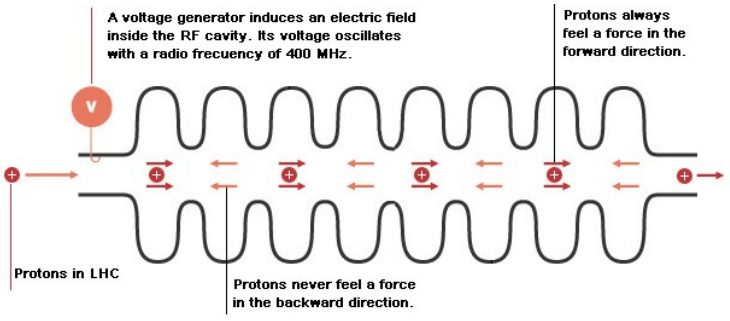


Figure 2.2: Schema of the acceleration of a proton inside the RF cavities [9]

The LHC accelerates proton beams to large energies and provides enough bending power to keep proton beams rotating within the double-bore magnet ring. Bending power is provided by the magnetic field injected into the arcs of the accelerator. However, the adoption of super-conducting magnets with an inserted double ring implies that both rings are magnetically coupled, which disturbs the bending of the two counter-rotating proton beams which requires two opposed magnetic fields in each beam ring. This issue is solved by using magnetic dipoles. These dipole magnets are developed to transport the protons within the ring circumference, providing the necessary acceleration to curve the beam. For the whole LHC, 1232 main dipoles made of NbTi Rutherford superconducting cables cooled down with superfluid helium to 1.9 K provide a nominal magnetic field of 8.33 T. The acceleration of the proton beams is performed in the straight sections of the LHC, where radiofrequency (RF) cavities are included. This acceleration is achieved via a varying electromagnetic field, provided by the RF power supply. The frequency of the field is 400 MHz and is reflected by the walls of the RF cavity. Cavities are built so that

the electromagnetic waves add up resonantly so that the proton beam is just accelerated in the forward direction. There are 16 RF cavities in the LHC, all of them placed at the Point 4, which are cooled down to 4.5 K [9]. Finally, to increase the rate of interactions when opposite bunches cross each other at the four interaction points of the LHC (ATLAS, CMS, LHCb, ALICE), beams are further concentrated by a system of 392 quadrupoles.

2.1.1 Beam injection complex

The LHC is the final accelerator of the proton bunches before collision. Previously, proton beams have passed through a system of pre-accelerators that adjusted and accelerated the beams prior to the injection in the main LHC ring. Proton source is a gaseous hydrogen ionized by an intense electromagnetic field that allows the separation of protons from electrons. The obtained protons are first accelerated by the LINAC2 linear accelerator up to an energy of 50 MeV. Protons are then injected into the PSB (Proton synchrotron booster) and later to the Proton Synchrotron (PS), which respectively accelerate the protons to 1.4 GeV and 25 GeV. In the PS, the beam is structured in bunches separated by 25 ns according to Run II conditions. The next step is the acceleration by the SPS (Super-Proton-Synchrotron) where beams reach energies up to 450 GeV. Protons are injected in the LHC at Point 1 and Point 8 for the clockwise and counter-clockwise rotating beams respectively.

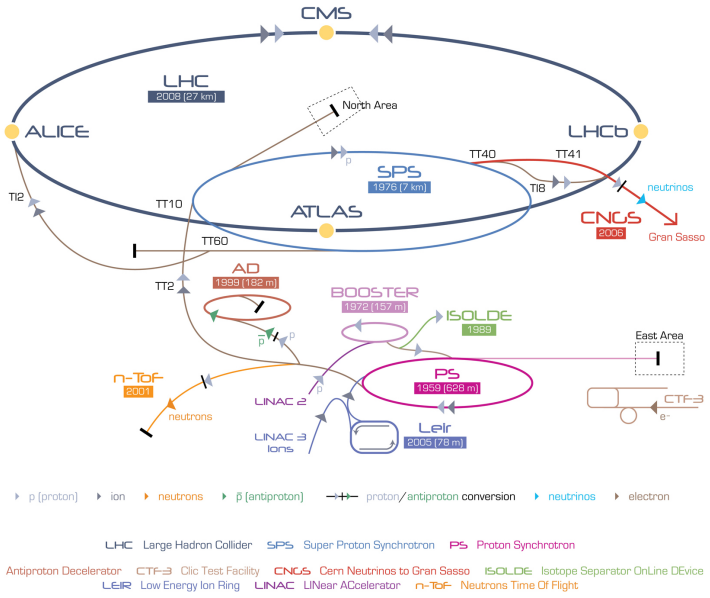


Figure 2.3: CERN acceleration complex [10].

2.1.2 Luminosity

In most LHC searches, the production of large statistics data samples is primordial to have a chance of observing very rare new physics processes. For instance, the discovery of the Higgs boson in the $h \to \gamma\gamma$ decay channel involved the production of few hundreds of bosons that decayed into two photons, which are very unlikely to be produced compared to the $\sim 10^9$ more frequent QCD interactions occurring between protons. Nevertheless, a more detailed study of the Higgs boson requires, among other things, the increase in the final number of events to get larger statistics. The performance of an accelerator is characterized by the energy at which particles are accelerated and by the number of collisions that it provides per unit of time. During Run II, the LHC is operating at a center-of-mass energy of 13 TeV, colliding beams of protons each with 6.5 TeV. Proton beams are composed of 2808 bunches separated 25 ns, each composed of $\sim 1 \times 10^{11}$ protons on average compressed into very small transverse and well defined longitudinal dimensions. Proton-proton collisions occur at the interaction points (IP) where

both beams cross. The number of events per second for a given process is given by:

$$\frac{dN_{\text{process}}}{dt} = L\sigma_{\text{process}} \tag{2.1}$$

where σ_{process} is the process cross-section which represents the probability that such process occurs, and L is the instantaneous luminosity delivered by the LHC, expressed as inverse cross-section units, e.g. $\text{cm}^{-2}\ \text{s}^{-1}$. The luminosity is a parameter that depends on the features of the accelerator, and provides an estimation of the number of collisions. The luminosity depends on several parameters and can be written for a Gaussian beam distribution as:

$$L = \frac{N_b^2 n_b f_{rev} \gamma_r}{4\pi\epsilon_n \beta^*} F \tag{2.2}$$

where:

- N_b is the number of particles per bunch.
- n_b is the number of bunches per beam.
- f_{rev} is the revolution frequency in the accelerator.
- γ_r is the relativistic Lorentz factor $\gamma = 1/\sqrt{1-\beta^2}$ of the beam in the lab frame.
- ϵ_n is the normalized beam transverse emittance. The emittance characterizes the transverse size of the beam at the collision point. A low emittance means that protons are confined in a very small dimension, almost presenting the same momentum.
- β^* is referred as the distance from the interaction point (IP) point at which the beam transverse width is twice as wide as its size at the interaction point. The smaller the β^*, the more squeezed the beam is at the interaction point and therefore the higher is the luminosity.
- F is the geometric reduction factor due to the crossing angle between beams at the IP.

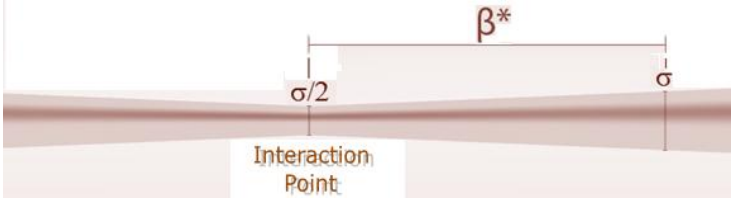


Figure 2.4: Illustration of the β^* parameter in Eq. 2.2 [11].

After the beam introduction, the luminosity is degraded due to the interactions taking place in the different interaction points where the same beams are colliding along time. In addition, protons may interact with residual gases in the beam rings or suffer Coulomb scatterings with other protons in the same bunches (also called Touschek effect [12]) or suffer operating errors (such as sudden beam losses). Taking into account all these interactions, the average lifetime (τ_L) of the LHC beam (estimated as the time that the beam intensity is reduced by a factor of $1/e$) is ~10h [13]. The instantaneous luminosity during beam circulation can be expressed as:

$$L_{\text{int}} = L_0 \tau_L \left[1 - e^{-t/\tau_L}\right] \tag{2.3}$$

where L_0 is the luminosity at the first collision. The total luminosity obtained during stable beam runs can then be estimated by integrating the previous equation:

$$L_{\text{tot}} = \int L_{\text{int}} dt \tag{2.4}$$

Total luminosity provided by the LHC during 2015 and 2016 data taking periods correspond to 42.7 fb^{-1} out of which ATLAS recorded 39.5 fb^{-1} taking into account the experimental efficiency requiring all ATLAS subdetectors to behave as expected. After requiring a full functionality of the different subdetectors, the total size of the dataset collected in 2015-2016 during Run II reduces to 36.1 fb^{-1}. Figures 2.5 present the performance of the LHC during Run I and Run II and the day-by-day luminosity provided by the LHC and collected by ATLAS during the 2015 and 2016 Run II period.

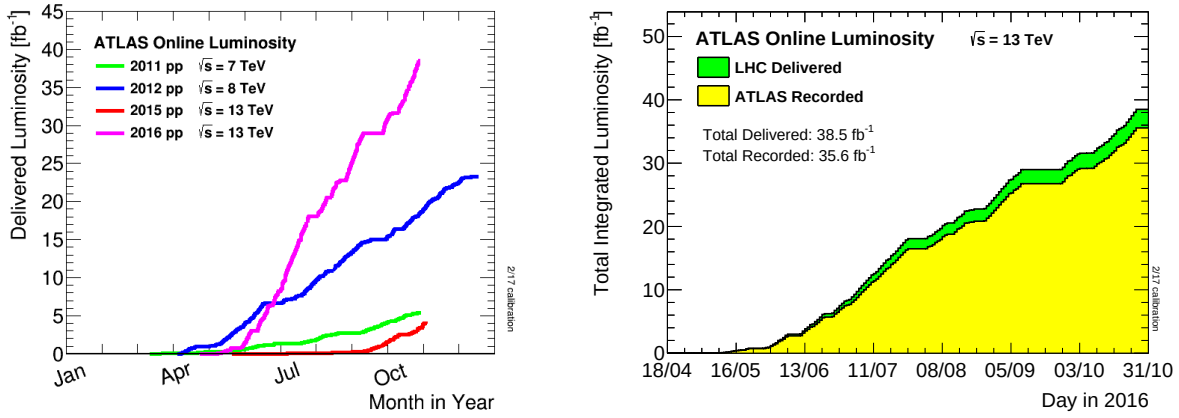


Figure 2.5: Instantaneous luminosity delivered by the LHC for the 2011-2017 period (left) and integrated luminosity provided by the LHC and recorded by ATLAS during 2016 data taking period (right) [14].

2.1.3 Expected number of interactions and pileup

The larger the instantaneous luminosity, the larger the number of pp collisions. However, this increase in luminosity implies that multiple interactions pp collisions may occur inside the same bunch crossing. These interactions then overlap with products of other interactions, either issued from collisions in the same bunch crossing (in-time) or from interactions between remnants of previous bunch-crossings (out-of-time). These multiple interactions are referred to as pileup. Pileup mean contributions to a given event of interest are closely related to the average number of interactions per bunch crossing ($\langle\mu\rangle$). Figure 2.6 presents the number of interactions during Run II 2015 and 2016 data taking. The 2015 period registered $\langle\mu\rangle \sim 14$ while the 2016 period registered $\langle\mu\rangle \sim 25$.

In the future, plans are made to increase the number of collisions by a factor of 10 (to $L \sim 10^{33}\text{cm}^2\text{s}^{-1}$) [15]. This increase in the luminosity implies a much larger pileup magnitude on average. An overall $\langle\mu\rangle \sim 200$ is predicted in such extreme conditions. Current detector performances would be rapidly degraded by this amount of interactions. Hence, upgrades on the different detectors are considered to be able to benefit from this increase of luminosity. Figure 2.7 presents the current schedule to upgrade the HL-LHC in 2024.

2.2 ATLAS detector

The ATLAS (A Toroidal LHC ApparatuS) detector [2] is a multipurpose particle physics detector with approximately forward-backward symmetric cylindrical geometry. It was designed to study the Standard Model physics (m_t, Higgs boson discovery, ...) and to scan for any hint of physics Beyond Standard Model (SUSY, extra dimensions, quantum black holes,..) in the new high energy domain allowed by the LHC. ATLAS uses a right-handed coordinate system with its origin at the nominal interaction point (IP) in the center of the detector. The z-axis is defined along the beam direction while the transverse plane is defined by the x-axis pointing from the nominal IP to the center of the LHC ring and the y-axis pointing upwards. Usually, particles direction is defined in polar coordinates (r, ϕ, θ), where r is the distance

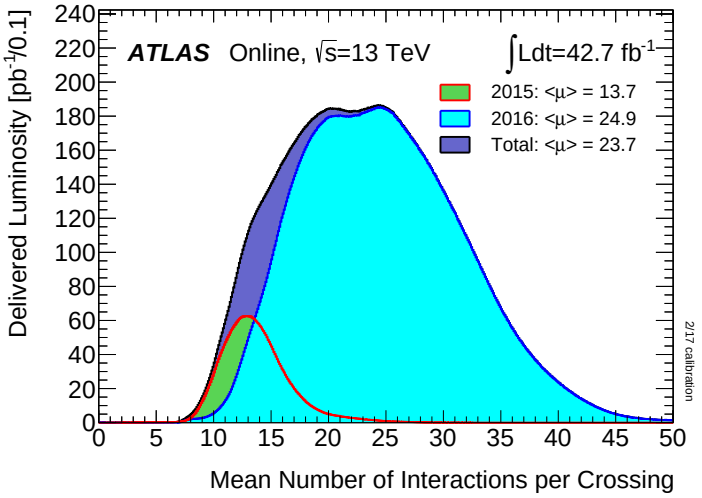


Figure 2.6: Registered number of interactions per bunch crossing during the data taking periods of 2015 and 2016, with pp collisions at $\sqrt{s} = 13$ TeV [14].

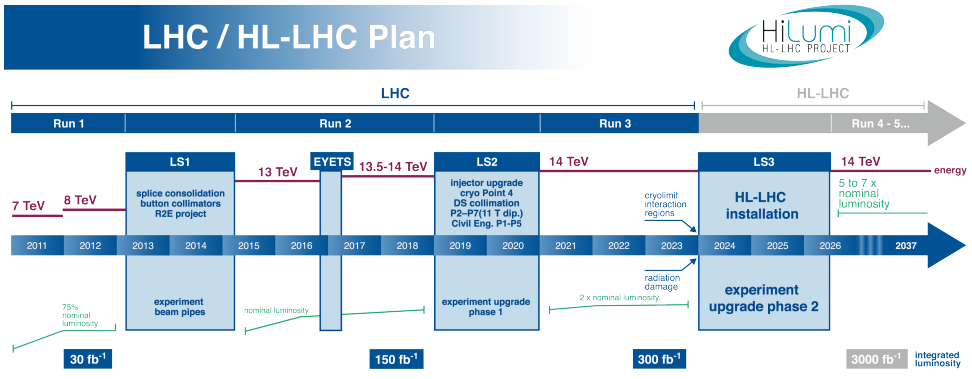


Figure 2.7: Plan of the HL-LHC phase [15].

between the particle and the interaction point, ϕ is the azimuthal angle in the transverse plane around the beam pipe and θ is the polar angle with respect to the z-axis. The pseudorapidity is defined in terms of the polar angle as $\eta = -\ln[\tan(\theta/2)]$.

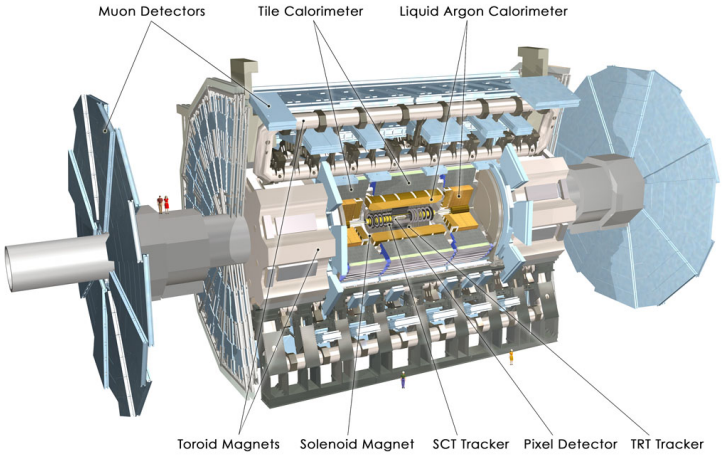


Figure 2.8: Schema of the ATLAS detectors and the different subdetectors [2].

The ATLAS detector is composed of several subsystems. The inner detector (ID) tracking system covers $|\eta| < 2.5$ and consists of a silicon pixel detector, a silicon microstrip detector and a transition radiation tracker (TRT). It allows a precise reconstruction of charged-particle trajectories and of decay vertices of long-lived particles and together with the magnetic field from the surrounding solenoid, it allows the measurement of the momenta of the different charged particles produced by the pp collisions. It also allows to discriminating electrons from charged hadrons thanks to the transition radiation tracker measurements. A lead/liquid-argon (LAr) sampling calorimeter measures the energy and the position of electromagnetic showers (electrons and photons) in the region $|\eta| < 3.2$. It includes a presampler (for $|\eta| < 1.8$) and three high-granularity sampling layers up to $|\eta| < 2.5$. LAr sampling calorimeters with copper and tungsten absorbers are also used to measure hadronic showers in the endcap ($1.5 < |\eta| < 3.2$) and forward ($3.1 < |\eta| < 4.9$) regions, while a steel/scintillator-tile calorimeter measures hadronic showers in the central region ($|\eta| < 1.7$). A thin superconducting solenoid provides up to 2 T of magnetic field surrounding the inner detector and three large superconducting toroids (one barrel and two end-caps) arranged around the calorimeters. The muon spectrometer surrounds the calorimeters and consists of three large superconducting air-core toroid magnets, each with eight coils, a system of precision tracking chambers ($|\eta| < 2.7$), and fast-tracking chambers for triggering ($|\eta| < 2.4$). Reconstructed events are selected by a two-level trigger system. The first-level trigger (L1) is a hardware-based system using information from different subdetectors to reduce the data rate from 40 MHz to 100kHz. The second-level trigger is software-based and uses more precise reconstructed variables to further reject non-interesting data until a rate of 1kHz is achieved and collected on disc [16]. This second level-trigger is usually called high-level trigger (HLT) and, during Run I, it was divided into a Level-2 (L2) trigger and an event filter during LHC Run I. These two farms were merged into a single one during the first long shutdown (LS1) to prepare the data collection to the expected increased rate in Run II.

Particles are produced from pp collisions at the IP and emitted into the fiducial area of the ATLAS detector. ATLAS detector provides discriminant detection power and identification between electrons, photons, muons and products from hadronic processes, leaving wide signals in the different detector subsystems called jets. Figure 2.9 illustrates the typical interaction that each of these particles has in the subsequent ATLAS subdetectors. Protons and neutrons represent the energy deposits left by charged and neutral hadrons respectively. The combined of all signals allow an identification of the various particles together with an estimation of their energy and direction.

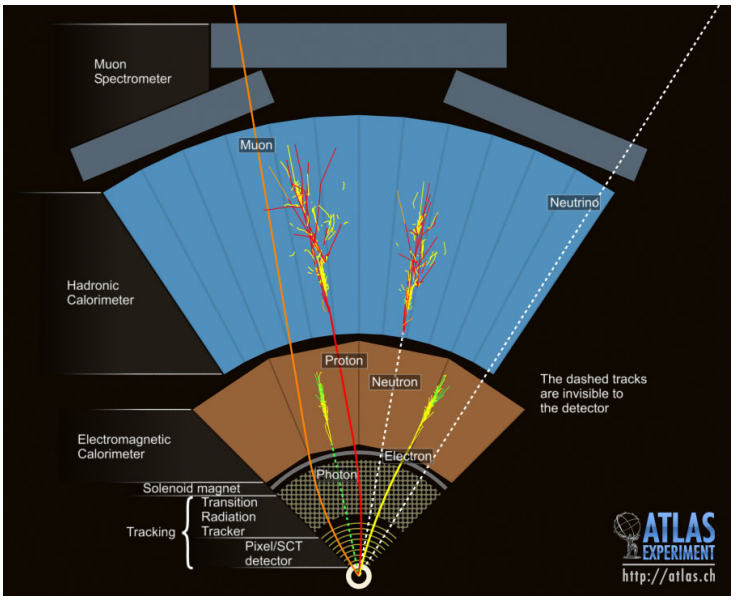


Figure 2.9: Illustration of the energy deposits expected for each measured particle in the ATLAS detector.

2.2.1 Magnets system

The magnet system of ATLAS (Fig. 2.10) is composed of a central solenoid, providing magnetic field to the inner tracking system, and a toroidal system providing magnetic field to the muon spectrometer. The total size of the system is 22 m in diameter and 26m in length:

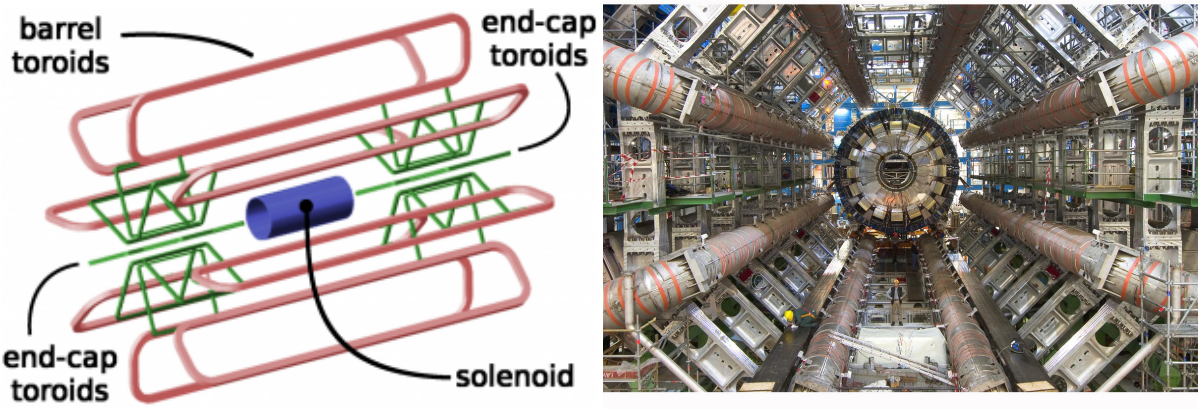


Figure 2.10: Illustration of the magnet system layout (a) and photograph of the final installation of the ATLAS detector (b), where barrel toroids may be observed in the foreground.

Solenoid magnet system: The solenoid system is composed of a single central barrel surrounding the inner detector and providing 2T axial field at a nominal operational current of 7730 kA. To improve object measurements and reduce the rate of interactions upstream the calorimeter, the solenoid layout was optimized to keep the material thickness as low as possible. It consists of a single superconductive coal layer wrapped internally around a support cylinder. The inner and outer diameters of the solenoid are 2.46 m and 2.56 m, and its axial length is 5.8 m.

Toroidal magnet system: The toroidal system consists of a barrel and two end-caps providing a magnetic field to the muon spectrometer in the central region and the end-caps of approximately 0.5 T and 1 T, respectively. The barrel toroid consists of eight coils encased in individual racetrack-shapped vacuum vessels made of stainless-steel which are distributed symmetrically around the

calorimeter. The muon spectrometer is installed in the core and around these vessels. The end-cap toroids are also composed of eight coils placed at both ends of the toroidal barrel and aligned with the central solenoid. Coils are distributed radially and symmetrically around the beam axis and they are rotated by 22.5° with respect to the barrel coils in order to provide radial overlap and to optimize the bending power at the interface. The end-cap muon spectrometer is placed upstream each end-cap toroid.

2.2.2 Inner detector

Approximately 1000 particles emerged from the collision point every 25 ns within $|\eta| < 2.5$. To achieve a very well resolved track momentum and vertex reconstruction, high-precision measurements must be made with fine detector granularity. The inner detector (Fig. 2.11) [17] achieves high precision measurements using three independent subdetectors and an insertable layer distributed around the beamline under a 2 T magnetic field. These subdetectors are ordered from the innermost to the outermost as:

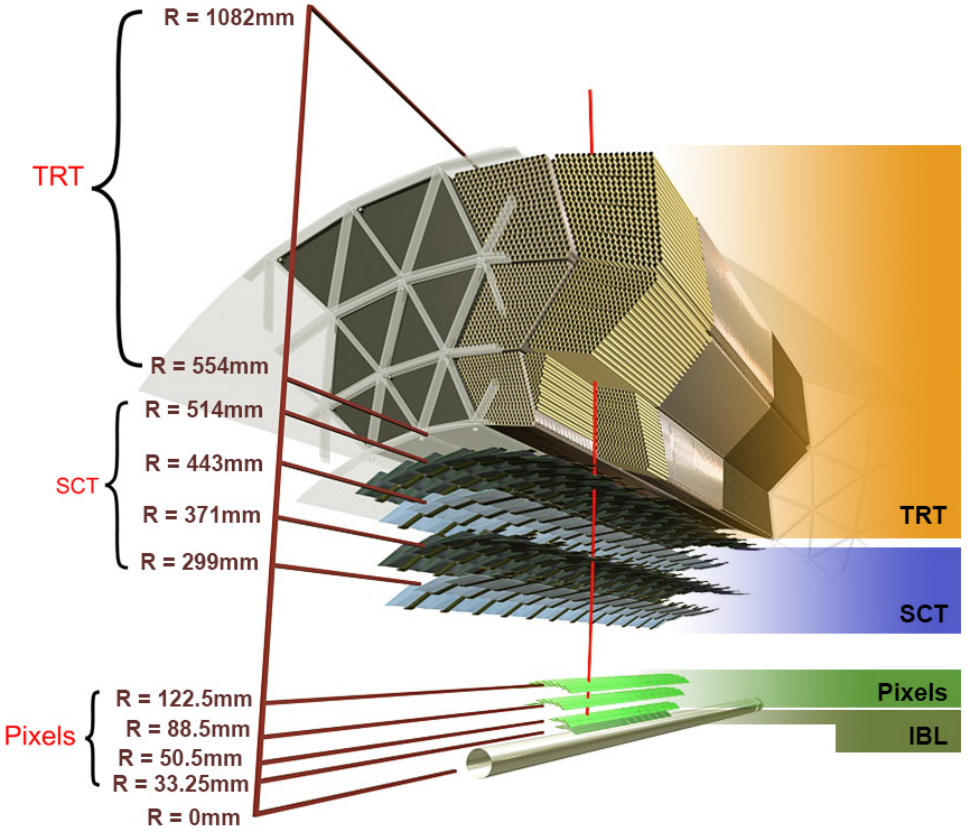


Figure 2.11: Illustration of the barrel region of the inner tracker showing the different subdetector layers and structures traversed by a charged particle created in collision point during Run II [18].

- **Insertable B layer (IBL):** The IBL detector [19] is an additional innermost pixel layer that has been built around the beam pipe and then inserted in the core of the ATLAS detector. The motivation to introduce it was the increased luminosity between Run I and Run II. This increase could provoke significant radiation damage of the inner layers of the detector, which implies that ATLAS would lose tracking efficiency, especially in tagging the decay of the beauty quark. Then, this layer is built so that it can easily replace the missing information from the pixel detector layers. It consists of 14 carbon fibre staves each 2 cm wide and 64 cm long surrounding the beam-pipe at a mean radius of 33 mm from the beamline and covering the region $|\eta| < 3$. Each stave is equipped with

32 front-end chips FE-I4, bump bonded to 26880 pixel cells of ($50\mu m \times 250\mu m$) organized in 80 columns and 336 rows.

- **Pixel detector:** The pixel detector is designed to provide a very high-granularity and high-precision set of measurements as close to the interaction point as possible. It covers the full ID pseudorapidity range ($|\eta| < 2.5$) and consists of three barrels of pixel sensors at a radius of ~ 5.05 cm, 8.85 cm and 12.25 cm and three end-cap disks placed between at 499mm, 554 mm and 799 mm from the interaction point. All disks are identical, with an inner radius of 115 mm and an outer radius of 212 mm from the beamline. 1744 identical sensors for a total of 80.4 millions of pixels are built covering a total surface of 1.7 m^2. These sensors initially operate at 150 V, although an increase of this potential is foreseen up to 600 V after ten years of operation in order to keep good charge collection efficiency depending on the sensor position. The nominal pixel size is $50 \times 400\mu m^2$, allowing around 46080 readout channels per sensor. The pixel detector is maintained at a constant temperature of -15 °C by evaporating C_3F_8 to minimize electronic noise.

- **Semiconductor tracker (SCT):**

  The semiconductor tracker is located after the pixel detector. In total, SCT uses 15912 silicon strip sensors grouped into 4088 two-sided modules representing 63 m^2 with approximately 6.3 million readout channels (silicon strips). It is organized into a barrel with 4 coaxial cylindrical layers and two end-caps containing 9 disk layers. Barrel layers are located radially at 299 mm, 371 mm, 443 mm and 514 mm from the beamline, containing in total 2112 modules. The end-cap strips instead extend radially from 80 cm to 280 cm from the interaction point (z=0) grouped in 988 modules per end-cap.

- **Transition Radiation Tracker (TRT):** This is the last detector upstream the calorimeter. It is located between 0.554 m and 1.082 m from the beamline and comprises many layers of drift tubes with a diameter of 4mm interleaved with transition radiation material. Tubes are filled with a gas mixture of Xe, $C0_2$ and 0_2. When a particle enters the TST, it ionizes the gas inside the straws. In the center of each tube, there is a gold-plated tungsten wire of 31 μm diameter for readout [20]. The resulting free electrons drift towards the wires for readout. TRT extents to $|\eta| < 2.0$ and it is divided into a barrel and two end-cap. 52544 straw tubes are arranged parallel to the beamline in the barrel, covering a range of $|\eta| < 1.0$. Both end-caps cover $1.0 < |\eta| < 2.0$ with 122880 tubes organized radially into two cylinder end-caps, one at each barrel side. The spaces between straws are filled with polymer fibres in the barrel and foils in the end-caps to create transition radiation that can be absorbed by Xe gas particles, thus increasing the readout amplitude. The TRT provides a resolution of 130μm for the track position per straw. Tracks leave on average 36 hits in this detector, hence providing a complementary tracking information that enhances the track pattern recognition and improves the momentum resolution (in $|\eta| < 2.0$) and electron identification.

Figure 2.12 illustrates the radial and pseudorapidity extension of the different subdetectors of the inner tracker.

2.2.3 Calorimetric system

The ATLAS calorimeters consist of a number of sampling calorimeter with full ϕ coverage around the beam axis. They are divided into electromagnetic and hadronic parts aiming to perform precise measurements on the position and energy of electromagnetic and hadronic particles from pp collisions.

- **Electromagnetic ATLAS calorimeter:** is a lead/liquid argon sampling calorimeter (Fig. 2.14) divided into a barrel ($|\eta| < 1.475$) and two end-caps ($1.375 < |\eta| < 3.2$). The barrel (EMB) is divided into two half barrels with an interface at z=0. Each symmetrical half-barrel is divided into 16 modules covering each a $\Delta\phi = 2\pi/16$ region, each containing 64 absorbers interleaved with kapton-copper electrodes. The end-caps (EMEC) are two wheels located at each side of the barrel calorimeter. Each end-cap consists of two different wheels, an outer wheel covering the $1.375 < |\eta| < 2.5$ and an inner wheel covering $2.5 < |\eta| < 3.2$. Absorbers and electrodes are shaped following an

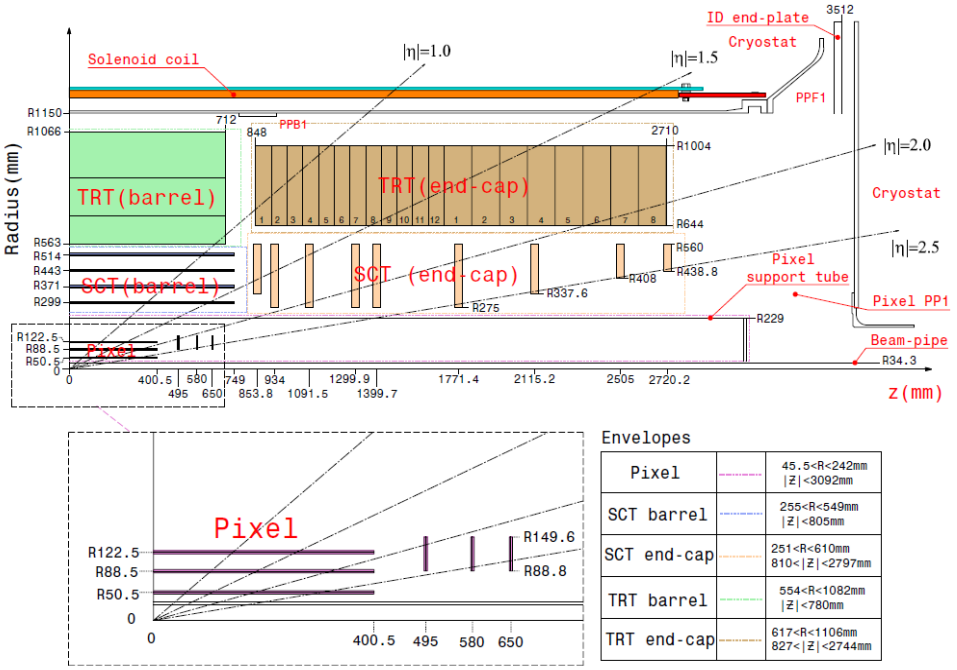


Figure 2.12: Views of a quarter section of the tracker not including the insertable B layer [2].

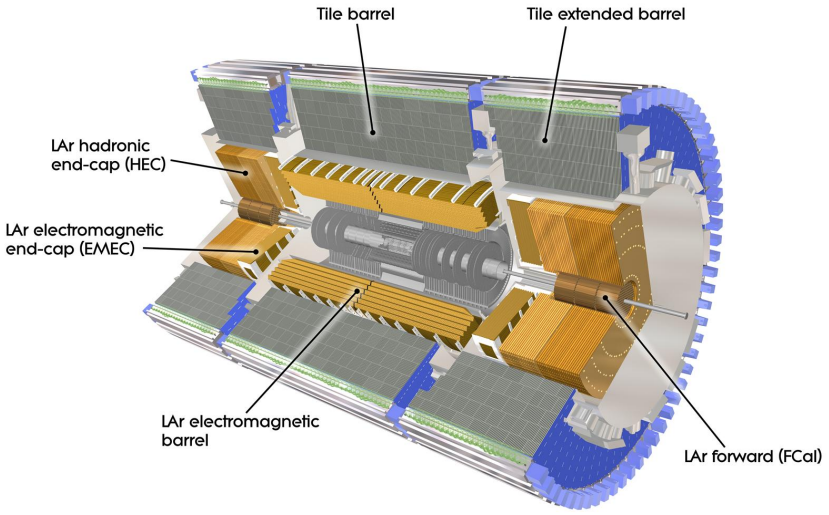


Figure 2.13: View of the ATLAS calorimeter geometry with the different subdetectors [2].

accordion structure. In the barrel, the accordion waves are axial and run in r and z. In the end-caps, the waves are parallel to the radial direction and run axially. Each end-cap wheel is further divided into 8 azimuthal modules. A more detail description of the electromagnetic calorimeter and of the detection principles permitting energy and position measurements, in particular of the electromagnetic barrel, will be presented in Chapter 3.

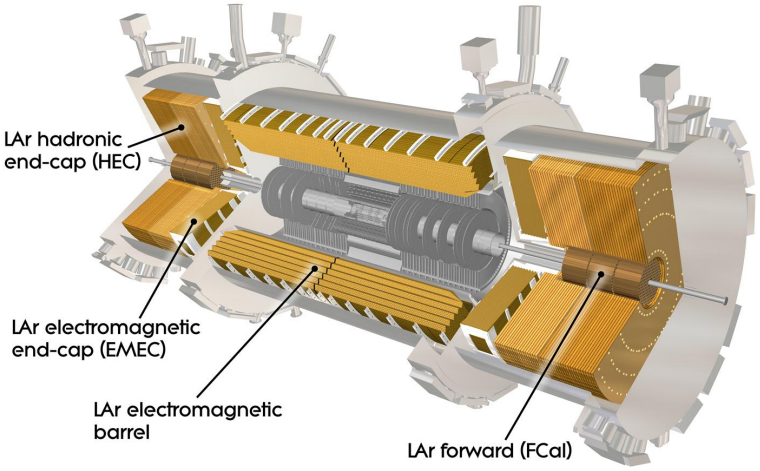


Figure 2.14: View of the liquid argon calorimeters, containing the electromagnetic calorimeter (on barrel and two end-caps) and the hadronic calorimeter end-caps (HEC) and forward calorimeters (FCal) [2].

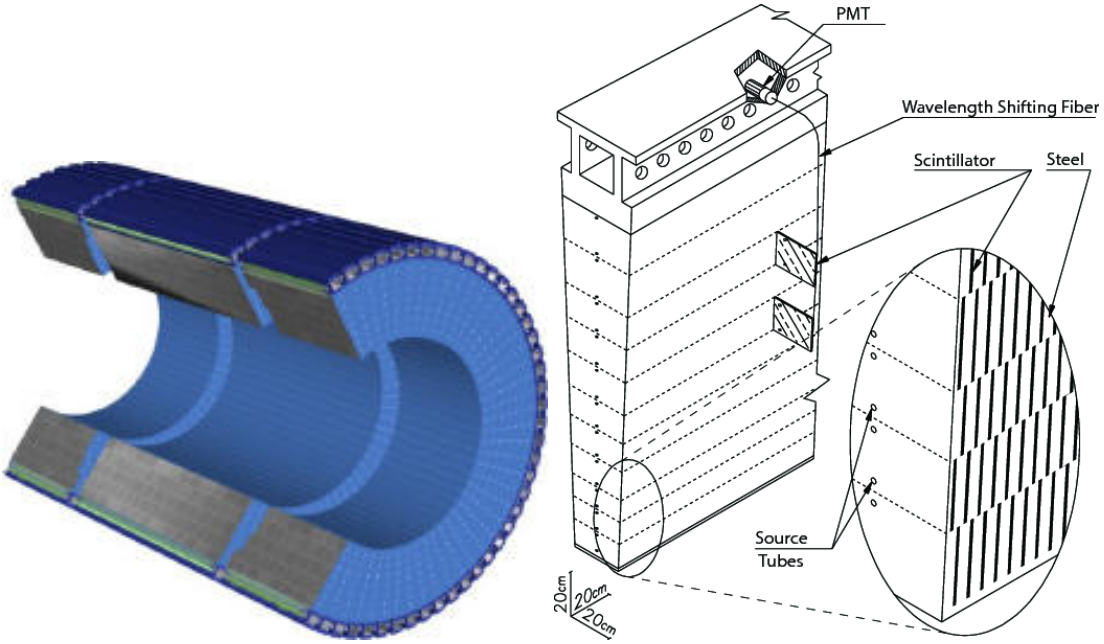


Figure 2.15: Schematic view of the tile calorimeter central region (left) and a slice of the tile calorimeter barrel (right) showing the disposition of the absorbers, the scintillating tiles and the readout PMT's [2].

- **Hadronic ATLAS calorimeters:** hadronic calorimeter system is composed of four subsystems covering different ranges in η. A scintillating tile calorimeter (Fig. 2.15) covers the region in $|\eta| < 1.7$ and is divided into two central barrels (LB) and two extended barrels (EB). Scintillating tiles are

ordered radially and normal to the beamline, interleaved with stainless-steel absorbers and fibres, which collect scintillation light from tiles. Fibres are connected to readout photomultiplier tubes (PMT's). The end-cap region of the hadronic calorimeter (HEC) is a sampling liquid argon calorimeter covering the range $1.5 < |\eta| < 3.2$. The HEC consists of two wheels, a front and a back wheel, each divided into 32 wedge-shaped modules. Front wheel modules are made of 24 copper plates, each 25 mm thick, plus a 12.5 mm thick front plate. In the rear wheels, modules are made of 16 copper plates, each 50 mm thick, plus a 25 mm thick front plate. And finally, two liquid argon calorimeters are placed in the forward regions ($3.1 < |\eta| < 4.9$). They are located at 4.7 m of the interaction point and are segmented into three longitudinal deep modules. One electromagnetic module (FCal1) and two hadronic modules (FCal2 and FCal3). FCal1 is made of copper rods parallel to the beamline arranged inside an outer tube with 250μm liquid argon gap in between. These rods and tubes are inserted in a matrix of copper plates also made of copper. FCal2 and FCal3 absorbers have the same structure than the FCal1, with the difference that tungsten rods are used in order to increase the radiation length to absorb the huge amount of radiation expected at these forward regions.

The liquid argon calorimeter barrel and the end-caps (composed of the EMEC, HEC and FCal) are placed in separate cryostats, instrumented with a cooling system based on liquid nitrogen which ensures a nominal LAr temperature of 88.5 K.

2.2.4 Muon spectrometer

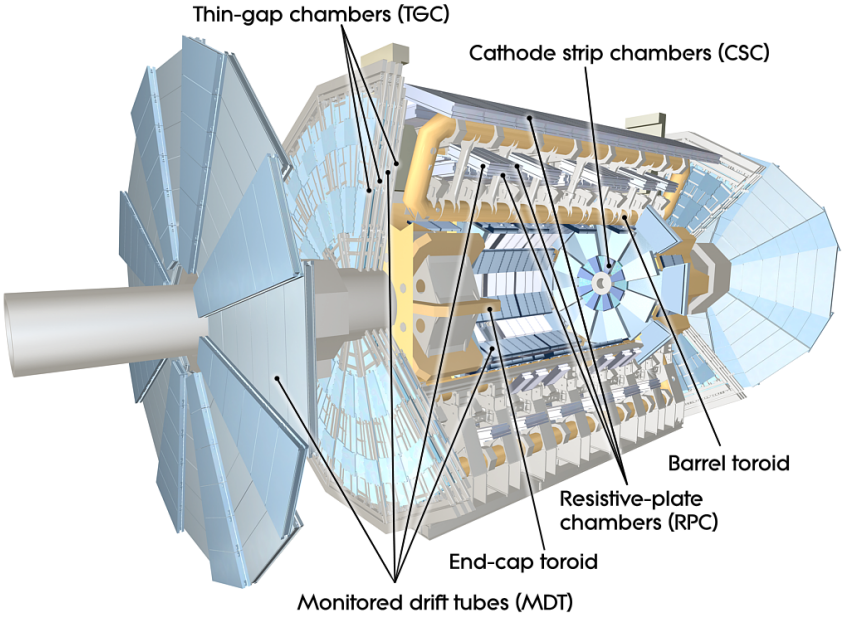


Figure 2.16: Structure of the ATLAS muon spectrometer [2].

The muon spectrometer (Fig. 2.16) consists of several types of detectors aiming to perform precision measurements of the momentum of muons up to $|\eta| < 2.7$ coming from pp interactions or from decays of intermediate hadronic particles. Precision chambers are placed between the toroidal magnet system rings in the barrel and after the toroid end-caps. Determination of the incoming particle momentum is made through accurate measurements of the track curvature. In most of the η range, precision measurements are provided by Monitoring Drift Tubes (MDT's). These are drift chambers formed by aluminium tubes with 3 cm diameter and length in the range 0.9 to 6.2 m. On each chamber the tubes are arranged in two multi-layers, each formed of three and four layers of tubes. A gas mixture of Ar-CO_2 kept at a 3 bar pressure fills the tubes and represents the active material for detection. An incoming muon ionizes the gas mixture and free charges are collected by the central tungsten-rhenium wire in the tube

(Fig 2.17.left). At large pseudorapidities, Cathode Strip Chambers (CSC's) with higher granularity are placed at $2 < |\eta| < 2.7$. These CSC's are multiwire proportional chambers with cathodes segmented into strips that are put in the large η regions to resist the background conditions and the demanding muon rate. In addition, muon trigger system consists of two detectors placed in the $|\eta| < 2.4$ region: Resistive Plate Chambers (RPC's) in the barrel ($|\eta| < 1.05$); and Thin Gap Chambers (TGC's) in the end-cap regions ($1.05 < |\eta| < 2.4$). The target of this system is to provide bunch-crossing identification, provide well-defined p_{T} thresholds, and measure the muon hit coordinates in the direction orthogonal to that determined by the MDT's and CSC's chambers.

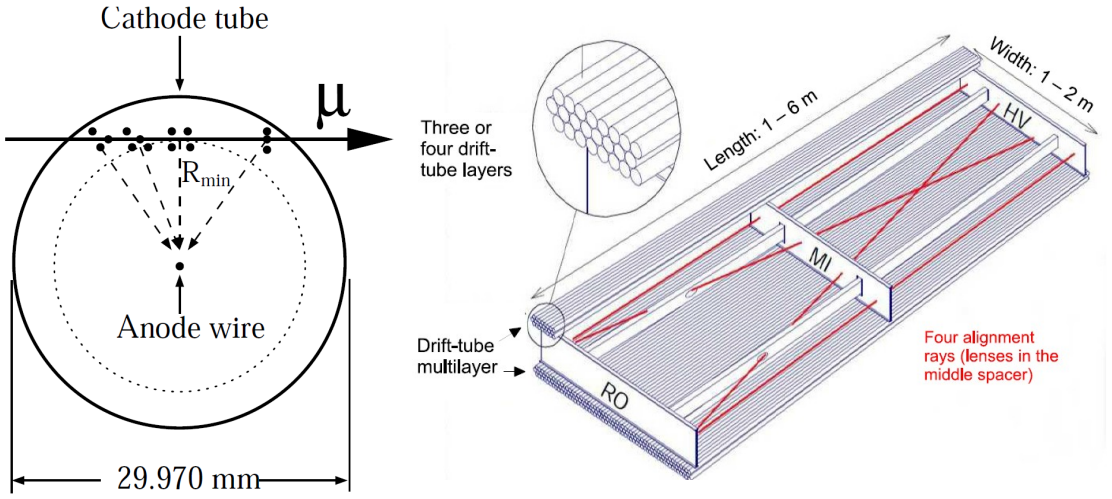


Figure 2.17: Section of an MDT tube (left) and schema of the structure of one MDT chambers (right) [2].

2.2.5 Trigger

LHC provides a pp bunch-crossing every 25 ns, which supposes a rate of 40 million bunch-crossings per second (40 MHz) within the ATLAS detector. At each bunch-crossing, 24 collisions occurred on average during Run II, which implies a huge amount of data measured every 25 ns by the ATLAS detector. Treating and storing all this data is an almost impossible task, thus a trigger system is put in place in order to identify which events present interesting high energy physics features and to reject the ones that don't. The trigger system (Fig. 2.18) consists of two levels of event selection: Level-1 (L1) and High Level Trigger (HLT). The L1 trigger is implemented using custom-made electronics, while the HLT is almost entirely based on algorithms run on conventional computers and networking hardware.

The L1 trigger searches for signatures in the whole detector from high-p_{T} electrons, photons, muons, τ-leptons, jets or large missing transverse momentum and aims to provide a reduced event rate of 100 kHz. It uses separate information from the calorimeters and the muon spectrometer:

- The Level 1 Calorimeter Trigger (L1Calo) selection is based on information from all calorimeters. It searches for signatures from photons, electrons, jets, missing transverse momentum, τ-lepton. The large amount of readout channels from the calorimeters cannot be fully treated by the readout chain. Thus, L1 trigger decision is made by using a coarser granularity readout of the calorimeters (Fig. 2.19). Signals read out from the calorimeter are first treated in the front-end electronics of the calorimeter, where a pre-processor digitizes and calibrates the analog signals from trigger towers, defined as regions of the calorimeter covering ($\Delta\eta \times \Delta\phi = 0.1 \times 0.1$). Signals are then sent to a Cluster Processor (CP) and Jet/Energy-sum Processor in parallel. The former identifies the electrons, photons and τ-leptons with E_{T} beyond a threshold for a sum of 2×2 trigger towers. The latter identifies jets and produce a complete sum of the missing transverse momentum and the scalar sum $\Sigma|E_{\mathrm{T}}|$.
- The Level 1 Muon Trigger uses information from the RPC's and TGC's and searches for hit patterns compatible with high-p_{T} muons originating from the interaction region.

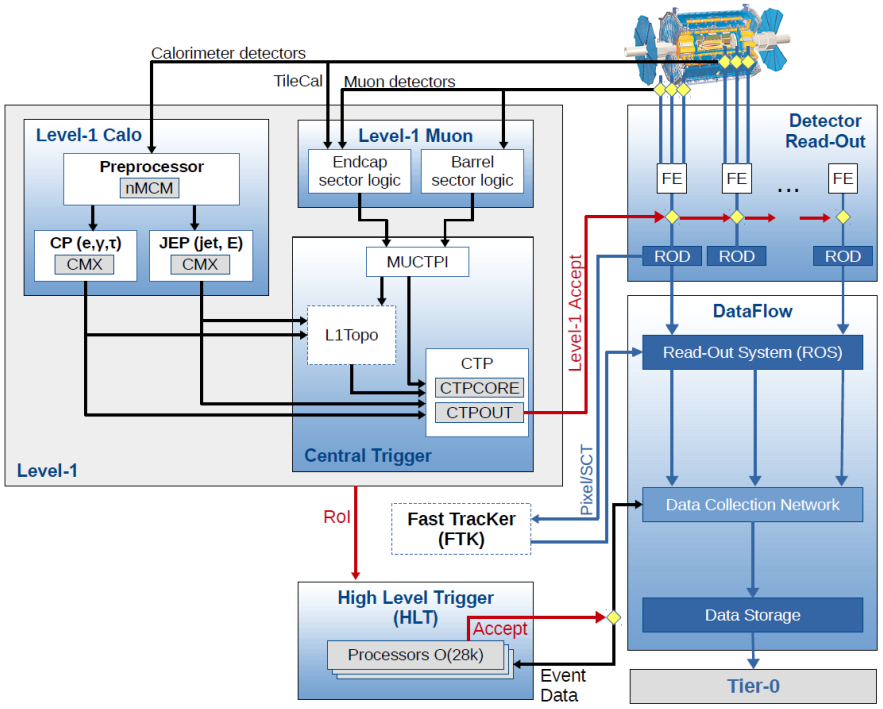


Figure 2.18: Layout of the ATLAS data acquisition system during Run II. FTK and L1 Topo were commissioned during Run II and therefore, they were not included in the trigger decision yet [16].

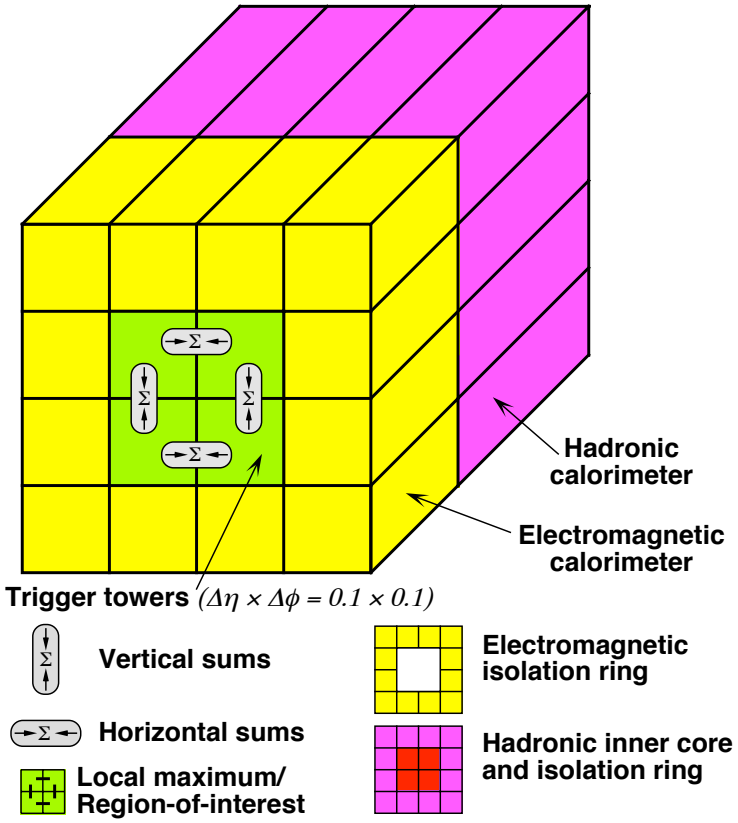


Figure 2.19: Layout of the ATLAS data acquisition system during Run II. FTK and L1 Topo were commissioned during Run II. L1Topo was included in the trigger decision but FTK is not [16].

Information from the L1 Calo and the L1 Muon trigger is combined in a Combined Trigger Processor (CTP) that makes the final trigger decision. During Run II, a topological trigger (L1Topo) was added to perform basic selections based on a geometric or kinematic association between the trigger objects from both trigger subsystems. The L1 accept decision is then sent into the front-end electronics and the readout drivers (RODs) to store (if accepted) the event information.

The HLT trigger is seeded by regions of interest (ROIs) provided by the L1 trigger step. They are regions where the L1 trigger identified possible high-p_{T} objects within the event, including their energy, coordinates and type of signature. HLT reconstructs from these ROI's the event using a finer granularity of the calorimeter information than the L1 trigger and including precision measurements of the muon spectrometer (MDT's and CSC's) and tracking information. However, HLT reconstruction may be also performed on other regions of the detector if needed, e.g for $E_{\mathrm{T}}^{\mathrm{miss}}$ for instance. This step reduces the event rate from 100 kHz at most to 1kHz.

L1 trigger and HLT trigger acceptance signals are issued if the event satisfies at least one set of cuts on energy and identification criteria from a predefined list of interesting event topology, called trigger menu. Table 2.1 presents the main trigger criteria used during 2012 and 2015. Variables used in the HLT event acceptance are reconstructed without applying the full set of corrections that are applied after the full acceptance of the event, in the event reconstruction step after storage. Reconstructed variables at the HLT step are referred to as *online* variables, while variables reconstructed later are referred as *offline*.

Year	2012		2015		
$\sqrt{s}$	8 TeV		13 TeV		
Peak luminosity	$7.7 \times 10^{33}\,\mathrm{cm}^{-2}\,\mathrm{s}^{-1}$		$5.0 \times 10^{33}\,\mathrm{cm}^{-2}\,\mathrm{s}^{-1}$		
	p_{T} threshold [GeV], criteria				
Category	L1	HLT	L1	HLT	Offline
Single electron	18	24i	20	24	25
Single muon	15	24i	15	20i	21
Single photon	20	120	20	120	125
Single tau	40	115	60	80	90
Single jet	75	360	100	360	400
Single b-jet	n/a	n/a	100	225	235
$E_{\mathrm{T}}^{\mathrm{miss}}$	40	80	50	70	180
Dielectron	2×10	2×12,loose	2×10	2×12,loose	15
Dimuon	2×10	2×13	2×10	2×10	11
Electron, muon	10, 6	12, 8	15, 10	17, 14	19, 15
Diphoton	16, 12	35, 25	2×15	35, 25	40, 30
Ditau	15i, 11i	27, 18	20i, 12i	35, 25	40, 30
Tau, electron	11i, 14	28i, 18	12i(+jets), 15	25, 17i	30, 19
Tau, muon	8, 10	20, 15	12i(+jets), 10	25, 14	30, 15
Tau, $E_{\mathrm{T}}^{\mathrm{miss}}$	20, 35	38, 40	20, 45(+jets)	35, 70	40, 180
Four jets	4×15	4×80	3×40	4×85	95
Six jets	4×15	6×45	4×15	6×45	55
Two b-jets	75	35b,145b	100	50b,150b	60
Four(Two) (b-)jets	4×15	2×35b, 2×35	3×25	2×35b, 2×35	45
B-physics (Dimuon)	6, 4	6, 4	6, 4	6, 4	6, 4

Table 2.1: Comparison of selected primary trigger thresholds (in GeV) at the end of Run 1 and during 2015 together with typical offline requirements applied in analyses [16].

References

[1] Lyndon Evans and Philip Bryant. "LHC Machine". In: *JINST* 3 (2008), S08001. DOI: 10.1088/1748-0221/3/08/S08001.

[2] G. Aad et al. "The ATLAS Experiment at the CERN Large Hadron Collider". In: *JINST* 3 (2008), S08003. DOI: 10.1088/1748-0221/3/08/S08003.

[3] S. Chatrchyan et al. "The CMS Experiment at the CERN LHC". In: *JINST* 3 (2008), S08004. DOI: 10.1088/1748-0221/3/08/S08004.

[4] A. Augusto Alves Jr. et al. "The LHCb Detector at the LHC". In: *JINST* 3 (2008), S08005. DOI: 10.1088/1748-0221/3/08/S08005.

[5] K. Aamodt et al. "The ALICE experiment at the CERN LHC". In: *JINST* 3 (2008), S08002. DOI: 10.1088/1748-0221/3/08/S08002.

[6] M Albrow et al. *CMS-TOTEM Precision Proton Spectrometer*. Tech. rep. CERN-LHCC-2014-021. TOTEM-TDR-003. CMS-TDR-13. Sept. 2014. URL: https://cds.cern.ch/record/1753795.

[7] O Adriani et al. *LHCf experiment: Technical Design Report*. Technical Design Report LHCf. Geneva: CERN, 2006. URL: https://cds.cern.ch/record/926196.

[8] James Pinfold et al. *Technical Design Report of the MoEDAL Experiment*. Tech. rep. CERN-LHCC-2009-006. MoEDAL-TDR-001. June 2009. URL: https://cds.cern.ch/record/1181486.

[9] LHC-closer. *RF Cavities*. URL: https://www.lhc-closer.es/taking_a_closer_look_at_lhc/0.rf_cavities.

[10] Christiane Lefèvre. "The CERN accelerator complex. Complexe des accélérateurs du CERN". Dec. 2008. URL: https://cds.cern.ch/record/1260465.

[11] LHC-closer webpage. *Beta and emittance*. URL: https://www.lhc-closer.es/taking_a_closer_look_at_lhc/0.beta___emittance.

[12] Wikipedia. *Touschek effect*. URL: https://en.wikipedia.org/wiki/Touschek_effect.

[13] LHC-closer. *Beam lifetime*. URL: https://www.lhc-closer.es/taking_a_closer_look_at_lhc/0.beam_lifetime.

[14] ATLAS collaboration. *Luminosity Public Results for Run2*. URL: https://twiki.cern.ch/twiki/bin/view/AtlasPublic/LuminosityPublicResultsRun2.

[15] HL-LHC project. *High Luminosity Large Hadron Collider*. URL: http://hilumilhc.web.cern.ch/about/hl-lhc-project.

[16] Morad Aaboud et al. "Performance of the ATLAS Trigger System in 2015". In: *Eur. Phys. J.* C77.5 (2017), p. 317. DOI: 10.1140/epjc/s10052-017-4852-3. arXiv: 1611.09661 [hep-ex].

[17] *ATLAS inner detector: Technical Design Report, 1*. Technical Design Report ATLAS. Geneva: CERN, 1997. URL: https://cds.cern.ch/record/331063.

[18] Karolos Potamianos. "The upgraded Pixel detector and the commissioning of the Inner Detector tracking of the ATLAS experiment for Run-2 at the Large Hadron Collider". In: *PoS* EPS-HEP2015 (2015), p. 261. arXiv: 1608.07850 [physics.ins-det].

[19] ATLAS Collaboration. *ATLAS Insertable B-Layer Technical Design Report*. CERN-LHCC-2010-013, ATLAS-TDR-19. 2010. URL: https://cds.cern.ch/record/1291633.

[20] A Vogel. *ATLAS Transition Radiation Tracker (TRT): Straw Tube Gaseous Detectors at High Rates*. Tech. rep. ATL-INDET-PROC-2013-005. Geneva: CERN, Apr. 2013. URL: https://cds.cern.ch/record/1537991.

Energy and time reconstruction in electromagnetic barrel

Contents

3.1 Calorimetry . . . 64
3.1.1 Precision of measurements in calorimeters . . . 65
3.2 Principles of electron and photon detection . . . 65
3.2.1 Electron and photon interaction with matter . . . 66
3.2.2 Longitudinal and lateral development . . . 68
3.3 Liquid argon barrel readout chain and energy reconstruction . . . 69
3.3.1 Layer and cell division of the electromagnetic calorimeter . . . 70
3.3.2 Charge collection in the liquid argon . . . 72
3.3.3 From charge collection to front-end electronics . . . 74
3.3.4 Front-end boards . . . 74
3.3.5 Electronic cell calibration . . . 76
3.4 Signal shape for physics signal . . . 77
3.4.1 Ionization signal . . . 77
3.4.2 Estimation of the ionization shape after readout . . . 78
3.5 Optimal filtering . . . 80
3.6 Passage from *ADC* to MeV . . . 81
3.6.1 Ramps . . . 82
3.6.2 Difference between physics and calibration peaks . . . 83
3.6.3 Calorimeter constants . . . 83
3.7 Energy and time reconstruction performance . . . 84

The detection of particles is based on the interactions of particles with matter. Scintillators, Geiger counters, photomultipliers, calorimeters, etc, are detectors developed during the last century allowing the identification and measurement of the interacting particles properties. They are all specific detectors for different types of particles and adapted for a certain range of energy.

Calorimeters are broadly used detectors in particle physics. They are blocks of matter in which the energy of incident particles is completely absorbed and measured. The main physics effects used in calorimeters are ionization, nuclear reactions and atom excitations giving rise to a cascade of daughter particles. In such a way, incoming particles initiate a cascade in the detector such that their energy is degraded and transmitted into the detector. Measurements on particle's properties are performed via the collection and study of the free charges from ionization and/or of the de-excitation radiation of material atoms. The propagation of the particle shower then stops when its energy is low enough so that it can be absorbed or recombine with the detector material.

The main focus of this chapter is to explain detection techniques employed in the ATLAS electromagnetic calorimeter to measure energy and time of incoming electrons and photons. For that, a summary of the main calorimetry techniques, the electron and photon interaction with matter and the ATLAS EM calorimeter is presented in Sections 3.1, 3.2 and 3.3. Incident particle energy is then measured by applying a scale to the obtained signal from the calorimeter specific for each calorimeter cell. Relevant steps to

determine this energy scale are exposed in Section 3.4 and Section 3.5. In addition, some calibration constants need to be determined from studies of the calorimeter. These constants as well as their obtained values are exposed in Section 3.6. Finally, the performance of the cell calibration process is presented in Section 3.7.

3.1 Calorimetry

Calorimeters are blocks of instrumented material on which interacting particles are absorbed. Particles entering the calorimeter initiate a particle shower. The particles of the shower interact with the material of the detector, which degrades the initial energy of the object, and leaves a trace of energy deposits that can be used to measure properties of the particle. Current calorimeters are built employing two possible strategies to measure the energy of the incident particle: either the energy is transmitted inside the calorimeter by material ionization, either the particles of the shower interact with the detector nuclei that later radiate the excitation energy in form of scintillation light. The magnitude of the deposited energy is then proportional to the number of free charges after the ionization or the intensity of the scintillating light. Additionally, calorimeters are also built to trigger and help the development of the shower. Three differentiated components are relevant for the development of the particle cascade: an active media, from which the energy deposition of the incident particle is measured; the vessel containing this material, with which the incident particle may interact in the first place; and, eventually, slices of other material which are added to help the shower development. These last components, called absorbers, are present in many calorimeters and permit to classify them as sampling (with absorbers) or homogeneous calorimeters, being the latter those calorimeters whose absorber and active materials are the same.

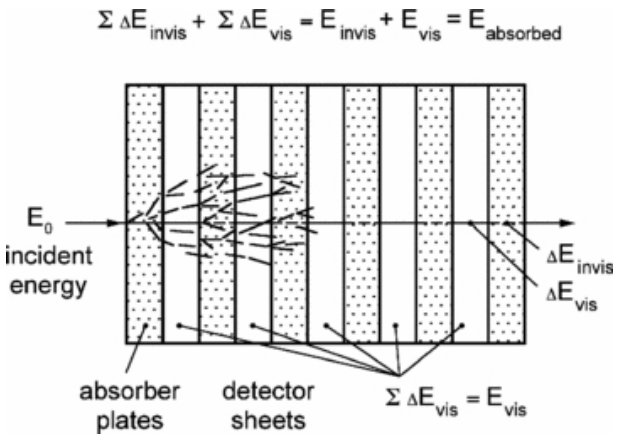


Figure 3.1: Shower development and energy depositions in a sampling calorimeter [1].

Homogenous calorimeters (CMS calorimeter [2]) are typically very high-density scintillating crystals with very large atomic number Z. Almost all the incident particle energy is deposited in the material and measured except for the intrinsical fluctuations that a particle shower may present and the possible interactions of with the vessel. The main drawback of these detectors is that if a low-density active material needs to be used, a fraction of the particle cascade from initial high energy particles may cross the whole calorimeter and be absorbed out of the detector fiducial volume. In order to avoid these leakages, homogeneous calorimeters are usually large for low-density active material. In this case, the addition of absorbers interleaved with the active material allows building more compact detectors (ATLAS calorimeter [3]). However, these absorbers are usually made of very high Z materials, such as lead or tungsten, for which the ionized charges or scintillation light are rapidly absorbed and cannot easily be collected. Therefore, the energy deposits inside the absorbers are lost and only the fraction of energy transmitted into the active material between two slices of absorber is measured. In Figure 3.1, these two energies are respectively outlined as $E_{\text{invisible}}$ and E_{vis}, such that the readout signal is the sum of the light or charges measured in each active material gaps (ΔE_{vis}).

3.1.1 Precision of measurements in calorimeters

The measurement of the energy with a calorimeter is based on the principle that the number of collected charges or the scintillation light intensity is proportional to the energy deposited by the incident particle. However, the configuration of the detector, the electronic noise or shower fluctuations may influence the energy measurement. The relative resolution of the energy is then estimated as the quadratic sum of three resolution terms:

$$\frac{\sigma_E}{E} = \underbrace{\frac{a}{\sqrt{E}}}_{\text{Stochastic term}} \oplus \underbrace{\frac{b}{E}}_{\text{Noise term}} \oplus \underbrace{c}_{\text{Constant term}} \tag{3.1}$$

where the different terms correspond to:

- **Stochastic term**

  This term is due to fluctuations of charges related to the development of the shower. Two terms can be differentiated: one coming from the intrinsic fluctuations on the shower development and other from sampling fluctuations. In homogeneous calorimeters, the fluctuation term only corresponds to the intrinsic shower fluctuations. Instead, in sampling calorimeters the number of particles in the shower strongly fluctuates at the crossing of the shower with the interleaved absorbers. These fluctuations follow a stochastic law, implying a resolution term in the number of measured particles proportional to $\sqrt{N_{\text{ch}}}$. Since the number of final charges or the intensity of the light is also proportional to the number of particles in the shower, the error on the measured energy is proportional to $\sigma_E/E \propto \sqrt{N_{\text{ch}}}/N_{\text{ch}} = a/\sqrt{E} = \sigma$. The coefficient a is a few percent in homogeneous calorimeters (3% in CMS) while it is of the order of 10% in sampling calorimeters (10.1% in ATLAS).

- **Noise term**

  This contribution comes from the electronic noise of the readout chain. This term depends on the features of the readout chain such as the detector capacitance and cables. Another contribution may come from spontaneous ionization of the liquid argon due to the excitation of electrons in the valence band by soft radiation or thermal excitation.

- **Constant term**

  Instrumental effects that cause variations of the calorimeter response in different regions cause non-uniformities. These non-uniformities can originate from the detector geometry, from imperfections in the detector structure or in the readout chain, temperature gradients, impurities etc. These defects usually occur in random regions of the calorimeter and cannot be corrected for. Nevertheless, if any imperfection shows a periodic pattern, some corrections can be applied to energy calculation. This constant term does not depend on the energy and becomes a dominant source of uncertainty for high-energy electrons and photons.

The current resolution values estimated for ATLAS [4] and CMS [5] are:

$$\text{ATLAS;} \qquad \frac{\sigma_E}{E} = \frac{10.1\%}{\sqrt{E}} \oplus \frac{250}{E} \oplus 0.7\% \tag{3.2}$$

$$\text{CMS;} \qquad \frac{\sigma_E}{E} = \frac{2.8\%}{\sqrt{E}} \oplus \frac{41.5}{E} \oplus 0.3\% \tag{3.3}$$

A more detailed description of the estimation of these parameters for the ATLAS calorimeter can be found in Section 3.7.

3.2 Principles of electron and photon detection

Calorimeters are optimized for each one measuring a different type of particle. The ATLAS electromagnetic calorimeter is built in order to perform high-quality measurements of incident electrons and

photons issued from pp collisions. In this configuration, when a high-energy electron or photon interacts with a thick absorber, it initiates an electromagnetic cascade as lower energy electrons and photons are produced. These particles subsequently interact with the detector material, giving rise to secondary electrons and photons. This process is repeated until the incoming energy has been reduced and split in many low energy electrons and photons that can be absorbed by the detector material. A schema of an electromagnetic shower is presented in Figure 3.2.

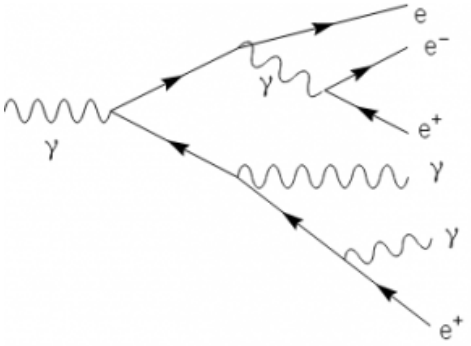


Figure 3.2: Schema of a shower for an incoming photon.

3.2.1 Electron and photon interaction with matter

The nature of the electron and photon interaction with matter depends on the initial energy and the matter composition itself. At high energies, electrons lose energy mainly through bremsstrahlung radiation, caused by the electron interactions with the electromagnetic field of the surrounding material nuclei. The differential cross-section of this process with respect to the emitted photon energy k is:

$$\frac{d\sigma}{dk} = \frac{A}{X_0 N_A k}(\frac{4}{3} - \frac{4}{3}y + y^2) \tag{3.4}$$

where $y = k/E$ and X_0 is called the radiation length of the material. This radiation length, who plays an important role in the longitudinal and lateral development of the shower as it will be explained later, depends on the type of material with which the electron is interacting:

$$\frac{1}{X_0} = 4\alpha r_e^2 \frac{N_A}{A}\{Z^2[\ln(184.15Z^{-1/3}) - f(Z)] + Z\ln(1194Z^{-2/3})\} \tag{3.5}$$

where $f(Z)$ can be approximated to Eq. 3.6 for lighter materials than uranium:

$$f(Z) = a^2[(1+a^2)^{-1} + 0.20206 - 0.0369a^2 + 0.0083a^4 - 0.002a^6] \tag{3.6}$$

where $a \propto Z$. At lower energies, other interactions take the leading role, such as the ionization of the surrounding media or Möller ($e^-e^- \rightarrow e^-e^-$) and Bhabha ($e^-e^+ \rightarrow e^-e^+$) scattering. These latter interactions corresponds to the last steps of the shower development, where the daughter particles are a bunch of low energy electrons and photons that are finally absorbed by the detector. Figure 3.3 presents the main energy loss processes for electrons in lead.

Besides, high energy photons tend to produce a stable electron and positron pair. The cross-section of the electron-positron pair creation is given by Equation 3.7, where in this case $x = E_{e^-}/E_\gamma$ with E_{e^-} is the energy of the electron:

$$\frac{d\sigma}{dx} = \frac{A}{X_0 N_A}[1 - \frac{4}{3}x(1-x)] \tag{3.7}$$

Low energy photons interact through photoelectric effect and Rayleigh (Compton) scattering with the material nuclei (electrons). Figure 3.4 presents photon interactions in carbon and lead. It can be observed a dominance of the pair creation process beyond $E_\gamma = 10$ MeV for the case of the lead. Likewise the

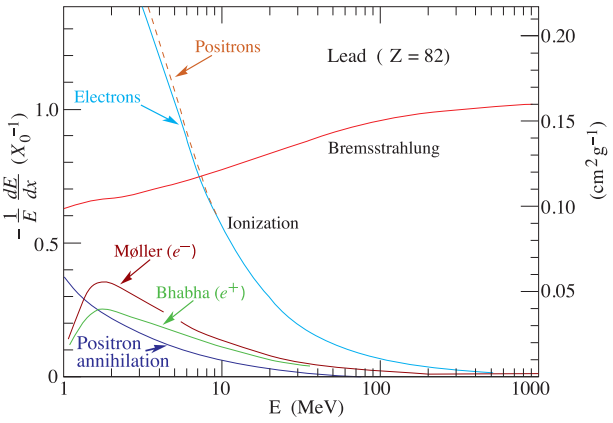


Figure 3.3: Electron (or positron) fractional loss of energy in lead [6].

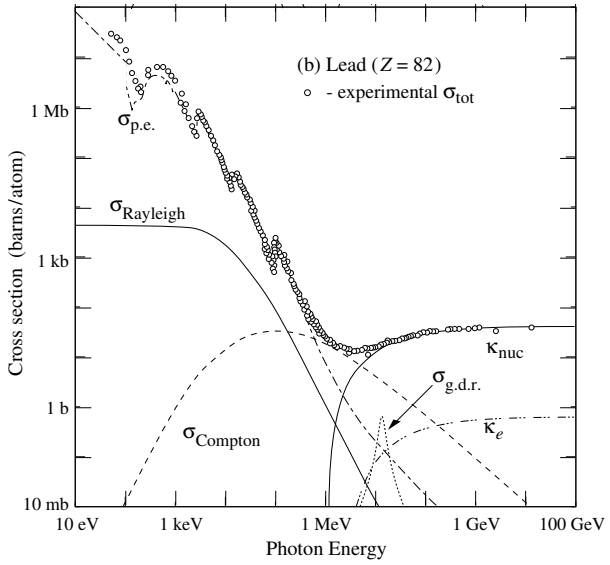


Figure 3.4: Photon total cross-sections as a function of energy in lead, showing the contributions of different processes [6], where the different cross-sections are: $\sigma_{\mathrm{p.e}}$, the atomic photoelectric effect cross-section; $\sigma_{\mathrm{Rayleigh}}$ for Rayleigh scattering–atom; $\sigma_{\mathrm{Compton}}$ stands for Compton scattering off an electron cross-section; κ_{nuc} accounts for the pair e^+e^- production by nuclear field and κ_e by the electron field; and $\sigma_{\mathrm{g.d.r.}}$ accounts for photonuclear interactions.

electron, high energy photons ($E_\gamma > 10$GeV) are measured in the EM calorimeter, thus the dominant activator of the photon EM shower is the e^+e^- pair production.

In summary, the electromagnetic cascades are initiated by bremsstrahlung or by pair-creation for electrons and photons respectively and they are developed by subsequent bremsstrahlung and pair-creation of the children electrons and photons. The children electrons of these interactions are less energetic than their parents, and apart from radiating bremsstrahlung photons, they also ionize the surrounding material. The strategy followed in ATLAS is to use these ionized charges of the active material, fixed to be liquid argon, to measure the energy of the incoming particle. It also needs to be noticed that electron bremsstrahlung and photon pair-creation cross-sections depend on the atomic number (Z) of the material with which they interact, what motivated the use of lead absorbers in the ATLAS EM calorimeter. Instead, energy is measured through scintillation light from $\mathrm{P_bWO_4}$ crystals of which the CMS ECAL is composed.

3.2.2 Longitudinal and lateral development

The electromagnetic shower begins when electrons and photons with enough energy produce secondary photon and stops when daughter electron and photons can be absorbed by the detector material. Between these two points, the shower has been propagated along the calorimeter and has transmitted all the initial particle energy into the detector. This transmission is not uniform, arriving at a maximum of energy deposition at a certain point in the shower development. In addition, daughter particles are emitted at a certain angle with respect to the parent electron or photon direction, which implies a cascade that is not only developed longitudinally but also laterally. The study of the development of the showers permit to acknowledge very important properties of the initial electron and photon. For instance, photons usually can travel the matter a bit longer before they produce the first conversion. In contrast, electrons usually interact much before given that they are charged particles. In addition, the lateral development of the shower may help to understand if the incoming particle is a photon that produces a first conversion or not (Fig. 3.5).

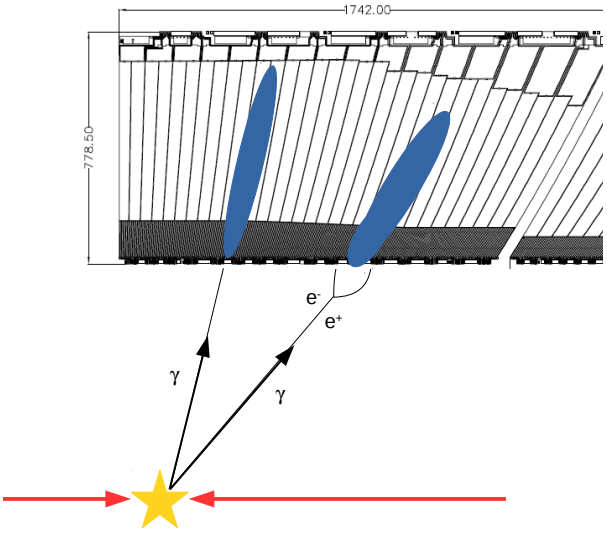


Figure 3.5: Schematic view of the effect that interactions upstream the calorimeter may present in the lateral shower development of two photons. The yellow star indicates the collision point. Red arrows present the two opposite bunches of protons and dark blue ellipses represent the shower of the incoming photons.

Longitudinal shower development can be described in terms of the radiation length X_0 (Eq. 3.5). Its usual unity is g cm^{-2} but by redefining it as $X_0(\mathrm{cm}) = X_0(\mathrm{gcm}^{-2})/\rho_{\mathrm{material}}$, it represents the mean length that the electron needs to travel to lose 1/e of its energy:

$$E = E_0 e^{-\frac{x}{X_0}} \tag{3.8}$$

where E_0 is the electron or photon initial energy. The mean longitudinal profile of the energy deposition by the shower is well modeled by a gamma function [7]:

$$\frac{dE}{dt} = E_0 b_t \frac{(bt)^{a_t - 1} e^{-b_t t}}{\Gamma(a_t)} \tag{3.9}$$

where t is the shower depth x in units of X_0 ($t = x/X_0$) and a_t and b_t are parameters depending on the material [6]. The point at which the cascade energy loss is maximum is determined by:

$$t_{max} = \frac{a_t - 1}{b_t} \tag{3.10}$$

ATLAS electromagnetic calorimeter varies with η, although it represents at most $33X_0$. The ending point of the electromagnetic shower is determined by given critical energy (E_C), which is here defined as the

energy of electrons at which the average energy losses caused by ionization and bremsstrahlung are equal. This variable depends on the absorber and detection materials and represents the energy below which the remaining electrons from the cascade are stopped by ionization and collisions with atoms. This critical energy is approximately given by:

$$E_C = \frac{610(710)\text{MeV}}{Z + 1.24(0.92)} \tag{3.11}$$

for solids and liquids (gases), where Z is the atomic number of the material.

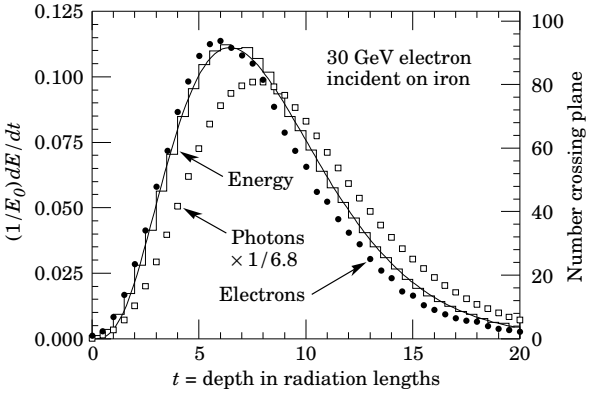


Figure 3.6: Simulation of a 30 GeV electron-induced cascade in iron. It is shown the fraction of energy deposited in the iron per radiation length. The curve is a gamma-function fit to the distribution for electrons. Circles indicate the number of electrons with total energy greater than 1.5 MeV crossing planes at $X_0/2$ intervals (scale on right) and the squares the number of photons with $E \geq 1.5$ MeV crossing the planes (scaled down to have the same area as the electron distribution). This figure is taken from [6].

On the other hand, the transverse development is given by the Molière radius R_M given by:

$$R_M = \frac{E_s}{E_c} \tag{3.12}$$

where $E_s \approx 21$ MeV and E_c is the critical energy. Simulations show that 90% of the whole energy of the cascade is within a radius R_M and the 99% within $3.5\ R_M$. The Molière radius for the ATLAS electromagnetic barrel is on average ~ 2.5 cm.

3.3 Liquid argon barrel readout chain and energy reconstruction

The ATLAS electromagnetic calorimeter barrel aims at performing high precision measurements of the electrons and photons with a large momentum. Charges from liquid argon ionization are read-out from the detector by a complex procedure, permitting precise measurements of the electromagnetic shower. The barrel calorimeter is divided into 109568 electronic cells (also called channels). Signals are collected from electrodes and are combined into summing and mother boards in the front and the back of the barrel. These latter send the resulting signals out of the calorimeter cryostat for their first treatment in the Front-End Boards (FEBs). This treatment includes the preamplification, shaping, sampling of the signals and acceptance by the Level 1 trigger. Then, data is sent to the readout drivers, outside the ATLAS cavern, where signal peak and arrival time are estimated and then transformed into energy measurements through a calibration technique, which converts the output charge intensity into MeV units.

Unless stated otherwise, the information in this section comes from [8, 9, 10].

3.3.1 Layer and cell division of the electromagnetic calorimeter

Accurate measurements of electrons and photons require an optimal segmentation of the calorimeter to precisely determine the longitudinal and lateral profiles of their shower and the amount of deposited energy on the detector. This sampling of each shower can be used to reconstruct the direction of the incoming particle and its impact point in the calorimeter. Moreover, it can also be used to better reconstruct the energy. Low energy particles tend to produce broader showers than high energy ones given that the first electrons and photons in the shower are produced at larger angles with regard to the original particle direction. Given that the shower shapes catch part of this behavior, one may use them in a multivariate regression algorithm [11] to improve the energy reconstruction at the calibration step.

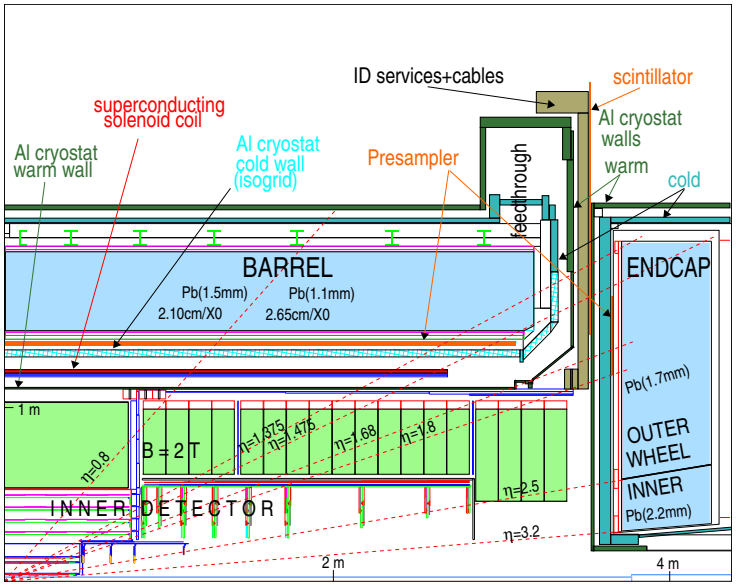


Figure 3.7: Section of the calorimeter showing the barrel and the end-cap together with η projections [12].

The electromagnetic calorimeter is divided into a barrel calorimeter ($|\eta| < 1.475$) and two end-caps ($1.375 < |\eta| < 3.2$), as illustrated in Figure 3.7. The barrel is segmented into three different longitudinal layers (or samplings) along the radial axis with a presampler in front (Fig. 3.8).

- The first layer measures the beginning of the electromagnetic shower. A fine segmentation is implemented in η for this layer in order to improve the separation between photons and neutral pions decaying into two photons. The branching ratio of $\pi^0 \to \gamma\gamma$ is 98.82% [6] and in case of very energetic π^0, the resulting two photons are boosted (almost colinear) so that they cannot easily be distinguished from prompt photons. This fact implies that π^0 is one of the most important backgrounds for final states with photons. Thus, the segmentation of the front layer is also optimized to allow a good separation between γ and $\pi^0 \to \gamma\gamma$. In addition, a precise determination of the impact point of the EM particle and its direction (this latter including second layer information), which allows reducing the pileup effect. Concerning the granularity in ϕ, the limited computing power imposes a reduction of the readout cells. In consequence, front cells size is fixed to $\Delta\eta \times \Delta\phi = 0.025/8 \times 0.1$. The depth of this layer varies with η, going up to four X_0.
- The second layer receives most of the energy deposit of the electromagnetic shower. The cell division of this layer is optimized taking into account that R_m ~2.5 cm in the barrel [13]. The second layer depth represents up to $22X_0$ and its lateral segmentation is of $\Delta\eta \times \Delta\phi = 0.025 \times 0.025$.
- The third layer is available for measuring the end of the cascade. It is contained between $r = 22X_0$ or $r = 33X_0$, with a cell size of $\Delta\eta \times \Delta\phi = 0.050 \times 0.025$. However, it ends at $|\eta| < 1.35$.

In addition, a presampler ($|\eta| < 1.52$) is placed in front of the barrel in order to measure possible electron or photon energy losses upstream the calorimeter. It is a very thin liquid argon layer (1mm) with

End-cap segmentation		
Sampling	η coverage	Cell segmentation ($\Delta\eta \times \Delta\phi$)
Layer 1	$1.375 < \|\eta\| < 1.425$	0.050×0.1
	$1.425 < \|\eta\| < 1.5$	0.025×0.1
	$1.5 < \|\eta\| < 1.8$	0.003×0.1
	$1.8 < \|\eta\| < 2.0$	0.004×0.1
	$2.0 < \|\eta\| < 2.4$	0.006×0.1
	$2.4 < \|\eta\| < 2.5$	0.025×0.1
	$2.5 < \|\eta\| < 3.2$	0.1×0.1
Layer 2	$1.375 < \|\eta\| < 1.425$	0.050×0.025
	$1.425 < \|\eta\| < 2.5$	0.025×0.025
	$2.5 < \|\eta\| < 3.2$	0.1×0.1
Layer 3	$1.5 < \|\eta\| < 2.5$	0.050×0.025

Table 3.1: Segmentation of the end-caps. Outer wheel covers the region $1.375 < |\eta| < 2.5$ and the inner wheel, $2.5 < |\eta| < 3.2$. Inner wheel presents a constant segmentation for all three layers while granularity varies for the outer wheel [3].

granularity $\Delta\eta \times \Delta\phi = 0.025 \times 0.1$. There is a barrel-end ($1.40 < |\eta| < 1.475$) where only two layers are setup with a coarser granularity than the preceding ones: the first with $\Delta\eta \times \Delta\phi = 0.025 \times 0.025$ cells and the second with $\Delta\eta \times \Delta\phi = 0.050 \times 0.025$ cells.

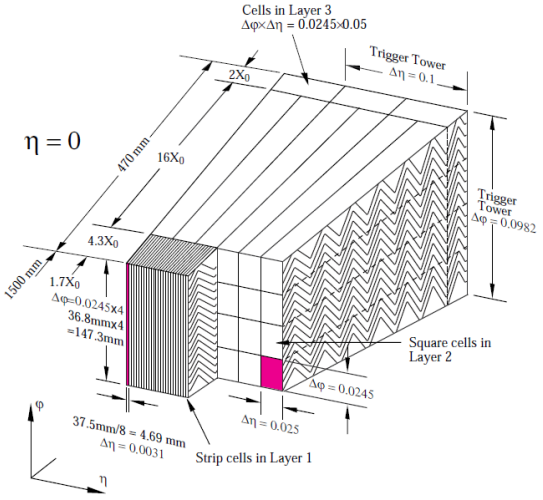


Figure 3.8: Section of the barrel calorimeter barrel showing the three radial layers with their corresponding cell segmentation [8].

The segmentation of the end-caps differs from the barrel one given that much more radiation from the collision is expected at larger η. Each end-cap is divided in an outer wheel ($1.375 < |\eta| < 2.5$) and an inner wheel ($2.5 < |\eta| < 3.2$). Both wheels are segmented into three longitudinal layers. In addition, a presampler layer is placed in front of the end-caps covering the region ($1.5 < |\eta| < 1.8$). The segmentation of the end-cap is presented in Table 3.1

During this thesis, specific studies have been made on the electromagnetic barrel calorimeter. Next sections will then be devoted to the precise description of the signal formation and energy measurements on this subdetector. However, more information about the end-caps can also be found in the references that are provided.

3.3.2 Charge collection in the liquid argon

In Section 3.1, it has been explained the basic strategy on sampling calorimeters. It was presented the alternance of absorbers and active material in order to help the development of the shower at the same time that a compact calorimeter can be built. In the case of the ATLAS EM barrel calorimeter, geometrical constraints impose a different structure of the absorbers and of the electrodes than the one presented in Figure 3.1. A schema of this configuration is presented in Figure 3.9.

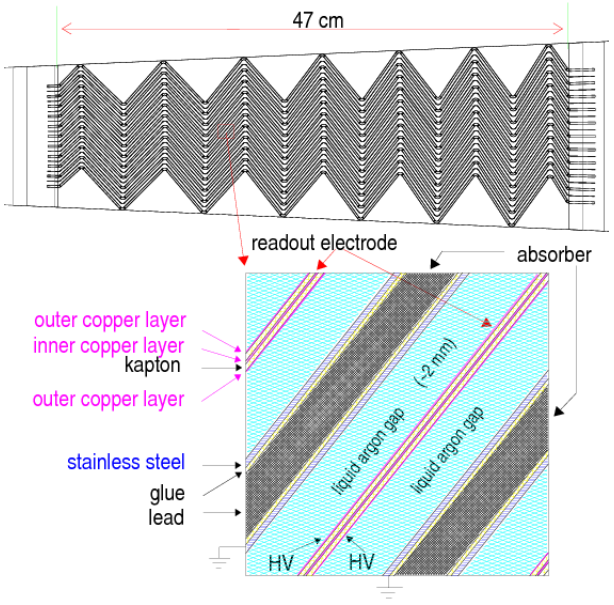


Figure 3.9: Schema of the absorber and electrode disposition in the EM calorimeter barrel.

The absorbers (Fig. 3.10) [3] are made of lead in order to provide good shower sampling at the same time that a compact detector is built. However, the cylindrical symmetry of the calorimeter poses certain geometrical issues. A detector geometry with straight absorbers placed perpendicularly to the radial direction would present cracks along ϕ in order to provide some space to accommodate the detector services (readout electronics). Thus, absorbers are bent following an accordion geometry. The bending angles vary from the front to the back in order to accommodate different layers of this absorber while preserving a constant spacing between them.

The weight of the absorbers could induce the deformation of the lead structure. To prevent this, the lead is reinforced with two layers of stainless-steel glued with a fibreglass preparation ("prepreg"). In addition, lead thickness is reduced from 1.5 mm at $|\eta| < 0.8$ to 1.1 mm at $|\eta| > 0.8$ to allow a good sampling of the shower while the projective angle evolution at increasing η makes the effective lead thickness to increase. The LAr gap is however kept constant by increasing the thickness of the prepreg layer.

Electrodes are interleaved with the absorber layers in order to collect charges from LAr ionization. They are composed of three copper layers (Fig. 3.11): two outer layers that serve to distribute a high-voltage (HV) around 2000V between the absorbers and the electrode and one internal copper layer which plays the role of the signal readout layer. These copper layers are separated by two insulating kapton-polyimide layers glued using a thermosetting epoxy adhesive. In addition, electrodes are divided into two separate elements, each covering $0 < |\eta| < 0.8$ and $0.8 < |\eta| < 1.45$, respectively. These two elements are called electrode A and electrode B for both half-barrels and correspond to the 2 different lead thicknesses. Once ionization charges are induced by EM objects traversing the liquid argon gap, electrons drift towards the HV layers and induce a proportional current by capacitive coupling into the signal layer.

Electrodes are disposed between absorbers in such a way that the gap between the electrode and the

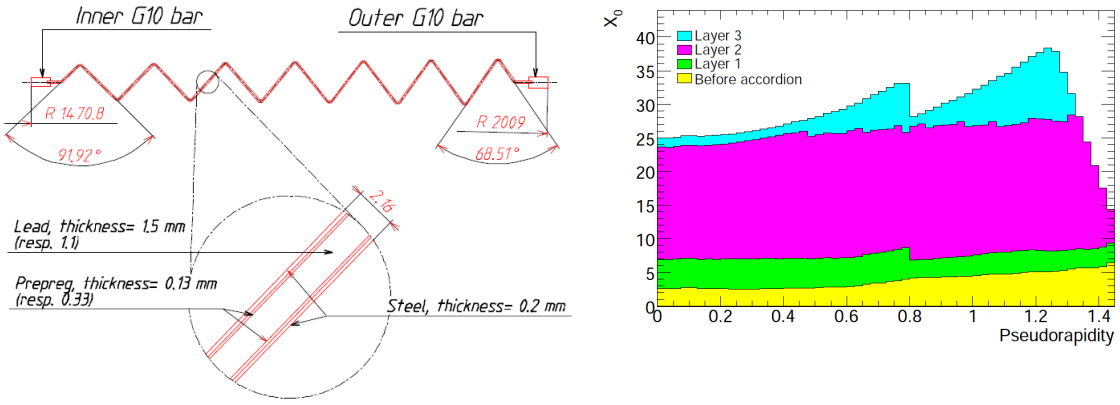
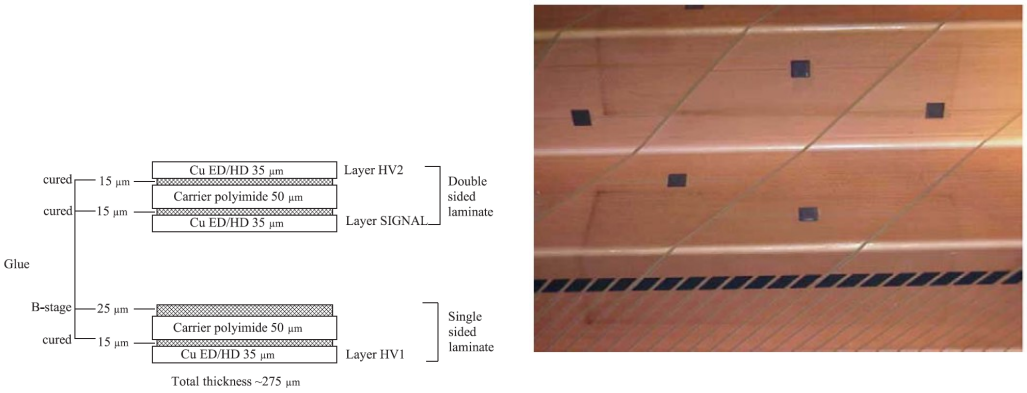


Figure 3.10: Left: schema of the absorber bending angle and composition [3]. Right: cumulative amount of material found by particles traversing the detector expressed as radiation lengths X_0 [8]. It can be observed an increase of the cumulative material in the EM calo with η. It can be observed the lead thickness change at $\eta = 0.8$.



(a) (b)

Figure 3.11: Electrode components of the liquid argon (a) and electrodes high-voltage layers before bending, cut into small compartments connected by ink resistors (b) ([10]).

absorbers is around 2.09mm wide. This disposition allows an equal charge collection from both sides of the electrode which prevents any deformation in the readout pulse. Honeycomb spacers are added between the electrode and the absorbers to further keep this gap size constant all along the calorimeter, thus ensuring a uniform charge collection (Figure 3.12).

To avoid that short circuits between the HV layer and the material spoil a complete electrode, HV layers are cut into independent sectors. In addition, the HV layer is further cut following the radial layers and η pattern exposed in Section 3.3.1. These different sectors are connected by ink resistors, directly silk screened on the HV layer, which ensure the HV distribution and uniformity along the LAr gaps. Resistors between compartments in the same layer are set to 10 kΩ while resistors between different layers are at least 200 kΩ [10] (occasionally, few resistors present 100 kΩ). Apart from ensuring the HV all along the calorimeter, resistances also allow charge evacuation from the LAr gap after that signal current inside the electrode signal layer is created by them through capacitive coupling.

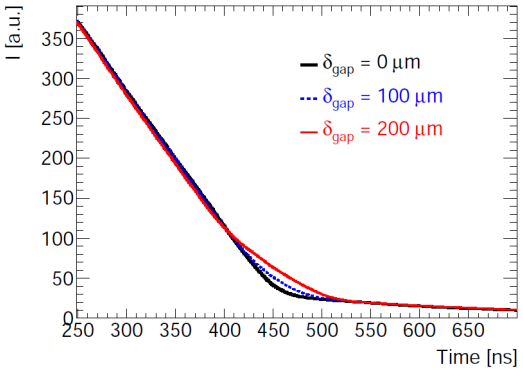


Figure 3.12: Current as a function of time for a perfect centering of the electrode with δ_{gap} = 0 μm and δ_{gap} = 100 μm and δ_{gap} = 200 μm [14].

3.3.3 From charge collection to front-end electronics

Signals from each electrode are sent to summing boards that assemble adjacent electrodes into electronic cells, with the layer-dependent granularity as explained in Section 3.3.1. Front layer signals are readout in the front of the calorimeter modules while signals from the middle and back cells are readout sitting on the back of the calorimeter modules. Each summing board reads one trigger tower of the barrel ($|\Delta\eta| \times |\Delta\phi| = 0.1 \times 0.1$). After charge summation, signals are sent into the mother boards mounted on the summing boards. Mother boards present 16 connectors, with one pin for each electronic cell. So, front mother boards have 32 pins per summing board while in the back, they present 16 pins for cells in the middle layer and 8 pins for cells in the back layer, following a pattern Middle-Back-Middle-Middle-Back-Middle as shown in Figure 3.13 right. Signals from the mother boards are sent to the electronics out of the calorimeter through one of the 64 signal feedthroughs. These feedthroughs are distributed radially around each end of the barrel cryostat(Fig 3.14.b). They are composed of two flanges, warm and cold, separated by stainless-steel bellows allowing vacuum in the transition region. Both flanges present 30 connectors separated in two rows, each with 64 pins. Each connector has a specific tasks, either allowing signal readout or calibration signal injection into the calorimeter, as shown in Fig. 3.14.a.

3.3.4 Front-end boards

After passing the feedthrough, signals are treated by the front-end electronics of the calorimeter. These front-end cards are placed in crates mounted on each feedthrough of the cryostat, called front-end crates (FECs). Each of these crates is mounted on two feedthroughs and can house 28 front-end boards (FEBs), each treating 128 electronic cells (also called channels). A feedthrough can provide signals for 14 FEBs in the barrel, with each front-end board receiving signals from an specific feedthrough connector. Apart from the FEB, each FEC houses 2 calibration and controller (for FEC control) boards, 4 monitoring boards (for calorimeter controlling) and a Tower Builder Board and a Tower Driver Board that ensures trigger related functions. The distribution of these cards is shown in Figure 3.15.

In FEB's, signals are first preamplified and split into four (Fig. 3.16). One of the split signals is combined with other channels forming a $|\eta| \times |\phi| = 0.1 \times 0.1$ trigger tower and sent to the L1 trigger system for processing. The lasting three are amplified again, each with a different gain: Low (1), Medium (10) or High (100). Three fast bipolar filters of type CR-RC^2 are then used for each gain to increase the signal-to-noise ratio. The single differentiation step serves to remove the long tail from the detector response, while the two integrations limit the bandwidth in order to reduce the noise. In order to reduce the quantity of information, these shaped signals are sampled at the LHC clock frequency (40 MHz) and then stored into a Switch Capacitor Array (SCA) analog pipeline with 144 capacitors, which allow to keep cell information during 2.5μ s while attending the trigger Level 1 decision. These samples are

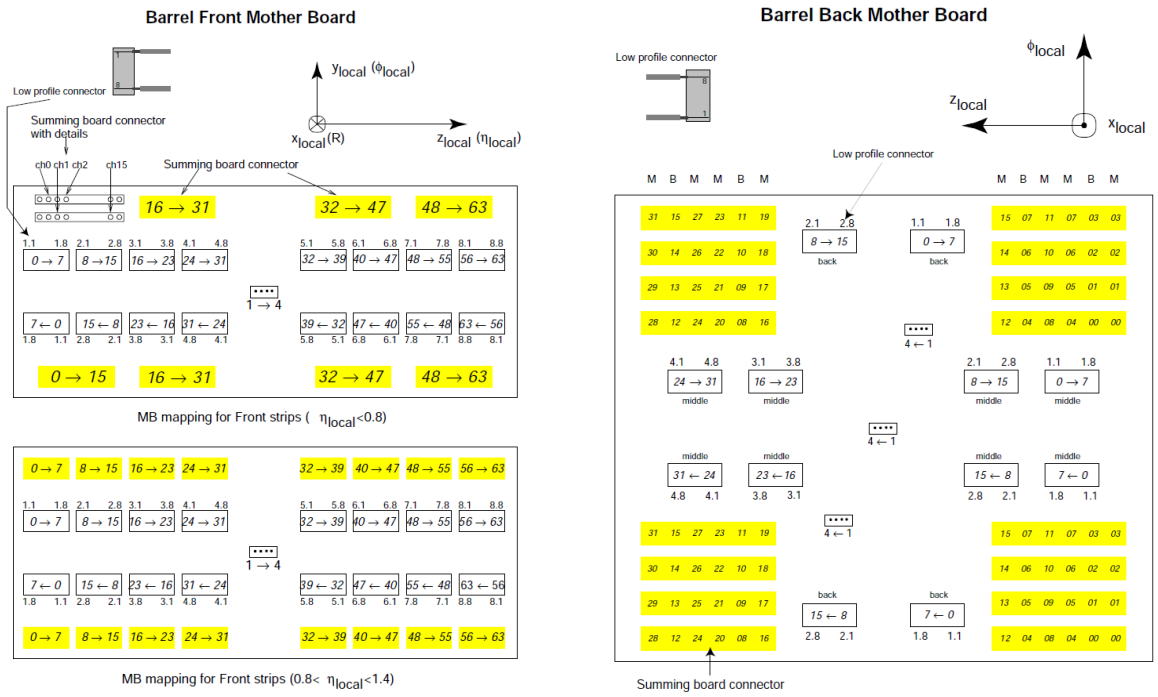


Figure 3.13: Front (left) and back (right) mother boards for the LAr barrel. Numbers on the connectors are attributed to each cell depending on their position [15].

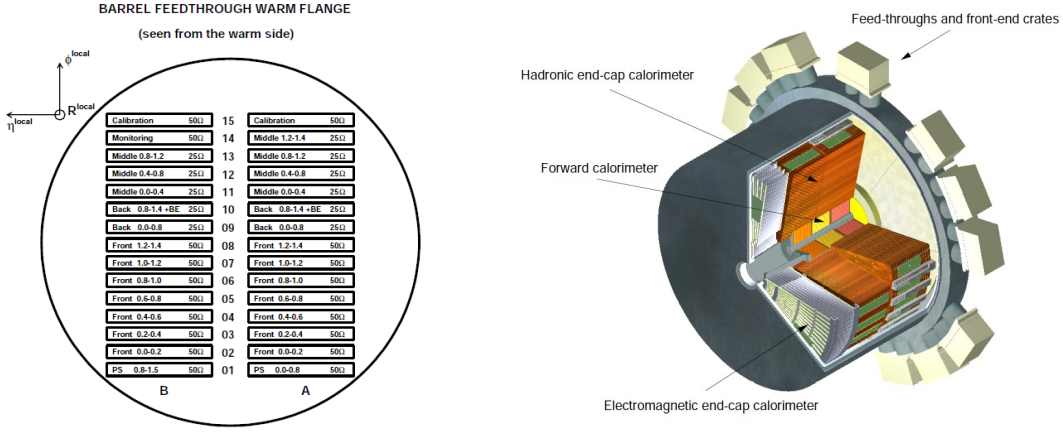


Figure 3.14: Feedthrough connectors distribution (left) [15] and feedthrough distribution in the cryostat of the end-cap(right), similar to the distribution of the feedthroughts around the barrel cryostat [8].

stored until the L1 trigger accepts the event, in which case the first four samples of the signal shape are digitized following L1 instructions through a 12-bit analog-to-digital (ADC) converter and sent to the read-out drivers (RODs). This digitization provides the signal amplitude in ADC counts, ranging from 0 to 4096, for one of the three gains. The optimal gain is determined depending on the ADC saturation. If high gain (signal $\times 100$) saturates the 4096 counts of the ADC, then the medium gain signal (signal $\times 10$) is digitized. If again a saturation of the 4096 occurs, signals are passed to the RODs at low gain. Samples are then combined together to find the waveform peak using a method called optimal filtering (OF). The conversion of the signal peak in ADC into MeV is done by means of a calibration system, explained in the next subsection.

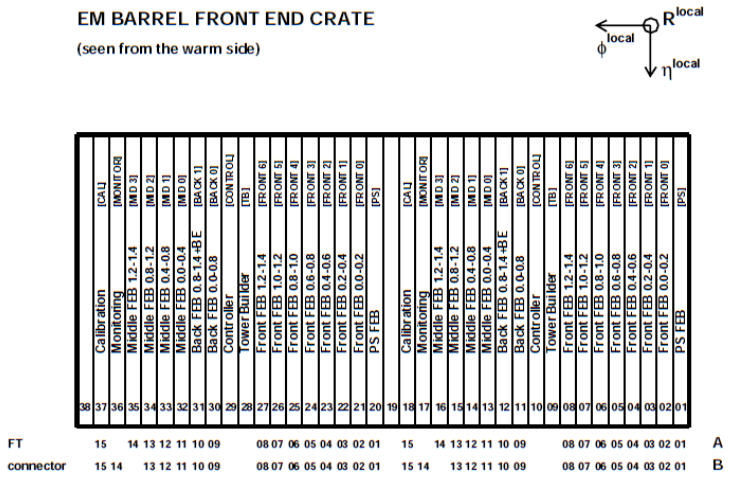


Figure 3.15: Boards distribution in the front-end crates for the barrel [15]

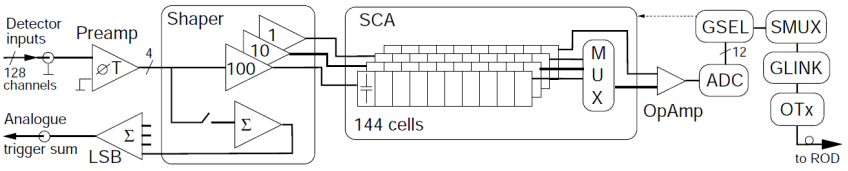


Figure 3.16: Diagram of the FEB architecture [8].

3.3.5 Electronic cell calibration

The calibration procedure sets the correspondence between a cell signal peak readout in ADC counts and the actual energy deposited in the cell and its peaking time (Fig. 3.17). This process uses a dedicated step to calibrate the full electronic chain by evaluating the relation between the read ADC counts and a known injected current μA on the electrode signal.

Calibration boards inject an exponential pulse with a decay time chosen to mimic the ionization pulse shape. This pulse is the result of a condensator discharge with a tunable amplitude. Calibration boards are mounted on the FECs. The calibration sequence is initiated by a command of the Trigger, Timing and Control board, after which the calibration board injects the signal with a certain delay t_0. This delay is allowed by two PHOS4 delay chips in the calibration board, which permit to shift the injected pulse by steps of 1.04 ns [16]. After this, a L1 accept signal is issued into the FEBs, programmable in steps of 25 ns. The amplitude of this pulse is controlled by a 16 digital-to-analog converter (DAC) system that provides a voltage according to requested command (done in DAC counts). The current enters the cryostat through the signal feedthroughs and is injected into the corresponding cell electrode through the mother boards. This injection path introduces differences between the calibration signal and the ionization signal. Since the objective of the calibration is to estimate the relation between ADC ionization pulse and its corresponding μA, calibration pulses must be corrected from these effects. Applied corrections to the calibration signal to emulate the physics one are explained in next section.

The conversion of ADC into MeV is then performed using the following formula:

$$E_{cell} = F_{\mu A \to MeV} F_{DAC \to \mu A} \frac{1}{\frac{M_{\text{phys}}}{M_{\text{calib}}}} \sum_{j=0}^{2} R_j \left(\sum_{i=0}^{4} a_i S_i \right)^j \tag{3.13}$$

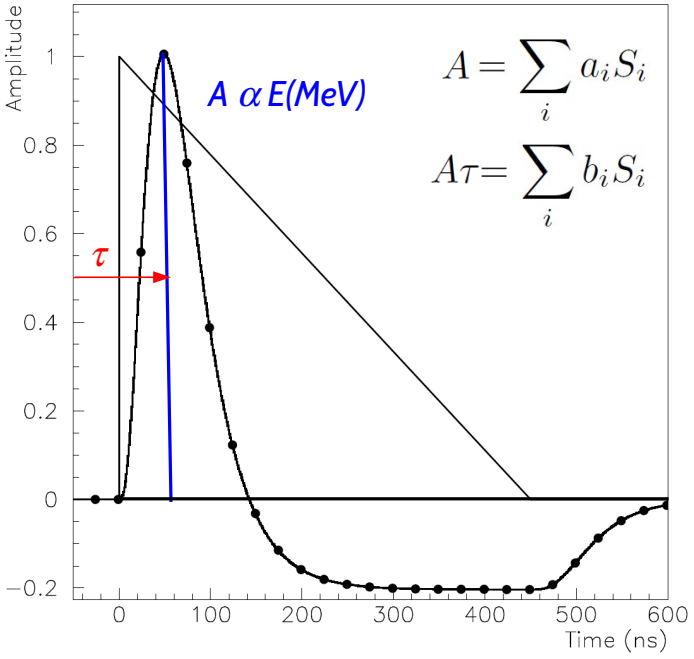


Figure 3.17: Sketch of the peaking time and amplitude of the physics signal and the estimation using optimal filtering coefficients (OFCs). The amplitude is proportional to the energy deposited in the cell.

where a_i are the optimal filtering coefficients (OFCs) for finding the signal peak (Section 3.5), R_j are the ramps transforming the ADC counts into DAC (digital counts) and $\frac{M_{\text{phys}}}{M_{\text{calib}}}$, $F_{\mu A \to MeV}$ and $F_{DAC \to \mu A}$ are electronic calibration constants, computed as explained in Section 3.6.

3.4 Signal shape for physics signal

The determination of calibration coefficients, in particular, the optimal filtering coefficients, is performed during regular calibration campaigns on a daily basis. However, the signal from calibration runs emulates the ionization signal but is not exactly the same. The OFCs are necessary to find the signal peak and therefore, they must be derived from signals similar to the ones expected during physics runs. Calibration pulses must then be corrected for their difference in shape.

3.4.1 Ionization signal

Ionization charges are deposited instantaneously and homogeneously in the LAr gap. The liquid argon is a material with high electron mobility. This implies that an important fraction of the created charges after ionization are collected without suffering important losses in their drift velocity within the material. Thus, under the action of an electric field E, the electrons drift to the readout electrode. Assuming that the charge density in the liquid argon is constant, the charge measured by the electrode falls with time following a linear law:

$$I(t) = I_0 \left(1 - \frac{t}{T_{\text{drift}}}\right) \theta(t)\theta(T_{\text{d}} - t) \tag{3.14}$$

where I_0 is the initial intensity i.e at signal rise time, which is quite fast (around 1ns after ionization). The signal obtained after liquid argon is ionized is a triangular signal decreasing with time. The ATLAS calorimeter high-voltage is set to 2000 V, which for a gap of 2.09 mm represents an electric field $E = 1\text{kV/mm}$. The drift velocity of the electrons under this field and at a LAr temperature of 88.5 K is

measured to be $v_D = 4.61 \pm 0.07 \mathrm{mm}/\mu\mathrm{s}$, with an average drift time (T_{drift}) of 457.9 ns in the barrel. A complete study of the drift time and velocity is performed in [14].

In addition, recombinations are quite rare in the liquid argon and positive ions contribute little to the signal charge due to their low mobility compared to electrons. However, it is very important to evacuate them to avoid any possible charge effect in the gaps. For instance, their accumulation in the absorbers would lead to a reduction of the electric field in the LAr gap, which affects the electron collection. In the barrel, this is currently not a problem although at high pileup conditions, like in large η regions (end-caps), it can become problematic.

3.4.2 Estimation of the ionization shape after readout

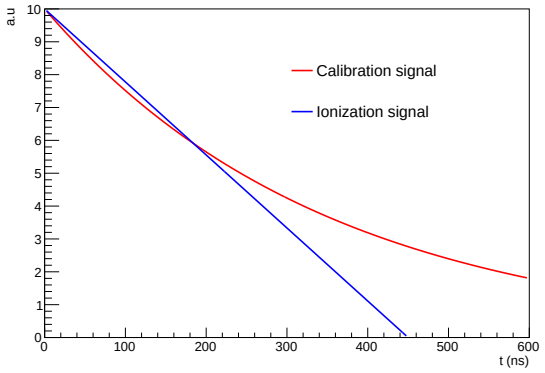


Figure 3.18: Representation of the calibration exponential pulse and ionization triangular signal.

After the injection of the calibration pulse at cell level, the read-out path is identical to physics signal one (Fig 3.19). The differences between the calibration and the ionization signals are then coming from the different initial shapes (exponential vs triangular as illustrated in Fig. 3.18) and the injection technique (calibration: injected on the signal electrode through the mother boards; physics: direct ionization of LAr).

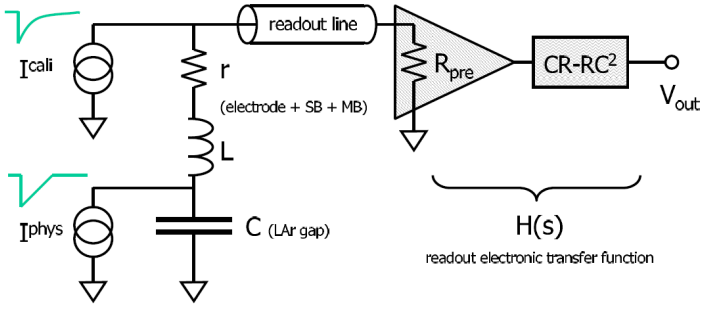


Figure 3.19: Basic equivalent circuit of the liquid argon detector cell readout [17].

The current estimation of the physics signal is performed by applying a Response Transformation Method (RTM) [17] on calibration signals. It consists of studying the effect that the injection and readout circuits have on signals and correct the calibration pulse from it. The differences are encoded in response functions of the system. The output of this method is the predicted physics signal, which can be expressed

as the convolution of the components:

$$g^{\text{phys}}(t) = g^{\text{cali}}(t) * g^{\text{exp}\to\text{tri}}(t) * g^{\text{MB}\to\text{detector}}(t) \tag{3.15}$$

The estimation of the response functions relies on our knowledge of the calorimeter readout system. These calculations are done in the Laplace domain.

Estimation of $g^{\text{exp}\to\text{tri}}(t)$

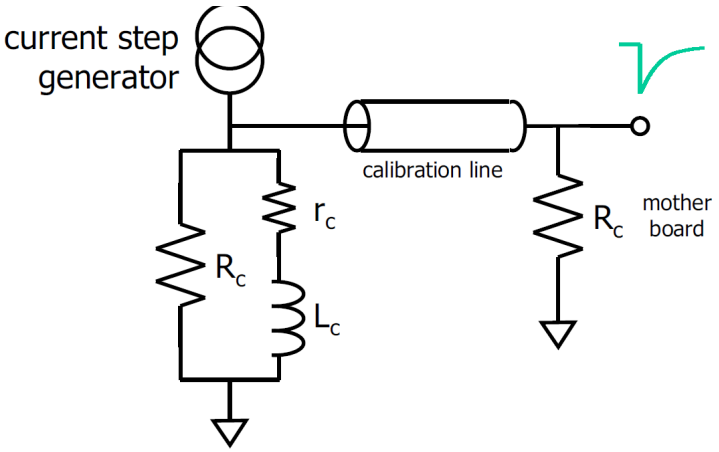


Figure 3.20: Simplified calibration board pulser circuit, showing the non-ideal nature of the inductance L_c in its resistive component r_c [17].

Although the exponential signal is tuned to emulate the ionization signal, differences are still present. The physics signal (Eq. 3.14) in the Laplace domain can be expressed as:

$$I^{\text{phys}}(s) = I_0^{\text{phys}} \left[\frac{1}{s} - \frac{1 - e^{-sT_{\text{drift}}}}{s^2 T_{\text{drift}}} \right] \tag{3.16}$$

As exposed in Section 3.3.5, the calibration board circuit (Fig. 3.20) alters the calibration signal due to a non-desired resistance r_c.

$$I^{\text{calib}}(s) = I_0^{\text{calib}} \left[\frac{f_{\text{step}} + s\tau_{\text{calib}}}{s(1+\tau_{\text{calib}})} \right]; \quad f_{\text{step}} = \left(\frac{r_c}{r_c + \frac{R_c}{2}} \right); \quad \tau_{\text{calib}} = \left(\frac{L_c}{r_c + \frac{R_c}{2}} \right) \tag{3.17}$$

The response function in Laplace domain is then estimated by $I^{\text{phys}}(s)$ and $I^{\text{calib}}(s)$, so that the final response function is the Laplace inverse of this factor:

$$\begin{aligned} g^{\text{exp}\to\text{tri}}(t) = \mathcal{L}^{-1}\left(\frac{I^{\text{phys}}(s)}{I^{\text{calib}}(s)} \right) = \delta(t) + \Bigg[& \frac{1 - f_{\text{step}}}{\tau_{\text{calib}}} e^{-f_{\text{step}} t/\tau_{\text{calib}}} \\ & + \frac{1}{f_{\text{step}} T_{\text{drift}}} \left((1 - f_{\text{step}}) e^{-f_{\text{step}} t/\tau_{\text{calib}}} - 1 \right) \Bigg] \theta(t) \\ & - \frac{1}{f_{\text{step}} T_{\text{drift}}} \left((1 - f_{\text{step}}) e^{-f_{\text{step}}(t - T_{\text{drift}})/\tau_{\text{calib}}} - 1 \right) \theta(t - T_{\text{drift}}) \end{aligned} \tag{3.18}$$

Estimation of $g^{\text{MB}\to\text{detector}}(t)$

Following the schema in Figure 3.19, the corresponding currents at the mother board injection are:

$$I_{\text{MB}}^{\text{phys}}(s) = I^{\text{phys}}(s) \frac{\frac{1}{sC}}{r + \frac{1}{sC} + sL + Z_{\text{line}}} \tag{3.19}$$

$$I_{\text{MB}}^{\text{calib}}(s) = I^{\text{calib}}(s) \frac{r + \frac{1}{sC} + sL}{r + \frac{1}{sC} + sL + Z_{\text{line}}} \tag{3.20}$$

where I^{calib} and $I^{\text{phys}}(s)$ are the calibration and physics pulsed that arrive at the mother board i.e. the exponential and triangular pulses. The response function taking into account the differences in the injection path is then:

$$g^{\text{MB}\to\text{det}}(t) = \mathcal{L}^{-1}\left(\frac{1}{1+s\tau_r+s^2\tau_0^2}\right) = \frac{2}{\tau_a}e^{-\frac{\tau_r}{2\tau_0^2}t}\sin\left(\frac{\tau_a}{2\tau_0^2}t\right)\theta(t); \tag{3.21}$$

with $\tau_r = rC; \quad \tau_0 = \sqrt{LC}; \quad \text{and} \quad \tau_a = \sqrt{4\tau_0^2 - \tau_r^2}$

Figure 3.21, a comparison between the calibration pulse after passing through the pre-amplifier and the shaper and the physics signal pulse. It can be observed that the width of pulse is softly smaller for physics signal while its peak is larger than calibration one.

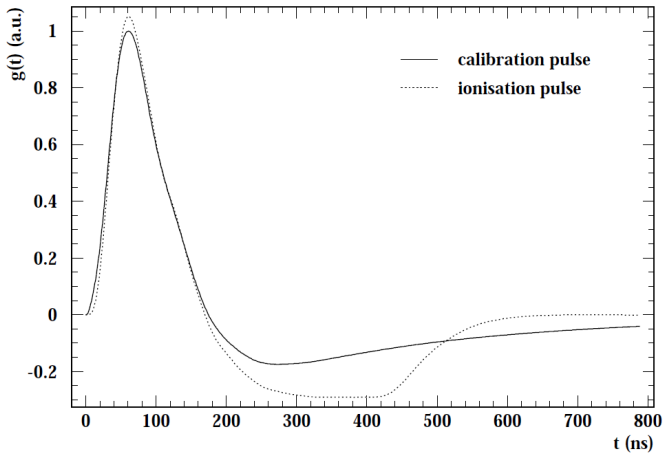


Figure 3.21: Comparison between calibration and physics pulse [17].

3.5 Optimal filtering

After the physics signal modeling, the next step is to determine the amplitude and timing of the pulse (pulse peaking time τ). The amplitude contains information about the number of charges that are collected and the timing permits to determine at which moment the shower ionizes the corresponding cell. Considering that particles are relativistic, and therefore that the mean time for crossing the calorimeter should be of the order of the nanoseconds, and that the shaping time is also constant for all readout cells, this pulse time helps to determine the time at which the incident particle arrived at the detector. This amplitude and peaking time τ (Fig. 3.17) could be determined just sampling the pulse at the peak. However, the presence of electronic and pileup noise would add fluctuations to this peak. This encourages the use of several samples of the pulse to achieve accurate measurements. The ponderated mean of these samples cancels the stochastic noise on average. Furthermore, positive fluctuations impact, such as the pileup noise, is reduced.

The optimal filtering method [18] aims at using two linear combinations of signal samples to recover the amplitude A of the signal and the start time τ:

$$u = \sum_i a_i S_i \quad ; \quad v = \sum_i b_i S_i \tag{3.22}$$

Considering the signal pulse S developed in first order Taylor expansion around $t = \tau$:

$$S_i = Ag(t_i - \tau) + n_i + \text{ped} \approx Ag(t_i) - A\tau\frac{dg(t)}{dt}|_{t_i} + n_i + \text{ped} \tag{3.23}$$

where i is the i-th sample of the pulse and n_i are the noise fluctuations and ped represents the pedestals, which is the average baseline value of the signal. Removing the pedestal contribution so that $S_i \to$

$S_i - \mathrm{ped}$, the equation 3.22 becomes:

$$\begin{aligned} < u >= \sum_i a_i \left(Ag(t_i) - A\tau \frac{dg(t)}{dt}|_{t_i} + < n_i > \right) \\ < v >= \sum_i b_i \left(Ag(t_i) - A\tau \frac{dg(t)}{dt}|_{t_i} + < n_i > \right) \end{aligned} \tag{3.24}$$

On average, $< n_i >$ is zero since noise fluctuations would cancel and $A =< u >$ and $A\tau =< v >$. These leads to the constraints:

$$\sum_i a_i g_i = 1, \quad \sum_i a_i \frac{dg}{dt}|_{t_i} = 0 \sum_i b_i g_i = 0, \quad \sum_i b_i \frac{dg}{dt}|_{t_i} = -1 \tag{3.25}$$

The coefficients a_i and b_i are determined by minimising the variances of u and v while satisfying constraints from Eqs 3.25 using Lagrange multipliers (λ,κ,μ,ρ):

$$Var(u) = \sum_{i,j} a_i a_j < n_i n_j >= \sum_{i,j} R_{ij} a_i a_j \quad ; \quad Var(v) = \sum_{i,j} R_{ij} b_i b_j \tag{3.26}$$

$$\begin{aligned} I_u = \sum_{i,j} R_{ij} a_i a_j - \lambda \left(\sum_i a_i g_i - 1 \right) - \kappa \sum_i a_i \frac{dg}{dt}|_{t_i} \\ I_v = \sum_{i,j} R_{ij} b_i b_j - \mu \sum_i b_i g_i - \rho \left(\sum_i b_i \frac{dg}{dt}|_{t_i} \right) \end{aligned} \tag{3.27}$$

The minimization of both I_u and I_v allow estimating a_i and b_i. The expression of the optimal filtering coefficients after minimization is:

$$\begin{aligned} a_i = \lambda \sum_j (R^{-1})_{ij} g(t_j) + \kappa \sum_j (R^{-1})_{ij} \frac{dg}{dt}|_{t_j}; \\ b_i = \mu \sum_j (R^{-1})_{ij} g(t_j) + \rho \sum_j (R^{-1})_{ij} \frac{dg}{dt}|_{t_j}; \end{aligned} \tag{3.28}$$

with λ, μ, ρ and κ being:

$$\begin{aligned} \lambda = \frac{\vec{g(t)}'^T R^{-1} \vec{g(t)}'}{\Delta}; \quad \kappa = -\frac{\vec{g(t)}'^T R^{-1} \vec{g(t)}}{\Delta} \\ \mu = \frac{\vec{g(t)}'^T R^{-1} \vec{g(t)}}{\Delta}; \quad \rho = -\frac{\vec{g(t)}^T R^{-1} \vec{g(t)}}{\Delta} \\ \Delta = (\vec{g(t)}^T R^{-1} \vec{g(t)})(\vec{g(t)}'^T R^{-1} \vec{g(t)}') - (\vec{g(t)}'^T R^{-1} \vec{g(t)})^2 \end{aligned} \tag{3.29}$$

$\vec{g(t)}$ and $\vec{g(t)}'$ are the vector of samples and the vector of samples of the time derivate of the waveform. These samples are determined cell-by-cell using calibration runs. The goodness of the method depends if the OF coefficients (OFCs) a_i and b_i are applied to the same samples ($S(t_i)$) on which they were derived. Since some delays may happen between the collision time and the arrival of the signal to the calorimeter, OFC's are estimated by delaying the calibration pulse by a phase, allowed by delay chips on the calibration boards presented in Section 3.3.5. Delay steps of 1.04 ns allow determining 24 sets of OFCs for each cell. During RunI, five signal samples were used to determine cell properties. Currently, four samples are considered.

3.6 Passage from ADC to MeV

After signal shape determination and the application of the optimal filtering technique to find the signal peak, the conversion from ADC counts into energy units require the determination of calibration

constants that depend on the calorimeter intrinsic behaviour, i.e, how a given energy is converted into a number of charges, whose derivation into the gap creates a current which induces an electrical tension that is sampled into ADC counts. Unless stated otherwise, information concerning these calorimeter constants presented in this section is based on the report [19].

3.6.1 Ramps

The signal peak is estimated in ADC while calibration boards send pulses with a desired amplitude, determined using DAC counts. A first step of the conversion is then to transform from ADC to DAC since one may correlate the DAC counts with the injected current by the calibration board. This DAC/ADC relation is mainly linear, as it can be observed in Figure 3.22 and 3.23 for all cells in the barrel and one cell, respectively.

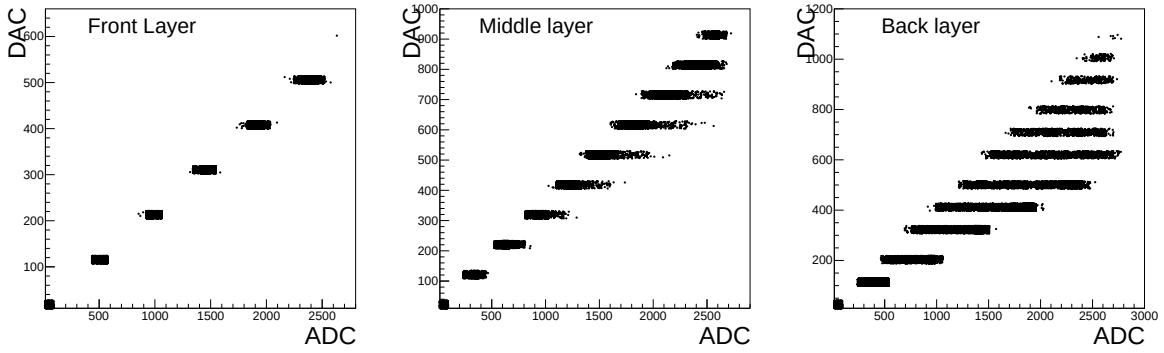


Figure 3.22: Run 00314180: DAC versus ADC_{peak} obtained in a high gain run for the 3 layers of the electromagnetic calorimeter.

However, possible non-linearities might be found coming from the electronic chain. In consequence, the DAC versus ADC curve is fitted with a second-order polynomial function:

$$DAC = R_0 + R_1 ADC_{peak} + R_2 ADC_{peak}^2 \tag{3.30}$$

where the coefficients R_0, R_1, R_2 are called *ramps*. The ADC output depends on the signal optimal gain (low, medium or high), so ramps are also gain-dependent quantities. However, this factor should be the factor between gains (1/10/100 for low, medium and high gain). For ramps estimation, several pulses are sent ($N_{triggers} = 100$) using different DAC values (typically 16 from 0 to 1500) and output ADC

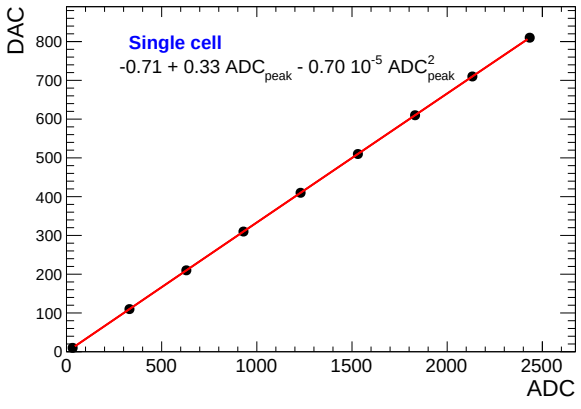


Figure 3.23: Run 00314180: DAC versus ADC_{peak} obtained in a high gain run for a single cell in the middle layer of the EM barrel calorimeter. The red line corresponds to the fitted curve describing the DAC vs ADC behaviour (Eq. 3.30).

samples are collected. The ADC peak is estimated and Equation 3.30 is used to get the ramps. The result for this calibration technique is presented in Figures 3.24 for R_1. These values correspond to a weekly calibration campaign performed on December 4^{th}, 2016 with RunNumber 00314180.

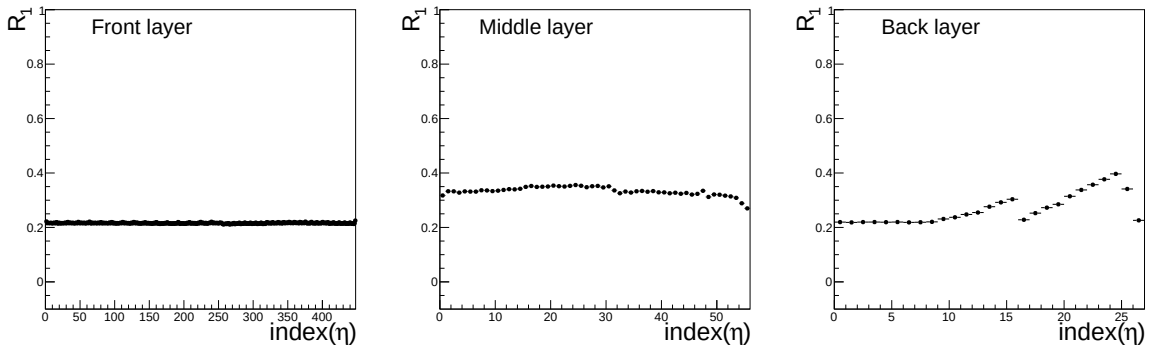


Figure 3.24: Run 00314180: value of R_1 from the fit of the DAC versus ADC distributions in Figure 3.22 with Equation 3.30.

3.6.2 Difference between physics and calibration peaks

Considering that $I_0^{\text{physics}} = I_0^{\text{calib}}$ in Section 3.3.3, the peak amplitudes of g^{phys} and g^{calib} differ as seen on Fig. 3.21. These differences are evaluated as the ratio of the physics and calibration peaks ($M_{\text{phys}} = \max(g^{\text{phys}})$ and $M_{\text{calib}} = \max(g^{\text{calib}})$) evaluated and can be applied on the energy calibration to correct for these amplitude differences. However, OFC's for physics signals are directly derived using g^{phys} shape estimated from calibration shapes with $M_{\text{calib}} = 1$. This implies that the output OFCs already including these $M_{\text{phys}}/M_{\text{calib}}$ factors, presented in Figure 3.25 for the three layers of the calorimeter barrel for a weekly calibration run with RunNumber 00314179 (December 4^{th}, 2016).

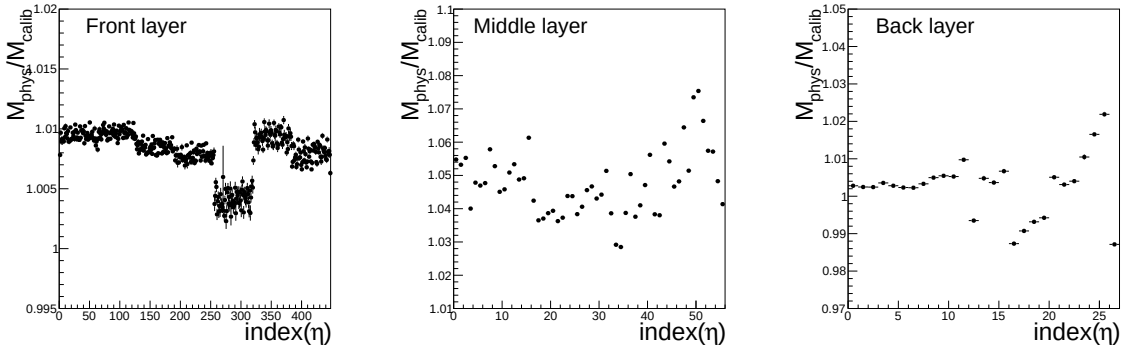


Figure 3.25: Run 00314179: value of $\frac{M_{\text{phys}}}{M_{\text{calib}}}$ for (a) the front layer, (b) the middle layer and (c) for the back layer of the electromagnetic barrel.

3.6.3 Calorimeter constants

The factor $F_{DAC\to\mu A}$ transforms the DAC counts into a current measurement. The amplitude of this pulse is controlled by the DAC system that provides a voltage according to requested command (done in DAC counts). This current is sent to the motherboards that distribute it into the chosen cells via a resistor system with R_{inj} resistance. The amplitude of the injected current in the cells then depends on

Barrel layers	Strips	Middle	Back
$F_{DAC\to\mu A}$ ($\mu A/DAC$)	0.0025464	0.150127	0.0751078

Table 3.2: Values of $F_{DAC\to\mu A}$ in 2004 test beam report [19].

Compartment	I/E ($\mu A/$ MeV)	f_{sampl}	$F_{\mu A\to\mathrm{MeV}}$
$\eta < 0.8$	0.016	0.1667	375
$\eta > 0.8$	0.016	0.1959	320

Table 3.3: Values of I/E, f_{sampl} and $F_{\mu A\to\mathrm{MeV}}$ in 2004 test beam report [19].

the initial value of the voltage over R_{inj}. The chosen current is:

$$F_{DAC\to\mu A} = \frac{75.295\mu V}{R_{inj}} \tag{3.31}$$

which yields values in Table 3.2.

The factor $F_{\mu A\to\mathrm{MeV}}$ converts the current expressed in μA into energy units MeV. For the barrel, $F_{\mu A\to\mathrm{MeV}}$ depends on the sampling performance of the calorimeters and the capacitance between the high-voltage and the electrode layers. It can be expressed as:

$$F_{\mu A\to\mathrm{MeV}} = \frac{1}{f_{sampl} I/E} \tag{3.32}$$

where I/E is the energy to current conversion factor and f_{sampl} is the sampling fraction for electrons. This factor translates the energy that was deposited in the liquid argon gaps (E_{vis}) into the total energy of the electron (E_{total}), which is not the same for sampling calorimeters as exposed in Section 3.1. In [19], values in Table 3.3 are found. These quantities are independent on the gain.

3.7 Energy and time reconstruction performance

The energy reconstruction in the electromagnetic calorimeter was tested in 2002 [20]. Using 5 samples for reconstructing the peak amplitude with OFC's, this test showed that the energy of electrons could be in most cases reconstructed within a 1‰ precision as seen in Figure 3.26.a (0.5% for electrons with $E >$ 20 GeV). In addition, the energy resolution parameters a, b and c from Eq. 3.1 were derived. Figure 3.26 shows that the constant term c of the energy resolution is around 0.17% while the stochastic term a corresponds to 10.1%. This disparity can, however, arrive up to 0.7% when the whole EM calorimeter is taken into account 0.7% [4]. In addition, the noise b is found to represent 250 MeV. This result is in agreement with expectations and test-beams presented in the TDR [3].

The time reconstruction of the electromagnetic barrel has also been tested during 2001-2002 test beam [9]. Several sources are found to contribute to time measurement, mainly related to the electronic chain and calorimeter problems. Two scintillation counters are added to the beamline in order to determine the time at which the electrons are being sent to the calorimeter. One of these scintillators is found to perform more precise timing measurements and then, its time measurement (t_2) is defined as reference time to this study.

Electronic chain contribution

The measurement is carried out by pulsing simultaneously two cells and comparing their reconstructed time with OF method. Three configurations are considered: cells that do not belong to the same calibration line; cells that do belong to the same calibration line and cells belong not only to the same calibration line but also to the same SCA pipeline. The results using the two last configurations show a dependence

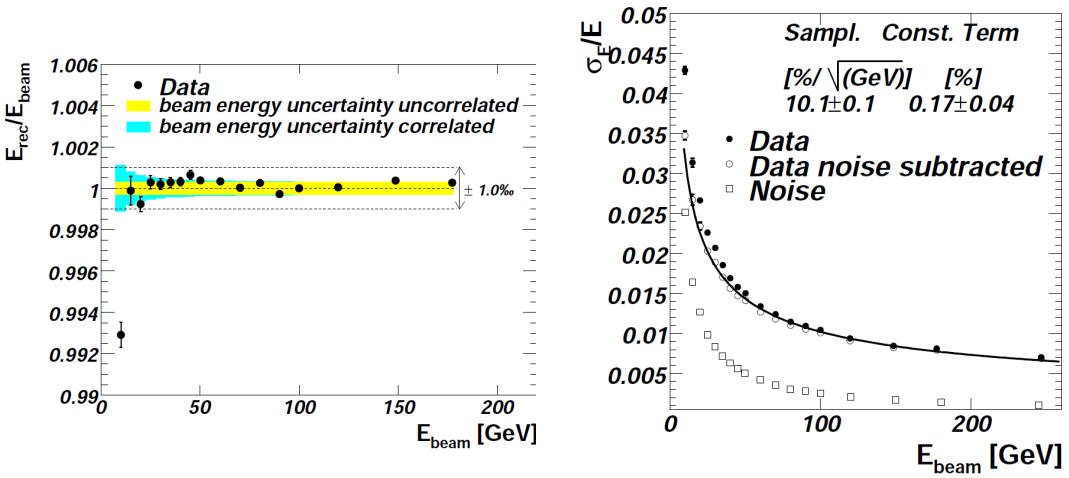


Figure 3.26: The ratio of the reconstructed electron energy to the beam energy (a) and the fractional energy resolution (b) as a function of the beam energy are presented [20]. In (b) data before (closed circles) and after (open circle) the gain dependent noise (open squares) subtraction are shown.

of the time resolution with the input amplitude of the signal pulse, which can be parametrized by:

$$\sigma_\tau = \frac{a_\tau}{E} \oplus c_\tau \tag{3.33}$$

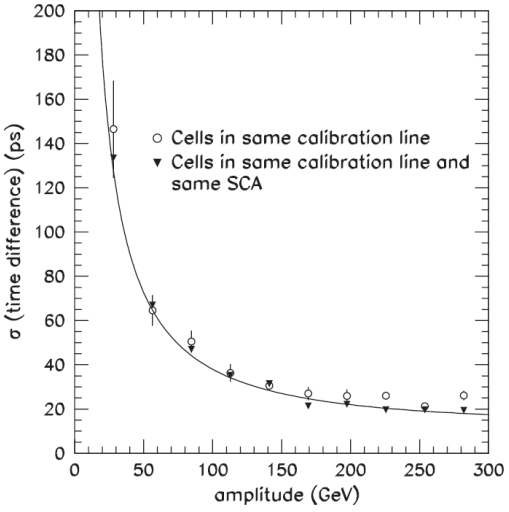


Figure 3.27: Resolution on the time difference between cells in calibration runs as a function of the amplitude [9].

The fitted function presents a constant term close to 20 ps in high gain for cells in the middle layer. This constitutes a lower limit to the time resolution. Table 3.4 presents the results for these different configurations.

Calorimeter problems

Due to the 1/E term in Eq. 3.33 and the fact that most of the shower energy is measured in the middle layer, the most accurate single cell based information on the injection time for a electromagnetic shower is given by the hottest cell in the middle layer. Tests are carried out using test beam data for the resolution of a 245 GeV electron beam. Comparisons between t_2 and reconstructed time by OF method present a

	Middle layer		Front layer	
	a_τ (ps * GeV)	c_τ (ps)	a_τ (ps * GeV)	c_τ (ps)
High gain	1620 ± 60	19 ± 14	510 ± 20	30 ± 8
Medium gain	2550 ± 15	13 ± 1	740 ± 50	18 ± 1
Medium gain, same SCA	2500 ± 20	9 ± 1	–	–

Table 3.4: Time resolution of the electronics readout for a single channel in the middle/front layer in high and medium gain. Measurement for the same calibration line and the same SCA could not be performed for the front layer due to the distribution of the calibration lines [9].

245 ps dispersion. A non-negligible fraction of this dispersion is found to come from SCA, phase and cross-talk effects.

1. It is found that if two cells are not treated by the same SCA capacitor in the FEB's, a linear bias on the reconstructed time t_{OF} appears. The correction of this effect leads to 239 ps of resolution.
2. The trigger setup during the test beam was asynchronous with the 40 MHz clock, usually providing the reference time for collisions in physics runs. This introduced a shift in the shape sampling before the SCA and therefore the reconstructed time got a small bias. However, this effect could be corrected. Overall resolution is reduced to 188 ps after corrections.
3. Cross-talk contribution is also affecting the time reconstruction. This effect distorts the signal shape and induces a bias in the time determination. It is found to be 94 ps and its correction allows to reduce the overall resolution to 163 ps. The cross-talk affects the energy reconstruction too, introducing a bias in the energy barycenter (η and ϕ position of the largest energy deposit). The larger is the cross-talk impact, the larger this bias could be. Figure 3.28 presents this bias depending on impact point position within the cell in η and ϕ.

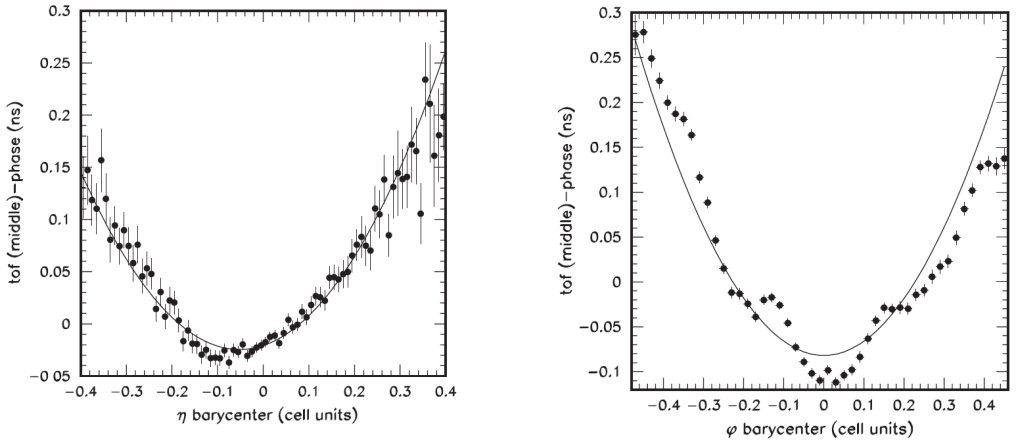


Figure 3.28: Difference between reconstructed OF time and trigger time depending on the barycenter of energy deposition in between cells in η and ϕ [9].

After correcting the resolution from these effects and possible sources coming from the trigger time resolution, the overall time resolution of the electromagnetic calorimeter shows a performance decreasing with the energy of the hottest middle cell and converging to a constant value of ~ 100 ps (Fig. 3.29). The change in the slope at $E \sim 40$ GeV corresponds to the change in the gain used to reconstruct the energy of the cell, given that typically at those energies the ADC counts in high gain are saturated.

Currently, the ATLAS calorimeter is performing very well. Almost all the readout channels are available and taking data, without any loss of data due to a bad operation of the liquid argon detectors. The L1-trigger can sustain a 110 kHz event rate, a bit larger than the nominal value of 100 kHz for L1 Calo Trigger 2.2.5.

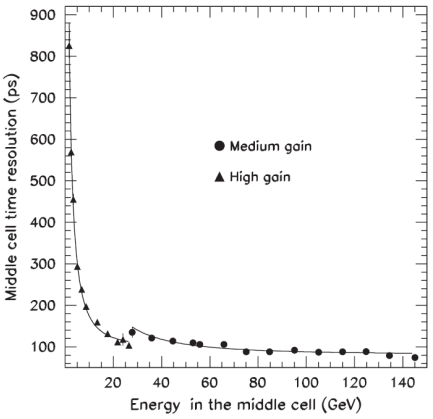


Figure 3.29: Time resolution (ps) as a function of the hottest middle layer cell.

References

[1] Klaus Pretzl. "Calorimeters in astro and particle physics". In: *Journal of Physics G: Nuclear and Particle Physics* 31.7 (2005), R133. URL: http://stacks.iop.org/0954-3899/31/i=7/a=R01.

[2] *The CMS electromagnetic calorimeter project: Technical Design Report*. Technical Design Report CMS. Geneva: CERN, 1997. URL: http://cds.cern.ch/record/349375.

[3] *ATLAS liquid-argon calorimeter: Technical Design Report*. Technical Design Report ATLAS. Geneva: CERN, 1996. URL: https://cds.cern.ch/record/331061.

[4] J. Colas et al. "Response Uniformity of the ATLAS Liquid Argon Electromagnetic Calorimeter". In: *Nucl. Instrum. Meth.* A582 (2007), pp. 429–455. DOI: 10.1016/j.nima.2007.08.157. arXiv: 0709.1094 [physics.ins-det].

[5] P Adzic. "Energy resolution of the barrel of the CMS Electromagnetic Calorimeter". In: *Journal of Instrumentation* 2.04 (2007), P04004. URL: http://stacks.iop.org/1748-0221/2/i=04/a=P04004.

[6] C. Patrignani et al. "Review of Particle Physics". In: *Chin. Phys.* C40.10 (2016), p. 100001. DOI: 10.1088/1674-1137/40/10/100001.

[7] Egidio Longo and Ignazio Sestili. "Monte Carlo calculation of photon-initiated electromagnetic showers in lead glass". In: *Nuclear Instruments and Methods* 128.2 (1975), pp. 283–307. ISSN: 0029-554X. DOI: http://dx.doi.org/10.1016/0029-554X(75)90679-5. URL: http://www.sciencedirect.com/science/article/pii/0029554X75906795.

[8] G. Aad et al. "The ATLAS Experiment at the CERN Large Hadron Collider". In: *JINST* 3 (2008), S08003. DOI: 10.1088/1748-0221/3/08/S08003.

[9] M. Aharrouche et al. "Time resolution of the ATLAS barrel liquid argon electromagnetic calorimeter". In: *Nucl. Instrum. Meth.* A597 (2008), pp. 178–188. DOI: 10.1016/j.nima.2008.08.142.

[10] Bernard Aubert et al. "Development and construction of large size signal electrodes for the ATLAS electromagnetic calorimeter". In: *Nucl. Instrum. Meth.* A539 (2005), pp. 558–594. DOI: 10.1016/j.nima.2004.11.005.

[11] A. Hoecker et al. "TMVA - Toolkit for Multivariate Data Analysis". In: *ArXiv Physics e-prints* (Mar. 2007). eprint: physics/0703039.

[12] *ATLAS calorimeter performance: Technical Design Report*. Technical Design Report ATLAS. Geneva: CERN, 1996. URL: https://cds.cern.ch/record/331059.

[13] A. Airapetian et al. "ATLAS calorimeter performance Technical Design Report". In: (1996).

[14] G. Aad et al. “Drift Time Measurement in the ATLAS Liquid Argon Electromagnetic Calorimeter using Cosmic Muons”. In: *Eur. Phys. J.* C70 (2010), pp. 755–785. DOI: 10.1140/epjc/s10052-010-1403-6. arXiv: 1002.4189 [physics.ins-det].

[15] C. et al. Cerna. *Cabling of the ATLAS liquid argon calorimeters*. URL: http://wwwlpsc.in2p3.fr/atlas/lucotte/3.SOFTWARE/NOTE_ONLINE_CABLING.pdf.

[16] N Massol. *ATLAS calibration delay chip study*. Tech. rep. ATL-ELEC-2004-001. Annecy-le-Vieux: Lab. Annecy Phys. Part., Nov. 2003. URL: http://cds.cern.ch/record/709445.

[17] D. Banfi, M. Delmastro, and M. Fanti. “Cell response equalisation of the ATLAS electromagnetic calorimeter without the direct knowledge of the ionisation signals”. In: *JINST* 1 (2006), P08001. URL: http://iopscience.iop.org/article/10.1088/1748-0221/1/08/P08001/pdf.

[18] W.E. Cleland and E.G. Stern. “Signal processing considerations for liquid ionization calorimeters in a high rate environment”. In: *Nuclear Instruments and Methods in Physics Research Section A: Accelerators, Spectrometers, Detectors and Associated Equipment* 338.2 (1994), pp. 467–497. ISSN: 0168-9002. DOI: http://dx.doi.org/10.1016/0168-9002(94)91332-3. URL: http://www.sciencedirect.com/science/article/pii/0168900294913323.

[19] Martin Aleksa et al. *ATLAS Combined Testbeam: Computation and Validation of the Electronic Calibration Constants for the Electromagnetic Calorimeter*. Tech. rep. ATL-LARG-PUB-2006-003. ATL-COM-LARG-2006-003. Geneva: CERN, Apr. 2006. URL: http://cds.cern.ch/record/942528.

[20] M. Aharrouche et al. “Energy linearity and resolution of the ATLAS electromagnetic barrel calorimeter in an electron test-beam”. In: *Nuclear Instruments and Methods in Physics Research Section A: Accelerators, Spectrometers, Detectors and Associated Equipment* 568.2 (2006), pp. 601–623. ISSN: 0168-9002. DOI: https://doi.org/10.1016/j.nima.2006.07.053. URL: http://www.sciencedirect.com/science/article/pii/S0168900206013222.

Photon and electron reconstruction

Contents

4.1 Cluster and track reconstruction . . . 91
4.1.1 Sliding-window clustering . . . 91
4.1.2 Topological clustering . . . 92
4.1.3 Track reconstruction . . . 93
4.2 Electron and photon reconstruction . . . 93
4.3 Electron and photon identification . . . 97
4.3.1 Electron identification . . . 97
4.3.2 Photon identification . . . 98
4.4 Isolation . . . 102
4.4.1 Calorimetric isolation . . . 102
4.4.2 Track isolation . . . 104
4.5 Photon and electron calibration . . . 105
4.5.1 MC-based calibration and uniformity corrections . . . 106
4.5.2 In-situ corrections . . . 109
4.5.3 Systematic uncertainties . . . 111

After pp collisions happen around the interaction point, the different ATLAS subdetectors present several energy deposits well above the ambient background and their respective electronic noise. A primordial task in ATLAS is to associate these energy deposits to possible particle candidates that were produced in the collisions, either electrons, photons, muons, τ-leptons or jets. In most of the cases, these particles leave significantly distinct signatures in the various subdetectors that can be easily recognized and used to identify the collision product. However, this identification is not so straightforward in some cases, and algorithms must be developed to identify the collision products. In this Chapter, we focus on the electron and photon reconstruction and identification algorithms.

Electrons and photons are reconstructed and identified using information from the ATLAS calorimeter and the inner detector. Electrons are particles that leave a trace of hits in the inner detector and an energy deposit in the electromagnetic calorimeter. They are reconstructed from clusters of cells in the calorimeter to which a track reconstructed from inner detector hits can be associated. In their way, electrons may interact with material from the inner detector and radiate bremsstrahlung photons, a fact that needs to be taken into account in its track reconstruction and that could also induce variations in the topology of their energy deposit in the calorimeter. Photons are instead neutral particles that can present isolated energy deposits in the electromagnetic calorimeter with no associated trace in the inner tracker system or associated with displaced tracks from the beamline due to photon conversionsFigures 4.1 show that these conversions are more likely to happen in regions where the detector presents larger material, such as the different silicon detector layers.

Apart from the separation between electrons and photons, calorimetric clusters can also be produced by the arrival of hadronic particles issued from the hadronization of a quark or gluon. However, these clusters tend to present a more extensive lateral profile and a significant fraction of energy in the hadronic calorimeter. A requirement on the fractional energy of the electron or photon found in this detector ($E_{\text{had}}/E_{\text{total}} < 0.1$) reduces the possible background coming from hadronic energy deposits. Besides,

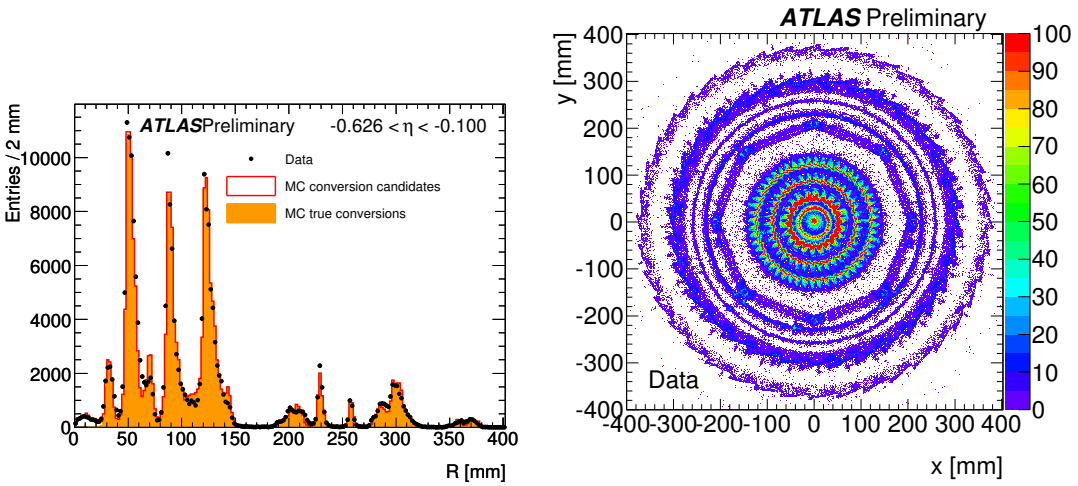


Figure 4.1: Distance to the beamline of reconstructed conversion vertices (left) and spatial distribution of reconstructed conversion vertices (right) in the transverse plane measured on 14nb^{-1} during June-July 2010 [1].

some of these particles produce very similar signatures. One of these cases, which is very important in the analysis presented in this thesis, is the identification of decaying neutral pions against true photons. Neutral pions π^0 tend to decay into two photons with a branching ratio of 98.82%. In the case of large energy π^0, these photons are almost collinear (Fig. 4.2), thus inducing a tighter lateral profile that can be misidentified with the one from an isolated photon. Due to the high QCD jet production, these decays are then an important source of photon background.

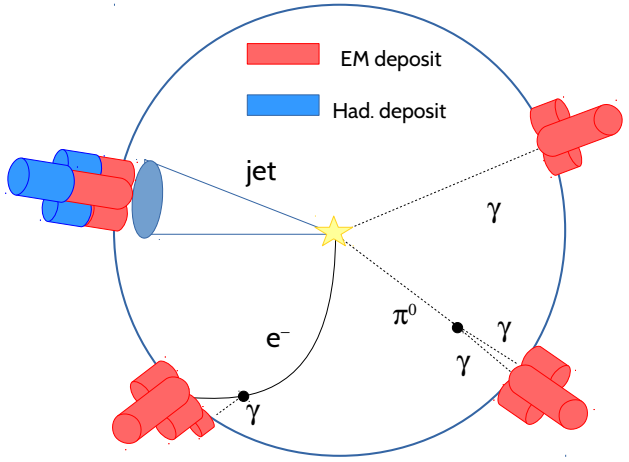


Figure 4.2: Schema of the expected energy deposits for jets, electrons, unconverted photons and neutral pions. Solid (dotted) lines represent tracks that (don't) leave traces in the inner detector. Red color stands for electromagnetic energy deposits in any of the calorimeters while blue color represent hadronic energy deposits.

On the other hand, the energy reconstruction technique explained in Chapter 3 shows that the ATLAS liquid argon barrel calorimeter reconstructs the energy from electromagnetic objects with a 0.5% accuracy. However, this performance cannot be extrapolated to electron and photon measurements after ATLAS installation, since final detector configuration varies significantly with regard to conditions during the test-beams. Some issues like calorimeter inhomogeneities, HV short circuits, calorimeter geometry effects (sagging caused by weight, intermodule effects, ..), cross-talk or absorbers and electrodes bending angles appear in the calorimeter. Furthermore, thicker passive material and the inner tracker (Figs. 4.3)

are present in ATLAS final configuration, thus increasing bremsstrahlung energy losses for electrons and photon conversions, as previously mentioned. All these changes affect the electron and photon shower development and ultimately the measurement of their energy. In consequence, a calibration procedure is developed to correct for all possible additional effects on electrons and photons energy.

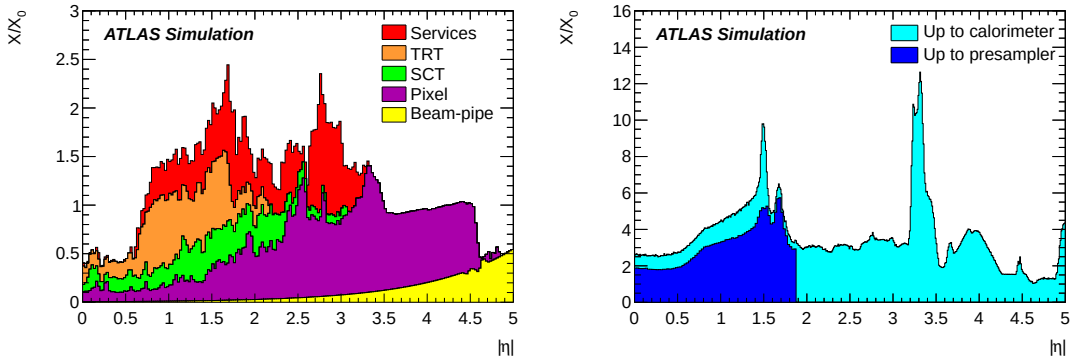


Figure 4.3: Material traversed by a particle in the ID (left) and the calorimeter (right) as a function of the pseudorapidity [2].

The electron and photon reconstruction is seeded by clusters found in the electromagnetic calorimeter. In Section 4.1, the main clustering and track reconstruction techniques are summarized. Later, tracking information and clusters are combined to reconstruct electron and photon candidates, as outlined in Section 4.2. The reconstruction technique, however, can identify as photon or electron candidates energy deposits coming from hadronic processes. This motivates the definition of a set of identification criteria to improve electron and photon separation from jets, as explained in Section 4.3. Electrons and photons are key particles in ATLAS physics analyses. SM and several BSM theories predict final states where a set of photons or electrons are produced either directly from the interaction point or as decay products of intermediate particles, i.e. the Higgs boson. Prompt particles coming from these decays are usually produced in an isolated way (no hadrons in their vicinity). On the other hand, hadron and τ or top decays may also present many of these particles in less isolated topologies, with much more activity around them. Then, the definition of isolation variables explained in Section 4.4 help to increase the purity of the final electron and photon sample. Finally, a precise energy calibration is primordial for achieving accurate measurements, e.g. of the Higgs mass. The ATLAS electron and photon calibration strategy is explained in Section 4.5.

4.1 Cluster and track reconstruction

After a pp collision, energy deposits are registered in all ATLAS subdetectors. In the case of photons and electrons, this deposited energy shows up as a localized cluster of cells, whose energies are well above their electronic noise. The identification of these cells and their association to disjoint clusters along the calorimeter is performed by two clustering techniques carried out during offline event reconstruction: sliding window and topological clustering (Fig. 4.4). These techniques can be applied to electromagnetic and hadronic deposits. Hadronic showers are beyond the scope of this chapter and all numbers presented below concern only electromagnetic showers, i.e. electrons and photons. Nevertheless, more information may be found in [3] and Section 6.1 about clustering techniques applied to jets.

4.1.1 Sliding-window clustering

The sliding-window technique consists of reconstructing the electromagnetic cluster by associating cells to a fixed-size rectangular window. The algorithm is divided into three steps:

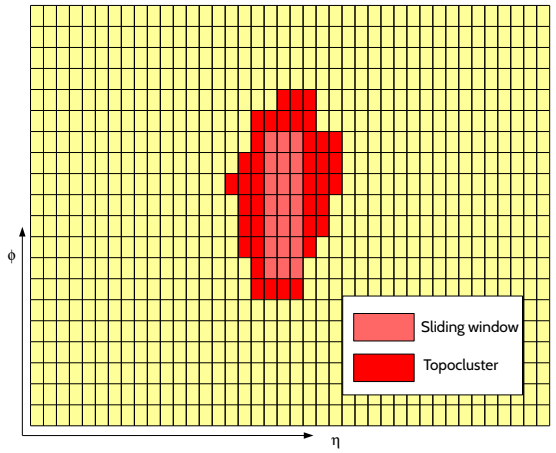


Figure 4.4: Schema of the calorimeter cells introduced in sliding-window and topocluster algorithms.

- **Tower building**

  The whole calorimeter is segmented into towers of size $\Delta\eta \times \Delta\phi = 0.025 \times 0.025$ in the $\eta - \phi$ plane. At the end of this step, the calorimeter is split into a grid of $N_\eta \times N_\phi = 200 \times 256$ towers, each one containing the energy of all three longitudinal layers in their $\Delta\eta \times \Delta\phi$. The energies of cells spanning several towers are distributed according to the fractional area of the cells intersected by each tower.

- **Pre-clustering**

  A fixed-size window is moved across each element of the tower grid defined above. If the window transverse energy (defined as the sum of the transverse energies of the towers contained in the window) is a local maximum above a threshold ($E_{\mathrm{T}}^{\mathrm{thresh}}$), a pre-cluster is formed. The size of the window, denoted in tower $\Delta\eta \times \Delta\phi$ units, and $E_{\mathrm{T}}^{\mathrm{thresh}}$ are optimized to reduce the number of fake clusters due to noise and to get the best efficiency for finding potential interesting clusters. The position of the pre-cluster is defined as the barycenter of the energy deposition, which is estimated using a window of $\Delta\eta \times \Delta\phi = 0.075 \times 0.075$. Overlaps between two clusters are possible, in which case only the pre-cluster with the largest transverse energy is preserved. Two pre-clusters overlap if they are found within a region of $\Delta\eta \times \Delta\phi = 0.05 \times 0.05$.

- **EM cluster reconstruction**

  Clusters are built from pre-clusters identified during the previous step. Pre-cluster barycenter is readjusted using a different sliding window size, optimized to minimize noise contribution. In this step, window scan is performed separately per longitudinal layer. First, the middle layer clusters are reconstructed. The pre-cluster barycenter serves as seed position of the new sliding window scan. Once the new barycenter is fixed, the middle layer cells entering the window are associated with the cluster. This process is repeated iteratively in the front, presampler and back layers. The seed position for the window scan in the front layer is the barycenter of the middle layer cluster, while the presampler and the back layers are processed using respectively the strip and middle clusters barycenter as seeds.

4.1.2 Topological clustering

The sliding window technique presents a very good performance for reconstructing photon and electron clusters and it is currently the main clustering technique used for electron and photon candidate reconstruction. However, jets and isolation variable reconstruction require more flexible clustering algorithms, with capability of adapting the cluster shape. The topological clustering is seeded by cells with large signal-to-noise ratio and iteratively associates to the cluster neighbouring cells that also present a significant energy with respect to their noise magnitude. There are three main steps:

- **Finding seeds**

  All cells with energy above a rather high signal-to-noise ratio ($t_{\text{seed}} > 6$ GeV for EM clusters) are identified and act as seeds to the topological cluster algorithm. Each seed cell starts a proto-cluster.

- **Finding neighbours**

  For each seed cell found in the calorimeter, all neighbours are considered. If any of the neighbours present a signal-to-noise higher than 3, they are added to the corresponding topocluster. After that, the same procedure is applied to the neighbour cells in the cluster. If one neighbour cell is adjacent to two proto-clusters, the two proto-clusters are merged into a single one.

- **Finalize**

  Proto-clusters with a $E_{\text{T}} < 5$ GeV are removed. The resulting topological clusters are then 3-dimensional clusters taking into account cells in the same layer, adjacent cells in the neighbouring layers and neighbouring cells in η and ϕ from the adjacent calorimeter.

The main advantage of this topological clustering is its efficiency for suppressing noise in clusters with large numbers of cells. However, this algorithm must be corrected in regions where significant energy deposits are expected in neighbouring cells. For instance, it is usual to record several overlapping clusters that come from different particles in the end-caps and the forward calorimeter. This fact is partially solved by splitting the proto-cluster into two smaller ones if two differentiated local energy maxima are identified. This algorithm associates a given fraction of the shared cells energy to each proto-cluster, depending on the distance between the two proto-clusters centroid to the shared cells and the energy of each cluster.

4.1.3 Track reconstruction

The standard ATLAS track reconstruction is seeded by three hits in the silicon detectors (pixel or SCT detectors). Track candidates are then extrapolated following the direction of the track seed. If more silicon hits are found in the extrapolation path, they are collected and judged using a Kalman filtering [4] and they are added to the track candidate or rejected. After the full set of track candidates in the silicon detectors (not including yet TRT hits) has been identified, an ambiguity solving procedure is applied to remove track candidates with incorrectly assigned hits. This ambiguity solving scores the track candidate depending on the number of hits that were successfully added to the track, the number of holes of the track[1] or the sub-detectors on which the hits are measured. After the reconstruction of tracks in the pixel and the SCT detectors, the successful candidates are extrapolated into the TRT volume and combined with measurements there. This technique is complemented with a back-tracking method, seeded by hits in the TRT detector and extending the track into the silicon detector [5]. Back-tracking is designed to reconstruct secondaries, which are particles produced in the interactions of particles issued from the collision point. Tracks with a TRT segment but no extension into the silicon detectors are referred to as TRT-only tracks. This complementary reconstruction is important for instance in the reconstruction of converted tracks, needed to identify photons.

4.2 Electron and photon reconstruction

Photons and electrons have very similar signatures in the EM calorimeter. However, they can be distinguished depending on the activity in the inner detector. A good electron reconstruction requires the association of a track with an EM cluster of the calorimeter. On the other hand, the reconstruction of photons may also involve the matching to an EM cluster of two (or one) tracks compatible to be produced in a conversion vertex or none, depending if the photon converts into an electron-positron pair before the calorimeter (converted) or if it arrived undisturbed into the calorimeter (unconverted). Some late conversions may occur in the space between the tracker and the calorimeter that could only be tagged using

[1] A hole represents a measurement on a detector surface that is expected, given the trajectory predictions, but not observed.

information of the calorimeter presampler. The reconstruction algorithm then proceeds in parallel [6, 7, 8] and a final algorithm decides if the resulting particle candidate is an electron, an unconverted photon or a converted photon.

The reconstruction is seeded by sliding window pre-clusters of size $\Delta\eta \times \Delta\phi = 0.075 \times 0.125$ with transverse momentum calibrated at the electronic cell energy scale (Eq. 3.13) larger than $E_{\mathrm{T}}^{\mathrm{thresh}}$ =2.5 GeV. In addition, clusters must be within $|\eta| < 2.5$. Once seed clusters are reconstructed, a search is performed for inner detector tracks. These tracks are reconstructed using data the standard strategy described in Section 4.1.3. However, this strategy sometimes fails to correctly evaluate electron tracks due to the larger bremsstrahlung losses that electrons may overcome in the inner tracker. The standard reconstruction considers the pion hypothesis to model energy losses due to the interactions with the tracking detectors material. Unfortunately, given the strong magnetic field and the amount of inner tracker material, electrons are very likely to undergo large energy losses due to bremsstrahlung. The pion hypothesis is then complemented with a modified algorithm which allows up to 30% energy loss at each intersection of the track with the detector material. If an electron track seed (consisting of three hits in different layers of the silicon detectors) with a transverse momentum larger than 1 GeV cannot be successfully extended to a full track of at least seven hits using the pion hypothesis and it falls within one of the EM cluster region of interest (regions of $\Delta R = 0.3$ size around EM clusters with $R_\eta > 0.65$ and $E_{\mathrm{had}}/E_{\mathrm{tot}} < 10\%$), a second attempt is performed using an electron hypothesis that allows for larger energy loss. This electron track reconstruction is performed using the same strategy than standard reconstruction [4] but the inclusion of a model of electron bremsstrahlung losses improves significantly the performance of electron track reconstruction.

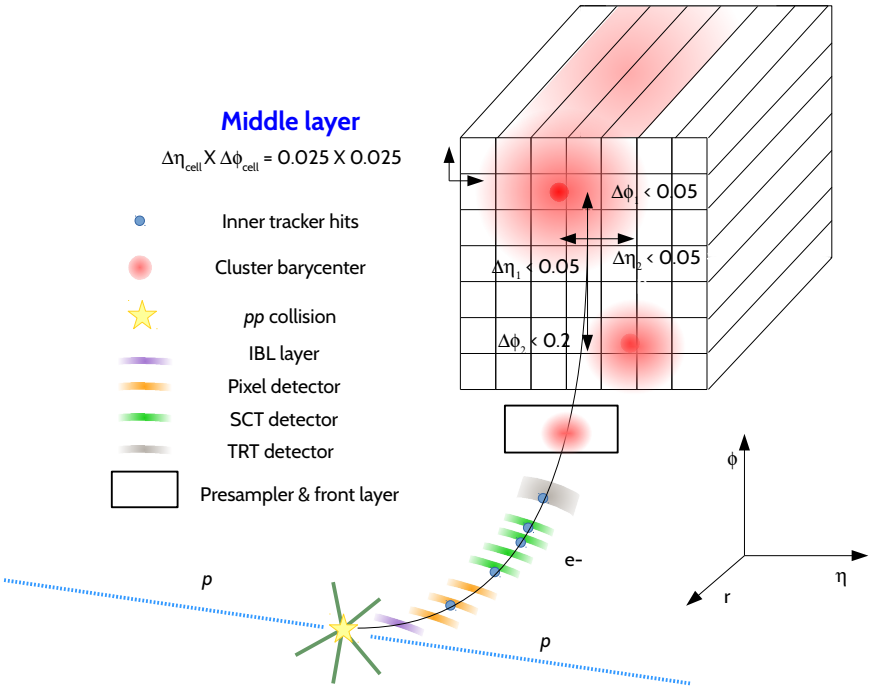


Figure 4.5: Picture illustrating the cluster-track matching for electrons and converted photons in the EM barrel calorimeter.

After tracks are reconstructed, tracks falling in an EM cluster region of interest are extrapolated to the middle layer of the calorimeter. This allows evaluating tracks as loosely matched to EM clusters if the angular distance along ϕ between the extrapolated track and the cluster barycentre is $|\phi_{\mathrm{track}} - \phi_{\mathrm{clus}}^{\mathrm{bary}}| < 0.05(0.2)$ in the direction (or opposite direction) of the bending of the track (Fig. 4.5). If matched tracks also present significant number of precision pixel or SCT hits ($\geq$4), they are refit using an optimised Gaussian Sum Filter (GSF) [9], which takes into account non-linear bremsstrahlung effects.

Conversion vertices are then reconstructed. These vertices can be reconstructed either using two recon-

structed tracks or one single track (Fig. 4.6):

- **Double-track conversion vertices**

  Pairs of opposite-charge reconstructed tracks are identified. These tracks pairs can be classified as Si-Si if both tracks present hits in the silicon, Si-TRT if only one does it and TRT-TRT if both tracks are TST-only. Conversion tracks are used for conversion vertex reconstruction if their relative distance is compatible to come from a conversion vertex[2] Then, a conversion vertex fit is performed. The conversion vertex reconstruction efficiency decreases for conversions taking place in the outermost layers of the tracker, given that one track usually fails to be reconstructed, either because its transverse momentum is too low or the two tracks are so close that they cannot be separated. However, the single-track vertex reconstruction helps to increase this efficiency in these regions.

- **Single-track conversion vertices**

  Tracks are considered to come from a conversion vertex if they present no hits in the B-layer and, either no hits in the TRT or with 95% likelihood to be an electron. Since the double-track conversion vertex reconstruction cannot be applied in this case, the conversion vertex is considered to be the first innermost hit in the tracker.

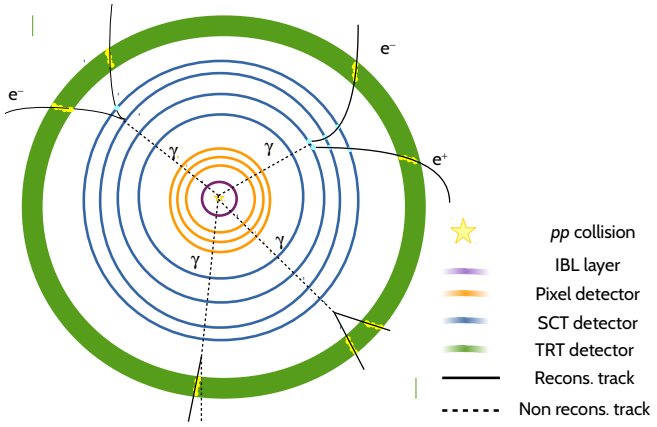


Figure 4.6: Picture illustrating the three track pairs that can be used to reconstruct conversion vertices. The rightmost pair represents Si-Si tracks; the bottom right pair represents TRT-TRT tracks and the last one, Si-TRT tracks. In addition, the bottom left photon presents two tracks from which one escapes detection (single-track conversion vertex).

Conversion tracks are then extrapolated to the middle layer of the calorimeter and loosely matched to clusters [7]. In addition, conversion vertices are matched to the clusters by requiring that the $\Delta\eta < 0.05$ and $\Delta\phi < 0.05$ between the conversion vertex and the cluster center. In the case of single tracks, $\Delta\phi$ is extended to be lower than 0.1 in the direction of the bending angle of the track.

Electromagnetic clusters are then classified as converted photon, unconverted photon and electron candidates. Figure 4.7 presents the different selection criteria applied to make this classification. In the case of electron candidates, if several tracks fulfill the matching condition, one is then chosen as primary track depending on the number of hits in the pixel and silicon layers of the track and the cluster-track distance.

After this classification, the cluster is re-formed into a $\Delta\eta \times \Delta\phi = 0.075 \times 0.175$ (0.125×0.125) in the EM barrel (end-caps). The initial energy of the photons and electrons is calculated by simply summing the energies of the cluster associated with them. This energy is then corrected from possible material and calorimeter effects following a procedure exposed in Section 4.5. The flight direction is determined

[2] $\Delta\cot\theta < 0.3(0.5)$ for Si-Si (Si-TRT or TRT-TRT) tracks with θ taken at the closest point to the primary vertices. In addition, the distance between the closest point of both tracks must be 10 mm (50 mm) for Si-Si (other) tracks and the $\Delta\phi$ between the two tracks is 0.05 (0.2). Finally, the sum of the helicies radii and the distance between helices center must be between -5 and 5 mm, -50mm and 10 mm and -25 and 10 mm for Si-Si, TRT-TRT or Si-TRT respectively.

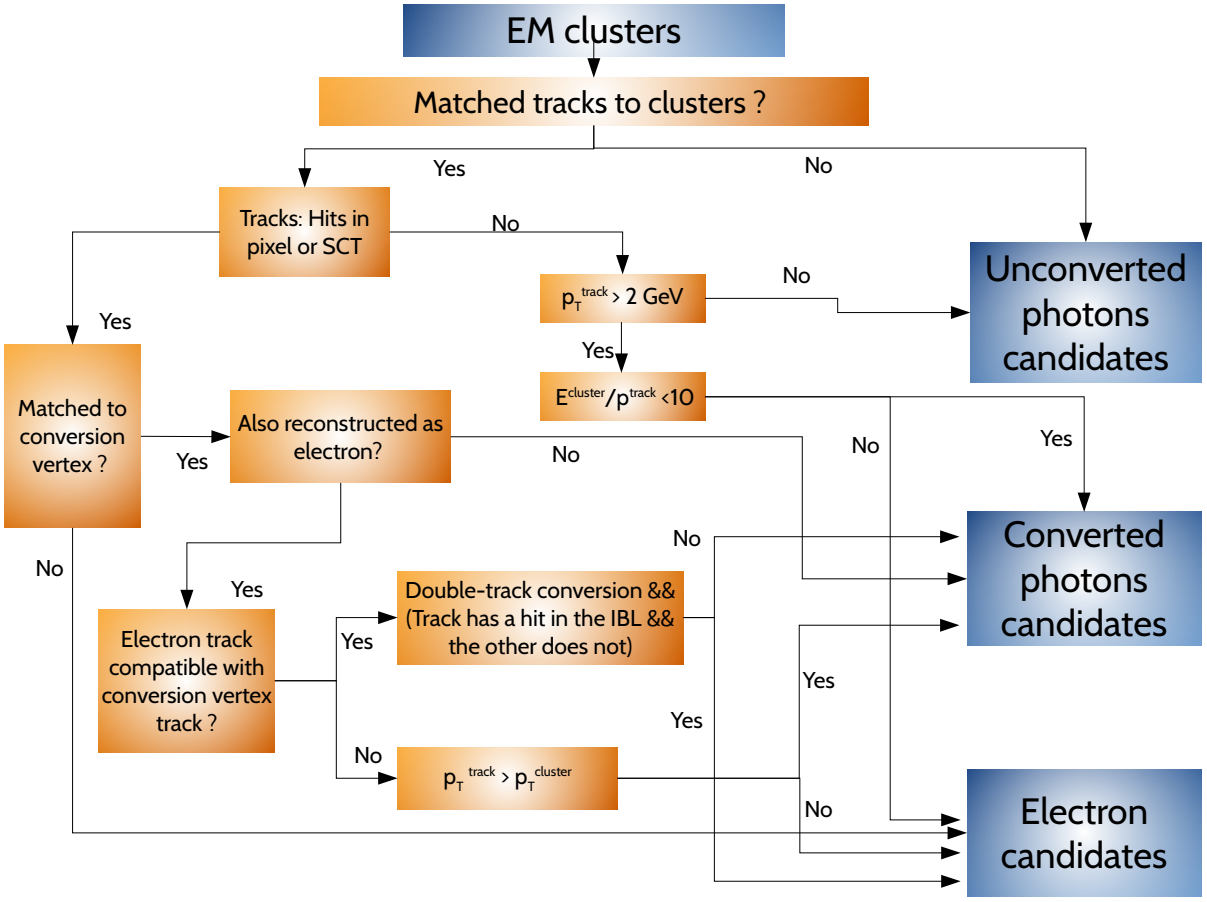


Figure 4.7: Scheme of the decision tree to initially separate electron, converted photon and unconverted photon candidates.

differently for electrons and photons. For electrons, the direction in η^e and ϕ^e is determined from the track parameters at the electron production vertex [10]. For an unconverted photon, this direction is initially determined from the η and ϕ coordinates of its associated cluster with regard to the interaction point. η^{cluster} is calculated through a weighted average of the layer 1 and layer 2 barycenters. Some corrections are applied to this initial η^{cluster} due to biases produced by the limited granularity of the calorimeter (S-shapes [11]), etc. ϕ^{cluster} corresponds to the ϕ of the layer 2 barycenter corrected from detector sagging and other detector effects [11]. This technique is also used for converted photons, unless they are Si+Si in which case η^γ and ϕ^γ are equated to the conversion vertex coordinates.

The efficiency of this reconstruction scheme is evaluated for electrons (Fig. 4.8). The evaluation is performed via a tag-and-probe method on $Z \rightarrow ee$ samples. This method imposes a strict selection on one of the electron candidates (called "tag") and together with the requirements on the di-electron invariant mass, it allows for a loose pre-identification of the other electron candidate ("probe"). Taking these initial events, a given selection is applied on the probe (either reconstruction or and identification working point, etc) and efficiencies are estimated as the number of events passing the probe selection over the number of initial events. An overall agreement is observed between data and MC efficiency measurements, with an average efficiency of 98.5% decreasing at low E_{T} and around the barrel-endcap transition regions ($|\eta| \sim 1.5$).

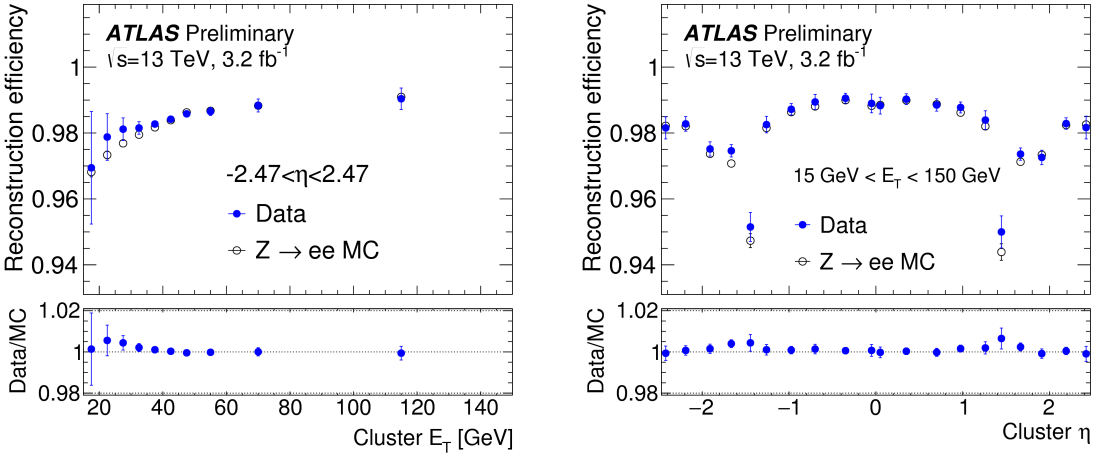


Figure 4.8: Measured reconstruction efficiencies for electrons as a function of E_{T} integrated over the full pseudorapidity range (left) and as a function of pseudo-rapidity for 15 GeV < E_{T} < 150 GeV (right) for the 2015 dataset. The shown uncertainties are statistical plus systematic errors [6].

4.3 Electron and photon identification

Clusters and tracks associated with electron or photon candidates must satisfy a set of identification (ID) criteria to determine whether the reconstructed objects are signal-like or background-like objects, such as electrons and photons or hadronic jets respectively. The identification algorithms are based on electrons and photons calorimeter shower shape variables, information from the TRT, track-cluster matching related quantities, track properties, and variables measuring bremsstrahlung effects.

4.3.1 Electron identification

Electrons are identified in Run II using a likelihood-based (LH) method that combines several properties of the electron track and shower shapes to make a decision. It is a multivariate analysis (MVA) technique that evaluates the probability of an object of being an electron using pre-determined signal and background probability density functions ($f_{S(B)}(x_i)$ where S and B stand for signal and background PDF of the i^{th} continuous variables). Based on these PDFs, overall signal ($\mathcal{L}_S$) and background ($\mathcal{L}_B$) likelihoods are calculated using each object characteristics x_i. These likelihoods are combined into a discriminant $d_{\mathcal{L}}$ on which a cut is applied:

$$d_{\mathcal{L}} = \frac{\mathcal{L}_S}{\mathcal{L}_S + \mathcal{L}_B}; \qquad \mathcal{L}_{S(B)}(x_i) = \prod_{i=1}^{N_{\mathrm{var}}} f_{S(B)}(x_i) \tag{4.1}$$

The discriminant variables x_i are defined in Table 4.1. Among these variables, w_{stot}, $\Delta\phi_2$, E/p and the track number of hits in the three inner detectors are not included in the algorithm as PDFs but as rectangular cuts. Figures 4.9 compare the distributions of several shower shape variables for electrons against the same distributions from jets mimicking an electron.

Three levels of identification are usually considered for electron ID. In increasing order of background rejection, these working points are *loose*, *medium* and *tight*. Each operating point uses the same variables to define the LH discriminant so that the distinction between them only lies on the requirements on each variable discriminant.

The performance of the electron ID for signal selection and background rejection is evaluated on $Z \rightarrow$

Type	Description	Name
Hadronic leakage	Ratio of E_{T} in the first layer of the hadronic calorimeter to E_{T} of the EM cluster (used over the range $\lvert\eta\rvert < 0.8$ or $\lvert\eta\rvert > 1.37$)	R_{had1}
	Ratio of E_{T} in the hadronic calorimeter to E_{T} of the EM cluster (used over the range $0.8 < \lvert\eta\rvert < 1.37$)	R_{had}
Back layer of EM calorimeter	Ratio of the energy in the back layer to the total energy in the EM accordion calorimeter. This variable is only used below 100 GeV because it is known to be inefficient at high energies.	f_3
Middle layer of EM calorimeter	Lateral shower width, $\sqrt{(\Sigma E_i \eta_i^2)/(\Sigma E_i) - ((\Sigma E_i \eta_i)/(\Sigma E_i))^2}$, where E_i is the energy and η_i is the pseudorapidity of cell i and the sum is calculated within a window of 3×5 cells	$w_{\eta 2}$
	Ratio of the energy in 3×3 cells over the energy in 3×7 cells centered at the electron cluster position	R_ϕ
	Ratio of the energy in 3×7 cells over the energy in 7×7 cells centered at the electron cluster position	R_η
Strip layer of EM calorimeter	Shower width, $\sqrt{(\Sigma E_i (i - i_{\mathrm{max}})^2)/(\Sigma E_i)}$, where i runs over all strips in a window of $\Delta\eta \times \Delta\phi \approx 0.0625 \times 0.2$, corresponding typically to 20 strips in η, and i_{max} is the index of the highest-energy strip	w_{stot}
	Ratio of the energy difference between the largest and second largest energy deposits in the cluster over the sum of these energies	E_{ratio}
	Ratio of the energy in the strip layer to the total energy in the EM accordion calorimeter	f_1
Track conditions	Number of hits in the innermost pixel layer; discriminates against photon conversions	n_{Blayer}
	Number of hits in the pixel detector	n_{Pixel}
	Number of total hits in the pixel and SCT detectors	n_{Si}
	Transverse impact parameter with respect to the beam-line	d_0
	Significance of transverse impact parameter defined as the ratio of d_0 and its uncertainty	d_0/σ_{d_0}
	Momentum lost by the track between the perigee and the last measurement point divided by the original momentum	$\Delta p/p$
TRT	Likelihood probability based on transition radiation in the TRT	eProbabilityHT
Track-cluster matching	$\Delta\eta$ between the cluster position in the strip layer and the extrapolated track	$\Delta\eta_1$
	$\Delta\phi$ between the cluster position in the middle layer and the track extrapolated from the perigee	$\Delta\phi_2$
	Defined as $\Delta\phi_2$, but the track momentum is rescaled to the cluster energy before extrapolating the track from the perigee to the middle layer of the calorimeter	$\Delta\phi_{\mathrm{res}}$
	Ratio of the cluster energy to the track momentum	E/p

Table 4.1: List of variables used in the electron identification.

ee and dijet events. Figure 4.10 shows the three identification criteria efficiencies as function of the transverse energy of the evaluated electron E_{T}. An increase in identification efficiency is observed at higher transverse momenta while background rejection is also improved. Tight identification permits to identify around 78.5% of good electrons at low E_{T}, increasing until 87% at high E_{T}, at the same time that fake rate from jets decreases from 0.6-0.1%, respectively.

4.3.2 Photon identification

Unlike the electrons, photon identification in ATLAS [7, 8] is a cut-based selection. Single photons typically present narrow showers well contained in the electromagnetic calorimeter. Instead, fake photons from jets tend to present broader distributions in the electromagnetic calorimeter and a significant fraction of energy in the hadronic calorimeter. In addition, the $\pi^0 \to \gamma\gamma$ decays, whose signature in the EMCAL is quite similar to prompt photons, are often characterized by two separate local energy maxima in the finely segmented strips of the first layer (Fig. 4.11). This motivates the definition of several

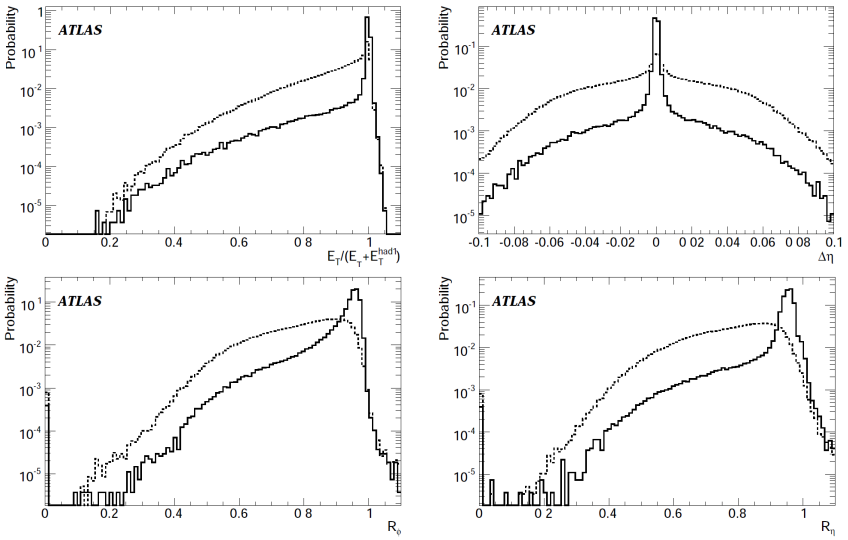


Figure 4.9: Top left: ratio between the transverse energy of the electron candidate and the sum of this trans- verse energy and that contained in the first layer of the hadronic calorimeter. Top right: $\Delta\eta$ between the cluster barycentre and the extrapolated track. Bottom: distribution of R_ϕ (left) and R_η (right), defined in Table 4.1. Dotted lines correspond to non-isolated electrons from hadrons evaluated on di-jet events while solid lines correspond to prompt electrons selected on a $Z \to ee$ simulation [12].

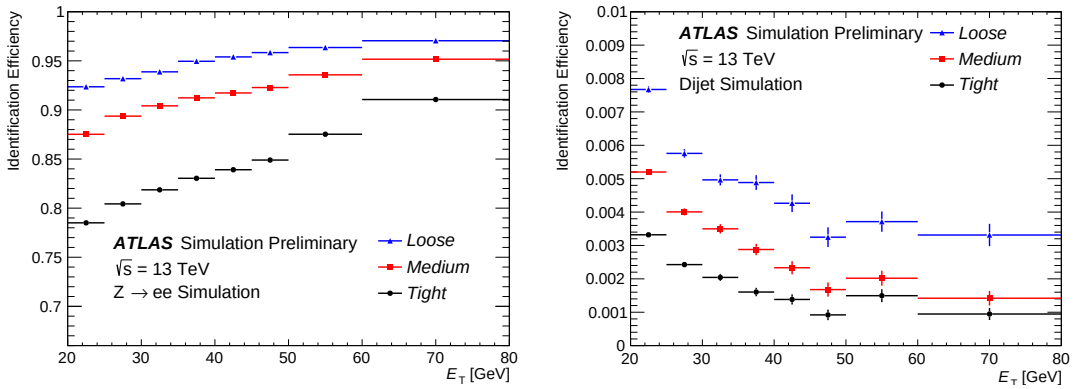


Figure 4.10: The efficiency to identify electrons from $Z \to ee$ decays (left) and the efficiency to identify hadrons as electrons (background rejection, right) estimated using simulated dijet samples. The efficiencies are obtained using Monte Carlo simulations, and are measured with respect to reconstructed electrons. The candidates are matched to true electron candidates for $Z \to ee$ events. For background rejection studies the electrons matched to true electron candidates are not included in the analysis [6].

discriminating variables using information from both calorimeters, with a special focus on shower shape variables on the ECAL front and middle layers.

Table 4.2 summarizes the variables used in photon identification. Some of these variables are presented in Fig. 4.12, where clear differences are observed between true photons and fake photons from jets.

Two working points are defined for classifying photons according to the level of identification: *loose* and *tight*. The loose selection is based only on shower shapes in the second layer of the electromagnetic calorimeter and on the energy deposited in the hadronic calorimeter.The tight identification includes the loose working points, with more stringent cuts, and adds information of the shower shapes in the strip layer. This definition aims to reduce the allowing a further discrimination of $\pi^0 \to \gamma\gamma$ backgrounds. This selection is separately optimized for converted and unconverted photons, providing an overall 85% identification efficiency for $E_{\mathrm{T}}^{\gamma} > 40\mathrm{GeV}$ photon candidates.

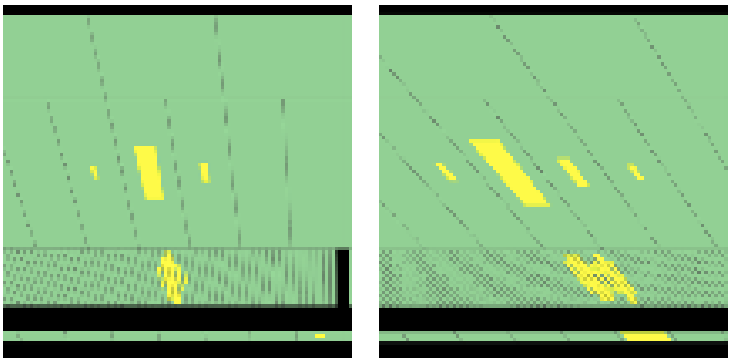


Figure 4.11: Shower shape comparison between a γ and a π^0 decaying into two photons.

Category	Description	Name	*loose*	*tight*
Acceptance	$\|\eta\| < 2.37$, with $1.37 < \|\eta\| < 1.52$ excluded	–	✓	✓
Hadronic leakage	Ratio of E_{T} in the first sampling layer of the hadronic calorimeter to E_{T} of the EM cluster (used over the range $\|\eta\| < 0.8$ or $\|\eta\| > 1.37$)	$R_{\mathrm{had_1}}$	✓	✓
	Ratio of E_{T} in the hadronic calorimeter to E_{T} of the EM cluster (used over the range $0.8 < \|\eta\| < 1.37$)	R_{had}	✓	✓
EM Middle layer	Ratio of 3×7 $\eta \times \phi$ to 7×7 cell energies	R_η	✓	✓
	Lateral width of the shower	$w_{\eta 2}$	✓	✓
	Ratio of 3×3 $\eta \times \phi$ to 3×7 cell energies	R_ϕ		✓
EM Strip layer	Shower width calculated from three strips around the strip with maximum energy deposit	$w_{s\,3}$		✓
	Total lateral shower width	$w_{s\,\mathrm{tot}}$		✓
	Energy outside the core of the three central strips but within seven strips divided by energy within the three central strips	F_{side}		✓
	Difference between the energy associated with the second maximum in the strip layer and the energy reconstructed in the strip with the minimum value found between the first and second maxima	ΔE		✓
	Ratio of the energy difference associated with the largest and second largest energy deposits to the sum of these energies	E_{ratio}		✓

Table 4.2: Discriminant variables used in the tight and loose photon identification criteria [7].

Figures 4.13 and 4.14 presents the measured efficiencies for tight and loose identification criteria evaluated using radiative Z, electron extrapolation and matrix methods. These methods optimize identification studies for different E_{T} regions but they may complement each other for certain values.

- **Radiative Z boson decays**

  This method relies on the use of a pure photon sample selected from radiative decays of the Z boson, $Z \to \ell^+\ell^-\gamma$. Selected events are fitted to a signal plus background model based on MC templates. The fit allows the variation of the signal and background normalization, so that the identification efficiency is estimated by dividing the number of fitted signal events after applying loose or tight ID criteria over the number of fitted signal events on the full selected $Z \to \ell^+\ell^-\gamma$ dataset:

$$\epsilon^{\mathrm{ID}} = \frac{N^{\mathrm{ID}}_{\mathrm{pass}}}{N_{\mathrm{probes}}} \tag{4.2}$$

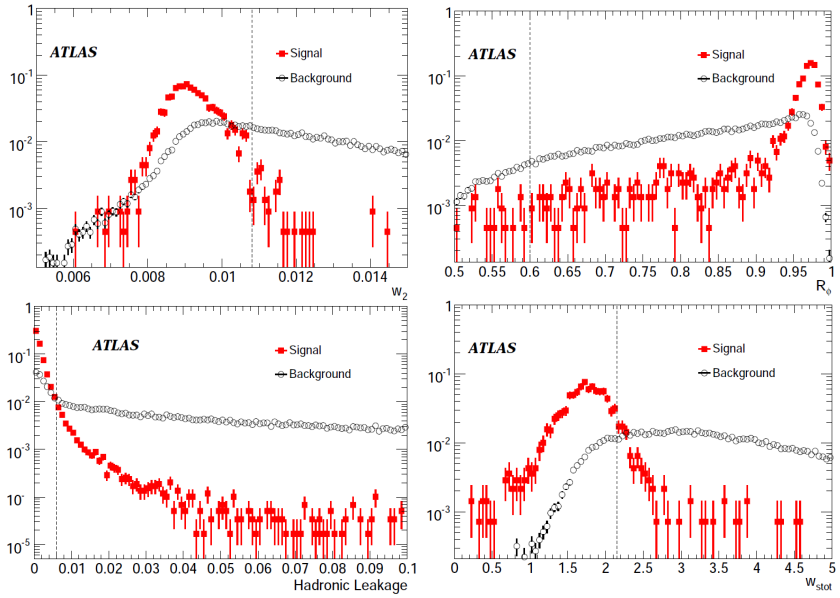


Figure 4.12: Illustrations comparing several shower shape variable distributions for boosted $\pi^0 \to \gamma\gamma$ (open black points) against prompt photons (red solid points) [12].

This technique allows a precise measurement in the low E_{T} region although due to the low number of events at high-E_{T} after $Z \to \ell^+\ell^-\gamma$ selection, a coarse granularity for E_{T} and η can be scanned.

- **Electron extrapolation**

  An electron sample from $Z \to ee$ decays is used to obtain a pure sample of electromagnetic showers from data. Showers developed by electrons are quite similar to those by photons. Then, differences are taken from the simulation (separately for converted and unconverted photons) and applied to observed showers from electrons to describe those produced by photons. Due to the Z decay kinematics, this method allows extending the identification studies to an intermediate E_{T} range.

- **Matrix method**

  This method exploits photons reconstructed in collision data, which are contaminated by hadronic background. Single photon events are selected by the trigger system by requiring one photon in the ECAL with 20 GeV < E_{T} < 1500 GeV. With this, a sample is built with N_{all} events. This sample includes true photons and background from hadronic processes. Immediately, another sample is built with photons passing one of the identification cuts (N_{pass}). The isolation of reconstructed photons is used as a discriminating property in order to extract the sample purity before and after the photon identification. Track isolation, explained in Section 4.4, is applied to both samples, building other two with $N_{\mathrm{all}}^{\mathrm{iso}}$ and $N_{\mathrm{pass}}^{\mathrm{iso}}$ number of events. Given that:

$$N_{\mathrm{all}} = N_{\mathrm{all}}^{\mathrm{signal}} + N_{\mathrm{all}}^{\mathrm{bkg}}, \tag{4.3}$$

$$N_{\mathrm{pass}} = N_{\mathrm{pass}}^{\mathrm{signal}} + N_{\mathrm{pass}}^{\mathrm{bkg}}, \tag{4.4}$$

$$N_{\mathrm{all}}^{\mathrm{iso}} = \epsilon_{\mathrm{all}}^{\mathrm{signal}} N_{\mathrm{all}}^{\mathrm{signal}} + \epsilon_{\mathrm{all}}^{\mathrm{bkg}} N_{\mathrm{all}}^{\mathrm{bkg}}, \tag{4.5}$$

$$N_{\mathrm{pass}}^{\mathrm{iso}} = \epsilon_{\mathrm{pass}}^{\mathrm{signal}} N_{\mathrm{pass}}^{\mathrm{signal}} + \epsilon_{\mathrm{pass}}^{\mathrm{bkg}} N_{\mathrm{pass}}^{\mathrm{bkg}}, \tag{4.6}$$

  so that the efficiency is:

$$\epsilon_{\mathrm{ID}} = \frac{\frac{\epsilon_{\mathrm{pass}} - \epsilon_{\mathrm{pass}}^{\mathrm{bkg}}}{\epsilon_{\mathrm{pass}}^{\mathrm{signal}} - \epsilon_{\mathrm{pass}}^{\mathrm{bkg}}} N_{\mathrm{pass}}}{\frac{\epsilon_{\mathrm{all}} - \epsilon_{\mathrm{all}}^{\mathrm{bkg}}}{\epsilon_{\mathrm{all}}^{\mathrm{signal}} - \epsilon_{\mathrm{all}}^{\mathrm{bkg}}} N_{\mathrm{all}}}, \tag{4.7}$$

This method has the advantage of covering a very large E_{T} range.

More information about these three methods may be found in [8].

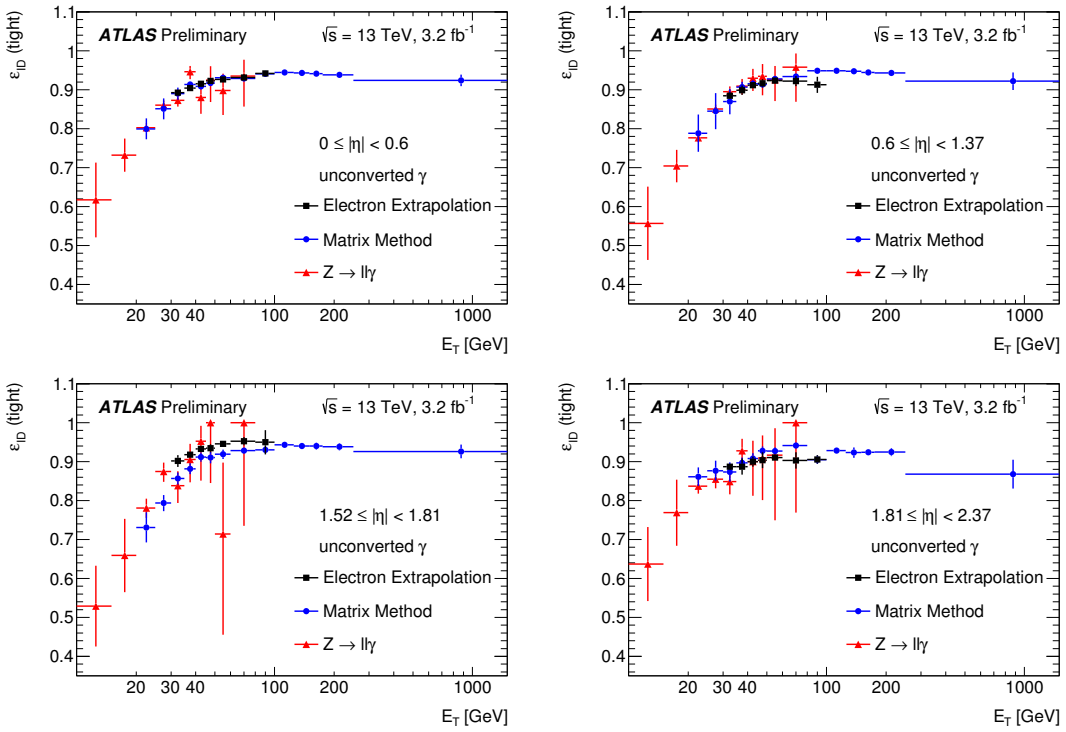


Figure 4.13: Tight identification efficiency for unconverted photons depending on η and E_{T}. Efficiencies are tested using three methods providing similar results.

4.4 Isolation

A higher purity on the photon and electron reconstruction can be improved by studying the activity around their vicinity. Prompt photons or electrons tend to present isolated topologies while hadronic energy deposits also mimicking electrons and photons tend to present larger energy deposits in their vicinity recorder by the inner tracker or the calorimeter. Then, it is convenient for searches expecting prompt particles to require a small of energy in a cone around the isolated particle, also called "isolation energy" [13]. This isolation requirement may increase the purity of the final selected sample at the same time that the probability of misidentifying a prompt particle with a hadron decay product is reduced. Activity around a prompt particle candidate can be evaluated either using the tracks in the inner detector, the calorimeter clusters or both.

4.4.1 Calorimetric isolation

A cone of radius $R = \sqrt{(\Delta\eta)^2 + (\Delta\phi)^2}$ is defined around the direction of the electron or photon, given by the position of the associated sliding-window calorimeter cluster used to reconstruct the electron or photon energy. The transverse energy component of all positive energy topological clusters whose barycentre falls within this cone are summed into what is called the raw *topoetcone* isolation $E_{\mathrm{T}}^{\mathrm{isol,raw}}$. This energy is estimated by default using $R = 0.2$ or 0.4, respectively defining the topoetcone20 or topoetcone40 isolation transverse energy, although other values of R can be scanned if needed. This

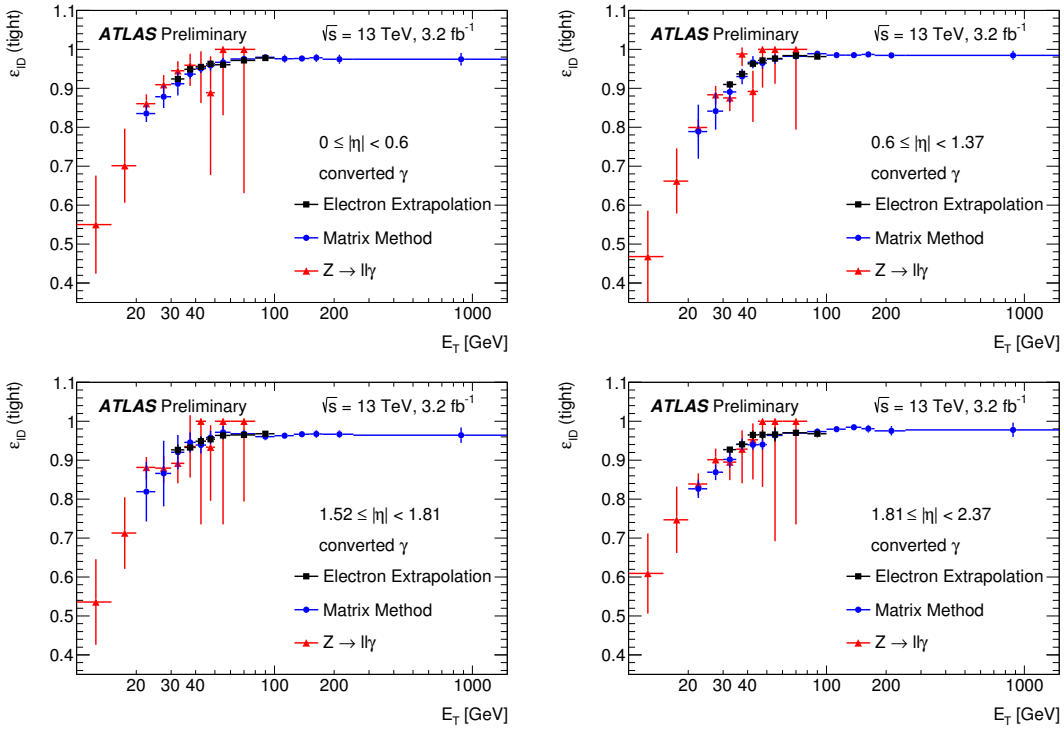


Figure 4.14: Tight identification efficiency for converted photons depending on η and E_{T}. Efficiencies are tested using three methods providing similar results.

raw isolation energy includes the energy of the electron or photon, called the transverse core energy $E_{\mathrm{T}}^{\mathrm{core}}$, the ambient pileup activity $E_{\mathrm{T}}^{\mathrm{PU}}$ and the transverse energy leakage $E_{\mathrm{T}}^{\mathrm{leak}}$, which corresponds to the transverse energy belonging to the electron or photon that falls out of the sliding window cluster. These contributions need to be subtracted to correctly evaluate the presence of other particles around an electron or a photon. These various contributions are computed in the following way:

- **Core subtraction:**

  It is done by subtracting a $N_\eta \times N_\phi = 5 \times 7$ cells around the barycenter of the shower. This subtraction has the advantage that a regular shape is removed from prompt and non-prompt particles. However, leakage energy is not completely removed, as illustrated in Fig. 4.15.

- **Leakage energy subtraction:**

  Leakage energy is evaluated using single-particle MC samples without pileup of electrons and photons. After core correction, the mean transverse isolation energy around the single-particle is evaluated and used as an estimator of the average leakage energy around electrons and photons.

- **Pileup energy subtraction:**

  Pileup energy correction is estimated using the ambient energy technique introduced in [14]. The median density ρ gives an estimate of the pileup energy density. This median density is calculated using jets reconstructed by the anti-k_t [15] algorithm with parameter 0.5 without any p_T threshold. These conditions enrich the jet sample with jets possibly coming from soft-interactions. $Z \rightarrow ee$ samples are used to determine this energy density, expressed in Equation 4.8:

$$\rho = \mathrm{median}\left(\frac{p_{\mathrm{T}}^{\mathrm{jet}}}{A^{\mathrm{jet}}}\right) \tag{4.8}$$

  where A^{jet} is the area of the jet [16]. $E_{\mathrm{T}}^{\mathrm{PU}}$ is then estimated by multiplying this energy density by the surface of the isolation cone, from which the core area is subtracted:

$$E_{\mathrm{T}}^{\mathrm{PU}} = \rho(\pi R^2 - A^{\mathrm{core}}) \tag{4.9}$$

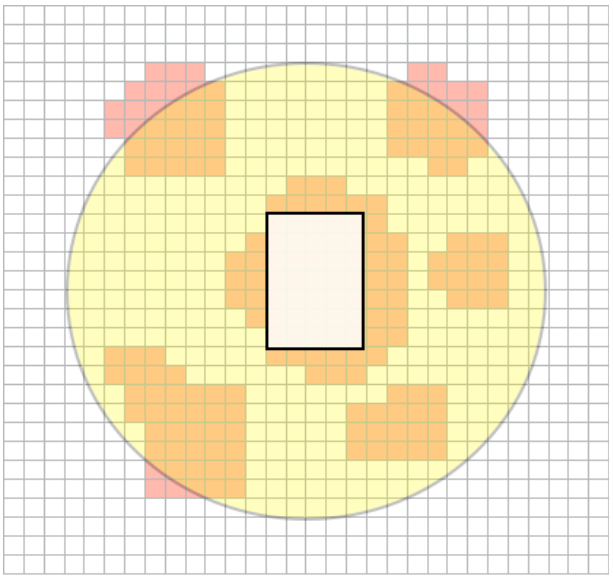


Figure 4.15: Schema of the *topoetcone* variable: the grid represents the middle calorimeter cells in the η and ϕ directions. The electron or photon is located in the center of the yellow cone representing the isolation cone. Topological clusters are represented in red. Those whose barycenter falls into the isolation cone are included in the isolation computation. The 5×7 cells white rectangle corresponds to the subtracted core cells. Energy around this core corresponds to the energy leakage that needs to be corrected [13].

Then, the transverse isolation energy $E_{\mathrm{T}}^{\mathrm{isol}}$ is defined as:

$$E_{\mathrm{T}}^{\mathrm{isol}} = E_{\mathrm{T}}^{\mathrm{isol,raw}} - E_{\mathrm{T}}^{\mathrm{PU}} - E_{\mathrm{T}}^{\mathrm{leak}} - E_{\mathrm{T}}^{\mathrm{core}} \tag{4.10}$$

An example of the E_T^{iso} is presented in Figures 4.16 on photons from a gluon-fusion $h \to \gamma\gamma$ MC sample and a jj sample, where the photon is faked by a jet. It can be observed a clearer that jets faking photons present larger transverse isolation energy than true photons.

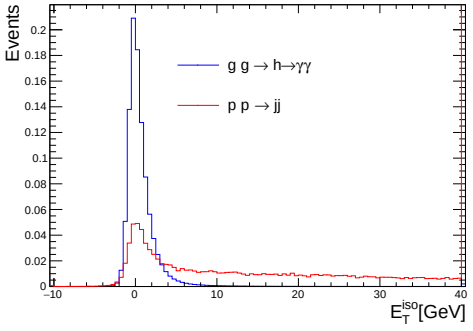


Figure 4.16: Comparison of the corrected topoetcone20 isolation transverse energies for photons from the gluon-fusion $h \to \gamma\gamma$ MC sample and a jj sample, where the photon is faked by a jet.

4.4.2 Track isolation

A track isolation variable, called *ptcone*, is computed by summing the transverse momentum of a set of tracks within a cone centered around the electron track or the photon direction determined from the calorimetric cluster. The selection of the tracks is detailed in the Table 4.3.

Criterium	$\lvert\eta\rvert$	N_{Si}	$N_{\mathrm{mod}}^{\mathrm{sh}}$	$N_{\mathrm{Si}}^{\mathrm{hole}}$	$N_{\mathrm{Pix}}^{\mathrm{hole}}$	p_{T}	$\lvert z_0 \sin\theta\rvert$
Cut value	< 2.5	≥ 7	≤ 1	≤ 2	≤ 1	$> 1\mathrm{GeV}$	< 3 mm

Table 4.3: Track selection for the track isolation. z_0 is the difference of longitudinal impact parameter of the track, and the position of a given vertex (by default the hardest vertex of the event); N_{Si} is the number of hits in silicon detectors (pixels and SCT); $N_{\mathrm{mod}}^{\mathrm{sh}}$ is the number of shared hits assigned to several tracks in the silicon detectors; $N_{\mathrm{Si}}^{\mathrm{hole}}$ and $N_{\mathrm{Pix}}^{\mathrm{hole}}$ is the number of missing hits in both silicon detectors and only pixel detector, respectively [13].

Contrary to the calorimeter isolation, where a cone with a radius smaller than 0.2 cannot be used (electron and photon clusters size is around $\Delta R = 0.175$ (0.125) in the calorimeter or the end-caps), the much finer angular resolution of the tracker allows using smaller cone size when needed. For example, in boosted signatures or very busy environements, different objects can end up very close to the particle direction. For such cases, a variable cone size depending on the electron or photon p_{T} is allowed. Consequently, a new track isolation variable [17], called *ptvarcone*, where the cone size $\Delta R_{\mathrm{track}}$ gets smaller for larger transverse momentum of the particle can be defined:

$$\Delta R_{\mathrm{track}} = \min\left(\frac{k_{\mathrm{T}}}{p_{\mathrm{T}}}, R_{\mathrm{track}}\right), \tag{4.11}$$

where k_T is a constant fixed to 10 GeV, p_T the transverse momentum of the photon or electron and R_{track} is the maximum cone size (0.2 to 0.4). Figure 4.17 shows the ptcone20 and ptcone40 isolation energies for photons from a gluon-fusion $h \to \gamma\gamma$ MC sample and a jj sample, where the two leading jets are misidentified as photons. It can be observed that jets faking photons present larger transverse isolation energy than true photons, although the rejection factor of background jj from a possible cut on track isolation is much lower than the calorimetric isolation previously presented.

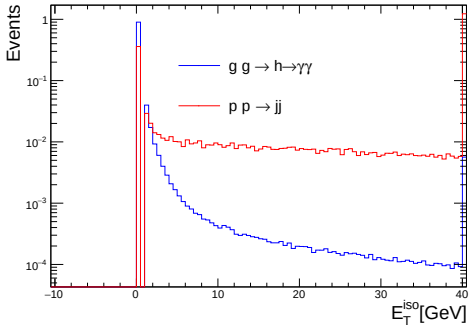


Figure 4.17: Comparison of the corrected ptcone20 isolation transverse energies for photons from the gluon-fusion $h \to \gamma\gamma$ MC sample and a jj sample, where the photon is faked by a jet.

4.5 Photon and electron calibration

The energy of electrons and photons is first estimated by summing the energies of all cells associated with their EM cluster. As presented in Chapter 3, detector calibration gives very good performance for measuring the energy deposited in the calorimeter. However, this performance was tested on a slice of the LAr barrel, without any upstream inner detector slice. After ATLAS full installation, a larger fraction of passive material is present upstream the calorimeter (Fig. 4.3.a) and, possibly, the calorimeter also present more imperfections and inhomogeneities, which influence the shower development and that worsen the performance of energy reconstruction. The current calibration technique was developed during Run I using 25 fb^{-1} [2] and re-evaluated during Run II using 3.2 fb^{-1} [18]. Figure 4.18 shows

the main steps of the calibration technique, based first on data-driven stability and shower development corrections, a MC-based calibration and an in-situ calibration. Optimizations are performed separately for electrons, unconverted photons and converted photons as a consequence of the different behaviour to variations in upstream material or uniformity measurements.

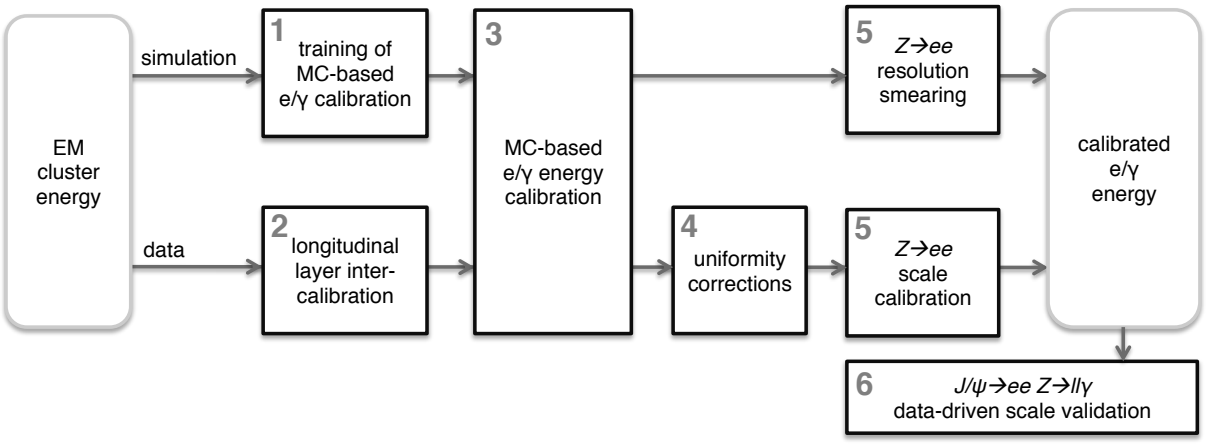


Figure 4.18: Calibration scheme for electrons and photons [2].

4.5.1 MC-based calibration and uniformity corrections

A correct calibration procedure relates the measured energy in the detector ($E_{\text{reco}}^{\text{data}}$) to the true energy ($E_{\text{true}}$) of the detected particle. This relation must first be studied on simulated samples between E_{true} and MC detector-level energy ($E_{\text{reco}}^{\text{MC}}$). Then, to calibrate data based on this relation, the differences between reconstructed energy in data and simulation due to detector mismodeling or shower development must be identified and corrected for.

Layer intercalibration

The shower shape development presents differences between data and MC coming from residual effects on upstream material mismodeling or electronic cell calibration presented in Chapter 3. Corrections are then applied based on data/MC differences observed on E_1/E_2 and E_0 distributions. No intercalibration is performed on layer 3 since its influence is negligible at the range of energies considered in the calibration study.

Muons entering the calorimeter interact like minimum ionizing particles and are not very affected by the upstream material on the calorimeter. This motivates the use of muons from $Z \to \mu\mu$ decays to study the intercalibration of the first and second calorimeter layers. Denoting $< E_{1/2} >=< E_1 > / < E_2 >$ the ratio of the mean energy deposited by muons in the strip and middle layers, the differences between data and MC are evaluated using $\alpha_{1/2} =< E_{1/2} >^{\text{data}} / < E_{1/2} >^{\text{MC}}$. The cause of divergences from $\alpha_{1/2} = 1$ are: the geometry of the read-out cells, the reduced electric field between the different calorimeter layers, the different electric field following the accordion geometry of the electrodes and absorbers and the modeling of the cross-talk between cells. Observed $\alpha_{1/2}$ biases (Fig 4.19) are removed by applying an $|\eta|-$dependent correction in the middle layer energy scale ($E_2^{\text{corr}} = E_2 \times \alpha_{1/2}$) in data as a direct comparison of E_2 in data and simulation shows that the observed pattern in Fig. 4.19 as a function of pseudorapidity. The presampler energy scale α_{PS} is determined from the ratio of the PS energy in data and MC for Z and W electron decays. However, before evaluating this scale, presampler energy needs to be corrected from passive material mismodeling upstream of the presampler, as an inaccurate material modeling affects the electron shower development. Corrections are derived by exploiting the correlation between E_0 and $E_{1/2}$ for electrons at a given η value under variations of passive material. After removing the dependence of $E_{1/2}$ from material mismodeling between the presampler and the calorimeter, the energy scale is estimated as $\alpha_{\text{PS}} = E_0^{\text{data}}/E_0^{\text{MC}}$, where E_0^{MC} is the MC energy corrected

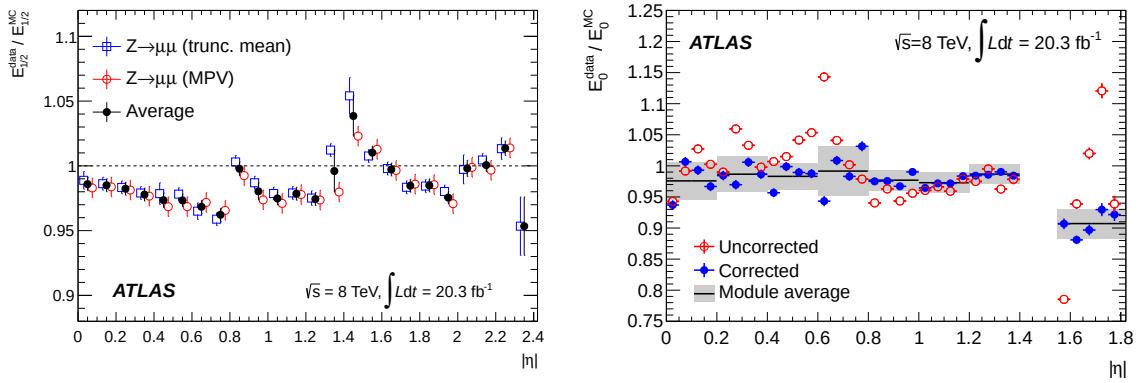


Figure 4.19: Energy scales $\alpha_{1/2}$ and $\alpha_{\rm PS}$ values depending on η for Run I [2]. Presented $\alpha_{1/2}$ values are derived using two methods for estimating $Z \to \mu\mu$ mean deposited energy in the first and second layer (fitting to a Landau or truncated mean of the distribution). $\alpha_{\rm PS}$ values are presented before and after correcting the presampler energy in MC from passive material mismodeling.

from material mismodeling.

$\alpha_{1/2}$ coefficients are cross-checked by studying the electron energy response in $Z \to ee$ events. In this case, the dependence of the invariant mass m_{ee} with respect to $E_{1/2}$ is studied. This invariant mass is not constant with $E_{1/2}$. To recover a constant slope, corrections are applied to the layer 1 response and to $\alpha_{1/2}$. It can be observed a certain difference in $\alpha_{1/2}$ derived on $Z \to ee$ and $Z \to \mu\mu$ events that is covered by the uncertainties affected the muon result and the electron result (Fig. 4.20).

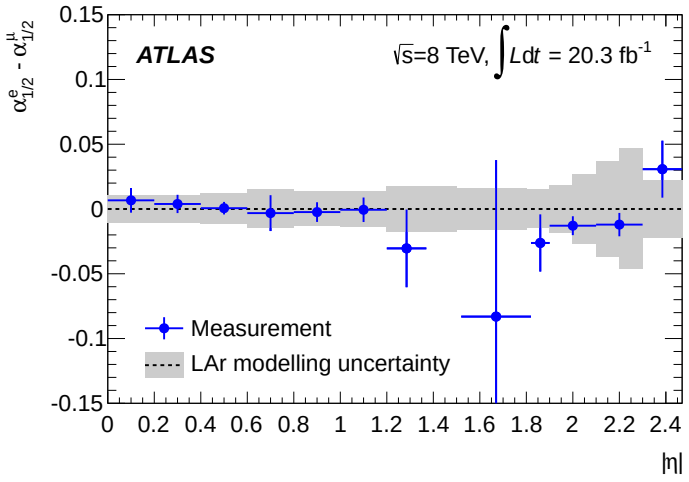


Figure 4.20: Differences in $\alpha_{1/2}$ after cross-checking the dependence of the invariant mass in $Z \to ee$ events with $E_{1/2}$ depending on η [2]. The error band represents the uncertainty on $\alpha_{1/2}$ when derived on the Z muon decay while the error bars represent the uncertainty on Z electron result.

Uniformity corrections

Apart from passive material effects, the ATLAS detector may present spatial inhomogeneities that are not correctly modeled by simulation. HV short circuits, azimuthal non-uniformity or different performances of gains are examples of such inhomogeneities, that usually are found in specific regions in the detector and that can only be corrected *a posteriori*, after comparing data and MC. Non-uniformities were evaluated during Run I and validated using 3.2 fb^{-1} data under Run II.

1. In few sectors of the EM calorimeter, the HV is set to a non-nominal value due to short circuits occurring in specific LAr gaps. This HV reduction increased the charge drift time before readout,

which induced a bias in the sampling phase at the FEBs that affected energy calculation. In addition, during Run I the presampler high-voltage nominal value was reduced from 2000 V to 1200 V (with some sectors at 800 V) (P2) passing through a period with 1600 V (P1). These effects are first corrected using the expected energy response dependence on HV. Corrections are verified on $Z \to ee$ invariant mass and found to present a residual effect in ϕ for the EM calorimeter and in η for the presampler. An empirical correction is put in place that restores the stability of the response. Figure 4.21 presents the effects on energy response carried out during Run I before and after the HV corrections. These effects are re-evaluated using Run II conditions [18], with an updated HV non-nominal value map.

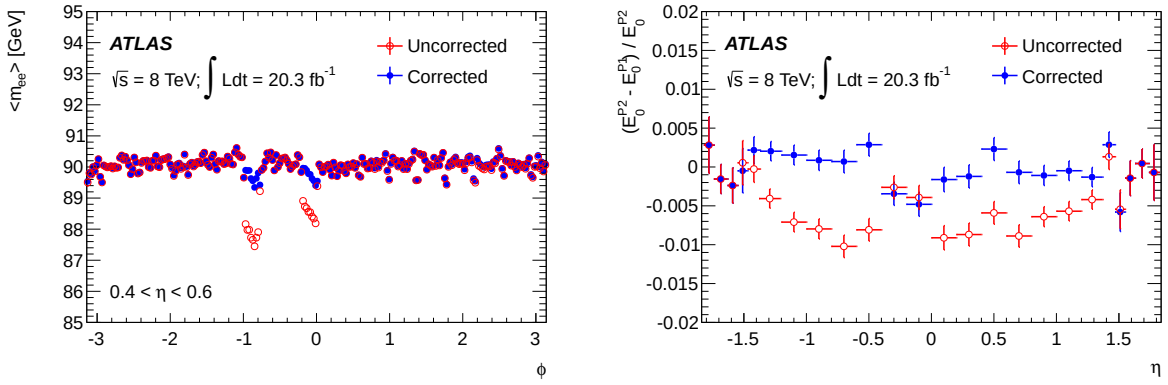


Figure 4.21: Left: average value of m_{ee} as a function of the azimuthal position of the leading decay electron with $0.4 < \eta < 0.6$ before and after the HV correction. Right: relative difference in the raw PS energy response due to the change in HV settings, as a function of η, before and after correction of the residual HV dependence [2].

2. In most of the calorimeter, the energy calibration is found to be electronic cell gain independent within uncertainties; however, a percent-level effect is seen in specific η regions (around $|\eta| \sim 0.6$ and $|\eta| \sim 1.6$). Corrections are then applied on the medium gain to remove this gain dependence. The same correction is assumed for the low gain.

3. When probing the energy response versus ϕ, a $\pi/8$-periodical structure is observed. The period and the location of the structures correspond to the transitions between the barrel calorimeter modules. The energy loss is adjusted with an empirical function used to correct the calorimeter response.

There is a residual azimuthal non-uniformity after previous corrections with an average magnitude of and 0.45% for $|\eta| < 0.8$ and 0.75 % for $|\eta| > 0.8$ during Run I.. In addition, a pileup instability of the response is found affecting within 0.1% to the energy response, as presented in Figure 4.22.

MVA calibration

After layer intercalibration and inhomogeneity corrections, the calibration procedure optimises the estimate of E_{true} at the interaction point from the detector-level observables. This step is based on a multivariate (MVA) boosted decision tree with gradient boosting feature trained using single-particle MC samples without pileup. This MVA relates several cluster level variables with E_{true} of the particle such as the total energy measured in the calorimeter (E_{calo}); the ratio of the presampler energy to the calorimeter energy, E_0/E_{calo}; the cluster barycentre pseudorapidity η_{cluster} in the ATLAS coordinate system; the η and ϕ barycentre within the calorimeter frame and the ratio between the strip layer and middle layer energy E_1/E_2 (in Run I, the longitudinal shower depth was used, defined as $X = \sum X_i E_i / \sum E_i$ where X_i is the calorimeter layer thickness). In addition, the amount of material traversed by the particles in $1.4 < |\eta| < 1.6$ before reaching the first active layer of the calorimeter represents from 5 to almost 10 radiation lengths, thus the energy resolution is very degraded. To mitigate this effect, the energy measured by the E4 scintillators installed in the transition region between the EM barrel and the end-cap

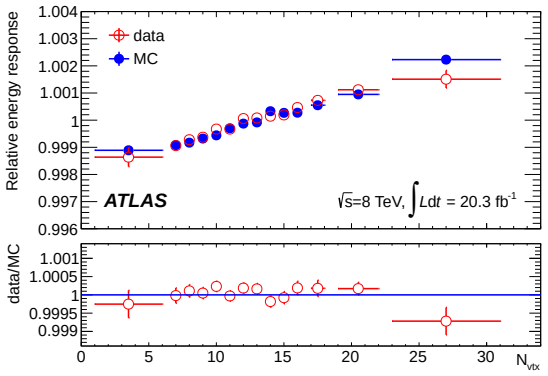


Figure 4.22: Pileup stability of the energy response in data and simulation [2].

is added to the MVA variables. The conversion radius R_{conv} is added in the case of converted photons if the vectorial sum of the conversion track momenta ($p_{\text{T}}^{\text{conv}}$) is larger than 3 GeV. In the case that both tracks are reconstructed with one hit in the SCT detector, further quantities are considered: $p_{\text{T}}^{\text{conv}}/E_{\text{calo}}$ and the ratio of the conversion momentum carried by the highest-p_{T} track, $p_{\text{T}}^{\text{max}}/p_{\text{T}}^{\text{conv}}$.

4.5.2 In-situ corrections

A residual disagreement in the energy scale and resolution may be present between data and simulation after the application of the MVA and data corrections. During Run I, residual disagreements were corrected by comparing $Z \to ee$ events invariant mass from data and the related MC samples with pileup. Scale factors to correct from energy mismeasurement are derived and applied to data. The energy miscalibration is defined as the difference in response between data and simulation, and is parametrized as:

$$E_i^{\text{data}} = E_i^{\text{MC}}(1 + \alpha_i) \tag{4.12}$$

where E_i^{data} and E_i^{MC} are the electron energies in data and simulation, and α_i represents the deviation from optimal calibration, in a given pseudorapidity region labeled i. On the $Z \to ee$ invariant mass, this scale on the electrons energy translates into a correction of type:

$$m_{ik}^{\text{data}} = m_{ik}^{\text{MC}}(1 + \alpha_{ij}); \qquad \alpha_{ij} \sim \frac{\alpha_i + \alpha_j}{2} \tag{4.13}$$

assuming that the angle between the two electrons is well-known and neglecting second order terms. Apart from energy miscalibration, comparisons between data and simulation energy resolution (σ_E/E) show a disagreement that is corrected by properly smearing the $Z \to ee$ MC invariant mass distribution. This difference can be modeled by an additional effective constant term ($c_i^{'}$) to the calorimeter resolution defined in Eq. 3.1:

$$\left(\frac{\sigma_E}{E}\right)_i^{\text{data}} = \left(\frac{\sigma_E}{E}\right)_i^{\text{MC}} \oplus c_i^{'} \tag{4.14}$$

for a given pseudorapidity region i. This resolution for each electron is then translated into the $Z \to ee$ invariant mass resolution as:

$$\left(\frac{\sigma_m}{m}\right)_{ij}^{\text{data}} = \left(\frac{\sigma_m}{m}\right)_{ij}^{\text{MC}} \oplus c_{ij}^{'} = \frac{1}{2}\left[\left(\frac{\sigma_E}{E}\right)_i^{\text{MC}} \oplus c_i^{'} \oplus \left(\frac{\sigma_E}{E}\right)_j^{\text{MC}} \oplus c_j^{'}\right] \tag{4.15}$$

$$c'_{ij} \sim \frac{c_i^{'} \oplus c_j^{'}}{2} \tag{4.16}$$

The factors α_i and $c_i^{'}$ are estimated then using histograms of the $Z \to ee$ invariant mass built separately for different electron pseudorapidity configurations (η_i, η_j). Then, template histograms are similarly built from simulation on which different α_{ij} or $c_{ij}^{'}$ factors are applied. The final α_{ij} and $c_{ij}^{'}$ for the (η_i, η_j) are calculated by performing a χ^2 minimisation of these templates on data, as illustrated in Figs. 4.23.

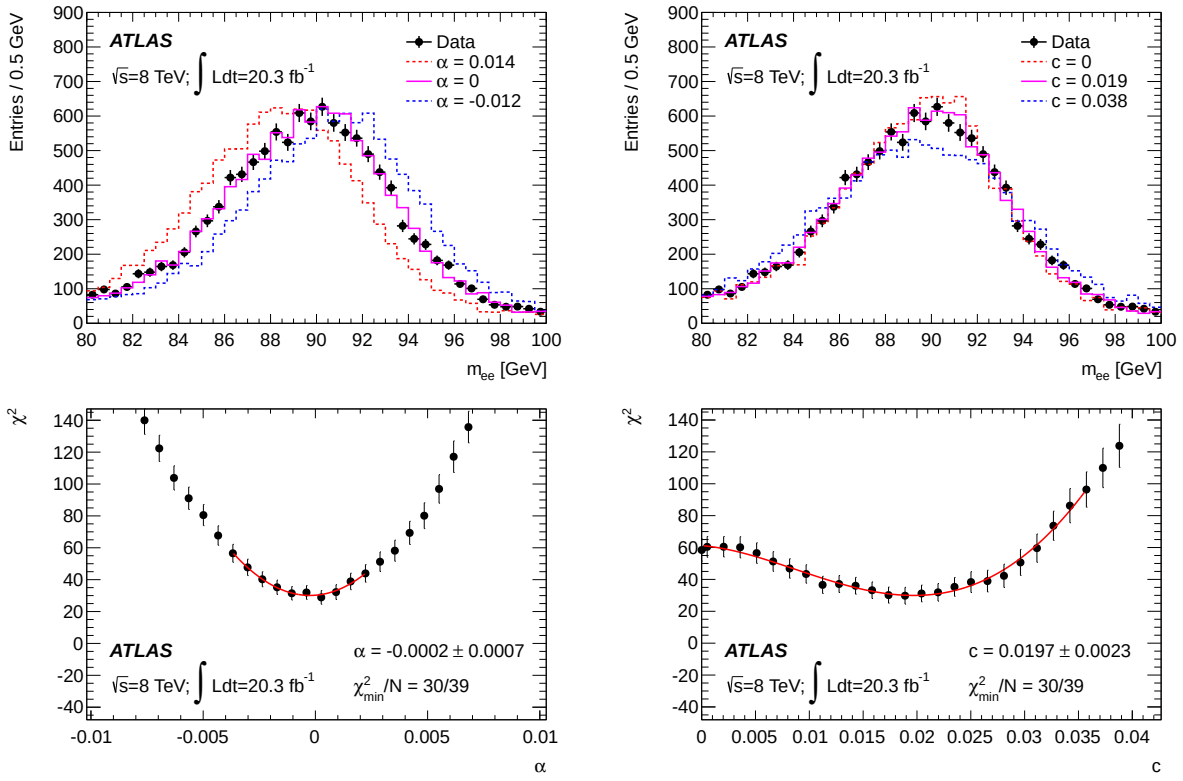


Figure 4.23: Top plots: electron pair invariant mass distribution for $Z \to ee$ candidates in data compared to MC templates. Different values of α_{ij} (left) are tested for a fixed value of $c_{ij}^{'}$ and viceversa (right). One electron is within $1.63 < \eta < 1.74$ and the other, within $2.3 < \eta < 2.4$. Bottom plots: χ^2 as a function of α_{ij} (left) and $c_{ij}^{'}$ (right) [2].

The obtained energy scale α_i and constant term $c_i^{'}$ for electrons in a particular pseudorapidity region is obtained then by solving Eqs. 4.13 and 4.16. Figure 4.24 presents the results on α_i and $c_i^{'}$ on 2015 $Z \to ee$ events. These scale factors and resolution term include any possible residual correction from pileup effects.

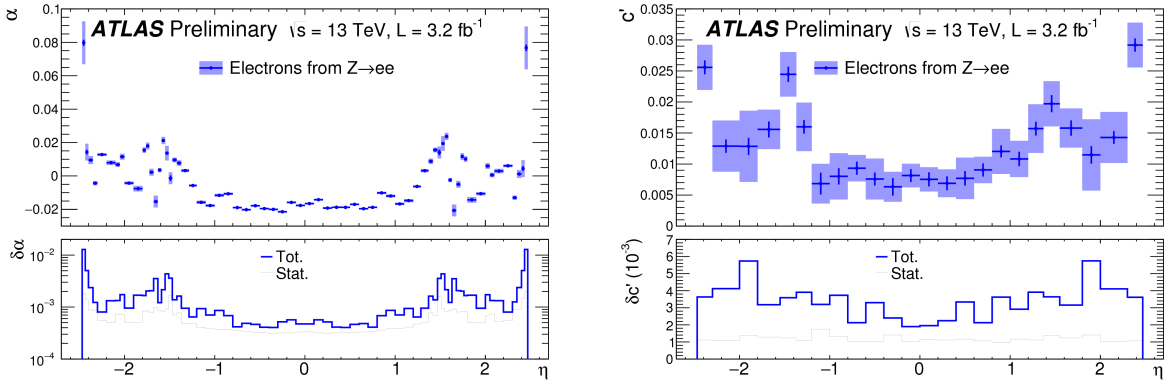


Figure 4.24: (a) Energy scale factor α and (b) additional constant term $c^{'}$ for energy resolution from $Z \to ee$ events as a function of η. The uncertainty bands on the top plots represent the total uncertainties on these quantities, while the thin black (resp. thick blue) lines at the bottom represent the statistical (resp. total) uncertainties. [18].

4.5.3 Systematic uncertainties

The main sources of uncertainties and their magnitude for the calibration procedure are presented in Figures 4.25, 4.26 and 4.27 for electron, unconverted and converted photons in $|\eta| < 0.6$. They correspond to uncertainties found in the presampler and layer intercalibration, detector non-uniformities (gain, material) and in-situ calibration. Pileup and temperature stability are accounted inside the in-situ calibration systematics. An 0.02% is added to the pileup uncertainty to account for the different pileup conditions between 2015 and 2016 datasets. An uncertainty on the E4 scintillators must be added for the region $1.4 < |\eta| < 1.6$.

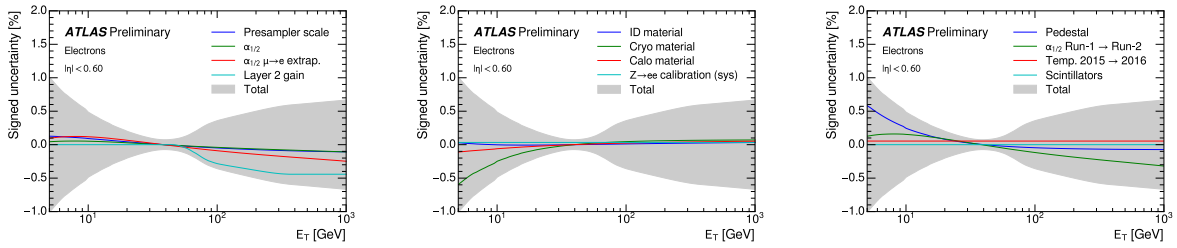


Figure 4.25: Uncertainties for the electron energy calibration using 2015 dataset with 3.2fb^{-1} total luminosity [18].

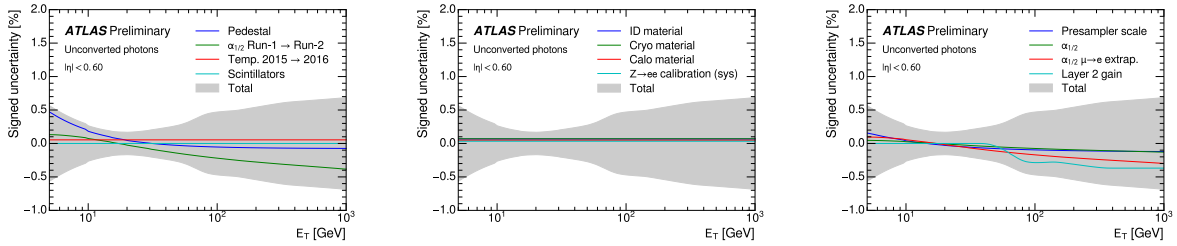


Figure 4.26: Uncertainties for the unconverted photons energy calibration using 2015 dataset with 3.2fb^{-1} total luminosity [18].

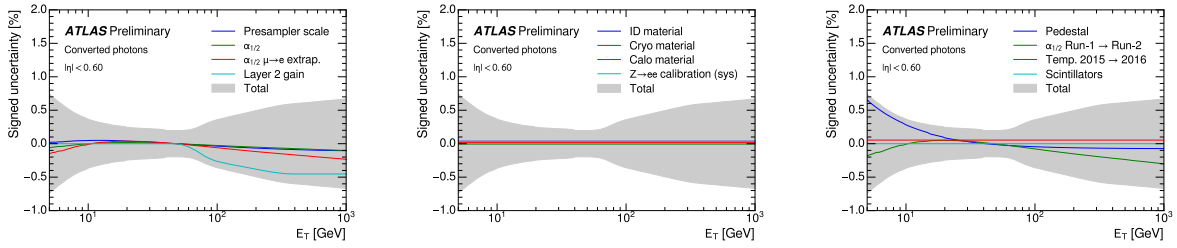


Figure 4.27: Uncertainties for the converted photons energy calibration using 2015 dataset with 3.2fb^{-1} total luminosity [18].

References

[1] ATLAS Collaboration. *Conversion radius public plots*. URL: https://atlas.web.cern.ch/Atlas/GROUPS/PHYSICS/EGAMMA/PublicPlots/20110216/ATL-COM-PHYS-2011-120/index.html.

[2] Georges Aad et al. "Electron and photon energy calibration with the ATLAS detector using LHC Run 1 data". In: *Eur. Phys. J.* C74.10 (2014), p. 3071. DOI: 10.1140/epjc/s10052-014-3071-4. arXiv: 1407.5063 [hep-ex].

[3] W Lampl et al. *Calorimeter Clustering Algorithms: Description and Performance*. Tech. rep. ATL-LARG-PUB-2008-002. ATL-COM-LARG-2008-003. Geneva: CERN, Apr. 2008. URL: https://cds.cern.ch/record/1099735.

[4] T G Cornelissen et al. "The global χ^2 track fitter in ATLAS". In: *Journal of Physics: Conference Series* 119.3 (2008), p. 032013. URL: http://stacks.iop.org/1742-6596/119/i=3/a=032013.

[5] *Performance of the ATLAS Inner Detector Track and Vertex Reconstruction in the High Pile-Up LHC Environment*. Tech. rep. ATLAS-CONF-2012-042. Geneva: CERN, Mar. 2012. URL: http://cds.cern.ch/record/1435196.

[6] *Electron efficiency measurements with the ATLAS detector using the 2015 LHC proton-proton collision data*. Tech. rep. ATLAS-CONF-2016-024. Geneva: CERN, June 2016. URL: http://cds.cern.ch/record/2157687.

[7] Morad Aaboud et al. "Measurement of the photon identification efficiencies with the ATLAS detector using LHC Run-1 data". In: *Eur. Phys. J.* C76.12 (2016), p. 666. DOI: 10.1140/epjc/s10052-016-4507-9. arXiv: 1606.01813 [hep-ex].

[8] *Photon identification in 2015 ATLAS data*. Tech. rep. ATL-PHYS-PUB-2016-014. Geneva: CERN, Aug. 2016. URL: http://cds.cern.ch/record/2203125.

[9] *Improved electron reconstruction in ATLAS using the Gaussian Sum Filter-based model for bremsstrahlung*. Tech. rep. ATLAS-CONF-2012-047. Geneva: CERN, May 2012. URL: http://cds.cern.ch/record/1449796.

[10] Georges Aad et al. "Electron performance measurements with the ATLAS detector using the 2010 LHC proton-proton collision data". In: *Eur. Phys. J.* C72 (2012), p. 1909. DOI: 10.1140/epjc/s10052-012-1909-1. arXiv: 1110.3174 [hep-ex].

[11] G. Aad et al. "Expected Performance of the ATLAS Experiment - Detector, Trigger and Physics". In: (2009), p. 49. arXiv: 0901.0512 [hep-ex].

[12] G. Aad et al. "Expected Performance of the ATLAS Experiment - Detector, Trigger and Physics". In: (2009). arXiv: 0901.0512 [hep-ex].

[13] Jean-Baptiste De Vivie De Regie et al. *ATLAS electron, photon and muon isolation in Run 2*. Tech. rep. ATL-COM-PHYS-2017-290. Geneva: CERN, Mar. 2017. URL: https://cds.cern.ch/record/2256658.

[14] Georges Aad et al. "Performance of pile-up mitigation techniques for jets in pp collisions at $\sqrt{s} =$ 8 TeV using the ATLAS detector". In: *Eur. Phys. J.* C76.11 (2016), p. 581. DOI: 10.1140/epjc/s10052-016-4395-z. arXiv: 1510.03823 [hep-ex].

[15] Matteo Cacciari, Gavin P. Salam, and Gregory Soyez. "The anti-k_t jet clustering algorithm". In: *JHEP* 04 (2008), p. 063. DOI: 10.1088/1126-6708/2008/04/063. arXiv: 0802.1189 [hep-ph].

[16] Matteo Cacciari, Gavin P. Salam, and Gregory Soyez. "The Catchment Area of Jets". In: *JHEP* 04 (2008), p. 005. DOI: 10.1088/1126-6708/2008/04/005. arXiv: 0802.1188 [hep-ph].

[17] Keith Rehermann and Brock Tweedie. "Efficient Identification of Boosted Semileptonic Top Quarks at the LHC". In: *JHEP* 03 (2011), p. 059. DOI: 10.1007/JHEP03(2011)059. arXiv: 1007.2221 [hep-ph].

[18] *Electron and photon energy calibration with the ATLAS detector using data collected in 2015 at* $\sqrt{s} =$ 13TeV. Tech. rep. ATL-PHYS-PUB-2016-015. Geneva: CERN, Aug. 2016. URL: http://cds.cern.ch/record/2203514.

Cross-Talk effects in the LAr EM barrel

Contents

5.1 Types of cross-talk . . . 114
5.1.1 Capacitive cross-talk . . . 114
5.1.2 Resistive cross-talk . . . 115
5.1.3 Inductive cross-talk . . . 116
5.2 Test-beam and calibration cross-talk . . . 117
5.3 Cross-talk in physics conditions . . . 121
5.3.1 Physics cross-talk shape determination . . . 123
5.3.2 Cross-talk estimation in the LAr barrel . . . 130
5.4 Shower shape corrections . . . 140

A precise energy reconstruction and particle identification were the experimental key points that allowed the discovery of the Higgs boson in the $\gamma\gamma$ decay channel in 2012. However, the ATLAS performance could still be improved by correcting several undesired effects in the detector that spoil the measurement accuracy. For instance, the correct identification of the electrons and photons requires a good determination of the shower shape variables introduced in the algorithm. The quality of this reconstruction lies on the correct description of these variables in the MC, which is affected by the mismodeling of several effects at detector level. Among all possible effects that could reduce these performances, this work has been devoted to study the cross-talk effect.

Cross-talk is the charge sharing among different electronic cells of the calorimeter due to non-desired connections in the readout chain. It can occur at electrode level between cells belonging to the same region of the calorimeter or directly somewhere along the electronic readout chain. These couplings affect the shower shapes by inducing lateral and longitudinal distortions, thus affecting the shower shapes reconstruction e.g. such as the w_{η_2} variable described in Chapter 4. Interestingly, the charge leakage between cells distorts the readout cell signal shape. This distortion of the shape thereby induces a certain bias on energy and time because OFCs are estimated using the signal shape without cross-talk in each cell. Given the energy and time extraction procedure, the time bias is dominant. As exposed in Section 3.7, the energies of several electron beams ranging from 10 to 245 GeV were successfully determined within a 5 ‰ accuracy during 2001 test beam campaign [1]. It was demonstrated that cross-talk induces around a 94 ps bias on the arrival time of a particle in the ECAL. This is an important effect since time measurements could in principle be used to estimate the interaction primary vertex from which the incoming EM particle is produced. Considering relativistic particles, a bias of ~ 3 cm is induced by the cross-talk effect, which represents about half the typical size of the region along the z-axis where pp collisions take place. Corrections of cross-talk effects could then improve particle identification and help to reduce the large amount of in-time pileup observed for Run II.

The different types of cross-talk are exposed in Section 5.1. The current setup of cross-talk estimation and the values used in the ATLAS simulation code are exposed in Section 5.2. A more accurate determination of the cross-talk effect requires the evaluation of which fraction of the cell energy leaks into other cells of the calorimeter. This implies the reconstruction of the cross-talk shape during data-taking, which is discussed in Section 5.3.1. After the cross-talk measurement protocol is described, cross-talk magnitude is estimated for the calorimeter barrel, as exposed in Section 5.3.2.

5.1 Types of cross-talk

The different sources of cross-talk can be modeled by electrical circuits with a set of resistances, capacitances and inductances. This allows classifying the cross-talk as either capacitive, resistive or inductive effects. These three types of cross-talk can be found all along the calorimeter and the readout chain. However, each layer usually presents a dominant contribution from one of them. The existence of these couplings is related to the structure of the readout electrodes, the mother-boards and the feedthroughs. This information has been detailed in Chapter 3 for the electromagnetic barrel calorimeter.

On the other hand, cross-talk may be registered between neighbouring cells in a given region of the calorimeter, or between cells in different regions of the calorimeter. The former cross-talk contribution is called *short distance cross-talk* and may be caused by the three different types of couplings. The latter is called *long distance cross-talk* and only resistive and inductive cross-talk sources have been observed.

5.1.1 Capacitive cross-talk

The capacitive cross-talk comes from capacitive couplings occurring on the electrodes. Electrodes are formed of three copper layers, the outer ones being devoted to provide HV to the LAr gap. These HV layers are segmented following the η division of the barrel, as explained in Section 3.3.1. The inner layer, devoted to the signal readout, is segmented according to the cell distribution in the barrel calorimeter. The signal layer segments are separated 0.5 mm and are glued to a kapton-polymide layer that acts as a dielectric between HV and signal layers. Despite that this signal layer segmentation avoids large charge transfer between the different cell electrodes, the presence of a dielectric between two signal electrode cells made of copper causes that some charges associated with a given cell that are collected by the signal layer migrate into regions of the electrode that are associated with a neighbouring cell.

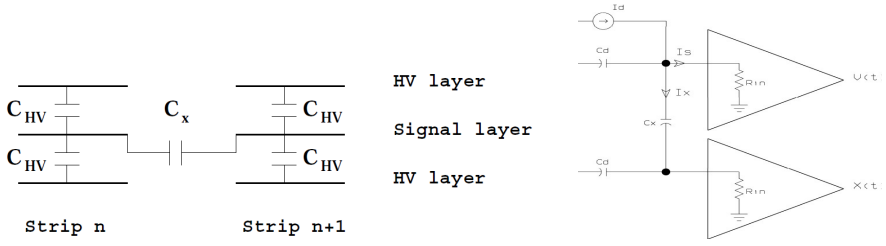


Figure 5.1: (left) Illustration of the capacitive coupling C_x between cells on a single electrode and comparison with the capacitive coupling C_{HV} between the inner layer and the two HV outer layers of the electrode. (right) Readout chain model used to estimate the capacitive coupling signal. In this model, $C_d = C_{\mathrm{HV}}$

The characteristic shape of the capacitive cross-talk is a derivative of the signal shape. The capacitive coupling can be modeled by a simple circuit [2] exposed in Figures 5.1. Making the approximation that C_x is small compared to C_d (ensured by a high R_{in} or $C_x << C_d$), the currents I_s and I_x that travel in the direct channel and the neighbouring channel respectively are expressed as:

$$I_s(s) = \frac{I_d}{1 + sR_{in}C_t} \qquad I_x(s) = \frac{sR_{in}C_xI_d}{(1 + sR_{in}C_t)^2} \tag{5.1}$$

where C_d is the detector capacitance, C_x the parasitic coupling capacitance and $C_t = C_x + C_d$. This equation shows that the relative magnitude of the capacitive cross-talk depends on the depends on the ratio C_x/C_d. The larger is this ratio, the larger is the relative magnitude between the cross-talk induced in the neighbouring cell and the signal collected by the ionized electronic cell. Given that the capacitance C_d is proportional to the surface of the electrode signal layer cell, the finer is the cell segmentation, the larger is the capacitive cross-talk. In consequence, capacitive coupling becomes the main source of charge leakage in the front layer, meanwhile it is strongly reduced in the second and the third layer.

The triangular detector current can be approximated by a step function $I_d(s) = I_o/s$ in the Laplace domain. After preamplification and shaping with the CR–RC^2 shaper, whose global transfer function is:

$$H(s) = \frac{V_{out}(s)}{I_{in}(s)} = R_f \frac{\tau s}{(1+\tau s)^3}, \tag{5.2}$$

with $\tau \sim 15$ ns being the shaping time, the output direct signal and cross-talk shapes can be written as:

$$V(s) = \frac{I_o}{s} \frac{1}{1+sR_{in}C_t} \frac{R_f \tau s}{(1+\tau s)^3}, \tag{5.3}$$

$$X(s) = \frac{I_o}{s} \frac{sR_{in}C_x}{(1+sR_{in}C_t)^2} \frac{R_f \tau s}{(1+\tau s)^3}. \tag{5.4}$$

Applying an inverse Laplace transform, the final formula for capacitive cross-talk is given by Equation 5.5 [2], where $x = t/\tau$ and $\lambda = R_{in}C_t/\tau$. Figure 5.2 shows a typical capacitive cross-talk shape in calibration runs compared to the corresponding pulsed cell waveform.

$$X(x) = -R_f I_0 \frac{\lambda C_x}{C_t} \left[\left(x - \frac{\lambda^2+2\lambda}{\lambda-1} \right) \frac{e^{-x/\lambda}}{(\lambda-1)^3} + \left(\frac{x^2}{2} + \frac{\lambda+1}{\lambda-1} x + \frac{\lambda^2+2\lambda}{(\lambda-1)^2} \right) \frac{e^{-x}}{(\lambda-1)^2} \right] \tag{5.5}$$

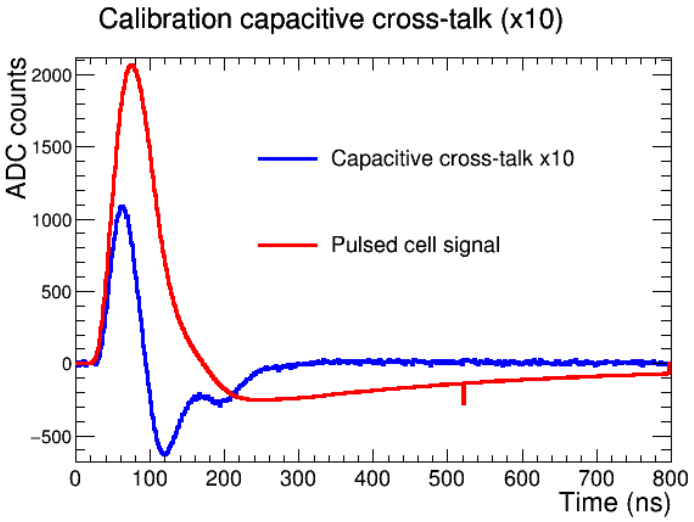


Figure 5.2: Capacitive cross-talk shape obtained from calibration data. A cell is pulsed in the front layer of the EM barrel. The cross-talk shape is retrieved from its closest neighbouring cell in η.

5.1.2 Resistive cross-talk

Silk screened resistors along the full HV layer (Fig. 3.11) produce a charge leakage between electronic cells. Since resistors connect cells in the same η region, as shown in Figure 5.3, resistive cross-talk is only present between cells in different layers belonging to the same η. The nature of the coupling implies that its shape is similar to the regular signal shape, represented in Figure 5.4. It represents the main source of charge leakage between the middle and front layers of the calorimeter while it can be considered negligible between the middle and the back layer cells.

In addition, long distance cross-talk can be observed if a middle layer is pulsed on first layer strips. These strips surround the front layer cells that are in front of a pulsed middle cell. However, they are not sharing any resistor with the pulsed middle cell. Nevertheless, these contributions are small compared to resistive cross-talk between front and middle cells in the same η line.

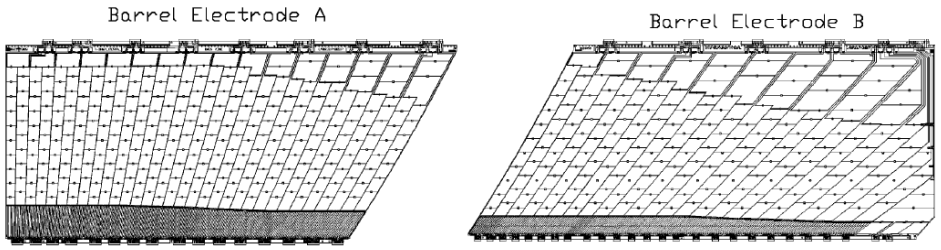


Figure 5.3: Layout of the resistors on the HV layer for the Electrode A and Electrode B of the LAr EM barrel [3].

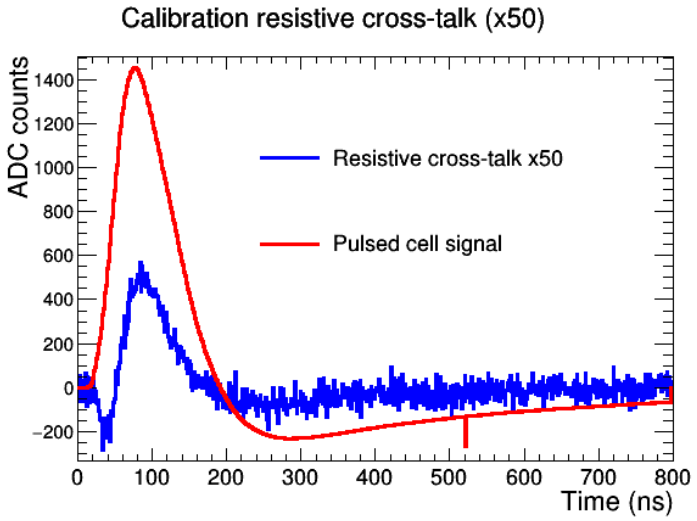


Figure 5.4: Resistive cross-talk shape obtained from calibration data. A cell is pulsed in the middle layer of the EM barrel. The cross-talk shape is retrieved from one of its neighbouring cell in the front layer.

5.1.3 Inductive cross-talk

The passage of charges through the readout chain (connectors and cables) may induce some charges by induction effect in the cables of other calorimeter cells. There are three possible sources of cross-talk:

- If several electrodes are connected in series to the same ground return, an inductive cross-talk is produced as a loop effect.
- In the mother board, a mutual inductance may appear between different channels. The proximity of the pins (Section 3.3.3) of middle and back layer cells may induce charges in the readout chain of neighbouring channels.
- On the feedthroughs, the passage of the signal may induce a current in neighbouring connectors. This contribution is long distance cross-talk and tends to be quite small. Its location thanks to the connectors pattern shown in Figure 3.14.

The first source encouraged a redesign of the mother-boards, which some ground pins were added [2]. This leaves the mutual inductance between mother board connectors as the dominant contribution of the inductive cross-talk (Fig. 5.5). There are two typical shapes: the first is well described by a time

shifted second derivative of the regular signal shape and the second, to a first derivative. This cross-talk dominates the cross-talk between middle-middle, back-back and middle-back cells.

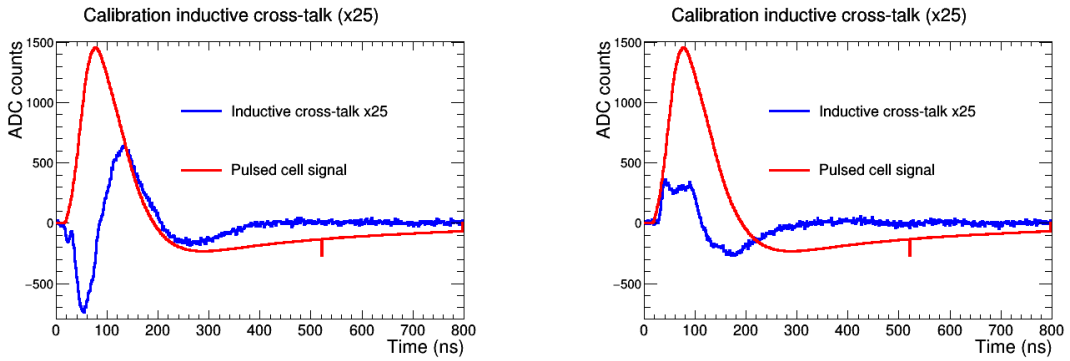


Figure 5.5: Inductive cross-talk shape obtained from calibration data. A cell is pulsed in the middle layer of the EM barrel. The cross-talk shape on the left is retrieved from its closest neighbouring cell in η while the one on the right is retrieved from its adjacent cell in the back layer.

5.2 Test-beam and calibration cross-talk

In this section, the strategy carried out during LAr barrel development is presented together with the measured values of cross-talk after final installation. Cross-talk was first studied in 1999 and 2000 test-

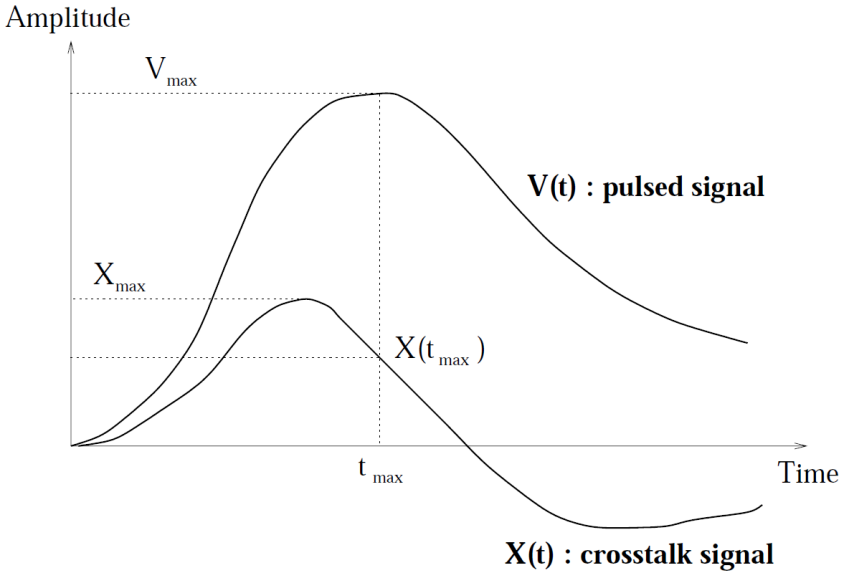


Figure 5.6: Diagram of the related quantities entering the cross-talk determination [4].

beams on the barrel [4, 5] and the end-caps [6, 7] during the ATLAS construction. Complementarily, a final test was performed in 2008 once the ATLAS detector was fully installed [8]. In this context, two techniques were developed to evaluate the cross-talk. The relevant quantities for estimating cross-talk are presented in Figure 5.6, being $X(t_{\max})$ the value of the cross-talk under the peak of the direct signal, $V(\max)$ the value of the injected signal peak and $X(\max)$ the peak of the resulting cross-talk:

- **Under-peak to peak estimation:**

  It is defined as the ratio of $X(t_{\max})$ by $V(\max)$. The sampling phase is tuned for each FEB of the calorimeter so that the peak of the signal is systematically stored. This estimation gives then the most realistic value of the cross-talk for each cell. However, these values are very dependent on fluctuations of the cross-talk signal or from a shift in the sampling phase.

- **Peak-to-peak estimation:**

  It is defined as the ratio of $X(\max)$ by $V(\max)$. This value is more stable in comparison to the under-peak to peak estimation but it just represents the most pessimistic value of the cross-talk in each cell. In consequence, this technique is used to estimate the maximum magnitude of the cross-talk effect.

$X(\max)$, $X(t_{\max})$ and $V(\max)$ are values expressed in ADC counts. In order to deal with energy measurements, gain factors translating ADC into MeV were applied. These factors substitute the standard calibration pattern exposed in Chapterch:energyreco, given that this procedure was not still fully implemented when these studies were performed. Their introduction does not affect the magnitude of the cross-talk between cells in the same layer, given that they preserve the same value cell-by-cell. Conversely, cross-talk magnitude between different layers cells is affected as gain factors vary between one layer and the other. The ratios between these gains are shown in Figures 5.7.

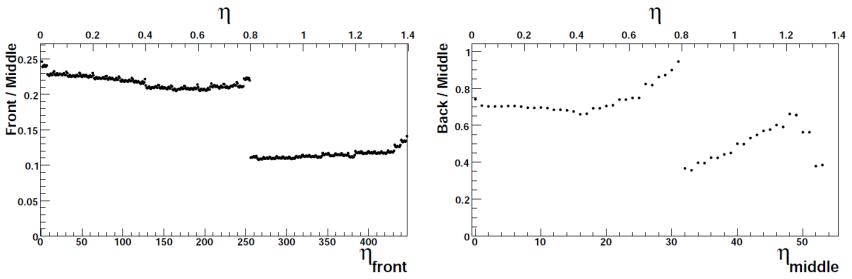


Figure 5.7: Gain factors ratio (MeV/ADC) between front and middle layers (left) and back and middle layers (right) [8].

2008 cross-talk results are presented in Figs. 5.8 and 5.9 using peak-peak and under-peak to peak methods, respectively. A capacitive cross-talk of around 4.3 % is found between cells in the front layer, with a maximum magnitude of 7.2%. In addition, capacitive coupling in the front layer is large enough to allow an energy leakage between cells separated by two η bins. This so-called *second neighbours* cross-talk represents up to 0.8% of the energy of the pulsed cell. Cross-talk between middle cells accounts for $\sim$ 0.44 % of the pulsed energy, while cross-talk contribution from middle layer to front and back cells is on average 0.07% (0.093% on the electrode B) and 0.6 % of the pulsed energy. The cross-talk between back cells represents at most -0.52% but can vary along the calorimeter up to 1.4%.

These results are in agreement within uncertainties with the 2000 test-beam results. Resistive and inductive long distance cross-talk contributions are considered negligible in comparison to short distance cross-talk and it is not evaluated in this study.

Estimation of the cross-talk effect using optimal filtering method.

Values using peak-peak and under-peak to peak methods are indicative of the magnitude of the cross-talk effect. However, in order to obtain more accurate values, energies of the cross-talk and the direct signal are estimated using the optimal filtering method on calibration signals (Fig. 5.10). The use of calibration signals and not physics signals requires that the optimal filtering coefficients are optimized to correctly find the peak of calibration waveforms. This is done using the method described in Section 3.5 with $g(t) = g^{\text{calib}}(t)$. After applying the OFCs on cross-talk and calibration pulses, their

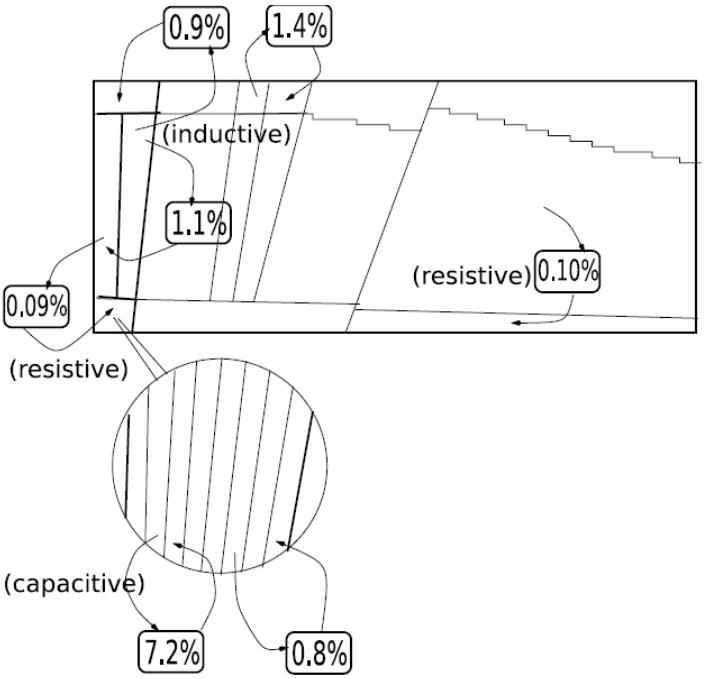


Figure 5.8: Schema of the different cross-talk magnitudes using the peak-peak estimation [8].

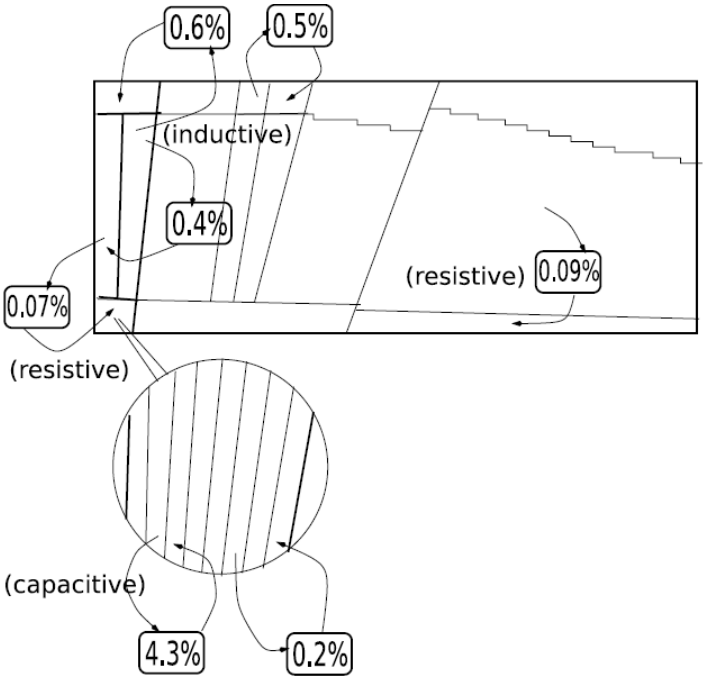


Figure 5.9: Schema of the different cross-talk magnitudes using the under-peak to peak estimation [8].

respective energies are expressed in ADC. Then, the relative cross-talk magnitude is evaluated as: $R = E^{\mathrm{ADC}}_{\mathrm{cross-talk}}/E^{\mathrm{ADC}}_{\mathrm{direct}}$ [9].

The resulting cross-talk ratios are exposed in Figures 5.11 for different bins in η. It is assumed that cross-talk magnitude does not vary significantly in the azimuthal direction. A decrease in cross-talk magnitude between strips is observed at increasing η for the electrode A ($|\eta| < 0.8$), which is expected

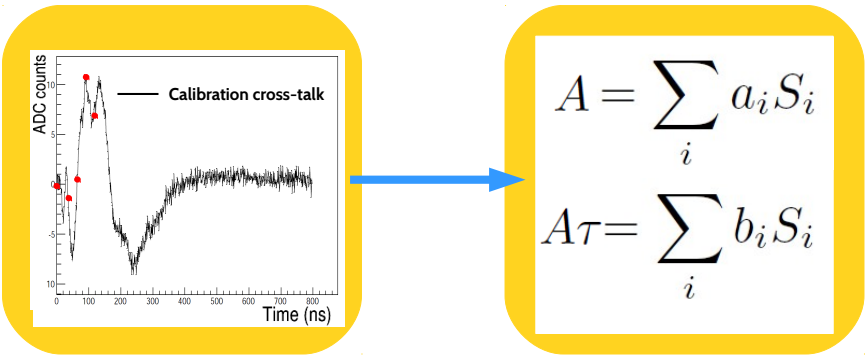


Figure 5.10: Schema of how cross-talk energy is estimated using the optimal filtering method on calibration signals .

	2000 test-beam		2008 results		OF method on calibration signals	
Type	Electrode A	Electrode B	A	B	A	B
Strip-to-strip	4.3%		4.34% ± 0.60%		4.31% ± 0.65%	
Strip-to-middle	0.05%	0.16%	0.070% ± 0.014%	0.093% ± 0.022%	0.070%± 0.008%	0.080% ± 0.016%
Middle-to-middle	0.85%		0.44% ± 0.26%		0.60% ± 0.24%	
Middle-to-back	0.36%		0.61% ± 0.18%		0.48% ± 0.17%	
Back-to-back	0.68%		-0.52% ± 0.28%		–	

Table 5.1: Cross-talk mean values in the LAr barrel. 2000 test-beam and 2008 results represent the cross-talk magnitude using under-peak to peak technique [8]. The uncertainties for the 2008 and OF method values correspond to the RMS of their corresponding ratios distribution for the full distribution of cells in each category.

due to the increase of the electrode cell surface (thus C_d) with η. At $|\eta| > 0.8$, the electrode length decreases at larger η, thus its surface too, and capacitive cross-talk tend to increase. Dips are observed every 16 (8) channels in the range $|\eta| < 0.8$ ($0.8 < |\eta| < 1.45$). These drops are due to a capacitive coupling [8] of $\sim$ 1–2% occurring between the summing board connectors in the motherboards (Fig. 3.13 in Chapter 3), where there is one connector per 16 channels in the region $|\eta| < 0.8$ and one connector per 8 channels in the region $0.8 < |\eta| < 1.45$. Besides, second neighbours contribution has a magnitude of 0.4% at $|\eta| < 1.1875$ and 0.5% beyond. The dip observed at $|\eta| = 0.8$ is due to the change of the electrodes. Concerning the cross-talk between middle and front layers, the increasing slope along η is correlated with a decrease in the number of resistances per η line, which can be observed in Figure 5.3. In addition, magnitude drops occur every 8 channels in the barrel due to larger resistances in the limiting channels of the group of 8 strips facing the middle cell [8]. Concerning the middle layer, a mean magnitude of 0.60% is found. Dips can be observed every two channels, explained by a lower coupling between channels that are not readout by the same summing board. The same reasoning can be applied to cross-talk between the middle and back layer cells. Contributions between back layer cells is not estimated.

Table 5.1 presents the main results of the cross-talk between 2000 test-beam, 2008 after final installation and OF calibration cross-talk values. It can be observed a general agreement between the three values, except for the middle layer cross-talk. In that case, the cross-talk is very dependent on the OF phase, thus a larger uncertainty is present. However, it can be observed that different values still agree under the uncertainties.

It must be noticed that strip-to-middle cross-talk ratios are considered equal to the cross-talk from middle-to-front cells. Similarly, cross-talk ratios between middle-to-back are assumed to be equal to back-to-middle contributions.

Cross-talk estimated from calibration signals has the advantage to be more noise resilient than the cross-talk estimated using under-peak to peak or peak-to-peak strategies. In consequence, cross-talk ratios

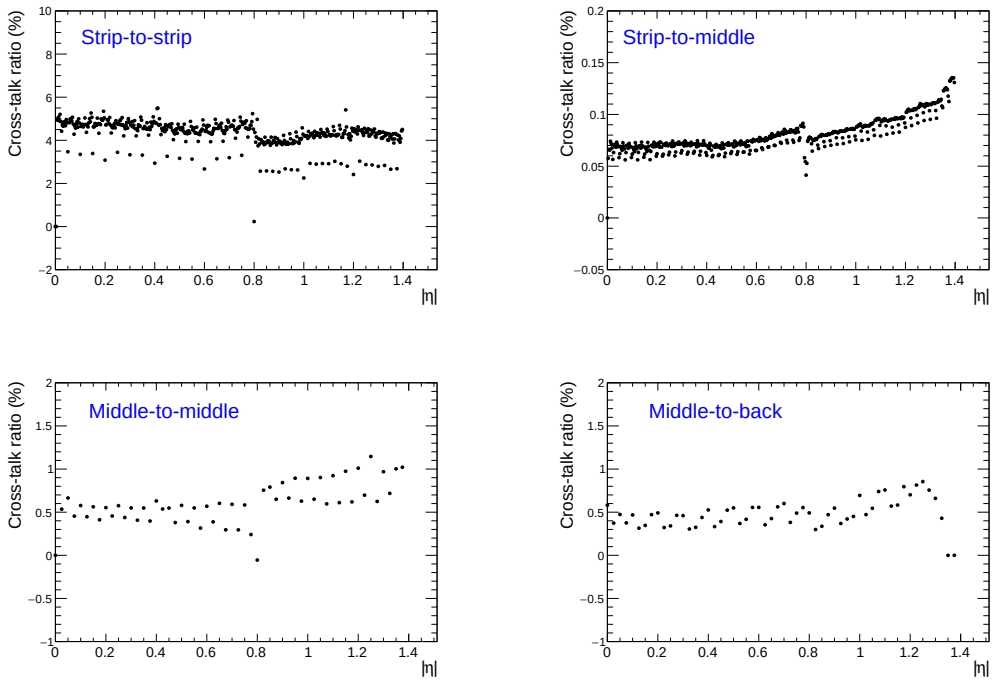


Figure 5.11: Cross-talk magnitude dependence on $|\eta|$. This magnitude represents the ratio of the cross-talk energy divided by the pulsed cell energy. Both energies are derived using the OF method explained in Section 3.5 where calibration OFCs were applied.

from OF method on calibration signals are the standard values used in ATLAS code to simulate the cross-talk effect. However, the calibration shape needs to be corrected from the different paths taken by calibration and ionization signals, as it was discussed previously in Section 3.4. In the following sections, a new technique is proposed to determine cross-talk using physics shapes.

5.3 Cross-talk in physics conditions

In physics runs, cross-talk contributions are sampled like direct signals in the FEBs. The energy of the cross-talk contribution is then derived applying the standard cell calibration to these samples. A precise estimation of the cross-talk effect in data requires to apply the same procedure, thus cross-talk physics shape must be estimated and then sampled to apply the cell calibration. Analogously to direct signals, cross-talk calibration shape must be corrected from different calibration and ionization pulses and injection paths. In the following, the cross-talk shape in calibration runs is called *calibration cross-talk* while the corrected shape is called *physics cross-talk*.

Similarly to ionization signals, physics cross-talk needs to be estimated from dedicated calibration runs, to which corrections are applied. In these runs, a single calibration line receives signals from the calibration board. These exponential pulses are sent to different cells belonging to the same layer following a unique pattern, determined by the cabling of the calorimeter. Individual cell pulsing is not possible, which is a limitation to the physics cross-talk estimation. However, patterns are determined so that calibration pulses are no affected by cross-talk coming from neighbouring cells. Calibration patterns for each calorimeter layer is presented in Figures 5.12. For the front layer, four η points are pulsed. These points are separated from each other by other four η values. This allows the estimation of the cross-talk between the closest and the second neighbouring cells in η in the front layer. Instead, all cells are pulsed for a given η point, which impedes to estimate cross-talk between adjacent strips in ϕ. Concerning the

middle layer, pulsed regions are separated by one η bin, which allow determining cross-talk from closest neighbours. In addition, cells are separated by one cell in ϕ in the same η region, which allows estimating the cross-talk between two adjacent cells in ϕ. The calibration pattern is shifted by one cell in ϕ between cells belonging to two different η regions so that closest neighbours in η are only receiving one cross-talk contribution. Finally, back calibration pattern leaves one cell of separation in η or ϕ between pulsed cells. In order to reduce the electronic noise contribution, each electronic cell is pulsed 200 times

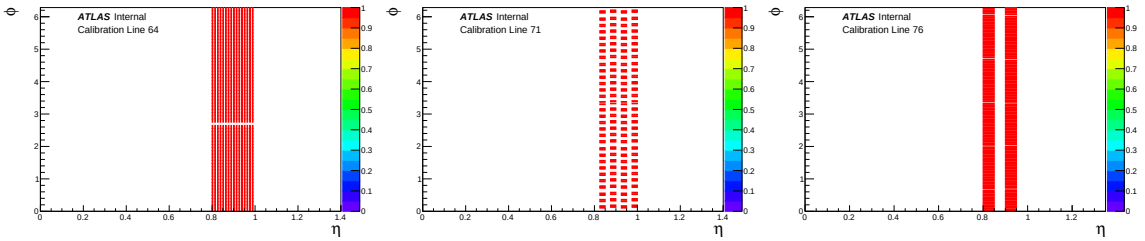


Figure 5.12: Calibration patterns for the front (left), middle (center) and back (right) layers.

and the resulting pulses are averaged to obtain a more accurate calibration shape. This reduces the effect of noise in the determination of the cell signal waveform. 200 is the usual number of pulses used to measure direct signals but, as it will be exposed later, it is not enough for cross-talk.

At the time of taking these runs, some of the cells were not receiving properly the calibration pulses, leading to unreal values that could fake the cross-talk magnitude in those channels. These channels have been identified and are represented in Figure 5.13.

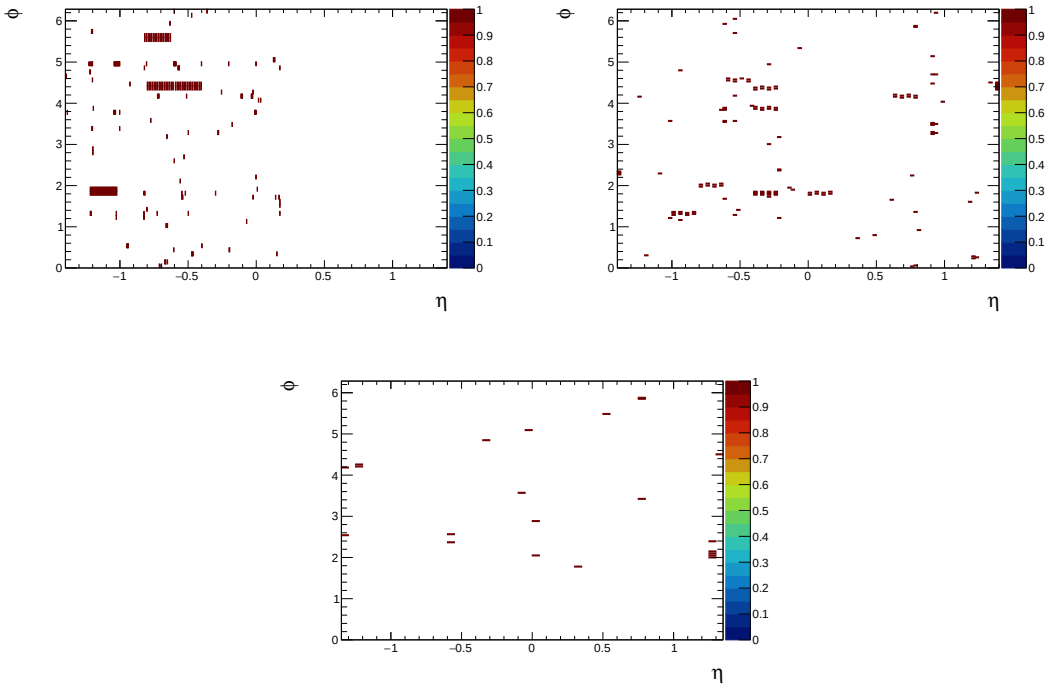


Figure 5.13: Bad channels found in the calibration runs used in the physics cross-talk study.

5.3.1 Physics cross-talk shape determination

Concerning the method to reconstruct the physics cross-talk shape from calibration runs, the Response Transform Method explained in Section 3.4.2 is first tested. It includes all the information about the electronic chain and successfully describes the direct signals obtained during data-taking after pre-amplification and shaping. Physics cross-talk ($g(t)^{\text{phys}}_{\text{xtalk}}$) is the convolution of a certain function $H(t)$ to the calibration shape ($g(t)^{\text{calib}}_{\text{xtalk}}$). This transfer function consisted of two terms, the first correcting from the difference in the initially injected shapes and the second correcting from the difference in the injection path of the calibration and the physics signal. Figure 5.14 illustrates how this method should be applied to cross-talk.

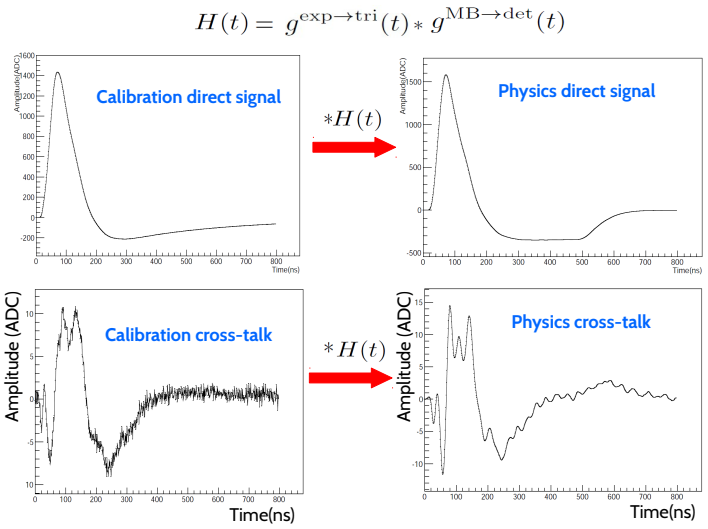


Figure 5.14: Illustration of the application of the RTM method to the cross-talk calibration shape, based on the method used for direct signals.

However, it is not straightforward that this reconstruction is well-adapted for estimating physics cross-talk shape with enough precision. As it can be observed in Figure 5.15, some instabilities appear in the RTM physics shape. Although this periodic oscillating structure is not important in the tails of the shape ($t > 150$ ns), a large fluctuation is observed around 100 ns of the signal. This could affect the determination of the cross-talk energy since this time region is very likely to be sampled and used in the OF processing. This motivated the search for alternative methods to determine the physics cross-talk waveform.

The fluctuations in the RTM cross-talk shape could be the result of the convolution of calibration signals with sinusoidal functions present in the response function (Eq. 3.21). Therefore, other strategies must avoid the convolution of sinusoidal functions. This can be achieved by introducing a technique that does not need the response functions to estimate the cross-talk shape.

$\mathcal{Z}$ transform

In the Laplace domain, convolutions are translated into a multiplication of the calibration waveform with the corresponding response functions. Similarly, deconvolutions are equivalent to the division of the physics waveform by the response functions. Then, convolutions applied in the RTM method can be expressed as Equation 5.6. Assuming that the transfer function $H(t)$ between calibration cross-talk and physics cross-talk is the same as for the direct signal, the physics cross-talk signal can be obtained by deconvoluting the calibration direct signal from the physics signal of the pulsed cell and applying the result to the calibration cross-talk signal in the Laplace domain (Eq 5.7). Then, the physics cross-talk signal can be obtained from the inverse Laplace transform of the resulting function (Eq. 5.8).

$$g^{\text{phys}}(t) = g^{\text{calib}}(t) * H(t) \xrightarrow{\text{Laplace transform}} g^{\text{phys}}(z) = g^{\text{calib}}(z)H(z) \tag{5.6}$$

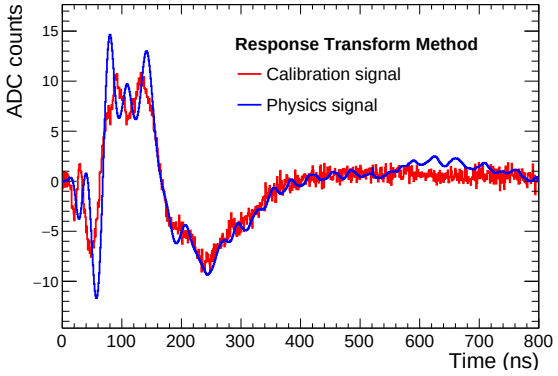


Figure 5.15: Calibration (red) and physics cross-talk signal presented in a middle cell layer of the calibration run 00227022. This cell corresponds to the previous neighbour in η of a pulsed cell of the calibration run. Physics shape is determined using the RTM method.

$$H(z) = \frac{g(z)^{\text{phys}}_{\text{direct}}}{g(z)^{\text{calib}}_{\text{direct}}} = \frac{g(z)^{\text{phys}}_{\text{xtalk}}}{g(z)^{\text{calib}}_{\text{xtalk}}} \longrightarrow g(z)^{\text{phys}}_{\text{xtalk}} = \frac{g(z)^{\text{calib}}_{\text{xtalk}} g(z)^{\text{phys}}_{\text{direct}}}{g(z)^{\text{calib}}_{\text{direct}}} \tag{5.7}$$

$$g^{\text{phys}}_{\text{xtalk}}(t) = \mathcal{L}^{-1}\left(g^{\text{phys}}_{\text{xtalk}}(z)\right) \tag{5.8}$$

This formulation considers continuous calibration and physics shapes. This is not exactly the practical case, since they are sampled in the FEBs during data-taking. In calibration runs, several pulses can be sent into the detector, for which the FEB sampling phase is delayed by steps of 1.04 ns. This allows a well-reconstructed signal which could justify the approach to a continuous shape for calibration and physics. However, the discretization of the signal is considered here in order to restrict the analysis to the actual ATLAS conditions. This discretization requires the application of the discrete equivalent of the Laplace transform, also called $\mathcal{Z}$ *transform*.

The $\mathcal{Z}$ transform [10] is defined as:

$$g(z) = \sum_{n=-\infty}^{\infty} z^{-n} g(t_n) \tag{5.9}$$

where $g(z)$ is the calibration (or physics) waveform in the Laplace domain and $g(t_n)$ is its corresponding waveform value at the time t_n in the time domain. For a reduced number of samples N_{samples}, this expression can be reduced to

$$g(z) = \sum_{n=0}^{N_{\text{samples}}} z^{-n} g(t_n) \tag{5.10}$$

where z is a complex number that can be expressed as $z = re^{i\omega}$. The convergence of this series is ensured unless any of the terms $|z^{-n}g(t_n)|$ goes to infinity.

In order to have a physics signal model independent from the RTM method, a theoretical physics signal shape is considered (from the paper [2]) and adapted for the different cell properties. Considered this, an inverse discrete Laplace transform (or inverse $\mathcal{Z}$ transform) must be performed to get the physics cross-talk signal shape in the time domain. Different techniques allow to perform such inverse transform:

- The matrix method: This method performs the inverse $\mathcal{Z}$ transform by inversing a matrix defined by a linear system of equations as explained a bit further.

- The partial fraction expansion method: it consists of decomposing the physics cross-talk signal in the Laplace domain as sum of terms whose inverse transform is well-known. The passage into the time domain is then done by direct inspection of the expansion terms.
- The χ^2 method: this method uses the same linear system of equations that the matrix method but the inversion is performed by a χ^2 minimization.

Matrix method

Provided that $g(z)^{\text{phys}}_{\text{xtalk}}$ is itself the $\mathcal{Z}$ transform of the physics cross-talk signal in the time domain, its formula is:

$$g(z)^{\text{phys}}_{\text{xtalk}} = \sum_{n=0}^{N-1} g(t_n)^{\text{phys}}_{\text{xtalk}} z^{-n} \tag{5.11}$$

Generating R random points z in the complex convergence disk of this serie [11] provides R relations that can be expressed as a linear system of equations with a coefficients matrix. The inverse $\mathcal{Z}$ transform is then performed by solving this system of equations, that expressed in matricial form is:

$$\overrightarrow{g(z_r)}^{\text{phys}}_{\text{xtalk}} = A^r_i \overrightarrow{g(t_i)}^{\text{phys}}_{\text{xtalk}} \longrightarrow \overrightarrow{g(t_i)}^{\text{phys}}_{\text{xtalk}} = (A^{-1})^i_r \overrightarrow{g(z_r)}^{\text{phys}}_{\text{xtalk}} \tag{5.12}$$

where the matrix A corresponds to:

$$A = \begin{pmatrix} A^0_0 & A^1_0 & A^2_0 & \cdots & A^i_0 \\ A^0_1 & A^1_1 & A^2_1 & \cdots & A^i_1 \\ \cdots & \cdots & \cdots & \cdots & \\ A^0_r & A^1_r & A^2_r & \cdots & A^i_r \end{pmatrix} = \begin{pmatrix} 1 & z_0^{-1} & z_0^{-2} & \cdots & z_0^{-i} \\ 1 & z_1^{-1} & z_1^{-2} & \cdots & z_1^{-i} \\ \cdots & \cdots & \cdots & \cdots & \\ 1 & z_r^{-1} & z_r^{-2} & \cdots & z_r^{-i} \end{pmatrix} \tag{5.13}$$

where $i = 1, ..., N$ and $r = 1....R$ are the respective indices of $\overrightarrow{g(t)}^{\text{phys}}_{\text{xtalk}}$ and $\overrightarrow{g(z)}^{\text{phys}}_{\text{xtalk}}$. The main milestone of this procedure is to estimate the inverse of the matrix A. Matrix inversion is a well know procedure and successfully computed for small dimension matrices. But in this case, where the whole physics signal would present at most 768 samples, $A-$matrix dimension is 768×768. Inversion algorithms usually present numerical problems at this matrix size and the results cannot be trusted. Matrix inversion must be achieved through specialized libraries implementing advanced matrix inversion techniques. The solution of this linear system is first implemented using a method from the Eigen library [12]. This method uses a singular value decomposition (SVD) [13] technique to diagonalize the matrix and estimate directly $g(t_i)^{\text{phys}}_{\text{xtalk}}$. The SVD decomposition consists of rewriting the matrix A as:

$$A = USV^{\dagger} \tag{5.14}$$

where U and V are unitary (or orthogonal) matrices of dimension $R \times R$ and $N \times N$ and S is a real diagonal matrix of dimension $N \times N$. The matrix inversion is then given by:

$$A^{-1} = VS^{-1}U^{\dagger} \tag{5.15}$$

The matrix method physics signal for 768 samples is presented in Fig. 5.16. It can be appreciated that no fluctuations are present in this physics signal, leading to a much smoother waveform. However, even if it seems to converge, this method is quite sensitive to noise. Since A^i_r is a function of z_r^{-i}, if the modulus of z is higher than 1, the last terms of the matrix approach to zero ($\approx z^{-768}$). It implies then that last terms of the signal in time have no impact on the construction of the $\mathcal{Z}$ transform function $g(z)^{\text{phys}}_{\text{xtalk}}$. On the opposite side, first terms of the time signal are determinant for the estimation of $g(z)^{\text{phys}}_{\text{xtalk}}$. Therefore, a small fluctuation in these terms induces a large difference in $g(z)^{\text{phys}}_{\text{xtalk}}$, thus introducing a large error in the inverse $\mathcal{Z}$ transform operation and in the estimation of $g(t)^{\text{phys}}_{\text{xtalk}}$. Indeed, a fluctuation on the first samples of the direct physics signal, the calibration direct signal or the cross-talk calibration signal induces a sizeable variation in $g(z)^{\text{phys}}_{\text{xtalk}}$. When the $\mathcal{Z}$ inversion is performed, this variation is propagated

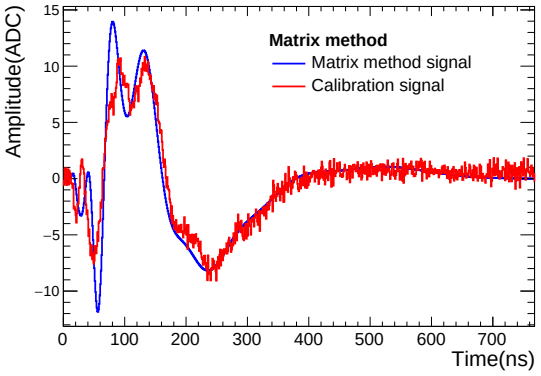


Figure 5.16: $g(t)^{\mathrm{phys}}_{\mathrm{xtalk}}$ after using matrix inversion.

into the $g(t)^{\mathrm{phys}}_{\mathrm{xtalk}}$ shape, possibly enhanced since the matrix A is not necessarily unitary. Figures 5.17 and 5.18 show the matrix method sensitivity to noise fluctuations. This study is performed by adding a random noise contribution to different samples of one of the input signals: either the direct calibration signals; the direct physics signal or the calibration cross-talk. This noise is randomly generated following a gaussian function centered at zero for different values of the standard deviation. This σ scan begins with σ =0.00 (nominal shapes without noise) and increases up to 1.25 in steps of 0.25. It is noticed that the matrix method is mainly affected by noise fluctuations on samples of the direct signals, either calibration or physics, even in cases where the noise fluctuation is restricted to small values ($\sigma = 0.25$). In addition, large fluctuations occur when the affected samples by noise are the first samples of the signal ($\leq$20), as expected.

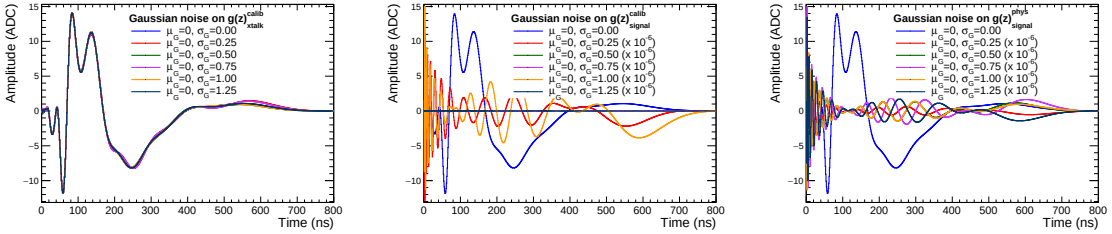


Figure 5.17: $g(t)^{\mathrm{phys}}_{\mathrm{xtalk}}$ estimated using the matrix inversion method. Left plot presents the obtained signal when a gaussian noise centered at zero and with varying σ is added to all terms of $g(t)^{\mathrm{calib}}_{\mathrm{xtalk}}$. Center and right plots present instead the obtained physics cross-talk shape when the gaussian noise is applied to $g(z)^{\mathrm{calib}}_{\mathrm{direct}}$ or $g(z)^{\mathrm{phys}}_{\mathrm{direct}}$, respectively.

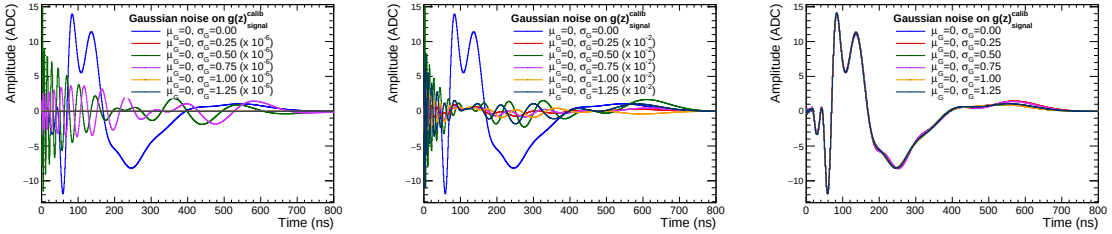


Figure 5.18: $g(t)^{\mathrm{phys}}_{\mathrm{xtalk}}$ estimated using the matrix inversion method. Left, center and right plots show the obtained signal when a gaussian noise centered at zero and with varying σ is added to the first 20 terms, 20^{th}-50^{th} terms and 50^{th}-100^{th} of $g(t)^{\mathrm{calib}}_{\mathrm{signal}}$, respectively. It can be observed that large fluctuations are obtained when the first samples are affected by noise, even by a small contribution.

The partial fraction expansion method

$g(z)^{\text{phys}}_{\text{xtalk}}$ is decomposed into a sum of fractions [14]. Assuming that the physics cross-talk in the Laplace domain can be expressed as a fraction of a numerator and a denominator, as shown in Equation 5.7, the decomposition is performed by factorizing the denominator as simple terms $(1 - d_i z^{-1})$. The d_i are the complex roots of the denominator polynomial. These terms possess a very well known partner in the time domain, and therefore the inverse $\mathcal{Z}$ transform can be performed by direct inspection of each term.

Calculations are done in a complex space, ensuring by the fundamental algebra theorem that the denominator of degree N has the same number of complex roots. Assuming a denominator of degree N and a numerator of degree M, at least three terms can be defined in the sum expansion:

- One term with a polynomial of degree M - N. It only appears in the case that the denominator has a lower degree N than the numerator M.
- One term concerning the roots of the denominator with multiplicity equal to one ($1 - d_i z^{-1}$).
- A last term concerning the roots of the denominator with higher multiplicities ($(1 - d_i z^{-1})^p$).

The partial expansion formula is the following:

$$g(z)^{\text{phys}}_{\text{xtalk}} = \sum_{r=0}^{M-N} A_r z^{-r} \quad + \quad \sum_{i=1, i\neq j}^{N-S} \frac{B_i}{(1 - d_i z^{-1})} \quad + \quad \sum_{j=1}^{S} \sum_{p=1}^{P} \frac{C_p}{(1 - d_j z^{-1})^p} \tag{5.16}$$

Solving this partial expansion method consists of finding the coefficients A_r, B_i and C_p. These coefficients can be estimated by the following formulas:

$$\sum_{r=0}^{M-N} A_r z_k^{-r} = g(z)^{\text{phys}}_{\text{xtalk}} \quad - \quad \sum_{i=1, i\neq j}^{N-S} \frac{B_i}{(1 - d_i z_k^{-1})} \quad - \quad \sum_{j=1}^{S} \sum_{p=1}^{P} \frac{C_p}{(1 - d_j z_k^{-1})^p} = Q(z_k) \tag{5.17}$$

where:

$$A_r = \begin{pmatrix} 1 & z_1^{-1} & z_1^{-2} & \cdots & z_1^{-r} \\ 1 & z_2^{-1} & z_2^{-2} & \cdots & z_2^{-r} \\ \cdots & \cdots & \cdots & \cdots & \\ 1 & z_k^{-1} & z_k^{-2} & \cdots & z_k^{-r} \end{pmatrix}^{-1} Q(z_k) \tag{5.18}$$

$$B_i = \frac{g(z)^{\text{calib}}_{\text{xtalk}} g(z)^{\text{phys}}_{\text{signal}}}{b_0 \prod_{k=0, k\neq i}^{N-S} (1 - d_k d_i^{-1})} \tag{5.19}$$

$$C_p = \frac{1}{(P-p)!(-d_j)^{P-p}} \left(\frac{d^{P-p}}{dz^{P-p}} [(1 - d_j z)^P g(z)^{\text{phys}}_{\text{xtalk}}] \right)_{w=d_j^{-1}} \tag{5.20}$$

It needs to be noticed that a matrix inversion is also used in this method, as in the matrix method, to estimate the coefficients A_r. However, the reduced number of terms in the expansion M-N could lead to a more accurate result that in the matrix method. In the $\mathcal{Z}$ transform formalism, two of these factors have direct images in the time domain:

$$\delta(t - n) \longrightarrow \mathcal{Z}(\delta(t - n)) = \sum_{i=-\infty}^{\infty} \delta(t - n)_i z^{-i} = z^{-n} \tag{5.21}$$

$$\mathcal{H}(t) \longrightarrow \mathcal{Z}(\mathcal{H}(t)) = \sum_{i=-\infty}^{\infty} \mathcal{H}(t)_i z^{-i} = \sum_{i=0}^{\infty} z^{-i} = \frac{1}{1 - \frac{1}{z}} = \frac{z}{z - 1} \tag{5.22}$$

$$a^t \mathcal{H}(t) \longrightarrow \mathcal{Z}(a^t \mathcal{H}(t)) = \sum_{i=-\infty}^{\infty} (a^t \mathcal{H}(t))_i z^{-i} = \sum_{i=0}^{\infty} a^i z^{-i} = \sum_{i=0}^{\infty} (a z^{-1})^i = \frac{1}{1 - \frac{a}{z}} = \frac{z}{z - a} \tag{5.23}$$

where $\mathcal{H}(t)$ is the Heaviside function defined as $\mathcal{H}(x < 0) = 0$ and $\mathcal{H}(x \geq 0) = 1$. It has been found that despite it requires a simpler technique for performing the matrix inversion, the expansion of the physics

cross-talk into these three terms requires more computing power than the matrix method for classifying the multiplicities of the roots and estimating A_r, B_i and C_p. In addition, the Equation 5.23 is a geometric series and thus, the conclusion is valid only if $|a| < 1$. This condition is not ensured for the denominator roots d_i for any kind of crosstalk shape. This process hasn't converged by now.

χ^2 method

The inverse $\mathcal{Z}$ transform is performed here by minimizing a χ^2 function built as:

$$\chi^2(a_0, a_1, ..., a_n) = \sum_{i=0}^{R} \left| \frac{\left(\sum_{n=0}^{N-1} a_n z_i^{-n} - \frac{g(z_i)^{\text{calib}}_{\text{xtalk}} g(z_i)^{\text{phys}}_{\text{direct}}}{g(z_i)^{\text{calib}}_{\text{direct}}} \right)^2}{\sigma^2} \right| \tag{5.24}$$

where another set of R complex points are generated (z_i) and where the noise σ corresponds to the combined noise of $y(z) = g(z_i)^{\text{calib}}_{\text{xtalk}} g(z_i)^{\text{phys}}_{\text{direct}} / g(z_i)^{\text{calib}}_{\text{direct}}$, which is the sum in quadrature of the noise in the Laplace domain of the separate signals:

$$\sigma = \frac{g(z_i)^{\text{calib}}_{\text{xtalk}} g(z_i)^{\text{phys}}_{\text{direct}}}{g(z_i)^{\text{calib}}_{\text{direct}}} \sqrt{\left(\frac{\Delta g(z_i)^{\text{calib}}_{\text{direct}}}{g(z_i)^{\text{calib}}_{\text{direct}}} \right)^2 + \left(\frac{\Delta g(z_i)^{\text{phys}}_{\text{direct}}}{g(z_i)^{\text{phys}}_{\text{direct}}} \right)^2 + \left(\frac{\Delta g(z_i)^{\text{phys}}_{\text{xtalk}}}{g(z_i)^{\text{phys}}_{\text{xtalk}}} \right)^2} \tag{5.25}$$

$$\Delta g\left(z_i\right) = \sqrt{\left(\sum_{n=0}^{N-1} \left(\sigma_{\text{pedestal}} z_i^{-n} \right)^2 \right)} \tag{5.26}$$

with a_n are the N physics cross-talk samples, σ_{pedestal} the root mean square of the electronic cell noise This method is carried out with ROOT and the minimization is performed using TMinuit and its method MIGRAD. Nor MINOS and other methods to enhance the error estimation accuracy are used. For a high quantity of values, MIGRAD usually fails to build a positive-definite error matrix (correlation matrix) and therefore, the final output of the minimization cannot be fully trusted. For the first stage of the method test, the binning of the initial signals is reduced to 128 samples (each bin correspond to 6 samples). The convergence then is ensured for a first test. This method seems to provide a finite result and be less sensitive to noise than the matrix method. However, it needs an initial set of parameters as input to MIGRAD. The signals output from the RTM and the matrix method are used as well as the calibration signal. The output of the χ^2 method is shown in Figures 5.19 and 5.20. It can be observed that this method does not resolve the problem about the signal peak when RTM physics shape is put as initial shape. Furthermore, it is noticed that the output depends on the input shape.

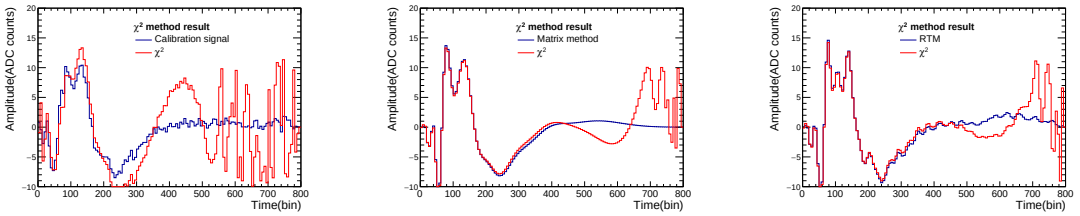


Figure 5.19: χ^2 method output using an initial shape: left figure, calibration signal; center figure, using the physics cross-talk output of the matrix method; and right figure, using the physics shape from applying RTM method.

This means that MIGRAD did not find the global minimum. The main reason is also related to the problem found in the matrix method. MIGRAD must minimize and estimate a_n samples whose coefficients decrease exponentially with n and, therefore, they lose weight in the minimization. In Figure 5.21, scans of the χ^2 have been performed fixing all a_n to their fixed and varying the value at each iteration for a given a_i. One can observe that χ^2 shape is not stable for a_i with $i \geq 5 - 10$ and therefore the global minimum is no longer a relative minimum of the function but it is associated with the interval where

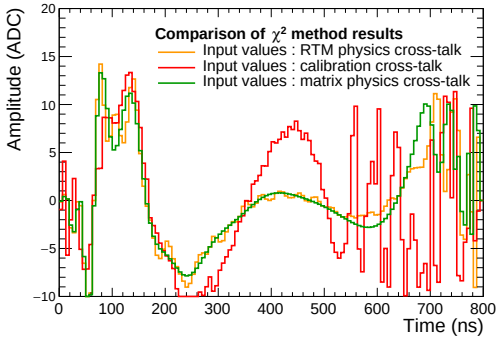
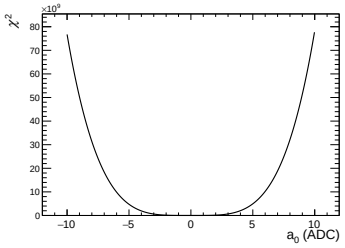
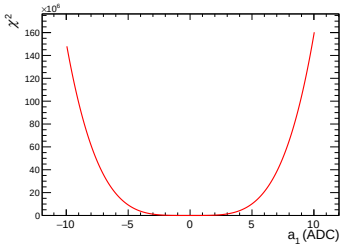


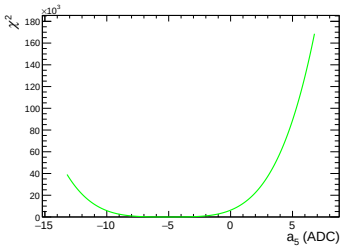
Figure 5.20: Comparison of χ^2 method outputs depending on the input signal



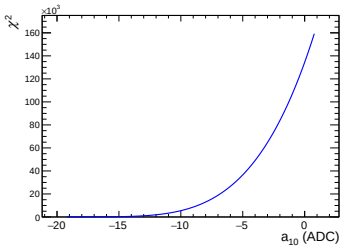
(a) χ^2 for different a_0 values



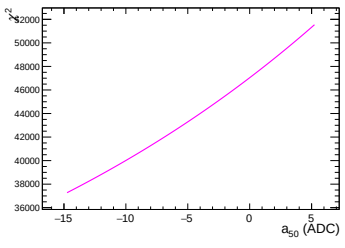
(b) χ^2 for different a_1 values



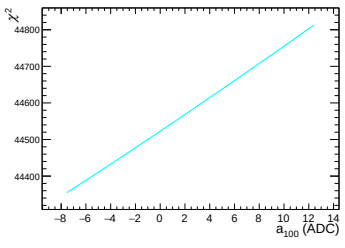
(c) χ^2 for different a_5 values



(d) χ^2 for different a_{10} values



(e) χ^2 for different a_{50} values



(f) χ^2 for different a_{100} values

Figure 5.21: χ^2 as a function of a given coefficient a_i. All coefficients a_n from Eq. 5.24 are fixed to their initial value except the coefficient stated in each subfigure caption.

the χ^2 is evaluated. However, this method gives a finite signal in a sizeable time. Further searches can be performed to refine this method in the future since I could not fully explore this option given the available time scale.

All these three methods are revealed to be inadequate to estimate physics cross-talk shape, in most cases being quite time-consuming. Giving its better performance in time and in direct signal reconstruction, the RTM method is used in the following for estimating the cross-talk signal.

RTM dependence on the number of averaged samples

LAr calorimeter direct physics signal is reconstructed using calibration runs that provide an average shape for each channel obtained from 200 individual calibration signals. This is sufficient because those signals are large compared to the noise. In the case of cross-talk signals, the ratio energy/noise is much higher (of the order of 50-100 times larger) and could require a larger averaging procedure to extract physics signals with a limited noise contribution. Dedicated runs have been requested with 2000 averaged pulses to study this possible issue. Figure 5.22 presents the comparison of the cross-talk shape obtained by applying the RTM method to a calibration signal averaged 200 times or 2000 times. It can be clearly noticed that the physics signal averaging over 2000 pulses present a smoother waveform than the one averaged over 200 pulses.

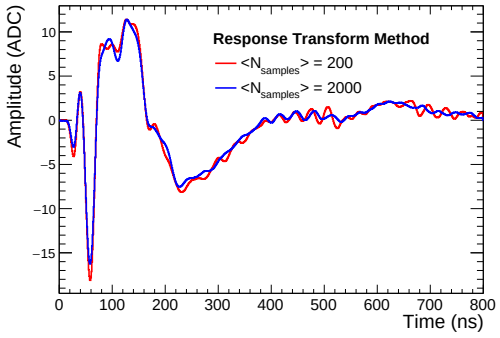


Figure 5.22: Comparison of the cross-talk signal in the same electronic cell if signals are averaged over 200 or 2000 samples.

More samples were requested for measuring cross-talk effect using 2000 samples. However, these runs could not be completely used because some problems occurred during the calibration campaign on which they were taken. Results presented in the following sections are then derived using calibration runs averaged over 200 pulses but this study will be performed soon.

5.3.2 Cross-talk estimation in the LAr barrel

The RTM cross-talk and direct signal shapes are used to estimate their respective energies the standard cell calibration procedure (Equation 3.13). Optimal filtering is applied on the first four samples of both shapes, separated by 25 ns each other. The calibration constants, OF coefficients and ramps are taken from a weekly calibration run performed on 6$^{\text{th}}$ December 2016.

- LArOFCPhys_00314179_EB-EMB*_4samples_Picked.root: calibration file used to retrieve the physics OF coefficients.
- LArParams_DefaultExtraction_00314179_EB-EMB*.root: it contains the cell constants necessary to perform the RTM method, e.g. τ_{calib}, f_{step}, etc (Section 3.4.2).
- LArRamp_00314180_EB-EMB*_StripsXtalkCorr_OFC.root: it contains the DAC and ADC values necessary to determine the ramps coefficients which are determined by fitting the DAC vs ADC curves with a second order polynomial, as outlined in Section 3.6.1.
- LArPedAutoCorr_00314172_EB-EMB*.root: it contains the average value of pedestals for all cells and their fluctuation size. This data is used in the study of the long distance cross-talk.

The values presented in Tables 3.2 and 3.3 are used for the constants $F_{DAC\to\mu A}$ and $F_{\mu A\to \mathrm{MeV}}$.

The cross-talk is evaluated for both halves of the LAr barrel except for the barrel-end ($1.4 < |\eta| < 1.475$). This region only presents two layers with a coarser granularity than the rest of the barrel. Front layer only presents three cells in η and the middle layer, one.

Cross-talk evaluation

The cross-talk magnitude from a pulsed cell into a non-pulsed cell is estimated as the ratio of the energy of both cells.

$$R_{\mathrm{cross-talk}} = \frac{E_{\mathrm{cross-talk}}}{E_{\mathrm{cell}}} \tag{5.27}$$

In the case that one cell is receiving cross-talk distributions from more than one pulsed cell, the cross-talk ratio associated with each pulsed cell is:

$$R_{\mathrm{cross-talk}} = \frac{E_{\mathrm{cross-talk}}}{E_{\mathrm{cell},1} + E_{\mathrm{cell},2}} \tag{5.28}$$

It is then necessary to first determine the neighbours to a given pulsed cell that can be affected by the cross-talk. This is performed using the current calorimeter description included in the ATLAS reconstruction code, which allows retrieving the neighbouring cells of a desired channel. This description provides same layer cells included in a 2D square of size $\Delta N_\eta \times \Delta N_\phi = 3 \times 3$ around the channel, other layer channels that are in front or behind and cells belonging to the tile calorimeter at the same η and ϕ than the channel. In the case of front layer cells, second neighbours are also included. Diagonal neighbours from the same layer ($\Delta N_\eta \times \Delta N_\phi = \pm 1 \times \pm 1$) and cells belonging to the barrel presampler and the tile calorimeter are removed. Figure 5.23 illustrates the ensemble of neighbour cells for which cross-talk contribution is estimated.

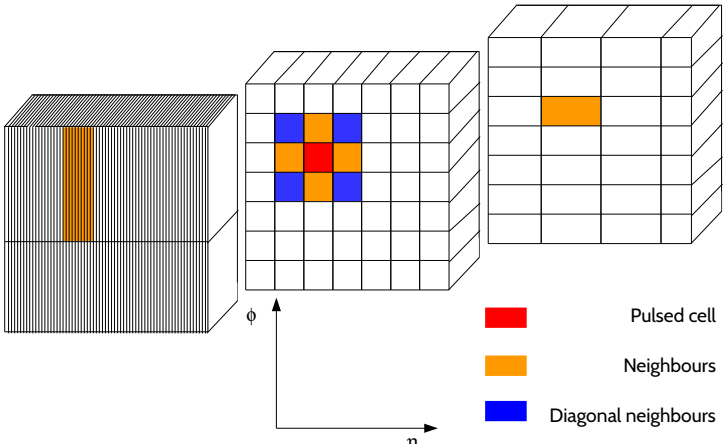


Figure 5.23: Illustration of the neighbours (orange) to a pulsed cell (red) assumed to receive a sizeable cross-talk contribution. Diagonal neighbours (blue) are not considered to receive cross-talk in this study.

The average contributions of physics cross-talk together with their dispersion (RMS) are presented on Table 5.2. These values are compared to the ones estimated using the OF method on calibration signals, presented in Section 5.2. Furthermore, these values can be compared with the under-peak to peak and peak-to-peak values presented in Table 5.1.

Cross-talk when pulsed cells are in the front layer: Calibration boards pulsing the front layer do not allow evaluating contributions between adjacent cells in ϕ. Therefore, the cross-talk is evaluated between neighbour strips in η. Second neighbours contributions are also estimated. Figure 5.24 presents the estimated cross-talk values between strip-to-strip, second neighbours and strip-to-middle cells. The relative energy transfer between two adjacent strips represents a 4.8% on average, decreasing between the electrode A and electrode B from 5.5% to 4.5%. The energy leakage

	Physics cross-talk results		Calibration cross-talk values	
Type	Mean	RMS	Mean	RMS
Strip-to-strip	4.78 %	1.20 %	4.31 %	0.65 %
Strip-to-middle	0.197%	0.177%	0.080%	0.017%
Second neighbours	0.373 %	0.205 %	0.4% (0.5%)	–
Middle-to-strip	0.102%	0.089 %	0.080%	0.017%
Middle-to-middle (neighbours in η)	0.315%	0.454%	0.60 %	0.24 %
Middle-to-middle (neighbours in ϕ)	-0.538%	0.409%	–	
Middle-to-back	0.804 %	0.699 %	0.48 %	0.17%
Back-to-middle	0.846%	0.465%	0.48 %	0.17%
Back-to-back (neighbours in η)	-0.721%	0.309%	–	
Back-to-back (neighbours in ϕ)	-0.389%	0.122%	–	

Table 5.2: Cross-talk mean values in the LAr barrel using physics cross-talk signals and calibration cross-talk signals (currently used in ATLAS simulation code Section 5.2). Physics cross-talk is estimated by averaging the contributions from all cells in the calorimeter. Both average magnitudes are estimated for all possible short-distance contributions. The RMS accounts for the cross-talk ratios dispersion around the central value. Calibration cross-talk values for middle-to-strip and back-to-middle contributions are respectively equated to the strip-to-middle and middle-to-back values, given that it is the procedure followed in ATLAS simulation code. For second neighbours contribution estimated using calibration runs, the magnitude between parentheses represents the contributions magnitude at $|\eta| > 1.1825$.

from front to middle layer cells presents an average value of 0.28% in the electrode A and 0.09% in the electrode B. Second neighbours cross-talk presents an average contribution of 0.37%, increasing with η from 0.25% to 0.6%.

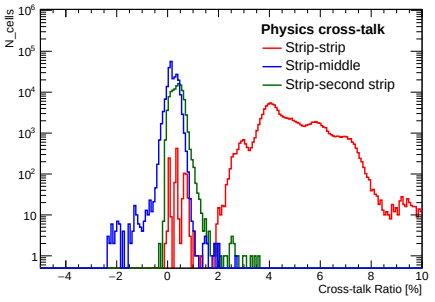


Figure 5.24: Distributions of the cross-talk ratios between pulsed cells in front layer and cells in the front, middle and back layers.

It can be observed in Figure 5.25 that the η dependence of cross-talk ratios between cells in the front layer are similar to current ATLAS cross-talk values (Fig. 5.11), while cross-talk ratios between front layer and middle layer as a function of η are different than the one observed in Figure 5.11. This divergence can be explained by the differences on how cross-talk ratios are estimated, either on calibration signals or using physics signals, and possibly on the differences on how ADC to MeV conversion is performed. However, this effect has not been studied yet.

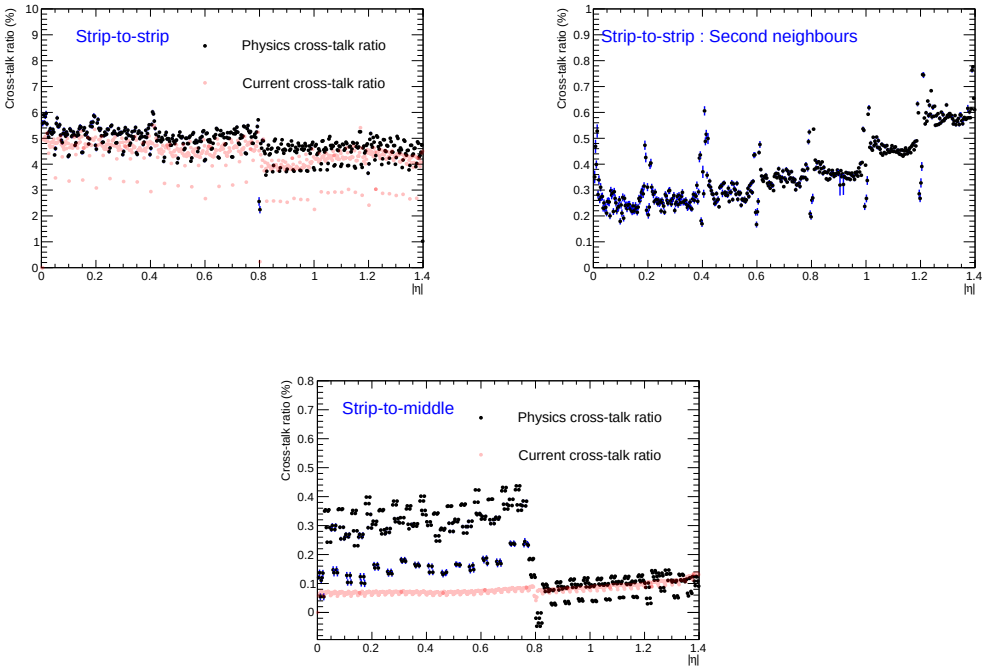


Figure 5.25: Cross-talk magnitude as a function of η with pulsed cells in front layer. Therefore, the strip-to-strip contribution corresponds to the cross-talk between adjacent cells in η. In addition, the cross-talk between strips separated by two cells in η is presented. Strip-to-middle contribution is evaluated between a pulsed strip and its corresponding middle cells. Distributions with calibration cross-talk results are overlaid.

Cross-talk when pulsed cells are in the middle layer: Pulsed cells in the middle cell (Figs. 5.26) present cross-talk values much lower than cells in the front layer . For cross-talk between cells in the middle layer, the middle layer calibration runs allow to determine contributions between neighbouring cells in ϕ. The average contribution is found to be 0.102%, but it can be divided between the positive 0.32% average contribution between η neighbours and the -0.54% cross-talk between ϕ neighbours. This difference is due to the fact that between η neighbours, some capacitive cross-talk may happen, inducing a peak in the signal in the first samples of the cross-talk shape that translate into positive energies. On the opposite, ϕ neighbours can only present pure inductive cross-talk, which tends to present negative energies when optimal filtering is applied. The cross-talk between front cells and pulsed middle cells presents an average relative magnitude of 0.05% and the cross-talk between middle and back cells, 0.95%.

Concerning the dependence in η of cross-talk magnitude, neighbouring cells in η present an increasing magnitude with larger η, with a remarkable step at $|\eta| \sim 0.8$. In the case of cross-talk between adjacent cells in ϕ present a decreasing magnitude at larger η except at $|\eta| \sim 0.8$, where the cross-talk increases. The reason for this behaviour has not been understood yet. For middle-to-front cells cross-talk, resistive contribution shows an inverse behaviour than the one observed in Figure 5.25.right. The reason is the $R_1^{\text{front}}/R_1^{\text{middle}}$ ramps (Section 3.6.1) ratio, which appears at calculating the cross-talk ratio. In the case of pulsed front cells cross-talk to middle cells, the ramps ratio that appears is $R_1^{\text{middle}}/R_1^{\text{front}}$. Finally, the cross-talk between the middle and back cells present a stable contribution on the electrode A while an increasing slope with η is found on electrode B. Similarly to middle-to-front cells cross-talk, the explanation of this slope (that is not present in the current simulation values as can be seen in Figure 5.27) is the difference in ramps between the middle and back layers in the electrode B. Nevertheless, the contribution in electrode A is found to be 0.4%, which is in agreement with the current values.

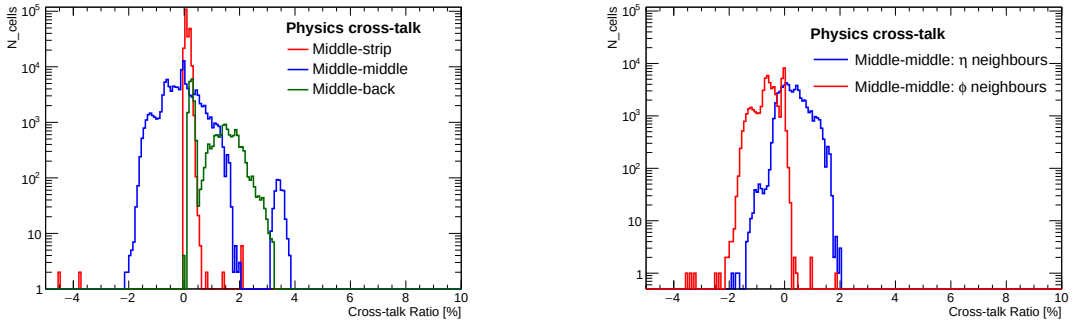


Figure 5.26: Left: distributions of the cross-talk ratios between pulsed cells in the middle layer and cells in the front, middle and back layers. Right: distribution of the cross-talk ratios between pulsed cells in the middle layer and their adjacent cells in η and ϕ.

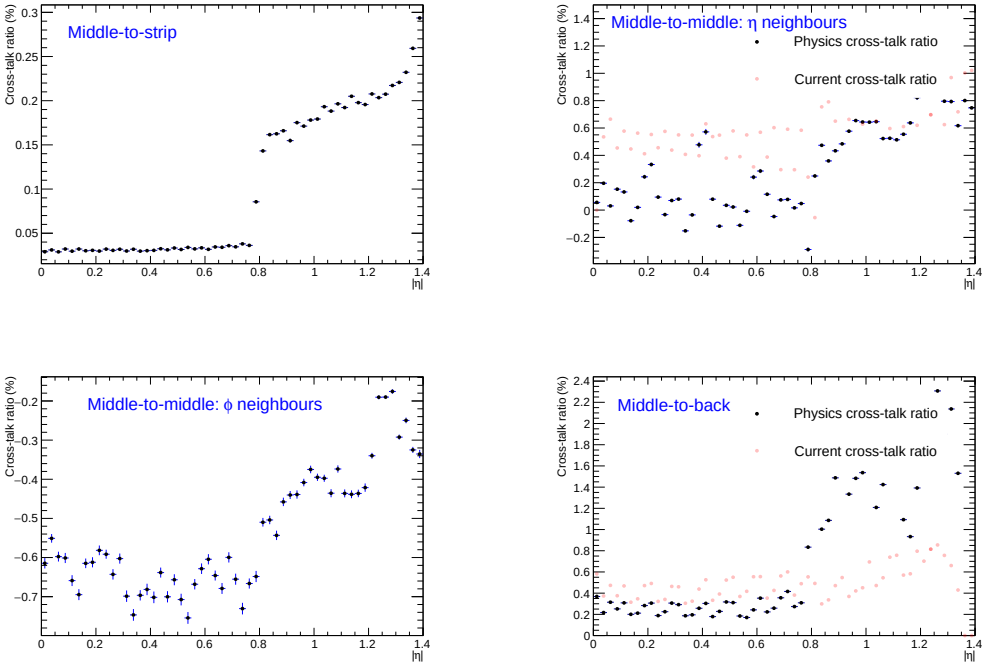


Figure 5.27: Cross-talk magnitude as a function of η with pulsed cells in the middle layer. Distributions between the same layer have been divided into the cross-talk contribution between adjacent cells in ϕ, with $\Delta\eta = 0$ and adjacent cells in η, with $\Delta\phi = 0$. Distributions with calibration cross-talk results are overlaid.

Cross-talk when pulsed cells are in the back layer: Similarly to the middle layer, calibration runs allow to separate the η and ϕ neighbours. η neighbours present a contribution of -0.72% on average, while ϕ neighbours present a mean value of -0.39%. The back to middle layer cross-talk presents the inverse behaviour than the middle to back cross-talk, as expected from the relation between both layer ramps. However, the electrode A presents in this time an increasing contribution at larger η that is not present in the opposite case. This dependence could be due to the increasing depth of the back layer.

A schema of the these cross-talk values is presented in Fig. 5.30. In general, the found values for cross-

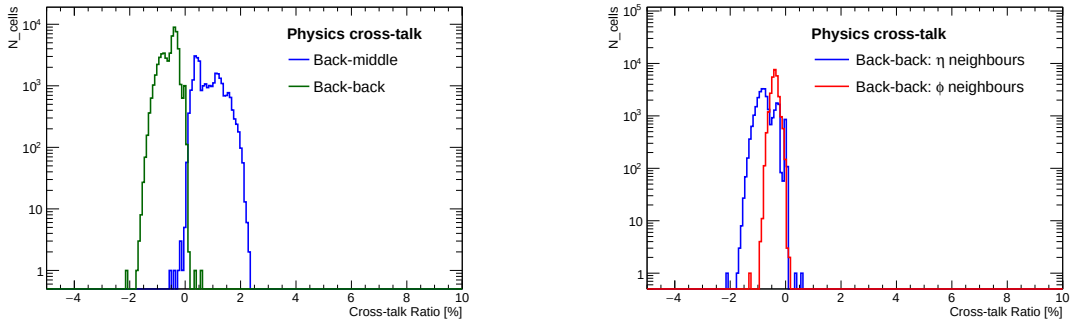


Figure 5.28: Left: distributions of the cross-talk ratios between pulsed cells in the back layer and cells in the front, middle and back layers. Right: distribution of the cross-talk ratios between pulsed cells in the back layer and their adjacent cells in η and ϕ.

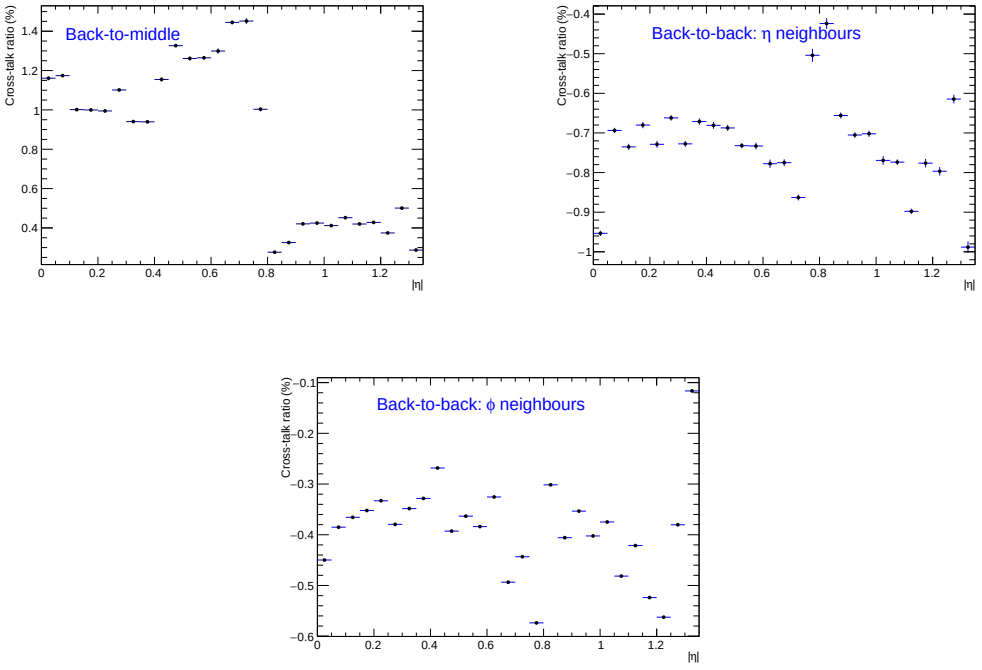


Figure 5.29: Cross-talk magnitude as a function of η with pulsed cells in the back layer. Distributions between the same layer have been divided into the cross-talk contribution between adjacent cells in ϕ, with $\Delta\eta = 0$ and adjacent cells in η, with $\Delta\phi = 0$.

talk differ significantly than the ones presented in Section 5.2. This is possibly due to the use of the standard calibration to estimate energies or to a possible dependence of the cross-talk on the number of samples used in the OF processing and the phase used to sample the cross-talk. This phase is invariably zero, but starting the sampling at another point could induce a different cross-talk magnitude.

Cross-talk dependence on the number of OF samples

Physics cross-talk ratios have also been estimated using 5 samples with the OF methods (5 samples were used during Run I data taking). Table 5.3 present the average magnitude of cross-talks. The obtained values are less scattered than 4 samples, which translates into smaller RMS. In general, 5 or 4 sample values differ as expected, but it is particularly remarkable the difference between front cells cross-talk,

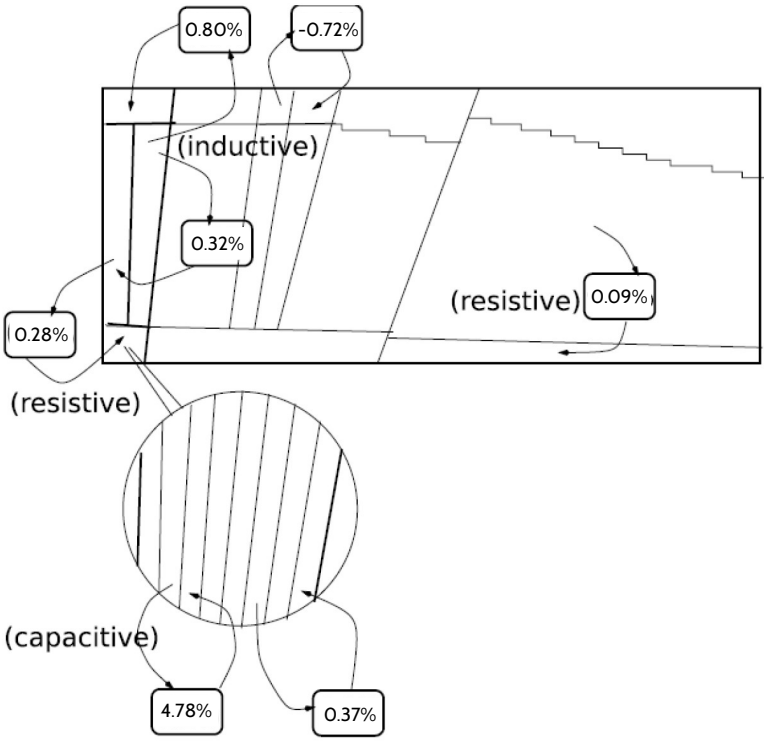


Figure 5.30: Illustration of the obtained cross-talk values obtained on physics signals. Cross-talk and signal energies are estimated using the full calibration chain. OF method uses 4 samples of the signal.

whose mean magnitude is reduced from 4.78 % to 3.69%. The η distributions of cross-talk are presented in Figures 5.31. If these figures are compared with their corresponding 4 samples case (Figs. 5.25, 5.27 and 5.29), it can be observed that calculating the cross-talk ratios using 4 samples or 5 does not affect significantly the cross-talk behaviour along η. The most remarkable difference comes from neighbours in ϕ, where there is a steep discontinuity at $|\eta| \sim 1.2$ not seen in the 4 samples case. A schema of these cross-talk values using 5 samples is presented in Fig. 5.32.

Cross-talk dependence on the sampling phase

The dependence of the cross-talk magnitude on the optimal filtering coefficients used to estimate the energy in ADC implies a dependence of the initial sampling phase. Signals are sampled every 25 ns, but the initial sample can be chosen among the first 24 samples separated 1.04 ns in time. In addition, the OFCs depend on the initial sample since different points of the signal are used to get the peak. While this phase dependence should not be very important on the direct signal, physics cross-talk shapes are usually less smooth and OFCs are not optimized for them, which implies a more marked energy dependence on the sampling phase. The evaluation of this effect is performed as follows:

- Scan on the shape peak vs sampling phase is only performed for cross-talk shapes while the direct signal energy in ADC is kept constant. OFCs (a_i^{phase}) for cross-talk are retrieved from LArOFCPhys_00314179_EB-EMBA_4samples.root to correctly determine the signal peak.
- The phase dependence can be highlighted just studying the evolution of $R_{\text{cross-talk}}$ in ADC counts. Contributions are then estimated as the ratio of the energy in ADC for cross-talk and direct signal issued after OF processing (calibration constants, e.g. ramps, are not applied).

$$R_{\text{cross-talk}}(\text{phase}) = \frac{\sum_{i=1}^{4} a_i^{\text{phase}} g_{\text{xtalk}}^{\text{phys}}(t = (i-1) * 25 + \text{phase})}{\sum_{i=1}^{4} a_i g_{\text{direct}}^{\text{phys}}(t = (i-1) * 25)} \tag{5.29}$$

Phase dependence is evaluated for a capacitive cross-talk signal (between two strips) and inductive

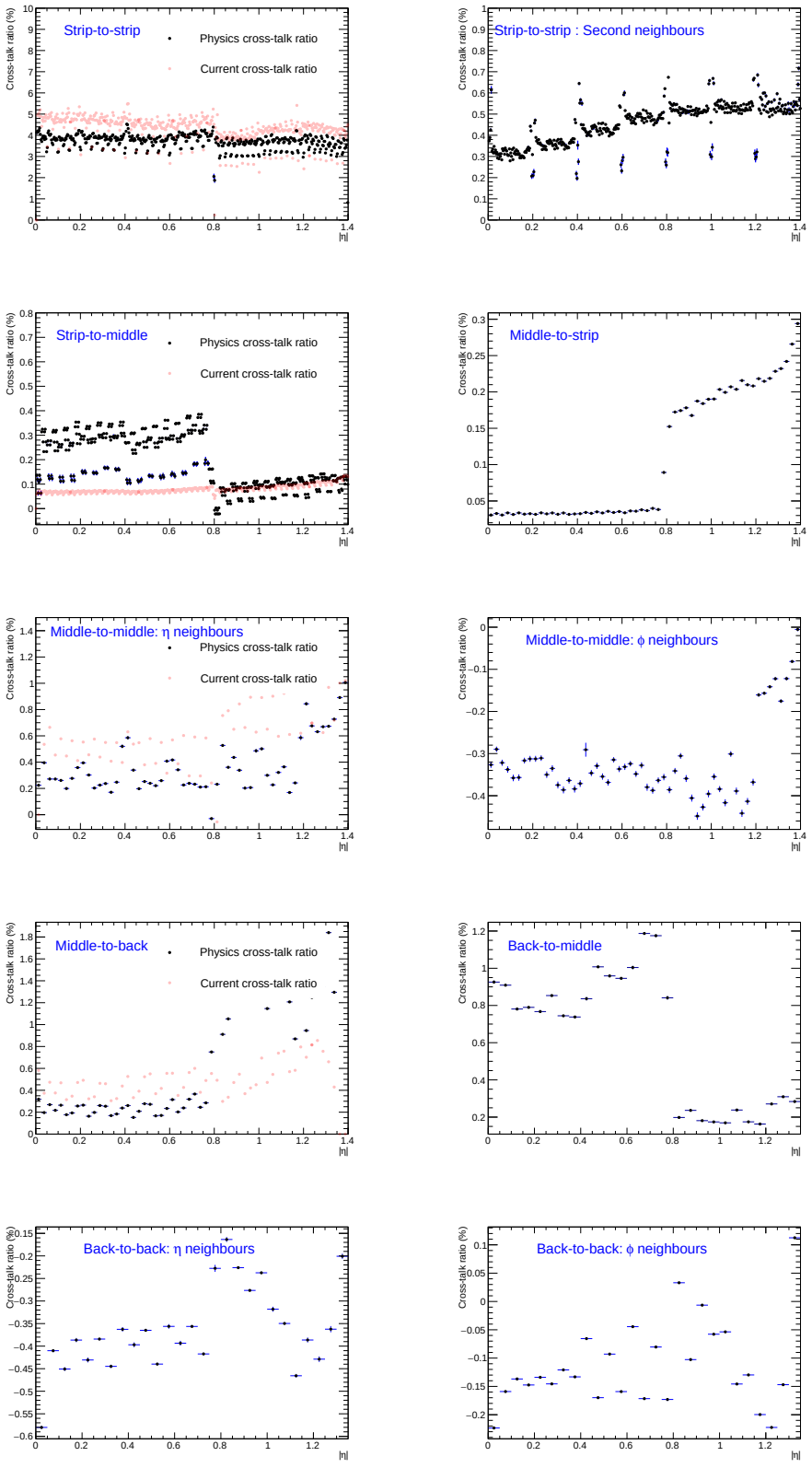


Figure 5.31: Cross-talk magnitude as a function of η between cells in all layers. Distributions for the second sampling have been divided into the cross-talk contribution between adjacent cells in ϕ, with $\Delta\eta = 0$ and adjacent cells in η, with $\Delta\phi = 0$. In the case of the front layer, there is no possibility of evaluating contributions between adjacent cells in ϕ. However, the cross-talk between strips separated by two cells in η is presented. Distributions with calibration cross-talk results are overlaid.

	Physics cross-talk results		Calibration cross-talk values	
Type	Mean	RMS	Mean	RMS
Strip-to-strip	3.69 %	0.77 %	4.31 %	0.65 %
Strip-to-middle	0.182%	0.156%	0.080%	0.017%
Second neighbours	0.453 %	0.143 %	0.4% (0.5%)	–
Middle-to-strip	0.108%	0.093 %	0.080%	0.017%
Middle-to-middle (neighbours in η)	0.359%	0.296%	0.60 %	0.24 %
Middle-to-middle (neighbours in ϕ)	-0.325%	0.244%	–	
Middle-to-back	0.702 %	0.588 %	0.48 %	0.17%
Back-to-middle	0.624%	0.399%	0.48 %	0.17%
Back-to-back (neighbours in η)	-0.363%	0.168%	–	
Back-to-back (neighbours in ϕ)	-0.114%	0.095%	–	

Table 5.3: Cross-talk mean values in the LAr barrel using physics cross-talk signals using 5 samples in the OF step. Physics cross-talk is estimated by averaging the contributions from all cells in the calorimeter. Both average magnitudes are estimated for all possible short-distance contributions. The RMS accounts for the cross-talk ratios dispersion around the central value. Physics contributions are compared to calibration cross-talk signals. Calibration cross-talk values for middle-to-strip and back-to-middle contributions are respectively equated to the strip-to-middle and middle-to-back values. For second neighbours contribution estimated using calibration runs, the magnitude between parentheses represents the contributions magnitude at $|\eta| > 1.1825$.

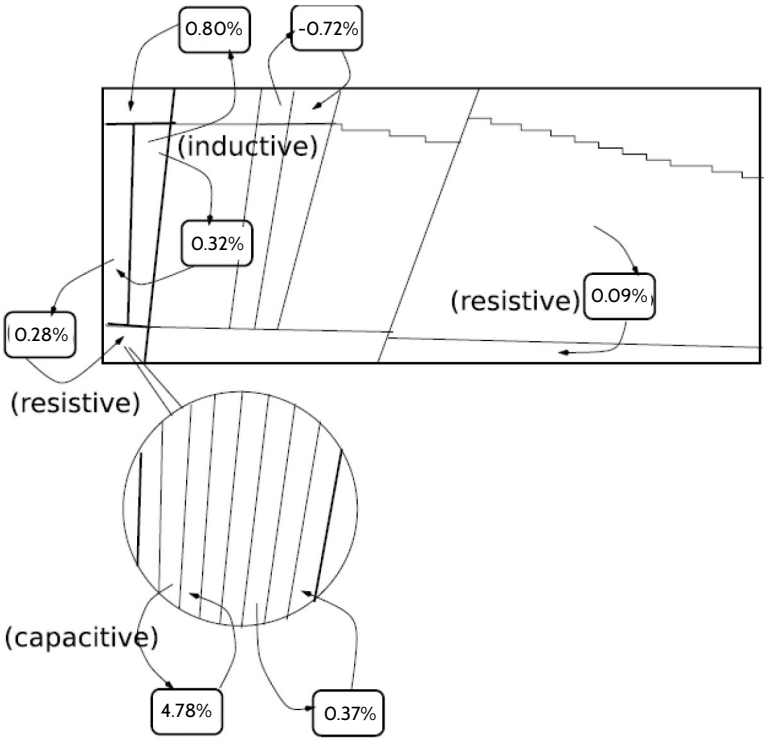


Figure 5.32: Illustration of the obtained cross-talk values obtained on physics signals. Cross-talk and signal energies are estimated using the full calibration chain. OF method uses 5 samples of the signal.

signals (between two middle cells and two back cells). Figures 5.33 present this dependence on the sampling phase. It can be observed that the choice of different sets of OFCs imply large variations of $R_{\mathrm{cross-talk}}$ magnitude, e.g. of 40% between strips, 43% between middle cells or 100% between back cells.

Long distance cross-talk vs short distance cross-talk

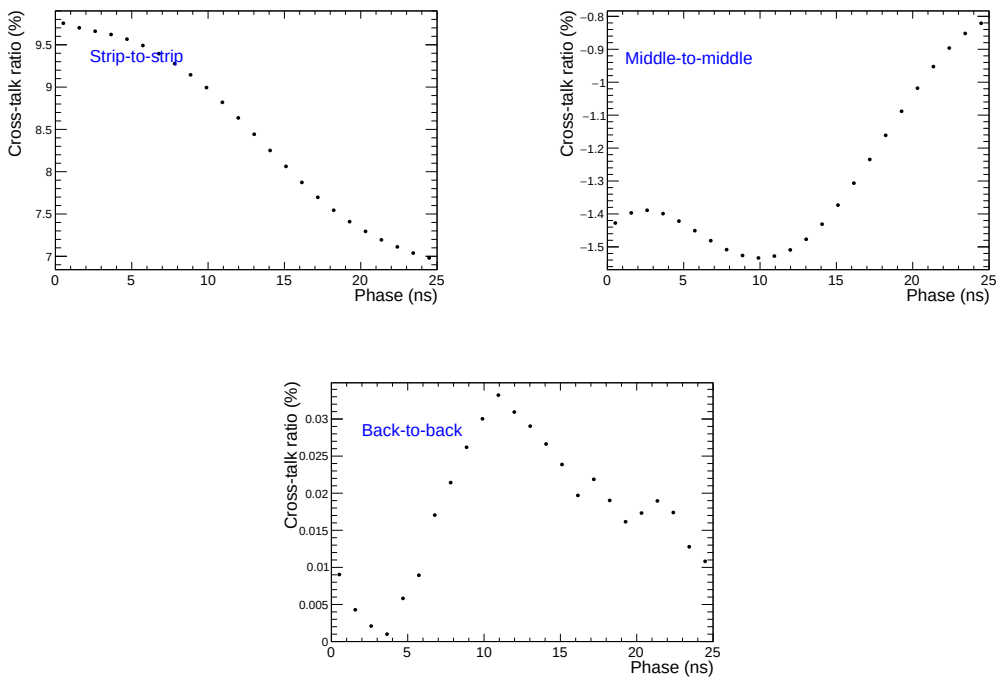


Figure 5.33: Sampling phase dependence of cross-talk magnitude.

As explained previously, long distance cross-talk is a charge leakage present between geometrically separated cells in the calorimeter. This cross-talk tends to present a smaller contribution than the short distance one. It is interesting to determine if the long distance contribution is a small contribution that in the following can be neglected. Thus, a comparison between long distance and short-distance cross-talk has been performed.

In the case of inductive cross-talk, there is no cell-to-cell correspondance that can be identified. However, calibration boards pulse a given region of the calorimeter which induces long distance effects in other regions of the calorimeter. On the other hand, resistive long distance cross-talk is registered between pulsed middle layer cells and the surrounding cells of the first layer adjacent to the front cells of the middle cell. A cell-to-cell cross-talk relation can be identified in this case. Then, the algorithm work as follows:

- All pulsed cells inside the calibration run are identified and their corresponding η and ϕ coordinates are stored.

- Cells are identified as neighbours of a pulsed cell or not using the calorimeter parametrization inside the ATLAS reconstruction code. After this step, a loop is performed on the collection of non-pulsed cells to determine if a cell is receiving energy from cross-talk or not. For doing so, it is requested to present a significant energy above its noise fluctuation, i.e. $E_{\mathrm{cell}} > 5 * \sigma_{\mathrm{cell}}^{\mathrm{noise}}$. This cell noise is determined from the pedestal runs. In addition, another cut is applied so that the energy of the cell must be larger in absolute value than $50\mathrm{MeV}/\sqrt{N_{\mathrm{pulses}}}$, with the denominator being the stochastic noise reduction factor due to the average of N_{pulses} calibration pulses per cell.

- Pulsed cells energies are not very different. This is due to the fact a single calibration line pulses with the same DAC value cells belonging to the same layer and to four close η values, thus the different calibration constants are quite similar. Assuming that long distance cells are receiving long distance cross-talk from a single pulsed cell, the corresponding cross-talk ratio is estimated by dividing the non-pulsed cell energy by the average energy of the pulsed cells: $R_{\mathrm{xtalk}} = E_{cell}^{\mathrm{non-pulsed}}/\langle E_{cells}^{\mathrm{pulsed}}\rangle$.

	Physics cross-talk results
Type	Long distance cross-talk results
Strip-to-back	0.0003% $\pm$ 0.0012%
Middle-to-middle	-0.0011% $\pm$ 0.00080%
Middle-to-back	-0.0003% $\pm$ 0.0040%
Back-to-medium	0.0005% $\pm$ 0.0011%
Back-to-back	-0.0027% $\pm$ 0.0013%

Table 5.4: Long distance contributions in the LAr barrel using 4 samples. The uncertainties values correspond to the RMS of their corresponding ratios distribution.

- Finally, calibration pulses may also induce cross-talk at the feedthrough level when they are injected into the calorimeter. It can be observed from Figure 3.14 that cross-talk could be induced in the middle layer, between $1.2 < |\eta| < 1.4$. This region is then blinded since these long distance contributions are not present during data-taking.

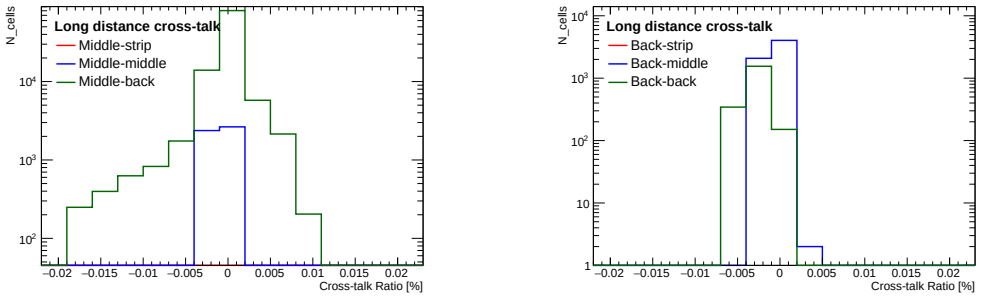


Figure 5.34: Long distance contribution derived on physics cross-talk shapes.

Figures 5.34 cross-talk present the long distance cross-talk magnitude for the middle and back layers of the barrel. No significant long distance cross-talk is found with pulsed front layer cells so they are not included in this study. Long distance cross-talk present very small contributions with regard to the short distance. It is a contribution that can then be neglected.

5.4 Shower shape corrections

These new cross-talk ratios are tested on the ATLAS simulation code. As previously outlined, the cross-talk distorts the shower shapes variables used in the electron and photon identification. Currently, simulations of these variables differ from data. 2015 differences in the shower shape variables between data and MC can be observed in Figs. 5.35 and 5.36, taken from [15]. The source of these differences are mainly the cross-talk and the modeling of the dead material crossed by the interacting particle. However, the relative magnitude associated with cross-talk or the dead material is not known. Corrections are applied by smearing and applying global shifts to the Monte-Carlo variables in order to fit the data distributions. In this section, smearing is not treated. Instead, shifts needed to be applied are studied, also called *fudge-factors*.

Simulations using physics cross-talk values presented in Section 5.3.2 are performed in order to evaluate the improvement on shower shapes description. These simulated samples correspond to events of $Z \rightarrow ee$. Pileup effects are not taken into account and detector effects are simulated using Geant 4. Shower shapes distributions can be compared (Figs. 5.37 and 5.38) if using the current cross-talk values (Table 5.1) and the new cross-talk values (Table 5.2). It can be observed that the f_1, E_{ratio} and R_ϕ are

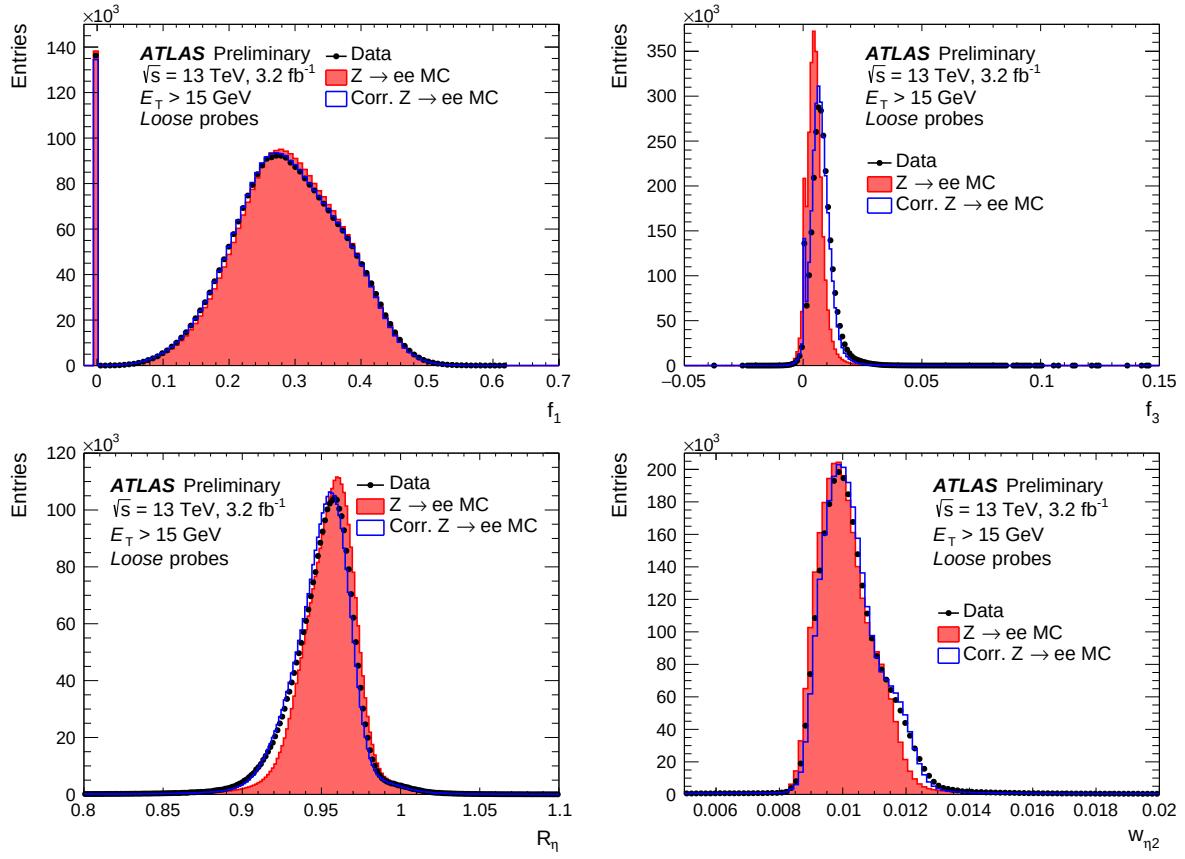


Figure 5.35: Distributions of variables (f_1, f_3, w_{η_2} and R_η) used in the electron identification. They are measured using a tag-and-probe method on $Z \to ee$ samples for probes passing the electron loose identification [15]. Corrected MC stand for the MC distributions corrected using the fudge factors and the widths determined in the study.

shifted using the physics cross-talk towards the data distributions, in the case of R_ϕ representing a 50 % of the current shift,as it can be noticed by comparing Figs. 5.37 and 5.38 in Figs. 5.35 and 5.36. On the other hand, description of variables concerning the second and third sampling is worsened, as it can be observed from the distributions of f_3, R_η and R_{had}.

There is a correlation between cross-talk values and the simulation of the dead material upstream the calorimeter. To provide a definitive conclusion on the influence of physics cross-talk in the shower shapes need to revisit this correlation, which is left for a future work.

References

[1] M. Aharrouche et al. "Energy linearity and resolution of the ATLAS electromagnetic barrel calorimeter in an electron test-beam". In: *Nuclear Instruments and Methods in Physics Research Section A: Accelerators, Spectrometers, Detectors and Associated Equipment* 568.2 (2006), pp. 601–623. ISSN: 0168-9002. DOI: https://doi.org/10.1016/j.nima.2006.07.053. URL: http://www.sciencedirect.com/science/article/pii/S0168900206013222.

[2] Jacques Colas et al. "Crosstalk in the ATLAS Electromagnetic Calorimeter". In: (1999).

[3] Bernard Aubert et al. "Development and construction of large size signal electrodes for the ATLAS electromagnetic calorimeter". In: *Nucl. Instrum. Meth.* A539 (2005), pp. 558–594. DOI: 10.1016/j.nima.2004.11.005.

[4] F. Hubaut et al. "Test Beam Measurement of the Crosstalk in the EM Barrel Module 0". In: (2000).

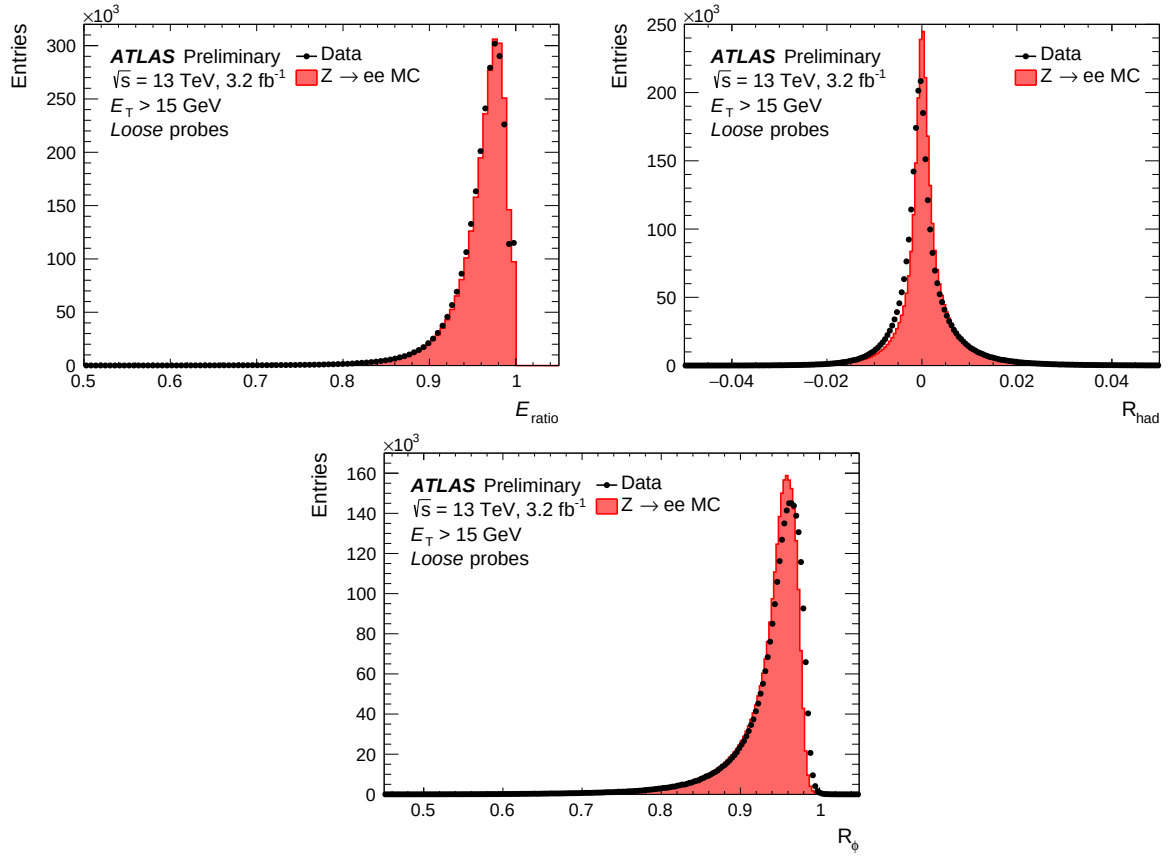


Figure 5.36: Distributions of variables (E_{ratio}, R_{had} and R_{ϕ}) used in the electron identification. They are measured using a tag-and-probe method on $Z \rightarrow ee$ samples for probes passing the electron loose identification [15].

[5] F. Hubaut. "Crosstalk Measurements in the EM Barrel Module 0 from 99', May 00' and July 00' Beam Tests". In: (2000).

[6] Pascal Pralavorio and D. Sauvage. "Review of the crosstalk in the module 0 of the Electromagnetic Endcap Calorimeter". In: (2001).

[7] Fabrice Hubaut et al. "Crosstalk in production modules of the Electromagnetic Endcap Calorimeter". In: (2003).

[8] J Labbe and R Ishmukhametov. *Crosstalk Measurements in the Electromagnetic Calorimeter during ATLAS Final Installation*. Tech. rep. ATL-LARG-INT-2009-004. ATL-COM-LARG-2008-012. Geneva: CERN, Dec. 2008. URL: https://cds.cern.ch/record/1143373.

[9] Guillaume Unal. *Private communication*.

[10] Alan V. Oppenheim and Ronald W. Schafer. *Discrete-Time Signal Processing*. 3rd. Upper Saddle River, NJ, USA: Prentice Hall Press, 2009. ISBN: 0131988425, 9780131988422.

[11] F. Merrikh-Bayat. "Two Methods for Numerical Inversion of the Z-Transform". In: *ArXiv e-prints* (Sept. 2014). arXiv: 1409.1727 [math.NA].

[12] Gaël Guennebaud, Benoît Jacob, et al. *Eigen v3*. http://eigen.tuxfamily.org. 2010.

[13] Andreas Hocker and Vakhtang Kartvelishvili. "SVD approach to data unfolding". In: *Nucl. Instrum. Meth.* A372 (1996), pp. 469–481. DOI: 10.1016/0168-9002(95)01478-0. arXiv: hep-ph/9509307 [hep-ph].

[14] J.F. Mahoney and B.D. Sivazlian. "Partial fractions expansion: a review of computational methodology and efficiency". In: *Journal of Computational and Applied Mathematics* 9.3 (1983), pp. 247–269. ISSN: 0377-0427. DOI: http://dx.doi.org/10.1016/0377-0427(83)90018-3. URL: http://www.sciencedirect.com/science/article/pii/0377042783900183.

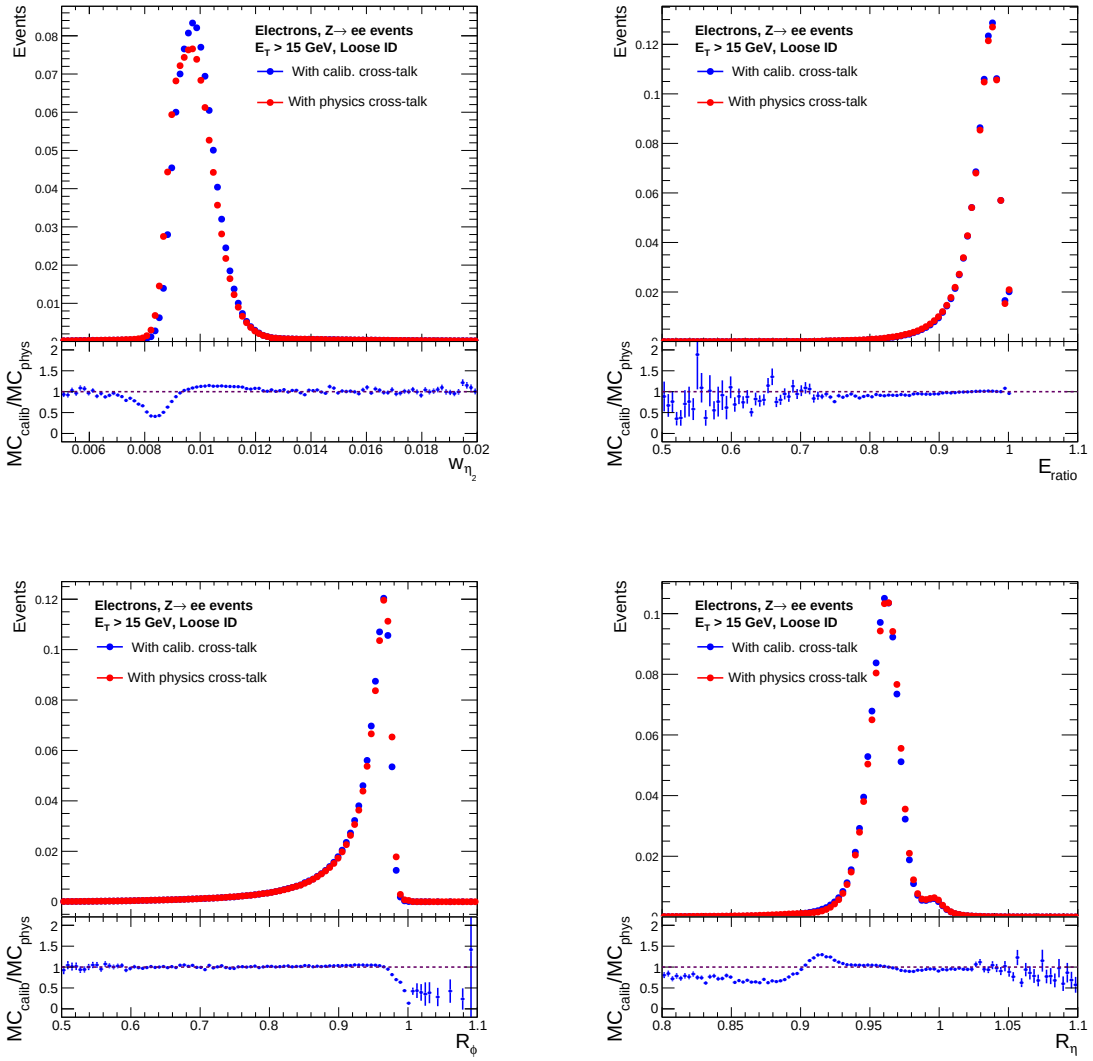


Figure 5.37: Distributions of variables (E_{ratio}, w_{η_2}, R_η and R_ϕ) used in the electron identification. Measured on $Z \rightarrow ee$ events simulated without any pileup effects. Electrons are required to pass loose identification and to present $E_T > 15$ GeV and $|\eta| < 1.475$. Calibration cross-talk stands for the current cross-talk values introduced in the simulation (Table 5.1) and the physics cross-talk estimated using 4 samples (Table 5.2).

[15] *Electron efficiency measurements with the ATLAS detector using the 2015 LHC proton-proton collision data*. Tech. rep. ATLAS-CONF-2016-024. Geneva: CERN, June 2016. URL: http://cds.cern.ch/record/2157687.

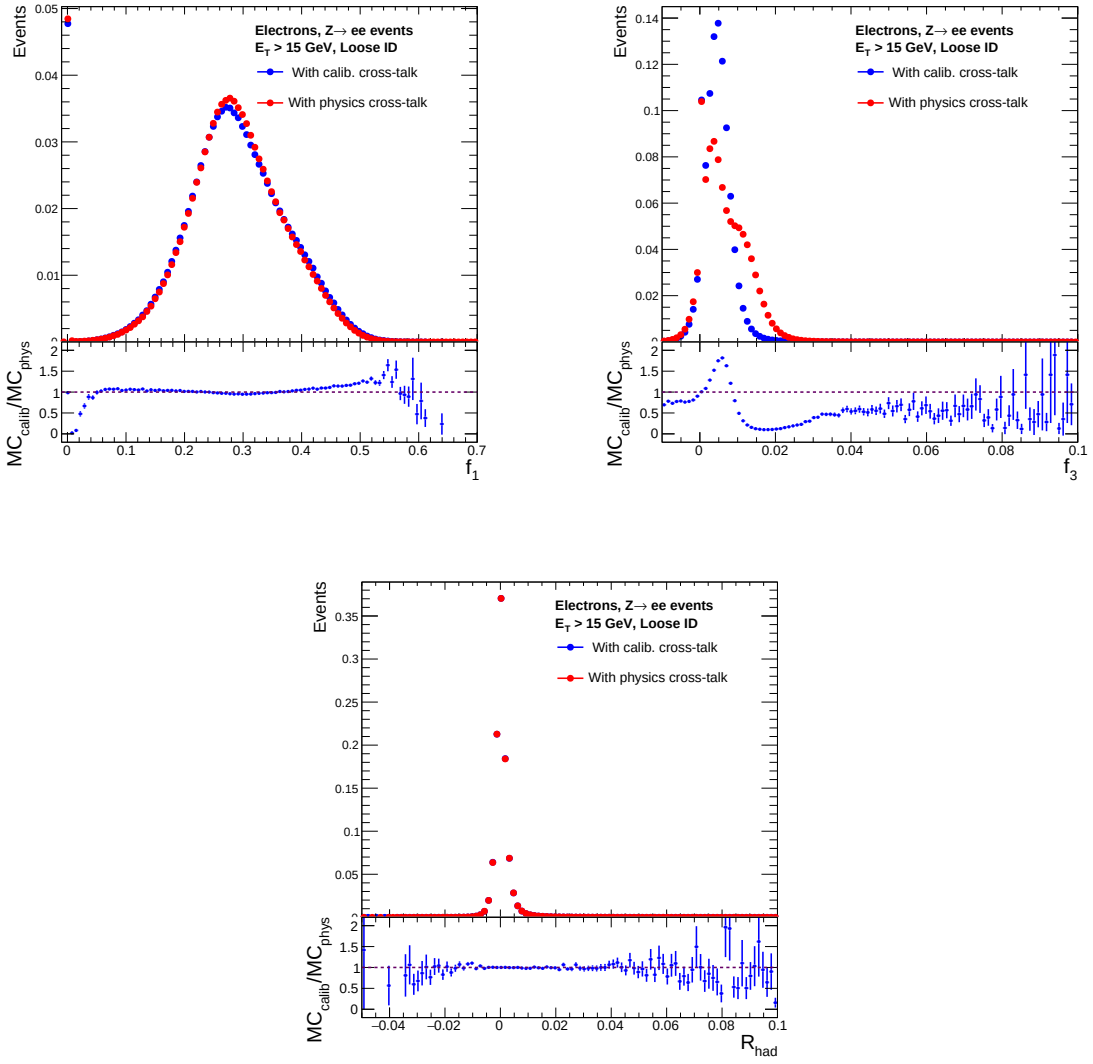


Figure 5.38: Distributions of variables (R_{had}, f_1 and f_3) used in the electron identification. Measured on $Z \rightarrow ee$ events simulated without any pileup effects. Electrons are required to pass loose identification and to present $E_T > 15$ GeV and $|\eta| < 1.475$. Calibration cross-talk stands for the current cross-talk values introduced in the simulation (Table 5.1) and the physics cross-talk estimated using 4 samples (Table 5.2).

Missing transverse momentum reconstruction

Contents

6.1 Jets reconstruction and calibration . . . 146
6.1.1 Pileup jets suppression in ATLAS . . . 148
6.2 Muon reconstruction and identification . . . 151
6.3 $E_{\mathrm{T}}^{\mathrm{miss}}$ reconstruction . . . 153
6.4 $E_{\mathrm{T}}^{\mathrm{miss}}$ reconstruction in $h \to \gamma\gamma$ events . . . 158
6.4.1 Diphoton vertex identification . . . 158
6.4.2 $E_{\mathrm{T}}^{\mathrm{miss}}$ performance in $h \to \gamma\gamma$ . . . 160
6.4.3 $E_{\mathrm{T}}^{\mathrm{miss}}$ magnitude reconstruction . . . 161
6.4.4 $E_{\mathrm{T}}^{\mathrm{miss}}$ pileup resilience . . . 162
6.4.5 $E_{\mathrm{T}}^{\mathrm{miss}}$ direction . . . 163

Momentum conservation in the transverse plane to the beam axis imposes that the sum of momentum vectors of all measured objects equals zero ($\sum \vec{p}_{\mathrm{T}}^{\,\mathrm{initial}} = \sum \vec{p}_{\mathrm{T}}^{\,\mathrm{final}} = \vec{0}$). An imbalance in this sum is known as missing transverse momentum and, by convention, it is also called missing transverse energy ($E_{\mathrm{T}}^{\mathrm{miss}}$). Since only particles that have been measured can be used to estimate the magnitude of the imbalance, the $E_{\mathrm{T}}^{\mathrm{miss}}$ expected at truth level is the sum of the p_{T} of invisible particles and the particles falling outside the fiducial region, or the negative sum of the visible particles p_{T}:

$$\sum \overrightarrow{p_{\mathrm{T}}^{\mathrm{initial}}} = \sum \overrightarrow{p_{\mathrm{T}}^{\mathrm{final}}} = \sum \overrightarrow{p_{\mathrm{T}}^{\mathrm{visible}}} + \sum \overrightarrow{p_{\mathrm{T}}^{\mathrm{out-of-detector}}} + \sum \overrightarrow{p_{\mathrm{T}}^{\mathrm{invisible}}} = \sum \overrightarrow{p_{\mathrm{T}}^{\mathrm{visible}}} + \overrightarrow{E_{\mathrm{T}}^{\mathrm{miss}}} \approx \vec{0} \quad (6.1)$$

This imbalance might be indicative of mismeasurements of the reconstructed objects such as miscalibration of the electron, photon or jet energies or a bias in their position measurements but also the result of unmeasured contributions from particles produced out of the detector fiducial region. Another possible contribution comes from pileup or relevant particles wrongly removed by the selection cuts. However, it might also mean that at least one dark matter particle leaving no trace in the detector is produced. For instance, neutrinos are one of these particles and is the only one in the Standard Model. Beyond the Standard Model instead, several particles could present this feature, such as stable neutralinos in supersymmetric theories or dark matter particles. This is the reason why $E_{\mathrm{T}}^{\mathrm{miss}}$ is used in many analyses searching for new physics and, in the search performed during this thesis, it becomes one of the key variables to detect DM production in association to a Higgs boson.

To correctly reconstruct $E_{\mathrm{T}}^{\mathrm{miss}}$, all physics objects must be reconstructed, correctly identified and calibrated to their respective scales. In addition, in order to reduce the bias from low-p_{T} particles not passing the reconstruction cuts, the transverse energy deposits in the different subdetectors not associated with any high energy objects are evaluated and summed in the $E_{\mathrm{T}}^{\mathrm{miss}}$ calculation. This strategy improves the $E_{\mathrm{T}}^{\mathrm{miss}}$ reconstruction but also increase contributions from pileup events.

Photon and electron reconstruction and identification have already been explained in Chapter 4. Section 6.2 and Section 6.1 present the reconstruction and calibration of muons and jets. Section 6.3 outlines the main algorithms used inside ATLAS to reconstruct $E_{\mathrm{T}}^{\mathrm{miss}}$. The general recommendations issued by the $E_{\mathrm{T}}^{\mathrm{miss}}$ performance group of ATLAS, however, must be taken carefully in the case of $h \to \gamma\gamma$ topologies, mainly due to the determination of the primary vertex of the event as presented in Section 6.4.1.

A major contribution of this Ph.D was to study the specific $E_{\mathrm{T}}^{\mathrm{miss}}$ performance for $h \to \gamma\gamma$ events, as explained in Section 6.4.

6.1 Jets reconstruction and calibration

Jets are reconstructed using an anti-k_t algorithm [1]. The inputs of this algorithm are either energy deposits in the calorimeter or track jets, which are then separated and ensembled in *calorimeter jets* or *track jets* respectively. A similar treatment is done for truth information from Monte Carlo models by using stable truth particles to build to *truth jets*. Truth jets are built from generated stable truth particles ($\tau_{\mathrm{life}} > 30ps$), excluding truth muons and truth neutrinos. The main parameter of this algorithm is the distance between the considered jet components $d_{i,j}$ and the beam distance $d_{i,B}$, defined as:

$$\begin{aligned} d_{i,j} &= \min\left(\frac{1}{p_{Ti}^2}, \frac{1}{p_{Tj}^2}\right)\frac{\Delta_{ij}^2}{R^2} \\ d_{i,B} &= \frac{1}{p_{Ti}^2} \end{aligned} \tag{6.2}$$

where $p_{T,i}$ is the transverse momentum of the i^{th} component, $\Delta_{ij}^2 = (y_i - y_j)^2 + (\phi_i - \phi_j)^2$ is the angular distance between components i and j and R is the radius parameter of the algorithm, which can be set to 0.4, 0.6 or 1.0. In $h \to \gamma\gamma + E_{\mathrm{T}}^{\mathrm{miss}}$ searches, jets with $R = 0.4$ are used and all the following results only concern that case. When two possible constituents of the jets are a hard particle i (high-p_{T}) and a soft particle j (low-p_{T}), the distance between these two particles is determined by the hard particle p_{T}, resulting in a small distance R. In the case of two soft particles, the distance is usually larger and depends on their p_T. Therefore, soft-particles tend to cluster around the hard particle, such that jets are formed. One of the main advantages of the anti-k_t algorithm is that the shape of the jet is not affected by soft-radiation. All particles such that $d_{i,j} < R$ are introduced in the jet cluster while others not. This feature leads to circular clusters representing the jets. However, the shape may vary depending on the number of hard particles found inside the radius R. In that case, soft-particles cluster around two separate jets. Clustering would result in circulars jets associated with the hardest particles while jets with more random shapes are associated with the softer particles. However, shapes in both cases are stable under the addition of new soft-particles.

Track jets are built using inner detector tracks which are reconstructed within the full acceptance of the ID ($p_{\mathrm{T}} > 500$MeV, $|\eta| < 2.5$). The inputs of the calorimeter jets are topoclusters containing cells from the whole calorimeter (electromagnetic and hadronic). They are assumed to originate from the center of the detector and are initially calibrated at the electromagnetic scale (EM) (Section 3.3.5). This scale correctly measures the energy deposited in the calorimeter by particles produced in electromagnetic showers. In a second step, calorimeter cells can be calibrated so that the hadronic contribution of jets is also taken into account. This calibration uses the local cell signal weighting (LCW) method that corrects for a variety of effects in the calorimeter [2, 3]. First, jets are classified as electromagnetic or hadronic such that the hadronic side measurement can be taken into account. Second, the energy falling outside the topocluster is estimated from the cluster isolation and finally the amount of energy falling out of the calorimeter is determined taking into account the position of the jet. Then, these topoclusters are further corrected following a calibration scheme that takes into account:

- **Non-compensating nature of the ATLAS calorimeters**, taking into account that the response of the calorimeters to hadronic showers is lower than for electromagnetic showers.
- **Dead material** losses in the inactive area of the detector (cryostat, services etc).
- **Energy leakage** of showers close to the calorimeter edges.
- **Out of calorimeter jet** contribution related to particles that enter in the truth jet but that are not included in its corresponding reconstructed jet.

- **Energy deposits below noise threshold** since only cells with energy beyond a noise threshold are included in the topocluster.
- **Pileup** energy contributions in the jets coming from energy deposits either produced in-time or out-of-time multiple pp collisions occurring at each bunch crossing.

The calibration process is divided into MC-based calibration, aiming to correct the jet energy to its associated truth jet, and in-situ corrections comparing the derived jet energy scale with data so that further corrections are applied to cope with possible inhomogeneities in calorimeter response. The scheme is shown in Figure 6.1.

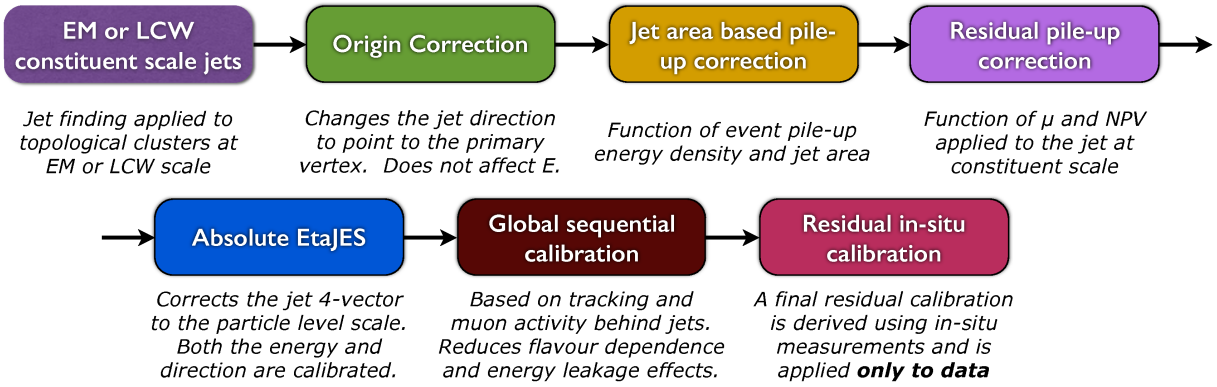


Figure 6.1: Calibration scheme of EM and LCW jets [4].

An origin correction modifies the jet four-momentum so that it points to the hardest vertex of the event instead of the center of the detector. Then, pileup is corrected by using an area-based correction explained in Section 4.4. Additionally, a residual correction is applied depending on the number of primary vertices (NPV) and the number of interactions per bunch crossing (μ) measured by the luminosity system and derived from MC. An absolute jet energy scale (JES) is derived from dijet simulated samples by fitting $E_{\text{jet}}^{\text{reco}}/E_{\text{jet}}^{\text{truth}}$ distributions binned in E_{truth} and η_{det}[1]. In addition, the jet η is corrected since a bias may appear due to sudden changes in the calorimeter granularity or different calorimeter technologies. This energy scale and η calibration are different for EM or LCW calibrated jets, referred in the following as EM+JES or LCW+JES jets. Non-trivial difference between quark or gluon initiated jets remain after the JES step for which a global sequential correction (GSC) is applied. In the analysis presenting in Chapter 7, EM+JES jets are used. Their absolute JES correction and the η calibration are exposed in Figures 6.2.

After the GSC step, some residual differences remain between data and MC, from which data must be corrected for. In-situ techniques further correct the energy of jets accounting for differences in the jet response between data and MC. These differences are quantified by balancing the p_{T} of a jet against other well-measured reference objects and comparing this response of the jets between data and MC events:

$$\alpha = \frac{R_{\text{data}}}{R_{\text{MC}}} = \frac{\langle p_T^{\text{jet}}/p_T^{\text{ref}}\rangle_{\text{data}}}{\langle p_T^{\text{jet}}/p_T^{\text{ref}}\rangle_{\text{MC}}} \tag{6.3}$$

These techniques can be divided into three categories:

- η **intercalibration:** a well-measured central jet is used to correct the energy scale of forward jets. This technique uses dijet events with one of the jets within $|\eta| < 0.8$ and the other jet in $0.8 < |\eta| < 4.5$. This step of the in-situ calibration aim to remove any η dependence of the jet energy correction.
- Z/γ**+jet:** this calibration uses a Z boson (decaying into a muon-antimuon or an electron-positron pair) or a photon as reference particle to evaluate the recoil jet p_{T} response in the central region

[1] η_{det} is the jet pointing from the geometric center of the detector.

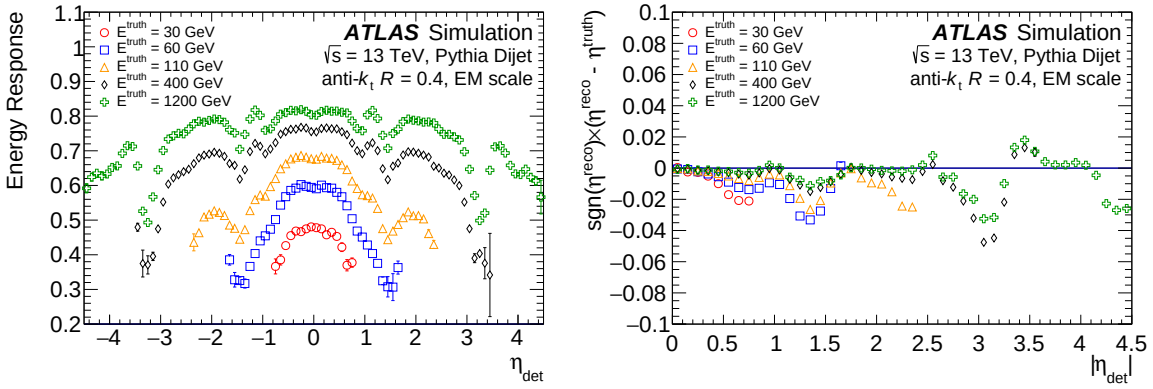


Figure 6.2: (Left) Average energy response as a function of $|\eta_{\mathrm{det}}|$ and the truth jet energy E^{truth}. Pileup and origin corrections are applied. (Right) Signed difference between the reconstructed η of the jet and the truth η as a function of $|\eta_{\mathrm{det}}|$ [5].

($|\eta| < 0.8$). The recoiling jet can be efficiently corrected for 20 GeV $< \mathrm{p_T} <$ 950 GeV. Given that η intercalibration is previously applied, this correction can be applied to jets in the whole pseudorapidity acceptance, not only to jets in ($|\eta| < 0.8$).

- **Mulijet calibration:** it is the last stage of the in situ calibration which is used to extend the calibration for p_T up to 2 TeV. Topologies with three or more jets are used to balance a high- p_{T} jet against a recoil system composed of several lower-p_{T} jets. The recoil jets are of sufficiently low p_{T} as to be in the range of Z/γ+jet calibrations so that this procedure is efficient to correct high-p_{T} jets.

The combined systematic error from the in-situ calibration as well as the contribution from each correction step are shown in Figures 6.3 as a function of p_T and η for EM+JES jets. It can be observed that the dominant source of systematic error is the absolute in-situ jet energy scale, which corresponds to Z/γ+jet and multijet calibration and becomes specially important for low-p_{T} jets. However, the relative JES determination (from η intercalibration) also plays a leading role at large $|\eta|$ values.

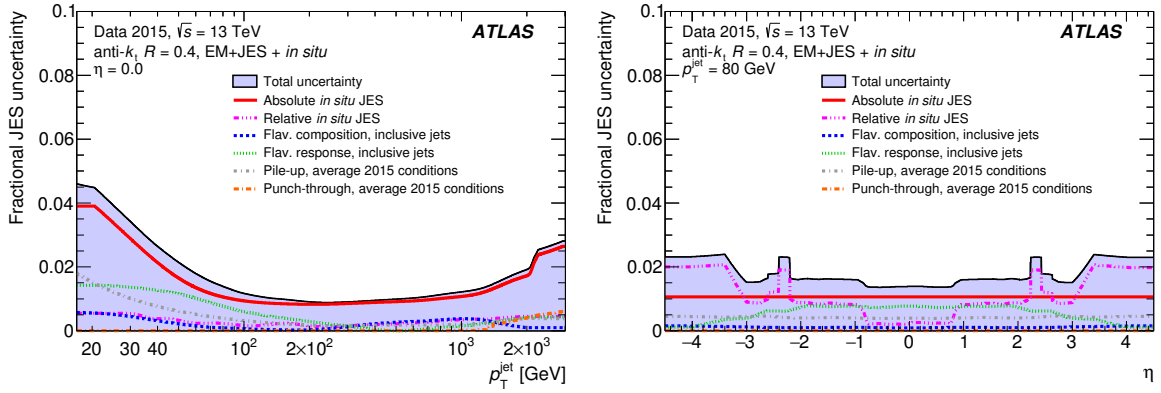


Figure 6.3: Combined uncertainty in the JES of fully calibrated jets as a function of (a) jet p_{T} at $\eta = 0$ and (b) η at $p_{\mathrm{T}} = 80$ GeV. Absolute in-situ JES corresponds to Z/γ+jet and multijet calibrations and relative in-situ calibration corresponds to η intercalibration. More systematic errors are presented corresponding to pileup, punch-through (one of the corrections of the GSC step) and jet flavour uncertainties are also included [5].

6.1.1 Pileup jets suppression in ATLAS

The multiple pp collisions per bunch crossing occurring in the LHC can reduce the performance of the ATLAS detector due to the production of additional particles. As it has been discussed, this pileup

activity affects the reconstruction of jets, photons and electrons and is corrected using ambient energy and MC based techniques at the calibration step. However, local fluctuations of the pileup activity of the event may result in spurious pileup jets that can be misidentified as a real hard jet of the collision.

The separation of hard and pileup jets becomes one important problem to improve measurements. During Run I, a jet-vertex-fraction (JVF) variable was used, achieving a significant reduction of pileup jets while keeping a significant amount of hard jets in the event. This variable tests the compatibility of the jet to have been produced in the largest $\sum_{\text{trk}} p_T^2$ vertex of the event (p_{T} being the transverse momentum of tracks associated with the vertex), also called *the hardest vertex of the event*. This vertex is identified as the point where the hard interaction took place. Hard jets correspond to partons such as quarks or gluons truly produced in the hard interaction issued from the collision. Pileup jets instead are caused by stochastical fluctuations of the pileup activity. Pileup corresponds here to soft-collisions and underlying events occurring around the hard interaction. Thus, they should not be associated with the hardest vertex given the good resolution of ATLAS track-vertex association [6]. Following this, JVF is defined as:

$$\text{JVF} = \frac{\sum_k p_T^{\text{trk}_k}(\text{PV}_0)}{\sum_l p_T^{\text{trk}_l}(\text{PV}_0) + \sum_{n\geq 1}\sum_l p_T^{\text{trk}_l}(\text{PV}_{\text{n}})} \tag{6.4}$$

where $p_T^{\text{trk}_k}(\text{PV}_0)$ corresponds to the transverse momentum of the k^{th} track associated with the jet and the hardest vertex of the event and $p_T^{\text{trk}_k}(\text{PV}_{\text{n}})$, to the n^{th} vertex. Pileup jets tend to present values close to zero while hard jets present distributions peaking at 1. The performance of this variable is dependent on the number of primary vertices (Fig. 6.4 left) so a new variable called corrJVF is introduced:

$$\text{corrJVF} = \frac{\sum_k p_T^{\text{trk}_k}(\text{PV}_0)}{\sum_l p_T^{\text{trk}_l}(\text{PV}_0) + \frac{\sum_{n\geq 1}\sum_l p_T^{\text{trk}_l}(\text{PV}_{\text{n}})}{k\cdot N_{\text{vtx}}}} \tag{6.5}$$

to reduce this pileup dependence (Fig. 6.4 right). Hard jets tend to present values close to 1 while pileup jets present values going to smaller values (Fig. 6.5.left), until zero (or -1, meaning that no tracks are associated with it).

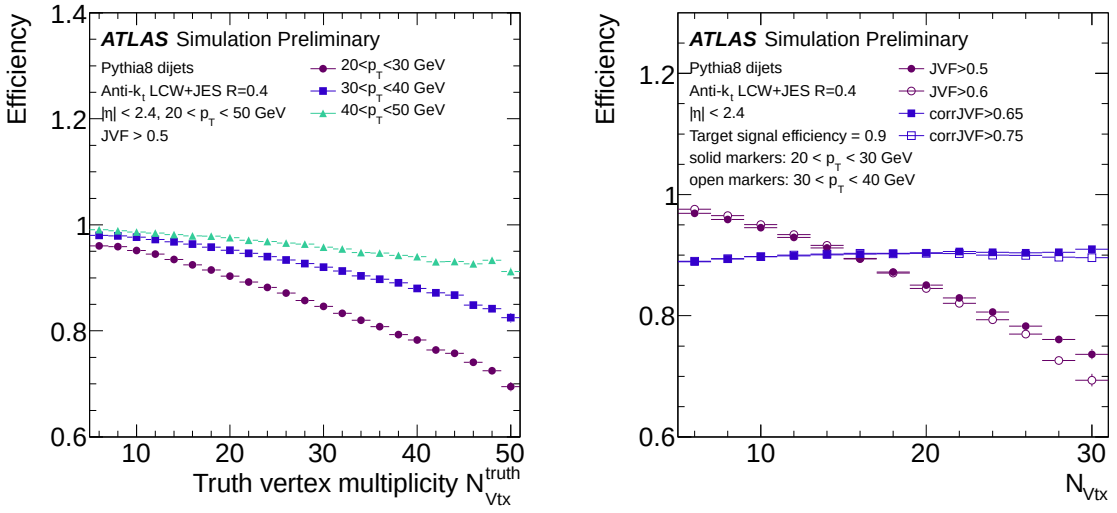


Figure 6.4: Left: performance of the JVF against pileup and for different jet p_T values. Right: comparison of corrJVF and JVF performance against pileup activity [7].

Apart from corrJVF, the ratio between sum of the transverse momentum of the jet associated tracks to the largest $\sum_{\text{trk}} p_T^2$ vertex and the calibrated transverse momentum of the jet is also used to reject pileup jets:

$$R_{pT} = \frac{\sum_k p_T^{\text{trk}_k}(\text{PV}_0)}{p_{\text{T}}^{\text{jet}}} \tag{6.6}$$

Pileup jets tend to present a R_{pT} distribution peaked at zero and steeply falling while hard jets present broader distributions (Fig. 6.5.right).

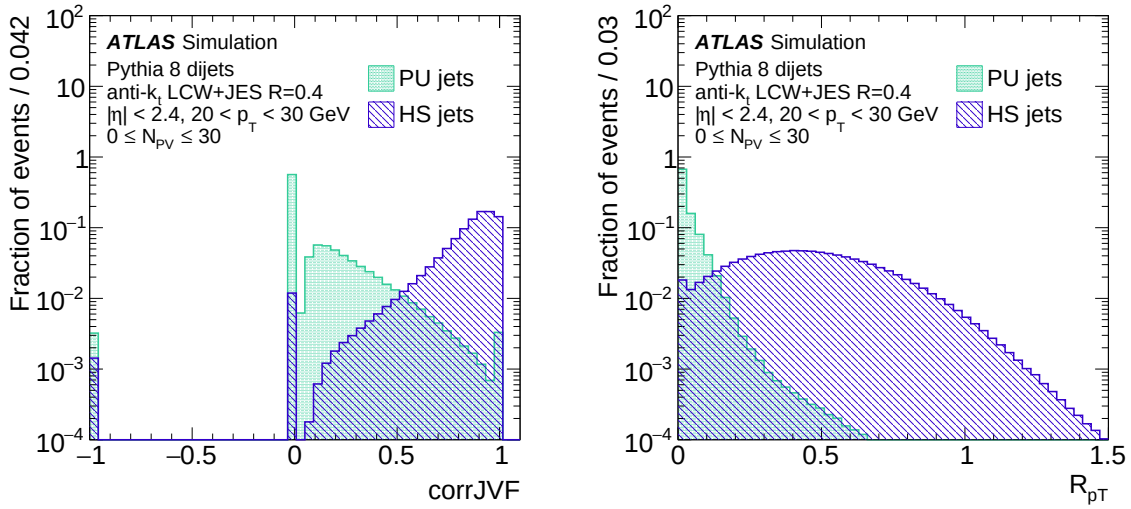


Figure 6.5: Left: Distribution of the corrJVF variable of pileup and hard jets. Right: Distribution of the R_{pT} variable of pileup and hard jets [7].

These two variables are combined into a new discriminant variable called jet-vertex-tagger (JVT) [7]. JVT is a 2-dimensional likelihood, based on a k-nearest neighbour algorithm [8], that can be applied to central jets ($|\eta| < 2.4$) presenting transverse momenta in the range $20\ \mathrm{GeV} < \mathrm{p_T} < 60\ \mathrm{GeV}$. Hard jets tend to present values close to 1 while pileup jets present values closer to zero although an overlap of both distributions is observed (Fig. 6.6 right).

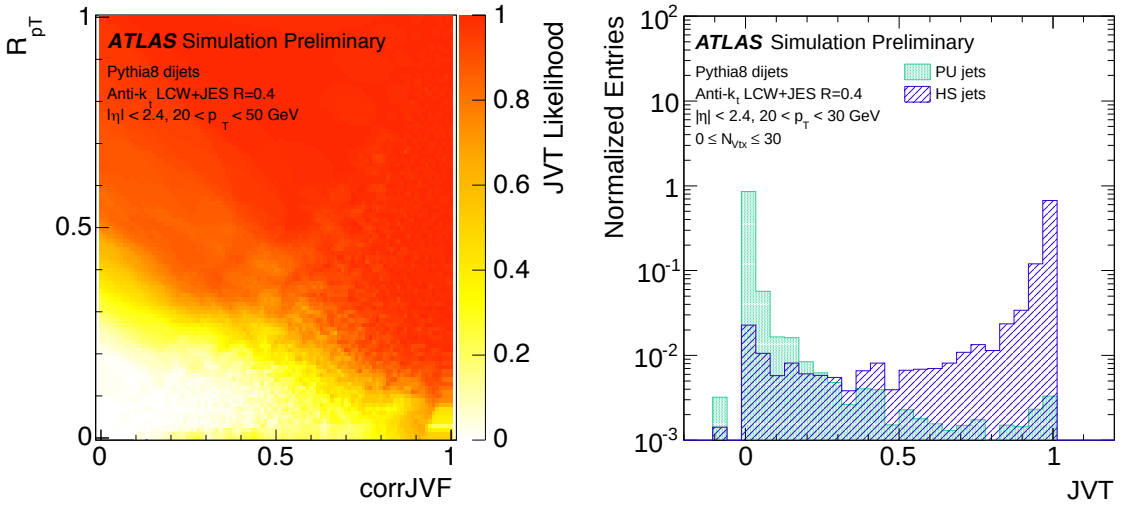


Figure 6.6: Left: JVT values depending on the corrJVF and R_{pT}. Right: JVT distributions for pileup and hard jets estimated on Pythia8 dijet MC events [7].

This new variable performs better than R_{pT} and corrJVF taken separately, as it can be observed in Figure 6.7. The optimal working point has been studied, which should combine a large acceptance of hard jets with a sufficiently small fake rate is performed. Before the Moriond 2017 conference, a JVT cut larger than 0.64 for central jets with $20\ \mathrm{GeV} < \mathrm{p_T} < 50\ \mathrm{GeV}$ was recommended. However, further studies led to change the recommendation to a JVT > 0.59 for jets with $20\ \mathrm{GeV} < \mathrm{p_T} < 60\ \mathrm{GeV}$, later used in the

analysis presented in this manuscript.

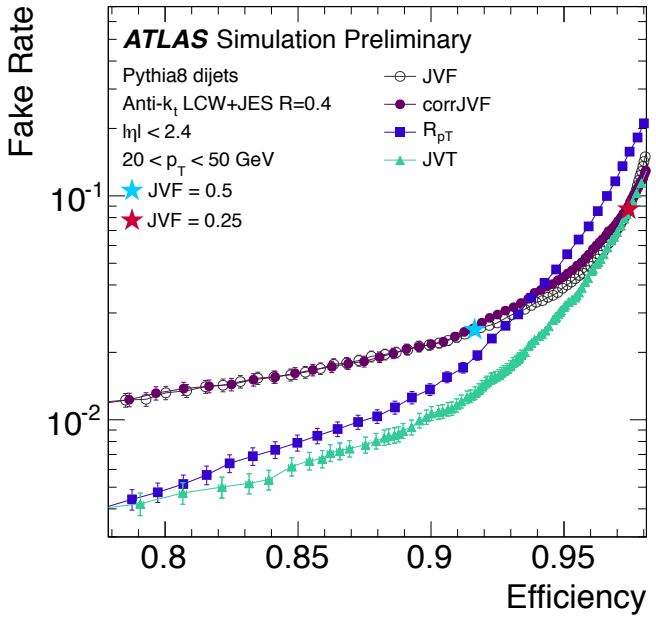


Figure 6.7: Efficiency and fake rate curves of the JVT variable in comparison with the corrJVF, R_{pT} and JVF variables [7].

6.2 Muon reconstruction and identification

This section summarizes muon reconstruction and identification based on the ATLAS most recent public results using of 3.2 fb^{-1} 2015 dataset [9]. Muons are charged particles that interact with the inner detector, the calorimeter and the muon spectrometer. Muons entering the calorimeter behave as minimum ionizing particles [10] while the energy deposited in the inner detector and the muon spectrometer are the main elements to perform the muon reconstruction. Muon reconstruction is first performed using separately inner detector or muon spectrometer information. This information is then combined to form muon tracks that are then used in the analysis. In the ID, muons are first reconstructed as other charged particles (tracks). In the MS, hit patterns in the different subdetectors are searched in first place to form MS segments. Then, a muon track candidate is built by fitting segments from different layers. At least two matching segments are required to build a track, except in the barrel-endcap transition region where a single high-quality segment with η and ϕ information can be used. Every segment may initiate several muon tracks so an overlap removal algorithm is applied. This algorithm either assigns the segment to the most probable candidate track or allows the segment to be shared between two tracks.

ID and MS tracks are then combined together to build the muon candidates. Four techniques are considered:

- **Combined muons (CB)**

  ID and muon-spectrometer tracks are reconstructed separately and combined with a global refit combining both subdetectors hits. In the global fit, reconstruction may take two directions: an outside-inside technique that first reconstructs tracks in the MS and then extrapolates it into the inner detector; and an inside-outside technique, which reconstructs the muon track in the opposite direction. The default muon track reconstruction is the former.

- **Segment-tagged muons (ST)**

  This reconstruction is available when muons cross one layer of the MS, reducing the performance of a CB reconstruction. In that case, an ID track is identified as a muon if it matches one CSC or MDT track segment once it is extrapolated.

- **Calorimeter-tagged muons (CT)**

  Muons are reconstructed if an ID track match energy deposits in the calorimeter compatible with a minimum ionizing particle. This reconstruction has the lowest purity of the muons but allows to increase muon reconstruction efficiency in regions where the MS coverage is only partial in order to accommodate calorimeters cabling and services.

- **Extrapolated muons (ME)**

  Muons are reconstructed only from MS segment tracks compatible as originating from the interaction point. At least, two MS layers (three in the forward region) must present hits and parameters of the muon track at interaction points are determined by extrapolating the MS track back to the interaction point. These reconstructed muons are useful for increasing muon reconstruction in the region $2.5 < |\eta| < 2.7$, where no ID coverage is provided.

A single μ collection is then built from these μ using an overlap removal procedure. When two muons share the same ID track, preference is given to CB muons, then to ST, and finally to CT.

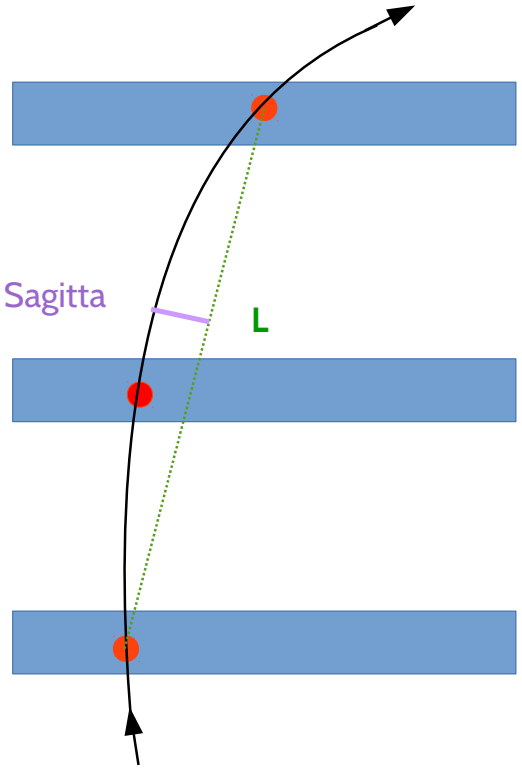


Figure 6.8: Illustration of the sagitta parameter.

Another important measurement concerning the muons is their *sagitta* parameter S (Fig 6.8). This parameter measured in the MS represents the curvature of the muon track in the R-ϕ plane. The sagitta is then used in the reconstruction of the transverse momentum of the muon [11]:

$$p_T = \frac{BL^2}{8S} \tag{6.7}$$

where B is the magnetic field strength.

After their reconstruction, prompt muons must be separated from muons coming from the in-flight decay of kaons or other hadronic particles. The latter kind of muons presents a distinctive "kink" in the reconstructed track. This distinction ca be made using a poor χ^2 of the track or a divergence between the muon momentum measured in the MS or the ID initial tracks. Four reconstruction quality criteria are defined:

- **Medium:** Only CB and ME muons are considered. The former are required to present at least 3 hits in at least two MDT, except in $|\eta| < 0.1$ where at least one MDT hit is required in regions without any MDT presenting holes. ME muons are required at least to have hits in three MDT/CSC layers. A loose selection in the compatibility between the ID and the MS tracks is also added to further suppress background: the charge over momentum significance (q/p)[2] is requested to be less than 7.

- **Loose:** All types of muons are considered. All muons CB and ME passing the Medium criteria and CT and ST muons within $|\eta| < 0.1$ are considered.

- **Tight:** Only CB muons passing Medium criteria and presenting hits in at least two MS stations are considered. In addition, the track fit $\chi^2/n.d.f$ is requested to be lower than 8 and p_T dependent cuts are performed on the q/p significance and the $\rho^{'}$ variable, which is defined as the absolute value of the difference between the ID and MS measured transverse momentum divided by the p_{T} of the combined fitted track.

- **High-p_{T} muons:** this collection includes only CB muons passing Medium criteria and presenting hits in the three MS stations. Sections of the MS where the alignment is suboptimal are vetoed as precaution.

The efficiency of the muon identification and reconstruction is evaluated using tag-and-probe methods on $Z \to \mu^+\mu^-$ and $J/\psi \to \mu^+\mu^-$ samples. The tag muon is requested to pass the Medium selection and efficiency is evaluated using the following formula:

$$\epsilon = \frac{N_R^{\mathrm{signal}} - N_R^{\mathrm{bkg}}}{N_P^{\mathrm{signal}} - N_P^{\mathrm{bkg}}} \tag{6.8}$$

where N_R stands for the number of reconstructed probes passing the considered ID selection and N_P, for the number of identified probes before imposing the identification working point. The indexes *signal* and *bkg* respectively stand for the probes identified to come from a Z or J/ψ decay and the number of background probes coming from other sources than Z or $J\psi$ decay but that are misidentified as such. The Medium working point is the standard muon identification criteria in ATLAS and is used in the present analysis. The reconstruction efficiencies of muons following Medium ID criteria is presented in Figures 6.9, where an overall 99% reconstruction efficiency is observed for muons within $0.1 < |\eta| < 2.5$.

6.3 $E_{\mathrm{T}}^{\mathrm{miss}}$ reconstruction

The $E_{\mathrm{T}}^{\mathrm{miss}}$ is reconstructed as the negative sum of transverse momenta of variable electrons, photons, muons, τ-leptons and jets. In addition, low energy deposits in the detectors that are not associated with any identified high energy particles, also called *soft-terms*, must be reconstructed and included in the calculation. These soft-terms correspond to energy deposits made by very low energy particles that could not pass the selection cuts of isolated leptons nor included in a jet. They are either coming from

[2] q/p significance is defined as the absolute value ratio of the charge and the momentum divided by the sum in quadrature of all the uncertainties.

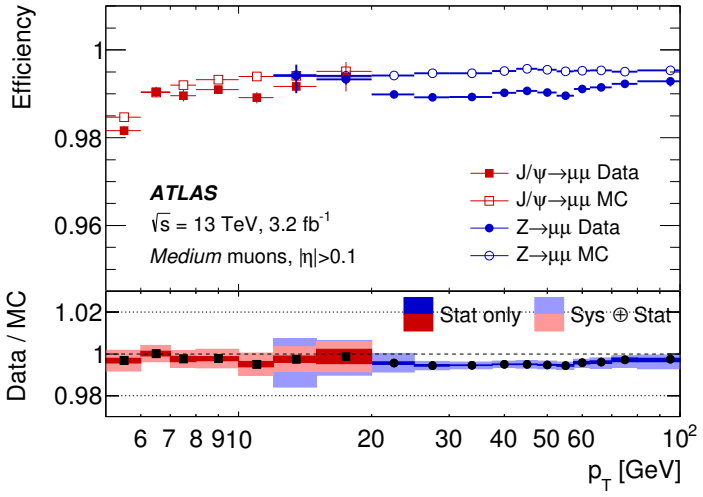


Figure 6.9: Reconstruction efficiency for the Medium muon selection as a function of the p_{T} of the muon, in the region $0.1 < |\eta| < 2.5$ as obtained with $Z \to \mu^+\mu^-$ and $J/\psi \to \mu^+\mu^-$ events in 2015 data and MC [9].

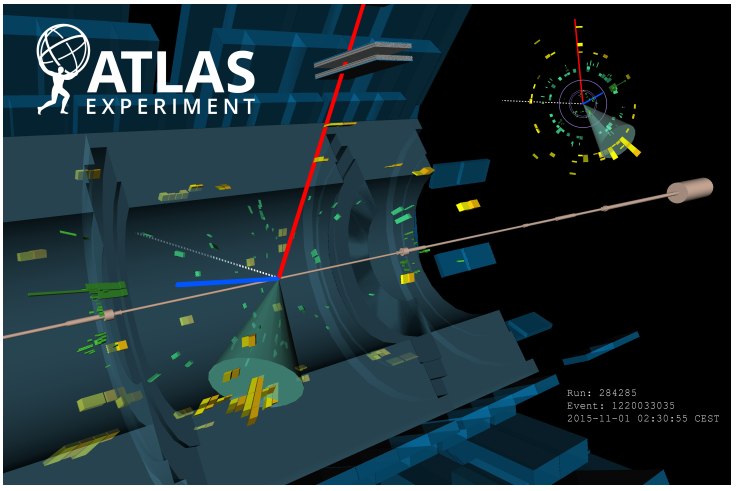


Figure 6.10: Example of an event with large $E_{\mathrm{T}}^{\mathrm{miss}}$ in ATLAS data: display of event 1220033035 in run 284285 recorded by ATLAS in LHC proton-proton collisions at a centre-of-mass energy of 13 TeV. This candidate is likely to be the production of a W boson in association with a single top quark in the dilepton channel. Two opposite charged leptons are reconstructed. The reconstructed electron is represented by the blue line and the reconstructed muon is represented by the red line. One b-jet is identified and represented by an azure cone and the missing transverse momentum coming from a neutrino is represented by the dotted white line [12].

true particles produced in the primary vertices or from pileup and underlying events. The $E_{\mathrm{T}}^{\mathrm{miss}}$ is then estimated as:

$$\vec{E}_{\mathrm{T}}^{\mathrm{miss}} = -\sum \vec{p}_{\mathrm{T}}{}^{\gamma} - \sum \vec{p}_{\mathrm{T}}{}^{\mathrm{j}} - \sum \vec{p}_{\mathrm{T}}{}^{\tau} - \sum \vec{p}_{\mathrm{T}}{}^{\mathrm{e}} - \sum \vec{p}_{\mathrm{T}}{}^{\mu} - \sum \vec{p}_{\mathrm{T}}{}^{\mathrm{soft-term}} \tag{6.9}$$

This definition provides a complete measurement of the transverse momentum imbalance in the event and its good reconstruction depends on the good measurement of all the measured objects inside an event. Among all objects, jets and soft-terms are the contributions that can introduce an important imbalance in the event, mainly due to their small pileup resilience and the uncertainty on their energy. The main contribution to $E_{\mathrm{T}}^{\mathrm{miss}}$ resolution come from jets calibration, mainly due to the absolute jet energy scale determination (Figs. 6.3). On the other hand, for an optimal reconstruction of soft-terms, it is important to take into account that a part of these deposits could come from pileup events. Several strategies have been developed to reconstruct soft-terms, defined during Run I [13]. However, two of these reconstructions are clearly the most important to focus on:

- **Calorimeter-based soft-terms (CST):**

The CST are reconstructed using calorimeter topoclusters transverse energy that could not be associated with any high p_{T} object. These topoclusters (Section 4.1.2) are calibrated to LCW scale given that most of these contributions come from hadronic events. This reconstruction has the advantage to take into account the contribution from charged and neutral particles. On the other hand, there is no association of these deposits with the hardest vertex due to the small accuracy of the calorimeter pointing. In consequence, all deposits are included in the soft-terms. Contributions from pileup vertices are expected to be deposited isotropically in the detector so that pileup contributions may balance in the vectorial sum of the final objects transverse momentum. This was the standard $E_{\mathrm{T}}^{\mathrm{miss}}$ reconstruction during Run I.

- **Track-based soft-terms (TST):**

  These soft terms are reconstructed using well-reconstructed ID tracks not associated with any hard object. These tracks must satisfy a $p_{\mathrm{T}} \geq 0.5$ GeV and $|\eta| < 2.5$ and at least 7 hits in the silicon detectors with less than 2 holes in the SCT or one hole in the pixel detector. Tracks must be associated with the hardest vertex of the event. This association is achieved if the transverse impact parameter (d_0) is less than 1.5 mm and that the transverse impact significance (d_0/σ_0) is less than 3. In addition, tracks are excluded if they are within $\Delta R = 0.5$ of an electron or a photon cluster, or within $\Delta R = 0.2$ of a hadronically-decaying tau-lepton. ID tracks from combined or segment-tagged muons are replaced by a combined fit to the ID and MS tracks. Tracks associated with jets using the ghost-association technique [14, 15] are removed, as well as tracks with momentum uncertainties larger than 40% or not matched to any calorimeter deposit. Associating tracks to the hardest primary vertex of the event allows to efficiently reject pileup tracks (associated with a different vertex). This implies a stronger soft-term immunity against pileup, which motivates that this is the standard $E_{\mathrm{T}}^{\mathrm{miss}}$ reconstruction during Run II. In addition, when a pileup jet is further rejected by requiring a JVT threshold to central jets (20 GeV $<$ $\mathrm{p_T}$ $<$ 60 GeV, $|\eta| < 2.4$), the related tracks are reconstructed in the soft-terms in case that they are associated with the vertex of the event. However, this is not the case in $h \to \gamma\gamma$ and is introducing some biases on the $E_{\mathrm{T}}^{\mathrm{miss}}$ reconstruction, which are exposed in Section 6.4.

Another $E_{\mathrm{T}}^{\mathrm{miss}}$ reconstruction can also be done based on tracks only, called Track-$E_{\mathrm{T}}^{\mathrm{miss}}$. The difference with TST $E_{\mathrm{T}}^{\mathrm{miss}}$ is that, in the former case, hard objects are not included in the reconstruction but only their associated tracks. This induces some imbalance in final states where neutral objects are expected, in particular photons, but allows reconstructing a very pileup resilient $E_{\mathrm{T}}^{\mathrm{miss}}$ when leading particles are charged.

The performance of the $E_{\mathrm{T}}^{\mathrm{miss}}$ reconstruction is evaluated using $Z \to \ell^-\ell^+$+jets and $W \to \ell\nu$+jets samples. The $Z \to \ell^-\ell^+$ sample final state is used to determine the performance each method in case where no genuine $E_{\mathrm{T}}^{\mathrm{miss}}$ is produced. Then, the size of the momentum imbalance helps to evaluate the goodness of the reconstruction method. In addition, pileup resilience can also be evaluated using these samples. On the other hand, $W \to \ell\nu$+jets serves to evaluate the linearity (Eq. 6.10) of the $E_{\mathrm{T}}^{\mathrm{miss}}$ variable, which is the relative difference between the reconstructed $E_{\mathrm{T}}^{\mathrm{miss}}$ and the truth $E_{\mathrm{T}}^{\mathrm{miss}}$ of the event on MC samples.

$$\text{Linearity} = \frac{E_{\mathrm{T,reco}}^{\mathrm{miss}} - E_{\mathrm{T,truth}}^{\mathrm{miss}}}{E_{\mathrm{T,truth}}^{\mathrm{miss}}} \tag{6.10}$$

These studies are performed selecting calibrated and isolated electrons with $p_{\mathrm{T}} > 10$ GeV, $|\eta| < 2.47$ without the crack region (1.37 < $|\eta|$ < 1.52) and passing Medium identification requirements. Selected muons pass $|\eta| < 2.5$ and medium selection criteria. Photons are selected if their p_{T} 25 GeV and $|\eta| <$ 2.37 without the crack region. Tight identification and isolation requirements are imposed to photon collection. They are also required to present hits in the muon spectrometer and the inner detector. Muon candidates with a large imbalance between the momentum measured by the ID and by the MS are rejected.The acceptance is extended to cover the range $2.5 < |\eta| < 2.7$ by allowing muons reconstructed in the MS only, but with tightened requirements on the number of MS track hits. In addition, muons are required to have p_{T} greater than 10 GeV. Hadronically decaying $\tau-$leptons are required to pass Medium selection [16] and $p_{\mathrm{T}} > 20$ GeV and $|\eta| < 2.5$ without the crack region. Finally, jets are reconstructed

using the anti-k_T algorithm with radius parameter $R = 0.4$ and calibrated to EM+JES scale [17]. They are required to have $p_{\mathrm{T}} > 20$ GeV. In this study, TST$E_{\mathrm{T}}^{\mathrm{miss}}$ reconstruction scheme uses a JVT> 0.64 cut to jets within the range 20 GeV $< p_{\mathrm{T}} < 50$ GeV, $|\eta| < 2.4$. Finally, jets are excluded if the overlap-removal with a muon would reduce the apparent jet p_{T} by more than 90%.

The distributions of $E_{\mathrm{T}}^{\mathrm{miss}}$ using $Z \rightarrow \mu^-\mu^+$+jets are presented in Figures 6.11. Since no $E_{\mathrm{T}}^{\mathrm{miss}}$ is expected, the best reconstruction scheme corresponds to the one presenting the smallest imbalance. $E_{\mathrm{T}}^{\mathrm{miss}}$ resolution is specially sensitive to the jets, as it can be observed. TST reconstruction is the most accurate reconstruction when all jets are included while events with no jets present a similar performance between Track-$E_{\mathrm{T}}^{\mathrm{miss}}$ and TST. In both cases, CST presents a worse accuracy. Concerning the pileup

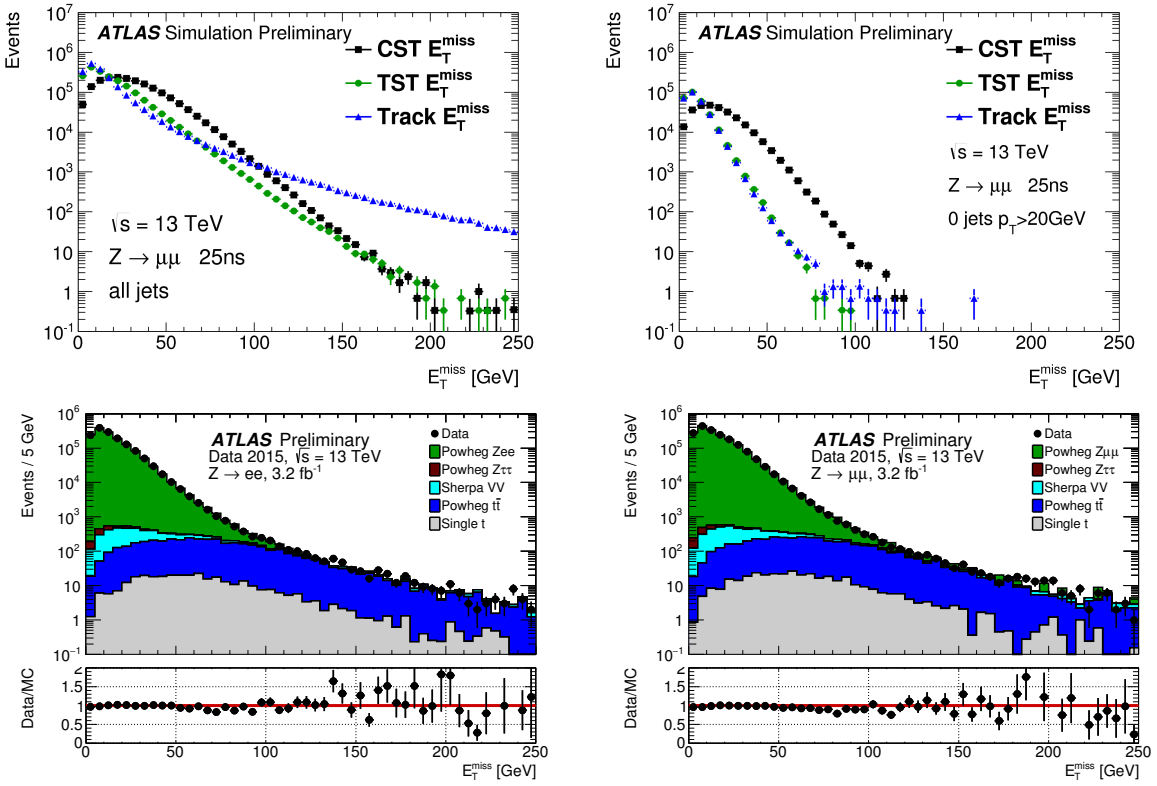


Figure 6.11: $E_{\mathrm{T}}^{\mathrm{miss}}$ distributions using CST, TST and Track-$E_{\mathrm{T}}^{\mathrm{miss}}$ on $Z \rightarrow \mu^-\mu^+$ MC samples (upper plots) and comparison between TST $E_{\mathrm{T}}^{\mathrm{miss}}$ in 2015 data (3.2 fb^{-1}) and MC. Upper left plot presents the distributions considering all events and the upper right plot, considering events with no reconstructed jet [18]. Bottom left plot presents the comparison between data and MC on $Z \rightarrow e^-e^+$ final state and bottom right plot, on $Z \rightarrow \mu^-\mu^+$ final state [19].

resilience, Figure 6.12 presents the evolution of the $E_{\mathrm{T}}^{\mathrm{miss}}$ resolution, encoded in the RMS of the $E_{\mathrm{T}}^{\mathrm{miss}}$ as a function of the number of primary vertices (NPV) in the event or the scalar sum ($\sum E_T$), which is defined in Equation 6.11.

$$\sum E_T = \sum |p_{\mathrm{T}}{}^{\gamma}| + \sum |p_{\mathrm{T}}{}^{\mathrm{j}}| + \sum |p_{\mathrm{T}}{}^{\tau}| + \sum |p_{\mathrm{T}}{}^{\mathrm{e}}| + \sum |p_{\mathrm{T}}{}^{\mu}| + \sum |p_{\mathrm{T}}{}^{\mathrm{soft-term}}| \tag{6.11}$$

The number of primary vertices is a very dependent variable on the number of interactions per collision as the $\sum E_T$ which accounts for the activity in the event, i.e, the number of particles produced in the collision. TST and Track-$E_{\mathrm{T}}^{\mathrm{miss}}$ clearly present the most pileup resilient $E_{\mathrm{T}}^{\mathrm{miss}}$ variable. TST-$E_{\mathrm{T}}^{\mathrm{miss}}$ presents the most performant variable in cases that all jets are included in the event. In case if events with no jets, TST and Track-$E_{\mathrm{T}}^{\mathrm{miss}}$ present a similar performance in the bulk of events, although Track-$E_{\mathrm{T}}^{\mathrm{miss}}$ induces larger tails than TST. The comparison between data and MC using TST reconstruction shows a good agreement between data and MC.

The scale on the parallel axis to the hard object (in this case, the Z boson) transverse momentum and the

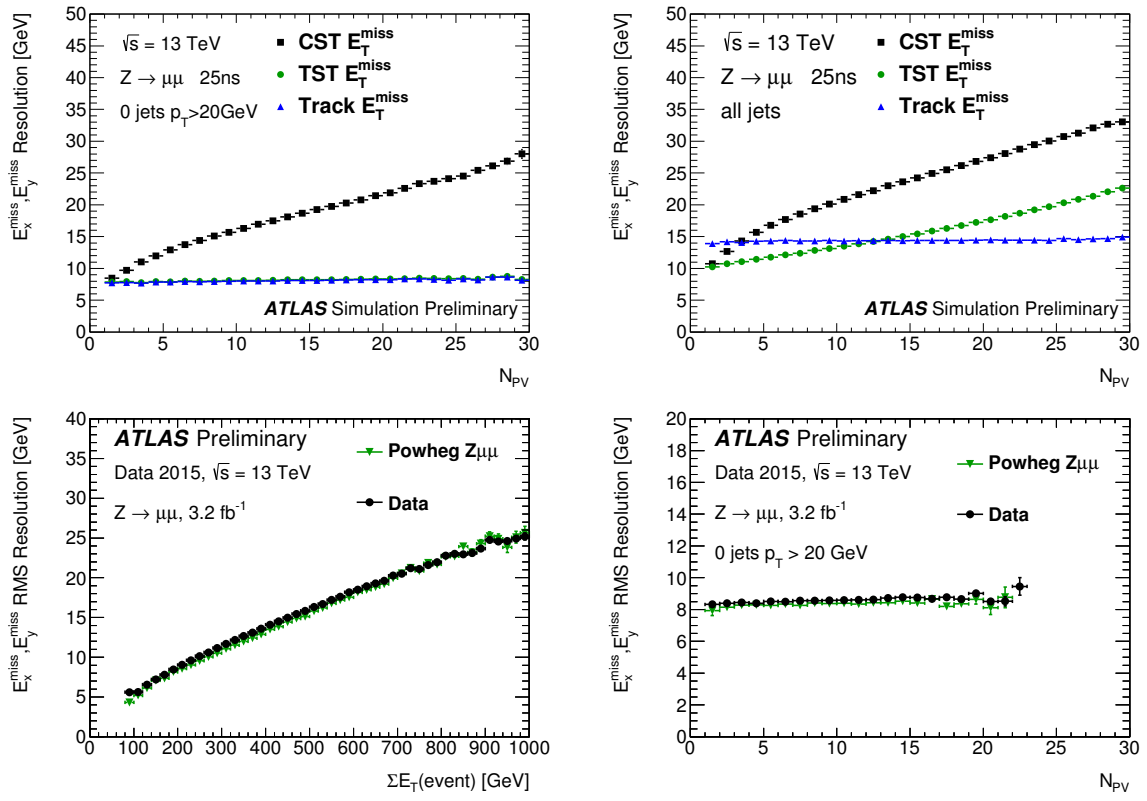


Figure 6.12: Resolution (RMS) of the $E_{\mathrm{x,y}}^{\mathrm{miss}}$ distributions using CST, TST and Track-$E_{\mathrm{T}}^{\mathrm{miss}}$ on $Z \to \mu^{-}\mu^{+}$ MC samples (upper plots) and comparison between TST $E_{\mathrm{T}}^{\mathrm{miss}}$ in 2015 data (3.2 fb^{-1}) and MC. Resolution is presented as a function of the number of primary vertices in the event in the upper plots, either considering all events (left) or events with no reconstructed jet (right) [18]. Bottom left plot presents the comparison between data and MC on 0-jet events as a function of the NPV and $\sum |E_T|$ using TST reconstruction scheme, both for events $Z \to \mu^{-}\mu^{+}$ [19].

linearity are variables to study the reconstruction of the $E_{\mathrm{T}}^{\mathrm{miss}}$. The scale is evaluated on the axis defined by the transverse momentum of the Z boson. Figures 6.13 present a better performance of TST than the other reconstruction algorithms. Therefore, due to its performance in estimating the correct magnitude of $E_{\mathrm{T}}^{\mathrm{miss}}$ and its pileup resilience, TST is the standard reconstruction algorithm in Run II. Distributions

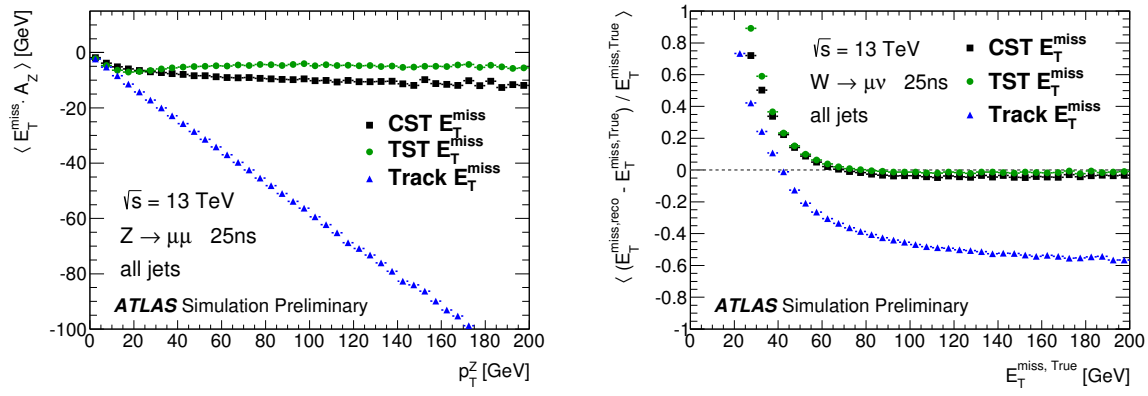


Figure 6.13: (Left) Scale of the $E_{\mathrm{T}}^{\mathrm{miss}}$ on the axis defined by the transverse momentum of the Z boson studied on $Z \to \mu^{-}\mu^{+}$ MC samples as a function of p_{T}^{Z}. (Right) linearity as a function of $E_{\mathrm{T,truth}}^{\mathrm{miss}}$ on $W \to \mu\nu$ MC events.

are presented in this section show the $E_{\mathrm{T}}^{\mathrm{miss}}$ performance for $Z \to \ell^+\ell^-$ and $W \to \mu\nu$ events, where the hardest vertex reconstructs the correct interaction vertex with a very high efficiency. However, in $h \to \gamma\gamma$, this is not the case since the largest p_{T} objects are photons, which leave no trace in the inner detector compatible with a primary vertex in the beamline. $E_{\mathrm{T}}^{\mathrm{miss}}$ calculation then needs to be optimized for $h \to \gamma\gamma$ topologies.

6.4 $E_{\mathrm{T}}^{\mathrm{miss}}$ reconstruction in $h \to \gamma\gamma$ events

6.4.1 Diphoton vertex identification

The beam spot position is determined with sub-millimeter accuracy in the transverse plane, while along the z-axis the spread is about 5-6 cm due to the overlap of proton bunches inside the LHC. Exploiting the longitudinal segmentation of the ATLAS EM calorimeter ("pointing") [20], one can locate the interaction point in $h \to \gamma\gamma$ decays within ~ 2 cm, depending on the photon energy and impact point. Combining this pointing technique with vertex information increase the correct Higgs production vertex reconstruction.

A multivariate method has been developed to identify the Higgs vertex during Run II [21] based on a boosted decision tree (BDT) [8] including the following variables:

- $(z_{\mathrm{common}} - z_{\mathrm{vertex}})/\sigma_{\mathrm{z}}$ where z_{vertex} is the position of the considered vertex on the z-axis and z_{common}, the weighted mean of the intersection of both photon trajectories on the beamline. These trajectories are estimated by using calorimeter "pointing" information in the case of unconverted and TRT-only converted photons or inner detector information for other types of converted photons, as explained in [20]. σ_{z} is the associated error.

- $log_{10}(\sum p_T)$ and $log_{10}(\sum p_T^2)$ where $\sum p_T$ is the scalar sum of the transverse momenta of all the tracks associated with the vertex and $\sum p_T^2$ is the corresponding sum of squared transverse momenta.

- $\Delta\phi(p_{\mathrm{T}}^{\gamma\gamma}, \sum \vec{p_T})$ where p_T is the sum of the vectorial tracks momenta associated with the primary vertex and $p_{\mathrm{T}}^{\gamma\gamma}$ is the transverse momenta of the diphoton system. This variable is expected to peak close to π for the correct vertex choice in case of no real missing transverse momentum, and to have a uniform distribution for pileup vertices.

This method evaluates the probability of the different vertices in the event to be the production vertex of the Higgs candidate. The vertex with the highest probability is identified as the production Higgs vertex and it is called in the following *the diphoton vertex* of the event. The performance of this method is estimated on MC samples for the different production modes of the Higgs boson, exposed in Section 1.2.1. Its efficiency to identify the truth Higgs production vertex is compared with the efficiency of the hardest vertex technique. Table 6.1 presents the efficiency for the inclusive set of events and Figures 6.14, 6.15 and 6.16 present the identification efficiency as a function of the number of primary vertices, the number of truth jets in the event and the diphoton system truth transverse momentum. There is a clear improvement using the diphoton vertex reconstruction, except for topologies where large number of jets and/or leptons are expected, such as ttH production. This is expected since in those cases, there are additional particles associated with the production vertex that present large momenta tracks. At high $p_{\mathrm{T}}^{\gamma\gamma}$, diphoton vertex and hardest vertex tend to perform quite similarly, even if one may observe a better performance of the hardest vertex in some cases. However, this difference is very small and it occurs in $p_{\mathrm{T}}^{\gamma\gamma}$ regions with a lower number of events for example in the case of associated production.

Production mode	Hardest vertex efficiency	Diphoton vertex efficiency
Gluon fusion	57.5%	81.4%
Vector-boson fusion	74.7%	85.6%
Associated production (WH)	90.6 %	94.0%
Associated production (ZH)	84.1%	90.4%
Top-antitop production	99.7%	97.7 %
Bottom-antibottom production	55.6%	79.7%

Table 6.1: Identification efficiency of the Higgs boson production vertex using the hardest vertex or the diphoton vertex.

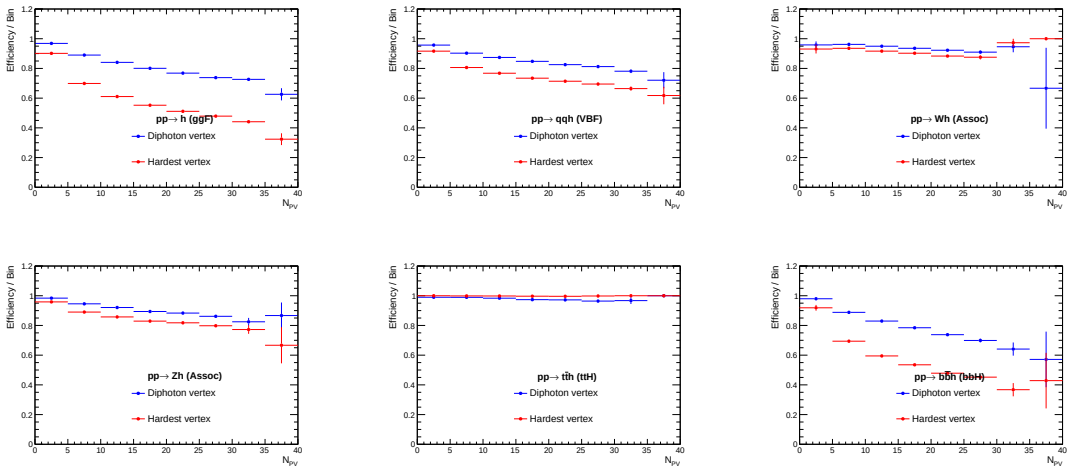


Figure 6.14: Truth Higgs boson production vertex identification efficiency using the diphoton or the hardest vertex method. Efficiency is presented as a function of the number of primary vertices.

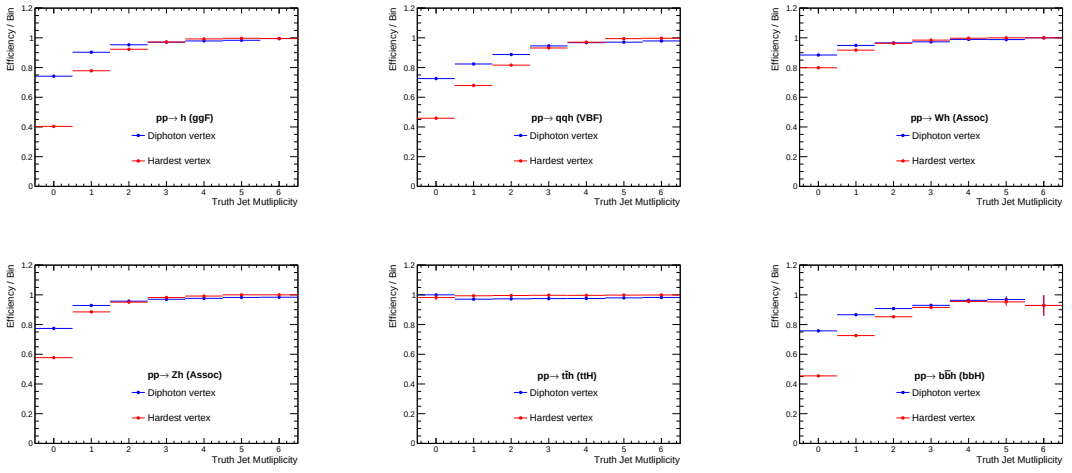


Figure 6.15: Truth Higgs boson production vertex identification efficiency using the diphoton or the hardest vertex method. Efficiency is presented as a function of the number of truth jets in the event.

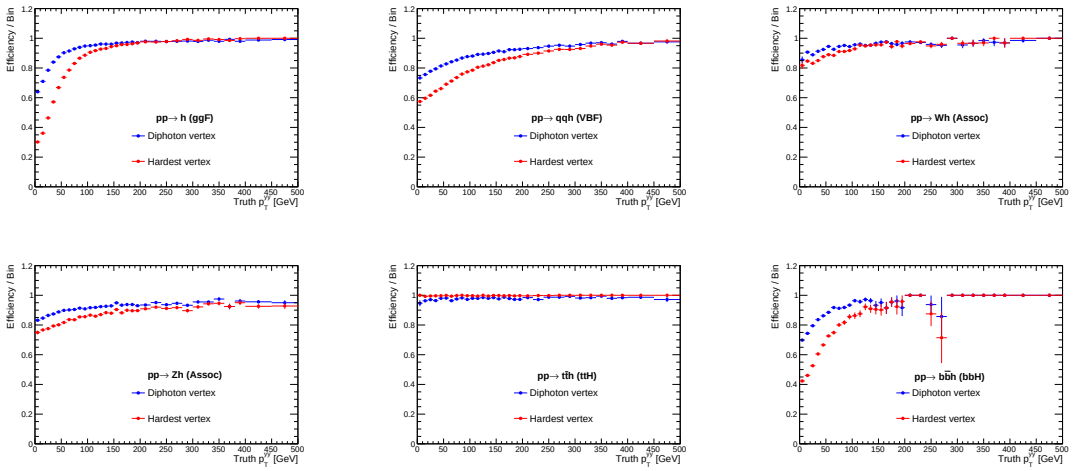


Figure 6.16: Truth Higgs boson production vertex identification efficiency using the diphoton or the hardest vertex methods. Efficiency is presented as a function of the transverse momenta of the truth diphoton system. Photons are previously matched as children of the truth Higgs boson.

6.4.2 $E_{\mathrm{T}}^{\mathrm{miss}}$ performance in $h \to \gamma\gamma$

The lower identification efficiency of the hardest vertex technique in $h \to \gamma\gamma$ topologies introduce a small bias in the TST $E_{\mathrm{T}}^{\mathrm{miss}}$ calculation. In particular, this bias is introduced in the soft-terms and the photon term. In the standard reconstruction, tracks entering the soft-terms must be associated with the hardest vertex. In the case where the hardest vertex is not the diphoton vertex, this condition would reject the tracks associated with the diphoton vertex and introduce tracks in the soft-terms coming from a pileup vertex. A correction is then applied to the standard TST algorithm where tracks are required to be associated with the diphoton vertex, not the hardest one. On the other hand, photon direction is by default corrected to match the hardest vertex of the event. Although the energy of the photon does not vary, η^{γ} varies and therefore p_T^{γ} too. This affects the photon vectorial sum in Equation 6.9 and is then corrected by recomputing η^{γ} with respect to the diphoton vertex.

TST $E_{\mathrm{T}}^{\mathrm{miss}}$ performance is evaluated on $h \to \gamma\gamma$ MC samples (using samples for ggF, VBF, Vh, tth and bbh production modes) either using the diphoton or the hardest vertex of the event. The selection applied to this performance study differs from the one explained in Section 6.3 in some aspects. $h \to \gamma\gamma$ standard selection is applied on photons, by requiring two isolated photons passing the tight ID and whose transverse momentum must be higher than 35 GeV(25 GeV) for the most energetic (second most energetic) photon. In addition, both photons must be found within $|\eta| < 2.37$ and present $p_T^{\gamma} > 0.35(0.25)m_{\gamma\gamma}$. No change in the muons nor electrons selection criteria is applied. τ-leptons are not reconstructed and they are included (if any) in the jet term of Equation 6.9 due to their expected low production in $h \to \gamma\gamma$ final state. Jets p_{T} and $|\eta|$ cuts are preserved. Most recent searches on JVT effect on $E_{\mathrm{T}}^{\mathrm{miss}}$ reconstruction lead to a different recommendation than the one exposed in Section 6.3, which suggest to apply a JVT> 0.59 cut on central jets passing $20\ \mathrm{GeV} < p_{\mathrm{T}} < 60\ \mathrm{GeV}$.

Two distributions indicate what is the most accurate reconstruction scheme. The first one is the $E_{\mathrm{T}}^{\mathrm{miss}}$ distribution subtracted from truth information (Fig. 6.17). The best reconstruction scheme should present values close to zero while values beyond or below indicate a bias on the $E_{\mathrm{T}}^{\mathrm{miss}}$ reconstruction. In addition, the distribution of $E_{\mathrm{T}}^{\mathrm{miss}}$ magnitude parallel to the diphoton system can help to understand if any possible bias depends on any miscalibration in the diphoton system or due to any other effect (see for instance Fig. 6.20). The strength of the TST reconstruction against pileup is studied using the resolution plots on $E_{\mathrm{T}}^{\mathrm{miss}}$ components on the x or y axes and checking that its slope as a function of the average number of interactions per bunch crossing ($\langle\mu\rangle$) is as low as possible. If the slope approaches to zero, it means that on average the resolution of the $E_{\mathrm{T}}^{\mathrm{miss}}$ distribution is not affected by pileup. Finally, a bad

reconstruction method may also induce a bias in the direction of the $E_{\mathrm{T}}^{\mathrm{miss}}$. This bias can be studied observing the azimuthal angle between the transverse diphoton momentum and the $E_{\mathrm{T}}^{\mathrm{miss}}$. In topologies where no genuine $E_{\mathrm{T}}^{\mathrm{miss}}$ is expected, $E_{\mathrm{T}}^{\mathrm{miss}}$ direction would tend to be random compared to the diphoton system direction depending on statistical fluctuations of the underlying event or remaining pileup contributions. When invisible particles are expected to be produced recoiling against the Higgs, as it is the case of associated production Vh or the tth production, then $E_{\mathrm{T}}^{\mathrm{miss}}$ would tend to oppose the diphoton system ($\Delta\phi \approx \pi$).

6.4.3 $E_{\mathrm{T}}^{\mathrm{miss}}$ magnitude reconstruction

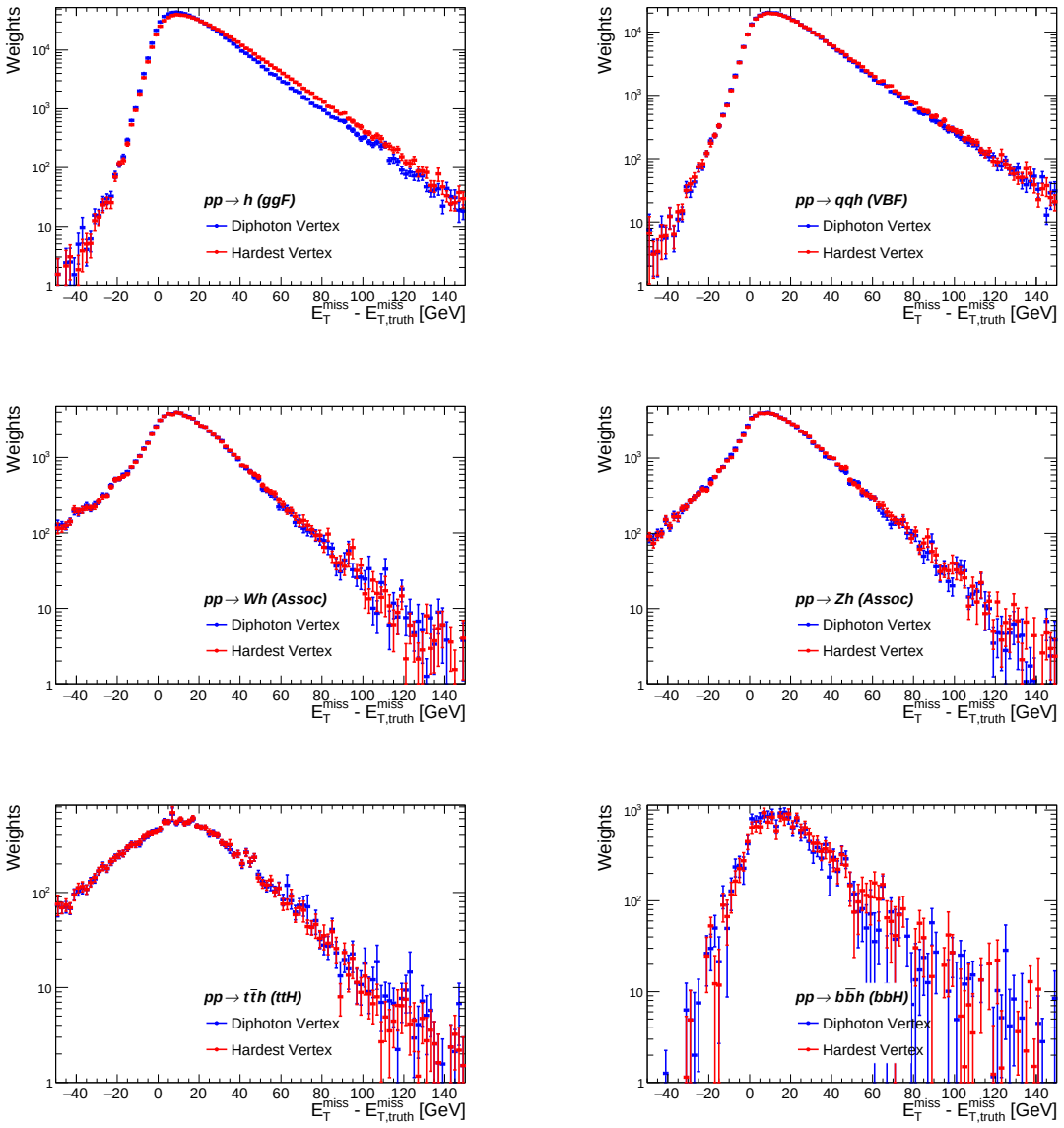


Figure 6.17: Reconstructed $E_{\mathrm{T}}^{\mathrm{miss}}$ distributions substracted from truth information for different Higgs production. TST reconstruction is compared if soft-terms are associated with the hardest vertex or the diphoton vertex of the event.

Figures 6.17 present the distributions of TST $E_{\mathrm{T}}^{\mathrm{miss}}$ estimated with regard to the hardest or the diphoton vertex. Both reconstructions introduce a bias in the $E_{\mathrm{T}}^{\mathrm{miss}}$, but it can be clearly observed a better per-

formance of the diphoton vertex TST given that the distribution mean presents a smaller value than the hardest vertex case, as seen in Tables 6.2 and 6.3. In addition, shorter tails and a better resolution can be observed in diphoton $E_{\mathrm{T}}^{\mathrm{miss}}$ distributions. Linearity plots in Figures 6.19 indicate that the diphoton vertex $E_{\mathrm{T}}^{\mathrm{miss}}$ performs better than hardest vertex TST when low truth $E_{\mathrm{T}}^{\mathrm{miss}}$ values are expected. This can be observed by the mean value of the linearity, which tends to be closer to zero than the hardest vertex TST $E_{\mathrm{T}}^{\mathrm{miss}}$ at $E_{\mathrm{T,truth}}^{\mathrm{miss}} < 10$ GeV for all production modes except tth. However, there is no such effect at larger $E_{\mathrm{T,truth}}^{\mathrm{miss}}$. This bias can also be observed in the scale evolution as a function of the diphoton system transverse momentum, shown in Figures 6.20. These distributions are only presented for gluon fusion and vector-boson fusion samples given that they are the production modes for which no $E_{\mathrm{T,truth}}^{\mathrm{miss}}$ is expected and potential biases can be more clearly measured. A linear decreasing bias is observed for $p_{\mathrm{T}}^{\gamma\gamma} < 25$ GeV in the gluon fusion production mode. This negative slope is explained by the fact that a $p_{\mathrm{T}} > 20$ GeV cut is applied on jets. Typically, ggF Higgs production would present soft-radiation recoiling against the diphoton system (Fig. 6.18). At low $p_{\mathrm{T}}^{\gamma\gamma}$ this soft-radiation would present very small p_{T} values and therefore it is very likely that these contributions are not associated with any jet, thus they are reconstructed in soft-terms. This bias increases with $p_{\mathrm{T}}^{\gamma\gamma}$, given that no other particles are produced and the soft-recoil should increase at larger $p_{\mathrm{T}}^{\gamma\gamma}$. This bias is reduced where the recoiling jets would present already larger transverse momentum, as seen around $p_{\mathrm{T}}^{\gamma\gamma} > 25$ GeV. At $p_{\mathrm{T}}^{\gamma\gamma} > 40$ GeV, the bias stabilizes, which indicate that it is due to the reconstruction itself. In conclusion, the TST soft-terms computed with tracks associated with the diphoton vertex allow a better reconstruction of the $E_{\mathrm{T}}^{\mathrm{miss}}$ magnitude than hardest vertex soft-terms.

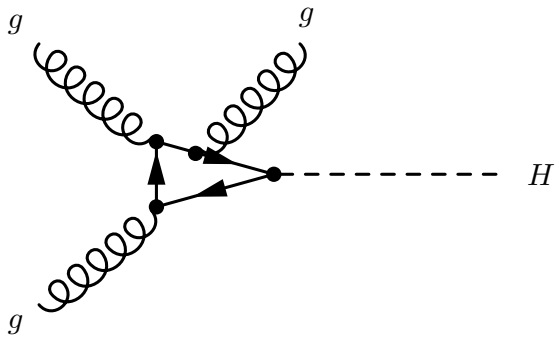


Figure 6.18: Feynman diagram of ggF Higgs production including soft-radiation from $t\bar{t}$ loop that could be rejected by jet selection cuts and introduce a bias in $E_{\mathrm{T}}^{\mathrm{miss}}$.

Mean of the $E_{\mathrm{T}}^{\mathrm{miss}}$ distribution.		
Production mode	Hardest vertex [GeV]	Diphoton vertex [GeV]
Gluon fusion	22.32 ± 0.03	19.74 ± 0.03
Vector-boson fusion	22.38 ± 0.04	21.72 ± 0.04
Associated production (WH)	14.12 ± 0.10	13.71 ± 0.10
Associated production (ZH)	14.97 ± 0.10	14.38 ± 0.10
Top-antitop production	12.83 ± 0.33	13.48 ± 0.34
Bottom-antibottom production	22.10 ± 0.64	20.44 ± 0.64

Table 6.2: Mean of the $E_{\mathrm{T}}^{\mathrm{miss}}$ distribution for the different Higgs production modes. Values are compared between diphoton vertex TST or hardest vertex TST. Both mean values are significantly different within their error intervals.

6.4.4 $E_{\mathrm{T}}^{\mathrm{miss}}$ pileup resilience

Figures 6.21 present the $E_{\mathrm{T}}^{\mathrm{miss}}$ resolution obtained using diphoton vertex or hardest vertex TST technique versus $\langle\mu\rangle$ It can be observed a general improvement of the resolution if diphoton TST method is used, except for tth production mode. Concerning the pileup resilience, the slopes of these distributions are

RMS of the $E_{\mathrm{T}}^{\mathrm{miss}}$ distribution.		
Production mode	Hardest vertex [GeV]	Diphoton vertex [GeV]
Gluon fusion	19.73 $\pm$ 0.02	18.29 $\pm$ 0.02
Vector-boson fusion	20.53 $\pm$0.03	20.05 $\pm$ 0.03
Associated production (WH)	21.33 $\pm$ 0.07	21.21 $\pm$ 0.07
Associated production (ZH)	21.34 $\pm$ 0.07	21.05 $\pm$ 0.07
Top-antitop production	27.92 $\pm$ 0.23	28.76 $\pm$0.24
Bottom-antibottom production	20.34 $\pm$ 0.08	20.35 $\pm$0.08

Table 6.3: RMS of the $E_{\mathrm{T}}^{\mathrm{miss}}$ distribution for the different Higgs production modes. Values are compared between diphoton vertex TST or hardest vertex TST. Both mean values are significantly different within their error intervals.

presented in Table 6.4. They tend to be larger for the hardest vertex TST except in tth production mode, which indicates a better performance for the diphoton vertex against pileup, as expected. On the other

Slope of the $E_{\mathrm{T}}^{\mathrm{miss}}$ resolution vs $<\mu>$ distribution.		
Production mode	Hardest vertex	Diphoton vertex
Gluon fusion	0.746 $\pm$ 0.005	0.661 $\pm$ 0.005
Vector-boson fusion	0.639 $\pm$ 0.007	0.598 $\pm$ 0.007
Associated production (WH)	0.360 $\pm$ 0.033	0.350 $\pm$ 0.034
Associated production (ZH)	0.394$\pm$ 0.030	0.362$\pm$ 0.030
Top-antitop production	0.285$\pm$ 0.060	0.291$\pm$ 0.062
Bottom-antibottom production	0.780$\pm$ 0.019	0.716$\pm$ 0.018

Table 6.4: Slope of the $E_{\mathrm{T}}^{\mathrm{miss}}$ resolution vs the average interaction versus the bunch crossing ($<\mu>$) for different Higgs production modes. Values are compared between diphoton vertex TST or hardest vertex TST.

hand, default JVT cut for TST reconstruction is set to 0.59. Other values could induce a better pileup resilience in $h \to \gamma\gamma$ events. Different JVT thresholds have been tested on simulated samples of ggF and VBF production modes. It can be observed on Figures 6.22 a very limited effect on the resolution slope if other working points were used. Thus, the default Jvt threshold of 0.59 is considered in the following for reconstructing TST $E_{\mathrm{T}}^{\mathrm{miss}}$.

6.4.5 $E_{\mathrm{T}}^{\mathrm{miss}}$ direction

The angle between the diphoton transverse momentum and the $E_{\mathrm{T}}^{\mathrm{miss}}$ for dominant Higgs production modes is presented in Figures 6.23. For topologies where no $E_{\mathrm{T,truth}}^{\mathrm{miss}}$ is expected, such as ggF and VBF, one expects the same number of events for all possible values of the azimuthal angle. However, it is observed in both distributions a bias using both diphoton and hardest vertex angle. A clear peak around $\Delta\phi \approx \pi$ is observed in both distributions which indicate a bias of the TST reconstruction. In addition, the VBF distribution presents another peak around $\Delta\phi \approx 0$. For samples where genuine $E_{\mathrm{T,truth}}^{\mathrm{miss}}$ is expected, diphoton vertex presents a peaked distribution around $\Delta\phi \approx \pi$ as expected. However, the performance on ggF or VBF does not allow to fully determine which method reconstructs the best the $E_{\mathrm{T}}^{\mathrm{miss}}$ direction.

References

[1] Matteo Cacciari, Gavin P. Salam, and Gregory Soyez. "The anti-k_t jet clustering algorithm". In: *JHEP* 04 (2008), p. 063. DOI: 10.1088/1126-6708/2008/04/063. arXiv: 0802.1189 [hep-ph].

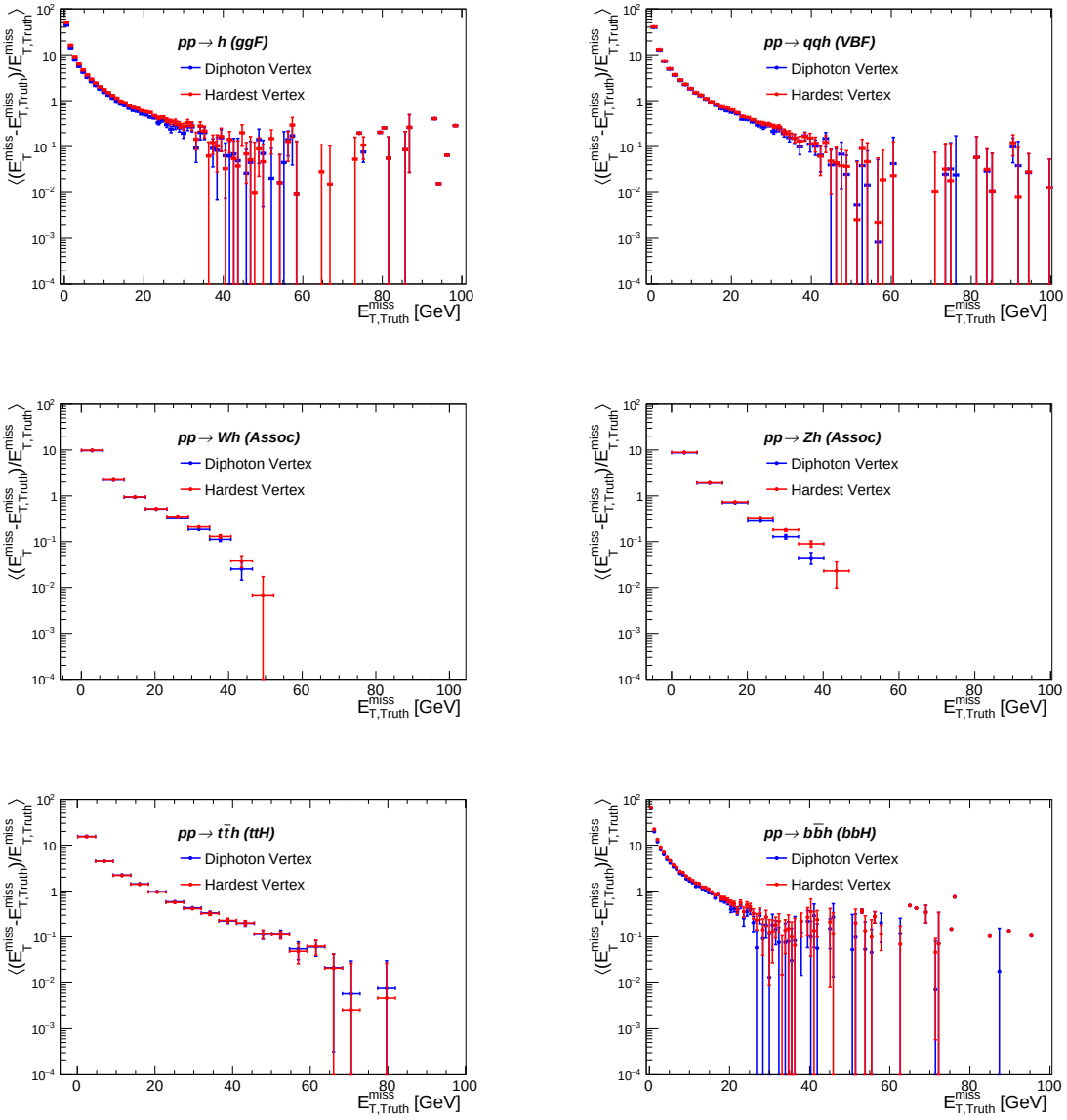


Figure 6.19: TST $E_{\mathrm{T}}^{\mathrm{miss}}$ linearity as a function of $E_{\mathrm{T,Truth}}^{\mathrm{miss}}$ for different Higgs production. TST reconstruction is compared with soft-terms either associated with the hardest vertex or to the diphoton vertex of the event.

[2] T Barillari et al. *Local Hadronic Calibration*. Tech. rep. ATL-LARG-PUB-2009-001-2. ATL-COM-LARG-2008-006. ATL-LARG-PUB-2009-001. Due to a report-number conflict with another document, the report-number ATL-LARG-PUB-2009-001-2 has been assigned. Geneva: CERN, June 2008. URL: http://cds.cern.ch/record/1112035.

[3] Georges Aad et al. "Jet energy measurement with the ATLAS detector in proton-proton collisions at $\sqrt{s} = 7$ TeV". In: *Eur. Phys. J.* C73.3 (2013), p. 2304. DOI: 10.1140/epjc/s10052-013-2304-2. arXiv: 1112.6426 [hep-ex].

[4] *Monte Carlo Calibration and Combination of In-situ Measurements of Jet Energy Scale, Jet Energy Resolution and Jet Mass in ATLAS*. Tech. rep. ATLAS-CONF-2015-037. Geneva: CERN, Aug. 2015. URL: http://cds.cern.ch/record/2044941.

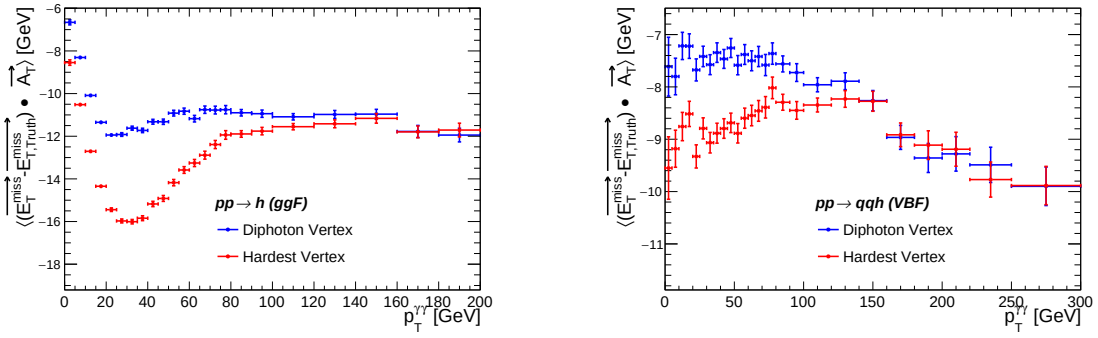


Figure 6.20: Reconstructed $E_{\mathrm{T}}^{\mathrm{miss}}$ distributions substracted from truth information for different Higgs production. TST reconstruction is compared to soft-terms either associated with the hardest vertex or to the diphoton vertex of the event.

[5] Morad Aaboud et al. "Jet energy scale measurements and their systematic uncertainties in proton-proton collisions at $\sqrt{s}$ = 13 TeV with the ATLAS detector". In: (2017). arXiv: 1703.09665 [hep-ex].

[6] Morad Aaboud et al. "Reconstruction of primary vertices at the ATLAS experiment in Run 1 proton-proton collisions at the LHC". In: *Eur. Phys. J.* C77.5 (2017), p. 332. DOI: 10.1140/epjc/s10052-017-4887-5. arXiv: 1611.10235 [physics.ins-det].

[7] ATLAS Collaboration. *Tagging and suppression of pileup jets*. ATL-PHYS-PUB-2014-001. 2014. URL: https://atlas.web.cern.ch/Atlas/GROUPS/PHYSICS/PUBNOTES/ATL-PHYS-PUB-2014-001/.

[8] A. Hoecker et al. "TMVA - Toolkit for Multivariate Data Analysis". In: *ArXiv Physics e-prints* (Mar. 2007). eprint: physics/0703039.

[9] ATLAS Collaboration. "Muon reconstruction performance of the ATLAS detector in proton-proton collision data at $\sqrt{s}$ =13 TeV". In: *Eur. Phys. J. C* 76.5 (2016), p. 292. DOI: 10.1140/epjc/s10052-016-4120-y. arXiv: 1603.05598 [hep-ex].

[10] G. Aad et al. "Expected Performance of the ATLAS Experiment - Detector, Trigger and Physics". In: (2009). arXiv: 0901.0512 [hep-ex].

[11] Jochem Snuverink. *Thesis: THE ATLAS MUON SPECTROMETER:COMMISSIONING AND TRACKING*. URL: https://www.nikhef.nl/pub/services/biblio/theses_pdf/thesis_J_Snuverink.pdf.

[12] ATLAS Collaboration. *Event Displays from Run 2 physics analyses*. URL: https://twiki.cern.ch/twiki/bin/view/AtlasPublic/EventDisplayRun2Physics.

[13] G. Aad et al. "Performance of algorithms that reconstruct missing transverse momentum in $\sqrt{s}$ = 8 TeV proton-proton collisions in the ATLAS detector". In: *Eur. Phys. J.* C77.4 (2017), p. 241. DOI: 10.1140/epjc/s10052-017-4780-2. arXiv: 1609.09324 [hep-ex].

[14] Matteo Cacciari, Gavin P. Salam, and Gregory Soyez. "The Catchment Area of Jets". In: *JHEP* 04 (2008), p. 005. DOI: 10.1088/1126-6708/2008/04/005. arXiv: 0802.1188 [hep-ph].

[15] Matteo Cacciari and Gavin P. Salam. "Pileup subtraction using jet areas". In: *Phys. Lett.* B659 (2008), pp. 119–126. DOI: 10.1016/j.physletb.2007.09.077. arXiv: 0707.1378 [hep-ph].

[16] Georges Aad et al. "Identification and energy calibration of hadronically decaying tau leptons with the ATLAS experiment in *pp* collisions at $\sqrt{s}$=8 TeV". In: *Eur. Phys. J.* C75.7 (2015), p. 303. DOI: 10.1140/epjc/s10052-015-3500-z. arXiv: 1412.7086 [hep-ex].

[17] *Data-driven determination of the energy scale and resolution of jets reconstructed in the ATLAS calorimeters using dijet and multijet events at* $\sqrt{s} = 8\ TeV$. Tech. rep. ATLAS-CONF-2015-017. Geneva: CERN, Apr. 2015. URL: https://cds.cern.ch/record/2008678.

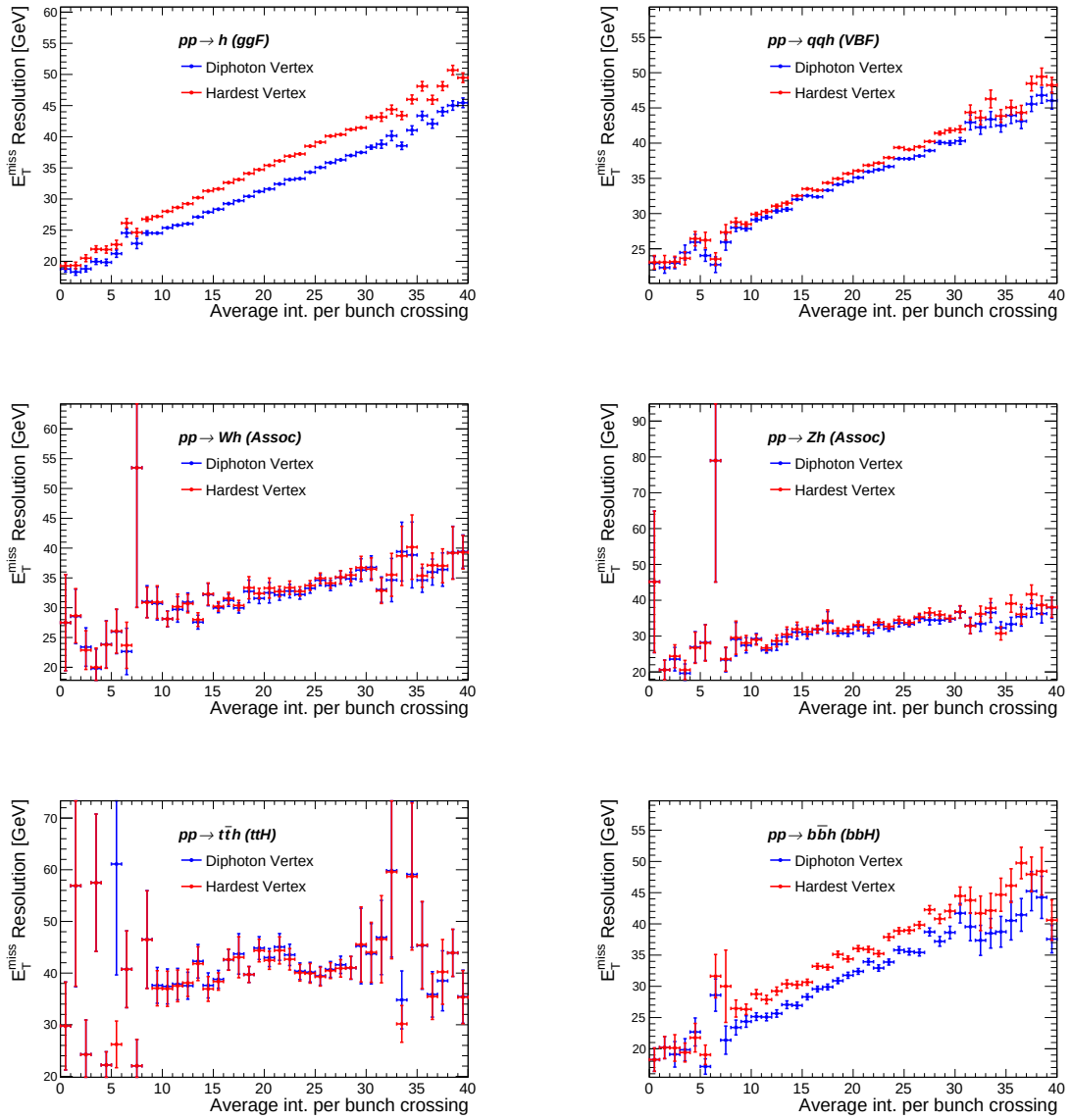


Figure 6.21: $E_{\mathrm{T}}^{\mathrm{miss}}$ resolution estimated as the RMS of the $E_{\mathrm{T}}^{\mathrm{miss}}$ distribution depending on the average number of interactions per bunch crossing. Truth information is substracted and TST reconstruction is compared to soft-terms either associated with the hardest vertex or to the diphoton vertex of the event.

[18] *Expected performance of missing transverse momentum reconstruction for the ATLAS detector at $\sqrt{s} = 13$ TeV*. Tech. rep. ATL-PHYS-PUB-2015-023. Geneva: CERN, July 2015. URL: http://cds.cern.ch/record/2037700.

[19] The ATLAS Collaboration. *Missing transverse energy performance and systematic uncertainties using the full 2015 dataset*. URL: http://atlas.web.cern.ch/Atlas/GROUPS/PHYSICS/PLOTS/JETM-2016-003/.

[20] M Escalier, L Fayard, and J-F Marchand. *Reconstruction of the z vertex and direction of the photon*. Tech. rep. ATL-COM-PHYS-2009-614. Geneva: CERN, Nov. 2009. URL: https://cds.cern.ch/record/1222687.

[21] Bruno Lenzi and David Delgove. *Selection of the diphoton production vertex using multivariate techniques for $H \to \gamma\gamma$ and other analyses*. Tech. rep. ATL-COM-PHYS-2015-1321. Geneva: CERN, Oct. 2015. URL: https://cds.cern.ch/record/2062239.

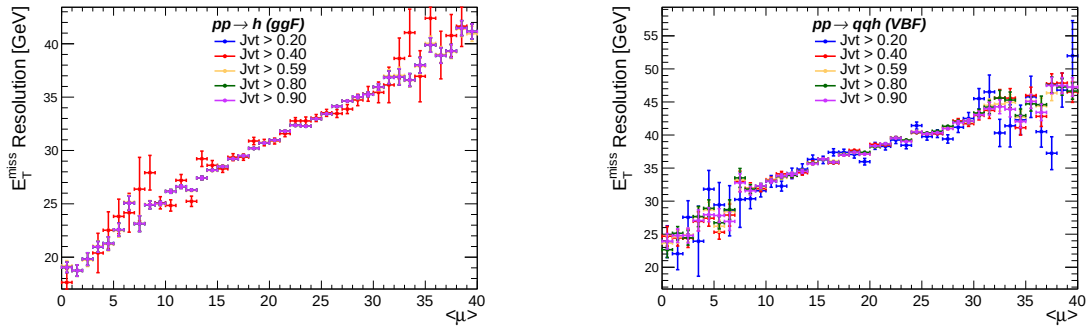


Figure 6.22: Dependence of $E_{\mathrm{T}}^{\mathrm{miss}}$ resolution as a function of the jet-vertex-tagger cut applied to central jets of the event ($20\ \mathrm{GeV} < \mathrm{p_T} < 60\ \mathrm{GeV}$, $|\eta| < 2.4$). Resolution is shown versus the average number of interactions per bunch crossing. Truth $E_{\mathrm{T}}^{\mathrm{miss}}$ is substracted and soft-terms are computed using tracks associated with the diphoton vertex of the event.

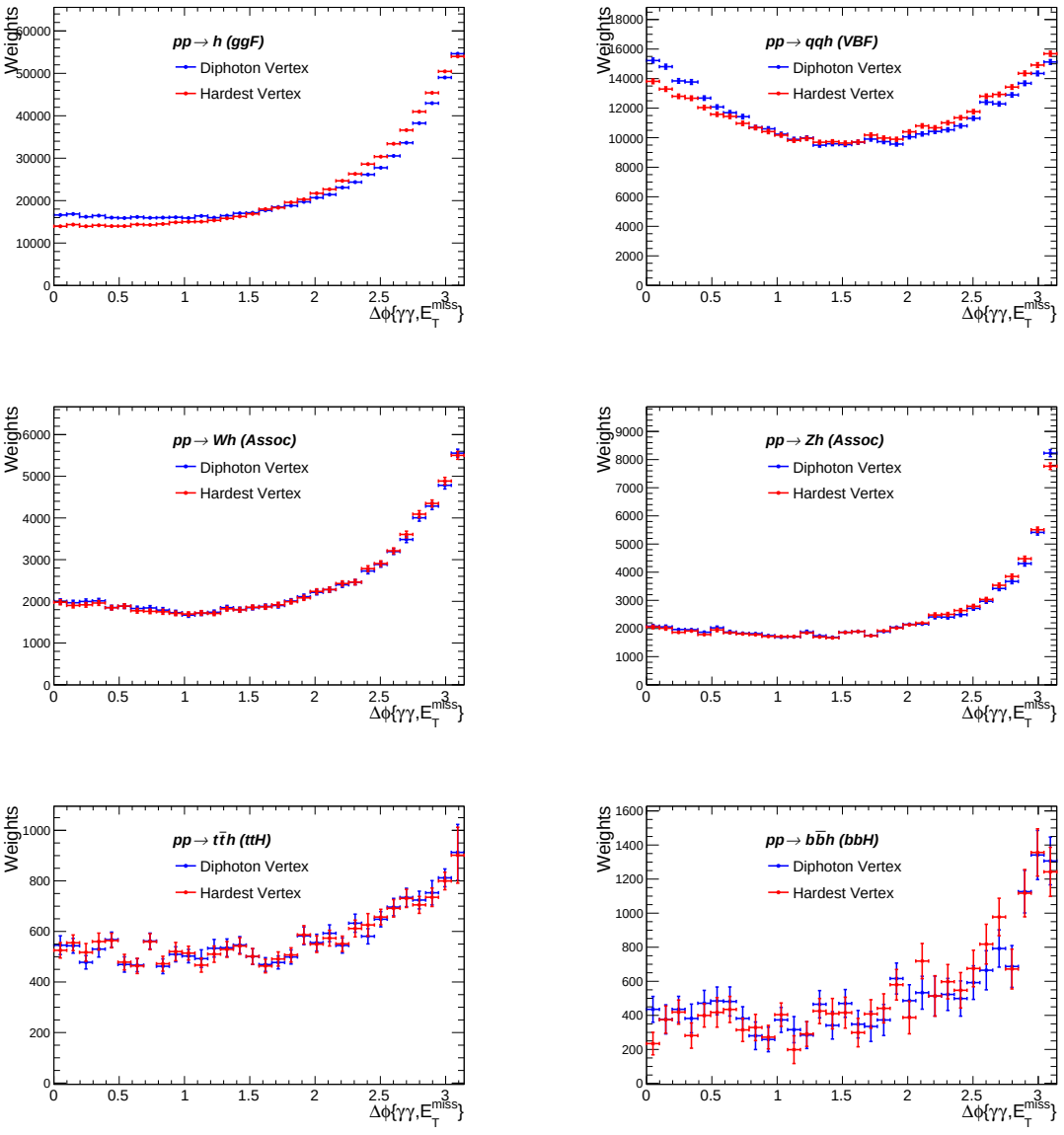


Figure 6.23: Distributions of the relative azimuthal angle between the diphoton transverse momentum and the $E_{\mathrm{T}}^{\mathrm{miss}}$ either computed from either hard or diphoton vertex TST $E_{\mathrm{T}}^{\mathrm{miss}}$. No truth information is substracted.

DM production in $h \to \gamma\gamma + E_{\mathrm{T}}^{\mathrm{miss}}$ channel

Contents

7.1 Data and simulated samples . . . 170
7.1.1 Signal samples . . . 170
7.1.2 Resonant background samples . . . 171
7.1.3 Non-resonant background samples . . . 175
7.2 Event reconstruction and selection . . . 176
7.2.1 Event reconstruction and pre-selection . . . 176
7.2.2 Event selection . . . 177
7.3 Categorization . . . 178
7.3.1 Optimization of the Mono-Higgs category . . . 178
7.3.2 Optimization of the heavy-scalar categories . . . 187
7.3.3 Final categorization . . . 188
7.4 Analysis strategy . . . 188
7.4.1 Signal and SM Higgs parametrization . . . 190
7.4.2 Non-resonant background parametrization . . . 190
7.5 Systematic uncertainties . . . 197
7.5.1 Theoretical systematic uncertainties . . . 197
7.5.2 Experimental systematic uncertainties . . . 199
7.6 Results . . . 201
7.6.1 Limits on the visible cross-section . . . 204
7.6.2 DM reweighting . . . 205
7.6.3 Interpretations of the Z'_B and Z'-2HDM models . . . 207
7.6.4 Interpretation of the heavy-scalar model . . . 211
7.7 Comparison of the ATLAS $h \to \gamma\gamma + E_{\mathrm{T}}^{\mathrm{miss}}$ with other measurements . . . 215
7.7.1 Mono-Higgs ATLAS $h \to b\bar{b}$ results . . . 215
7.7.2 CMS $h \to \gamma\gamma$ results . . . 217

The discovery of a particle consistent with a Standard Model (SM) Higgs boson in 2012 by the ATLAS [1] and CMS [2] collaborations has opened up new possibilities in searches for physics beyond the SM (BSM). The analysis presented here examines the case when a significant missing transverse momentum is produced in association with a Higgs boson. The Higgs boson decay into two photons is chosen to benefit from the high-resolution measurements of photons, which leads to a more precise Higgs mass reconstruction. This allows fighting against background contributions. This search is performed using full 2015-2016 ATLAS dataset of 36.1 fb^{-1} collected at $\sqrt{s} = 13$ TeV. Events passing selection criteria are classified into several categories in order to increase the sensitivity of the analysis to observe BSM phenomena. Signal yields from the benchmark models are then estimated through a fit of the data $m_{\gamma\gamma}$ spectrum in the different categories around the SM Higgs boson mass ($m_{\gamma\gamma} = 125.09$ GeV). As it will be explained later, the DM simplified models signal yields are estimated by fitting one of the categories while heavy scalar signal yields are deduced from a fit in all categories. All these details concerning the analysis may be found in Ref. [3].

The optimization and the interpretation of the analysis results is based on the three models explained in Section 1.5 (Z'_B, Z'-2HDM and heavy scalar models). This is chapter is organized as follows: data

collection and simulation procedure are described in Section 7.1. In Section 7.2, object and event selection are detailed. In Section 7.3, a complete description of the event categorization is presented. In Section 7.4, signal and background parametrization are explained. Main theoretical and experimental systematics are shown in Section 7.5. Results for this search are presented in Section 7.6. Finally, Section 7.7 compares the final results in $h \to \gamma\gamma$ channel with most recent results from ATLAS $h \to b\bar{b}$ and CMS $h \to \gamma\gamma$ channels.

7.1 Data and simulated samples

The analysis uses pp collision data with a bunch crossing interval of 25 ns, collected in 2015 and 2016 at $\sqrt{s} = 13$ TeV with the ATLAS detector (Chapter 2). Only events that were recorded when relevant detector components were functioning properly are considered. Events are collected using a diphoton trigger (Section 2.2.5) requiring two reconstructed photon candidates with transverse energies of at least 35 and 25 GeV for the E_{T}-ordered leading and sub-leading photons, respectively. In addition, a loose online identification criteria must be satisfied by those photons. The trigger efficiency with respect to the offline-reconstructed photons is 99% using the same method as described in Ref. [4]. The data sample corresponds to an integrated luminosity of $36.1\ \mathrm{fb}^{-1}$.

Simulation of signal and background processes are used to optimize the selection criteria, evaluate uncertainties and study the shape of the signal and background ($m_{\gamma\gamma}$) distribution, although the final statistical analysis uses data-driven normalization to extract background contribution. In this search for DM particles, three signal model are simulated for different values of their parameters of interest, as explained in Section 1.5. The dominant backgrounds are resonant SM $h \to \gamma\gamma$, and non-resonant $\gamma\gamma$, γ+jet, $W\gamma$, $Z\gamma$, $W\gamma\gamma$ and $Z\gamma\gamma$ productions.

7.1.1 Signal samples

Signal events from Z'_B, Z'-2HDM, and the heavy-scalar models are generated using MADGRAPH 5_aMC@NLO 2.2.3 [5] at leading order (LO) in QCD using the NNPDF3.0LO [6] parton distribution function (PDF) sets. Parton showering and hadronization are handled by the PYTHIA 8 [7] event generator with the A14 [8] set of tuned parameters (tune), using the NNPDF2.3LO PDF sets [9].

- **Simulation of heavy-scalar model**

  For the heavy-scalar model, events are generated for different values of m_{H} in steps of 10 GeV in the interval $260 \leq m_{\mathrm{H}} \leq 270$ GeV and $300 \leq m_{\mathrm{H}} \leq 350$ GeV and in steps of 5 GeV in the interval $270 \leq m_{\mathrm{H}} \leq 300$ GeV for $m_{\chi} = 50, 60$ GeV.

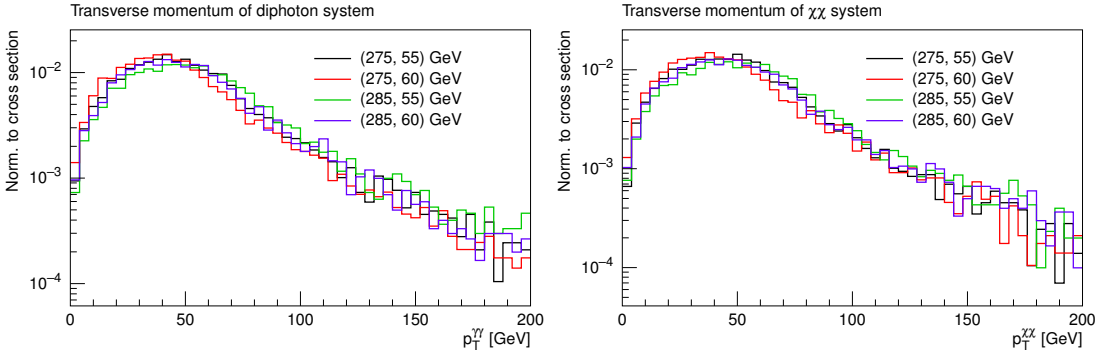


Figure 7.1: Heavy scalar model comparison for several mass points in the [m_{H} m_{χ}] plane.

Given that the heavy-scalar model predicts the production of the heavy-scalar intermediate state through gluon-fusion mediated by an effective coupling of type $\beta_g \kappa_{hgg}^{SM}$ (Section 1.5), simulated

samples are normalized using the cross-sections of the ggF SM Higgs like particle at the same mass at NNLO+NNLL.

- **Simulation of Z'_B model**

  MC samples for the Z'_B model are generated assuming a DM mass m_χ between 1 to 1000 GeV and a range of mediator masses $m_{Z'_B}$ from 1 to 2000 GeV. Figures 7.2 show that the larger is the simulated $m_{Z'_B}$ the wider are the $p_{\mathrm{T}}^{\gamma\gamma}$ and $E_{\mathrm{T}}^{\mathrm{miss}}$ distributions for a fixed mass of the dark matter particle. In addition, azimuthal angular distance $\Delta\phi(\gamma_1, \gamma_2)$ between the two leading photons tend to be reduced as higher $m_{Z'_B}$, following a more back-to-back configuration between the diphoton system and $E_{\mathrm{T}}^{\mathrm{miss}}$. This highlights a more boosted topology at higher $m_{Z'_B}$. On the other hand, an increase of m_χ also tend to boost two both photons, as it could be expected due to the increasing recoil against the Higgs particle. It needs to be noticed that off-shell Z'_B configurations show less dependent kinematic distributions on $m_{Z'}$ than on-shell ones. The Z'_B model samples are normalized to the LO cross-sections predicted by MADGRAPH 5_aMC@NLO 2.2.3.

- **Simulation of $Z'-$2HDM model**

  Similarly, the MC samples for the Z'-2HDM model are generated for ranges of the mediator mass $m_{Z'} = 400$ to 1400 GeV and pseudoscalar boson mass $m_{A^0} = 200$ to 800 GeV for which the search is sensitive with the present dataset. Due to the required on-shell decay of the A^0 boson, kinematic distributions in this model are different in Z'_B. In particular, they tend to present higher $E_{\mathrm{T}}^{\mathrm{miss}}$ and $p_{\mathrm{T}}^{\gamma\gamma}$ and therefore, high cuts on $E_{\mathrm{T}}^{\mathrm{miss}}$ induce a larger discriminant power for this model than for Z'_B one. Kinematics is dependent on the $m_{Z'}$ -m_{A^0} difference. The smaller this difference is, the harder $E_{\mathrm{T}}^{\mathrm{miss}}$ and $p_{\mathrm{T}}^{\gamma\gamma}$ and the less boosted diphoton system. In general, a significant fraction of events is present at $E_{\mathrm{T}}^{\mathrm{miss}} > 100$ GeV although this could be different for $m_{Z'} < 600$ GeV, given that $E_{\mathrm{T}}^{\mathrm{miss}}$ is reduced at lower $m_{Z'}$ and m_{A^0}. In this region of the parameter space, $E_{\mathrm{T}}^{\mathrm{miss}}$ and $p_{\mathrm{T}}^{\gamma\gamma}$ can present similar shapes as if they were produced by the heavy-scalar model [10]. Dedicated studies are performed in the Appendix B demonstrating that, despite the similarities between both models, kinematics distributions disagree and therefore they are treated as two separate models interesting to consider. The Z'_B model samples are normalized to the LO cross-sections predicted by MADGRAPH 5_aMC@NLO 2.2.3.

Detector effects are simulated using a fast-simulation of the ATLAS detector, developed inside the ATLAS collaboration and known as AtlFastII [11]. Pileup effects are also included in the simulation by overlaying generated events with a minimum-bias sample produced using PYTHIA 8 and EvtGen [12] with the MSTW2008LO PDF sets and the A2 [13] tune.

7.1.2 Resonant background samples

The resonant background is associated with all the Standard Model production processes with a Higgs boson h in the final state as detailed in Section 1.2.1. These samples are normalized to the cross-sections presented in Table 1.3, calculated up to high orders of QCD. Different generators are specialized to simulate each Higgs production sample with the highest possible precision:

- **Gluon-gluon fusion (ggF) process** is the dominant production of the SM Higgs at $m_h = 125.09$ GeV. The ggF sample is generated by POWHEG-BOX 2 [14, 15, 16, 17] at next-to-leading order in QCD and interfaced to PYTHIA 8 with the AZNLO [18] tune and the CT10 PDF set [19]. This contribution dominates the resonant background when no requirement is applied on $E_{\mathrm{T}}^{\mathrm{miss}}$. A fake imbalance may be created in the total transverse momentum sum mainly due to jet and soft-terms mismeasurements. A significant number of events present low and intermediate $E_{\mathrm{T}}^{\mathrm{miss}}$ values, implying the dominance of this process also in categories where intermediate $E_{\mathrm{T}}^{\mathrm{miss}}$ values are scanned. Besides, the ggF contribution becomes a secondary contribution to resonant background at large values of $E_{\mathrm{T}}^{\mathrm{miss}}$. However, this constitutes an irreducible background.

- **Vector-boson fusion (VBF) process** is the second dominant production mode of the SM Higgs, with two forward jets in the final state. The VBF sample is generated by POWHEG-BOX 2 [14, 15,

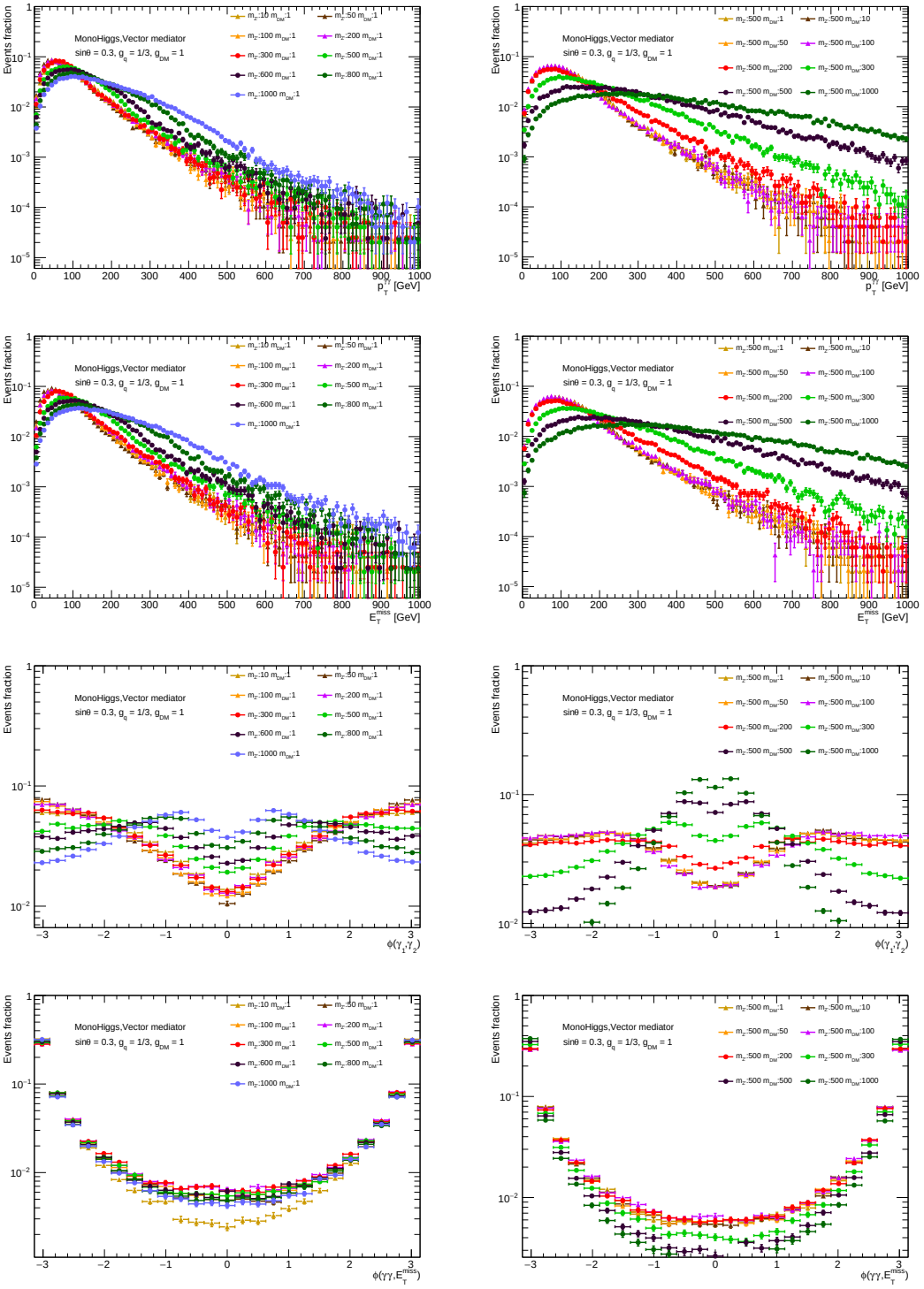


Figure 7.2: Z'_B model comparison for several mass points in the [$m_{Z'_B}$ m_χ] plane (g_q = 1/3, g_{DM} = 1 and sinθ = 0.3). Left column: comparison for a fixed m_χ. Right column: comparison for a fixed $m_{Z'_B}$. The two rows on the top present the $p_{\mathrm{T}}^{\gamma\gamma}$ and $E_{\mathrm{T}}^{\mathrm{miss}}$ distributions for different simulated samples. It can be observed that at larger $m_{Z'_B}$ and m_χ, both distributions tend to higher values. Concerning the two bottom rows, they present the angular azimuthal difference between the two photons direction and the diphoton system and the $E_{\mathrm{T}}^{\mathrm{miss}}$. It can be observed that at larger $m_{Z'_B}$ and m_χ, the former distribution tend to peak at values closer to zero, indicating that both photons are closer (more boosted). This is not the case however, while $m_{Z'_B} \gtrsim m_\chi$, in which case both photons tend to be separated given that the intermediate h momentum should not be high. The latter present lower number of events in the central region and a more defined peak at π at larger $m_{Z'_B}$ and m_χ difference, which indicates a larger back-to-back topology between the $\gamma\gamma$ and the $\chi\bar{\chi}$ systems.

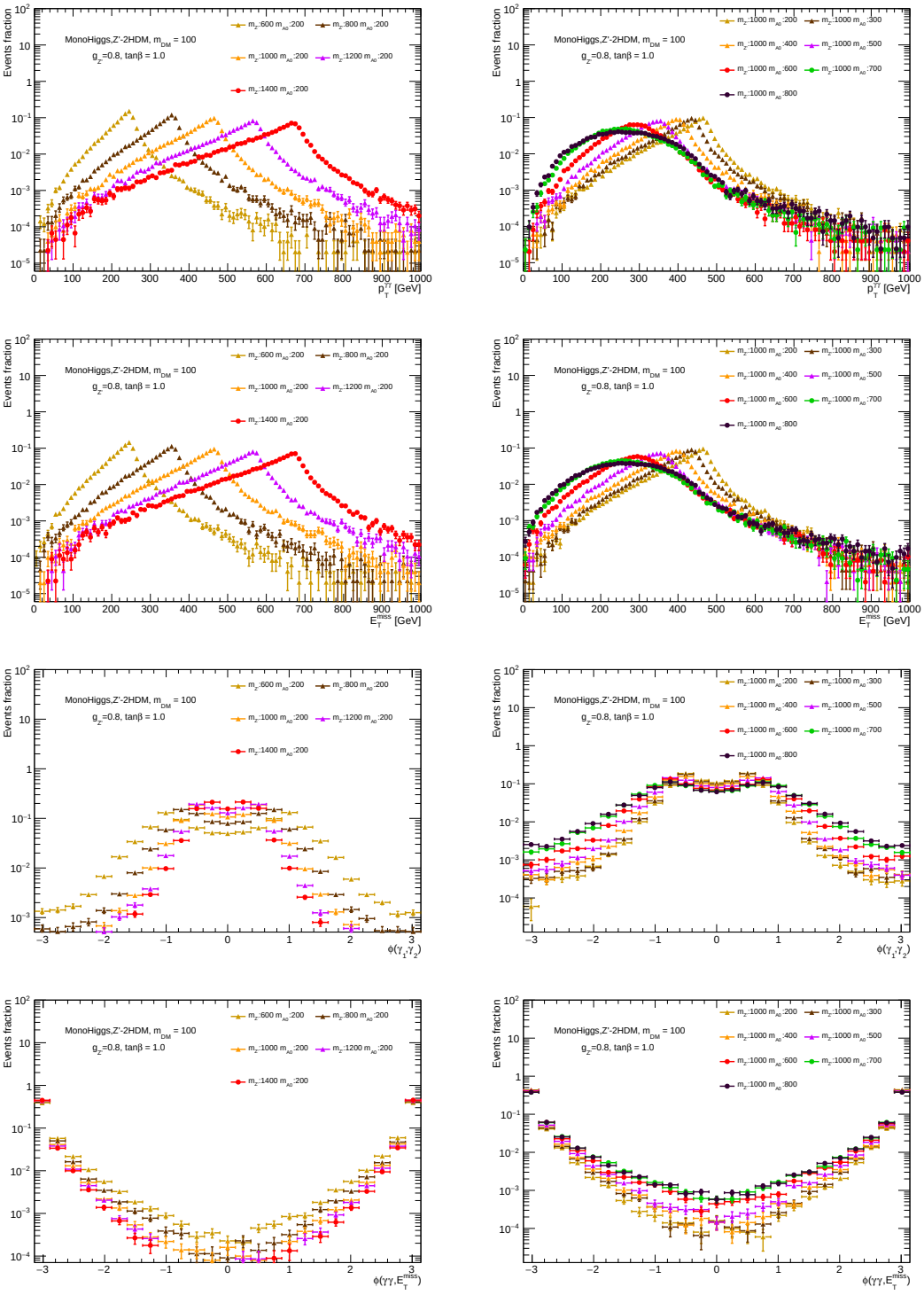
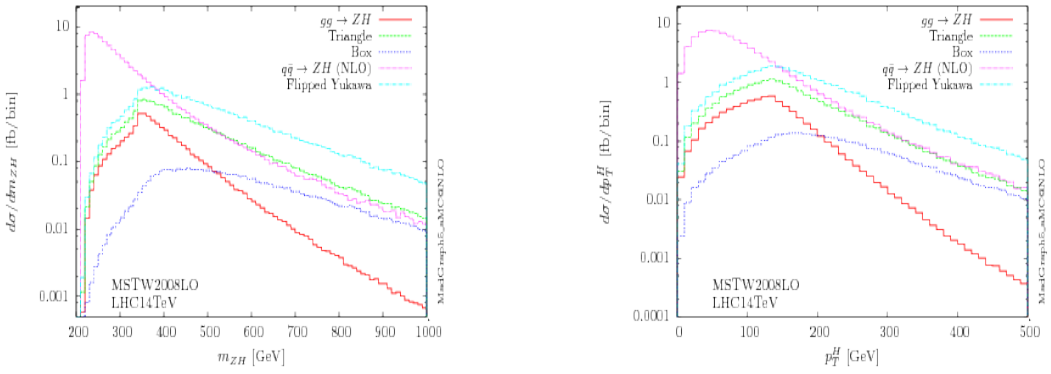


Figure 7.3: Z'-2HDM comparison for several mass points in the [$m_{Z'}$ m_{A^0}] plane ($g_{Z'}$ = 0.8, tanβ = 1.0 and $m_\chi = 100$GeV) Left column: comparison for a fixed m_{A^0}. Right column: comparison for a fixed $m_{Z'}$. The two rows on the top present the $p_{\mathrm{T}}^{\gamma\gamma}$ and $E_{\mathrm{T}}^{\mathrm{miss}}$ distributions for different simulated samples. It can be observed that at larger $m_{Z'}$ -m_{A^0} difference, harder are the kinematic distributions. Concerning the two bottom rows, they present the angular azimuthal difference between the two photons direction and the diphoton system and the $E_{\mathrm{T}}^{\mathrm{miss}}$. It can be observed that at larger $m_{Z'}$ -m_{A^0} difference, the former distribution tend to peak at values closer to zero, indicating that both photons are closer (more boosted). The latter present lower number of events in the central region and a more defined peak at π at larger $m_{Z'}$ -m_{A^0} difference, which indicates a larger back-to-back topology between the $\gamma\gamma$ and the $\chi\bar{\chi}$ systems.

16, 17] interfaced to PYTHIA 8 with the AZNLO [18] tune and the CT10 PDF set [19], as the ggF sample. Similarly to the ggF contribution, its $E_{\mathrm{T}}^{\mathrm{miss}}$ is mainly due to fake contributions. It also constitutes the irreducible background of the present search.

- **Associated production (Vh) process** , where V stands for W or Z bosons, corresponds to another important Higgs production mode, being the dominant source of background at high values of $E_{\mathrm{T}}^{\mathrm{miss}}$ of the present analysis. This contribution has two initial state configurations: gluon-fusion ($gg \to Zh$) or quark annihilation ($q\bar{q} \to Vh$). Quark annihilation samples are generated using PYTHIA 8 with the A14 tune and the NNPDF2.3LO PDF set. Gluon-fusion production is generated instead using POWHEG-BOX 2 with NNPDF3.0 due to the presence of a quark-loop, which is not correctly handled by PYTHIA 8. In this case, parton shower is performed with PYTHIA 8 with AZNLO tune. Figure 7.4 shows a comparison of the expected differential cross-sections between both production modes, as presented in [20], where simulations are performed using MADGRAPH 5_aMC@NLO. Inclusive (hadronic and leptonic) vector-boson decays are considered. In this case,



(a) (b)

Figure 7.4: Comparison between $q\bar{q} \to Zh$ and $gg \to Zh$ production [20]. $gg \to Zh$ process tend to present higher production rate at larger values of (a) m_{Zh} and (b) p_{T}^{H}, mainly due to the present of soft-QCD radiation (from the quark-loop or the colliding gluons) recoiling against the Higgs. Both contributions presented in these figures are generated at NLO+PS.

the leptonic decay channel is a reducible background for the DM search that can be removed by applying a lepton veto to the event. The other contributions are included in the irreducible background.

- **Top-antitop ($t\bar{t}h$) production.** The $t\bar{t}h$ events are generated withMADGRAPH 5_aMC@NLO 2.2.3 [5] interfaced to PYTHIA 8 with the NNPDF3.0LO [6] PDF set. The contribution of this sample is negligible in front of the other production modes, at low-$E_{\mathrm{T}}^{\mathrm{miss}}$ regions, mainly due to its small cross-section. However, in high-$E_{\mathrm{T}}^{\mathrm{miss}}$ regions, this contribution may become larger than production modes where no genuine DM is expected, e.g. ggF and VBF, due to the possible production of neutrinos from W boson leptonic decays issued from the t-quark decay.

- **Bottom-antibottom ($b\bar{b}h$) production.** The sample of $b\bar{b}h$ is generated by MADGRAPH 5_aMC@NLO 2.2.3 interfaced to PYTHIA 8 with the A14 tune and the NNPDF2.3LO PDF set. The contribution of this sample is negligible with respect to the other Higgs production modes due to its low expected cross-section.

Detector effects are implemented using a full simulation [11] of the ATLAS detector using Geant4 [21]. This procedure has the advantage of performing a more accurate simulation of the particles interaction with the detector compared to AtlFastII. This accuracy is needed at least on the SM Higgs samples, provided that they are the most important irreducible background contributions and no background shape nor normalization can be directly extracted from data. In addition, pileup effects are also included using the same method than for signal samples.

7.1.3 Non-resonant background samples

Non-resonant background is composed of all processes that are or mimic events with two photons in the final state but that are not expected to provide a resonant structure in the $m_{\gamma\gamma}$ spectrum. In $h \to \gamma\gamma$ searches, these backgrounds can be determined by fitting the sidebands of the $m_{\gamma\gamma}$ spectrum ($[105, 120] \bigcup [130, 160]$GeV) Section 7.4 around the Higgs resonance. However, the parametrization of the background is performed using MC samples to allow a subsequent study of the systematic uncertainties:

- **Diphoton background ($\gamma\gamma$)**

  Diphoton production is the dominant source of background at low and intermediate $E_{\mathrm{T}}^{\mathrm{miss}}$ regions due to its high cross-section and to the high efficiency of these backgrounds to pass selection the analysis selection (see Section 7.2.2). At large $E_{\mathrm{T}}^{\mathrm{miss}}$, its contribution is very limited since no non-interacting recoiling particle is produced in this process, where $E_{\mathrm{T}}^{\mathrm{miss}}$ only results from experimental effects. Large $E_{\mathrm{T}}^{\mathrm{miss}}$ is generated from misidentification of pileup jets or by mismeasurement of the photons energy or $E_{\mathrm{T}}^{\mathrm{miss}}$ soft-terms. Samples are simulated using SHERPA 2.1.1 [22] with CT10 tuning. Matrix elements are calculated with up to three hard partons at LO and merged with the SHERPA parton shower [23] using the ME+PS@LO prescription [24]. The CT10 PDF set is used in conjunction with a dedicated parton shower tuning developed by SHERPA authors. The main Feynman diagrams of this process are presented in Fig. 7.5:

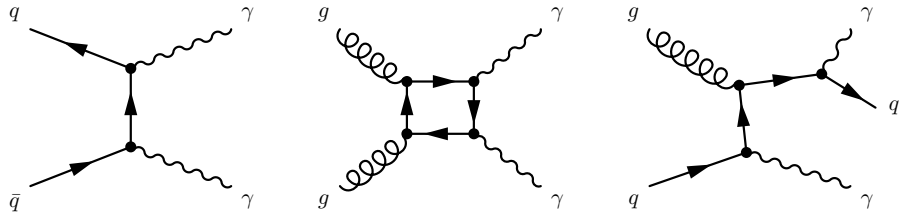


Figure 7.5: Dominant Feynman diagrams of the $\gamma\gamma$ background.

- **γ+jet background**

  This process is the second dominant contribution of the SM non-resonant background. It is due to the misidentification of a hard-jet in the event as a photon, thus representing the first reducible background. In contrast to irreducible $\gamma\gamma$ background, its relative contribution is expected to increase at larger $E_{\mathrm{T}}^{\mathrm{miss}}$ since a misidentification of the hard jet as a photon would induce an imbalance in the final p_{T} sum due to the miscalibration of the jet. Simulated samples are produced using PYTHIA 8 together with the NNPDF23 at LO and A14 tune. The main processes diagram are shown in Fig 7.6

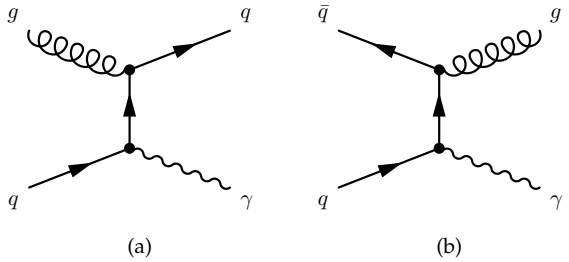


Figure 7.6: Dominant Feynman diagrams of the γj background.

- **$V\gamma\gamma$ and $V\gamma$**

These reducible backgrounds are generated using SHERPA 2.1.1 with CT10 PDF set. The $V\gamma$ contribution comes from the misidentification of one of the electrons from the vector boson reconstructed as a photon due to track reconstruction inefficiency. Their contribution at low and intermediate $E_{\mathrm{T}}^{\mathrm{miss}}$ is negligible, accounting for less than 1 % of the total background. Instead, at high $E_{\mathrm{T}}^{\mathrm{miss}}$, neutrino decays of the Z boson and the leptonic decays of the W boson imply that these processes become non-negligible, since $\gamma\gamma$ and γ+jet contributions drastically decrease in that region. Their leading order diagrams are shown in Fig 7.7:

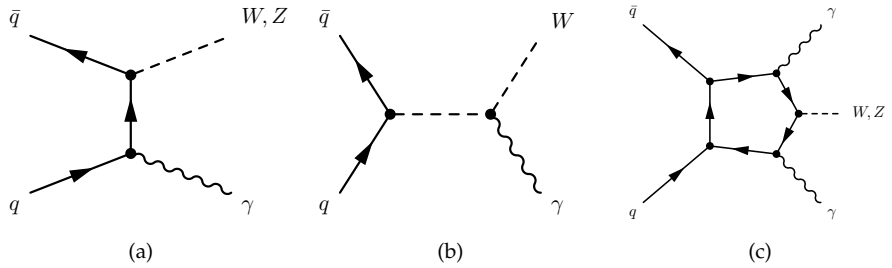


Figure 7.7: Dominant Feynman diagrams of the $V\gamma$(a,b) and $V\gamma\gamma$ (c) backgrounds.

- **Other background samples**

  Other possible background samples contributing to these final states are the dijet (jj) process, Drell-Yan and the $t\bar{t}\gamma$ processes. These backgrounds are simulated due their low expected rate at intermediate and high $E_{\mathrm{T}}^{\mathrm{miss}}$ regions, although they are present in the collected data.

Diphoton sample is passed to AtlFast II for fast-simulation and γ+jet, Vγ and V$\gamma\gamma$ samples are reconstructed using full detector simulation. Pileup effects are simulated according to the procedure used for SM Higgs samples.

7.2 Event reconstruction and selection

In each event, the observed final state is reconstructed from physics objects (photons, leptons, jets and $E_{\mathrm{T}}^{\mathrm{miss}}$) which are built combining the related measurements provided by the various subdetectors of the ATLAS experiment. Object reconstruction, identification and calibration procedures are described in Chapter 4 and Chapter 6.

7.2.1 Event reconstruction and pre-selection

The event reconstruction and pre-selection applied in this analysis corresponds to the common selection criteria used in the ATLAS $h \to \gamma\gamma$ group. Tight identification criteria are applied to photons, which constitute the main objects of the selection, while looser selection criteria are applied to electrons, muons and jets.

Reconstructed photons are required to pass tight identification criteria. In addition, photons are considered if they satisfy $E_{\mathrm{T}} > 25$ GeV and $|\eta| < 2.37$ excluding the electromagnetic calorimeter "crack" region ($1.37 < |\eta| < 1.52$), which leads to an identification efficiency of 85%, as presented in Section 4.3.2. Tight isolation criteria is also required, considering a E_T dependent calorimetric isolation topoetcone20 $< 0.065\ E_T$ (Section 4.4.1) and a track isolation ptcone$< 0.05\ E_T$ (Section 4.4.2). This isolation criterion leads to an overall 82%-90% efficiency on SM Higgs production modes, evaluated on simulated MC samples [25].

Electrons are required to satisfy $|\eta| < 2.47$, excluding the EM calorimeter transition region $1.37 < |\eta| < 1.52$, and to have $p_{\mathrm{T}} > 10$ GeV. The LH Medium criteria (Section 4.3.1) is applied, providing an identification efficiency from 85% to 95% as a function of E_{T} [26]. Loose calorimeter and track isolation requirements are applied to electrons. The combined efficiency in the inclusive diphoton sample of the isolation requirements is 98% [27].

Muons are required to have $p_{\mathrm{T}} > 10$ GeV and $|\eta| < 2.7$ [28]. The muon candidates are also required to pass calorimeter and track isolation criteria which lead on overall to a muon identification efficiency of 96% [29]. The combined isolation efficiency is between 95% to 99% as a function of p_{T} from 25 GeV to 60 GeV [29].

The diphoton primary vertex is selected according to Section 6.4.1. Photon pseudorapidity and p_{T} ($p_{\mathrm{T}}^{\gamma} = E^{\gamma}/cosh\eta^{\gamma}$) are recalculated with respect to the diphoton vertex. In addition, electron and muon tracks are required to be compatible as originating from the diphoton vertex, by requiring that their track transverse impact parameter significance ($|d_0|/\sigma_{d_0}$) with respect to the diphoton primary vertex, is less than 5.0 for electrons and 3.0 for muons. Furthermore, their longitudinal impact parameter z_0 must satisfy $|z_0| \sin\theta < 0.5$ mm, where θ is the polar angle of the track with respect to the beamline at the vertex.

Jets are reconstructed from three-dimensional topological clusters using the anti-k_t algorithm [30] with a radius parameter of $R = 0.4$. They are initially calibrated at the electromagnetic scale and are recalibrated using the process explained in Section 6.1. Jets are required to have $p_{\mathrm{T}} > 25$ GeV and $|\eta| < 4.4$. In addition, jets within $|\eta| < 2.4$ and $p_{\mathrm{T}} < 60$ GeV must pass a JVT > 0.59, which dedicated studies in [31] demonstrated to allow the proper identification of 92% of all hard-jets on average.

$E_{\mathrm{T}}^{\mathrm{miss}}$ is reconstructed using the TST reconstruction scheme, as discussed in Section 6.3. Selected photons, electrons and muons are included in this calculation. Jets are included if $p_{\mathrm{T}} > 20$ GeV and $|\eta| < 4.4$. Soft-terms are reconstructed from tracks associated with the primary vertex. Central jets ($|\eta| < 2.4$ and $p_{\mathrm{T}} < 60$ GeV) and not passing the JVT condition (JVT > 0.59) are included in the soft-term calculation.

Finally, an overlap removal after $E_{\mathrm{T}}^{\mathrm{miss}}$ calculation is applied on selected objects to remove possible particle misidentification. Candidate electrons, muons or jets are removed if they are found within a cone of $\Delta R = 0.4$ around a photon candidate. In addition, jets are removed if they are found within a cone of $\Delta R = 0.2$ around an electron candidate, and electrons and muons are removed if they are found inside a cone of size $\Delta R = 0.4$ around a jet.

7.2.2 Event selection

Pairs of photons are combined to form Higgs boson candidates used in the analysis. From these sample, only events that were recorded when relevant detector components were functioning properly, are considered. Selection requirements are further applied to photon pairs to increase the selection of good event candidates:

- Events are collected using a diphoton trigger requiring two reconstructed photon candidates with transverse energies (E_{T}) of at least 35 and 25 GeV for the E_{T}-ordered leading and sub-leading photons, respectively. In addition, a loose online identification criteria (Section 2.2.5) must be satisfied by those photons. The trigger efficiency with respect to the offline-reconstructed photons is 99% using the same method as described in Ref. [4].
- Diphoton candidates are further required to present an invariant mass within the range $105\ \mathrm{GeV} < \mathrm{m}_{\gamma\gamma} < 160\ \mathrm{GeV}$, where $m_{\gamma\gamma}$ is the invariant mass of the two selected photons and is calculated assuming that the photons originate from the common diphoton primary vertex. Ths cut allows a fit of the $m_{\gamma\gamma}$ where background is constraint on the sidebands and signal is searched in the region of interest, usually fixed to $120\ \mathrm{GeV} < \mathrm{m}_{\gamma\gamma} < 130\ \mathrm{GeV}$.
- Both photons issued from a Higgs decay tend to present momentum distributions at larger p_{T} than other SM processes. The leading and sub-leading photon candidates are then requested to fulfill

$E_{\mathrm{T}}^{\gamma}/m_{\gamma\gamma} > 0.35$ and 0.25, respectively.

In addition, quality criteria are applied to the jets, and events with jets consistent with noise in the calorimeter or non-collision backgrounds are vetoed [32].

7.3 Categorization

Events passing the selection criteria are further divided into categories optimizing the possibility of finding signals predicted by each model, in order to allow an increase of sensitivity to a possible excess from heavy-scalar or Mono-Higgs signals in the intermediate ($\sim$ 50 GeV) and large $E_{\mathrm{T}}^{\mathrm{miss}}$ (> 90 GeV) regions. As explained in Sections 1.5 and 7.1,the heavy-scalar spectra of $E_{\mathrm{T}}^{\mathrm{miss}}$ and $p_{\mathrm{T}}^{\gamma\gamma}$ are typically shifted to smaller values, thus this interpretation is more sensitive to excesses in events with intermediate $E_{\mathrm{T}}^{\mathrm{miss}}$ although it presents also a significant number of events at large $E_{\mathrm{T}}^{\mathrm{miss}}$. In contrast, Z'_B and Z'-2HDM models only predict a significant DM production at high values of $E_{\mathrm{T}}^{\mathrm{miss}}$ and $p_{\mathrm{T}}^{\gamma\gamma}$. Intermediate and large $E_{\mathrm{T}}^{\mathrm{miss}}$ regions are categorized using the heavy-scalar model since they present a sizeable sensitivity in all regions. However, the very high $E_{\mathrm{T}}^{\mathrm{miss}}$ region is categorized using the Mono-Higgs signal samples given that the sensitivity of these models is much higher than the heavy-scalar ones. The definition and optimization of these categories is tightly related to the analysis strategy described in Section 7.4.Z'_B and Z'-2HDM like excesses are tested by performing fits only to the high $E_{\mathrm{T}}^{\mathrm{miss}}$ category, while the heavy-scalar like signals are tested using a simultaneous fit of all the categories.

7.3.1 Optimization of the Mono-Higgs category

Topologies in Z'_B and Z'-2HDM models tend to present a higher event rate at large values of $E_{\mathrm{T}}^{\mathrm{miss}}$ and $p_{\mathrm{T}}^{\gamma\gamma}$. Oppositely, $\gamma\gamma$, γ+jet, ggF and VBF Higgs backgrounds present lower rates at higher values of $E_{\mathrm{T}}^{\mathrm{miss}}$, thus a variable related to $E_{\mathrm{T}}^{\mathrm{miss}}$ is used in the categorization in order to reduce the contribution of these backgrounds. On the other hand, contributions from Zh, Wh, tth, $V\gamma$ and $V\gamma\gamma$ are backgrounds that would present true production of invisible particles and would increase their relative contribution at larger $E_{\mathrm{T}}^{\mathrm{miss}}$ values. In Run I analysis [33], $E_{\mathrm{T}}^{\mathrm{miss}} > 90\mathrm{GeV}$ and $p_{\mathrm{T}}^{\gamma\gamma} > 90\mathrm{GeV}$ criteria were applied. This threshold was enlarged using 3.2 fb^{-1} to 100 GeV for both variables.

With higher statistics during 2016, the $E_{\mathrm{T}}^{\mathrm{miss}}$ variable was substituted by $S_{E_{\mathrm{T}}^{\mathrm{miss}}}$ variable (Eq. 7.1):

$$S_{E_{\mathrm{T}}^{\mathrm{miss}}} = \frac{E_{\mathrm{T}}^{\mathrm{miss}}}{\sqrt{\sum |E_{\mathrm{T}}|}} \tag{7.1}$$

The reason for this change is the higher pileup resilience obtained for $S_{E_{\mathrm{T}}^{\mathrm{miss}}}$ (Fig. 7.8.right), mainly due to the introduction of $\sum |E_{\mathrm{T}}|$. This variable stands for the scalar sum of the transverse momentum of all the objects used in the $E_{\mathrm{T}}^{\mathrm{miss}}$ calculation (electrons, photons, muons, jets and soft-terms). Events with large pileup activity, and therefore with a significant fake $E_{\mathrm{T}}^{\mathrm{miss}}$, also present large $\sum |E_{\mathrm{T}}|$, leading to a reduced $S_{E_{\mathrm{T}}^{\mathrm{miss}}}$. On the other hand, events with genuine $E_{\mathrm{T}}^{\mathrm{miss}}$ do not necessarily present a large $\sum |E_{\mathrm{T}}|$, thus $S_{E_{\mathrm{T}}^{\mathrm{miss}}}$ tends to increase. A cut in $S_{E_{\mathrm{T}}^{\mathrm{miss}}}$ is then very useful to reject fake $E_{\mathrm{T}}^{\mathrm{miss}}$ backgrounds(Fig. 7.8.left).

Other variables have been scanned aiming to get the highest possible significance for each model for all simulated points in the [$m_{Z'}$,$m_{\chi}(m_{A^0})$]. Three possible variables are defined:

- **Angular distance between diphoton system and $E_{\mathrm{T}}^{\mathrm{miss}}$ ($\Delta\phi(p_{\mathrm{T}}^{\gamma\gamma}, E_{\mathrm{T}}^{\mathrm{miss}})$)**

  The importance of this variable lies that in boosted topologies, as when dark matter is produced, the diphoton system and $E_{\mathrm{T}}^{\mathrm{miss}}$ tend to be back-to-back. Then, a cut at values of the $\Delta\phi(p_{\mathrm{T}}^{\gamma\gamma}, E_{\mathrm{T}}^{\mathrm{miss}})$ close to π could increase the expected significance with respect to the previous categorization. In

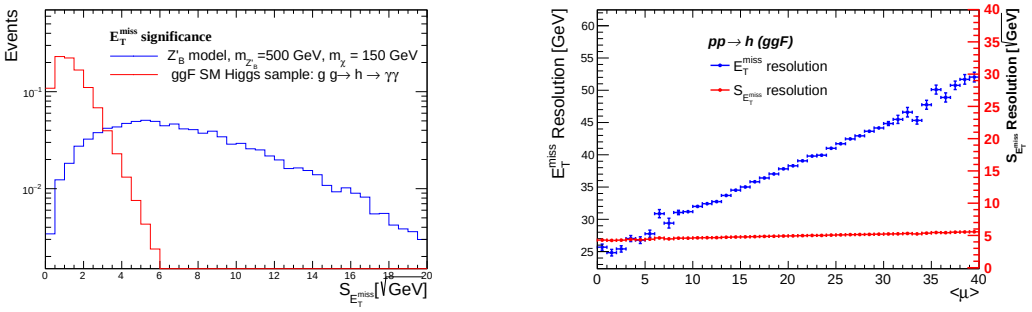


Figure 7.8: Left plot: $S_{E_{\mathrm{T}}^{\mathrm{miss}}}$ distributions comparing events from a Z'_B simulated sample ($m_{Z'_B} = 500$ GeV and $m_\chi = 150$ GeV) against events from the ggF SM Higgs simulated sample. It can be observed the discriminating power of this variable between samples presenting genuine $E_{\mathrm{T}}^{\mathrm{miss}}$ (Z'_B sample) or fake $E_{\mathrm{T}}^{\mathrm{miss}}$ (ggF sample). Right plot: comparison of the $S_{E_{\mathrm{T}}^{\mathrm{miss}}}$ and $E_{\mathrm{T}}^{\mathrm{miss}}$ resolution dependence in a ggF SM Higgs sample, where fake $E_{\mathrm{T}}^{\mathrm{miss}}$ is expected. Arbitrary units are used given that the aim of this plot is to compare the slope both distributions. It can be observed a higher pileup resilience of the $S_{E_{\mathrm{T}}^{\mathrm{miss}}}$ variable than the $E_{\mathrm{T}}^{\mathrm{miss}}$.

addition, it could be possible to observe the effect of this variable for different generated samples, as this effect would become more important with increasing m_χ for the Z'_B and at increasing m_{A^0} for the Z'-2HDM model.

- **Angular distance between all reconstructed objects and $E_{\mathrm{T}}^{\mathrm{miss}}$ ($\Delta\phi(\mathrm{H_T}, E_{\mathrm{T}}^{\mathrm{miss}})$)**

  The choice of this variable, defined in Eq. 7.3, is motivated by the fact that the most imprecise contribution in $E_{\mathrm{T}}^{\mathrm{miss}}$ calculation are the soft-terms. Soft-terms are estimated from tracks associated with the primary vertex but not associated with any object in the event. This increases $E_{\mathrm{T}}^{\mathrm{miss}}$ pileup immunity by not including low energy deposits in the calorimeter because they cannot be associated with any primary vertex. However, this feature also induces an imbalance in the total transverse momentum of the event due to the lack of neutral particle contribution. This fake $E_{\mathrm{T}}^{\mathrm{miss}}$ is expected to present a back-to-back direction with all the system defined by all the objects in the event. On the other hand, events with a miscalibrated jet or photon are expected to present flatter distributions. Events with genuine $E_{\mathrm{T}}^{\mathrm{miss}}$ are also expected to peak at π like in the $\Delta\phi(p_{\mathrm{T}}^{\gamma\gamma}, E_{\mathrm{T}}^{\mathrm{miss}})$ distribution although H_T is much more correlated with $E_{\mathrm{T}}^{\mathrm{miss}}$ than $p_{\mathrm{T}}^{\gamma\gamma}$ which leads to distributions peaking around π and rapidly decreasing towards 0.

$$\overrightarrow{\mathrm{H_T}} = \sum_i^{\mathrm{RecoObj}} \overrightarrow{p_{\mathrm{T}}}^i = \sum \overrightarrow{p_{\mathrm{T}}}^{\gamma} + \sum \overrightarrow{p_{\mathrm{T}}}^{\mathrm{j}} + \sum \overrightarrow{p_{\mathrm{T}}}^{\mathrm{e}} + \sum \overrightarrow{p_{\mathrm{T}}}^{\mu} \tag{7.2}$$

$$\Delta\phi(\overrightarrow{\mathrm{H_T}}, \overrightarrow{E_{\mathrm{T}}}^{\mathrm{miss}}) = \Delta\phi\left(\sum_i^{\mathrm{RecoObj}} \overrightarrow{p_{\mathrm{T}}}^i, \overrightarrow{E_{\mathrm{T}}}^{\mathrm{miss}}\right) \tag{7.3}$$

- **Number of leptons in the event**

  Wh, $W\gamma$ and $W\gamma\gamma$ backgrounds are important at high $E_{\mathrm{T}}^{\mathrm{miss}}$ since at least one neutrino is produced in the event. However, a lepton is also produced. A lepton veto can the remove these backgrounds and significantly increase our sensitivity of the analysis in high $E_{\mathrm{T}}^{\mathrm{miss}}$ categories.

The distributions of these three variables are presented in Fig. 7.9. The number of leptons in the event is split into the number of electrons and muons. It can be observed that angular variables $\Delta\phi(p_{\mathrm{T}}^{\gamma\gamma}, E_{\mathrm{T}}^{\mathrm{miss}})$ and $\Delta\phi(\mathrm{H_T}, E_{\mathrm{T}}^{\mathrm{miss}})$ can be used to reject background if a cut of $\Delta\phi \gtrsim 2$. Concerning the number of leptons, Z'_B and Z'-2HDM models tend to present very reduced fraction of events with leptons in comparison with respect to the background. Then, indeed, a lepton veto could increase the sensitivity.

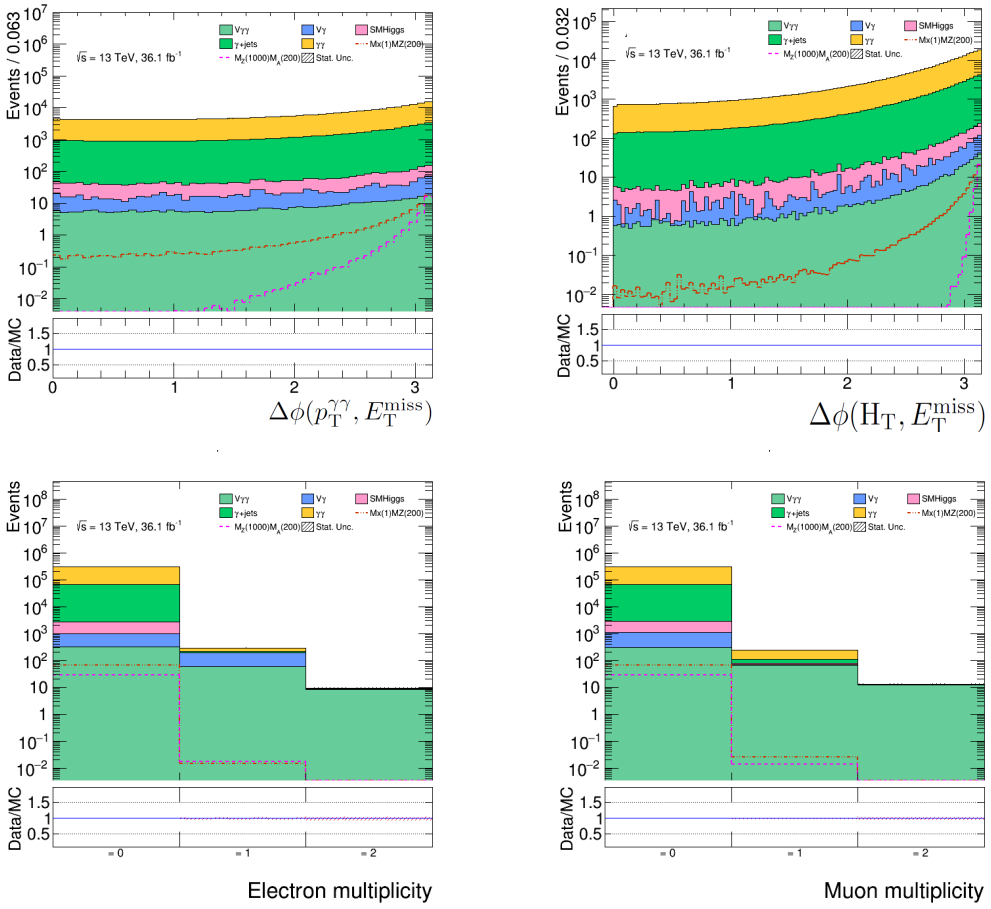


Figure 7.9: Distributions of the $\Delta\phi(p_{\mathrm{T}}^{\gamma\gamma}, E_{\mathrm{T}}^{\mathrm{miss}})$ (top-left), $\Delta\phi(\mathrm{H_T}, E_{\mathrm{T}}^{\mathrm{miss}})$ (top-right), N_e (bottom-left) and N_μ (bottom-right) based on simulated samples for signal models, SM Higgs models and non-resonant background.

Expected significance are estimated using Eq. 7.4 [34] with S being the expected number of signal events and B the expected background events. $p_{\mathrm{T}}^{\gamma\gamma}$, $\Delta\phi(p_{\mathrm{T}}^{\gamma\gamma}, E_{\mathrm{T}}^{\mathrm{miss}})$ or $\Delta\phi(\mathrm{H_T}, E_{\mathrm{T}}^{\mathrm{miss}})$ are tested for different cuts in $S_{E_{\mathrm{T}}^{\mathrm{miss}}}$. The cuts in these variables must leave a reasonable number of background events in the final sample given that non-resonant background on the signal region is estimated by a direct fit on the $m_{\gamma\gamma}$ sidebands, as explained later in Section 7.4. Thus, only cuts allowing at the end at least $N^{\mathrm{side-band}} > 10$ in the sidebands are considered.

$$Z = \sqrt{2(S+B)\ln(1+S/B) - 2S} \tag{7.4}$$

Figures 7.10–7.15 present the results of this optimization study for different masses of $m_{Z'}$ and $m_\chi(m_{A^0})$. In the Z'-2HDM sample $m_{Z'} = 400\,\mathrm{GeV}$ and $m_{A^0} = 200\,\mathrm{GeV}$ as well as for Z'_B models, best-significance is achieved at values of $S_{E_{\mathrm{T}}^{\mathrm{miss}}} > 7\sqrt{\mathrm{GeV}}$. These plots show that categorization using $\Delta\phi(\mathrm{H_T}, E_{\mathrm{T}}^{\mathrm{miss}})$ or $\Delta\phi(p_{\mathrm{T}}^{\gamma\gamma}, E_{\mathrm{T}}^{\mathrm{miss}})$ are usually less optimal than using $p_{\mathrm{T}}^{\gamma\gamma}$. Additionally, lepton veto induces a general improvement in the significance, as it can be observed in Table 7.1. The Mono-Higgs optimal then category requires events with no reconstructed lepton and that pass $S_{E_{\mathrm{T}}^{\mathrm{miss}}} > 7\sqrt{\mathrm{GeV}}$, $p_{\mathrm{T}}^{\gamma\gamma} > 90\mathrm{GeV}$. This category is called in the following the "Mono-Higgs" category and provides a significant discovery power for all simulated signals from both models, Z'_B and Z'-2HDM.

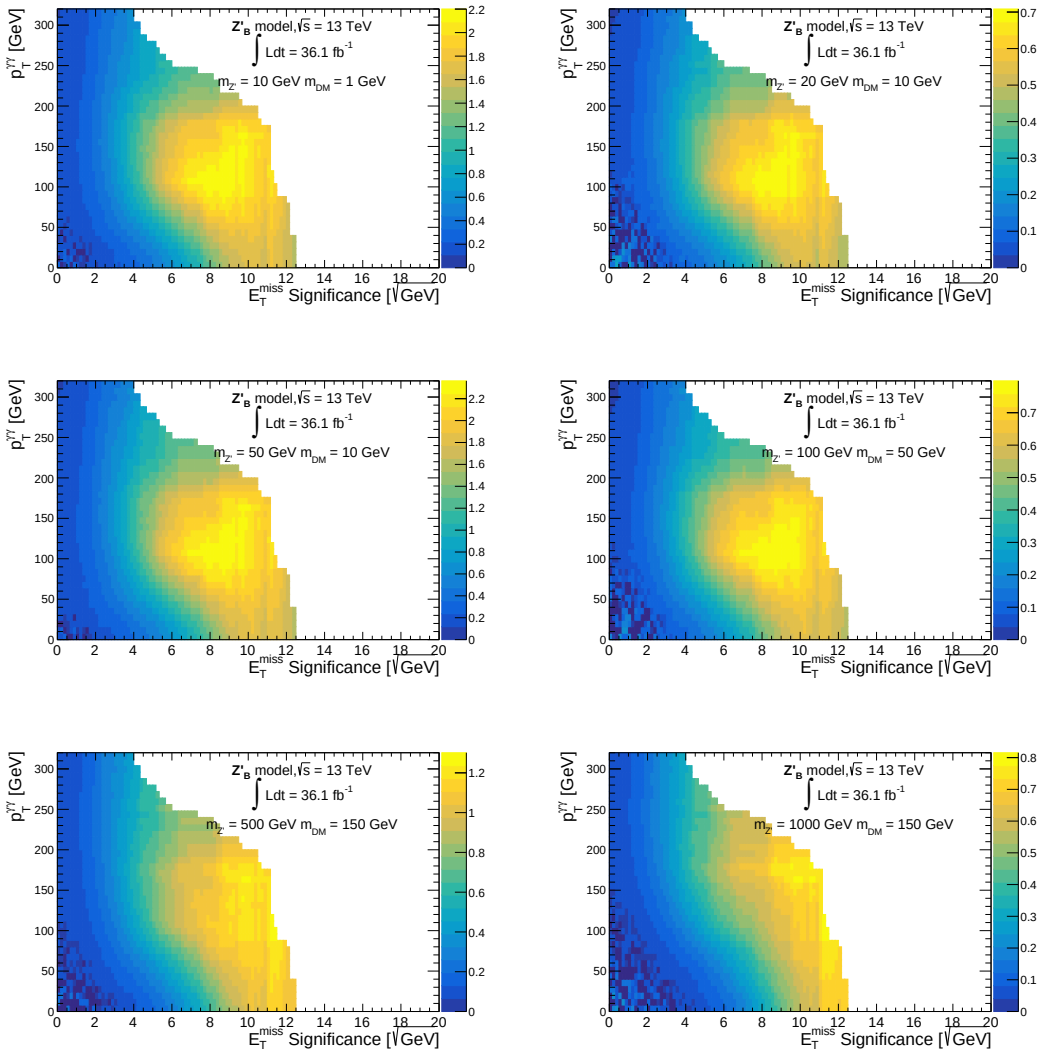


Figure 7.10: Significance scan for various masses of the Z'_B boson and DM particle depending on the $S_{E_{\mathrm{T}}^{\mathrm{miss}}}$ and $p_{\mathrm{T}}^{\gamma\gamma}$ variables for the Z'_B model. Event weights are applied and signal and background samples are scaled to their corresponding cross-sections or purity ($\gamma\gamma$ and γ+jet).

Table 7.1: Best significance for few benchmark samples of Z'-2HDM and Z'_B models. Values in parentheses correspond to best significance vetoing leptons in the event.

Sample	$p_{\mathrm{T}}^{\gamma\gamma}$	$\Delta\phi(p_{\mathrm{T}}^{\gamma\gamma}, E_{\mathrm{T}}^{\mathrm{miss}})$	$\Delta\phi(\mathrm{H_T}, E_{\mathrm{T}}^{\mathrm{miss}})$
Z'-2HDM $m_{Z'} = 400$ GeV, $m_{A^0} = 200$ GeV	5.06 (5.32)	3.68 (3.77)	2.75 (2.81)
Z'-2HDM $m_{Z'} = 1000$ GeV, $m_{A^0} = 200$ GeV	6.66 (6.65)	6.54 (6.54)	6.46 (6.52)
Z'-2HDM $m_{Z'} = 1200$ GeV, $m_{A^0} = 600$ GeV	0.23 (0.23)	0.23 (0.23)	0.23 (0.23)
Z'_B $m_{Z'_B} = 10$ GeV, $m_\chi = 1$ GeV	2.20 (2.28)	2.19 (2.22)	1.83 (1.96)
Z'_B $m_{Z'_B} = 100$ GeV, $m_\chi = 10$ GeV	2.55 (2.64)	2.48 (2.52)	2.05 (2.18)
Z'_B $m_{Z'_B} = 500$ GeV, $m_\chi = 150$ GeV	1.30 (1.32)	1.28 (1.31)	1.20 (1.28)

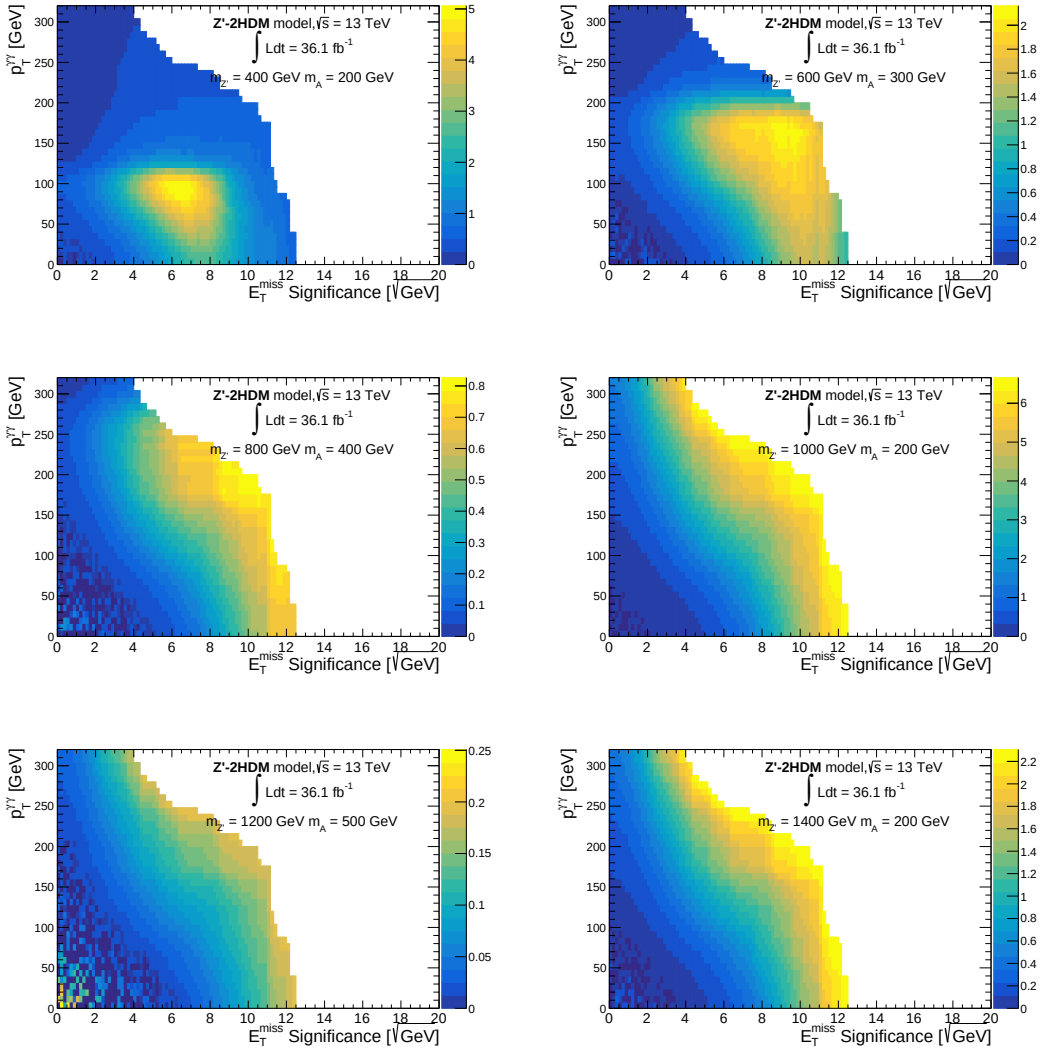


Figure 7.11: Significance scan for various masses of the Z' boson and pseudo-scalar A^0 depending on the $S_{E_{\mathrm{T}}^{\mathrm{miss}}}$ and $p_{\mathrm{T}}^{\gamma\gamma}$ variables for the Z'-2HDM model. Event weights are applied and signal and background samples are scaled to their correspoding cross-sections or purity ($\gamma\gamma$ and γ+jet).

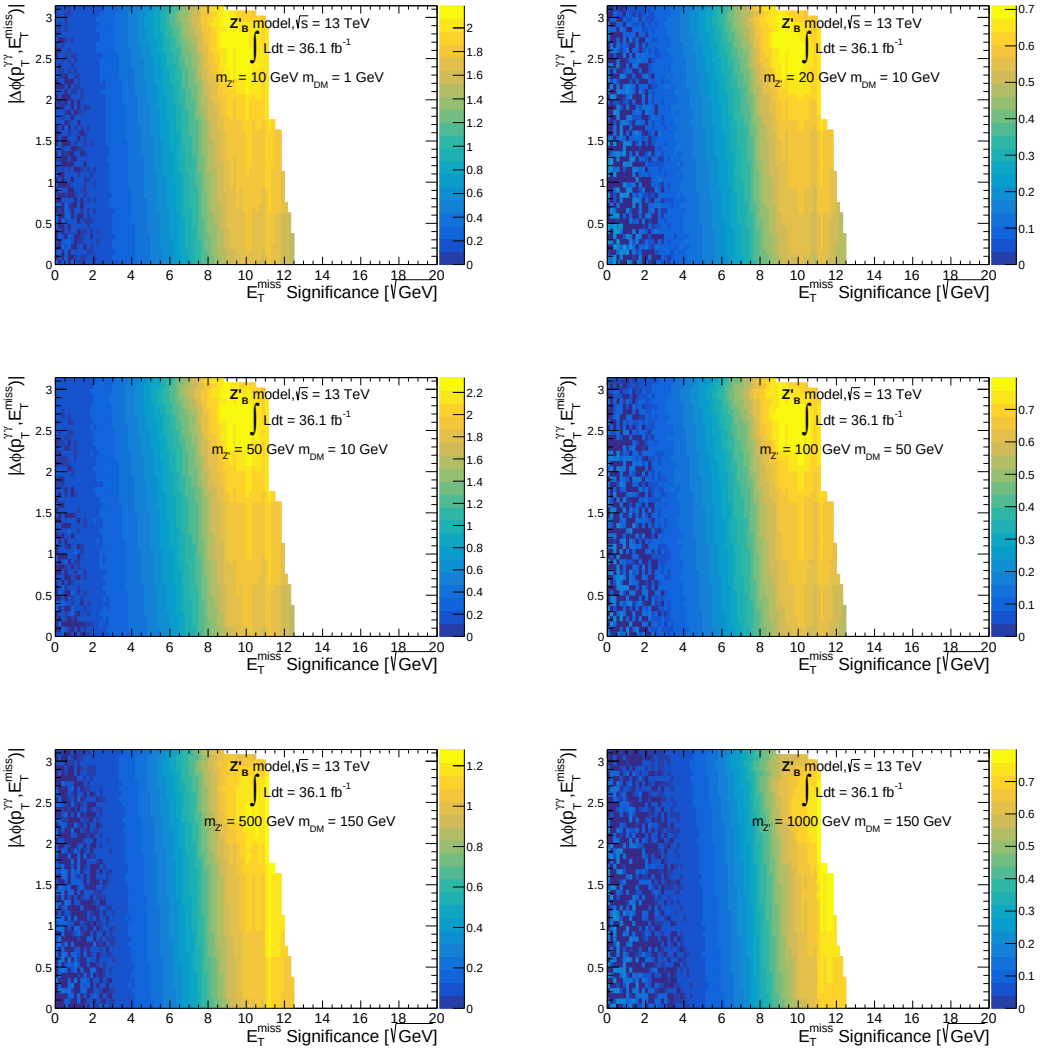


Figure 7.12: Significance scan for various masses of the Z'_B boson and DM particle depending on the $S_{E_{\mathrm{T}}^{\mathrm{miss}}}$ and $\Delta\phi(p_{\mathrm{T}}^{\gamma\gamma}, E_{\mathrm{T}}^{\mathrm{miss}})$ variables for the Z'_B model. Event weights are applied and signal and background samples are scaled to their correspoding cross-sections or purity ($\gamma\gamma$ and γ+jet).

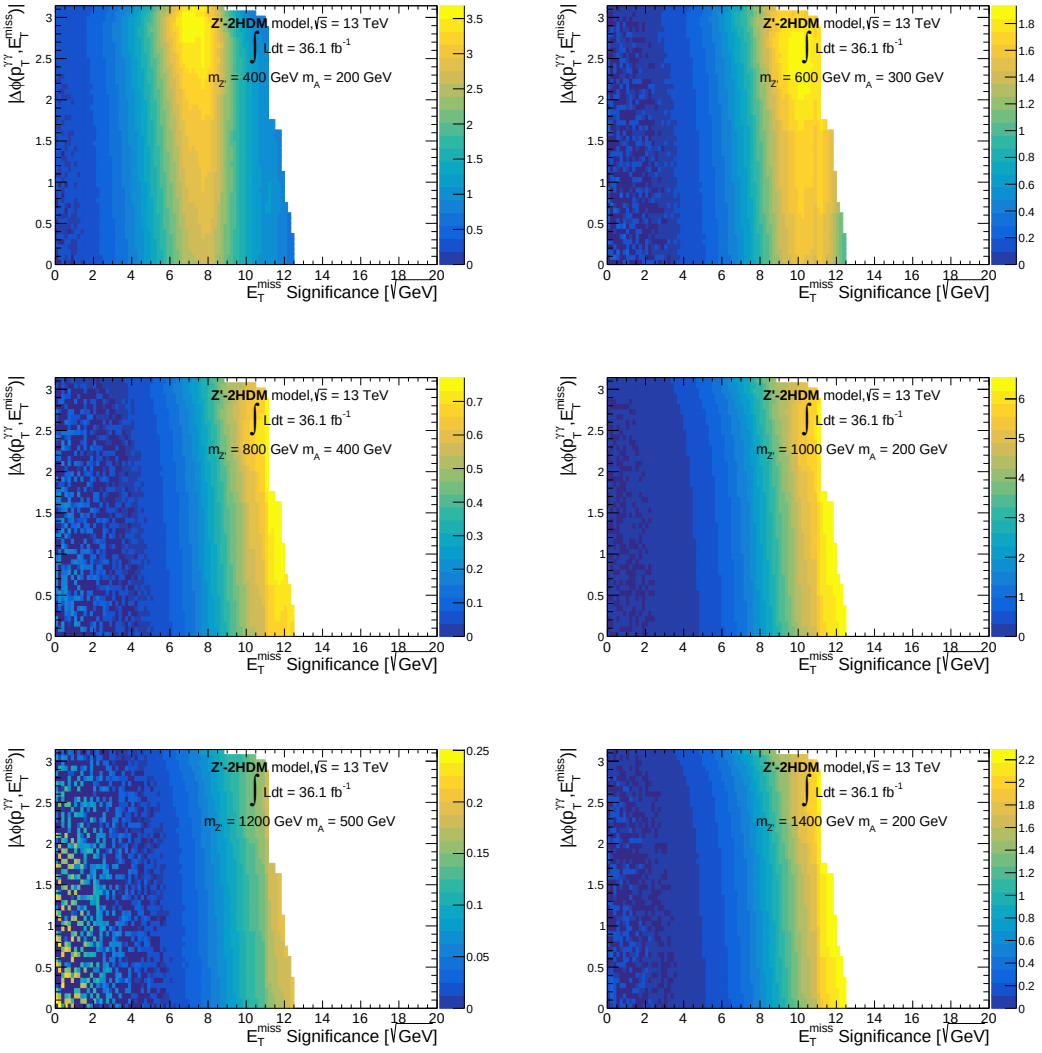


Figure 7.13: Significance scan for various masses of the Z' boson and pseudo-scalar A^0 depending on the $S_{E_{\mathrm{T}}^{\mathrm{miss}}}$ and $\Delta\phi(p_{\mathrm{T}}^{\gamma\gamma}, E_{\mathrm{T}}^{\mathrm{miss}})$ variables for the Z'-2HDM model. Event weights are applied and signal and background samples are scaled to their correspoding cross-sections or purity ($\gamma\gamma$ and γ+jet).

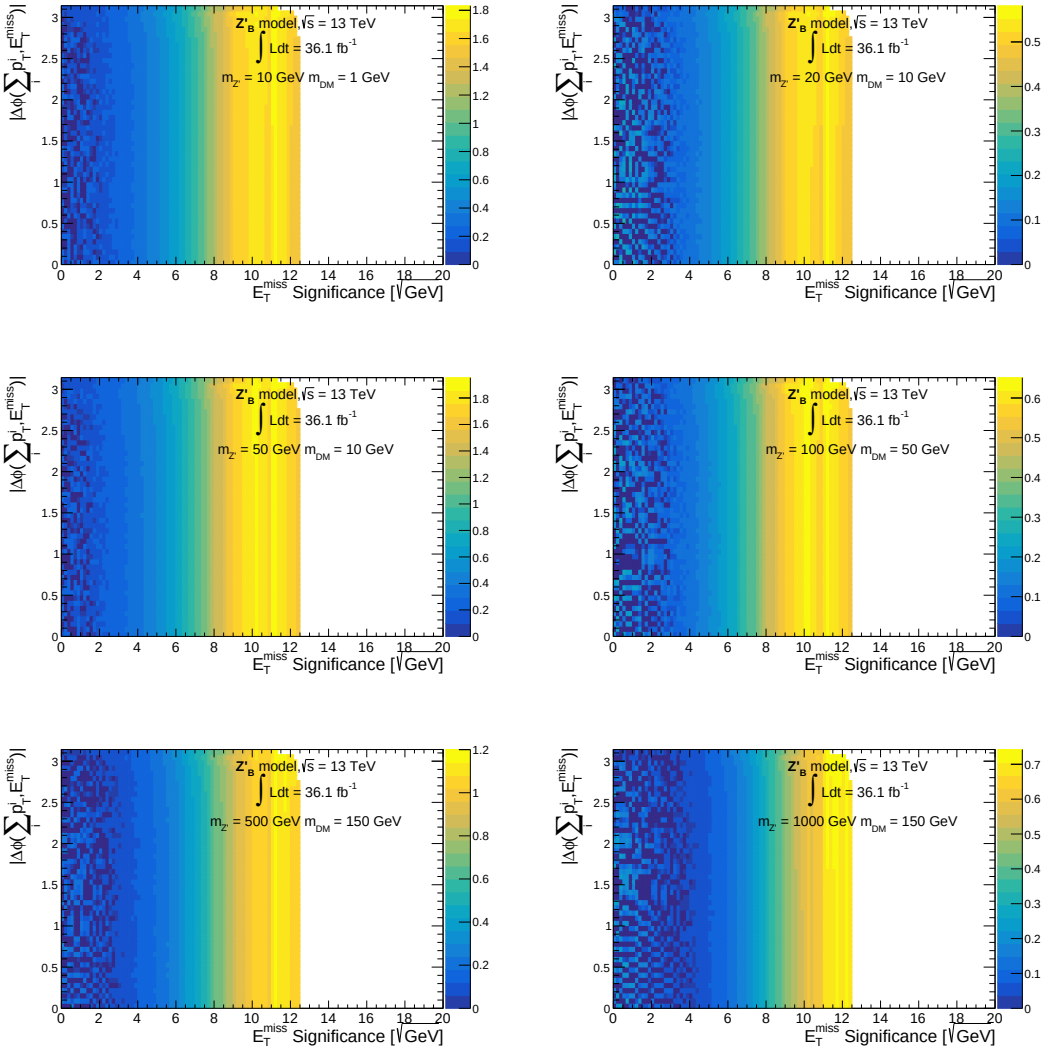


Figure 7.14: Significance scan for various masses of the Z'_B boson and DM particle depending on the $S_{E_{\mathrm{T}}^{\mathrm{miss}}}$ and $\Delta\phi(\mathrm{H_T}, E_{\mathrm{T}}^{\mathrm{miss}})$ variables for the Z'_B model. Event weights are applied and signal and background samples are scaled to their correspoding cross-sections or purity ($\gamma\gamma$ and γ+jet).

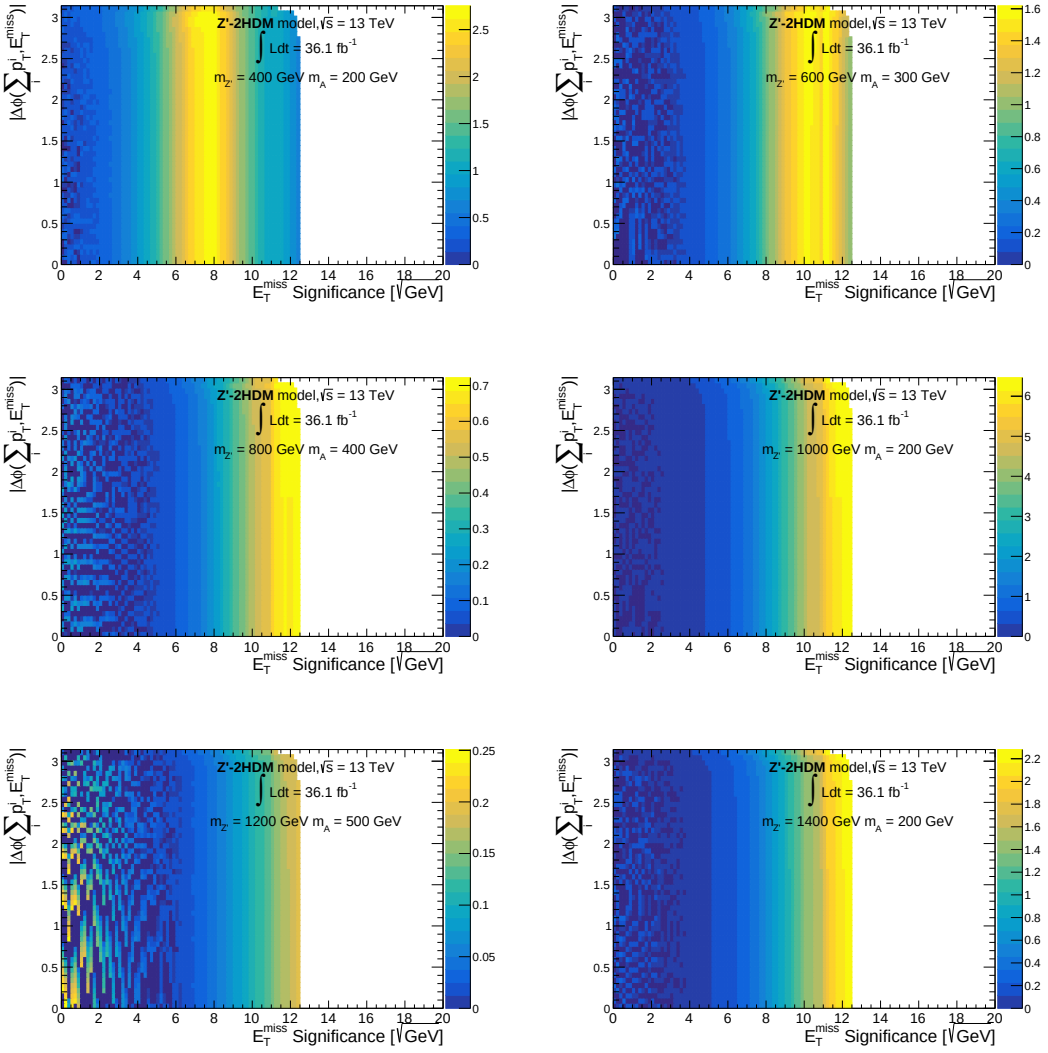


Figure 7.15: Significance scan for various masses of the Z' boson and pseudo-scalar A^0 depending on the $S_{E_{\mathrm{T}}^{\mathrm{miss}}}$ and $\Delta\phi(\mathrm{H_T}, E_{\mathrm{T}}^{\mathrm{miss}})$ variables for the Z'-2HDM model. Event weights are applied and signal and background samples are scaled to their correspoding cross-sections or purity ($\gamma\gamma$ and γ+jet).

7.3.2 Optimization of the heavy-scalar categories

Intermediate regions of $E_{\mathrm{T}}^{\mathrm{miss}}$ and $p_{\mathrm{T}}^{\gamma\gamma}$ have fake $E_{\mathrm{T}}^{\mathrm{miss}}$ backgrounds that become dominant in comparison to the high $E_{\mathrm{T}}^{\mathrm{miss}}$ region. Consequently, $S_{E_{\mathrm{T}}^{\mathrm{miss}}}$ is still a variable with an important discriminant power in these $E_{\mathrm{T}}^{\mathrm{miss}}$ ranges but reduced in comparison to the simplified models category. On the other hand, $p_{\mathrm{T}}^{\gamma\gamma}$ does not present a significant discriminant power to reject this fake $E_{\mathrm{T}}^{\mathrm{miss}}$ events, mainly coming from jet mismeasurements and pileup. Lepton veto is also inadequate here given that events with leptons are subdominant. Background is mainly dominated by ggF, VBF, $\gamma\gamma$ and γ+jet contributions. Additional discriminant variables are then studied, aiming to reject events where a mismeasurement of jets or large pileup contributions are present:

- **Coincidence of the diphoton vertex and the hardest vertex**

  The background events that survive the intermediate $E_{\mathrm{T}}^{\mathrm{miss}}$ requirement but are not expected to present any truth $E_{\mathrm{T}}^{\mathrm{miss}}$ (coming from invisible particles) mostly have one or several high-p_{T} pileup jets since the JVT > 0.59 condition only applies for jets with $p_{\mathrm{T}} < 60$ GeV. These pileup jets usually originate from a pileup vertex with larger Σp_{T}^2 than the diphoton primary vertex, where p_{T} is the track transverse momentum associated with a single vertex. Requiring the diphoton primary vertex to be the hardest vertex in each event helps to suppress pileup effects and reduce a large fraction of the fake $E_{\mathrm{T}}^{\mathrm{miss}}$ events.

  During Run II, ATLAS resolution for vertex reconstruction is on average of the order of few tens of μm in the x,y and z direction [35]. Coincidence between diphoton and hardest vertices can then be asked by requiring $|z_{PV}^{\mathrm{hard}} - z_{PV}^{\gamma\gamma}| < 0.1$ mm. Figure 7.16 presents the event rate for which the diphoton vertex is identified with the hardest vertex of the event as a function of the reconstructed $S_{E_{\mathrm{T}}^{\mathrm{miss}}}$ in the event. It is observed that the diphoton sample (Sherpa) event rate is reduced as a function of the $S_{E_{\mathrm{T}}^{\mathrm{miss}}}$ while for heavy-scalar and Z'_B signal samples, event rate remains almost constant.

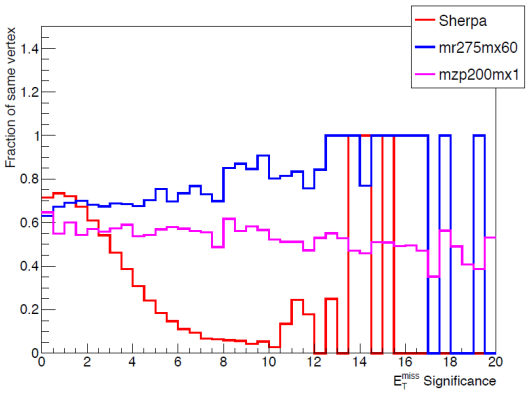


Figure 7.16: Event rate of coincidence between the diphoton vertex and the hardest vertex of the event. Rates as function of the $S_{E_{\mathrm{T}}^{\mathrm{miss}}}$ variable are presented. Red curve correspond to event rates for the diphoton non-resonant background sample while blue and pink curves show event rates for a chosen benchmark sample for the heavy-scalar and Z'_B models, respectively. This demonstrates that the background is reduced when the two vertices coincide.

- **Sum of two leading photons and jets in the event ($p_{\mathrm{T}}^{\mathrm{hard}}$)**

  $p_{\mathrm{T}}^{\mathrm{hard}}$ is a variable that provides additional separation power on rejecting fake $E_{\mathrm{T}}^{\mathrm{miss}}$ events in the low reconstructed $E_{\mathrm{T}}^{\mathrm{miss}}$ region. It is defined as the magnitude of the vectorial sum of both leading photons and all jets p_{T} in the event passing the Jvt and jet selection cuts (Eq. 7.5). The motivation for using this variable is that events containing a large quantity of pileup jets would present lower values of $p_{\mathrm{T}}^{\mathrm{hard}}$ since pileup jets contribution will tend to cancel. On the opposite, events with a lower number of pileup jets, and therefore more likely to present genuine $E_{\mathrm{T}}^{\mathrm{miss}}$, may present larger

values of $p_{\mathrm{T}}^{\mathrm{hard}}$, so a separation of events is possible.

$$p_{\mathrm{T}}^{\mathrm{hard}} = |\sum_{i=1}^{N_\gamma=2} \overrightarrow{p_{\mathrm{T,i}}}^{\gamma} + \sum_{i=1}^{N_{\mathrm{jets}}} \overrightarrow{p_{\mathrm{T,i}}}^{j}| \tag{7.5}$$

7.3.3 Final categorization

The resulting categorization scheme is shown in Table 7.2 where each event is tested against the first to the fith category in decreasing order unless a category accommodates this event. Ecents that cannot be matched to the fifth category are not used in the analysis. Simplified models present a better performance in Mono-Higgs category and heavy-scalar model presents, in addition, a very good sensitivity in the High-$E_{\mathrm{T}}^{\mathrm{miss}}$ and the Intermediate-$E_{\mathrm{T}}^{\mathrm{miss}}$ categories too. The last two categories are defined where heavy-scalar model has much lower significance: Different-vertex and Rest categories. Despite it, these two categories still bring some information about the signal normalization if a simultaneous fit is performed in all categories.

Table 7.2: Optimized criteria used in the categorization. Each category excludes events that are in the upper categories.

Number	Category	Requirements
Cat. 1	Mono-Higgs	$S_{E_{\mathrm{T}}^{\mathrm{miss}}} > 7\ \sqrt{\mathrm{GeV}}$, $p_{\mathrm{T}}^{\gamma\gamma} > 90$ GeV, lepton veto
Cat. 2	High-$E_{\mathrm{T}}^{\mathrm{miss}}$	$S_{E_{\mathrm{T}}^{\mathrm{miss}}} > 5.5\ \sqrt{\mathrm{GeV}}$, $\lvert z_{PV}^{\mathrm{hard}} - z_{PV}^{\gamma\gamma}\rvert < 0.1$ mm
Cat. 3	Intermediate-$E_{\mathrm{T}}^{\mathrm{miss}}$	$S_{E_{\mathrm{T}}^{\mathrm{miss}}} > 4\ \sqrt{\mathrm{GeV}}$, $p_{\mathrm{T}}^{\mathrm{hard}} > 40$ GeV, $\lvert z_{PV}^{\mathrm{hard}} - z_{PV}^{\gamma\gamma}\rvert < 0.1$ mm
Cat. 4	Different-Vertex	$S_{E_{\mathrm{T}}^{\mathrm{miss}}} > 4\ \sqrt{\mathrm{GeV}}$, $p_{\mathrm{T}}^{\mathrm{hard}} > 40$ GeV, $\lvert z_{PV}^{\mathrm{hard}} - z_{PV}^{\gamma\gamma}\rvert > 0.1$ mm
Cat. 5	Rest	$p_{\mathrm{T}}^{\gamma\gamma} > 15$ GeV

Figure 7.17 shows the distributions of $S_{E_{\mathrm{T}}^{\mathrm{miss}}}$, $p_{\mathrm{T}}^{\mathrm{hard}}$ and $p_{\mathrm{T}}^{\gamma\gamma}$ after the selection of diphoton candidates in the range $120\ \mathrm{GeV} < \mathrm{m}_{\gamma\gamma} < 130\ \mathrm{GeV}$. Expected signal distributions are shown for the Z'_B model with $m_{Z'_B} = 200$ GeV and $m_\chi = 1$ GeV, the Z'-2HDM model with $m_{Z'} = 1000$ GeV, $m_{A^0} = 200$ GeV and $m_\chi = 100$ GeV, and a heavy-scalar model with $m_{\mathrm{H}} = 275$ GeV and $m_\chi = 60$ GeV. These overlaid signal points are representative of the model kinematics. Concerning the backgrounds, SM h, $V\gamma$ and $V\gamma\gamma$ are normalized to their corresponding cross-section times the luminosity $\mathcal{L}$ =36.1 fb^{-1} of the data sample used in this analysis and the $\gamma\gamma$ and γ+jet contributions are normalized to their measured purity [36] (79% and 19% respectively extracted from data-driven measurements) times the number of data events in the signal region.

Data and MC are in agreement within uncertainties. The slight discrepancies observed in the $p_{\mathrm{T}}^{\gamma\gamma}$ distribution indicate a possible mismodeling of the non-resonant background. However, non-resonant background is directly estimated from data as it is explained later in Section 7.4, thus no impact is expected on our results from these discrepancies.

7.4 Analysis strategy

In this analysis, the presence of any excesses from DM production in association to a Higgs is evaluated by either fitting simultaneous the $m_{\gamma\gamma}$ distribution of the five categories in the case of the heavy-scalar model or only the Mono-Higgs category in the case of the simplified DM models. In both cases, each category is fitted by a single function divided into three components: a resonant function describing the signal described either by Mono-Higgs models or by the heavy-scalar model; the resonant background coming from SM Higgs production; and the non-resonant background. This strategy requires a previous knowledge on the optimal functional forms to model each of these contributions.

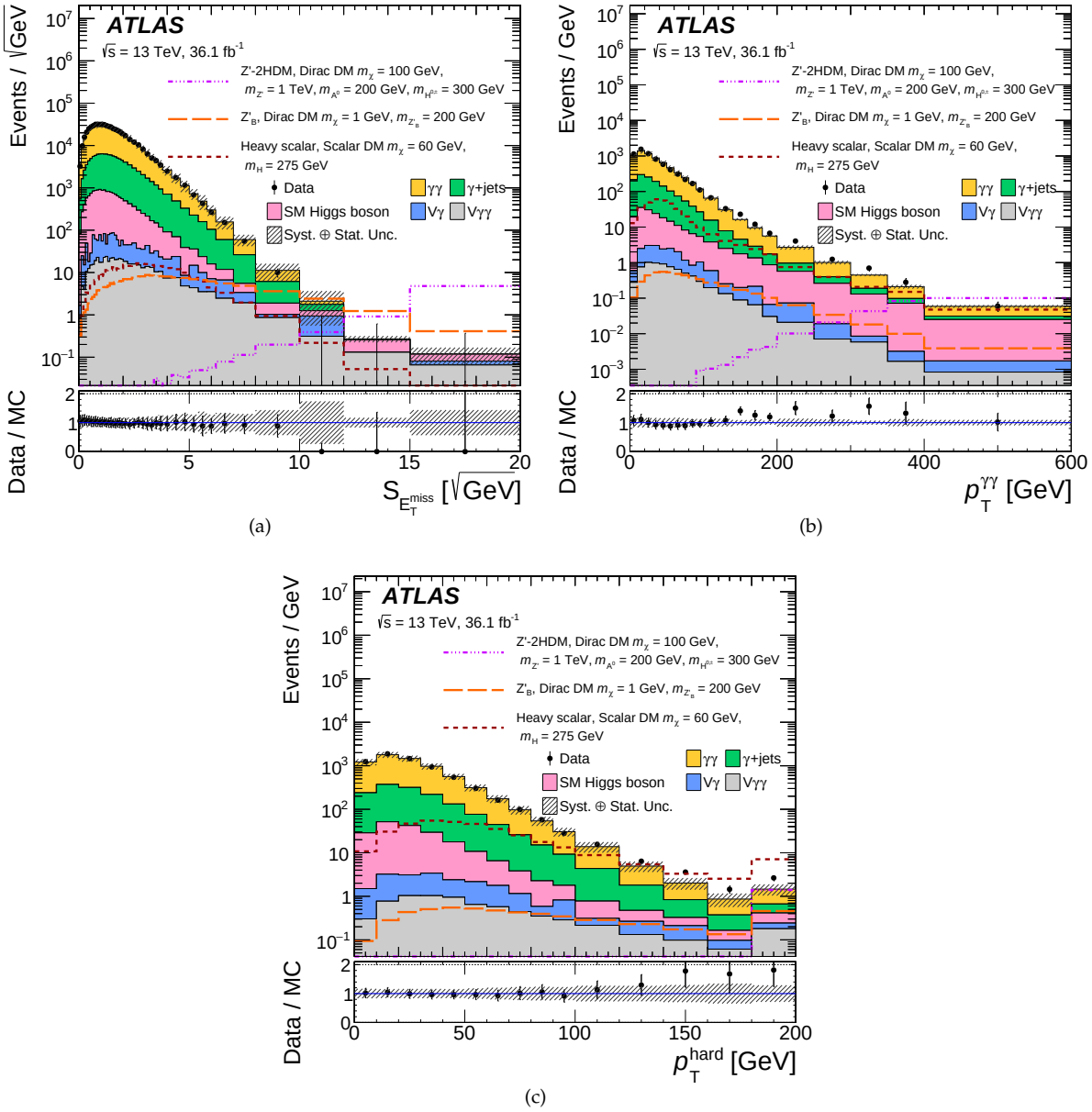


Figure 7.17: The distribution of (a) $S_{E_{\mathrm{T}}^{\mathrm{miss}}}$, (b) $p_{\mathrm{T}}^{\gamma\gamma}$ and (c) $p_{\mathrm{T}}^{\mathrm{hard}}$ after the selection of diphoton candidates in 120 GeV $< \mathrm{m}_{\gamma\gamma} <$ 130 GeV [3]. Expected signal distributions are shown for a Z'_B signal with $m_{Z'_B} =$ 200 GeV and Dirac fermion DM $m_\chi = 1$ GeV, a Z'-2HDM signal with $m_{Z'} = 1000$ GeV, $m_{A^0} = 200$ GeV and Dirac fermion DM $m_\chi = 100$ GeV and a heavy-scalar model with $m_{\mathrm{H}} = 275$ GeV and scalar DM $m_\chi = 60$ GeV. These overlaid signal points chosen are representative of the model kinematics. Only the sum of the MC statistical and experimental systematic uncertainties on the total background is shown as the hatched bands, while the theoretical uncertainties on the background normalization are not included. Overflow events are included in the rightmost bins.

7.4.1 Signal and SM Higgs parametrization

Higgs resonance is modeled using a double-sided Crystal-Ball function (DSCB), which is defined as[1]:

$$N \cdot \begin{cases} e^{-t^2/2} & \text{if } -\alpha_{Low} \geq t \geq \alpha_{High} \\ \frac{e^{-0.5\alpha_{Low}^2}}{\left[\frac{\alpha_{Low}}{n_{Low}}\left(\frac{n_{Low}}{\alpha_{Low}} - \alpha_{Low} - t\right)\right]^{n_{Low}}} & \text{if } t < -\alpha_{Low} \\ \frac{e^{-0.5\alpha_{High}^2}}{\left[\frac{\alpha_{High}}{n_{High}}\left(\frac{n_{High}}{\alpha_{High}} - \alpha_{High} + t\right)\right]^{n_{High}}} & \text{if } t > \alpha_{High}, \end{cases} \tag{7.6}$$

where $t = \Delta m_X/\sigma_{CB}$, $\Delta m_X = m_X - \mu_{CB}$, N is a normalization parameter, μ_{CB} is the peak of the Gaussian distribution, σ_{CB} represents the width of the Gaussian part of the function, α_{Low} (α_{High}) is the point where the Gaussian becomes a power law on the low (high) mass side, n_{Low} (n_{High}) is the exponent of this power law. An illustrative drawing of the double-sided Crystal Ball function is provided in Figure 7.18. The exact parametrization is done using Signal and SM Higgs Monte Carlo samples, whose different kinematic behaviour reflects in small differences in the Higgs peak shape.

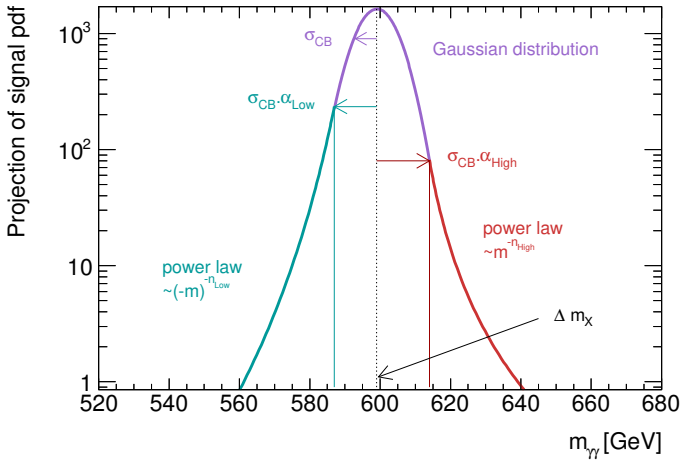


Figure 7.18: Description of the double-sided Crystal Ball function parameters, for a signal mass m_X = 600 GeV. Different parameters are described in the text.

Studies have been performed for different Z'_B Z'-2HDM and heavy-scalar samples. The fitted diphoton mass spectra of $h \to \gamma\gamma$ in theZ'-2HDM model and the the Z'_B model are shown in Figs. 7.19 and 7.20 respectively.

In the case of heavy-scalar, all $m_{\rm H}$ present very similar topologies (Figs. 7.1) and therefore, there is no need to determine signal parametrization sample by sample. All heavy-scalar samples are summed up and all $m_{\rm H}$ DSCB parameters are fixed to the result of this single fit. Concerning the SM contribution, the DSCB are fixed from a fit on a combinated shape of all the Higgs production modes. Both fits are shown for each category in Fig 7.21 and Fig 7.22.

7.4.2 Non-resonant background parametrization

Non-resonant background is expected to present a decreasing smooth behaviour in all the selected $m_{\gamma\gamma}$ spectrum. The choice of the best functional form to fit this spectrum must however be studied very carefully. Background mis-modeling can induce a fake signal in the spectrum that can misleadingly be interpreted as an excess of events at $m_h = 125.09$ GeV. To prevent this, background functional form is chosen by previously studying the non-resonant background shape.

[1]A double-sided Crystal Ball function is composed of a Gaussian distribution at the core, with two power law distributions describing the lower and upper tails.

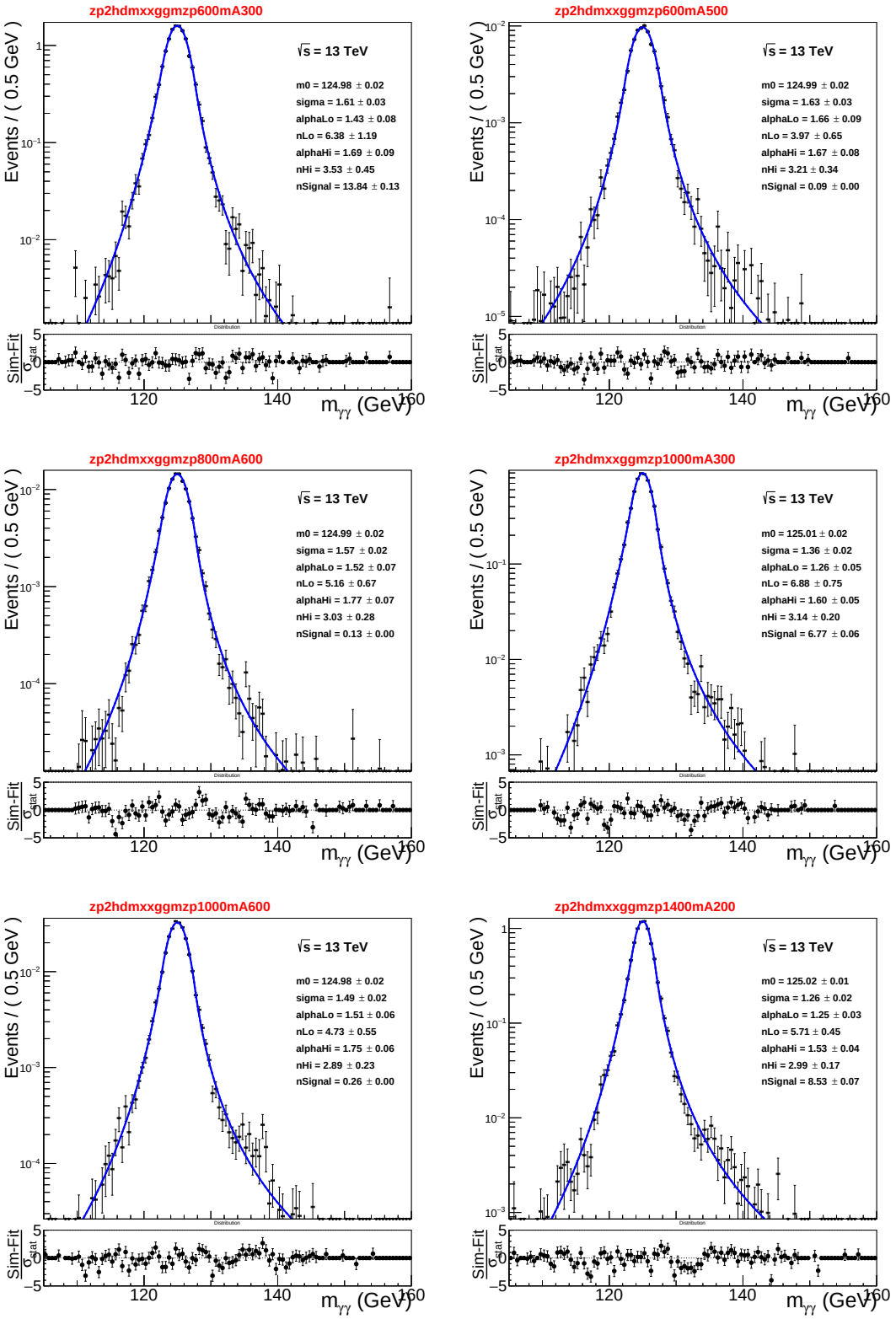


Figure 7.19: Fits of the Z'-2HDM signal line-shape for different sets of signal samples (red title).

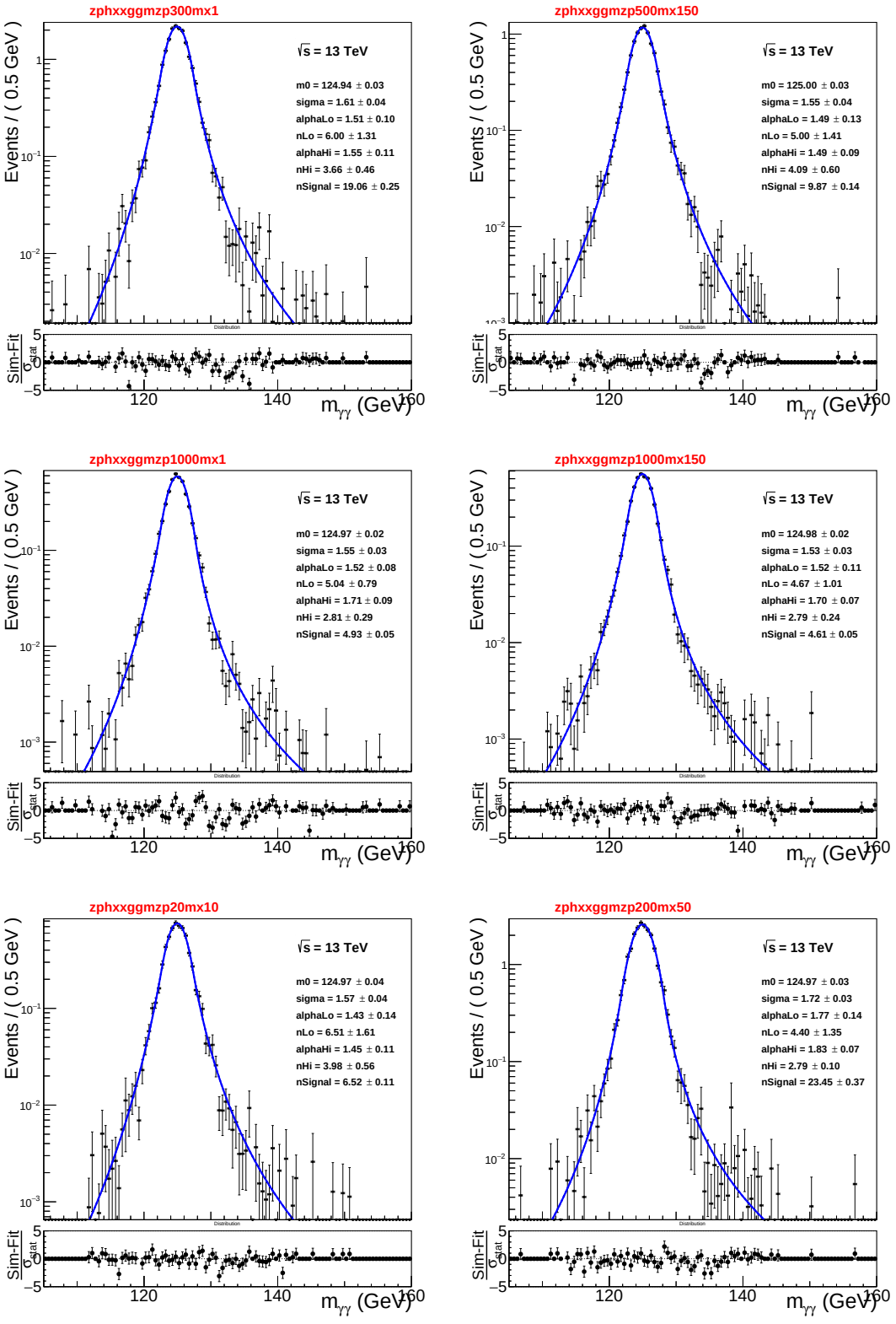


Figure 7.20: Fitted diphoton mass spectra of some Z'_B signals in the mono-Higgs category.

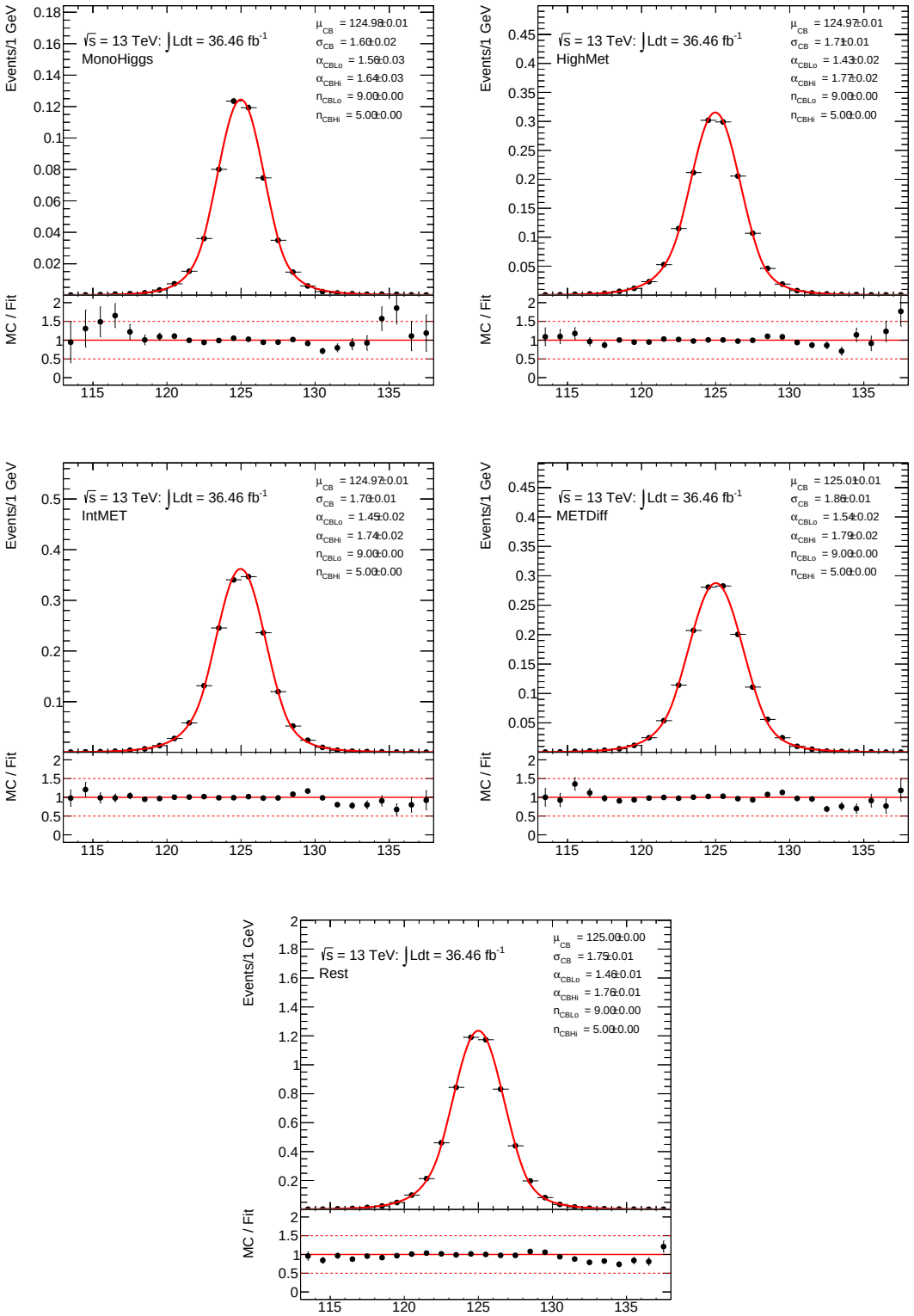


Figure 7.21: Results of a single fit of a DSCB function (lines) for a sample where all Heavy scalar processes are summed.

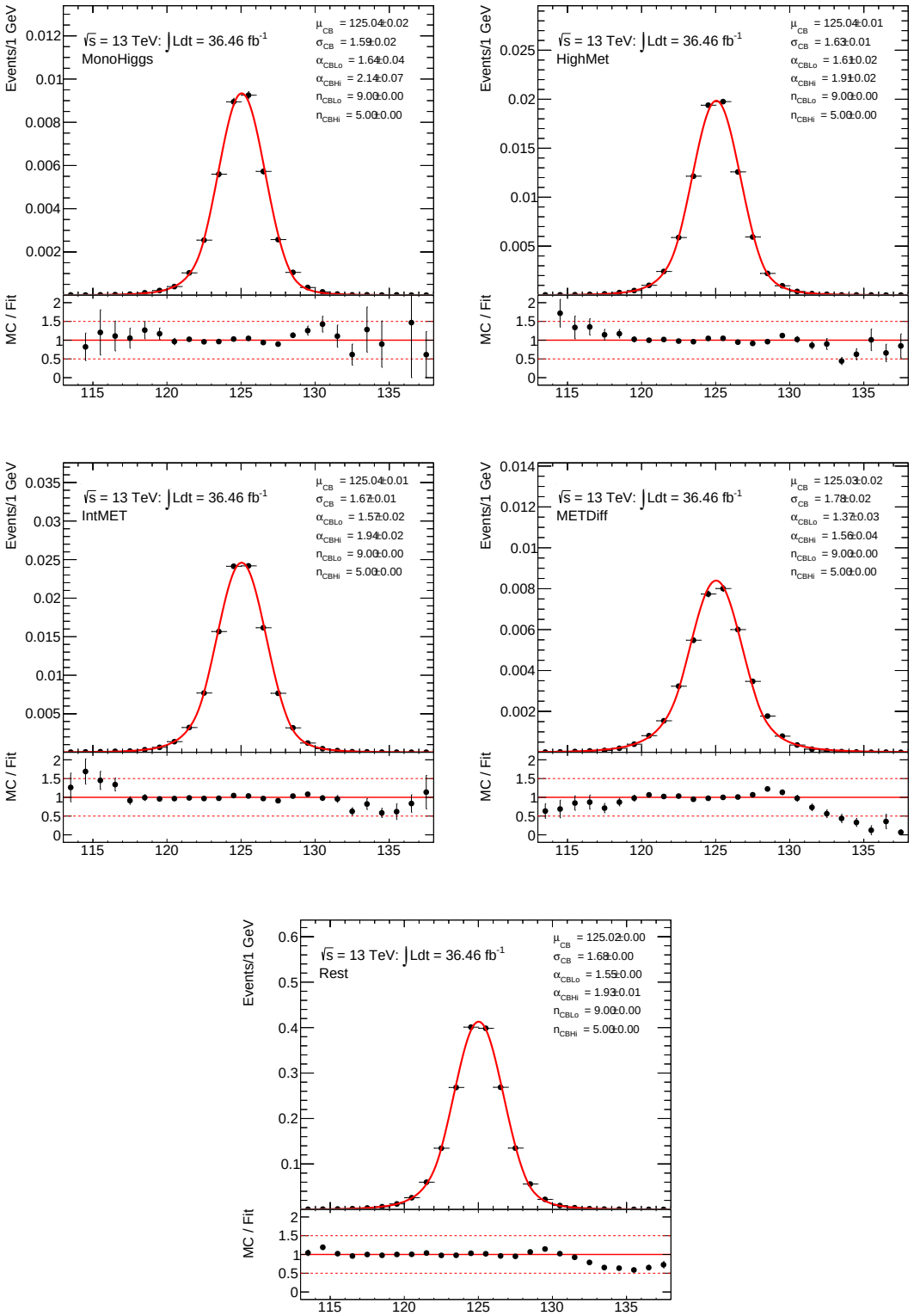


Figure 7.22: Results of a single fit of a DSCB function (lines) for a sample where all Standard Model Higgs processes are summed.

The $V\gamma$ and $V\gamma\gamma$ $m_{\gamma\gamma}$ shapes are taken from simulations as explained in Section 7.1. Besides, the γ+jet shape is taken from an enriched control region where one of the photons is required to fail the tight identification criteria, although it is also required to match the loose ID criteria. This data-driven technique is setup because the γ+jet MC sample has very low statistics after event selection is applied, due mainly to a large rejection factor and a limited CPU capacity to generate large samples. This leads to a inaccurate $m_{\gamma\gamma}$ shape prediction (Fig 7.23.left). This control region is enriched with γ+jet samples although it is also contaminated by diphoton, $V\gamma$ and $V\gamma\gamma$ backgrounds. Their contribution are estimated from MC samples and subtracted from the control region. The result is a very pure γ+jet sample that is extrapolated to the signal region by a reweighting of the $m_{\gamma\gamma}$ distribution of the diphoton MC sample. This reweighting procedure uses weights defined by Eq. 7.7, which are derived on by dividing the diphoton and the γ+jet $S_{E_{\mathrm{T}}^{\mathrm{miss}}}$ shapes in the control region:

$$w_{\gamma+\mathrm{jet}/\gamma\gamma} = \left(\frac{S^{\gamma+\mathrm{jet}}_{E_{\mathrm{T}}^{\mathrm{miss}}}}{S^{\gamma\gamma}_{E_{\mathrm{T}}^{\mathrm{miss}}}} \right)_{\mathrm{AntiID}} \tag{7.7}$$

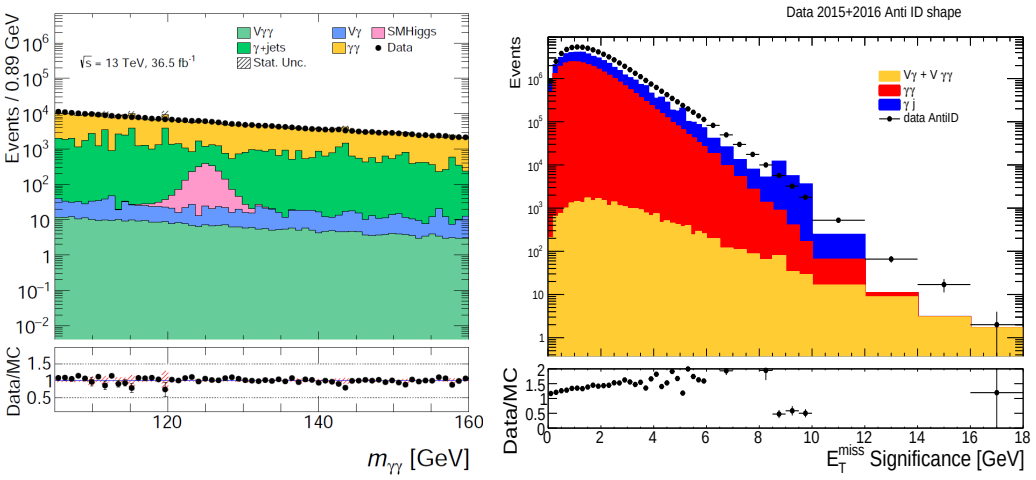


Figure 7.23: Comparison of Pythia8 γ+jet sample in the signal (left) and the control region (right). One can clearly observe that large fluctuations are present in this sample due to bad MC modeling. $\gamma\gamma$, $V\gamma$ and $V\gamma\gamma$ MC contributions are also included in both plots. Control region plot shows the $S_{E_{\mathrm{T}}^{\mathrm{miss}}}$ distribution since contribution of the γ+jet is extracted from this variable.

The aggregated $\gamma\gamma$, γ+jet $V\gamma$ and $V\gamma\gamma$ $m_{\gamma\gamma}$ shapes are combined (Figs. 7.24) and fitted using several test smooth functions to model the non-resonant component, plus a double-sided Crystall-Ball to estimate the bias on the signal, also called spurious signal.

A criterion is setup to define if one functional form is adequate to be used in the final fit without generating an acceptable spurious signal. For categories where a large number of events from signal and/or SM Higgs background are expected, spurious signal values must represent less than 10 % of the expected signal or SM h contribution or less than 20% of the background uncertainty under the signal peak. In addition, the fitting function must present a reasonable χ^2. A scan of the signal DSCB μ_{CB} parameter is made inside a window of 118 GeV $< \mu_{\mathrm{CB}} <$ 132 GeV for checking the stability of the spurious signal in a large mass window around $m_h = 125.09$ GeV. The considered spurious signal is the maximum bias found in this scan. In the case that two or more functions pass all these requirements, the parametrization presenting the lowest spurious signal is selected. However, this criterion cannot be applied to categories where a small number of signal and background events are expected. In these categories, statistical fluctuations dominate the uncertainty on the background shape and the spurious signal is then representative of the statistical uncertainty of the non-resonant background sample, thus overestimating the possible bias. In this case, the optimal parametrization is the one providing the lowest spurious signal, together with a small χ^2.

Table 7.3 shows the final decision of the functions used in the fit of each category. For comparison,

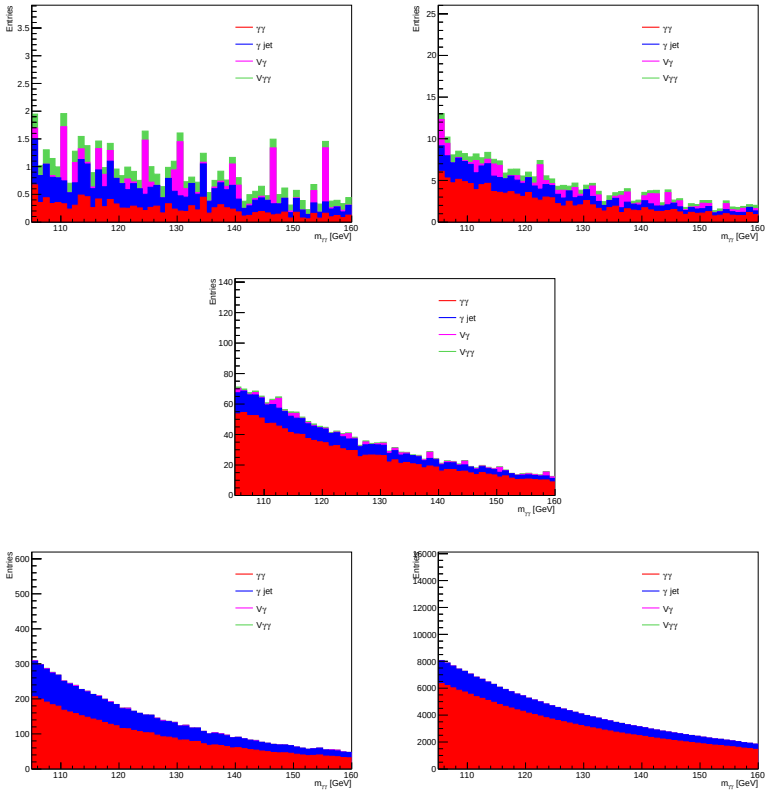


Figure 7.24: Merged non-resonant background distributions. $\gamma\gamma$ contribution is normalized to 79% of number of events in data in the inclusive category and γ+jet to 19% following data-driven measurements. $V\gamma$ and $V\gamma\gamma$ contributions are normalized to their predicted cross-section times the 36.1fb^{-1} luminosity.

Table 7.4 shows the integrated non-resonant background yields and their corresponding statistical uncertainty within the range $m_{\gamma\gamma} \in [122, 128]$ GeV. The spurious signal is added to the fit as a bias to the defined likelihood function (Section 7.6) to protect the final limits from any possible fake signal.

Table 7.3: The analytical functions used to model the non-resonant $m_{\gamma\gamma}$ distribution, the uncertainty on the signal due to the spurious signal (Spur. signal). The variable x is defined as $m_{\gamma\gamma}/\sqrt{s}$ while a and b are parameters of the background functions. For the Rest category, the fitting function is a Bernstein polynomial of order 3, where C_3^j are binomial coefficients and $b_{j,3}$ are Bernstein polynomial coefficients [37]. The relative magnitude of the spurious signal is also presented with regard to the expected number of the background events (N_{back}) and signal events (N_{signal}) in the range 120 GeV $< m_{\gamma\gamma} <$ 130 GeV. N_{signal} represents the expected yield of the Z'_B model sample for $m_{Z'_B} = 200$ GeV and $m_\chi = 1$ GeV in the Mono-Higgs category. For the other categories, it represents the expected signal yield of the heavy-scalar sample with $m_{\text{H}} = 275$ GeV and $m_\chi = 60$ GeV.

Category	Function	Spur. signal	Spur. signal/N_{back} [%]	Spur. signal/N_{signal} [%]
Mono-Higgs	$\exp(a \cdot x)$	1.2	9.8	6.0
High-$E_{\text{T}}^{\text{miss}}$	$(1-x^{1/3})^b \cdot x^a$	2.7	4.0	11
Intermediate-$E_{\text{T}}^{\text{miss}}$	$\exp(a \cdot x + b \cdot x^2)$	5.8	1.3	14
Different-Vertex	$\exp(a \cdot x + b \cdot x^2)$	8.4	0.5	26
Rest	$\sum_{j=0}^{3} C_3^j x^j (1-x)^{3-j} b_{j,3}$	61	< 0.1	28

Table 7.4: The MC yields and uncertainty in the in 122 to 128 GeV$m_{\gamma\gamma}$ window. Here no pile up reweighing is applied.

Category	MC yields	MC uncertainty
Mono-Higgs	4.40	1.13
High-$E_{\mathrm{T}}^{\mathrm{miss}}$	30.1	1.9
Intermediate-$E_{\mathrm{T}}^{\mathrm{miss}}$	226.0	3.4
Different-Vertex	794.8	5
Rest	28021	28

7.5 Systematic uncertainties

Uncertainties from both experimental and theoretical quantities affect the final yields in each category of the SM Higgs boson contribution and the signal samples. Migration between categories or uncertainty in the produced number of events must be taken into account in the final fit in order to evaluate if the fitted resonance can be explained by just a resonant background fluctuation or by a net production of DM signals. Migrations mainly involve resolution effects coming from uncertainties on the reconstruction, identification and/or calibration of the different objects in ATLAS. On the other hand, variations in the number of produced events mainly come from uncertainties on the theoretical magnitudes, such as the cross-section of the considered process or the Higgs decay branching ratio, and from uncertainties on the LHC provided luminosity.

7.5.1 Theoretical systematic uncertainties

Theoretical systematics account for all the possible uncertainties on the production cross-sections of the various mechanisms involved in the presented search on the branching ratio of the h boson to two photons.

They can be divided into several categories:

- **QCD scale uncertainties:**

  Cross-sections are calculated until a certain order in the perturbative QCD development. Higher-order terms are not taken into account in the calculation, which translates into an uncertainty on the cross-section. These uncertainties are estimated by varying the factorization and renormalization scales up and down from their nominal values by a factor of two, recalculating the cross-section in each case, and taking the largest deviation from the nominal cross-section as the uncertainty.

- **PDF uncertainties:**

  As explained in Section 1.1.7, the parton distribution functions model the parton substructure of the protons. These PDFs are determined experimentally and depending on the parametrization or the PDF that is used, the total cross-section may vary significantly. In addition, each PDF presents internal uncertainties that induce some systematic effect on the final cross-section calculation. These two sources of uncertainties, called inter-PDF and intra-PDF, are then estimated by evaluating the effect on the final cross-section of using a different PDF set than the nominal one and of varying the parameters of the nominal PDF within their uncertainties obtained from the fit of the experimental data. For SM h samples, the corresponding systematics are studied in [38] for each production mode of the Higgs.

- **Branching ratio uncertainty:**

The branching ratio of the diphoton Higgs decay is $\mathrm{Br}(h \to \gamma\gamma) = 0.02272$ for $m_h = 125.09$ GeV. These values are estimated using HDECAY [39] taking into account NLO electroweak corrections, leading to an uncertainty on the branching ratio of 1.73% of the nominal value [38].

- **Uncertainty on the multiple parton-parton interactions:**

  In the same proton-proton collision, multiple hard collisions between proton constituents may occur due to the composite nature of hadrons. The impact of such parasitic collisions is estimated by switching them on and off in PYTHIA 8 in the production of the ggF SM Higgs-boson sample. The resulting uncertainty in the number of events in this sample conservatively reaches 0.4% in the Rest category, 5.8% in the Different-Vertex category, 3.8% Intermediate-$E_{\mathrm{T}}^{\mathrm{miss}}$ and Different-Vertex category, 3.4% in the High-$E_{\mathrm{T}}^{\mathrm{miss}}$ category and 1.4% in the Mono-Higgs category.

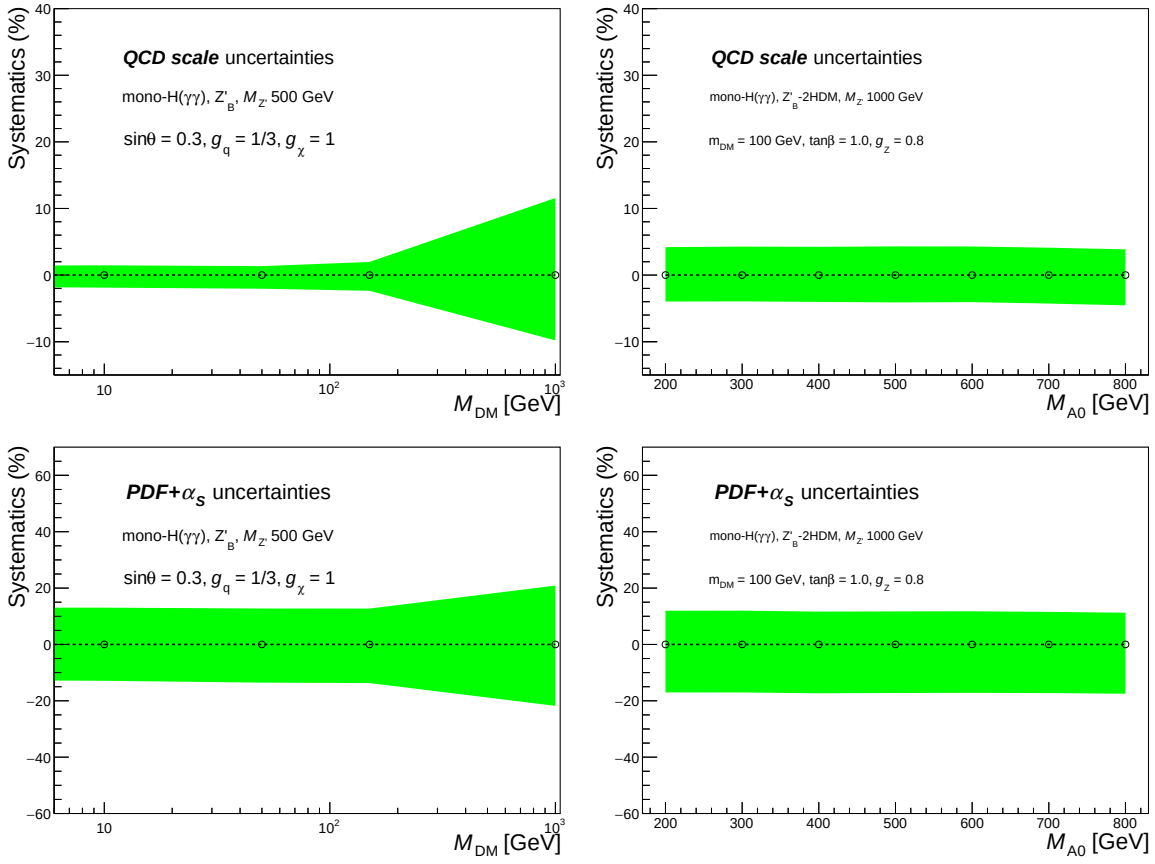


Figure 7.25: Relative scale (top) and PDF (bottom) uncertainty for Z'_B (left) and Z'-2HDM (right) models.

For signal samples, both theoretical uncertainties are evaluated using MADGRAPH 5_aMC@NLO and its associated library SysCalc [40]. The PDF uncertainty is evaluated using the recommendations of PDF4LHC [41]. Figures 7.25 show that PDF uncertainties dominate the theoretical uncertainty for Z'_B and Z'-2HDM samples. Intra-PDF uncertainties are obtained by varying the parameters of the NNPDF3.0LO PDF set, while inter-PDF uncertainties are evaluated using CT14 [42] at LO and MMHT2014 [43] at LO. Figures 7.26 and 7.27 present the scale and PDF uncertainties in the parameter space defined by the mediator and the dark matter particle mass (or the pseudo-scalar mass in the case of Z'-2HDM). On the other hand, theoretical uncertainties for the SM Higgs boson production are taken from [38]. Table 7.5 and 7.6 present the estimation of the QCD scale and PDF+α_s uncertainties on SM Higgs cross-sections.

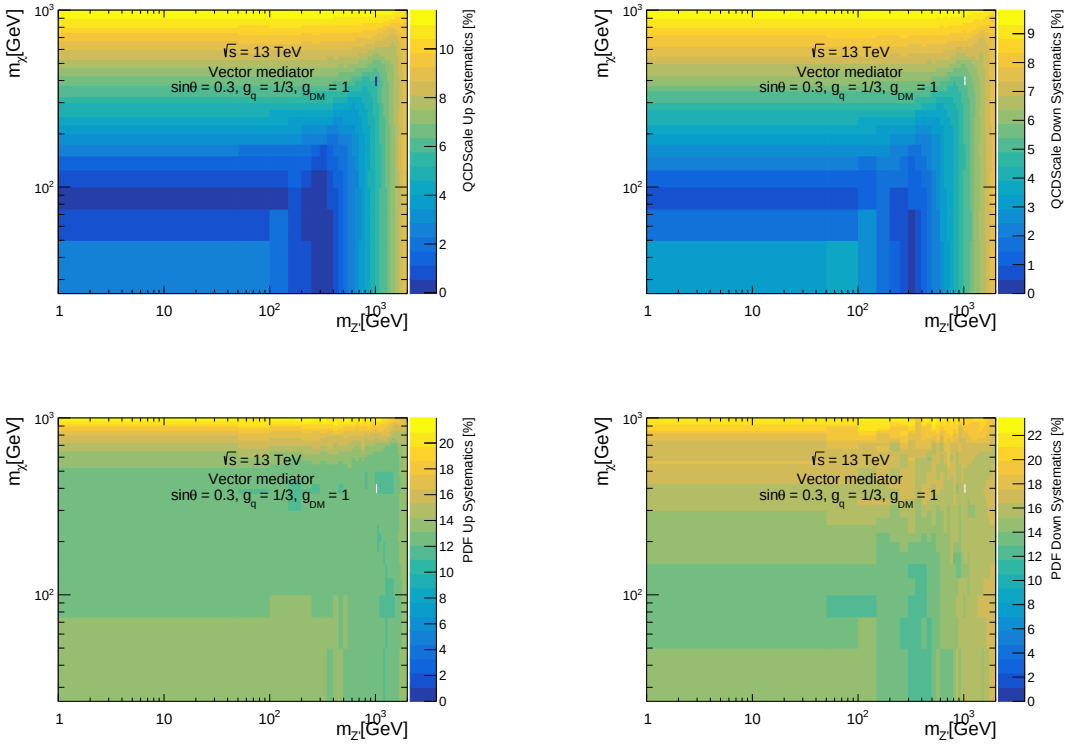


Figure 7.26: QCD (top) and PDF (bottom) systematic relative variation (%) for Z'_B model comparison for different DM mass and $m_{Z'_B}$.

Table 7.5: Relative factorization and renormalization scale uncertainty for SM Higgs boson samples.

Syst (%)	ggF	VBF	WH	ZH	ttH	bbH
Up	4.6	0.4	0.5	3.8	5.8	20.2
Down	-6.7	-0.3	-0.7	-3.1	-9.2	-23.9

Table 7.6: Relative PDF+α_s uncertainty on SM Higgs boson samples.

Syst (%)	ggF	VBF	WH	ZH	ttH	bbH
Up	3.2	2.1	1.9	1.6	3.6	6.1
Down	-3.2	-2.1	-1.9	-1.6	-3.6	-6.1

7.5.2 Experimental systematic uncertainties

Uncertainties on the signal yields for each category may be due to uncertainties on some measured quantities, that either affect the expected number of events after the event selection or that may imply event migrations between categories. Luminosity, trigger efficiencies and vertex selection efficiencies are examples of measured quantities that affect the number of events after selection. On the other hand, migrations between categories may occur due to the uncertainties on the reconstructed objects calibration, identification or isolation steps. A systematic list is provided by all the ATLAS performance groups, each one of them affecting different reconstructed objects. The effect of these uncertainties on the number of events per category is then estimated on MC samples by varying the affected magnitudes the size of the systematic error and re-applying the selection and categorization criteria to the output events. The observed relative variation per category corresponds to the systematic uncertainty on the yields per category. The full set of experimental systematic uncertainty and their effects on the yields are evaluated:

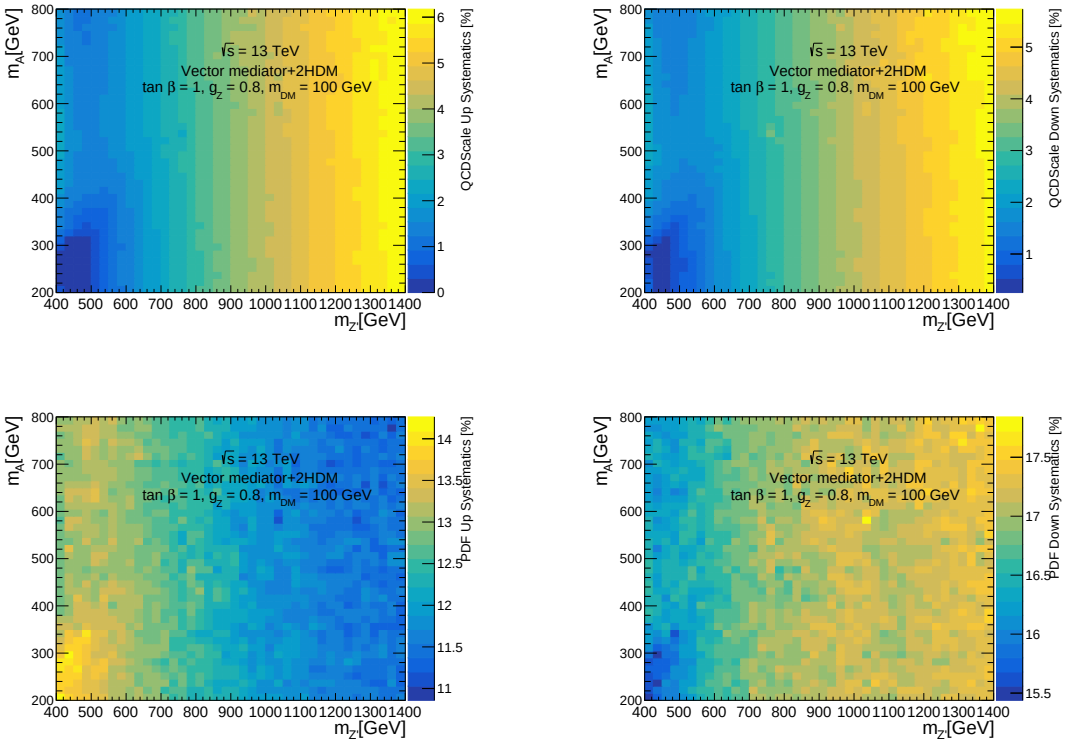


Figure 7.27: QCD (top) and PDF (bottom) systematic relative variation (%) for Z'-2HDM model comparison for different m_A and $m_{Z'_B}$.

Luminosity: The uncertainty in the combined 2015 and 2016 integrated luminosity is 3.2%. It is derived, following a methodology similar to that detailed in **[Lumi2]**, from a calibration of the luminosity scale using x–y beam-separation scans performed in August 2015 and May 2016.

Trigger efficiency: The efficiency of the diphoton trigger used to select events is evaluated in MC simulation using a trigger matching technique and in data using a bootstrap method [44]. In the diphoton invariant mass window of $105\ \text{GeV} < \text{m}_{\gamma\gamma} < 160\ \text{GeV}$, the trigger efficiency uncertainty is found to be 0.4%.

Vertex selection efficiency: The uncertainty in the vertex selection efficiency is assessed by comparing the efficiency of finding photon-pointing vertices in $Z \to e^+e^-$ events in data and MC simulation [4], for which each electron track is removed and its cluster is recalibrated as a photon cluster. The efficiency of this selection in data is found to be in agreement with the simulation within 0.01%.

Pileup reweighting: The MC samples on which systematics are estimated do not present the same profile of average interactions per bunch crossing as data. A reweighting technique is then used to adapt this distribution on MC to the collected data one. However, an uncertainty on this reweighting appears due to the statistical uncertainty on either MC and data, which induces migrations between different categories. The effect of this so-called pileup reweighting uncertainty is taken into account by propagating it through the event selection. This propagation results in a 0.2%–5.6% uncertainty in the event yield of the signal and SM Higgs-boson samples.

Photon experimental uncertainties: The systematic uncertainties due to the photon energy scale and resolution are adapted from Run-1 results [45], with minor updates in case of data-driven corrections using the Run II data. The uncertainty on the energy scale is less than 1% in the p_{T} range of the photons used in this analysis; the uncertainty on the energy resolution is smaller than 2%. Differences on the photon identification efficiency between data and simulation are encoded in scale

factors, which were estimated on data and MC samples of $Z \to \ell\ell\gamma$ process [46]. The uncertainty on these scale factors then induces an uncertainty on the categories yields. The resulting uncertainty on the yields from the photon identification efficiency is lower than 3.8% for SM Higgs background in all categories, 2.9% for simplified model samples and 4.3% for the heavy-scalar model. The uncertainty in the photon calorimeter isolation efficiency is calculated from efficiency differences between applying and not applying corrections derived from inclusive photon events to the isolation variables in simulation. The measurements of the efficiency correction factors using inclusive photon events are used to derive the efficiency uncertainty in the photon track isolation uncertainty. The photon isolation efficiency uncertainty is found to be smaller than 1.6% for the SM Higgs background and 1.2% for all signal samples.

Jets and soft-term uncertainties: Migration of events among categories occurs owing to changes in the energy of identified particles and jets, mostly due to the misreconstruction of jets and $E_{\mathrm{T}}^{\mathrm{miss}}$. The uncertainties in jet energy scale, resolution and jet vertex tagger are propagated to the $E_{\mathrm{T}}^{\mathrm{miss}}$ calculation. In addition, the uncertainties in the scale and resolution of the $E_{\mathrm{T}}^{\mathrm{miss}}$ soft term are estimated in 2016 data using the method described in Ref. [47]. The overall jet and $E_{\mathrm{T}}^{\mathrm{miss}}$ uncertainties in the SM Higgs-boson processes are 6%, 8%, 23%, 22% and 1% for the Mono-Higgs, High-$E_{\mathrm{T}}^{\mathrm{miss}}$, Intermediate-$E_{\mathrm{T}}^{\mathrm{miss}}$, Different-Vertex and Rest categories, respectively. For signal processes, the overall jet and $E_{\mathrm{T}}^{\mathrm{miss}}$ uncertainties range from 1.0% to 1.4%.

$E_{\mathrm{T}}^{\mathrm{miss}}$ diphoton vertex reconstruction uncertainty: Apart from the jets and TST $E_{\mathrm{T}}^{\mathrm{miss}}$ reconstruction, the choice of the diphoton vertex affects the $E_{\mathrm{T}}^{\mathrm{miss}}$ reconstruction. It introduces an additional uncertainty derived from the data-to-MC comparison in $Z \to e^+e^-$ events. This systematic uncertainty affects the processes with no genuine $E_{\mathrm{T}}^{\mathrm{miss}}$ and is estimated in each category. For the SM Higgs-boson production, it is found to be 0.5% in the Mono-Higgs category and up to 1.9% in the other categories. It is less than 0.1% for signal processes.

Efficiency of diphoton/hardest vertex coincidence: Categories requiring the equality of the diphoton vertex and the hardest vertex of the event present an additional uncertainty. This uncertainty accounts for the differences between the expected efficiency of the diphoton/hardest vertex equality in data and MC. A 6% uncertainty is found for the SM Higgs-boson production in the High-$E_{\mathrm{T}}^{\mathrm{miss}}$ and the Intermediate-$E_{\mathrm{T}}^{\mathrm{miss}}$ categories and 1.8% in the heavy-scalar signals in those categories.

Spurious signal: The ratio of the potential bias in the signal yield from the non-resonant background modeling ($N_{\mathrm{bkg}}^{\mathrm{spurious}}/N_{\mathrm{bkg}}^{\mathrm{signal+SMbkg}}$) in the range $120\ \mathrm{GeV} < \mathrm{m}_{\gamma\gamma} < 130\ \mathrm{GeV}$ is 9.8% in the Mono-Higgs category, 4.0% in the High-$E_{\mathrm{T}}^{\mathrm{miss}}$ category, 1.3% in the Intermediate-$E_{\mathrm{T}}^{\mathrm{miss}}$ category, 0.5% in the Different-Vertex category and 0.1% in the Rest category. The spurious signal is taken as an absolute uncertainty in the fit as explained in the previous section.

Experimental systematics inducing migrations are presented in Figures 7.28– 7.30 for three signal models and Figures 7.31 for the SM Higgs background. A summary of all the experimental and theoretical uncertainties is presented in Table 7.7.

7.6 Results

The results for the analysis are derived from a likelihood fit of the $m_{\gamma\gamma}$ distribution in the range $105\ \mathrm{GeV} < m_{\gamma\gamma} < 160\ \mathrm{GeV}$. The SM Higgs boson mass is set to 125.09 GeV [48]. The parameter of interest of the fit is the strength parameter of the signal model, denoted as μ, which stands for the ratio between the observed number of events and the expected yields. Signal and backgrounds yields, the background shape parameters and the associated parameters encoding the systematic uncertainties are also allowed to vary, constituting the *nuisance* parameters of the fit. The signal strength, the non-resonant background yield, the nuisance parameters representing the systematic uncertainties or the SM Higgs yields are profiled, which means that the systematic uncertainty of each nuisance parameter is taken into account by multiplying the likelihood by a Gaussian penalty function ($G(\theta)$). This penalty function is centered on the nominal value of this parameter with a width set to its uncertainty. The impact on the fit due to the

Table 7.7: Breakdown of the dominant systematic uncertainties in the range of 105 GeV $< m_{\gamma\gamma} <$ 160 GeV [3]. The uncertainties in the yield of signals, the background from SM Higgs-boson processes, and non-resonant background are shown. All production modes of the SM Higgs boson are considered together. Values for the impact on all categories are shown, unless one of the systematic uncertainties is not applicable to the sample, in which case the value is substituted by a "-". If a given source has a different impact on the various categories, the given range corresponds to the smallest and largest impacts among categories or among the different signal models used in the analysis. In addition, the potential bias coming from non-resonant background mismodeling is shown relative to the background.

Source	Signals [%]	Backgrounds [%]	
		SM Higgs boson	Non-resonant background
Experimental			
Luminosity		3.2	-
Trigger efficiency		0.4	-
Vertex selection		< 0.1	-
Photon energy scale	0.1-2.0	0.1-1.4	-
Photon energy resolution	0.1-0.2	0.1-1.1	-
Photon identification efficiency	2.9-4.3	1.9-3.8	-
Photon isolation efficiency	1.2	0.8-1.6	-
$E_{\mathrm{T}}^{\mathrm{miss}}$ reconstruction (diphoton vertex)	< 0.1	0.5-1.9	-
$E_{\mathrm{T}}^{\mathrm{miss}}$ reconstruction (jets, soft term)	1.0-1.4	0.8-23	-
Diphoton/hardest vertices equality	< 0.1 -1.9	< 0.1-6.0	-
Pileup reweighting	0.2-5.6	0.7-11	-
Non-resonant background modeling	-	-	$0.1 - 9.8$
Theoretical			
Factorization and renormalization scale	0.6-11	2.5-6.0	-
PDF+α_{S}	$11 - 25$	1.2-2.9	-
Multiple parton-parton interactions	<1	0.4-5.8	-
$\mathcal{B}(H \to \gamma\gamma)$		1.73	-

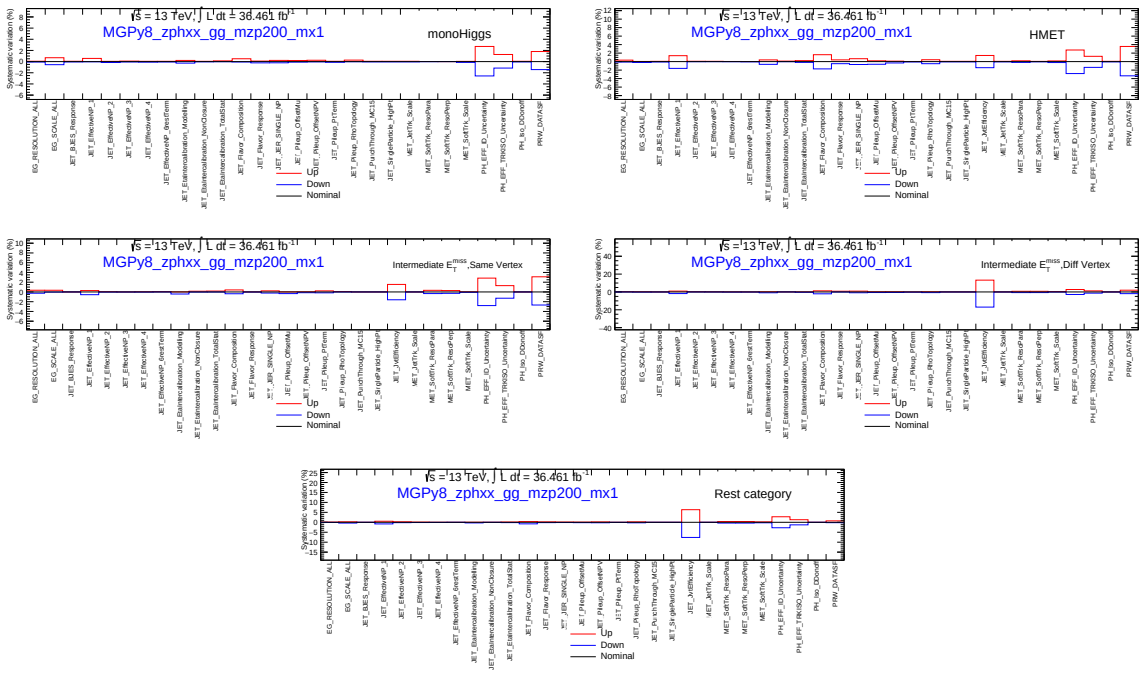


Figure 7.28: Systematic relative variation (%) for the Z'_B $m_\chi = 1$ GeV and $m_{Z'_B} = 200$ GeV sample in the five categories.

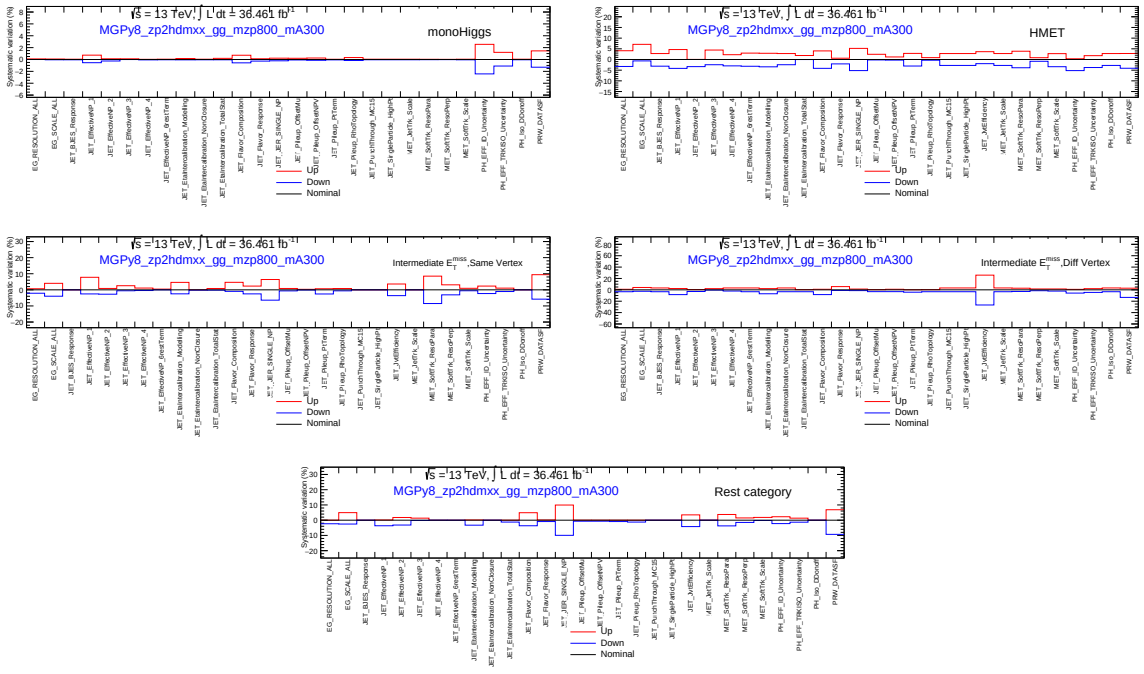


Figure 7.29: Systematic relative variation (%) for the Z'-2HDM $m_{A^0} = 300$ GeV and $m_{Z'} = 800$ GeV sample in the five categories.

signal and SM Higgs shape nuisance parameters is negligible, thus those nuisance parameters are fixed to a value derived with fits on the signal and SM Higgs MC samples. The likelihood function used in this fit is then defined as:

$$\mathcal{L}_c = \text{Pois}(n_c|N_c) \cdot \prod_{i=1}^{n_c} f_c(m^i_{\gamma\gamma}; \mu, \theta) \cdot G(\theta), \tag{7.8}$$

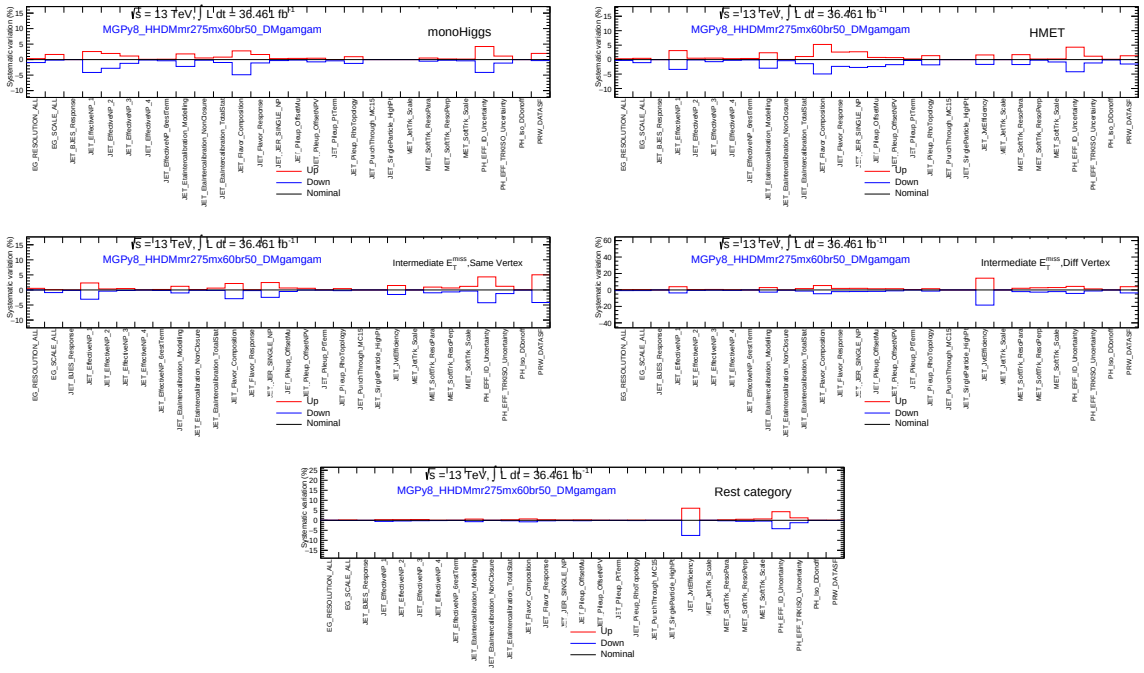


Figure 7.30: Systematic relative variation (%) for the heavy-scalar $m_\chi = 60$ GeV and $m_{\rm H} = 275$ GeV sample in the five categories.

where $f_c(m^i_{\gamma\gamma}, \theta)$ corresponds to the fitting function of category c including the signal and background (resonant, non-resonant and spurious signal) contributions.As explained in previous sections, the results are only obtained from Mono-Higgs category for both the Z'_B and Z'-2HDM signals. Nevertheless, a simultaneous fit has been tested to derive results for these two models, resulting in a negligible improvement of the sensitivity (1%). In contrast, results for the heavy-scalar model are obtained from a simultaneous fit of all the categories.

The event yields in the observed data, expected signal and backgrounds in the five categories within a window of 120 GeV $< \mathrm{m}_{\gamma\gamma} <$ 130 GeV are shown in Table 7.8. The signal samples shown correspond to a Z'_B signal with $m_{Z'_B} = 200$ GeV and $m_\chi = 1$ GeV, a Z'-2HDM signal with $m_{Z'} = 1000$ GeV, $m_{A^0} = 200$ GeV and $m_\chi = 100$ GeV, and a heavy-scalar signal with $m_{\rm H} = 275$ GeV and $m_\chi = 60$ GeV. For each benchmark signal model, the selection efficiency times acceptance denoted by "$\mathcal{A} \times \epsilon$" is also given. The yields for the non-resonant background are obtained from a fit to data while SM Higgs-boson events are estimated from the simulation. The uncertainties correspond to the quadrature sum of the statistical and systematic uncertainties.

7.6.1 Limits on the visible cross-section

The observed yields agree with the SM background predictions, as shown in Table 7.8, and no significant excess of events is observed. Upper limits are set on the visible cross-section $\sigma^{\rm BSM}_{\rm vis} \equiv (\mathcal{A} \times \epsilon \times \sigma \times \mathcal{B})^{\rm BSM}$ for BSM physics processes producing missing transverse momentum and a SM Higgs boson decaying into two photons. Table 7.9 shows the observed and expected 95% confidence level (CL) upper limits on $\sigma^{\rm BSM}_{\rm vis}$, which are calculated using a one-sided profile-likelihood ratio and the $\mathrm{CL_s}$ formalism [49] (see Appendix A) with the asymptotic approximation in Ref. [34]. The same parameterizations for the BSM signal and the total SM Higgs-boson background are used in each of the five different categories. The fits are performed individually in each category. The statistical uncertainty is dominant. The systematic uncertainties worsen the limits by about 10% (7% from the non-resonant background modeling and 3% from the other systematic uncertainties). The $\pm 1\sigma$ variations from the expected limits are also given. For the Mono-Higgs category, visible cross-sections $\sigma^{\rm BSM}_{\rm vis} > 0.19$ fb are excluded. The ranges of the

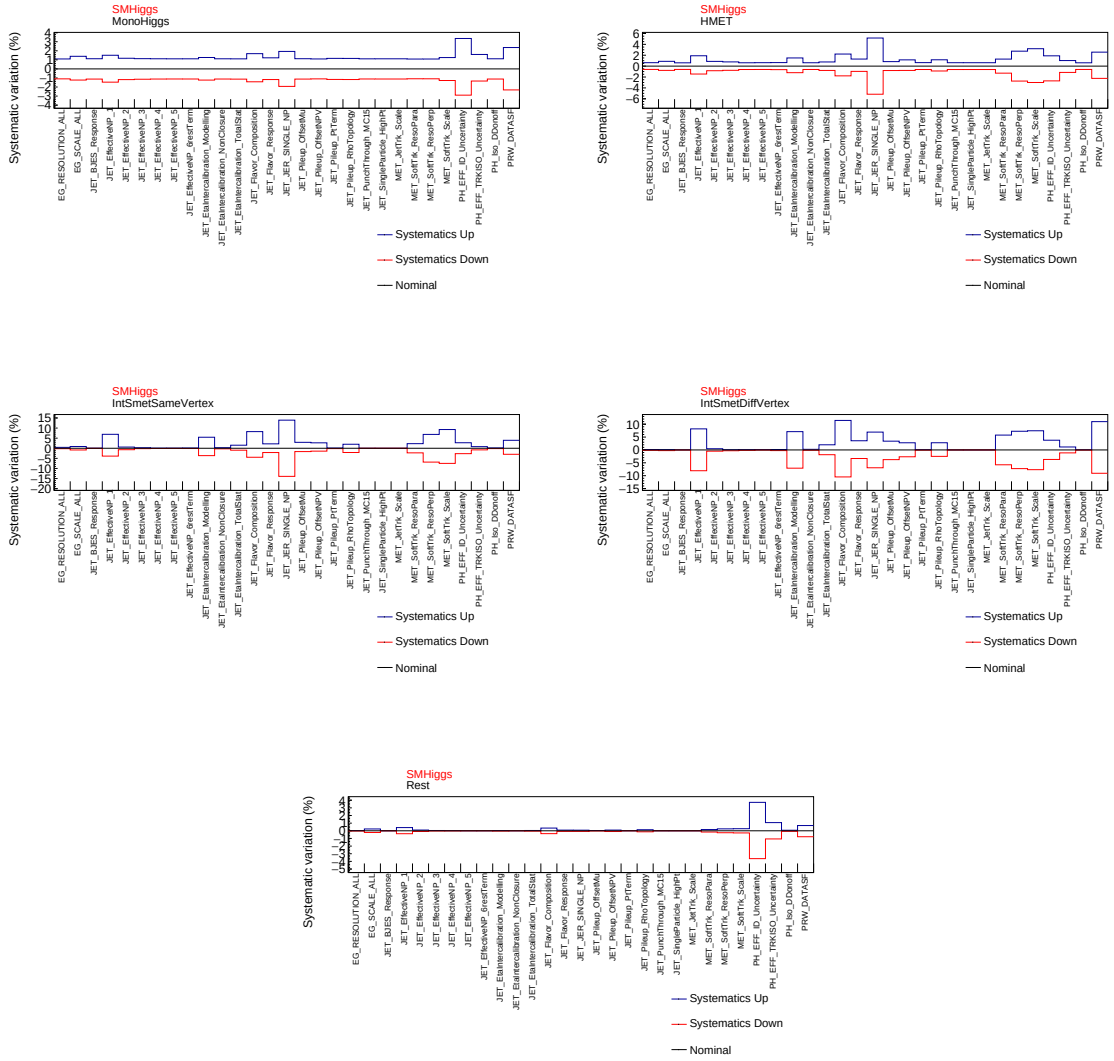


Figure 7.31: Systematic relative variation (%) for the combined SM Higgs samples in the five categories. The combination is the result of the square sum of the total error per production mode divided by the total number of expected events in each category.

acceptance times efficiency ($\mathcal{A} \times \epsilon$) for all three different models considered in this analysis are also shown. For the Z'_B model, signals with DM mass m_χ between 1 and 1000 GeV and mediator mass $m_{Z'_B}$ between 1 and 2000 GeV are taken into consideration. The samples with the mediator mass $m_{Z'} = 400$–1400 GeV and pseudoscalar boson mass $m_{A^0} = 200$–450 GeV are added for the Z'-2HDM model. For the heavy-scalar model, the values are taken from the signals points with m_{H} = 260 to 350 GeV and $m_\chi = 60$ GeV.

7.6.2 DM reweighting

As no excess is observed, excluded regions are defined for Z'_B and Z'-2HDM models in a two-dimensional space defined by the mediator mass $m_{Z'}$ and the dark matter mass m_χ (m_{A^0}) of the simulated Z'_B (Z'-2HDM) sample. The exclusion region is then bounded by the interpolated line between the points from which the exclusion limit $\sigma^{\mathrm{limit}}_{95\%\mathrm{CL}}$ equals the expected cross-section σ_{theo} of a given model. However, the limited number of generated and reconstructed samples imply that the interpolated exclusion bound is

Table 7.8: Event yields in the range of 120 GeV $< m_{\gamma\gamma} <$ 130 GeV for data, signal models, the SM Higgs-boson background and non-resonant background in each analysis category, for an integrated luminosity of 36.1 fb^{-1} [3]. The signal samples shown correspond to a heavy-scalar sample with $m_{\mathrm{H}} = 275$ GeV and $m_{\chi} = 60$ GeV, a Z'_B signal with $m_{Z'_B} = 200$ GeV and $m_{\chi} = 1$ GeV and a Z'-2HDM signal with $m_{Z'} = 1000$ GeV, $m_{A^0} = 200$ GeV, $m_{H^{0,\pm}} = 300$ GeV and $m_{\chi} = 100$ GeV. For each benchmark signal model, the selection efficiency times acceptance denoted as "$\mathcal{A} \times \epsilon$" is also shown. The yields for non-resonant background are obtained from a fit to data while SM Higgs-boson events are estimated from the simulation. The uncertainties correspond to the quadrature sum of the statistical and systematic uncertainties.

Category	Mono-Higgs	High-$E_{\mathrm{T}}^{\mathrm{miss}}$	Intermediate-$E_{\mathrm{T}}^{\mathrm{miss}}$	Different-Vertex	Rest
Data	9	72	464	1511	46804
Backgrounds					
SM Higgs boson	2.43 ± 0.22	4.2 ± 0.6	11.9 ± 2.7	44 ± 10	1360 ± 110
Non-resonant	9.9 ± 1.9	62 ± 5	418 ± 10	1490 ± 18	45570 ± 110
Total background	12.3 ± 1.9	67 ± 5	430 ± 10	1535 ± 21	46930 ± 170
Z'_B model, $m_{Z'_B} = 200$ GeV, $m_{\chi} = 1$ GeV					
Expected yields	20.0 ± 4.5	–	–	–	–
$\mathcal{A} \times \epsilon$ [%]	17.4 ± 0.2	–	–	–	–
Z'-2HDM model, $m_{Z'} = 1000$ GeV, $m_{A^0} = 200$ GeV, $m_{H^{0,\pm}} = 300$ GeV, and $m_{\chi} = 100$ GeV					
Expected yields	28.0 ± 5.3	–	–	–	–
$\mathcal{A} \times \epsilon$ [%]	70.7 ± 0.2	–	–	–	–
Heavy-scalar model, $m_{\mathrm{H}} = 275$ GeV, $m_{\chi} = 60$ GeV					
Expected yields	10.9 ± 1.4	23.8 ± 3.2	43 ± 5	33 ± 5	222 ± 20
$\mathcal{A} \times \epsilon$ [%]	1.22 ± 0.07	2.67 ± 0.10	4.82 ± 0.14	3.65 ± 0.13	24.9 ± 0.4

Table 7.9: Observed and expected upper limits (at 95% CL) on the visible cross-section for BSM physics processes producing missing transverse momentum and a SM Higgs boson decaying into two photons [3]. Limits are presented for the five different categories. The $\pm 1\sigma$ exclusion from expected limits are also given. For all the simulated signal points, the lowest and largest values of the acceptance times efficiency ($\mathcal{A} \times \epsilon$) for all three models are presented as a range. For the Z'_B model, signals with DM mass m_{χ} between 1 and 1000 GeV and mediator mass $m_{Z'_B}$ between 1 and 2000 GeV are taken into consideration. The samples with the mediator mass $m_{Z'} = 400$–1400 GeV and pseudoscalar boson mass $m_{A^0} = 200$–450 GeV are added for the Z'-2HDM model. For the heavy-scalar model, the values are taken from the signals points with m_{H} = 260 to 350 GeV and $m_{\chi} = 60$ GeV.

Category	$\sigma_{\mathrm{vis}}^{\mathrm{BSM}}$ [fb]		$\mathcal{A} \times \epsilon$ [%]		
	Observed	Expected	Z'-2HDM	Z'_B	Heavy scalar
Mono-Higgs	0.19	$0.23^{+0.11}_{-0.07}$	$53 - 74$	$15 - 63$	$1.0 - 4.0$
High-$E_{\mathrm{T}}^{\mathrm{miss}}$	0.67	$0.52^{+0.23}_{-0.15}$	$0.2 - 12$	$1.3 - 7.1$	$1.8 - 8.4$
Intermediate-$E_{\mathrm{T}}^{\mathrm{miss}}$	1.6	$1.2^{+0.5}_{-0.3}$	$0.05 - 5.0$	$0.6 - 5.5$	$3.9 - 6.6$
Different-Vertex	1.5	$2.5^{+1.1}_{-0.7}$	$0.04 - 11$	$0.9 - 10$	$2.5 - 7.4$
Rest	11	15^{+6}_{-4}	$0.06 - 5.5$	$1.1 - 22$	$14 - 27$

not precise. For solving this, instead of requesting one fully reconstructed MC sample for each working point a reweighting scheme using generator level DM MC samples has been investigated in the framework of the present analysis.

The detailed procedure is as follows:

1. Two large statistics FastSim samples are produced. These samples are base samples for this reweighting technique (one for each model);
2. For each required grid point (m_χ or m_{A^0}, $m_{Z'}$), a sample of $\sim$ 100000 events is generated using MADGRAPH 5_aMC@NLO interfaced by PYTHIA 8.
3. For each of these samples, the weights $w(X)$ needed to reweight the base samples are calculated by dividing the generator level (truth) $E_{\mathrm{T}}^{\mathrm{miss}}$ and $p_{\mathrm{T}}^{\gamma\gamma}$ distributions of each sample and the one from the base sample using histograms;
4. The weights $w(X)$ are applied on an event by event basis to the base sample to get the reco level corrected shape for each sample of (m_χ, $m_{Z'}$);
5. A closure test is done to assess a systematic uncertainty to the full procedure in order to check the goodness of the previous reweighting, FastSim samples are produced for few points in the parameter space to compare their reco level variables with the ones obtained using the reweighted base sample. Cut efficiency differences using both kinds of sample are used as a source of extra systematic uncertainty associated with the reweighting procedure and are included in the fit of each reweighted data sample. Those relative differences are presented for the Z'_B and Z'-2HDM models in Fig. 7.32 and appears to be at maximum of 5%.

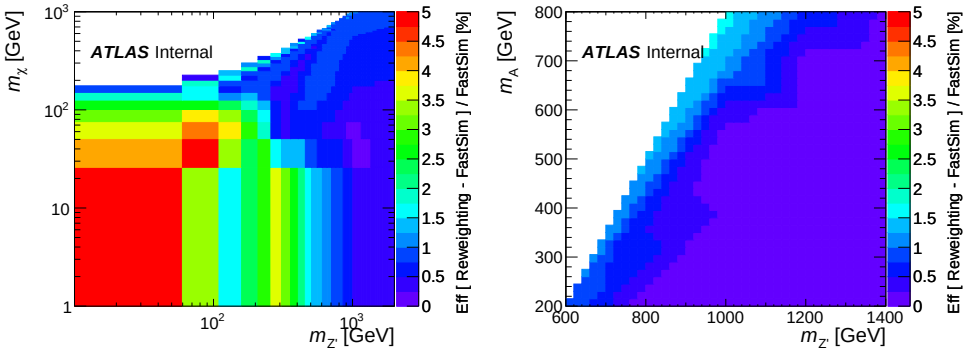


Figure 7.32: Relative differences of selection efficiencies for the Z'_B and Z'-2HDM models computed using a FastSim MC sample or the reweighted base sample as explained in the text.

Figures 7.33 and 7.35 present a comparison of the MET spectrum obtained either from the reweighted base sample or with a FastSim sample for different points in the parameter space of the $Z' - 2HDM$ and Z'_B models respectively. Figures 7.34 and 7.36 present a comparison of the diphoton transverse momentum spectrum obtained either from the reweighted base sample or with a FastSim sample for different points in the parameter space of the Z'-2HDM and Z'_B models respectively. Given that the analysis is limited by statistical uncertainties, the maximum 5% uncertainty found in the closure test is added as a systematic to all the reweighted samples efficiency. This reweighting technique is used for the DM models interpretation. Heavy scalar interpretation uses just the simulated samples presented in Section 7.1.1 so this 5% systematic uncertainty is not applied to it.

7.6.3 Interpretations of the Z'_B and Z'-2HDM models

Figure 7.37 shows the ATLAS data $m_{\gamma\gamma}$ distributions in the Mono-Higgs category as well as the fits for a Z'_B benchmark point with $m_{Z'_B}$ = 200 GeV and m_χ = 1 GeV. No significant excess is observed in this cate-

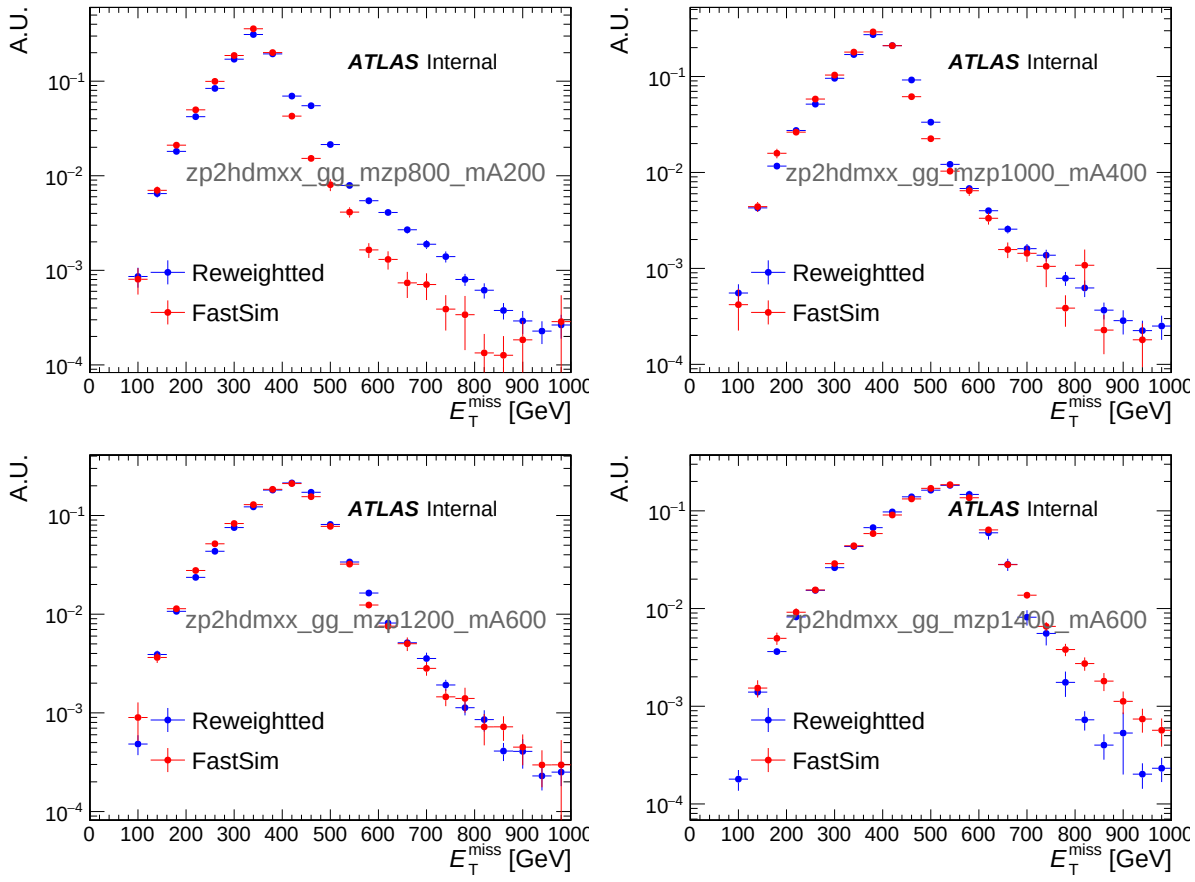


Figure 7.33: Comparison of the MET spectrum obtained either from the reweighted base sample or with a FastSim sample for different points in the parameter space of the $Z' - 2HDM$ model

gory. Upper limits are set on the production cross-sections in the two theoretical models considered. Figure 7.38(a) shows the observed and median expected 95% CL upper limits on $\sigma(pp \to h\chi\bar{\chi}) \times \mathcal{B}(h \to \gamma\gamma)$ as a function of the mediator mass $m_{Z'_B}$ for a DM mass of 1 GeV. Cross sections times branching fraction of $h \to \gamma\gamma$ larger than 2.3 fb are excluded for the full range of $m_{Z'_B}$ between 10 and 2000 GeV at 95% CL, and the Z'_B model is excluded with Z'_B masses below 850 GeV for a DM mass of 1 GeV.

In the Z'-2HDM scenario, the observed and median expected 95% CL upper limits on $\sigma(pp \to h\chi\bar{\chi}) \times \mathcal{B}(h \to \gamma\gamma)$ are shown in Figure 7.38(b), as a function of the pseudoscalar boson mass m_{A^0} for m_χ = 100 GeV and $m_{Z'} = 1000$ GeV. The masses of the neutral CP-even scalar (H^0) and the charged scalars ($H^\pm$) from Z'-2HDM model are set to 300 GeV.The theoretical cross-section starts from $m_{A^0} = 201$ GeV. The working point with $m_{A^0} = 200$ GeV is excluded since the resonant production of DM particles at $m_\chi = 100$ GeV significantly increases the cross-section of the process. To avoid the resonant regime where $m_{A^0} = 200$ GeV and $m_\chi = 100$ GeV and allow a better limit interpolation, the point $m_{A^0} = 201$ GeV is shown in this plot instead of 200 GeV. The drop of the theoretical prediction at $m_{A^0} = 345$ GeV is due to a rapid change in the width of $A^0 \to \chi\bar{\chi}$ when A^0 decaying to $t\bar{t}$ is kinematically allowed. Pseudoscalar boson masses below 280 GeV are excluded for $m_{Z'} = 1000$ GeV and m_χ = 100 GeV. Tables 7.10 and 7.11 present the 95% CL observed and median expected limits on $\sigma(pp \to h\chi\bar{\chi}) \times \mathcal{B}(h \to \gamma\gamma)$, respectively, for the Z'_B benchmark model for different Z'_B masses and the Z'-2HDM model for different pseudoscalar A^0 masses. The corresponding expected limits with one standard deviation are also shown.

The observed and expected 95% CL limit contours for the signal strength $\sigma^{\text{obs}}/\sigma^{\text{th}}$ are shown in Figure 7.39 for both the Z'_B and Z'-2HDM models, in which σ^{obs} is the observed limit on the model cross-section at a given point of the parameter space and σ^{th} is the predicted cross-section in the model at the same point. A fine grid of exclusion limits is built using the DM reweighting technique presented in

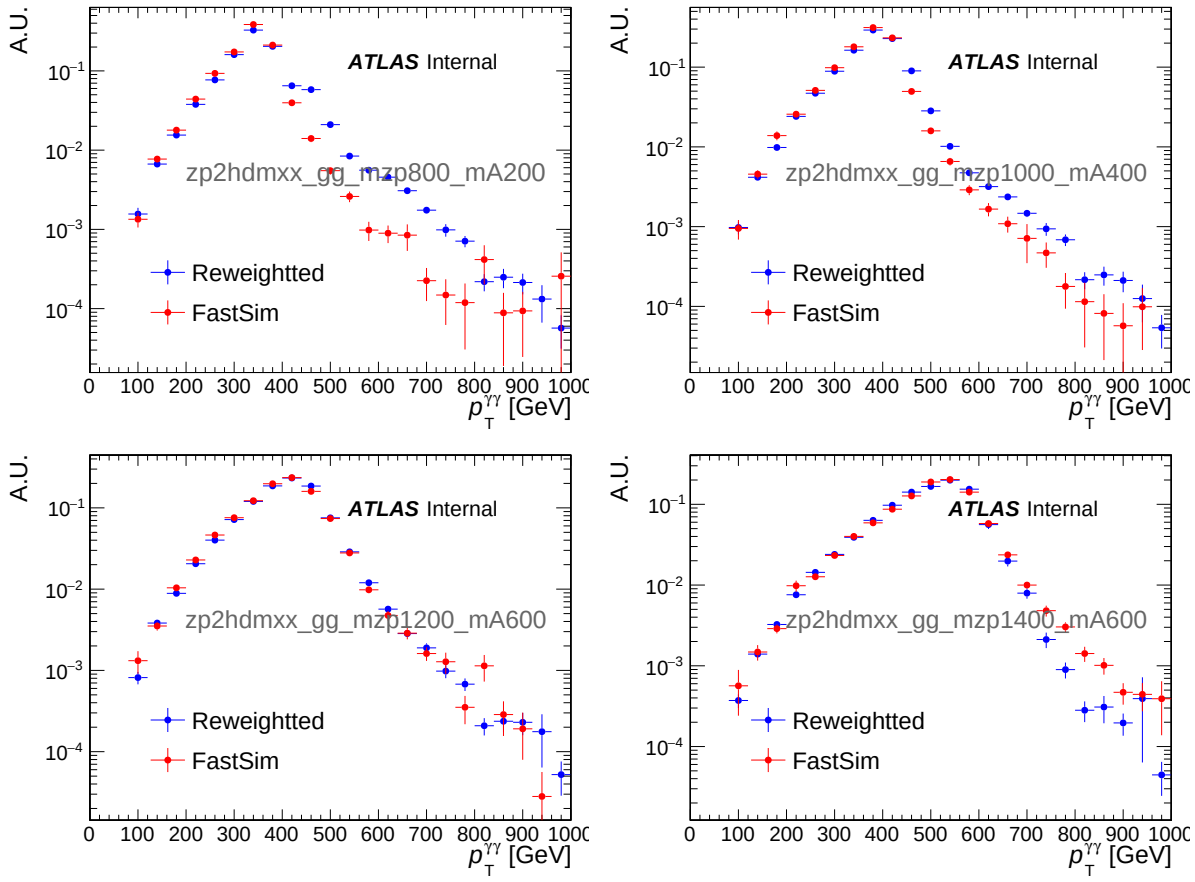


Figure 7.34: Comparison of the diphoton pair transverse energy spectrum obtained either from the reweighted base sample or with a FastSim sample for different points in the parameter space of the $Z' - 2HDM$ model

Section 7.6.2

Table 7.10: Observed and expected 95% CL upper limits (in fb) on $\sigma(pp \to h\chi\bar{\chi}) \times \mathcal{B}(h \to \gamma\gamma)$ and associated expected $\pm 1\sigma$ upper limits for the Z'_B benchmark model for different $m_{Z'_B}$ and for a fixed mass $m_\chi = 1$ GeV [3].

$m_{Z'_B}$ [GeV]	Observed	Expected	Expected $+1\sigma$	Expected -1σ
10	1.83	2.33	3.61	1.56
20	1.98	2.51	3.91	1.68
50	2.26	2.88	4.47	1.93
100	2.04	2.60	4.03	1.74
200	1.78	2.26	3.48	1.52
300	1.67	2.15	3.29	1.45
500	0.99	1.25	1.92	0.85
1000	0.59	0.74	1.16	0.50
2000	0.42	0.51	0.81	0.34

Figure 7.40 shows a comparison of the inferred limits to the constraints from direct detection experiments on the spin-independent (SI) DM–nucleon cross section in the context of the Z'_B simplified model with vector couplings using the relation [50]:

$$\sigma^{\mathrm{SI}}_{N\chi} = \frac{\mu^2_{N\chi}}{\pi A^2} \left[Z f_p - (A - Z) f_n \right]^2 , \tag{7.9}$$

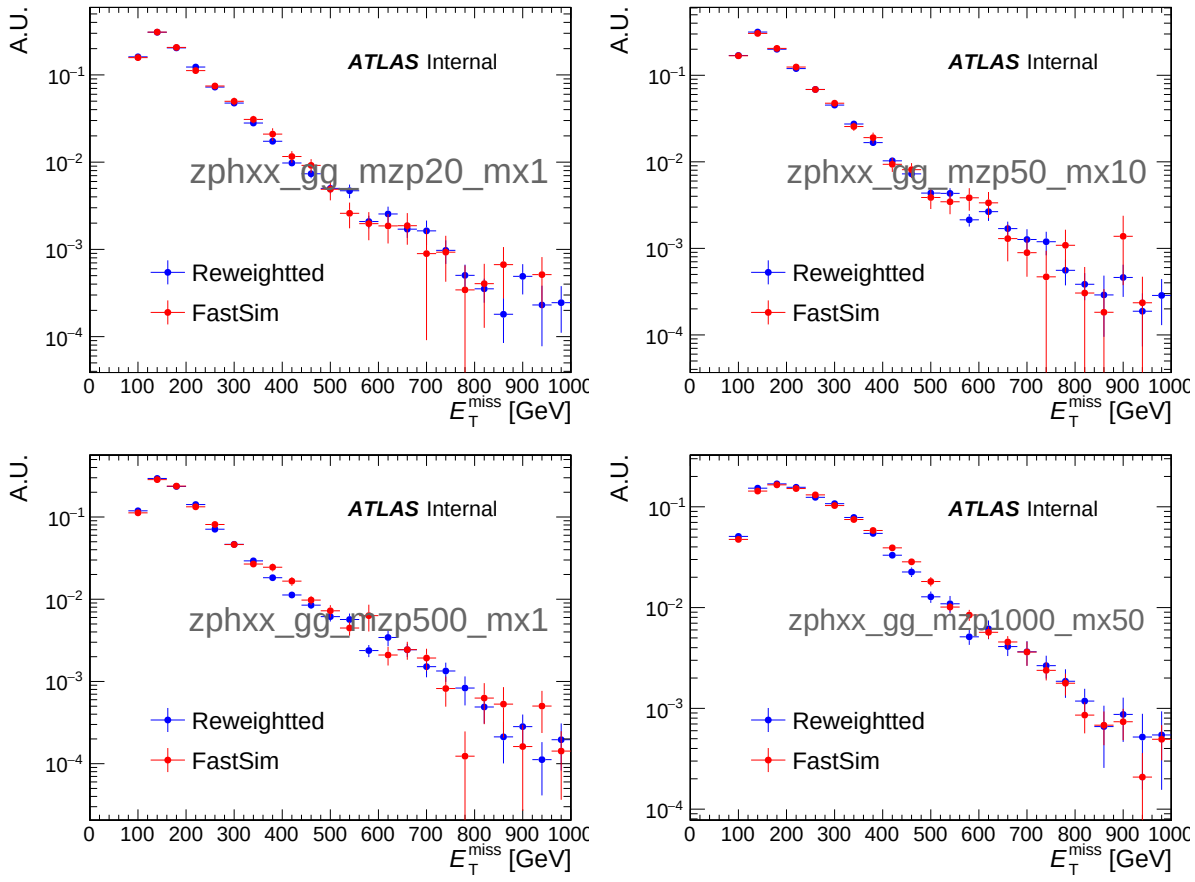


Figure 7.35: Comparison of the MET spectrum obtained either from the reweighted base sample or with a FastSim sample for different points in the parameter space of the Z'_B model

Table 7.11: Observed and expected 95% CL upper limits (in fb) on $\sigma(pp \to h\chi\bar{\chi}) \times \mathcal{B}(h \to \gamma\gamma)$ and the associated expected $\pm 1\sigma$ upper limits for the Z'-2HDM benchmark model for different m_{A^0} and $m_{Z'} = 1000$ GeV, $m_\chi = 100$ GeV [3].

m_{A^0} [GeV]	Observed	Expected	Expected $+1\sigma$	Expected -1σ
200	0.33	0.41	0.65	0.27
300	0.34	0.42	0.65	0.28
400	0.35	0.43	0.67	0.28
500	0.38	0.45	0.70	0.30
600	0.39	0.47	0.74	0.31
700	0.40	0.51	0.80	0.34
800	0.40	0.51	0.80	0.34

in which $\mu_{N\chi} = m_\chi m_N/(m_\chi+m_N)$ is the reduced mass of the DM–nucleon system, and $f_{p,n} = 3g_q g_\chi/m^2_{Z'_B}$ are the specific couplings between DM particles and protons and neutrons for spin-independent direct detection [50]. Following this convention, the SI cross-section limit becomes:

$$\sigma^{\text{SI}}_{N\chi} = \frac{\mu^2_{N\chi}}{\pi} f_p, \tag{7.10}$$

The parameter Z is the number of protons in the considered nucleus and A the number of nucleons and are both conventionally set to 1 to allow comparisons between direct detection and collider limits. Limits are shown at 90% CL. For comparison, results from direct detection experiments (LUX [51], PandaX-II [52], XENON [53], superCDMS [54], and CRESST-II [55]) are also shown. The comparison is model-

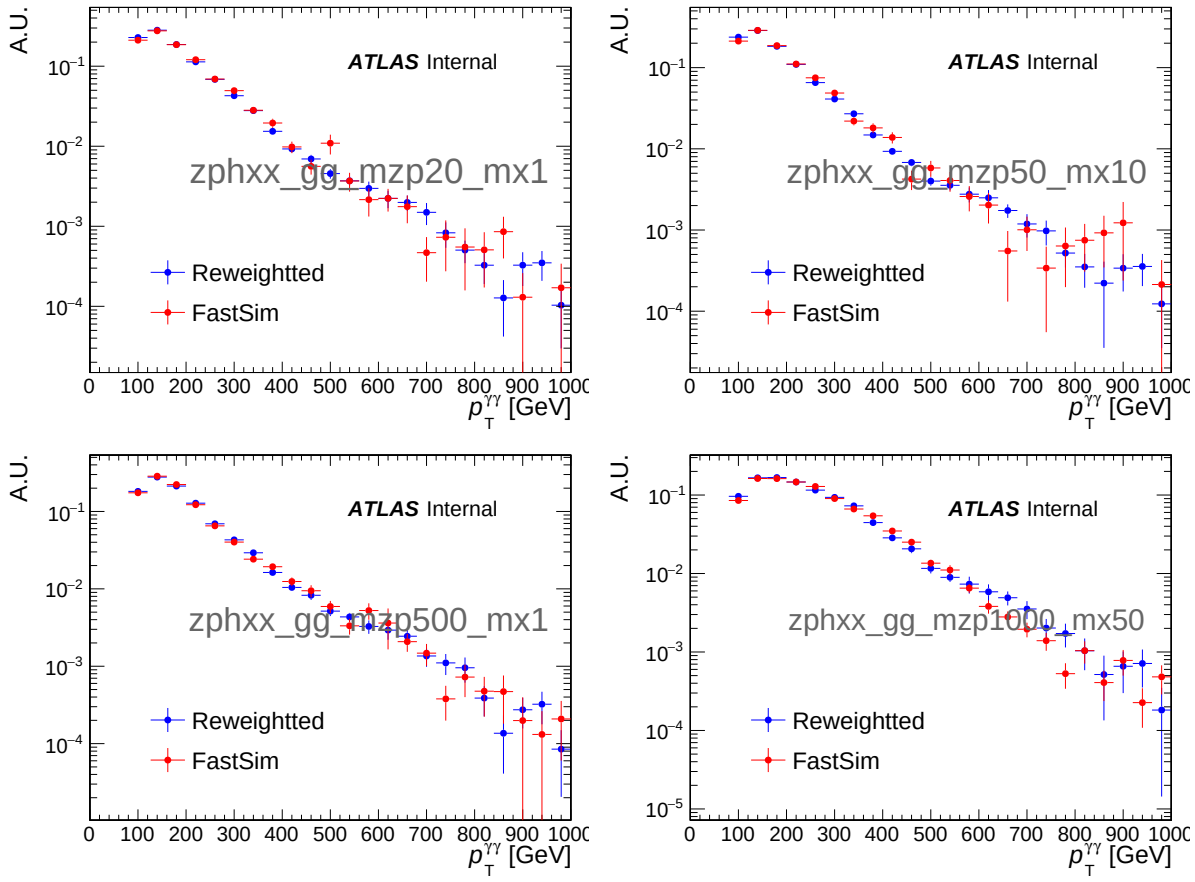


Figure 7.36: Comparison of the diphoton pair transverse energy spectrum obtained either from the reweighted base sample or with a FastSim sample for different points in the parameter space of the Z'_B model

dependent and solely valid in the context of this model. The results for the Z'_B model, with couplings $g_q = 1/3$ and $g_\chi = 1$ for this search, are more stringent than direct detection experiments for $m_\chi < 2.5$ GeV and extend to DM masses well below 1 GeV. The shape of the exclusion line at DM mass $m_\chi \sim 200$ GeV to low masses is due to the loss of sensitivity in Z'_B models where DM particles are produced via an off-shell process. The impact of renormalization-group evolution effects [56, 57] when comparing collider and direct detection limits is not taken into consideration here. This is a good example of the complementary information brought by collider searches and direct detection searches explained in Section 1.4.4. Models used in these analysis cannot however be used to add complementary information to spin-dependent cross-section limits. This is due to the mediation of Z' vector bosons, given that spin-dependent cross-sections involve interactions mediated by axial-mediators [58].

7.6.4 Interpretation of the heavy-scalar model

Figure 7.41 shows the $m_{\gamma\gamma}$ distributions in the five categories simultaneously as the fitted contribution of a heavy-scalar boson for illustration. No significant excess is observed in any category. In the heavy-scalar interpretation, the 95% CL upper limits on the $\sigma(pp \to H) \times \mathcal{B}(H \to \gamma\gamma\chi\chi)$ as a function of $m_{\rm H}$ for m_χ = 60 GeV are shown in Figure 7.42 and Table 7.12, where a 100% branching fraction is assumed for $H \to h\chi\chi$. The upper limit at 95% CL is 15.4 fb for $m_{\rm H} = 260$ GeV, and 4.3 fb for $m_{\rm H} = 350$ GeV.

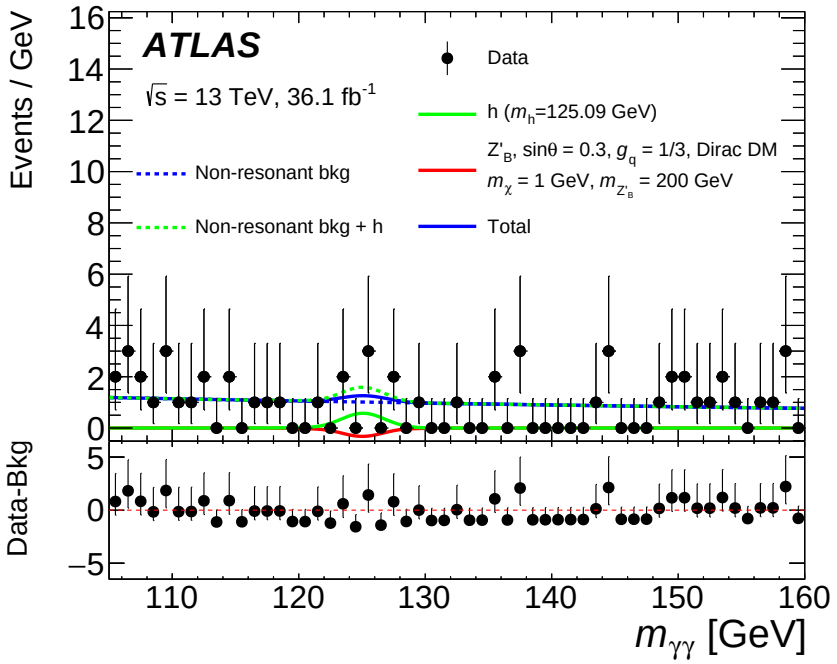


Figure 7.37: Diphoton invariant mass distribution for data and the corresponding fitted signal and background in the Mono-Higgs category for the Z'_B benchmark model fit using $g_q = 1/3$, $g_\chi = 1$, $\sin\theta = 0.3$ and Dirac fermion DM $m_\chi = 1$ GeV as an illustration [3]. A negative best-fit DM signal is found. The data is shown as dots with asymmetric error bars that represent central Poissonian confidence intervals at 68% CL. The fitted signal (solid red line), SM Higgs boson (solid green line), non-resonant background (dashed blue line) and the non-resonant background plus the SM Higgs boson (dashed green line) are shown as well as the total of all those contributions (solid blue line).

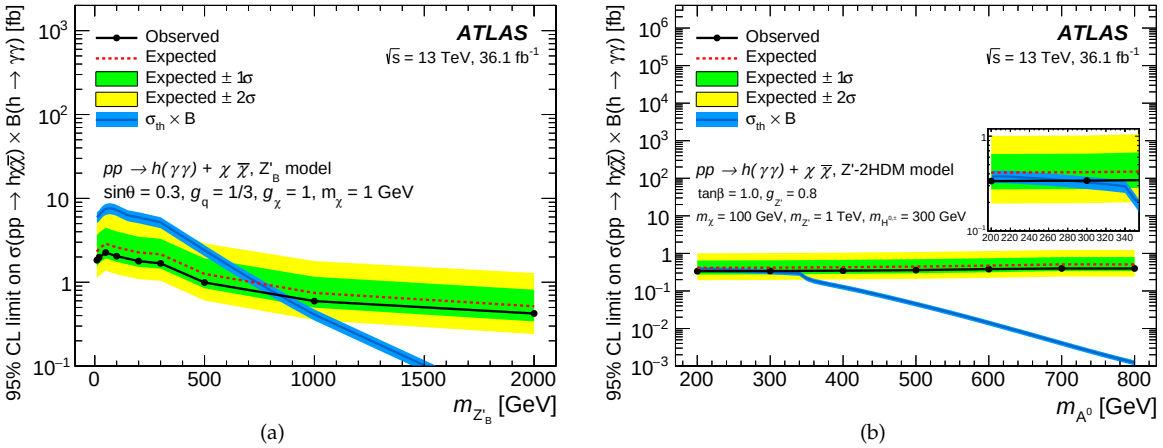


Figure 7.38: Expected (dashed lines) and observed (solid lines) 95% CL upper limits on $\sigma(pp \to h\chi\bar{\chi}) \times \mathcal{B}(h \to \gamma\gamma)$ for (a) the Z'_B model for $g_q = 1/3$, $g_\chi = 1$, $\sin\theta = 0.3$ and Dirac fermion DM $m_\chi = 1$ GeV and (b) the Z'-2HDM model for $\tan\beta = 1$, $g_{Z'} = 0.8$, $m_{Z'}$=1000 GeV and Dirac fermion DM $m_\chi = 100$ GeV, as a function of $m_{Z'_B}$ and m_{A^0}, respectively [3]. The masses of the neutral CP-even scalar (H^0) and the charged scalars ($H^\pm$) from Z'-2HDM model are set to 300 GeV. The theoretical predictions of $\sigma(pp \to h\chi\bar{\chi}) \times \mathcal{B}(h \to \gamma\gamma)$ for these two models (dark-blue lines with blue bands representing their associated theoretical systematic uncertainties) are also shown. The inset shows a zoomed-in view of the same figure in narrower ranges of both the x and y axes.

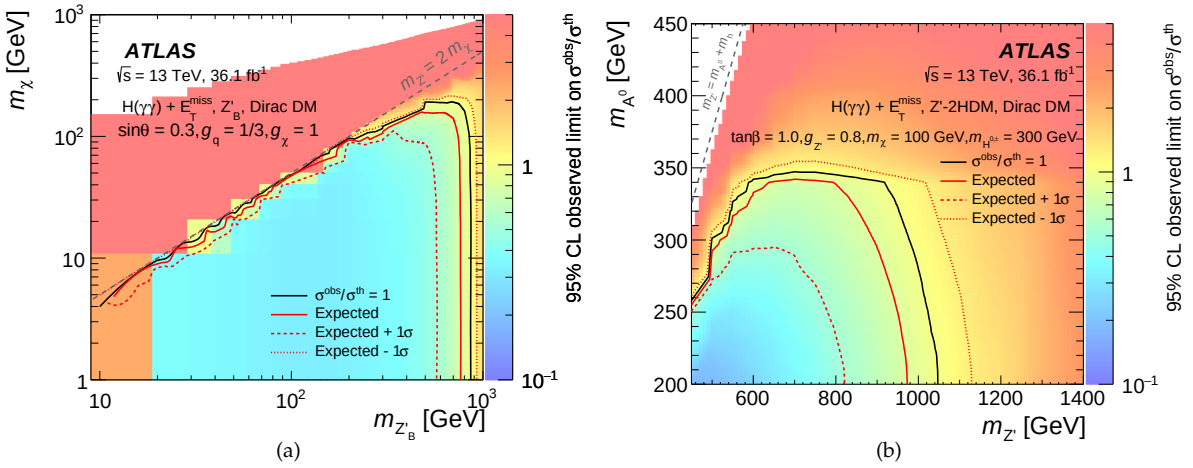


Figure 7.39: The ratios of the observed and expected 95% CL upper limits on the signal cross-section to the predicted signal cross-sections for (a) the Z'_B model in the (m_χ, $m_{Z'_B}$) plane and (b) the Z'-2HDM model in the (m_{A^0}, $m_{Z'}$) plane [3]. For the Z'_B model, the mixing angle $\sin\theta = 0.3$, and the coupling values $g_q = 1/3$ and $g_\chi = 1$ are used. In the scenario of Z'-2HDM model, the ratio of the two-Higgs-doublet vacuum expectation values $\tan\beta = 1.0$, Dirac fermion DM mass $m_\chi = 100$ GeV, and the coupling value $g_{Z'} = 0.8$ are used. The masses of the neutral CP-even scalar (H^0) and the charged scalars ($H^\pm$) from Z'-2HDM model are set to 300 GeV. The plus and minus one standard deviation expected exclusion curves are also shown as red dashed and dotted lines. The regions below the lines (i.e. with $\sigma^{\text{obs}}/\sigma^{\text{th}} < 1$) are excluded. In both figures, the gray dashed line corresponds to the boundary of the region above which the Z' boson is produced off-shell.

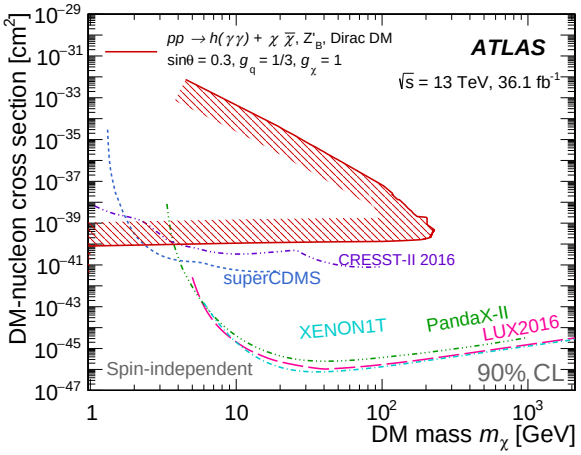
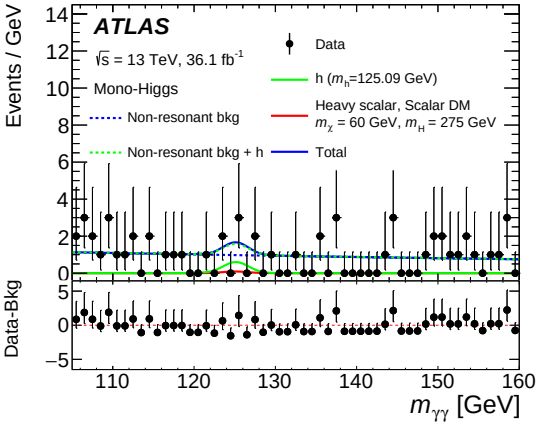
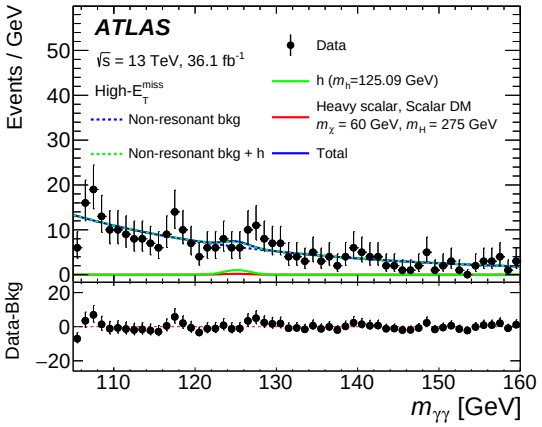


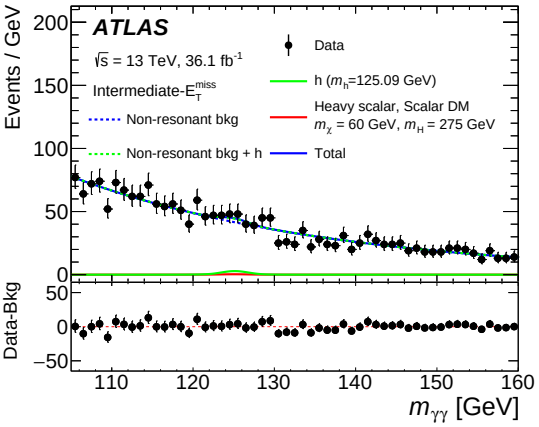
Figure 7.40: A comparison of the inferred limits to the constraints from direct detection experiments on the spin-independent DM–nucleon cross section in the context of the Z'_B simplified model with vector couplings [3]. Limits are shown at 90% CL. The results from this analysis, in which the region inside the contour is excluded, are compared with limits from the LUX [51], PandaX-II [52], XENON [53], superCDMS [54], and CRESST-II [55] experiments. The comparison is model-dependent and solely valid in the context of this model, assuming Dirac fermion DM, mixing angle $\sin\theta = 0.3$, and the coupling values $g_q = 1/3$ and $g_\chi = 1$. The impact of renormalization-group evolution effects [56, 57] when comparing collider and direct detection limits is not taken into consideration here.



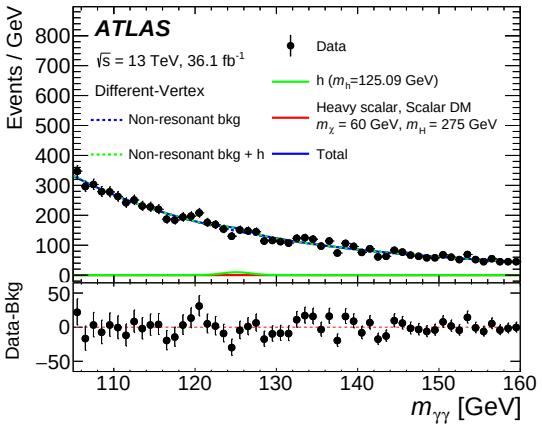
(a)



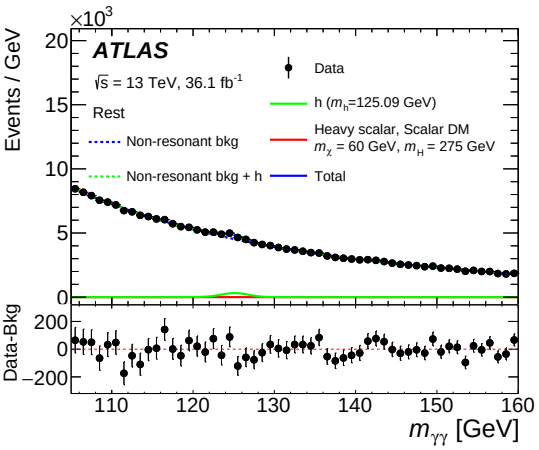
(b)



(c)



(d)



(e)

Figure 7.41: Diphoton invariant mass distribution for data and the corresponding fitted signal and background in the five categories, (a) Mono-Higgs category, (b) High-$E_{\mathrm{T}}^{\mathrm{miss}}$ category, (c) Intermediate-$E_{\mathrm{T}}^{\mathrm{miss}}$ category, (d) Different-Vertex category and (e) Rest category taken from Ref. [3]. On each plot, the data (dots with asymmetric error bars) is shown. The error bars represent the central Poissonian confidence intervals at 68% CL. The simultaneous fit result including a heavy-scalar signal (solid red line), SM Higgs boson (solid green line), the non-resonant background (dashed blue line) and the non-resonant background plus the SM Higgs boson (dashed green line) are shown as well as the sum of all those contributions (solid blue line). The fitted heavy-scalar signal shown here corresponds to $m_{\mathrm{H}} = 275$ GeV and scalar DM $m_{\chi} = 60$ GeV.

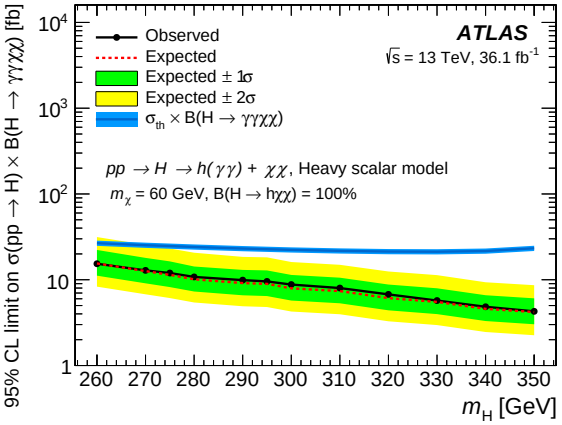


Figure 7.42: Observed and expected 95% CL upper limits on the $\sigma(pp \to H) \times \mathcal{B}(H \to \gamma\gamma\chi\chi)$ with a scalar DM candidate mass of 60 GeV as a function of the heavy-scalar-boson mass in the range 260 GeV $< m_{\mathrm{H}} <$ 350 GeV [3]. A 100% branching fraction is assumed for $H \to h\chi\chi$. The theoretical prediction for the model (dark-blue lines with blue bands representing their associated theoretical systematic uncertainties) is also shown. The theoretical cross-section is assumed to be equal to that of a SM Higgs boson with the same mass produced in gluon–gluon fusion.

Table 7.12: Observed and expected 95% CL upper limits (in fb) on the $\sigma(pp \to H) \times \mathcal{B}(H \to \gamma\gamma\chi\chi)$, where a 100% branching fraction is assumed for $H \to h\chi\chi$, and the associated expected $\pm 1\sigma$ upper limits for the heavy-scalar model for different mediator masses and $m_\chi = 60$ GeV [3].

m_{H} [GeV]	Observed	Expected	Expected $+1\sigma$	Expected -1σ
260	15.4	15.5	22.3	11.2
270	12.9	12.6	18.0	9.1
275	12.0	11.4	16.4	8.2
285	10.8	11.1	14.3	7.3
290	9.9	9.1	13.0	6.6
295	9.6	9.0	12.8	6.5
300	8.8	7.9	11.4	5.7
310	8.0	7.4	10.6	5.3
320	6.8	6.1	8.8	4.4
330	5.7	5.5	7.9	4.0
340	4.8	4.6	6.6	3.3
350	4.3	4.2	6.1	3.0

7.7 Comparison of the ATLAS $h \to \gamma\gamma + E_{\mathrm{T}}^{\mathrm{miss}}$ with other measurements

7.7.1 Mono-Higgs ATLAS $h \to b\bar{b}$ results

DM searches have also been performed in other final states in ATLAS. Z'-2HDM model is also studied in the $h \to b\bar{b} + E_{\mathrm{T}}^{\mathrm{miss}}$ final state [59].

As in $h \to \gamma\gamma + E_{\mathrm{T}}^{\mathrm{miss}}$ searches, the signal in $h \to b\bar{b} + E_{\mathrm{T}}^{\mathrm{miss}}$ channel is characterized by a high $E_{\mathrm{T}}^{\mathrm{miss}}$ and no leptons in the final state. A signal region is defined requiring no lepton and $E_{\mathrm{T}}^{\mathrm{miss}} > 150$ GeV. This signal region is then divided into four bins in $E_{\mathrm{T}}^{\mathrm{miss}}$ in order to improve the signal sensitivity: 150 GeV $\leq E_{\mathrm{T}}^{\mathrm{miss}} <$ 200 GeV, 200 GeV $\leq E_{\mathrm{T}}^{\mathrm{miss}} <$ 350 GeV, 350 GeV $\leq E_{\mathrm{T}}^{\mathrm{miss}} <$ 500 GeV $E_{\mathrm{T}}^{\mathrm{miss}} \geq$ 500 GeV regions. The first three categories belong to a regime called "resolved" regime. In this case, the Higgs particle is tagged by two small radius jets reconstructed using the anti-k$_t$ algorithm with radius parameter $R = 0.4$. One of

the jets must be tagged as a b-jet [60, 61] and the invariant mass of the Higgs particle is reconstructed either using the two most energetic b-tagged jets of the event or the b-jet and the most energetic non-b jet of the event. On the other hand, large $E_{\mathrm{T}}^{\mathrm{miss}}$ topology in the last category implies that Higgs boson is highly boosted in the opposite direction of the $E_{\mathrm{T}}^{\mathrm{miss}}$. This causes that the two final b-jets cannot be reconstructed separately. A large-R jet ($R = 1.0$) is then considered as the Higgs candidate particle. Dominant backgrounds in these searches correspond to $Z(\to \nu\nu)$+jets, W+jets and $t\bar{t}$. Apart from signal regions, two control regions are further defined per signal region to constrain these backgrounds. The first control region requires a muon in the event and is used to constraint the W+jets and $t\bar{t}$ backgrounds. A second control region collects events that present two leptons in the event, used to constrain $Z(\to \ell\ell)$+jets normalization and shapes. $Z(\to \nu\nu)$+jets contribution is estimated by using these constrain $Z(\to \ell\ell)$+jets sample by considering that the dilepton system kinematics are similar to the kinematics of the the di-neutrino system. Then, the $E_{\mathrm{T}}^{\mathrm{miss}}$ distribution of $Z(\to \nu\nu)$+jets background is equated to the dilepton transverse momentum distribution in $Z(\to \ell\ell)$+jets.A summary of all the selection criteria applied on signal regions and control regions is presented in Fig. 7.44.

Region	SR	1μ-CR	2ℓ-CR
Trigger	$E_{\mathrm{T}}^{\mathrm{miss}}$	$E_{\mathrm{T}}^{\mathrm{miss}}$	Single lepton
Leptons	No e or μ	Exactly one μ	Exactly two e or μ 83 GeV < m_{ee} < 99 GeV 71 GeV < $m_{\mu^{\pm}\mu^{\mp}}$ < 106 GeV
Resolved	$E_{\mathrm{T}}^{\mathrm{miss}} \in [150, 500)$ GeV $p_{\mathrm{T}}^{\mathrm{miss,trk}} > 30$ GeV (1 b-tag only) $\min\left[\Delta\phi\left(\vec{E}_{\mathrm{T}}^{\mathrm{miss}}, \vec{p}_{\mathrm{T}}^{j}\right)\right] > \pi/9$ $\Delta\phi\left(\vec{E}_{\mathrm{T}}^{\mathrm{miss}}, \vec{p}_{\mathrm{T}}^{\mathrm{miss,trk}}\right) < \pi/2$ –	$p_{\mathrm{T}}(\mu, E_{\mathrm{T}}^{\mathrm{miss}}) \in [150, 500)$ GeV $p_{\mathrm{T}}(\mu, \vec{p}_{\mathrm{T}}^{\mathrm{miss,trk}}) > 30$ GeV $\min\left[\Delta\phi\left(\vec{E}_{\mathrm{T}}^{\mathrm{miss}}, \vec{p}_{\mathrm{T}}^{j}\right)\right] > \pi/9$ $\Delta\phi\left(\vec{E}_{\mathrm{T}}^{\mathrm{miss}}, \vec{p}_{\mathrm{T}}^{\mathrm{miss,trk}}\right) < \pi/2$ –	$p_{\mathrm{T}}(\ell, \ell) \in [150, 500)$ GeV – – – $E_{\mathrm{T}}^{\mathrm{miss}} \times \left(\sum_{\mathrm{jets,leptons}} p_{\mathrm{T}}\right)^{-1/2} < 3.5\ \mathrm{GeV}^{1/2}$
	Number of central small-R jets ≥ 2 Leading Higgs candidate small-R jet $p_{\mathrm{T}} > 45$ GeV $H_{\mathrm{T},2j} > 120$ GeV for 2 jets, $H_{\mathrm{T},3j} > 150$ GeV for > 2 jets $\Delta\phi\left(\vec{E}_{\mathrm{T}}^{\mathrm{miss}}, \vec{p}_{\mathrm{T},h}\right) > 2\pi/3$ Veto on τ-leptons $\Delta R\left(\vec{p}_h^{\,j_1}, \vec{p}_h^{\,j_2}\right) < 1.8$ Veto on events with > 2 b-tags Sum of p_{T} of two Higgs candidate jets and leading extra jet > $0.63 \times H_{\mathrm{T,all\,jets}}$ b-tagging : one or two small-R calorimeter jets **Final discriminant = Dijet mass**		
Merged	$E_{\mathrm{T}}^{\mathrm{miss}} \geq 500$ GeV $p_{\mathrm{T}}^{\mathrm{miss,trk}} > 30$ GeV $\min\left[\Delta\phi\left(\vec{E}_{\mathrm{T}}^{\mathrm{miss}}, \vec{p}_{\mathrm{T}}^{j}\right)\right] > \pi/9$ $\Delta\phi\left(\vec{E}_{\mathrm{T}}^{\mathrm{miss}}, \vec{p}_{\mathrm{T}}^{\mathrm{miss,trk}}\right) < \pi/2$	$p_{\mathrm{T}}(\mu, E_{\mathrm{T}}^{\mathrm{miss}}) \geq 500$ GeV $p_{\mathrm{T}}(\mu, \vec{p}_{\mathrm{T}}^{\mathrm{miss,trk}}) > 30$ GeV $\min\left[\Delta\phi\left(\vec{E}_{\mathrm{T}}^{\mathrm{miss}}, \vec{p}_{\mathrm{T}}^{j}\right)\right] > \pi/9$ $\Delta\phi\left(\vec{E}_{\mathrm{T}}^{\mathrm{miss}}, \vec{p}_{\mathrm{T}}^{\mathrm{miss,trk}}\right) < \pi/2$	$p_{\mathrm{T}}(\ell, \ell) \geq 500$ GeV – – –
	Number of large-R jets ≥ 1 Veto on τ-lepton not associated to large-R jet Veto on b-jets not associated to large-R jet H_{T}-ratio selection (<0.57) b-tagging : one or two ID track jets matched to large-R jet **Final discriminant = Large-R jet mass**		

Figure 7.43: Summary of the $h \to b\bar{b} + E_{\mathrm{T}}^{\mathrm{miss}}$ analysis selection criteria. The notation $p_{\mathrm{T}}(A, B)$ is defined as the vector sum of the $p_{\mathrm{T}}$for the objects A and B [59].

A simultaneous fit is performed in the different categories for signal and control regions. No significant excess is found (Figs. 7.44) so that 95% CL limits are derived. Visible cross-section times branching ratio limits are also derived for this channel. Table 7.46 present these limits for the four categories in $E_{\mathrm{T}}^{\mathrm{miss}}$ defined in the analysis. In addition, limits on the 2D plane defined by the masses of the vector boson Z' and pseudo-scalar A^0 are calculated (Fig. 7.45). Masses of the Z' vector boson are excluded up to 2.6 TeV and masses of the pseudo-scalar A^0 are excluded up to 600 GeV. Comparing with the limits on the Z'-2HDM model from $h \to \gamma\gamma$+$E_{\mathrm{T}}^{\mathrm{miss}}$ in Fig. 7.38.b, mono-Higgs $h \to b\bar{b}$ searches exclude a larger region of the parameter space than $h \to \gamma\gamma$ searches. However, masses $m_{Z'} < 500$ GeV cannot be excluded due

to the low sensitivity at low $E_{\mathrm{T}}^{\mathrm{miss}}$ and the high $E_{\mathrm{T}}^{\mathrm{miss}}$ trigger applied in the event selection of $h \to b\bar{b}$. On the other hand, this is a very sensitive region for $h \to \gamma\gamma$ searches given that the applied diphoton trigger allows scanning regions of low-$E_{\mathrm{T}}^{\mathrm{miss}}$. These two searches are then complementary.

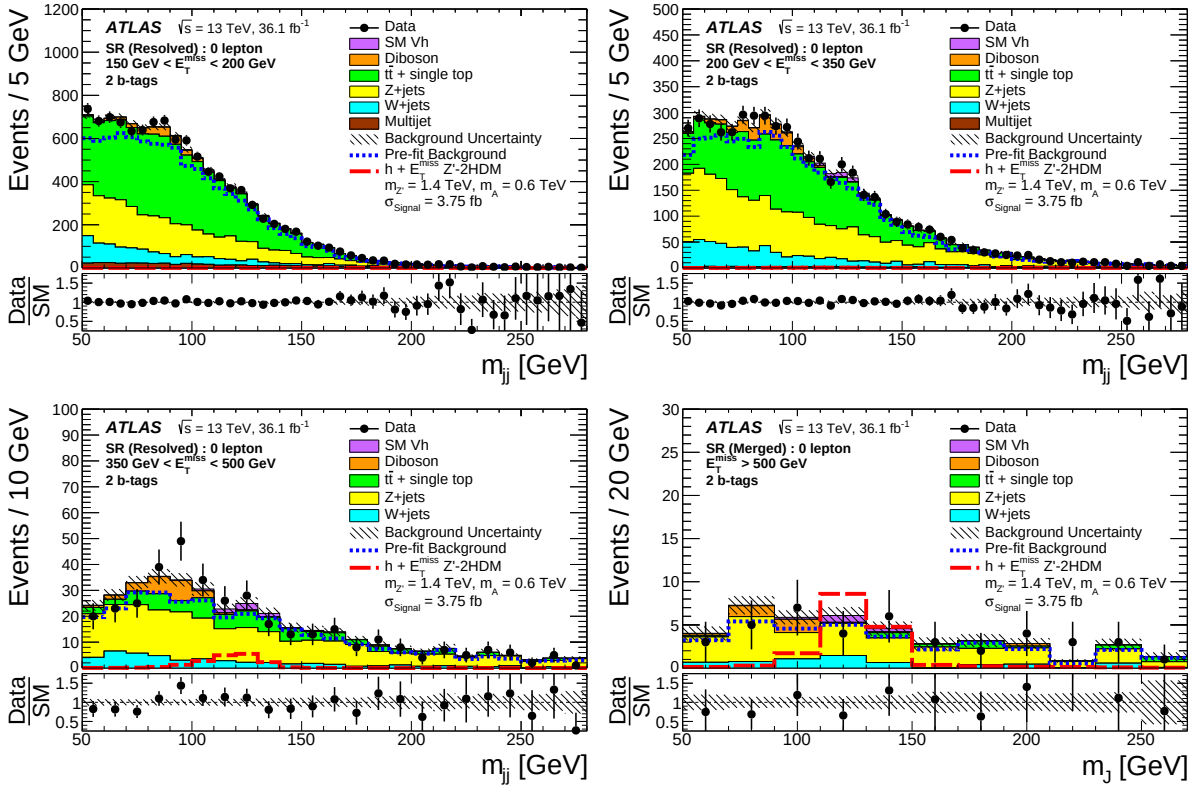


Figure 7.44: Distributions of the invariant mass of the Higgs boson candidates mh,reco=mjj,mJ with two b-tags in the SR for the four $E_{\mathrm{T}}^{\mathrm{miss}}$ categories that are used as inputs to the fit. The upper panels show a comparison of data to the SM expectation before (dashed lines) and after the fit (solid histograms) with no signal included. The lower panels display the ratio of data to SM expectations after the fit, with its systematic uncertainty considering correlations between individual contributions indicated by the hatched band. The expected signal from a representative Z'-2HDM model is also shown (long-dashed line). [59]

Z'_B model is not studied yet in the final state although studies are being performed to include this interpretation in the future.

7.7.2 CMS $h \to \gamma\gamma$ results

CMS collaboration has recently published the CMS latest results on Mono-Higgs signals in the $h \to \gamma\gamma + E_{\mathrm{T}}^{\mathrm{miss}}$ channel using 35.9 fb^{-1} at $\sqrt{s} = 13$ TeV [62].

Events are selected by requiring two photons in $|\eta| < 1.44$ or $1.57 < |\eta| < 2.5$ with a p_{T} larger than 30/20 GeV for the leading/subleading photon respectively. In addition, the invariant mass of the system must be above $m_{\gamma\gamma} > 95$ GeV and $p_{\mathrm{T}}\ /m_{\gamma\gamma} < 1/3(1/4)$ for the leading (subleading) photon. Two categories are defined according to the requirement on $E_{\mathrm{T}}^{\mathrm{miss}}$ (called $p_{\mathrm{T}}^{\mathrm{miss}}$):

The analysis strategy is quite similar to the one exposed for the present ATLAS search. Signal and resonant backgrounds are added to the final fitting functions. The non-resonant background is estimated directly from data by fitting the sidebands of the $m_{\gamma\gamma}$ distribution. The chosen fitted function is a sum

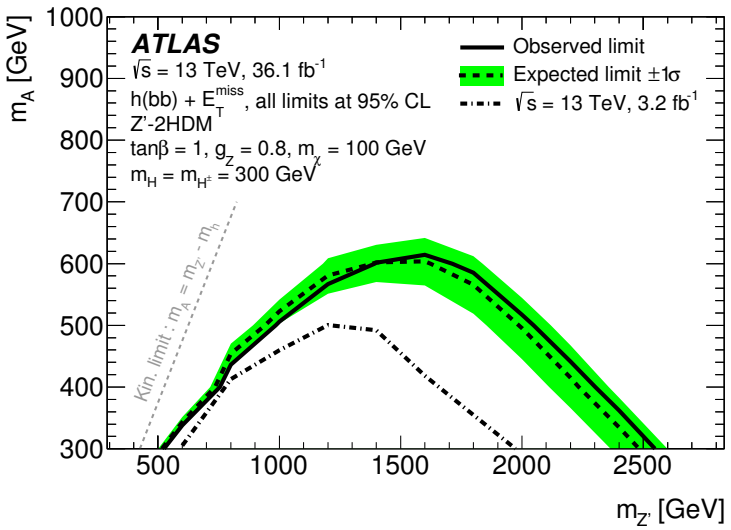


Figure 7.45: Exclusion contours for the Z'-2HDM scenario in the ($m_{Z'}$,m_{A^0}) plane for $\tan\beta = 1$, $g_{Z'} = 0.8$, and $m_\chi = 100$ GeV. The observed limits (solid line) are consistent with the expectation under the SM-only hypothesis (dashed line) within uncertainties (filled band). Observed limits from previous ATLAS results at $\sqrt{s} = 13$ TeV (dash-dotted line) [31] are also shown. [59]

Range in $E_{\mathrm{T}}^{\mathrm{miss}}$ [GeV]	$\sigma^{\mathrm{obs}}_{\mathrm{vis},h(b\bar{b})+\mathrm{DM}}$ [fb]	$\sigma^{\mathrm{exp}}_{\mathrm{vis},h(b\bar{b})+\mathrm{DM}}$ [fb]	$\mathcal{A}\times\varepsilon$ [%]
[150, 200)	19.1	$18.3^{+7.2}_{-5.1}$	15
[200, 350)	13.1	$10.5^{+4.1}_{-2.9}$	35
[350, 500)	2.4	$1.7^{+0.7}_{-0.5}$	40
[500, ∞)	1.7	$1.8^{+0.7}_{-0.5}$	55

Figure 7.46: Observed (obs) and expected (exp) upper limits at 95% CL on σ_{vis} of $h(\to b\bar{b}) + E_{\mathrm{T}}^{\mathrm{miss}}$ events. Also shown are the acceptance $\times$ efficiency probabilities to reconstruct and select an event in the same $E_{\mathrm{T}}^{\mathrm{miss}}$ bin as generated. [59]

Variable	Low-$p_{\mathrm{T}}^{\mathrm{miss}}$ category	High-$p_{\mathrm{T}}^{\mathrm{miss}}$ category
$p_{\mathrm{T}}^{\gamma_1}/m_{\gamma\gamma}$	> 0.45	> 0.5
$p_{\mathrm{T}}^{\gamma_2}/m_{\gamma\gamma}$	> 0.25	> 0.25
$p_{\mathrm{T}}^{\gamma\gamma}$	> 75 GeV	> 90 GeV
$p_{\mathrm{T}}^{\mathrm{miss}}$	[50,130] GeV	> 130 GeV
$\lvert\Delta\phi(\gamma\gamma, p_{\mathrm{T}}^{\mathrm{miss}})\rvert$	> 2.1	
$\min\lvert\Delta\phi(\mathrm{Jet}(\mathrm{p_T} > 50\ \mathrm{GeV}), p_{\mathrm{T}}^{\mathrm{miss}})\rvert$	> 0.5	
$N_{\mathrm{jets}}(p_{\mathrm{T}}^{\mathrm{jets}} > 30\ \mathrm{GeV})$	< 3	

Table 7.13: Categorization of the diphoton events inside the CMS collaboration [62].

of power law, defined as:

$$P(x) = \sum_{i=1}^{N} \beta_i x^{-\alpha_i} \tag{7.11}$$

These background functions are determined using a different procedure than the spurious signal technique explained in Section 7.4.2: non-resonant background MC samples are used as templates to generate toy datasets. The optimal function to model the non-resonant background is chosen among this set of functions by testing the size of the bias that they induce in the background estimation. This bias is estimated by fitting the toy datasets with the function candidate and estimating the difference between the simulated number of events injected in the toy dataset minus the number of events estimated by the fit function, all of it divided by the uncertainties of the fit ($(N_{\mathrm{fit}}^{\mathrm{non.resbkg}} - N_{\mathrm{toy}}^{\mathrm{non.resbkg}})/\sigma_{\mathrm{fit}}$). The bias of the optimal function is required to be less than 0.2 to ensure that the background bias is subdominant compared to the other systematics in the analysis.

The analysis is dominated by statistical uncertainties, as in the ATLAS case. Results are derived by fitting simultaneously low-$p_{\mathrm{T}}^{\mathrm{miss}}$ and high-$p_{\mathrm{T}}^{\mathrm{miss}}$ categories $m_{\gamma\gamma}$ distributions. Figures 7.47 present the simultaneous fit results for both categories. It can be observe a small excess of events in the low-$p_{\mathrm{T}}^{\mathrm{miss}}$ category, representing 2.0 σ excess if the low-$p_{\mathrm{T}}^{\mathrm{miss}}$ category is fitted alone. However, simultaneous fit does not show any significant excess of events, thus the results are interpreted as 95% CL limits. Figures 7.48 present the limits for the Z'-2HDM and Z'_B models. The Z'-2HDM limits allow to exclude masses up to $m_{Z'} < 800$ GeV and $m_{A^0} < 300$ GeV. The excluded region is contained in the ATLAS one (Fig. 7.39.b), although the limits of these excluded region become less precise given that no reweighting technique is applied. For the Z'_B model, the 1D limit can be compared with the ATLAS one presented in Fig. 7.38.a. ATLAS and CMS results are quite similar, excluding masses of $m_{Z'} < 800$ GeV for $m_\chi < 1$ GeV. However, this comparison is not fully conclusive given that for both models, some parameters are fixed to different values. These differences in the parameter configuration lead to different predicted cross-sections by CMS or ATLAS for both models, which ultimately translates into different excluded regions. Further details on this issue are presented in the Appendix C.

References

[1] ATLAS Collaboration. "Observation of a new particle in the search for the Standard Model Higgs boson with the ATLAS detector at the LHC". In: *Phys. Lett. B* 716 (2012), pp. 1–29. DOI: 10.1016/j.physletb.2012.08.020. arXiv: 1207.7214 [hep-ex].

[2] CMS Collaboration. "Observation of a new boson at a mass of 125 GeV with the CMS experiment at the LHC". In: *Phys. Lett. B* 716 (2012), pp. 30–61. DOI: 10.1016/j.physletb.2012.08.021. arXiv: 1207.7235 [hep-ex].

[3] Morad Aaboud et al. "Search for dark matter in association with a Higgs boson decaying to two photons at $\sqrt{s}$= 13 TeV with the ATLAS detector". In: (2017). arXiv: 1706.03948 [hep-ex].

[4] ATLAS Collaboration. "Search for resonances in diphoton events at $\sqrt{s}$=13 TeV with the ATLAS detector". In: *JHEP* 09 (2016), p. 001. DOI: 10.1007/JHEP09(2016)001. arXiv: 1606.03833 [hep-ex].

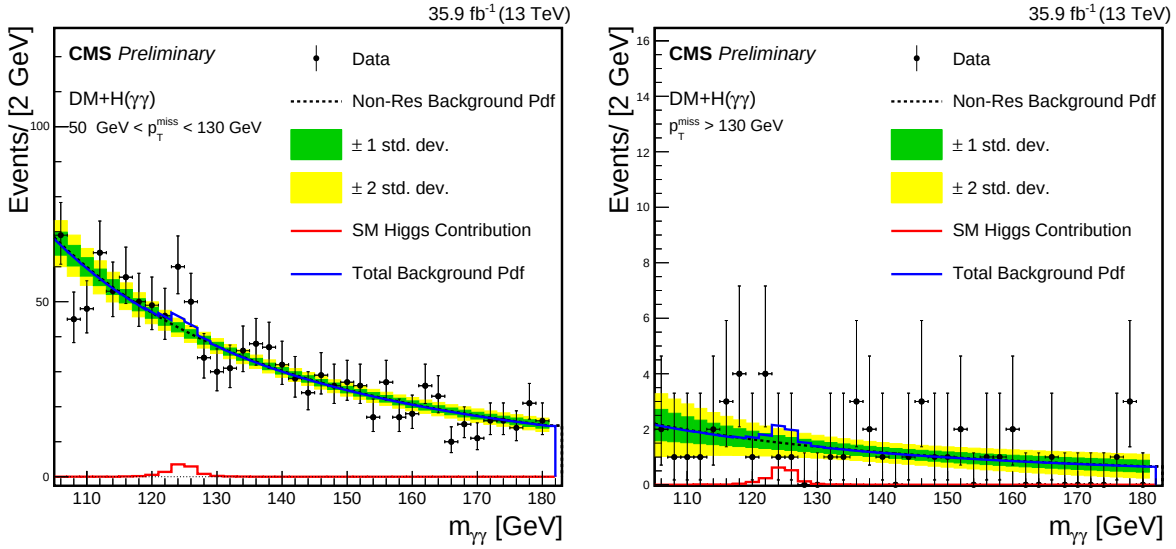


Figure 7.47: The dashed black line presents the fitted non-resonant background and the solid red line, the SM $h \to \gamma\gamma$ contribution for both categories (left: low-$p_{\mathrm{T}}^{\mathrm{miss}}$;right: high-$p_{\mathrm{T}}^{\mathrm{miss}}$) category. The sum of the non-resonant and resonant background shapes is shown in blue [62].

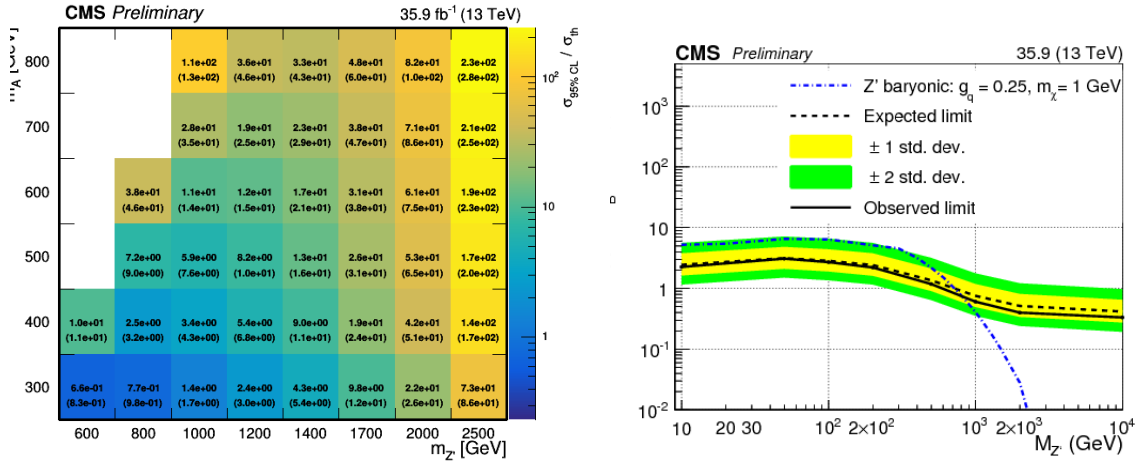


Figure 7.48: The observed (expected) 95% CL limits on the signal strength ($\sigma_{95\%\mathrm{CL}}/\sigma_{th}$) for all Z'-2HDM mass points shown in a grid of $m_{Z'}$ and m_{A^0}. Regions presenting values lower than 1 can be considered excluded by the analysis. The theoretical cross-section for each point is calculated assuming $g_{Z'}$= 0.8. Right: 95 % CL upper limits on cross-section for the baryonic Z' scenario as a function of $m_{Z'}$ for m_χ= 1 GeV. The theoretical cross-section (blue) is calculated assuming g_q= 0.25 and sinθ= 0.3 [62].

[5] J. Alwall et al. "The automated computation of tree-level and next-to-leading order differential cross sections, and their matching to parton shower simulations". In: *JHEP* 07 (2014), p. 79. DOI: 10.1007/JHEP07(2014)079. arXiv: 1405.0301 [hep-ph].

[6] Richard D. Ball et al. "Parton distributions for the LHC run II". In: *JHEP* 04 (2015), p. 040. DOI: 10.1007/JHEP04(2015)040. arXiv: 1410.8849 [hep-ph].

[7] T. Sjostrand, S. Mrenna, and P. Skands. "A brief introduction to PYTHIA 8.1". In: *Comput. Phys. Commun.* 178 (2008), pp. 852–867. DOI: 10.1016/j.cpc.2008.01.036. arXiv: 0710.3820 [hep-ph].

[8] ATLAS Collaboration. *ATLAS Run 1 Pythia8 tunes*. ATL-PHYS-PUB-2014-021. 2014. URL: https://cds.cern.ch/record/1966419.

[9] Richard D. Ball et al. "Parton distributions with LHC data". In: *Nucl. Phys. B* 867 (2013), pp. 244–289. DOI: 10.1016/j.nuclphysb.2012.10.003. arXiv: 1207.1303 [hep-ph].

[10] Stefan von Buddenbrock. *Heavy scalar model theory overview and comparisons to mono Higgs*. URL: https://indico.cern.ch/event/543351/contributions/2206780/attachments/1293901/1928658/svb_hbsm_darkmatter_06_15_16.pdf.

[11] ATLAS Collaboration. "The ATLAS Simulation Infrastructure". In: *Eur. Phys. J. C* 70 (2010), pp. 823–874. DOI: 10.1140/epjc/s10052-010-1429-9. arXiv: 1005.4568 [physics.ins-det].

[12] D. J. Lange. "The EvtGen particle decay simulation package". In: *Nucl. Instrum. Meth. A* 462 (2001), pp. 152–155. DOI: 10.1016/S0168-9002(01)00089-4.

[13] ATLAS Collaboration. *Summary of ATLAS Pythia 8 tunes*. ATL-PHYS-PUB-2012-003. 2012. URL: https://cds.cern.ch/record/1474107/.

[14] Paolo Nason. "A new method for combining NLO QCD with shower Monte Carlo algorithms". In: *JHEP* 11 (2004), p. 040. DOI: 10.1088/1126-6708/2004/11/040. arXiv: hep-ph/0409146 [hep-ph].

[15] Simone Alioli et al. "NLO Higgs boson production via gluon fusion matched with shower in POWHEG". In: *JHEP* 04 (2009), p. 002. DOI: 10.1088/1126-6708/2009/04/002. arXiv: 0812.0578 [hep-ph].

[16] Paolo Nason and Carlo Oleari. "NLO Higgs boson production via vector-boson fusion matched with shower in POWHEG". In: *JHEP* 02 (2010), p. 037. DOI: 10.1007/JHEP02(2010)037. arXiv: 0911.5299 [hep-ph].

[17] Simone Alioli et al. "A general framework for implementing NLO calculations in shower Monte Carlo programs: the POWHEG BOX". In: *JHEP* 06 (2010), p. 043. DOI: 10.1007/JHEP06(2010)043. arXiv: 1002.2581 [hep-ph].

[18] ATLAS Collaboration. *Example ATLAS tunes of Pythia8, Pythia6 and Powheg to an observable sensitive to Z boson transverse momentum*. ATL-PHYS-PUB-2013-017. 2013. URL: https://cds.cern.ch/record/1629317.

[19] Hung-Liang Lai et al. "New parton distributions for collider physics". In: *Phys. Rev. D* 82 (2010), p. 074024. DOI: 10.1103/PhysRevD.82.074024. arXiv: 1007.2241 [hep-ph].

[20] B. Hespel, F. Maltoni, and E. Vryonidou. "Higgs and Z boson associated production via gluon fusion in the SM and the 2HDM". In: *JHEP* 06 (2015), p. 065. DOI: 10.1007/JHEP06(2015)065. arXiv: 1503.01656 [hep-ph].

[21] S. Agostinelli et al. "GEANT4 – A Simulation toolkit". In: *Nucl. Instrum. Meth. A* 506 (2003), pp. 250–303. DOI: 10.1016/S0168-9002(03)01368-8.

[22] T. Gleisberg et al. "Event generation with SHERPA 1.1". In: *JHEP* 02 (2009), p. 007. DOI: 10.1088/1126-6708/2009/02/007. arXiv: 0811.4622 [hep-ph].

[23] Steffen Schumann and Frank Krauss. "A Parton shower algorithm based on Catani-Seymour dipole factorisation". In: *JHEP* 03 (2008), p. 038. DOI: 10.1088/1126-6708/2008/03/038. arXiv: 0709.1027 [hep-ph].

[24] Stefan Höche et al. "QCD matrix elements and truncated showers". In: *JHEP* 05 (2009), p. 053. DOI: 10.1088/1126-6708/2009/05/053. arXiv: 0903.1219 [hep-ph].

[25] Jahred Adelman et al. *Supporting note: Selection and performance for the $h \to \gamma\gamma$ and $h \to Z\gamma$ analyses, Spring 2017*. Tech. rep. ATL-COM-PHYS-2017-357. Geneva: CERN, Apr. 2017. URL: https://cds.cern.ch/record/2258158.

[26] ATLAS Collaboration. *Electron identification measurements in ATLAS using $\sqrt{s}$ = 13 TeV data with 50 ns bunch spacing*. ATL-PHYS-PUB-2015-041. 2015. URL: https://cds.cern.ch/record/2048202.

[27] ATLAS Collaboration. "Measurements of fiducial and differential cross sections for Higgs boson production in the diphoton decay channel at $\sqrt{s} = 8$ TeV with ATLAS". In: *JHEP* 09 (2014), p. 112. DOI: 10.1007/JHEP09(2014)112. arXiv: 1407.4222 [hep-ex].

[28] ATLAS Collaboration. "Measurement of the muon reconstruction performance of the ATLAS detector using 2011 and 2012 LHC proton-proton collision data". In: *Eur. Phys. J. C* 74.11 (2014), p. 3130. DOI: 10.1140/epjc/s10052-014-3130-x. arXiv: 1407.3935 [hep-ex].

[29] ATLAS Collaboration. "Muon reconstruction performance of the ATLAS detector in proton-proton collision data at $\sqrt{s}$ =13 TeV". In: *Eur. Phys. J. C* 76.5 (2016), p. 292. DOI: 10.1140/epjc/s10052-016-4120-y. arXiv: 1603.05598 [hep-ex].

[30] Matteo Cacciari, Gavin P. Salam, and Gregory Soyez. "The anti-k_t jet clustering algorithm". In: *JHEP* 04 (2008), p. 063. DOI: 10.1088/1126-6708/2008/04/063. arXiv: 0802.1189 [hep-ph].

[31] ATLAS Collaboration. *Tagging and suppression of pileup jets*. ATL-PHYS-PUB-2014-001. 2014. URL: https://atlas.web.cern.ch/Atlas/GROUPS/PHYSICS/PUBNOTES/ATL-PHYS-PUB-2014-001/.

[32] Morad Aaboud et al. "Jet energy scale measurements and their systematic uncertainties in proton-proton collisions at $\sqrt{s} = 13$ TeV with the ATLAS detector". In: (2017). arXiv: 1703.09665 [hep-ex].

[33] ATLAS Collaboration. "Search for Dark Matter in Events with Missing Transverse Momentum and a Higgs Boson Decaying to Two Photons in pp Collisions at $\sqrt{s} = 8$ TeV with the ATLAS Detector". In: *Phys. Rev. Lett.* 115.13 (2015), p. 131801. DOI: 10.1103/PhysRevLett.115.131801. arXiv: 1506.01081 [hep-ex].

[34] Glen Cowan et al. "Asymptotic formulae for likelihood-based tests of new physics". In: *Eur. Phys. J. C* 71 (2011). [Erratum: Eur. Phys. J.C73,2501(2013)], p. 1554. DOI: 10.1140/epjc/s10052-011-1554-0. arXiv: 1007.1727 [physics.data-an].

[35] The ATLAS Collaboration. *2016 Primary Vertex Performance Plots*. 2016. URL: https://atlas.web.cern.ch/Atlas/GROUPS/PHYSICS/PLOTS/IDTR-2016-007/.

[36] Xifeng Ruan et al. *Search for a Higgs boson with the di-photon 2 decay in association with missing energy in p p collisions at 3 p s = 13 TeV with the ATLAS detector*. Tech. rep. ATL-COM-PHYS-2016-1732. Geneva: CERN, Nov. 2016. URL: https://cds.cern.ch/record/2235629.

[37] UC Davis. *BERNSTEIN POLYNOMIALS*. URL: http://graphics.cs.ucdavis.edu/education/CAGDNotes/Bernstein-Polynomials/Bernstein-Polynomials.html.

[38] D. de Florian et al. "Handbook of LHC Higgs Cross Sections: 4. Deciphering the Nature of the Higgs Sector". In: (2016). arXiv: 1610.07922 [hep-ph].

[39] A. Djouadi, J. Kalinowski, and M. Spira. "HDECAY: A Program for Higgs boson decays in the standard model and its supersymmetric extension". In: *Comput. Phys. Commun.* 108 (1998), pp. 56–74. DOI: 10.1016/S0010-4655(97)00123-9. arXiv: hep-ph/9704448 [hep-ph].

[40] Johan Alwall et al. "MadGraph 5 : Going Beyond". In: *JHEP* 06 (2011), p. 128. DOI: 10.1007/JHEP06(2011)128. arXiv: 1106.0522 [hep-ph].

[41] Michiel Botje et al. "The PDF4LHC Working Group Interim Recommendations". In: (2011). arXiv: 1101.0538 [hep-ph].

[42] Sayipjamal Dulat et al. "New parton distribution functions from a global analysis of quantum chromodynamics". In: *Phys. Rev. D* 93.3 (2016), p. 033006. DOI: 10.1103/PhysRevD.93.033006. arXiv: 1506.07443 [hep-ph].

[43] L. A. Harland-Lang et al. "Parton distributions in the LHC era: MMHT 2014 PDFs". In: *Eur. Phys. J. C* 75.5 (2015), p. 204. DOI: 10.1140/epjc/s10052-015-3397-6. arXiv: 1412.3989 [hep-ph].

[44] Morad Aaboud et al. "Performance of the ATLAS Trigger System in 2015". In: *Eur. Phys. J.* C77.5 (2017), p. 317. DOI: 10.1140/epjc/s10052-017-4852-3. arXiv: 1611.09661 [hep-ex].

[45] Georges Aad et al. "Electron and photon energy calibration with the ATLAS detector using LHC Run 1 data". In: *Eur. Phys. J.* C74.10 (2014), p. 3071. DOI: 10.1140/epjc/s10052-014-3071-4. arXiv: 1407.5063 [hep-ex].

[46] *Photon identification in 2015 ATLAS data*. Tech. rep. ATL-PHYS-PUB-2016-014. Geneva: CERN, Aug. 2016. URL: http://cds.cern.ch/record/2203125.

[47] *Expected performance of missing transverse momentum reconstruction for the ATLAS detector at* $\sqrt{s} = 13$ *TeV*. Tech. rep. ATL-PHYS-PUB-2015-023. Geneva: CERN, July 2015. URL: http://cds.cern.ch/record/2037700.

[48] Georges Aad et al. "Combined Measurement of the Higgs Boson Mass in pp Collisions at $\sqrt{s} = 7$ and 8 TeV with the ATLAS and CMS Experiments". In: *Phys. Rev. Lett.* 114 (2015), p. 191803. DOI: 10.1103/PhysRevLett.114.191803. arXiv: 1503.07589 [hep-ex].

[49] Alexander L. Read. "Presentation of search results: The CL_s technique". In: *J. Phys. G* 28 (2002), pp. 2693–2704. DOI: 10.1088/0954-3899/28/10/313.

[50] Linda Carpenter et al. "Mono-Higgs-boson: A new collider probe of dark matter". In: *Phys. Rev. D* 89.7 (2014), p. 075017. DOI: 10.1103/PhysRevD.89.075017. arXiv: 1312.2592 [hep-ph].

[51] LUX Collaboration. "Results from a Search for Dark Matter in the complete LUX exposure". In: *Phys. Rev. Lett.* 118.2 (2017), p. 021303. DOI: 10.1103/PhysRevLett.118.021303. arXiv: 1608.07648 [astro-ph.CO].

[52] PandaX-II Collaboration. "Dark Matter Results from First 98.7 Days of Data from the PandaX-II Experiment". In: *Phys. Rev. Lett.* 117.12 (2016), p. 121303. DOI: 10.1103/PhysRevLett.117.121303. arXiv: 1607.07400 [hep-ex].

[53] E. Aprile et al. "First Dark Matter Search Results from the XENON1T Experiment". In: (2017). arXiv: 1705.06655 [astro-ph.CO].

[54] SuperCDMS Collaboration. "New Results from the Search for Low-Mass Weakly Interacting Massive Particles with the CDMS Low Ionization Threshold Experiment". In: *Phys. Rev. Lett.* 116.7 (2016), p. 071301. DOI: 10.1103/PhysRevLett.116.071301. arXiv: 1509.02448 [astro-ph.CO].

[55] CRESST Collaboration. "Results on light dark matter particles with a low-threshold CRESST-II detector". In: *Eur. Phys. J. C* 76.1 (2016), p. 25. DOI: 10.1140/epjc/s10052-016-3877-3. arXiv: 1509.01515 [astro-ph.CO].

[56] Andreas Crivellin, Francesco D'Eramo, and Massimiliano Procura. "New Constraints on Dark Matter Effective Theories from Standard Model Loops". In: *Phys. Rev. Lett.* 112 (2014), p. 191304. DOI: 10.1103/PhysRevLett.112.191304. arXiv: 1402.1173 [hep-ph].

[57] Francesco D'Eramo and Massimiliano Procura. "Connecting dark matter UV complete models to direct detection rates via effective field theory". In: *JHEP* 04 (2015), p. 054. DOI: 10.1007/JHEP04(2015)054. arXiv: 1411.3342 [hep-ph].

[58] C. Patrignani et al. "Review of Particle Physics". In: *Chin. Phys.* C40.10 (2016), p. 100001. DOI: 10.1088/1674-1137/40/10/100001.

[59] Morad Aaboud et al. "Search for Dark Matter Produced in Association with a Higgs Boson Decaying to $b\bar{b}$ using 36 fb^{-1} of pp collisions at $\sqrt{s} = 13$ TeV with the ATLAS Detector". In: (2017). arXiv: 1707.01302 [hep-ex].

[60] *Optimisation of the ATLAS b-tagging performance for the 2016 LHC Run*. Tech. rep. ATL-PHYS-PUB-2016-012. Geneva: CERN, June 2016. URL: https://cds.cern.ch/record/2160731.

[61] *Boosted Higgs* ($\to b\bar{b}$) *Boson Identification with the ATLAS Detector at* $\sqrt{s} = 13$ *TeV*. Tech. rep. ATLAS-CONF-2016-039. Geneva: CERN, Aug. 2016. URL: https://cds.cern.ch/record/2206038.

[62] *Search for Dark Matter Produced in Association with a Higgs Boson Decaying to Two Photons*. Tech. rep. CMS-PAS-EXO-16-054. Geneva: CERN, 2017. URL: http://cds.cern.ch/record/2264691.

Conclusion and prospects

The search for dark matter in association with a Higgs boson decaying to two photons in ATLAS has been presented. This study is based on data collected in 2015 and 2016 by the ATLAS detector, corresponding to an integrated luminosity of $36.1\ \mathrm{fb}^{-1}$ of proton–proton collisions at the LHC at a center-of-mass energy of 13 TeV. Given that this search is driven by the performances on the photon and missing transverse momentum variables, I also contributed to revisit the cross-talk effect affecting both quantities and to study the $E_{\mathrm{T}}^{\mathrm{miss}}$ reconstruction in the specific case of a diphoton final state.

From the cross-talk side, a new technique to estimate the magnitude of the cross-talk effect has been developed, based on physics cross-talk signals derived from dedicated calibration runs. Physics cross-talk contributions are estimated on average and their magnitude as a function of the pseudorapidity is presented. Values are in most cases compatible with the previous 2000 and 2008 cross-talk studies and the currently values used in the ATLAS simulation code. However, significant discrepancies have been observed in the cross-talk magnitude between cells in the front layer and in the cross-talk behavior along η. In addition, cross-talk evaluation between neighbouring cells in ϕ has been included for middle and back layers. The effect of these new cross-talk in the description of shower shapes has been evaluated. A 50 % shift between data but MC observed in some variables can be explained by the inclusion of physics cross-talk at the same time that the description of other variables related to the η size of the shower seem to be worsened. However, a conclusion on the cross-talk effect in shower shapes and the introduction of the physics cross-talk values in ATLAS simulation require to revisit the correlation between dead material and cross-talk in shower shapes. Finally, corrections of the cross-talk on the arrival time could not be implemented during this thesis and they are left for a future work.

From the missing transverse momentum, my work allowed to reconstruct better the $E_{\mathrm{T}}^{\mathrm{miss}}$ quantity in $h \to \gamma\gamma$. The comparison of its magnitude with regard to the true $E_{\mathrm{T}}^{\mathrm{miss}}$ showed a clear improvement of reconstructing the soft-terms with regard to the vertex pointed by the two photons in the event instead of using the standard ATLAS technique. An improvement on the mean value of $E_{\mathrm{T}}^{\mathrm{miss}}$ and its resolution is observed. In addition, a more pileup resilience is achieved for this quantity. For future studies, other $E_{\mathrm{T}}^{\mathrm{miss}}$ reconstruction schemes can be considered. In particular, it is very important to consider the implementation of a particle flow (p-flow) algorithm in the jet reconstruction [1]. At high jet energy, p-flow algorithm reconstructs worst the jet transverse momentum resolution than the current strategy, explained in Chapter 6. But at low jet energies, the inclusion of the jet tracks in the total energy calculation improves the resolution with regard to the current scheme, as it can be observed in Figures 7.49. If this algorithm is then applied to soft-terms, it is possible that soft-terms are reconstructed more accurately at the same time that some neutral contributions to the soft-terms are recuperated (TST reconstruction only uses tracks so no neutral soft radiation is included). In addition, the inclusion of an extended inner tracker (ITk) and a high granularity detector at large pseudorapidity (HGTD) foreseen for the HL-LHC phase could help to extend the soft-terms reconstruction at high η.

From the analysis side, the search for dark matter in association with a Higgs boson decaying to two photons in ATLAS has been presented. No significant excess beyond Standard Model predictions has been observed. For Mono-Higgs signals, upper limits at 95% CL have been set on the production cross section times branching fraction of the Higgs boson decaying into two photons. Limits on the Z'_B model exclude a significant region of the parameter space at low and intermediate masses of the Z'_B vector boson and to masses of the dark matter particle up to 100 GeV. Limits on the Z'-2HDM model exclude masses of the Z' boson up to 1 TeV and m_{A^0} up to 350 GeV. Heavy scalar boson (H) signals have been completely

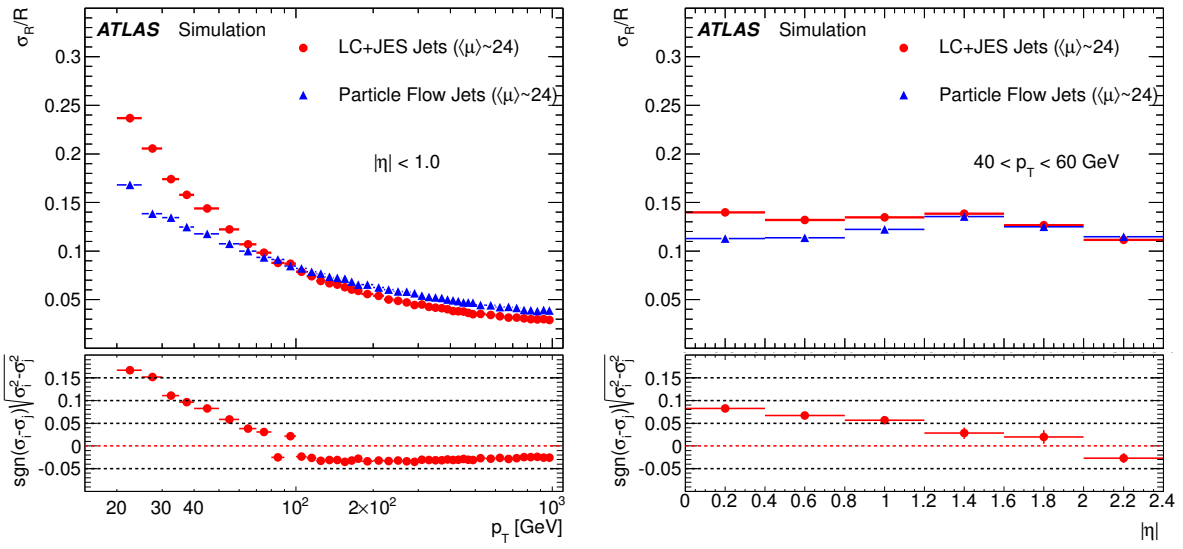


Figure 7.49: The jet transverse momentum resolution as determined in dijet MC events for calorimeter jets and particle flow jets with regard to the (a) jet transverse momentum and the (b) jet pseudo-rapidity [1].

excluded for all benchmark points investigated by a simulatenous fit in all the categories. Additionally, the results for the Z'_B model have been interpreted in terms of 90% CL limits on the dark-matter–nucleon scattering cross section, as a function of the dark matter particle mass, for a spin-independent scenario. Visible cross-section times branching ratio 95% CL have also been derived. Results have been compared between the ATLAS $h \to \gamma\gamma + E_{\mathrm{T}}^{\mathrm{miss}}$ and $h \to b\bar{b} + E_{\mathrm{T}}^{\mathrm{miss}}$ searches. Due to its larger Higgs branching ratio and sensitivity at large $E_{\mathrm{T}}^{\mathrm{miss}}$, $h \to b\bar{b} + E_{\mathrm{T}}^{\mathrm{miss}}$ excludes a larger region of the Z'-2HDM model than the $h \to \gamma\gamma + E_{\mathrm{T}}^{\mathrm{miss}}$ search, but at low $E_{\mathrm{T}}^{\mathrm{miss}}$ regions the diphoton channel becomes more sensitivie because it is not based on a large $E_{\mathrm{T}}^{\mathrm{miss}}$ trigger. CMS results for the $h \to \gamma\gamma + E_{\mathrm{T}}^{\mathrm{miss}}$ have also been compared to ATLAS ones and present very similar exclusion limits on the Mono-Higgs signals.

This analysis will be updated in the next months using the 2017 dataset delivered by the LHC pp collisions at $\sqrt{s} = 13$ TeV. Two more models will be possibly included: one model considering supersymmetric signals predicting a Higgs boson production in association to a W boson and two LSP neutralinos [2][3]; and a new model introducing a pseudo-scalar mediator coupled to a two Higgs doublet sector [4]. The optimization of these models need the redefinition of the different categories in the analysis. In addition, the implementation of visible cross-section limits as a function of the reconstructed $E_{\mathrm{T}}^{\mathrm{miss}}$ cut is considered in order to improve the reinterpretation of current limits for a larger variety of models. The current $S_{E_{\mathrm{T}}^{\mathrm{miss}}}$ definition showed a very good performance. However, a new implementation of the $S_{E_{\mathrm{T}}^{\mathrm{miss}}}$ is being considered in the ATLAS $E_{\mathrm{T}}^{\mathrm{miss}}$ performance group that could help to improve the fake $E_{\mathrm{T}}^{\mathrm{miss}}$ background rejection. This will be tested and possibly included in the future. Finally, the expected increase in statistics for Run 3 and the HL-LHC phases will allow to reduce the statistical error in the defined categories at the same time that more signal events will be expected. However, during HL-LHC, a significant increase of $\langle\mu\rangle$ is also foreseen, from 25 to 200. This implies a worst performance of the object reconstruction algorithms and the variables used in the analysis, in particular $S_{E_{\mathrm{T}}^{\mathrm{miss}}}$. If this decrease can be compensated either by the scheduled improvements in detectors (e.g. HGTD or ITk) and/or by more performing reconstruction algorithms (e.g. jet, precise time reconstruction in LAr to reject pileup and $E_{\mathrm{T}}^{\mathrm{miss}}$ particle flow), more stringent limits could be derived combining larger statistics with a similar (or better) signal and background separation.

References

[1] Morad Aaboud et al. "Jet reconstruction and performance using particle flow with the ATLAS Detector". In: *Eur. Phys. J.* C77.7 (2017), p. 466. DOI: 10.1140/epjc/s10052-017-5031-2. arXiv: 1703.10485 [hep-ex].

[2] Georges Aad et al. "Search for direct pair production of a chargino and a neutralino decaying to the 125 GeV Higgs boson in $\sqrt{s} = 8$ TeV pp collisions with the ATLAS detector". In: *Eur. Phys. J.* C75.5 (2015), p. 208. DOI: 10.1140/epjc/s10052-015-3408-7. arXiv: 1501.07110 [hep-ex].

[3] Vardan Khachatryan et al. "Searches for electroweak neutralino and chargino production in channels with Higgs, Z, and W bosons in pp collisions at 8 TeV". In: *Phys. Rev.* D90.9 (2014), p. 092007. DOI: 10.1103/PhysRevD.90.092007. arXiv: 1409.3168 [hep-ex].

[4] Martin Bauer, Ulrich Haisch, and Felix Kahlhoefer. "Simplified dark matter models with two Higgs doublets: I. Pseudoscalar mediators". In: *JHEP* 05 (2017), p. 138. DOI: 10.1007/JHEP05(2017)138. arXiv: 1701.07427 [hep-ph].

Appendices

Statistical framework

In particle physics, it is usual to search for signals that has been predicted but have not been observed yet, such as the production of the dark matter or supersymmetry. The sensitivity of an analysis, the optimization of the selection cuts, the observation of a signal over the well-known background and lastly the evaluation of the significance of the excess need the definition of an statistical framework to provide information on these subjects.

A.1 Hypothesis test

In the context of the search presented in this thesis, the analysis aims to test the existence of a predicted signal (for instance, the production of dark matter) over a well-known background. This test is performed by previously defining hypothesis on how the data would behave and requires the definition of a statistical framework capable to evaluate the probability that data follows any of these hypothesis. Usually, two hypothesis are considered:

- The null hypothesis (H_0) that predicts that data can be described by the well-known background alone and that no signal is present in data.
- The alternative hypothesis (H_1) that predicts that data can be described by the known processes and the signal of the predicted new process.

Associated to each hypothesis, there is an underlying model of how data is, defined by: a probability density function $f_{\mathrm{s(b)}}(x, \theta_{\mathrm{s(b)}})$, where θ stands for the different parameters of the functions (shape parameters and systematic errors) so-called nuisance parameters and x for the variable on which the data is observed; the expected number of events s_{tot} and b_{tot}; and the strength parameter of the signal $\mu = s_{\mathrm{tot}}^{\mathrm{obs}}/s_{\mathrm{tot}}^{\mathrm{exp}}$, which is the strength parameter and the parameter of interest of the search, representing the number of observed signal events over the number of expected events. In total, data is fitted with a function of the type:

$$F(x; \mu, \theta_{\mathrm{s}}, \theta_{\mathrm{b}}) = \mu s_{\mathrm{tot}} f_{\mathrm{s}}(x, \theta_{\mathrm{s}}) + b_{\mathrm{tot}} f_{\mathrm{b}}(x, \theta_{\mathrm{b}}) \tag{A.1}$$

provided that the null hypothesis model corresponds to the special case where $\mu = 0$ and the alternative hypothesis model, to the case that μ equals to an expected strength, denoted μ'.

The level of agreement of one hypothesis with the observed data is quantified by calculating a p-value, which corresponds to the probability that the data can be described by the signal plus background model defined by the alternative hypothesis. In particle physics, this p-value is usually expressed in terms of a significance Z, deduced as the quantile (inverse of the cumulative distribution) of the standard Gaussian:

$$Z = \Phi^{-1}(1 - p) \tag{A.2}$$

Two outcomes may be obtained from an hypothesis test evaluating the presence of a new signal. Either there is a disagreement between the null hypothesis and the data, in which case a discovery test is performed, or there is an agreement, so that limits are set on the production cross-section of new processes

encoded in the alternative hypothesis. Particle physics community tends to claim for a signal discovery when the p-value of the null hypothesis is equal or lower than 2.7×10^{-7}, which corresponds to a significance equal or greater than 5. On the other hand, when no significant signal is observed and data can be described by fluctuations of the known processes, limits are set if signals present p-values lower or equal to 0.05 (95 % confidence level), which represents a $Z = 1.64$. p-values are determined using a frequentist significance test based on a likelihood ratio as a test statistic.

A.1.1 Likelihood

Discovery of exclusion is evaluated by fitting the distribution of a given variable x (in the analysis presented in this thesis, $m_{\gamma\gamma}$) using the models of both hypothesis. The best estimate of the parameters of the fit is determined by maximizing a variable called *likelihood* (L). For binned distributions, the expectation number of events per distribution bin corresponds to:

$$E_i = \mu s_i + b_i \tag{A.3}$$

where s_i and b_i represent the expected number of signal and background events:

$$s_i = s_{\mathrm{tot}} \int_{\mathrm{bin_i}} dx f_{\mathrm{s}}(x, \theta_{\mathrm{s}}) \tag{A.4}$$

$$b_i = b_{\mathrm{tot}} \int_{\mathrm{bin_i}} dx f_{\mathrm{b}}(x, \theta_{\mathrm{b}}) \tag{A.5}$$

In data, this numbers may fluctuate per bin following a Poisson distribution. The likelihood function is then defined as:

$$L(\mu, \theta) = \prod_{i=1}^{N_{\mathrm{bin}}} \frac{(\mu s_i + b_i)^{n_i}}{n_i!} e^{-(\mu s_i + b_i)} \tag{A.6}$$

For unbinned analysis, the likelihood analysis is defined differently. In this case, the number of events is not estimated by bin but as the normalization multiplying the corresponding probability density function. The likelihood function is then defined as:

$$L(\mu, \theta) = \mathrm{Pois}(n|N) \cdot \prod_{i=1}^{n} F(m^i_{\gamma\gamma}; \mu, \theta) \tag{A.7}$$

where N stands for the expected number of events, n is the observed occurences after the fit and F is defined in Eq. A.1. The θ symbol stands for the different parameters describing the shape of the signal or the background. These shape parameters are usually determined previously on MC samples and either profiled (fixed to the mean value and corrected by the systematic error) or allowed to vary freely in the final fit (free parameter). The profiling of these parameters consists of fixing the parameters to their MC mean values and introducing new nuisance parameters that multiply the profiled variable.

$$\theta \rightarrow \langle\theta\rangle \left(\prod_{i=1}^{N_{syst.source}} e^{\epsilon_i^a} \right) \tag{A.8}$$

where the nuisance parameters ϵ represent the systematic errors and are then allowed to vary within the magnitude of the systematic error. There is one parameter ϵ_i^a per profiled parameter and source of uncertainty affecting it. Furthermore, constraints are added to the likelihood function when systematic errors are introduced. These constraints are applied using standard gaussian distribution centered at zero ($G(\theta)$) with a standard deviation equal to the mangitude of the statistical error, so that the likelihood value is reduced if one of the ϵ_i^a is pulled to more than one mangitude of its initial size. The likelihood function becomes:

$$L'(\mu, \theta) = \mathrm{Pois}(n|N) \cdot \prod_{i=1}^{n} F(m^i_{\gamma\gamma}; \mu, \langle\theta\rangle \left(\prod_{j=1}^{N_{syst.source}} e^{\epsilon_j} \right)) \cdot G(\epsilon_j), \tag{A.9}$$

where L' is the likelihood function that is used in the following. This is used to define a test statistic and perform the hypothesis test.

A.1.2 Test statistics and p-value

The test of an hypothesized value is performed considering the profile likelihood ratio:

$$\lambda(\mu) = \frac{L(\mu, \hat{\hat{\theta}})}{L(\hat{\mu}, \hat{\theta})} \tag{A.10}$$

where $\hat{\hat{\theta}}$ correspond to the value of the nuisance parameters maximizing the likelihood for a previously fixed value of the parameter of interest μ (conditional maximum likelihood estimators). On the other hand, $\hat{\mu}$ and $\hat{\theta}$ correspond to the values of μ and θ that maximize the likelihood function when all parameters are allowed to vary in the fit (maximum likelihood estimators).

From this definition, it can be inferred that $0 \leq \lambda(\mu) \leq 1$, with $\lambda(\mu)$ near one implying a good agreement between data and the hypothesized value of μ. It is convenient to use the test statistics:

$$t_\mu = -2\ln\lambda(\mu) \tag{A.11}$$

as basis of the statistical analysis. Higher values of t_μ correspond to larger disagreement between data and the hypothesized value. For each hypothesis, the distribution of t_μ is calculated. This is done using several toy MC samples emulating the distribution of the variable x for given μ. Fits are then performed and for each toy sample, a value of t_μ is obtained. This allows to build the probability density functions $f(t_\mu|\mu)$ of the t_μ variable under the assumption of that data presents a parameter of interest μ for both hypothesis. Then, data is fitted and its observed t_μ^{obs} is compared against both distributions. The p-value is then computed as:

$$p\text{−value} = \int_{t_\mu^{\text{obs}}}^{\infty} f(t_\mu|\mu)dt_\mu \tag{A.12}$$

This relation between the p-value and the observed t_μ and also with the significance Z are illustrated in Fig. A.1.

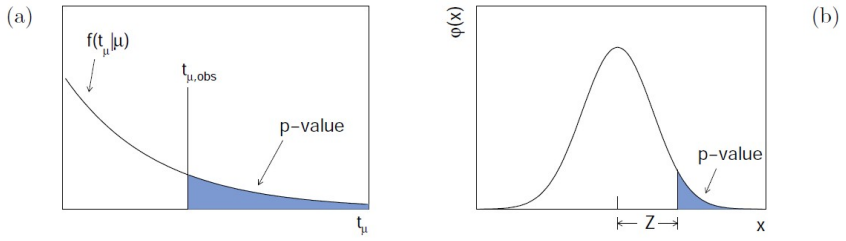


Figure A.1: (a) Illustration of the relation between the p-value obtained from an observed value of the test statistic t_μ. (b) The standard normal distribution showing the relation between the significance Z and the p-value [1].

This p-value is used either to evaluate the discovery of a new signal, if the null hypothesis p-value (also called p_0) is very low or exclusion limits if the p-value of the alternative hypothesis is low. Low p-values may be due to two distinct reasons: either the observed $\hat{\mu}$ is larger than the hypothesized value or lower. This implies that rejected values of μ may be found at both sides of the observed μ value i.e. one may obtain two-sided confidence interval for μ.

In some cases, special $\lambda(\mu)$ are defined:

Test statistics for a positive signal discovery: Often it is assumed that the presence of a new signal can only increase the mean event rate beyond what is expected from background alone. Asumming that the parameter of interest is the signal strength, this implies that the signal process necessarily has $\mu \geq 0$. To take this into account an alternative test statistic is defined called $\tilde{t_\mu}$. Given that

statistical fluctuations may be observed that reduce the event rate below the expected background in the signal region, $\tilde{\lambda_\mu}$ is also defined for data with $\mu < 0$:

$$\tilde{\lambda(\mu)} = \begin{cases} \frac{L(\mu,\hat{\theta(\mu)})}{L(\hat{\mu},\hat{\theta(\mu)})}; & \hat{\mu} \geq 0 \\ \frac{L(\mu,\hat{\theta(\mu)})}{L(0,\hat{\theta(0)})}; & \hat{\mu} < 0 \end{cases} \tag{A.13}$$

where $\hat{\theta(0)}$ and $\hat{\theta(\mu)}$ represent the conditional likelihood estimators given a strength parameter of 0 and μ respectively. The definition of $\tilde{\lambda_\mu}$ is then straightforward:

$$\tilde{t_\mu} = \begin{cases} -2\ln\frac{L(\mu,\hat{\theta(\mu)})}{L(\hat{\mu},\hat{\theta(\mu)})}; & \hat{\mu} \geq 0 \\ -2\ln\frac{L(\mu,\hat{\theta(\mu)})}{L(0,\hat{\theta(0)})}; & \hat{\mu} < 0 \end{cases} \tag{A.14}$$

The p-value can be calculated as in previous section. Still, a one-sided or two-sided confidence interval of μ can be obtained if μ is larger or lower than $\hat{\mu}$.

An special case of this test statistic is used to test the $\mu = 0$. This statistic is appropiate in the case that a positive signal is being searched for and tested against the null hypothesis described above. In this special case, the test statistics t_0 becomes:

$$\tilde{t_0} = \begin{cases} -2\ln\lambda(0); & \hat{\mu} \geq 0 \\ 0; & \hat{\mu} < 0 \end{cases} \tag{A.15}$$

The p-value (p_0) is then estimated as explained previously:

$$p_0 = \int_{t_0^{obs}}^{\infty} f(t_0|0)dt_0 \tag{A.16}$$

As explained previously, a low p_0 implies that the null hypothesis is less likely to explain the data and, if the significance is larger or equal than 5, that new phenomena has been observed.

Test statistics for upper limits: In the case that no excess is observed on data, the usual technique is to derive upper limits on the signal strength. In this case, a test statistic is defined:

$$\tilde{t_\mu} = \begin{cases} -2\ln\lambda(\mu); & \hat{\mu} \leq \mu \\ 0; & \hat{\mu} > \mu \end{cases} \tag{A.17}$$

We set $\tilde{t_\mu} = 0$ for values of $\hat{\mu} > \mu$ because, when setting an upper limit, we would not regard data such that the fitted μ is greater than the hypothesized μ. Such data would represent less compatibility with μ than the data obtained, and therefore this is not taken as part of the rejection region of the test. Similarly to t_0, the p-value is estimated by integrating the resulting distribution between the observed value and infinity.

A.2 Asymptotic formulae

In order to perform the statistic analysis explained in the previous sections, it is necessary to determine the test statistics pdfs $f(t_\mu|\mu)$. The technique explained in previous section using toy samples is usually the safest one to determine the pdf of t_μ. However, building a sufficiently smooth distribution in the tails requires to spend a lot fo time and computing power. In consequence, test statistics pdfs ($f(t_\mu|\mu)$) may be reconstructed using approximative formulas for analyses where large statistics are expected. In case of approximate distribution of the profile likelihood ratio we can expand the term $\ln\lambda$ [2] as:

$$-2\ln\lambda = \frac{(\mu - \hat{\mu})^2}{\sigma^2} + \mathcal{O}(\frac{1}{\sqrt{N}}) \tag{A.18}$$

Here $\hat{\mu}$ follows a Gaussian distribution with a mean μ and standard deviation σ, and N represents the data sample size. The standard deviation σ of $\hat{\mu}$ is obtained from the covariance matrix of the estimators for all the parameters $V_{ij}^{-1} = -E\partial^2 \ln L/\partial\theta_i \partial\theta_j$ where θ_i represent μ and the different nuisance parameters. We can use this approximation to evaluate $f(t_\mu; \Lambda)$.

$$f(t_\mu; \Lambda) = \frac{1}{2\sqrt{t_\mu}} \frac{1}{\sqrt{2\pi}} \left[exp\left(-\frac{1}{2}(\sqrt{t_\mu} + \sqrt{\Lambda})^2 \right) + exp\left(-\frac{1}{2}(\sqrt{t_\mu} - \sqrt{\Lambda})^2 \right) \right] \tag{A.19}$$

with Λ representing the number of standard deviations:

$$\Lambda = \frac{(\mu - \hat{\mu})^2}{\sigma^2} \tag{A.20}$$

To estimate σ, an alternative method may be used related to a special artificial data set that we call the Asimov data set [1]. The Asimov data set is defined such that when one uses it to evaluate the estimators for all parameters, one obtains the true parameter values. In practice, these are the values that would be estimated from the Monte Carlo model using a very large data sample. We can use the Asimov data set to evaluate the Asimov likelihood L_A and the corresponding profile likelihood ratio λ_A. Two ways may be used: evaluate the derivatives of $\ln(L_A)$ numerically, use this to find the inverse covariance matrix, and then invert and extract the variance of μ; given that the Asimov dataset gives the true parameter values, $\hat{\mu} = \mu'$ where μ' is the parameter used to create the Asimov data set and:

$$\sigma_A^2 = \frac{(\mu - \mu')^2}{t_{\mu,A}} \tag{A.21}$$

That is, from the Asimov data set one obtains an estimate of the non centrality parameter Λ that characterizes the distribution. Test statistic distributions from the previous section are simplified assuming Eq. A.18. The possitive signal test statistic is reduced to:

$$\tilde{\lambda(\mu)} = \begin{cases} \frac{(\mu-\hat{\mu})^2}{\sigma^2}; & \hat{\mu} \geq 0 \\ \frac{\mu^2}{\sigma^2} - \frac{1\mu\hat{\mu}}{\sigma^2}; & \hat{\mu} < 0 \end{cases} \tag{A.22}$$

t_0 then becomes:

$$\tilde{t_0} = \begin{cases} \frac{\hat{\mu}^2}{\sigma^2}; & \hat{\mu} \geq 0 \\ 0; & \hat{\mu} < 0 \end{cases} \tag{A.23}$$

and the upper limits test statistics becomes:

$$\tilde{t_\mu} = \begin{cases} \frac{(\mu-\hat{\mu})^2}{\sigma^2}; & \hat{\mu} \leq \mu \\ 0; & \hat{\mu} > \mu \end{cases} \tag{A.24}$$

A.3 Confidence level formalism

Usually, limits on a new signal process cross-section are set using the alternative hypothesis model and testing it against the data. If the p-value of this model is beyond 0.05, limits are set to 95 % confidence level. However, this interpretation should be corrected. In the case that λ_{s+b} and λ_b distributions are separated, it is easy to reject the alternative hypothesis if data agrees with the null hypothesis. However, sometimes searches are dominated by background and no significant signals are expected. In that case, both distributions are overlapping and there is a non-negligible probabiliy that the alternative hypothesis is rejected while the experiment has very low sensitivity to reject it. In this situation, the confidence intervals for the parameter of interest are not very accurate if the p-value of the alternative hypothesis is the only one taken into account. In order to perform more accurate limit setting, the confidence level limit CL_s [3] is re-defined:

$$\mathrm{CL}_s = \frac{\mathrm{CL}_{s+b}}{1 - \mathrm{CL}_b} = \frac{p_{s+b}}{1 - p_b} \tag{A.25}$$

where p_{s+b} is the p-value found for data on the t_μ distributions using the alternative hypothesis (for $\mu = \mu'$) or the null hypothesis (for $\mu = 0$), shown in Fig. A.2 for the Higgs searches at LEP. Limits are then set if $\mathrm{CL}_s \leq 1 - \alpha$, where α is the confidence level (usually 90% or 95 %).

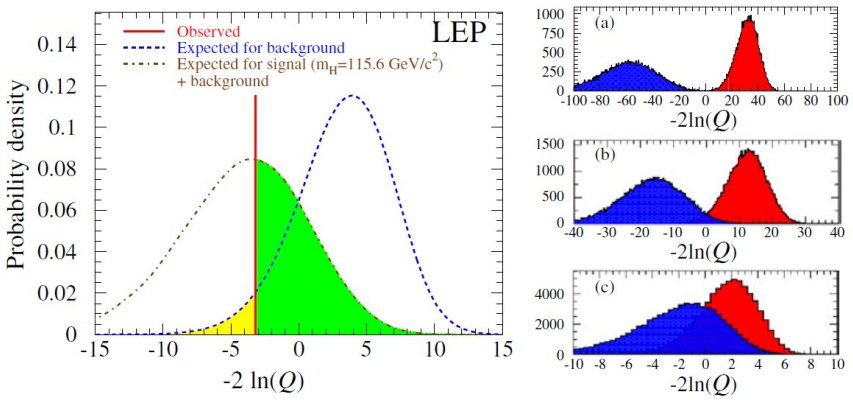


Figure A.2: On the left, the pdf of the test statistics for the Higgs search at LEP for the background (right) and signal+background hypotheses (left) are illustrated. The light yellow region to the left of the observation is $1 - \mathrm{CL}_b$ and the dark green is CL_{s+b}. On the right, the evolution of the pdfs is presented with falling search sensitivity from (a) to (c) as the Higgs mass hypothesis is increased and the production cross-section falls [3].

References

[1] Glen Cowan et al. "Asymptotic formulae for likelihood-based tests of new physics". In: *Eur. Phys. J. C* 71 (2011). [Erratum: Eur. Phys. J.C73,2501(2013)], p. 1554. DOI: 10.1140/epjc/s10052-011-1554-0. arXiv: 1007.1727 [physics.data-an].

[2] Abraham Wald. "Tests of Statistical Hypotheses Concerning Several Parameters When the Number of Observations is Large". In: *Transactions of the American Mathematical Society* 54.3 (1943), pp. 426–482. ISSN: 00029947. URL: http://www.jstor.org/stable/1990256.

[3] Alexander L. Read. "Presentation of search results: The CL_s technique". In: *J. Phys. G* 28 (2002), pp. 2693–2704. DOI: 10.1088/0954-3899/28/10/313.

Comparison between Z'-2HDM and Heavy Scalar model

In order to check the interest to include the Heavy Scalar model to cover the search of new physics in the intermediate $E_{\mathrm{T}}^{\mathrm{miss}}$ regime, a comparison of this model with the Z'-2HDM in a region of the parameter space where this latest model could have a much softer $E_{\mathrm{T}}^{\mathrm{miss}}$ distribution. The outcome of this comparison is that even if the $E_{\mathrm{T}}^{\mathrm{miss}}$ distribution can be similar, the other important kinematic distributions appear to be very different as shown on the figures below, especially the jet number distribution is cleary dissimilar between the two models.

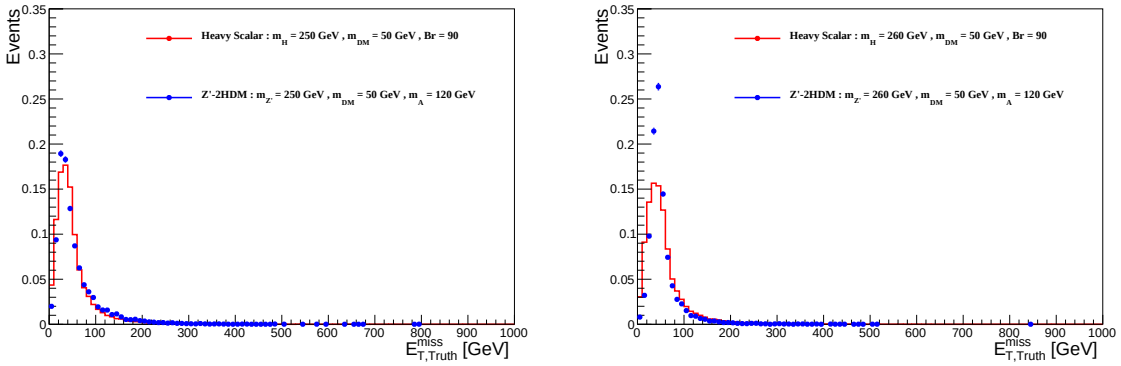


Figure B.1: Comparison of $E_{\mathrm{T}}^{\mathrm{miss}}$ spectrum of Z'-2HDM versus Heavy scalar model for same mediator and DM particle masses ($m'_Z = 250$ or 280 GeV, $m_\chi = 50$ GeV)

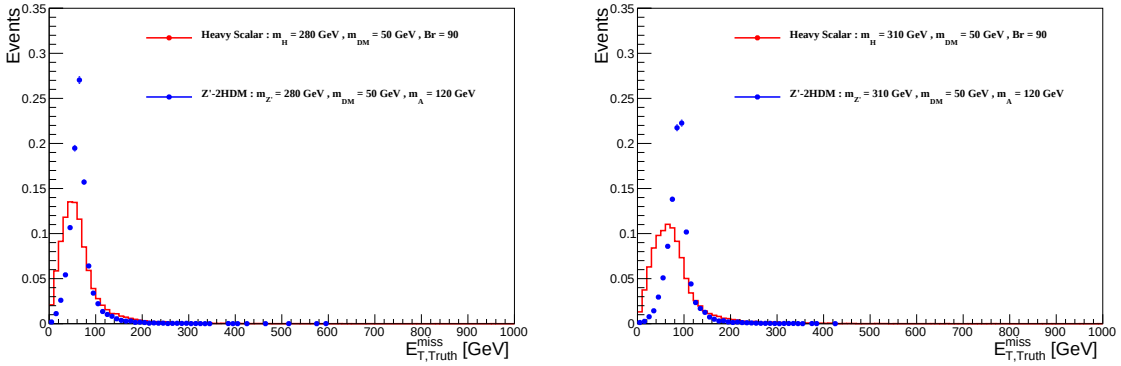


Figure B.2: Comparison of $E_{\mathrm{T}}^{\mathrm{miss}}$ spectrum of Z'-2HDM versus Heavy scalar model for same mediator and DM particle masses ($m'_Z = 280$ or 310 GeV, $m_\chi = 50$ GeV)

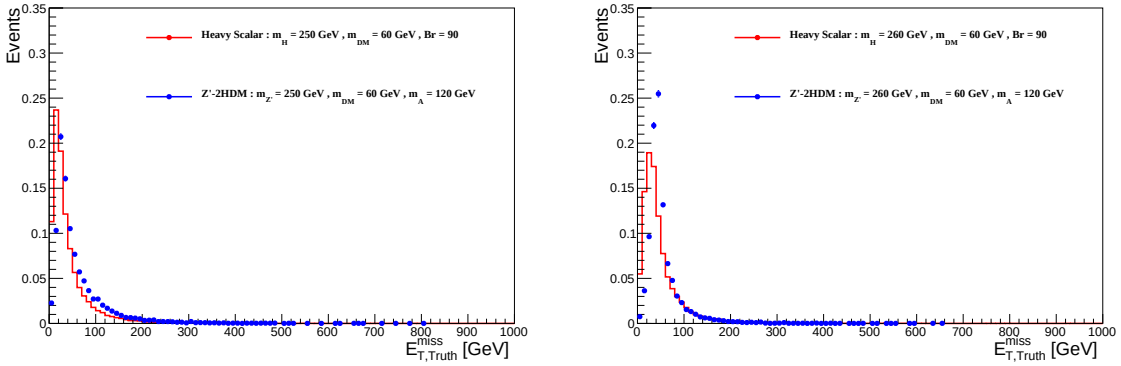


Figure B.3: Comparison of $E_{\mathrm{T}}^{\mathrm{miss}}$ spectrum of Z′-2HDM versus Heavy scalar model for same mediator and DM particle masses ($m'_Z = 250$ or 260 GeV, $m_\chi = 60$ GeV)

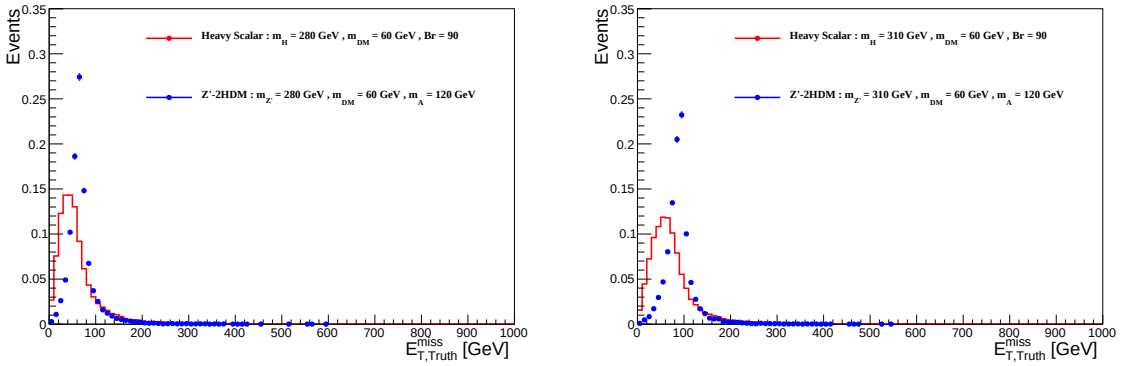


Figure B.4: Comparison of $E_{\mathrm{T}}^{\mathrm{miss}}$ spectrum of Z′-2HDM versus Heavy scalar model for same mediator and DM particle masses ($m'_Z = 280$ or 310 GeV, $m_\chi = 60$ GeV)

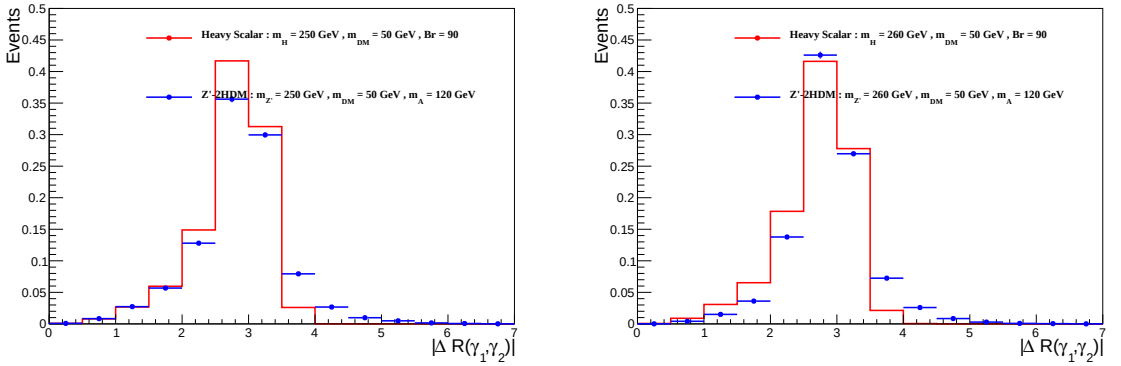


Figure B.5: Comparison of kinematic distributions between Z′-2HDM and Heavy scalar models for the same mediator and DM particle masses ($m'_Z = 250$ or 260 GeV, $m_\chi = 50$ GeV)

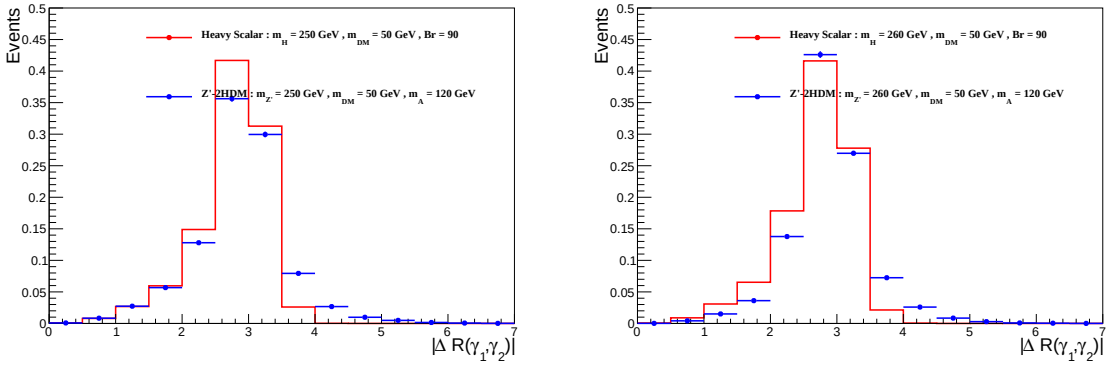


Figure B.6: Comparison of kinematic distributions between Z′-2HDM and Heavy scalar models for the same mediator and DM particle masses ($m'_Z = 250$ or 260 GeV, $m_\chi = 50$ GeV)

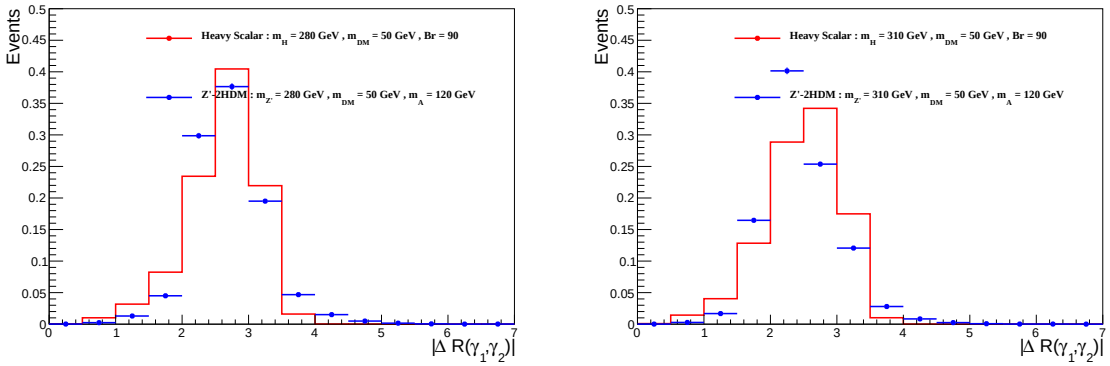


Figure B.7: Comparison of kinematic distributions between Z′-2HDM and Heavy scalar models for the same mediator and DM particle masses ($m'_Z = 280$ or 310 GeV, $m_\chi = 50$ GeV)

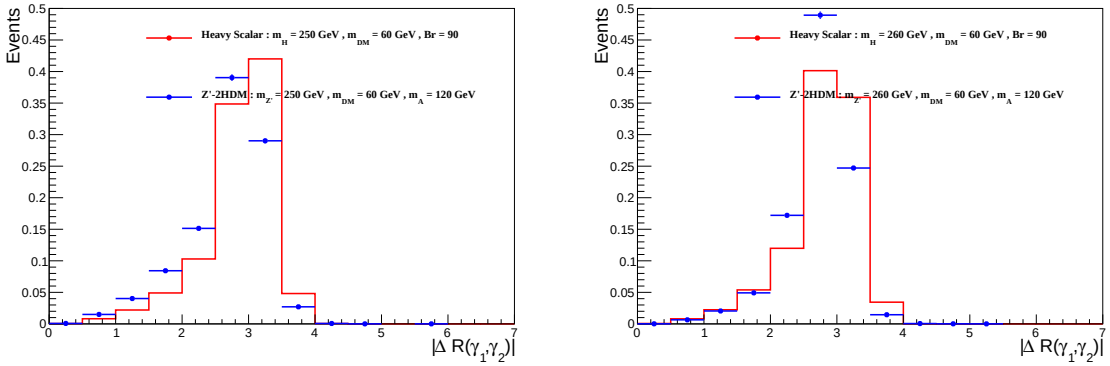


Figure B.8: Comparison of kinematic distributions between Z′-2HDM and Heavy scalar models for the same mediator and DM particle masses ($m'_Z = 250$ or 260 GeV, $m_\chi = 60$ GeV)

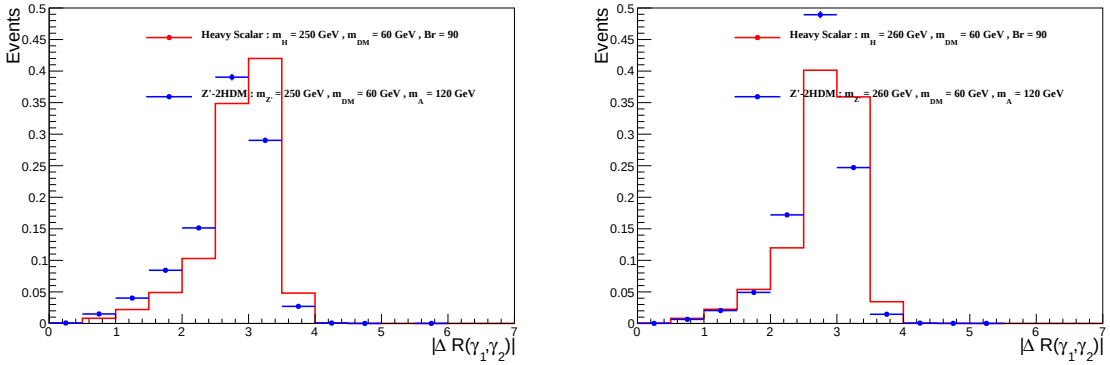


Figure B.9: Comparison of kinematic distributions between Z′-2HDM and Heavy scalar models for the same mediator and DM particle masses ($m'_Z = 250$ or 260 GeV, $m_\chi = 50$ GeV)

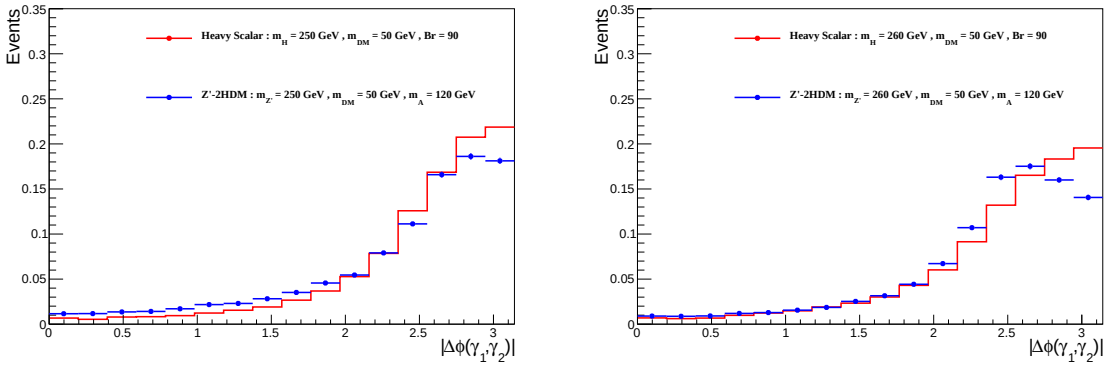


Figure B.10: Comparison of kinematic distributions between Z′-2HDM and Heavy scalar models for the same mediator and DM particle masses ($m'_Z = 250$ or 260 GeV, $m_\chi = 50$ GeV)

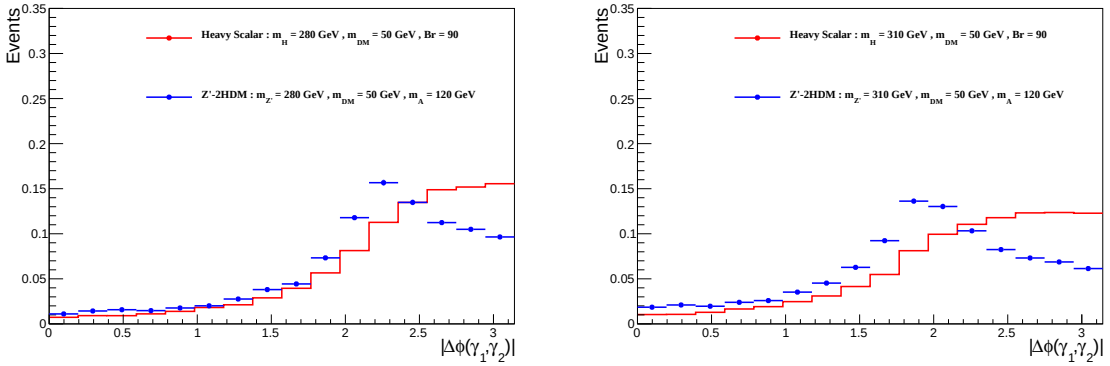


Figure B.11: Comparison of kinematic distributions between Z′-2HDM and Heavy scalar models for the same mediator and DM particle masses ($m'_Z = 280$ or 310 GeV, $m_\chi = 50$ GeV)

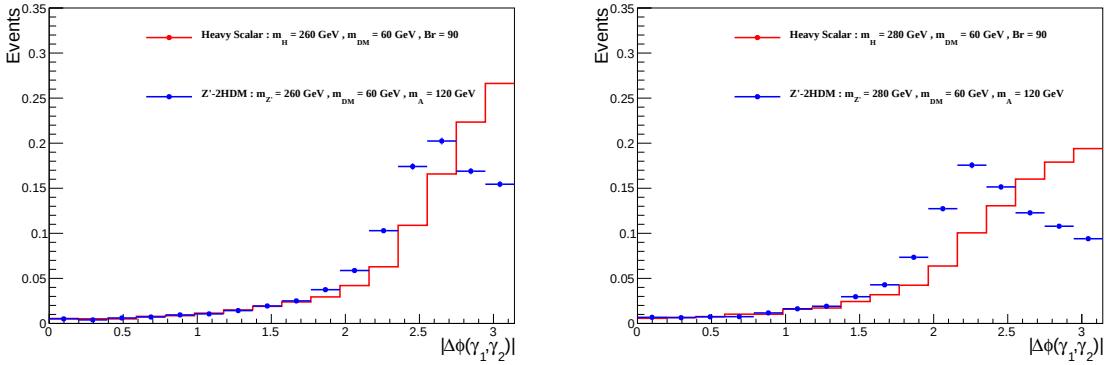


Figure B.12: Comparison of kinematic distributions between Z′-2HDM and Heavy scalar models for the same mediator and DM particle masses ($m'_Z = 260$ or 280 GeV, $m_\chi = 60$ GeV)

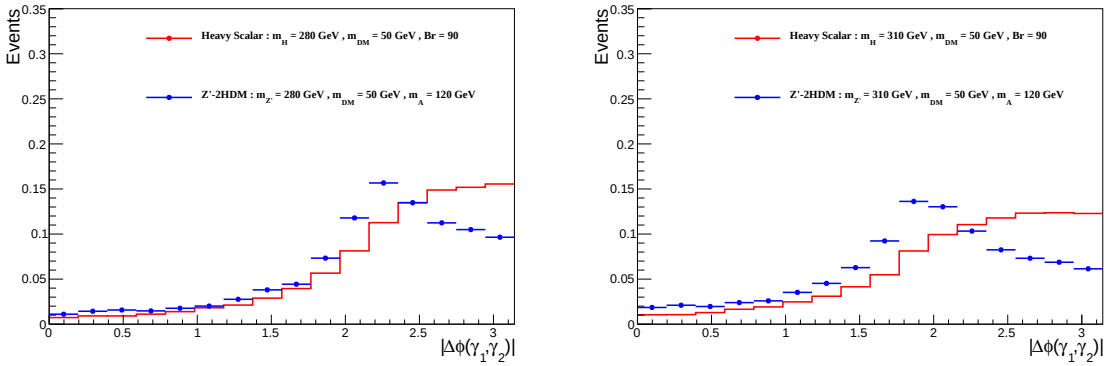


Figure B.13: Comparison of kinematic distributions between Z′-2HDM and Heavy scalar models for the same mediator and DM particle masses ($m'_Z = 280$ or 310 GeV, $m_\chi = 50$ GeV)

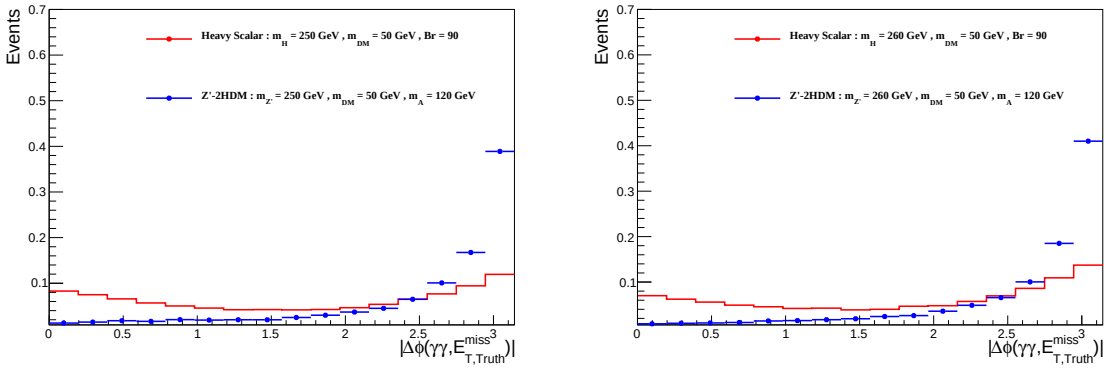


Figure B.14: Comparison of kinematic distributions between Z′-2HDM and Heavy scalar models for the same mediator and DM particle masses ($m'_Z = 250$ or 260 GeV, $m_\chi = 50$ GeV)

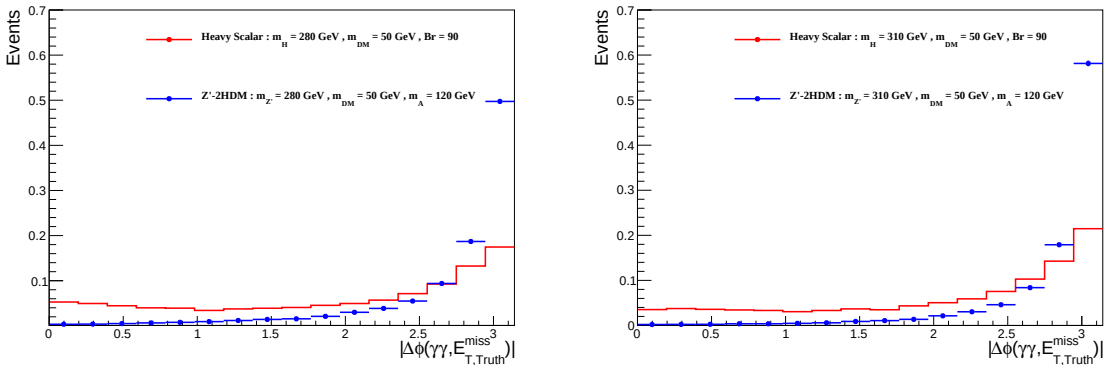


Figure B.15: Comparison of kinematic distributions between Z'-2HDM and Heavy scalar models for the same mediator and DM particle masses ($m'_Z = 280$ or 310 GeV, $m_\chi = 50$ GeV)

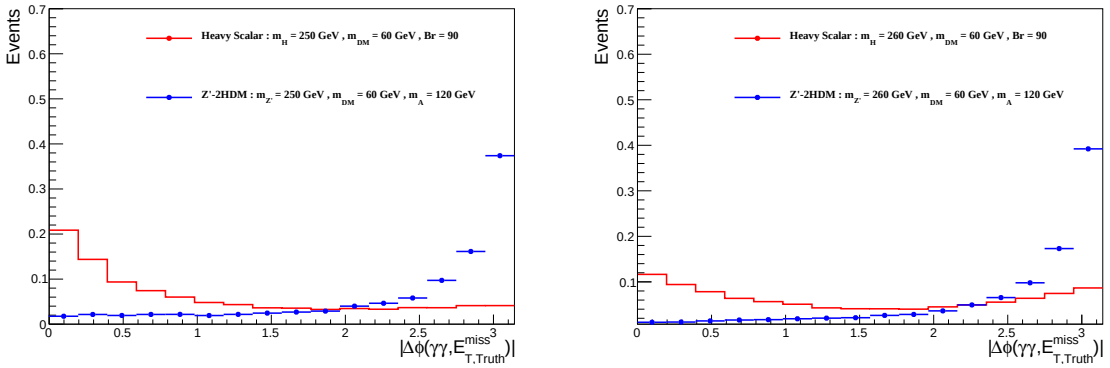


Figure B.16: Comparison of kinematic distributions between Z'-2HDM and Heavy scalar models for the same mediator and DM particle masses ($m'_Z = 250$ or 260 GeV, $m_\chi = 60$ GeV)

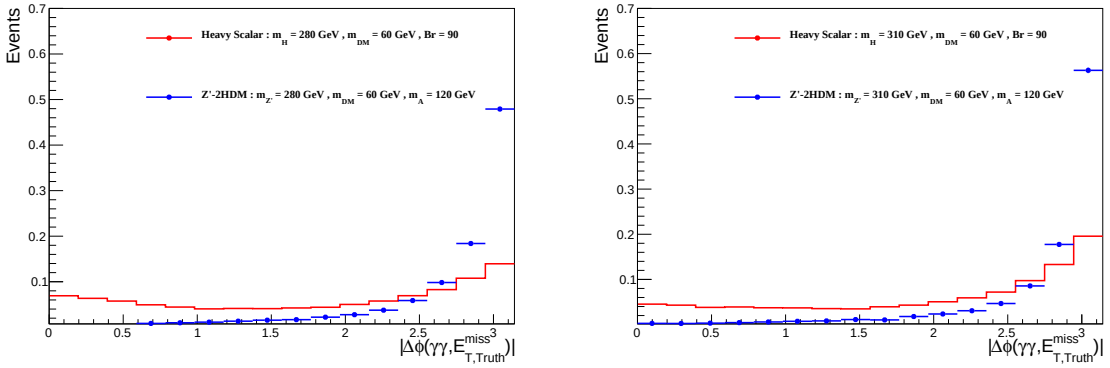
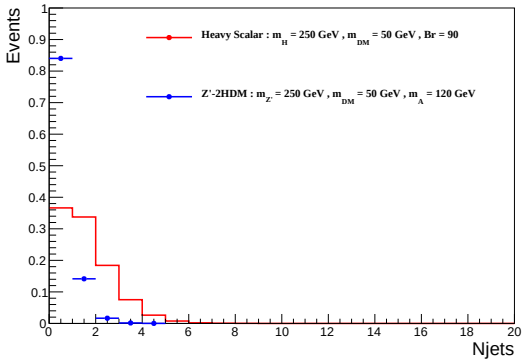


Figure B.17: Comparison of kinematic distributions between Z'-2HDM and Heavy scalar models for the same mediator and DM particle masses ($m'_Z = 280$ or 310 GeV, $m_\chi = 60$ GeV)



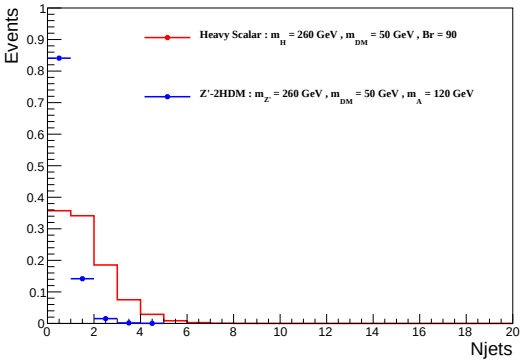
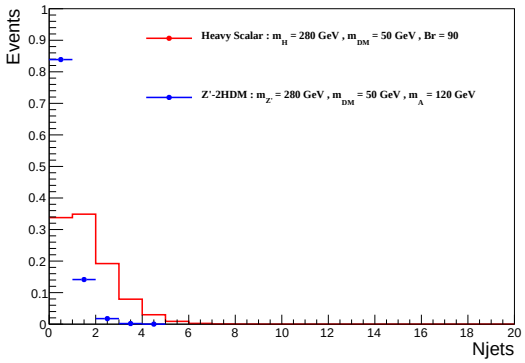


Figure B.18: Comparison of kinematic distributions between Z′-2HDM and Heavy scalar models for the same mediator and DM particle masses ($m'_Z = 250$ or 260 GeV, $m_\chi = 50$ GeV)



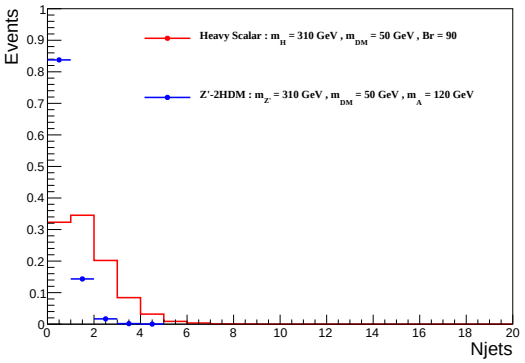
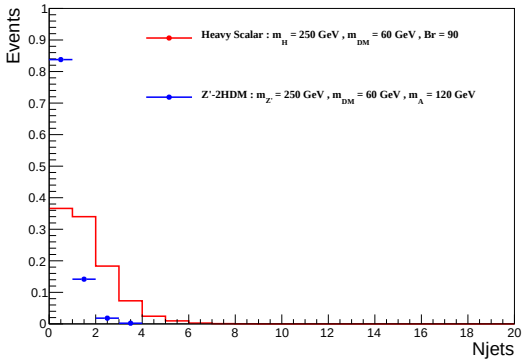


Figure B.19: Comparison of kinematic distributions between Z′-2HDM and Heavy scalar models for the same mediator and DM particle masses ($m'_Z = 280$ or 310 GeV, $m_\chi = 50$ GeV)



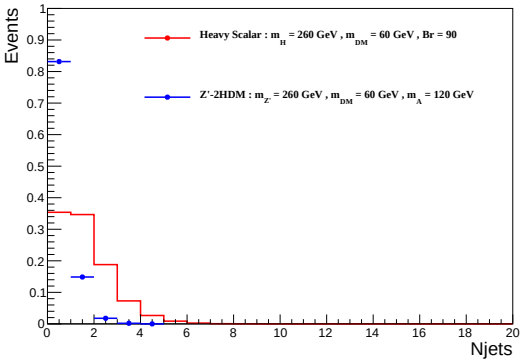
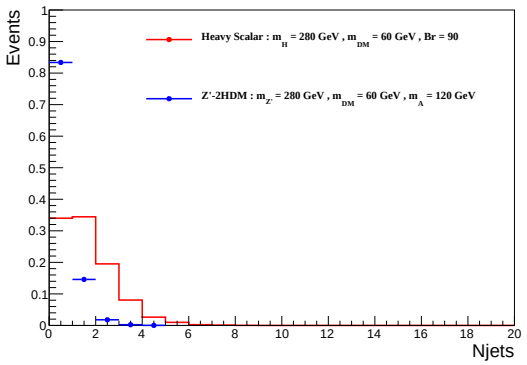


Figure B.20: Comparison of kinematic distributions between Z′-2HDM and Heavy scalar models for the same mediator and DM particle masses ($m'_Z = 250$ or 260 GeV, $m_\chi = 60$ GeV)



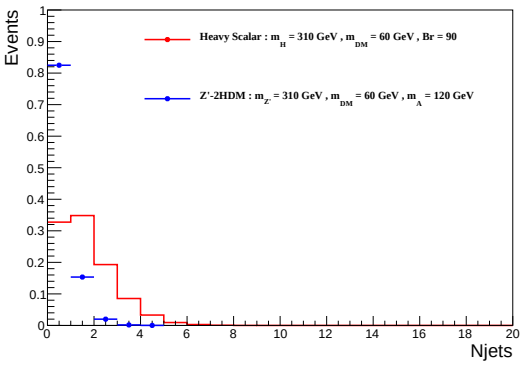
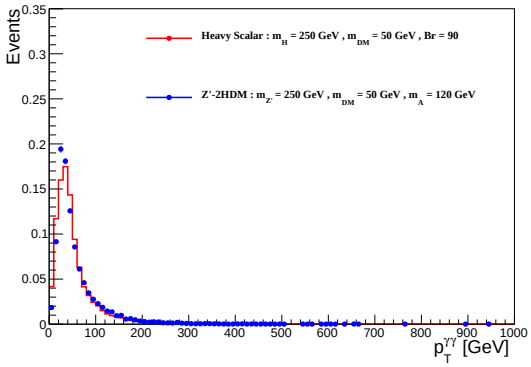


Figure B.21: Comparison of kinematic distributions between Z′-2HDM and Heavy scalar models for the same mediator and DM particle masses ($m'_Z = 280$ or 310 GeV, $m_\chi = 60$ GeV)



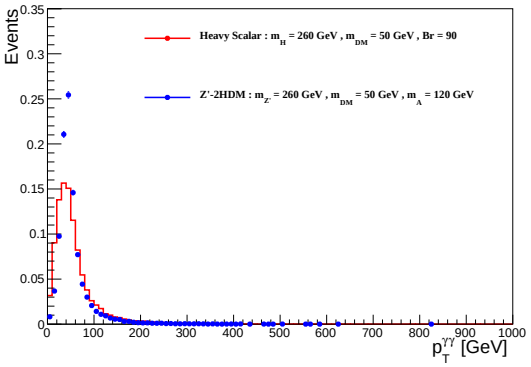
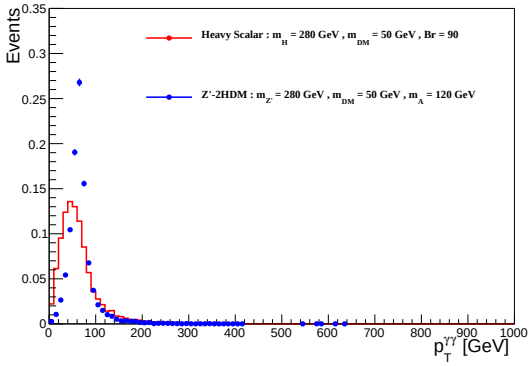


Figure B.22: Comparison of kinematic distributions between Z′-2HDM and Heavy scalar models for the same mediator and DM particle masses ($m'_Z = 250$ or 260 GeV, $m_\chi = 50$ GeV)



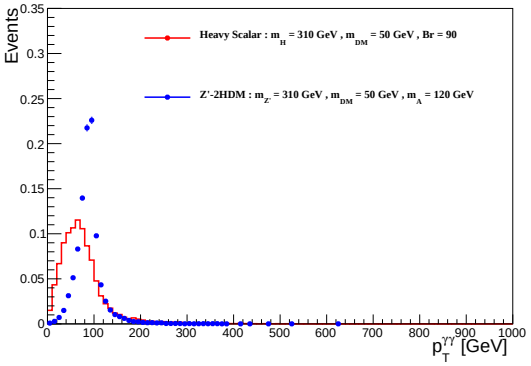


Figure B.23: Comparison of kinematic distributions between Z′-2HDM and Heavy scalar models for the same mediator and DM particle masses ($m'_Z = 280$ or 310 GeV, $m_\chi = 50$ GeV)

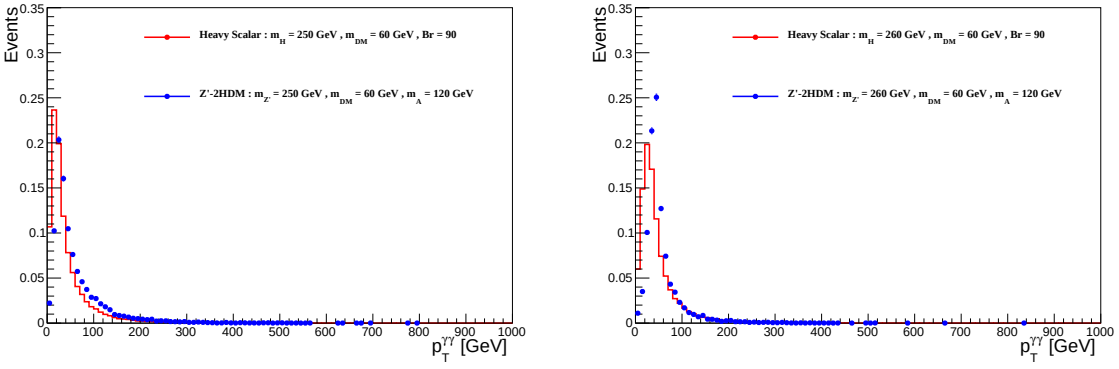


Figure B.24: Comparison of kinematic distributions between Z′-2HDM and Heavy scalar models for the same mediator and DM particle masses ($m'_Z = 250$ or 260 GeV, $m_\chi = 60$ GeV)

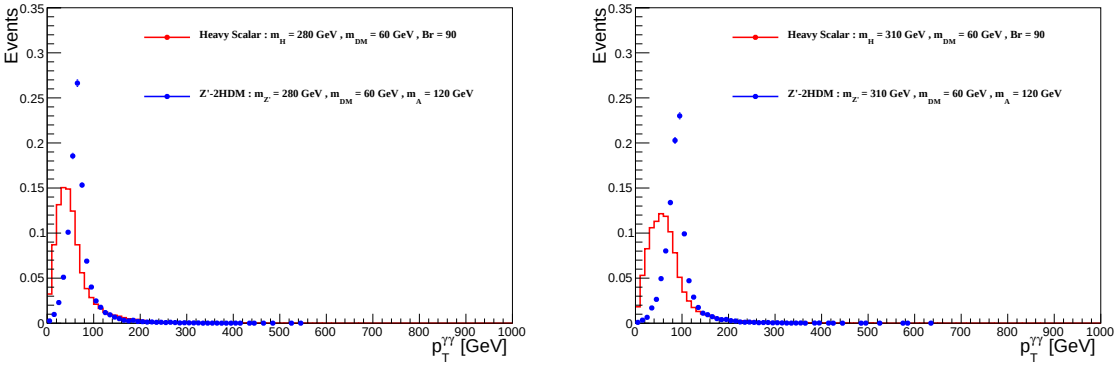


Figure B.25: Comparison of kinematic distributions between Z′-2HDM and Heavy scalar models for the same mediator and DM particle masses ($m'_Z = 280$ or 310 GeV, $m_\chi = 60$ GeV)

Cross-section checks between CMS and ATLAS DM models

Mono-Higgs models depend on several parameters that are previously fixed. Some of these parameters however are not fixed to the same values between CMS and ATLAS, which may induce different cross-sections, and possibly kinematic distributions. Each model presents their own differences:

C.1 Z'_B model g_q parameter

ATLAS and CMS configurations fixed the coupling g_q between the Z' vector boson and quarks to different values ($g_\chi^{\mathrm{ATLAS}} = 1/3$, $g_\chi^{\mathrm{CMS}} = 0.25$). This difference is not negligible since production cross-sections of the Z' boson at the LHC depend quadratically ($\propto g_q^2$) on this paramater. A study was performed within the DM Forum [1] on the effect of this coupling and it was found to affect negligibly the kinematic distributions of the model. Another study is now performed in order to estimate the scale factor needed to combine CMS and ATLAS limits. In this context, g_q effect on cross-sections is studied. Its effect on kinematic distributions is also studied to verify that certainly no other bias must be taken into account. Samples are generated using MadGraph5 version 2.3.3 interfaced with Pythia8. Four g_q values are considered: 0.4,1/3,0.25 and 0.10. Figures C.1– C.4 present the kinematic distributions for samples of the Z'_B model for these different g_q values. It can be observed that all distributions are compatible within their uncertainties, representing each the statistical error on the bin of the distribution.

Cross-sections are presented in Table C.1 presents the cross-sections for these samples with their corresponding ratio with the ATLAS benchmark cross-section ($\sigma_{g_q=1/3}$). It can be observed that between $g_q = 1/3$ and $g_q = 0.25$ cross-section values, cross-sections are lower in the second case, as expected. This would translate into more stringent limits in CMS using ATLAS configuration. However, the expected dependence of the cross-section on this parameter is not observed. The expected scales are: $\sigma_{g_q=0.4}/\sigma_{g_q=1/3} \sim 1.78$, $\sigma_{g_q=0.25}/\sigma_{g_q=1/3} \sim 0.69$ and $\sigma_{g_q=0.25}/\sigma_{g_q=1/3} \sim 0.11$. This is not observed. Further studies are beyond the scope of this work but it could be studied the dependence of the cross-section on the Madraph version, the study of the different diagrams from the Z'_B model contributing to the cross-section and the studies of ratios between CMS and ATLAS configurations for a finer grid of points. This last step would allow the conversion of the ATLAS limits into CMS limits, leading to a more precise comparison.

C.2 Z'-2HDM cross-sections dependence on CP-even boson masses

In Spring 2017, there was a cross-check between ATLAS and CMS cross-sections for a future combination of mono-Higgs final results. However, it was found a divergence between the cross-sections. The difference was due to the fixed mass of the CP-even heavy-scalars ($H^{\pm}$,H) issued from the two higgs doublets after EW symmetry breaking. ATLAS fixed their mass to $m_{H^\pm} = m_{H^0} = 300$ GeV while CMS equals these masses to the pseudo-scalar mass m_{A^0}. This is a non-negligible fact given that the width of the $A^0 \to \chi\overline{\chi}$ decay depends on the mass of m_{A^0}, $m_{H^\pm}$ and m_{H^0}. If $m_{A^0} > m_{H^\pm}, m_{H^0}$, new channel

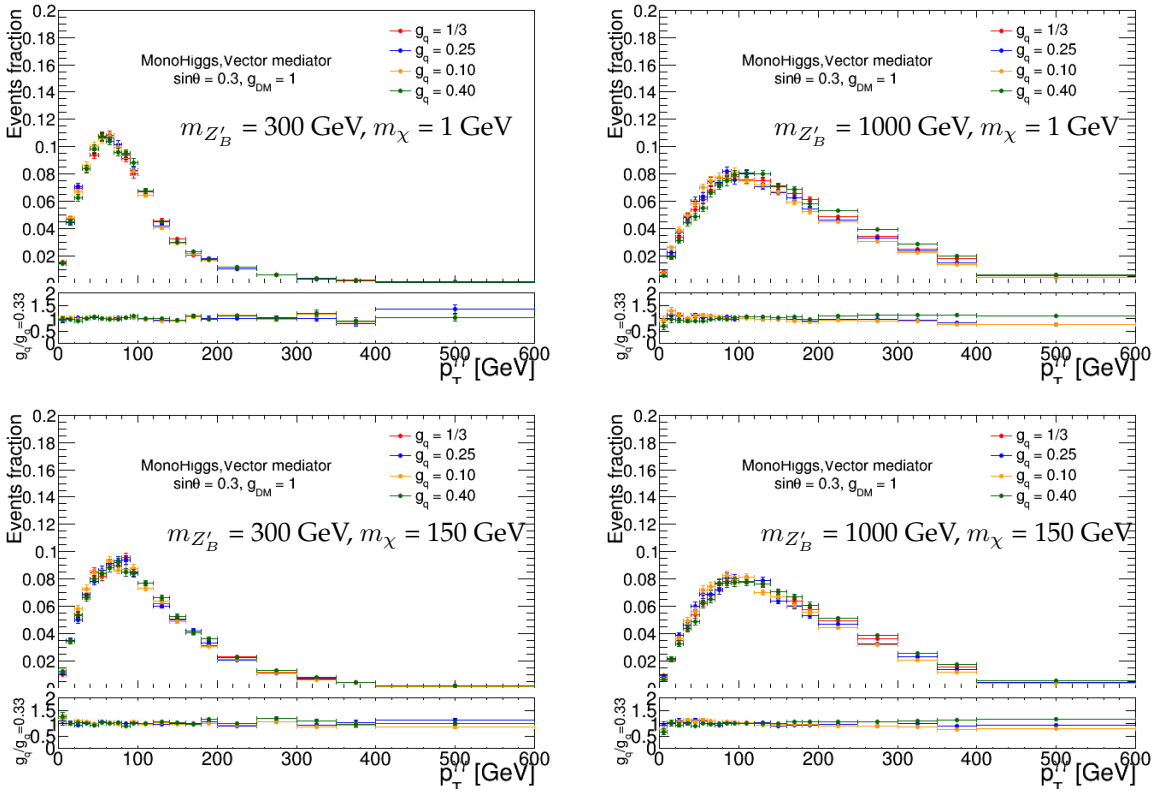


Figure C.1: $p_{\mathrm{T}}^{\gamma\gamma}$ distributions of the Z'_B model of four mass points ($m_{Z'_B}$, m_χ) and four different values of g_q.

$[m_{Z'}(\mathrm{GeV}), \mathrm{m}_\chi(\mathrm{GeV})]$	$\sigma_{g_q=0.4}$ (pb)	$\sigma_{g_q=1/3}$ (pb)	$\sigma_{g_q=0.25}$ (pb)	$\sigma_{g_q=0.1}$ (pb)
[300,1]	2.483 (1.088)	2.282 (1)	1.864 (0.817)	0.573 (0.251)
[300,150]	0.287 (1.061)	0.2705 (1)	0.2361 (0.873)	0.125 (0.462)
[1000,1]	0.1796 (0.99)	0.1813 (1)	0.1616 (0.891)	0.056 (0.306)
[1000,150]	0.1737 (0.989)	0.1756 (1)	0.1573 (0.896)	0.054 (0.308)

Table C.1: Cross-section values for the Z'_B model fixing different values of the g_q parameter. Values in parentheses correspond to the ratio between the given cross-section and the reference cross-section, fixed to be $\sigma_{g_q=1/3}$. Other parameters are fixed to their proposed values in [1] ($sin\theta = 0.3$, $g_{chi} = 1$ and $g_{hZ'Z'} = m_{Z'}$).

possibilities open up and the $\Gamma(A^0 \to \chi\overline{\chi})$ decreases. This affects not only the total cross-section but also the kinematic distributions. Table C.2 present values of Z'-2HDM cross-sections for several mass points using these two configurations.

$[m_{Z'}(\mathrm{GeV}), \mathrm{m}_{\mathrm{A}^0}(\mathrm{GeV})]$	σ_{ATLAS} (fb)	σ_{CMS}(fb)
[800,500]	21.1	37.7
[1000,600]	6.2	19.5
[1200,400]	32.6	35.2
[1400,800]	0.7	5.7

Table C.2: Cross-section values for Z'-2HDM model mass points using ATLAS ($m_{H^\pm} = m_{H^0} = 300$ GeV) and CMS ($m_{H^\pm} = m_{H^0} = m_{A^0}$) configurations. Other parameters are fixed to the values presented in DM Forum [1] ($\tan\beta = 1$, $g_{Z'} = 0.8$ and $m_{\mathrm{dm}} = 100$ GeV).

This leads to more stringent limits in CMS case that in ATLAS. However, both configurations are correct in a theoretical point of view. However, to converge between both experiments, the current CMS

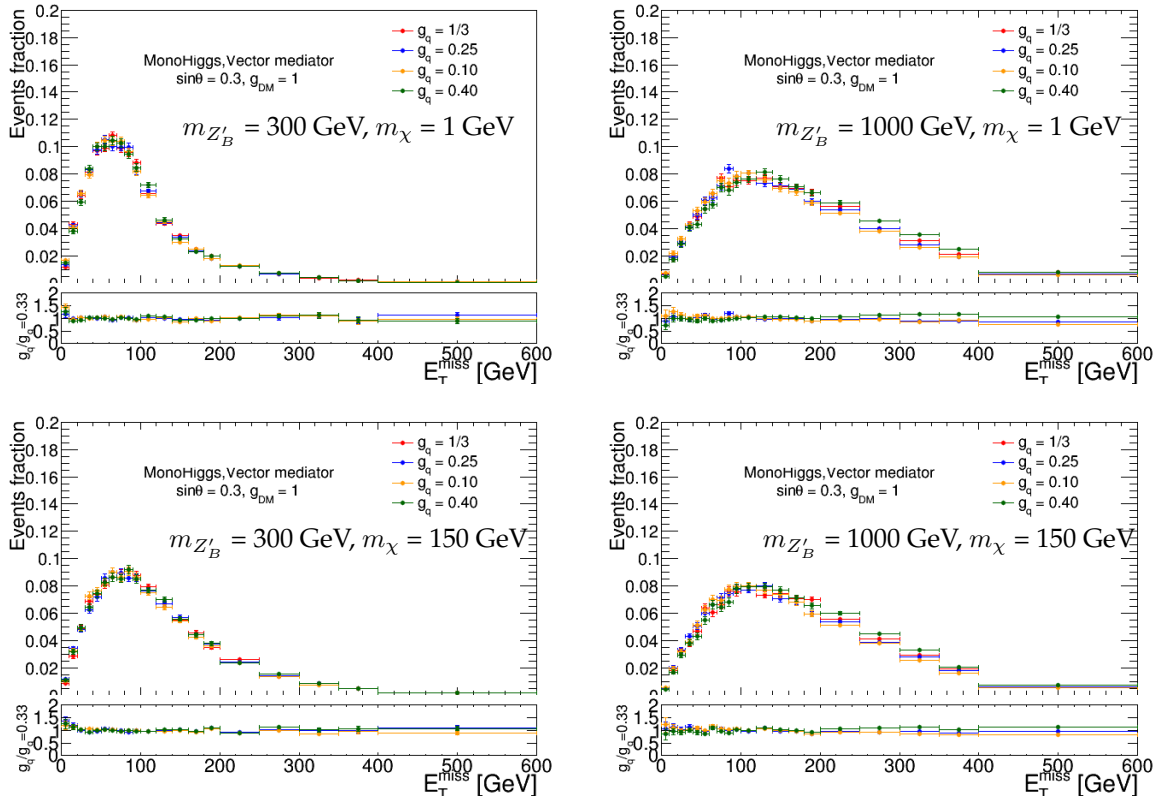


Figure C.2: $E_{\mathrm{T}}^{\mathrm{miss}}$ distributions of the Z'_B model of four mass points ($m_{Z'_B}$, m_χ) and four different values of g_q.

configuration will be used in the future.

References

[1] Daniel Abercrombie et al. "Dark Matter Benchmark Models for Early LHC Run-2 Searches: Report of the ATLAS/CMS Dark Matter Forum". In: (2015). arXiv: 1507.00966 [hep-ex].

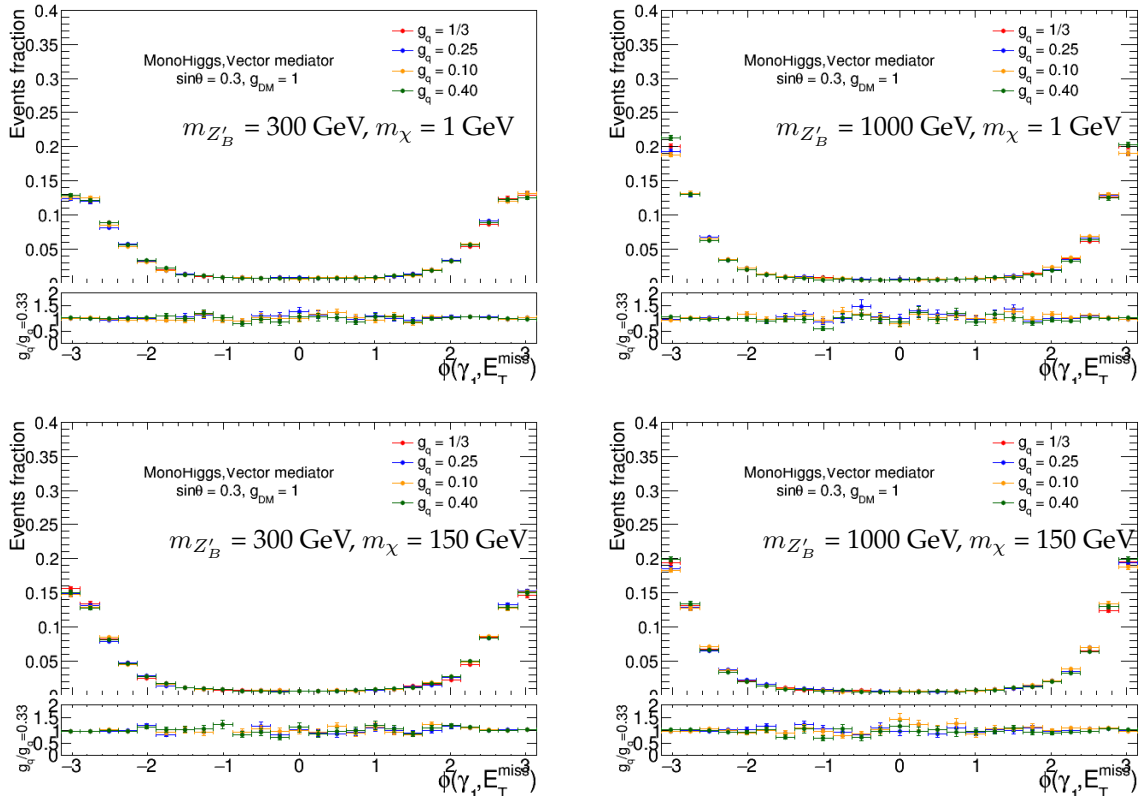


Figure C.3: $\Delta\phi(\gamma_1, E_{\mathrm{T}}^{\mathrm{miss}})$ distributions of the Z'_B model of four mass points ($m_{Z'_B}$, m_χ) and four different values of g_q.

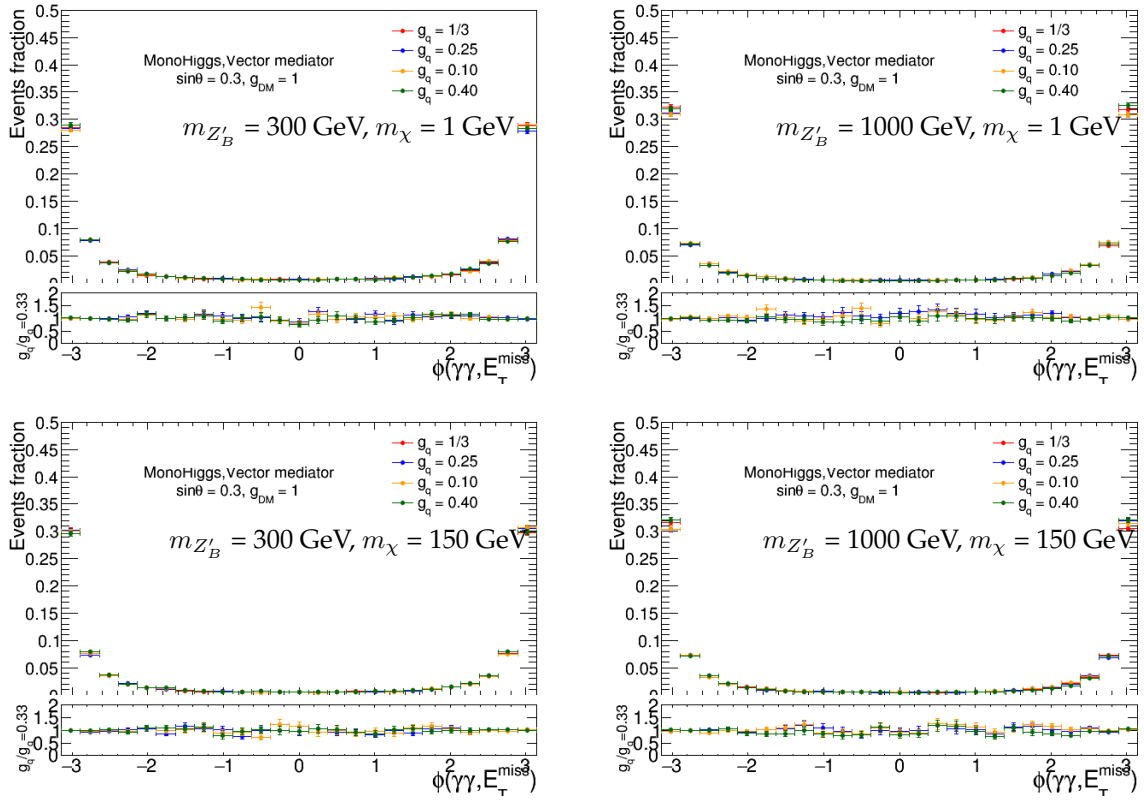


Figure C.4: $\Delta\phi(\gamma\gamma, E_{\mathrm{T}}^{\mathrm{miss}})$ distributions of the Z'_B model of four mass points ($m_{Z'_B}$, m_χ) and four different values of g_q.

List of Figures

1.1 Feynman diagram of the Deep Inelastic Scattering process. An electron interacts with a quark inside the proton. The scattered electron energy and angular distributions provide information about the structure inside the proton. . . . 5

1.2 Feynman diagrams representing the leading order contributions to the interaction between an initial electron and a muon in the t-channel. The tree-level diagram corresponds to the exchange of a photon between the electron and the muon. In addition, the leading order loop correction to the electron-muon interaction is also shown. 9

1.3 Higgs potential form represented in a 3D plot as a function of the imaginary and real part of the Higgs field. Ground state degeneracy is observed. . . . 10

1.4 Running coupling α_s as a function of the interaction energy ($\alpha_s = g_s^2/4\pi$) and representation of the confinement effect after the emission of quarks or gluons issued from an interaction. It can be observed how quarks and gluons scatter out of the collision point. As partons move away, g_s running coupling increases and at one point, quark-antiquark pairs are created from the vacuum and combine with the outcoming partons to form hadrons. . . . 14

1.5 General picture of elementary particles and force carriers included in the Standard Model [30]. . . . 15

1.6 Prediction of the mass of the Higgs boson by comparing the measured masses of the top and the W boson and measured 95 % CL limits on the Higgs production cross-section at Tevatron with 10 fb^{-1} integrated luminosity [48, 49]. . . . 17

1.7 Individual and combined values of the SM Higgs-like resonance using 2011-2012 ATLAS+CMS data at $\sqrt{s} = 7$ and 8 TeV [54]. $h \to \gamma\gamma$ and $h \to 4\ell$ are used because they offer the best mass resolution. Mass measurements are performed allowing strength parameters for selected production and decay modes to vary in the fit. It is done in order to obtain a mass measurement as independent as possible of SM assumptions. The red vertical line and the gray shaded column indicate the central value and the total uncertainty of the combined measurement. . . . 17

1.8 Combined measurements of the SM Higgs-like resonance production and decay couplings using 2011-2012 ATLAS+CMS data from LHC Run I at $\sqrt{s} = 7$ and 8 TeV [55]. All production modes are considered while only $b\bar{b}$, $\gamma\gamma$, $\tau^+\tau^-$, $W^\pm W^\mp$ and ZZ final state branching cross-section $\times$ branching ratios are extracted in units of the SM predictions. . 18

1.9 Example of the leading order Feynman diagrams for Higgs production at LHC: gluon fusion production (a), vector-boson fusion (b), associated production (c) and $t\bar{t}H$ (d) and $b\bar{b}H$ (e). . . . 19

1.10 Higgs production cross-section for leading production modes. The left plot shows production the cross-section at $\sqrt{s} = 13$ TeV while the right plot at $\sqrt{s} = 14$ TeV. Bolded regions correspond to the Higgs cross-section uncertainties. . . . 19

1.11 Leading-order Feynman diagrams for main Higgs boson decay modes at $m_h = 125.09$GeV: Higgs boson decay to $b\bar{b}$ and $c\bar{c}$ (a); $\tau^+\tau^-$ and $\mu^+\mu^-$ (b); decay into two vector bosons, one off-shell and other on-shell (c); decay to two photons $\gamma\gamma$ (d); to $Z\gamma$ and to two gluons (e). . . . 21

1.12 Branching ratios of the Standard Model Higgs boson decay modes as a function of the Higgs mass. Left plot shows the mass dependence of the branching ratio inside a region of $m_h \in [80, 200]\text{GeV}$ and right plot shows this dependence around the combined ATLAS+CMS 2011-2012 Higgs-like resonance mass $m_h \approx 125.09$ GeV [56]. 22
1.13 Fermion loop corrections to the Higgs self-interaction term. The dominant contribution corresponds to the top loop, due to the large $t - h$ coupling. 23
1.14 Standard Model and Minimal Supersymmetric Standard Model electromagnetic, weak and strong running couplings. Coupling unification in MSSM (plot taken from [58]). . . 23
1.15 Stability of the Higgs potential extrapolated to the Planck scale from [59]. 24
1.16 Rotational curves for (a) Andromeda galaxy, presented by Vera Rubin and Kent Ford in their article [73]; and (b) of the galaxy NGC 6503 [75]. Both galaxies are spiral. 25
1.17 Bullet cluster image, taken from the NASA measured by the Chandra X-ray observatory [77]. 26
1.18 Schema of the Universe evolution since from Big Bang until today [78]. 27
1.19 Evolution of the dark matter abundance before and at the moment of freeze-out. It can be observed that at one moment the dark matter decoupled from the interaction with the rest of the plasma species and for that time onward, its relic density remained constant [81]. 29
1.20 90 % CL limits on WIMP-nucleon spin-independent cross-section are presented. Left: comparisons between most recent results for Xenon100 [92], DarkSide-50 [85], LUX [86] and PandaX-II [87] are presented. The plot is taken from [92]. Right: latest results from Xenon1T [84] experiment and comparison with LUX [86], Xenon100 [92] and PandaX-II [87] results. 30
1.21 γ-ray data measured by Fermi-LAT in a region of size 15°×15°around the galactic center. It is found that model fits better the γ-ray spectra when including a contribution of WIMP dark matter annihilation distributed at the galactic center following a Navarro-Frenk-White profile distribution. Two possible distributions are considered, being shown on the center plot results using the standard NFW distribution and, on the right plot, a NFW distribution corrected with a power law [93]. In this pictures, one of the four IEM's is presented. 31
1.22 Summary of H.E.S.S. 10-year observation and results on the GC γ-ray spectrum. The top plot presents the signal (ON) and background (OFF) regions observed to study the galactic background. The bottom left plot presents the limits on WIMP thermal averaged cross-section $\langle\sigma v\rangle$ depending on the DM particle mass using the Einasto [97] profile distribution. The bottom right plot presents the dependence of H.E.S.S. limits on the DM spatial distribution model. All plots are taken from [96]. 32
1.23 Positron excess observed by PAMELA, Fermi-LAT and AMS-02 [101]. 32
1.24 Feynman diagrams from a simplified model (left) and an effective field theory (right). . . 33
1.25 The ratio R_Λ for $\sqrt{s} = 8$ TeV at $|\eta| = 0$ from [102]. A mono-jet EFT is used. These plots show the validity of the EFT depending on the hard-jet p_{T} and/or m_χ. It can be observed that EFT is valid only considering large values of Λ. For lower values, a part of the generated events presents interactions with $Q_{tr} > \Lambda$, where predictions are no longer valid. 34
1.26 Feynman diagrams of the production of DM (χ) in association with a SM-like Higgs boson (h) arising from Z'_B models: born process (a); t-channel production of the Z'_B (b); and leading NLO box diagram producing mono-Higgs signals in the final state (c). The latter diagram is not simulated since signal events are produced at leading-order in QCD, as explained in Section 7.1. 35
1.27 Z'_B kinematics dependence on g_χ (left) and $g_{hZ'Z'}$ (right) parameters [107]. 35
1.28 Feynman diagrams of the production of DM (χ) in association with a SM-like Higgs boson (h) arising from Z'-2HDM model. 36
1.29 Z'-2HDM kinematics dependence on m_χ (left) and $\tan\beta$ (right) parameters [107]. 37
1.30 Feynman diagrams of the production of DM (χ) in association with a SM-like Higgs boson (h) arising from the heavy-scalar model. 37

2.1 LHC layout with the positioning of the four experiments and the structure of the SPS+LHC acceleration system. 46

2.2 Schema of the acceleration of a proton inside the RF cavities [9] . . . 46
2.3 CERN acceleration complex [10]. . . . 47
2.4 Illustration of the β^* parameter in Eq. 2.2 [11]. . . . 48
2.5 Instantaneous luminosity delivered by the LHC for the 2011-2017 period (left) and integrated luminosity provided by the LHC and recorded by ATLAS during 2016 data taking period (right) [14]. . . . 49
2.6 Registered number of interactions per bunch crossing during the data taking periods of 2015 and 2016, with pp collisions at $\sqrt{s} = 13$ TeV [14]. . . . 50
2.7 Plan of the HL-LHC phase [15]. . . . 50
2.8 Schema of the ATLAS detectors and the different subdetectors [2]. . . . 51
2.9 Illustration of the energy deposits expected for each measured particle in the ATLAS detector. . . . 52
2.10 Illustration of the magnet system layout (a) and photograph of the final installation of the ATLAS detector (b), where barrel toroids may be observed in the foreground. . . . 52
2.11 Illustration of the barrel region of the inner tracker showing the different subdetector layers and structures traversed by a charged particle created in collision point during Run II [18]. . . . 53
2.12 Views of a quarter section of the tracker not including the insertable B layer [2]. . . . 55
2.13 View of the ATLAS calorimeter geometry with the different subdetectors [2]. . . . 55
2.14 View of the liquid argon calorimeters, containing the electromagnetic calorimeter (on barrel and two end-caps) and the hadronic calorimeter end-caps (HEC) and forward calorimeters (FCal) [2]. . . . 56
2.15 Schematic view of the tile calorimeter central region (left) and a slice of the tile calorimeter barrel (right) showing the disposition of the absorbers, the scintillating tiles and the readout PMT's [2]. . . . 56
2.16 Structure of the ATLAS muon spectrometer [2]. . . . 57
2.17 Section of an MDT tube (left) and schema of the structure of one MDT chambers (right) [2]. 58
2.18 Layout of the ATLAS data acquisition system during Run II. FTK and L1 Topo were commissioned during Run II and therefore, they were not included in the trigger decision yet [16]. . . . 59
2.19 Layout of the ATLAS data acquisition system during Run II. FTK and L1 Topo were commissioned during Run II. L1Topo was included in the trigger decision but FTK is not [16]. . . . 59

3.1 Shower development and energy depositions in a sampling calorimeter [1]. . . . 64
3.2 Schema of a shower for an incoming photon. . . . 66
3.3 Electron (or positron) fractional loss of energy in lead [6]. . . . 67
3.4 Photon total cross-sections as a function of energy in lead, showing the contributions of different processes [6], where the different cross-sections are: $\sigma_{\text{p.e}}$, the atomic photoelectric effect cross-section; σ_{Rayleigh} for Rayleigh scattering–atom; σ_{Compton} stands for Compton scattering off an electron cross-section; κ_{nuc} accounts for the pair e^+e^- production by nuclear field and κ_e by the electron field; and $\sigma_{\text{g.d.r.}}$ accounts for photonuclear interactions. . . . 67
3.5 Schematic view of the effect that interactions upstream the calorimeter may present in the lateral shower development of two photons. The yellow star indicates the collision point. Red arrows present the two opposite bunches of protons and dark blue ellipses represent the shower of the incoming photons. . . . 68
3.6 Simulation of a 30 GeV electron-induced cascade in iron. It is shown the fraction of energy deposited in the iron per radiation length. The curve is a gamma-function fit to the distribution for electrons. Circles indicate the number of electrons with total energy greater than 1.5 MeV crossing planes at $X_0/2$ intervals (scale on right) and the squares the number of photons with $E \geq 1.5$ MeV crossing the planes (scaled down to have the same area as the electron distribution). This figure is taken from [6]. . . . 69
3.7 Section of the calorimeter showing the barrel and the end-cap together with η projections [12]. . . . 70
3.8 Section of the barrel calorimeter barrel showing the three radial layers with their corresponding cell segmentation [8]. . . . 71

3.9 Schema of the absorber and electrode disposition in the EM calorimeter barrel. 72
3.10 Left: schema of the absorber bending angle and composition [3]. Right: cumulative amount of material found by particles traversing the detector expressed as radiation lengths X_0 [8]. It can be observed an increase of the cumulative material in the EM calo with η. It can be observed the lead thickness change at $\eta = 0.8$. 73
3.11 Electrode components of the liquid argon (a) and electrodes high-voltage layers before bending, cut into small compartments connected by ink resistors (b) ([10]). 73
3.12 Current as a function of time for a perfect centering of the electrode with δ_{gap} = 0 μm and δ_{gap} = 100 μm and δ_{gap} = 200 μm [14]. 74
3.13 Front (left) and back (right) mother boards for the LAr barrel. Numbers on the connectors are attributed to each cell depending on their position [15]. 75
3.14 Feedthrough connectors distribution (left) [15] and feedthrough distribution in the cryostat of the end-cap(right), similar to the distribution of the feedthroughts around the barrel cryostat [8]. 75
3.15 Boards distribution in the front-end crates for the barrel [15] 76
3.16 Diagram of the FEB architecture [8]. 76
3.17 Sketch of the peaking time and amplitude of the physics signal and the estimation using optimal filtering coefficients (OFCs). The amplitude is proportional to the energy deposited in the cell. 77
3.18 Representation of the calibration exponential pulse and ionization triangular signal. . . . 78
3.19 Basic equivalent circuit of the liquid argon detector cell readout [17]. 78
3.20 Simplified calibration board pulser circuit, showing the non-ideal nature of the inductance L_c in its resistive component r_c [17]. 79
3.21 Comparison between calibration and physics pulse [17]. 80
3.22 Run 00314180: DAC versus ADC_{peak} obtained in a high gain run for the 3 layers of the electromagnetic calorimeter. 82
3.23 Run 00314180: DAC versus ADC_{peak} obtained in a high gain run for a single cell in the middle layer of the EM barrel calorimeter. The red line corresponds to the fitted curve describing the DAC vs ADC behaviour (Eq. 3.30). 82
3.24 Run 00314180: value of R_1 from the fit of the DAC versus ADC distributions in Figure 3.22 with Equation 3.30. 83
3.25 Run 00314179: value of $\frac{M_{\text{phys}}}{M_{\text{calib}}}$ for (a) the front layer, (b) the middle layer and (c) for the back layer of the electromagnetic barrel. 83
3.26 The ratio of the reconstructed electron energy to the beam energy (a) and the fractional energy resolution (b) as a function of the beam energy are presented [20]. In (b) data before (closed circles) and after (open circle) the gain dependent noise (open squares) subtraction are shown. 85
3.27 Resolution on the time difference between cells in calibration runs as a function of the amplitude [9]. 85
3.28 Difference between reconstructed OF time and trigger time depending on the barycenter of energy deposition in between cells in η and ϕ [9]. 86
3.29 Time resolution (ps) as a function of the hottest middle layer cell. 87

4.1 Distance to the beamline of reconstructed conversion vertices (left) and spatial distribution of reconstructed conversion vertices (right) in the transverse plane measured on 14nb^{-1} during June-July 2010 [1]. 90
4.2 Schema of the expected energy deposits for jets, electrons, unconverted photons and neutral pions. Solid (dotted) lines represent tracks that (don't) leave traces in the inner detector. Red color stands for electromagnetic energy deposits in any of the calorimeters while blue color represent hadronic energy deposits. 90
4.3 Material traversed by a particle in the ID (left) and the calorimeter (right) as a function of the pseudorapidity [2]. 91
4.4 Schema of the calorimeter cells introduced in sliding-window and topocluster algorithms. 92
4.5 Picture illustrating the cluster-track matching for electrons and converted photons in the EM barrel calorimeter. 94

4.6 Picture illustrating the three track pairs that can be used to reconstruct conversion vertices. The rightmost pair represents Si-Si tracks; the bottom right pair represents TRT-TRT tracks and the last one, Si-TRT tracks. In addition, the bottom left photon presents two tracks from which one escapes detection (single-track conversion vertex). . 95
4.7 Scheme of the decision tree to initially separate electron, converted photon and unconverted photon candidates. 96
4.8 Measured reconstruction efficiencies for electrons as a function of E_{T} integrated over the full pseudorapidity range (left) and as a function of pseudo-rapidity for 15 GeV < E_{T} < 150 GeV (right) for the 2015 dataset. The shown uncertainties are statistical plus systematic errors [6]. 97
4.9 Top left: ratio between the transverse energy of the electron candidate and the sum of this trans- verse energy and that contained in the first layer of the hadronic calorimeter. Top right: $\Delta\eta$ between the cluster barycentre and the extrapolated track. Bottom: distribution of R_ϕ (left) and R_η (right), defined in Table 4.1. Dotted lines correspond to non-isolated electrons from hadrons evaluated on di-jet events while solid lines correspond to prompt electrons selected on a $Z \to ee$ simulation [12]. 99
4.10 The efficiency to identify electrons from $Z \to ee$ decays (left) and the efficiency to identify hadrons as electrons (background rejection, right) estimated using simulated dijet samples. The efficiencies are obtained using Monte Carlo simulations, and are measured with respect to reconstructed electrons. The candidates are matched to true electron candidates for $Z \to ee$ events. For background rejection studies the electrons matched to true electron candidates are not included in the analysis [6]. 99
4.11 Shower shape comparison between a γ and a π^0 decaying into two photons. 100
4.12 Illustrations comparing several shower shape variable distributions for boosted $\pi^0 \to \gamma\gamma$ (open black points) against prompt photons (red solid points) [12]. 101
4.13 Tight identification efficiency for unconverted photons depending on η and E_{T}. Efficiencies are tested using three methods providing similar results. 102
4.14 Tight identification efficiency for converted photons depending on η and E_{T}. Efficiencies are tested using three methods providing similar results. 103
4.15 Schema of the *topoetcone* variable: the grid represents the middle calorimeter cells in the η and ϕ directions. The electron or photon is located in the center of the yellow cone representing the isolation cone. Topological clusters are represented in red. Those whose barycenter falls into the isolation cone are included in the isolation computation. The 5×7 cells white rectangle corresponds to the subtracted core cells. Energy around this core corresponds to the energy leakage that needs to be corrected [13]. 104
4.16 Comparison of the corrected topoetcone20 isolation transverse energies for photons from the gluon-fusion $h \to \gamma\gamma$ MC sample and a jj sample, where the photon is faked by a jet. 104
4.17 Comparison of the corrected ptcone20 isolation transverse energies for photons from the gluon-fusion $h \to \gamma\gamma$ MC sample and a jj sample, where the photon is faked by a jet. . . 105
4.18 Calibration scheme for electrons and photons [2]. 106
4.19 Energy scales $\alpha_{1/2}$ and α_{PS} values depending on η for Run I [2]. Presented $\alpha_{1/2}$ values are derived using two methods for estimating $Z \to \mu\mu$ mean deposited energy in the first and second layer (fitting to a Landau or truncated mean of the distribution). α_{PS} values are presented before and after correcting the presampler energy in MC from passive material mismodeling. 107
4.20 Differences in $\alpha_{1/2}$ after cross-checking the dependence of the invariant mass in $Z \to ee$ events with $E_{1/2}$ depending on η [2]. The error band represents the uncertainty on $\alpha_{1/2}$ when derived on the Z muon decay while the error bars represent the uncertainty on Z electron result. 107
4.21 Left: average value of m_{ee} as a function of the azimuthal position of the leading decay electron with $0.4 < \eta < 0.6$ before and after the HV correction. Right: relative difference in the raw PS energy response due to the change in HV settings, as a function of η, before and after correction of the residual HV dependence [2]. 108
4.22 Pileup stability of the energy response in data and simulation [2]. 109

4.23 Top plots: electron pair invariant mass distribution for $Z \to ee$ candidates in data compared to MC templates. Different values of α_{ij} (left) are tested for a fixed value of $c_{ij}^{'}$ and viceversa (right). One electron is within $1.63 < \eta < 1.74$ and the other, within $2.3 < \eta < 2.4$. Bottom plots: χ^2 as a function of α_{ij} (left) and $c_{ij}^{'}$ (right) [2]. 110
4.24 (a) Energy scale factor α and (b) additional constant term $c^{'}$ for energy resolution from $Z \to ee$ events as a function of η. The uncertainty bands on the top plots represent the total uncertainties on these quantities, while the thin black (resp. thick blue) lines at the bottom represent the statistical (resp. total) uncertainties. [18]. 110
4.25 Uncertainties for the electron energy calibration using 2015 dataset with 3.2fb^{-1} total luminosity [18]. 111
4.26 Uncertainties for the unconverted photons energy calibration using 2015 dataset with 3.2fb^{-1} total luminosity [18]. 111
4.27 Uncertainties for the converted photons energy calibration using 2015 dataset with 3.2fb^{-1} total luminosity [18]. 111

5.1 (left) Illustration of the capacitive coupling C_x between cells on a single electrode and comparison with the capacitive coupling C_{HV} between the inner layer and the two HV outer layers of the electrode. (right) Readout chain model used to estimate the capacitive coupling signal. In this model, $C_d = C_{\mathrm{HV}}$ 114
5.2 Capacitive cross-talk shape obtained from calibration data. A cell is pulsed in the front layer of the EM barrel. The cross-talk shape is retrieved from its closest neighbouring cell in η. 115
5.3 Layout of the resistors on the HV layer for the Electrode A and Electrode B of the LAr EM barrel [3]. 116
5.4 Resistive cross-talk shape obtained from calibration data. A cell is pulsed in the middle layer of the EM barrel. The cross-talk shape is retrieved from one of its neighbouring cell in the front layer. 116
5.5 Inductive cross-talk shape obtained from calibration data. A cell is pulsed in the middle layer of the EM barrel. The cross-talk shape on the left is retrieved from its closest neighbouring cell in η while the one on the right is retrieved from its adjacent cell in the back layer. 117
5.6 Diagram of the related quantities entering the cross-talk determination [4]. 117
5.7 Gain factors ratio (MeV/ADC) between front and middle layers (left) and back and middle layers (right) [8]. 118
5.8 Schema of the different cross-talk magnitudes using the peak-peak estimation [8]. 119
5.9 Schema of the different cross-talk magnitudes using the under-peak to peak estimation [8]. 119
5.10 Schema of how cross-talk energy is estimated using the optimal filtering method on calibration signals 120
5.11 Cross-talk magnitude dependence on $|\eta|$. This magnitude represents the ratio of the cross-talk energy divided by the pulsed cell energy. Both energies are derived using the OF method explained in Section 3.5 where calibration OFCs were applied. 121
5.12 Calibration patterns for the front (left), middle (center) and back (right) layers. 122
5.13 Bad channels found in the calibration runs used in the physics cross-talk study. 122
5.14 Illustration of the application of the RTM method to the cross-talk calibration shape, based on the method used for direct signals. 123
5.15 Calibration (red) and physics cross-talk signal presented in a middle cell layer of the calibration run 00227022. This cell corresponds to the previous neighbour in η of a pulsed cell of the calibration run. Physics shape is determined using the RTM method. . 124
5.16 $g(t)^{\mathrm{phys}}_{\mathrm{xtalk}}$ after using matrix inversion. 126
5.17 $g(t)^{\mathrm{phys}}_{\mathrm{xtalk}}$ estimated using the matrix inversion method. Left plot presents the obtained signal when a gaussian noise centered at zero and with varying σ is added to all terms of $g(t)^{\mathrm{calib}}_{\mathrm{xtalk}}$. Center and right plots present instead the obtained physics cross-talk shape when the gaussian noise is applied to $g(z)^{\mathrm{calib}}_{\mathrm{direct}}$ or $g(z)^{\mathrm{phys}}_{\mathrm{direct}}$, respectively. 126

5.18 $g(t)^{\text{phys}}_{\text{xtalk}}$ estimated using the matrix inversion method. Left, center and right plots show the obtained signal when a gaussian noise centered at zero and with varying σ is added to the first 20 terms, 20^{th}-50^{th} terms and 50^{th}-100^{th} of $g(t)^{\text{calib}}_{\text{signal}}$, respectively. It can be observed that large fluctuations are obtained when the first samples are affected by noise, even by a small contribution. . . . 126
5.19 χ^2 method output using an initial shape: left figure, calibration signal; center figure, using the physics cross-talk output of the matrix method; and right figure, using the physics shape from applying RTM method. . . . 128
5.20 Comparison of χ^2 method outputs depending on the input signal . . . 129
5.21 χ^2 as a function of a given coefficient a_i. All coefficients a_n from Eq. 5.24 are fixed to their initial value except the coefficient stated in each subfigure caption. . . . 129
5.22 Comparison of the cross-talk signal in the same electronic cell if signals are averaged over 200 or 2000 samples. . . . 130
5.23 Illustration of the neighbours (orange) to a pulsed cell (red) assumed to receive a sizeable cross-talk contribution. Diagonal neighbours (blue) are not considered to receive cross-talk in this study. . . . 131
5.24 Distributions of the cross-talk ratios between pulsed cells in front layer and cells in the front, middle and back layers. . . . 132
5.25 Cross-talk magnitude as a function of η with pulsed cells in front layer. Therefore, the strip-to-strip contribution corresponds to the cross-talk between adjacent cells in η. In addition, the cross-talk between strips separated by two cells in η is presented. Strip-to-middle contribution is evaluated between a pulsed strip and its corresponding middle cells. Distributions with calibration cross-talk results are overlaid. . . . 133
5.26 Left: distributions of the cross-talk ratios between pulsed cells in the middle layer and cells in the front, middle and back layers. Right: distribution of the cross-talk ratios between pulsed cells in the middle layer and their adjacent cells in η and ϕ. . . . 134
5.27 Cross-talk magnitude as a function of η with pulsed cells in the middle layer. Distributions between the same layer have been divided into the cross-talk contribution between adjacent cells in ϕ, with $\Delta\eta = 0$ and adjacent cells in η, with $\Delta\phi = 0$. Distributions with calibration cross-talk results are overlaid. . . . 134
5.28 Left: distributions of the cross-talk ratios between pulsed cells in the back layer and cells in the front, middle and back layers. Right: distribution of the cross-talk ratios between pulsed cells in the back layer and their adjacent cells in η and ϕ. . . . 135
5.29 Cross-talk magnitude as a function of η with pulsed cells in the back layer. Distributions between the same layer have been divided into the cross-talk contribution between adjacent cells in ϕ, with $\Delta\eta = 0$ and adjacent cells in η, with $\Delta\phi = 0$. . . . 135
5.30 Illustration of the obtained cross-talk values obtained on physics signals. Cross-talk and signal energies are estimated using the full calibration chain. OF method uses 4 samples of the signal. . . . 136
5.31 Cross-talk magnitude as a function of η between cells in all layers. Distributions for the second sampling have been divided into the cross-talk contribution between adjacent cells in ϕ, with $\Delta\eta = 0$ and adjacent cells in η, with $\Delta\phi = 0$. In the case of the front layer, there is no possibility of evaluating contributions between adjacent cells in ϕ. However, the cross-talk between strips separated by two cells in η is presented. Distributions with calibration cross-talk results are overlaid. . . . 137
5.32 Illustration of the obtained cross-talk values obtained on physics signals. Cross-talk and signal energies are estimated using the full calibration chain. OF method uses 5 samples of the signal. . . . 138
5.33 Sampling phase dependence of cross-talk magnitude. . . . 139
5.34 Long distance contribution derived on physics cross-talk shapes. . . . 140
5.35 Distributions of variables (f_1, f_3, w_{η_2} and R_η) used in the electron identification. They are measured using a tag-and-probe method on $Z \to ee$ samples for probes passing the electron loose identification [15]. Corrected MC stand for the MC distributions corrected using the fudge factors and the widths determined in the study. . . . 141
5.36 Distributions of variables (E_{ratio}, R_{had} and R_ϕ) used in the electron identification. They are measured using a tag-and-probe method on $Z \to ee$ samples for probes passing the electron loose identification [15]. . . . 142

5.37 Distributions of variables (E_{ratio}, w_{η_2}, R_η and R_ϕ) used in the electron identification. Measured on $Z \to ee$ events simulated without any pileup effects. Electrons are required to pass loose identification and to present $E_T > 15$ GeV and $|\eta| < 1.475$. Calibration cross-talk stands for the current cross-talk values introduced in the simulation (Table 5.1) and the physics cross-talk estimated using 4 samples (Table 5.2). 143
5.38 Distributions of variables (R_{had}, f_1 and f_3) used in the electron identification. Measured on $Z \to ee$ events simulated without any pileup effects. Electrons are required to pass loose identification and to present $E_T > 15$ GeV and $|\eta| < 1.475$. Calibration cross-talk stands for the current cross-talk values introduced in the simulation (Table 5.1) and the physics cross-talk estimated using 4 samples (Table 5.2). 144

6.1 Calibration scheme of EM and LCW jets [4]. 147
6.2 (Left) Average energy response as a function of $|\eta_{\text{det}}|$ and the truth jet energy E^{truth}. Pileup and origin corrections are applied. (Right) Signed difference between the reconstructed η of the jet and the truth η as a function of $|\eta_{\text{det}}|$ [5]. 148
6.3 Combined uncertainty in the JES of fully calibrated jets as a function of (a) jet p_{T} at $\eta = 0$ and (b) η at $p_{\text{T}} = 80$ GeV. Absolute in-situ JES corresponds to Z/γ+jet and multijet calibrations and relative in-situ calibration corresponds to η intercalibration. More systematic errors are presented corresponding to pileup, punch-through (one of the corrections of the GSC step) and jet flavour uncertainties are also included [5]. 148
6.4 Left: performance of the JVF against pileup and for different jet p_T values. Right: comparison of corrJVF and JVF performance against pileup activity [7]. 149
6.5 Left: Distribution of the corrJVF variable of pileup and hard jets. Right: Distribution of the R_{pT} variable of pileup and hard jets [7]. 150
6.6 Left: JVT values depending on the corrJVF and R_{pT}. Right: JVT distributions for pileup and hard jets estimated on Pythia8 dijet MC events [7]. 150
6.7 Efficiency and fake rate curves of the JVT variable in comparison with the corrJVF, R_{pT} and JVF variables [7]. 151
6.8 Illustration of the sagitta parameter. 152
6.9 Reconstruction efficiency for the Medium muon selection as a function of the p_{T} of the muon, in the region $0.1 < |\eta| < 2.5$ as obtained with $Z \to \mu^+\mu^-$ and $J/\psi \to \mu^+\mu^-$ events in 2015 data and MC [9]. 154
6.10 Example of an event with large $E_{\text{T}}^{\text{miss}}$ in ATLAS data: display of event 1220033035 in run 284285 recorded by ATLAS in LHC proton-proton collisions at a centre-of-mass energy of 13 TeV. This candidate is likely to be the production of a W boson in association with a single top quark in the dilepton channel. Two opposite charged leptons are reconstructed. The reconstructed electron is represented by the blue line and the reconstructed muon is represented by the red line. One b-jet is identified and represented by an azure cone and the missing transverse momentum coming from a neutrino is represented by the dotted white line [12]. 154
6.11 $E_{\text{T}}^{\text{miss}}$ distributions using CST, TST and Track-$E_{\text{T}}^{\text{miss}}$ on $Z \to \mu^-\mu^+$ MC samples (upper plots) and comparison between TST $E_{\text{T}}^{\text{miss}}$ in 2015 data (3.2 fb^{-1}) and MC. Upper left plot presents the distributions considering all events and the upper right plot, considering events with no reconstructed jet [18]. Bottom left plot presents the comparison between data and MC on $Z \to e^-e^+$ final state and bottom right plot, on $Z \to \mu^-\mu^+$ final state [19]. 156
6.12 Resolution (RMS) of the $E_{\text{x,y}}^{\text{miss}}$ distributions using CST, TST and Track-$E_{\text{T}}^{\text{miss}}$ on $Z \to \mu^-\mu^+$ MC samples (upper plots) and comparison between TST $E_{\text{T}}^{\text{miss}}$ in 2015 data (3.2 fb^{-1}) and MC. Resolution is presented as a function of the number of primary vertices in the event in the upper plots, either considering all events (left) or events with no reconstructed jet (right) [18]. Bottom left plot presents the comparison between data and MC on 0-jet events as a function of the NPV and $\sum |E_T|$ using TST reconstruction scheme, both for events $Z \to \mu^-\mu^+$ [19]. 157
6.13 (Left) Scale of the $E_{\text{T}}^{\text{miss}}$ on the axis defined by the transverse momentum of the Z boson studied on $Z \to \mu^-\mu^+$ MC samples as a function of p_{T}^Z. (Right) linearity as a function of $E_{\text{T,truth}}^{\text{miss}}$ on $W \to \mu\nu$ MC events. 157

6.14 Truth Higgs boson production vertex identification efficiency using the diphoton or the hardest vertex method. Efficiency is presented as a function of the number of primary vertices. . . . 159

6.15 Truth Higgs boson production vertex identification efficiency using the diphoton or the hardest vertex method. Efficiency is presented as a function of the number of truth jets in the event. . . . 159

6.16 Truth Higgs boson production vertex identification efficiency using the diphoton or the hardest vertex methods. Efficiency is presented as a function of the transverse momenta of the truth diphoton system. Photons are previously matched as children of the truth Higgs boson. . . . 160

6.17 Reconstructed $E_{\mathrm{T}}^{\mathrm{miss}}$ distributions substracted from truth information for different Higgs production. TST reconstruction is compared if soft-terms are associated with the hardest vertex or the diphoton vertex of the event. . . . 161

6.18 Feynman diagram of ggF Higgs production including soft-radiation from $t\bar{t}$ loop that could be rejected by jet selection cuts and introduce a bias in $E_{\mathrm{T}}^{\mathrm{miss}}$. . . . 162

6.19 TST $E_{\mathrm{T}}^{\mathrm{miss}}$ linearity as a function of $E_{\mathrm{T,Truth}}^{\mathrm{miss}}$ for different Higgs production. TST reconstruction is compared with soft-terms either associated with the hardest vertex or to the diphoton vertex of the event. . . . 164

6.20 Reconstructed $E_{\mathrm{T}}^{\mathrm{miss}}$ distributions substracted from truth information for different Higgs production. TST reconstruction is compared to soft-terms either associated with the hardest vertex or to the diphoton vertex of the event. . . . 165

6.21 $E_{\mathrm{T}}^{\mathrm{miss}}$ resolution estimated as the RMS of the $E_{\mathrm{T}}^{\mathrm{miss}}$ distribution depending on the average number of interactions per bunch crossing. Truth information is substracted and TST reconstruction is compared to soft-terms either associated with the hardest vertex or to the diphoton vertex of the event. . . . 166

6.22 Dependence of $E_{\mathrm{T}}^{\mathrm{miss}}$ resolution as a function of the jet-vertex-tagger cut applied to central jets of the event ($20\ \mathrm{GeV} < \mathrm{p_T} < 60\ \mathrm{GeV}$, $|\eta| < 2.4$). Resolution is shown versus the average number of interactions per bunch crossing. Truth $E_{\mathrm{T}}^{\mathrm{miss}}$ is substracted and soft-terms are computed using tracks associated with the diphoton vertex of the event. . . . 167

6.23 Distributions of the relative azimuthal angle between the diphoton transverse momentum and the $E_{\mathrm{T}}^{\mathrm{miss}}$ either computed from either hard or diphoton vertex TST $E_{\mathrm{T}}^{\mathrm{miss}}$. No truth information is substracted. . . . 168

7.1 Heavy scalar model comparison for several mass points in the [m_{H} m_{χ}] plane. . . . 170

7.2 Z'_B model comparison for several mass points in the [$m_{Z'_B}$ m_{χ}] plane (g_q = 1/3, g_{DM} = 1 and sinθ = 0.3). Left column: comparison for a fixed m_{χ}. Right column: comparison for a fixed $m_{Z'_B}$. The two rows on the top present the $p_{\mathrm{T}}^{\gamma\gamma}$ and $E_{\mathrm{T}}^{\mathrm{miss}}$ distributions for different simulated samples. It can be observed that at larger $m_{Z'_B}$ and m_{χ}, both distributions tend to higher values. Concerning the two bottom rows, they present the angular azimuthal difference between the two photons direction and the diphoton system and the $E_{\mathrm{T}}^{\mathrm{miss}}$. It can be observed that at larger $m_{Z'_B}$ and m_{χ}, the former distribution tend to peak at values closer to zero, indicating that both photons are closer (more boosted). This is not the case however, while $m_{Z'_B} \gtrsim m_{\chi}$, in which case both photons tend to be separated given that the intermediate h momentum should not be high. The latter present lower number of events in the central region and a more defined peak at π at larger $m_{Z'_B}$ and m_{χ} difference, which indicates a larger back-to-back topology between the $\gamma\gamma$ and the $\chi\bar{\chi}$ systems. . . . 172

7.3 Z'-2HDM comparison for several mass points in the [$m_{Z'}$ m_{A^0}] plane ($g_{Z'}$ = 0.8, tanβ = 1.0 and $m_\chi = 100$GeV) Left column: comparison for a fixed m_{A^0}. Right column: comparison for a fixed $m_{Z'}$. The two rows on the top present the $p_{\mathrm{T}}^{\gamma\gamma}$ and $E_{\mathrm{T}}^{\mathrm{miss}}$ distributions for different simulated samples. It can be observed that at larger $m_{Z'}$ -m_{A^0} difference, harder are the kinematic distributions. Concerning the two bottom rows, they present the angular azimuthal difference between the two photons direction and the diphoton system and the $E_{\mathrm{T}}^{\mathrm{miss}}$. It can be observed that at larger $m_{Z'}$ -m_{A^0} difference, the former distribution tend to peak at values closer to zero, indicating that both photons are closer (more boosted). The latter present lower number of events in the central region and a more defined peak at π at larger $m_{Z'}$ -m_{A^0} difference, which indicates a larger back-to-back topology between the $\gamma\gamma$ and the $\chi\bar{\chi}$ systems. 173

7.4 Comparison between $q\bar{q} \to Zh$ and $gg \to Zh$ production [20]. $gg \to Zh$ process tend to present higher production rate at larger values of (a) m_{Zh} and (b) p_{T}^{H}, mainly due to the present of soft-QCD radiation (from the quark-loop or the colliding gluons) recoiling against the Higgs. Both contributions presented in these figures are generated at NLO+PS. 174

7.5 Dominant Feynman diagrams of the $\gamma\gamma$ background. 175

7.6 Dominant Feynman diagrams of the γj background. 175

7.7 Dominant Feynman diagrams of the $V\gamma$(a,b) and $V\gamma\gamma$ (c) backgrounds. 176

7.8 Left plot: $S_{E_{\mathrm{T}}^{\mathrm{miss}}}$ distributions comparing events from a Z'_B simulated sample ($m_{Z'_B} = 500$ GeV and $m_\chi = 150$ GeV) against events from the ggF SM Higgs simulated sample. It can be observed the discriminating power of this variable between samples presenting genuine $E_{\mathrm{T}}^{\mathrm{miss}}$ (Z'_B sample) or fake $E_{\mathrm{T}}^{\mathrm{miss}}$ (ggF sample). Right plot: comparison of the $S_{E_{\mathrm{T}}^{\mathrm{miss}}}$ and $E_{\mathrm{T}}^{\mathrm{miss}}$ resolution dependence in a ggF SM Higgs sample, where fake $E_{\mathrm{T}}^{\mathrm{miss}}$ is expected. Arbitrary units are used given that the aim of this plot is to compare the slope both distributions. It can be observed a higher pileup resilience of the $S_{E_{\mathrm{T}}^{\mathrm{miss}}}$ variable than the $E_{\mathrm{T}}^{\mathrm{miss}}$. 179

7.9 Distributions of the $\Delta\phi(p_{\mathrm{T}}^{\gamma\gamma}, E_{\mathrm{T}}^{\mathrm{miss}})$ (top-left), $\Delta\phi(\mathrm{H_T}, E_{\mathrm{T}}^{\mathrm{miss}})$ (top-right), N_e (bottom-left) and N_μ (bottom-right) based on simulated samples for signal models, SM Higgs models and non-resonant background. 180

7.10 Significance scan for various masses of the Z'_B boson and DM particle depending on the $S_{E_{\mathrm{T}}^{\mathrm{miss}}}$ and $p_{\mathrm{T}}^{\gamma\gamma}$ variables for the Z'_B model. Event weights are applied and signal and background samples are scaled to their corresponding cross-sections or purity ($\gamma\gamma$ and γ+jet). 181

7.11 Significance scan for various masses of the Z' boson and pseudo-scalar A^0 depending on the $S_{E_{\mathrm{T}}^{\mathrm{miss}}}$ and $p_{\mathrm{T}}^{\gamma\gamma}$ variables for the Z'-2HDM model. Event weights are applied and signal and background samples are scaled to their correspoding cross-sections or purity ($\gamma\gamma$ and γ+jet). 182

7.12 Significance scan for various masses of the Z'_B boson and DM particle depending on the $S_{E_{\mathrm{T}}^{\mathrm{miss}}}$ and $\Delta\phi(p_{\mathrm{T}}^{\gamma\gamma}, E_{\mathrm{T}}^{\mathrm{miss}})$ variables for the Z'_B model. Event weights are applied and signal and background samples are scaled to their correspoding cross-sections or purity ($\gamma\gamma$ and γ+jet). 183

7.13 Significance scan for various masses of the Z' boson and pseudo-scalar A^0 depending on the $S_{E_{\mathrm{T}}^{\mathrm{miss}}}$ and $\Delta\phi(p_{\mathrm{T}}^{\gamma\gamma}, E_{\mathrm{T}}^{\mathrm{miss}})$ variables for the Z'-2HDM model. Event weights are applied and signal and background samples are scaled to their correspoding cross-sections or purity ($\gamma\gamma$ and γ+jet). 184

7.14 Significance scan for various masses of the Z'_B boson and DM particle depending on the $S_{E_{\mathrm{T}}^{\mathrm{miss}}}$ and $\Delta\phi(\mathrm{H_T}, E_{\mathrm{T}}^{\mathrm{miss}})$ variables for the Z'_B model. Event weights are applied and signal and background samples are scaled to their correspoding cross-sections or purity ($\gamma\gamma$ and γ+jet). 185

7.15 Significance scan for various masses of the Z' boson and pseudo-scalar A^0 depending on the $S_{E_{\mathrm{T}}^{\mathrm{miss}}}$ and $\Delta\phi(\mathrm{H_T}, E_{\mathrm{T}}^{\mathrm{miss}})$ variables for the Z'-2HDM model. Event weights are applied and signal and background samples are scaled to their correspoding cross-sections or purity ($\gamma\gamma$ and γ+jet). 186

7.16 Event rate of coincidence between the diphoton vertex and the hardest vertex of the event. Rates as function of the $S_{E_{\mathrm{T}}^{\mathrm{miss}}}$ variable are presented. Red curve correspond to event rates for the diphoton non-resonant background sample while blue and pink curves show event rates for a chosen benchmark sample for the heavy-scalar and Z'_B models, respectively. This demonstrates that the background is reduced when the two vertices coincide. . . . 187
7.17 The distribution of (a) $S_{E_{\mathrm{T}}^{\mathrm{miss}}}$, (b) $p_{\mathrm{T}}^{\gamma\gamma}$ and (c) $p_{\mathrm{T}}^{\mathrm{hard}}$ after the selection of diphoton candidates in $120\ \mathrm{GeV} < \mathrm{m}_{\gamma\gamma} < 130\ \mathrm{GeV}$ [3]. Expected signal distributions are shown for a Z'_B signal with $m_{Z'_B} = 200$ GeV and Dirac fermion DM $m_\chi = 1$ GeV, a Z'-2HDM signal with $m_{Z'} = 1000$ GeV, $m_{A^0} = 200$ GeV and Dirac fermion DM $m_\chi = 100$ GeV and a heavy-scalar model with $m_{\mathrm{H}} = 275$ GeV and scalar DM $m_\chi = 60$ GeV. These overlaid signal points chosen are representative of the model kinematics. Only the sum of the MC statistical and experimental systematic uncertainties on the total background is shown as the hatched bands, while the theoretical uncertainties on the background normalization are not included. Overflow events are included in the rightmost bins. . . . 189
7.18 Description of the double-sided Crystal Ball function parameters, for a signal mass m_X = 600 GeV. Different parameters are described in the text. . . . 190
7.19 Fits of the Z'-2HDM signal line-shape for different sets of signal samples (red title). . . . 191
7.20 Fitted diphoton mass spectra of some Z'_B signals in the mono-Higgs category. . . . 192
7.21 Results of a single fit of a DSCB function (lines) for a sample where all Heavy scalar processes are summed. . . . 193
7.22 Results of a single fit of a DSCB function (lines) for a sample where all Standard Model Higgs processes are summed. . . . 194
7.23 Comparison of Pythia8 γ+jet sample in the signal (left) and the control region (right). One can clearly observe that large fluctuations are present in this sample due to bad MC modeling. $\gamma\gamma$, $V\gamma$ and $V\gamma\gamma$ MC contributions are also included in both plots. Control region plot shows the $S_{E_{\mathrm{T}}^{\mathrm{miss}}}$ distribution since contribution of the γ+jet is extracted from this variable. . . . 195
7.24 Merged non-resonant background distributions. $\gamma\gamma$ contribution is normalized to 79% of number of events in data in the inclusive category and γ+jet to 19% following data-driven measurements. $V\gamma$ and $V\gamma\gamma$ contributions are normalized to their predicted cross-section times the $36.1\mathrm{fb}^{-1}$ luminosity. . . . 196
7.25 Relative scale (top) and PDF (bottom) uncertainty for Z'_B (left) and Z'-2HDM (right) models. . . . 198
7.26 QCD (top) and PDF (bottom) systematic relative variation (%) for Z'_B model comparison for different DM mass and $m_{Z'_B}$. . . . 199
7.27 QCD (top) and PDF (bottom) systematic relative variation (%) for Z'-2HDM model comparison for different m_A and $m_{Z'_B}$. . . . 200
7.28 Systematic relative variation (%) for the Z'_B $m_\chi = 1$ GeV and $m_{Z'_B} = 200$ GeV sample in the five categories. . . . 203
7.29 Systematic relative variation (%) for the Z'-2HDM $m_{A^0} = 300$ GeV and $m_{Z'} = 800$ GeV sample in the five categories. . . . 203
7.30 Systematic relative variation (%) for the heavy-scalar $m_\chi = 60$ GeV and $m_{\mathrm{H}} = 275$ GeV sample in the five categories. . . . 204
7.31 Systematic relative variation (%) for the combined SM Higgs samples in the five categories. The combination is the result of the square sum of the total error per production mode divided by the total number of expected events in each category. . . . 205
7.32 Relative differences of selection efficiencies for the Z'_B and Z'-2HDM models computed using a FastSim MC sample or the reweighted base sample as explained in the text. . . . 207
7.33 Comparison of the MET spectrum obtained either from the reweighted base sample or with a FastSim sample for different points in the parameter space of the $Z' - 2HDM$ model 208
7.34 Comparison of the diphoton pair transverse energy spectrum obtained either from the reweighted base sample or with a FastSim sample for different points in the parameter space of the $Z' - 2HDM$ model . . . 209
7.35 Comparison of the MET spectrum obtained either from the reweighted base sample or with a FastSim sample for different points in the parameter space of the Z'_B model 210

7.36 Comparison of the diphoton pair transverse energy spectrum obtained either from the reweighted base sample or with a FastSim sample for different points in the parameter space of the Z'_B model 211

7.37 Diphoton invariant mass distribution for data and the corresponding fitted signal and background in the Mono-Higgs category for the Z'_B benchmark model fit using g_q = 1/3, g_χ = 1, $\sin\theta$ = 0.3 and Dirac fermion DM $m_\chi = 1$ GeV as an illustration [3]. A negative best-fit DM signal is found. The data is shown as dots with asymmetric error bars that represent central Poissonian confidence intervals at 68% CL. The fitted signal (solid red line), SM Higgs boson (solid green line), non-resonant background (dashed blue line) and the non-resonant background plus the SM Higgs boson (dashed green line) are shown as well as the total of all those contributions (solid blue line). 212

7.38 Expected (dashed lines) and observed (solid lines) 95% CL upper limits on $\sigma(pp \to h\chi\bar{\chi}) \times \mathcal{B}(h \to \gamma\gamma)$ for (a) the Z'_B model for g_q = 1/3, g_χ = 1, $\sin\theta$ = 0.3 and Dirac fermion DM $m_\chi = 1$ GeV and (b) the Z'-2HDM model for $\tan\beta$ = 1, $g_{Z'}$ = 0.8, $m_{Z'}$=1000 GeV and Dirac fermion DM $m_\chi = 100$ GeV, as a function of $m_{Z'_B}$ and m_{A^0}, respectively [3]. The masses of the neutral CP-even scalar (H^0) and the charged scalars ($H^\pm$) from Z'-2HDM model are set to 300 GeV. The theoretical predictions of $\sigma(pp \to h\chi\bar{\chi}) \times \mathcal{B}(h \to \gamma\gamma)$ for these two models (dark-blue lines with blue bands representing their associated theoretical systematic uncertainties) are also shown. The inset shows a zoomed-in view of the same figure in narrower ranges of both the x and y axes. 212

7.39 The ratios of the observed and expected 95% CL upper limits on the signal cross-section to the predicted signal cross-sections for (a) the Z'_B model in the (m_χ, $m_{Z'_B}$) plane and (b) the Z'-2HDM model in the (m_{A^0}, $m_{Z'}$) plane [3]. For the Z'_B model, the mixing angle $\sin\theta = 0.3$, and the coupling values $g_q = 1/3$ and $g_\chi = 1$ are used. In the scenario of Z'-2HDM model, the ratio of the two-Higgs-doublet vacuum expectation values $\tan\beta = 1.0$, Dirac fermion DM mass $m_\chi = 100$ GeV, and the coupling value $g_{Z'} = 0.8$ are used. The masses of the neutral CP-even scalar (H^0) and the charged scalars ($H^\pm$) from Z'-2HDM model are set to 300 GeV. The plus and minus one standard deviation expected exclusion curves are also shown as red dashed and dotted lines. The regions below the lines (i.e. with $\sigma^{\text{obs}}/\sigma^{\text{th}} < 1$) are excluded. In both figures, the gray dashed line corresponds to the boundary of the region above which the Z' boson is produced off-shell. 213

7.40 A comparison of the inferred limits to the constraints from direct detection experiments on the spin-independent DM–nucleon cross section in the context of the Z'_B simplified model with vector couplings [3]. Limits are shown at 90% CL. The results from this analysis, in which the region inside the contour is excluded, are compared with limits from the LUX [51], PandaX-II [52], XENON [53], superCDMS [54], and CRESST-II [55] experiments. The comparison is model-dependent and solely valid in the context of this model, assuming Dirac fermion DM, mixing angle $\sin\theta = 0.3$, and the coupling values $g_q = 1/3$ and $g_\chi = 1$. The impact of renormalization-group evolution effects [56, 57] when comparing collider and direct detection limits is not taken into consideration here. 213

7.41 Diphoton invariant mass distribution for data and the corresponding fitted signal and background in the five categories, (a) Mono-Higgs category, (b) High-$E_{\text{T}}^{\text{miss}}$ category, (c) Intermediate-$E_{\text{T}}^{\text{miss}}$ category, (d) Different-Vertex category and (e) Rest category taken from Ref. [3]. On each plot, the data (dots with asymmetric error bars) is shown. The error bars represent the central Poissonian confidence intervals at 68% CL. The simultaneous fit result including a heavy-scalar signal (solid red line), SM Higgs boson (solid green line), the non-resonant background (dashed blue line) and the non-resonant background plus the SM Higgs boson (dashed green line) are shown as well as the sum of all those contributions (solid blue line). The fitted heavy-scalar signal shown here corresponds to $m_{\text{H}} = 275$ GeV and scalar DM $m_\chi = 60$ GeV. 214

7.42 Observed and expected 95% CL upper limits on the $\sigma(pp \to H) \times \mathcal{B}(H \to \gamma\gamma\chi\chi)$ with a scalar DM candidate mass of 60 GeV as a function of the heavy-scalar-boson mass in the range 260 GeV $< m_{\mathrm{H}} <$ 350 GeV [3]. A 100% branching fraction is assumed for $H \to h\chi\chi$. The theoretical prediction for the model (dark-blue lines with blue bands representing their associated theoretical systematic uncertainties) is also shown. The theoretical cross-section is assumed to be equal to that of a SM Higgs boson with the same mass produced in gluon–gluon fusion. 215
7.43 Summary of the $h \to b\bar{b} + E_{\mathrm{T}}^{\mathrm{miss}}$ analysis selection criteria. The notation $p_{\mathrm{T}}(A, B)$ is defined as the vector sum of the $p_{\mathrm{T}}$for the objects A and B [59]. 216
7.44 Distributions of the invariant mass of the Higgs boson candidates mh,reco=mjj,mJ with two b-tags in the SR for the four $E_{\mathrm{T}}^{\mathrm{miss}}$ categories that are used as inputs to the fit. The upper panels show a comparison of data to the SM expectation before (dashed lines) and after the fit (solid histograms) with no signal included. The lower panels display the ratio of data to SM expectations after the fit, with its systematic uncertainty considering correlations between individual contributions indicated by the hatched band. The expected signal from a representative Z'-2HDM model is also shown (long-dashed line). [59] 217
7.45 Exclusion contours for the Z'-2HDM scenario in the ($m_{Z'}$,m_{A^0}) plane for $\tan\beta$ = 1, $g_{Z'}$ = 0.8, and m_χ = 100 GeV. The observed limits (solid line) are consistent with the expectation under the SM-only hypothesis (dashed line) within uncertainties (filled band). Observed limits from previous ATLAS results at $\sqrt{s} = 13$ TeV (dash-dotted line) [31] are also shown. [59] 218
7.46 Observed (obs) and expected (exp) upper limits at 95% CL on σ_{vis} of $h(\to b\bar{b}) + E_{\mathrm{T}}^{\mathrm{miss}}$ events. Also shown are the acceptance $\times$ efficiency probabilities to reconstruct and select an event in the same $E_{\mathrm{T}}^{\mathrm{miss}}$ bin as generated. [59] 218
7.47 The dashed black line presents the fitted non-resonant background and the solid red line, the SM $h \to \gamma\gamma$ contribution for both categories (left: low-$p_{\mathrm{T}}^{\mathrm{miss}}$;right: high-$p_{\mathrm{T}}^{\mathrm{miss}}$) category. The sum of the non-resonant and resonant background shapes is shown in blue [62]. 220
7.48 The observed (expected) 95% CL limits on the signal strength ($\sigma_{95\%\mathrm{CL}}/\sigma_{th}$) for all Z'-2HDM mass points shown in a grid of $m_{Z'}$ and m_{A^0}. Regions presenting values lower than 1 can be considered excluded by the analysis. The theoretical cross-section for each point is calculated assuming $g_{Z'}$= 0.8. Right: 95 % CL upper limits on cross-section for the baryonic Z' scenario as a function of $m_{Z'}$ for m_χ= 1 GeV. The theoretical cross-section (blue) is calculated assuming g_q= 0.25 and sinθ= 0.3 [62]. 220
7.49 The jet transverse momentum resolution as determined in dijet MC events for calorimeter jets and particle flow jets with regard to the (a) jet transverse momentum and the (b) jet pseudo-rapidity [1]. 226

A.1 (a) Illustration of the relation between the p-value obtained from an observed value of the test statistic t_μ. (b) The standard normal distribution showing the relation between the significance Z and the p-value [1]. 233
A.2 On the left, the pdf of the test statistics for the Higgs search at LEP for the background (right) and signal+background hypotheses (left) are illustrated. The light yellow region to the left of the observation is $1 - \mathrm{CL}_b$ and the dark green is CL_{s+b}. On the right, the evolution of the pdfs is presented with falling search sensitivity from (a) to (c) as the Higgs mass hypothesis is increased and the production cross-section falls [3]. 236

B.1 Comparison of $E_{\mathrm{T}}^{\mathrm{miss}}$ spectrum of Z'-2HDM versus Heavy scalar model for same mediator and DM particle masses ($m'_Z = 250$ or 280 GeV, $m_\chi = 50$ GeV) 237
B.2 Comparison of $E_{\mathrm{T}}^{\mathrm{miss}}$ spectrum of Z'-2HDM versus Heavy scalar model for same mediator and DM particle masses ($m'_Z = 280$ or 310 GeV, $m_\chi = 50$ GeV) 237
B.3 Comparison of $E_{\mathrm{T}}^{\mathrm{miss}}$ spectrum of Z'-2HDM versus Heavy scalar model for same mediator and DM particle masses ($m'_Z = 250$ or 260 GeV, $m_\chi = 60$ GeV) 238
B.4 Comparison of $E_{\mathrm{T}}^{\mathrm{miss}}$ spectrum of Z'-2HDM versus Heavy scalar model for same mediator and DM particle masses ($m'_Z = 280$ or 310 GeV, $m_\chi = 60$ GeV) 238

B.5 Comparison of kinematic distributions between Z′-2HDM and Heavy scalar models for the same mediator and DM particle masses ($m'_Z = 250$ or 260 GeV, $m_\chi = 50$ GeV) 238
B.6 Comparison of kinematic distributions between Z′-2HDM and Heavy scalar models for the same mediator and DM particle masses ($m'_Z = 250$ or 260 GeV, $m_\chi = 50$ GeV) 239
B.7 Comparison of kinematic distributions between Z′-2HDM and Heavy scalar models for the same mediator and DM particle masses ($m'_Z = 280$ or 310 GeV, $m_\chi = 50$ GeV) 239
B.8 Comparison of kinematic distributions between Z′-2HDM and Heavy scalar models for the same mediator and DM particle masses ($m'_Z = 250$ or 260 GeV, $m_\chi = 60$ GeV) 239
B.9 Comparison of kinematic distributions between Z′-2HDM and Heavy scalar models for the same mediator and DM particle masses ($m'_Z = 250$ or 260 GeV, $m_\chi = 50$ GeV) 240
B.10 Comparison of kinematic distributions between Z′-2HDM and Heavy scalar models for the same mediator and DM particle masses ($m'_Z = 250$ or 260 GeV, $m_\chi = 50$ GeV) 240
B.11 Comparison of kinematic distributions between Z′-2HDM and Heavy scalar models for the same mediator and DM particle masses ($m'_Z = 280$ or 310 GeV, $m_\chi = 50$ GeV) 240
B.12 Comparison of kinematic distributions between Z′-2HDM and Heavy scalar models for the same mediator and DM particle masses ($m'_Z = 260$ or 280 GeV, $m_\chi = 60$ GeV) 241
B.13 Comparison of kinematic distributions between Z′-2HDM and Heavy scalar models for the same mediator and DM particle masses ($m'_Z = 280$ or 310 GeV, $m_\chi = 50$ GeV) 241
B.14 Comparison of kinematic distributions between Z′-2HDM and Heavy scalar models for the same mediator and DM particle masses ($m'_Z = 250$ or 260 GeV, $m_\chi = 50$ GeV) 241
B.15 Comparison of kinematic distributions between Z′-2HDM and Heavy scalar models for the same mediator and DM particle masses ($m'_Z = 280$ or 310 GeV, $m_\chi = 50$ GeV) 242
B.16 Comparison of kinematic distributions between Z′-2HDM and Heavy scalar models for the same mediator and DM particle masses ($m'_Z = 250$ or 260 GeV, $m_\chi = 60$ GeV) 242
B.17 Comparison of kinematic distributions between Z′-2HDM and Heavy scalar models for the same mediator and DM particle masses ($m'_Z = 280$ or 310 GeV, $m_\chi = 60$ GeV) 242
B.18 Comparison of kinematic distributions between Z′-2HDM and Heavy scalar models for the same mediator and DM particle masses ($m'_Z = 250$ or 260 GeV, $m_\chi = 50$ GeV) 243
B.19 Comparison of kinematic distributions between Z′-2HDM and Heavy scalar models for the same mediator and DM particle masses ($m'_Z = 280$ or 310 GeV, $m_\chi = 50$ GeV) 243
B.20 Comparison of kinematic distributions between Z′-2HDM and Heavy scalar models for the same mediator and DM particle masses ($m'_Z = 250$ or 260 GeV, $m_\chi = 60$ GeV) 243
B.21 Comparison of kinematic distributions between Z′-2HDM and Heavy scalar models for the same mediator and DM particle masses ($m'_Z = 280$ or 310 GeV, $m_\chi = 60$ GeV) 244
B.22 Comparison of kinematic distributions between Z′-2HDM and Heavy scalar models for the same mediator and DM particle masses ($m'_Z = 250$ or 260 GeV, $m_\chi = 50$ GeV) 244
B.23 Comparison of kinematic distributions between Z′-2HDM and Heavy scalar models for the same mediator and DM particle masses ($m'_Z = 280$ or 310 GeV, $m_\chi = 50$ GeV) 244
B.24 Comparison of kinematic distributions between Z′-2HDM and Heavy scalar models for the same mediator and DM particle masses ($m'_Z = 250$ or 260 GeV, $m_\chi = 60$ GeV) 245
B.25 Comparison of kinematic distributions between Z′-2HDM and Heavy scalar models for the same mediator and DM particle masses ($m'_Z = 280$ or 310 GeV, $m_\chi = 60$ GeV) 245

C.1 $p_{\mathrm{T}}^{\gamma\gamma}$ distributions of the Z'_B model of four mass points ($m_{Z'_B}$, m_χ) and four different values of g_q. 248
C.2 $E_{\mathrm{T}}^{\mathrm{miss}}$ distributions of the Z'_B model of four mass points ($m_{Z'_B}$, m_χ) and four different values of g_q. 249
C.3 $\Delta\phi(\gamma_1, E_{\mathrm{T}}^{\mathrm{miss}})$ distributions of the Z'_B model of four mass points ($m_{Z'_B}$, m_χ) and four different values of g_q. 250
C.4 $\Delta\phi(\gamma\gamma, E_{\mathrm{T}}^{\mathrm{miss}})$ distributions of the Z'_B model of four mass points ($m_{Z'_B}$, m_χ) and four different values of g_q. 251

List of Tables

1.1 Fundamental interactions and relative strength together with their range of action in meters. This table summarizes the current knowledge of these interactions and it is the subject of ongoing searches. . . . 7

1.2 Quark and lepton families as seen by the electroweak interaction. Fermions grouped in parentheses are elements of a doublet under the isospin symmetry. Main quantum numbers corresponding to the electroweak symmetries are shown for each weak interaction doublet ($I_3 = \pm\frac{1}{2}$) and singlets ($I_3 = 0$). Indexes L and R show the chirality of the considered particles. . . . 11

1.3 Production cross-sections of the Standard Model Higgs boson at the LHC for $\sqrt{s} = 13$ TeV [56]. . . . 20

1.4 Branching ratios of the Standard Model Higgs through all channels in Figures 1.11 at $m_h = 125.09$ GeV for $\sqrt{s} = 13$ TeV [56]. . . . 22

2.1 Comparison of selected primary trigger thresholds (in GeV) at the end of Run 1 and during 2015 together with typical offline requirements applied in analyses [16]. . . . 60

3.1 Segmentation of the end-caps. Outer wheel covers the region $1.375 < |\eta| < 2.5$ and the inner wheel, $2.5 < |\eta| < 3.2$. Inner wheel presents a constant segmentation for all three layers while granularity varies for the outer wheel [3]. . . . 71

3.2 Values of $F_{DAC\to\mu A}$ in 2004 test beam report [19]. . . . 84

3.3 Values of I/E, f_{sampl} and $F_{\mu A\to \mathrm{MeV}}$ in 2004 test beam report [19]. . . . 84

3.4 Time resolution of the electronics readout for a single channel in the middle/front layer in high and medium gain. Measurement for the same calibration line and the same SCA could not be performed for the front layer due to the distribution of the calibration lines [9]. . . . 86

4.1 List of variables used in the electron identification. . . . 98

4.2 Discriminant variables used in the tight and loose photon identification criteria [7]. . . . 100

4.3 Track selection for the track isolation. z_0 is the difference of longitudinal impact parameter of the track, and the position of a given vertex (by default the hardest vertex of the event); N_{Si} is the number of hits in silicon detectors (pixels and SCT); $N_{\mathrm{mod}}^{\mathrm{sh}}$ is the number of shared hits assigned to several tracks in the silicon detectors; $N_{\mathrm{Si}}^{\mathrm{hole}}$ and $N_{\mathrm{Pix}}^{\mathrm{hole}}$ is the number of missing hits in both silicon detectors and only pixel detector, respectively [13]. . . . 105

5.1 Cross-talk mean values in the LAr barrel. 2000 test-beam and 2008 results represent the cross-talk magnitude using under-peak to peak technique [8]. The uncertainties for the 2008 and OF method values correspond to the RMS of their corresponding ratios distribution for the full distribution of cells in each category. . . . 120

5.2 Cross-talk mean values in the LAr barrel using physics cross-talk signals and calibration cross-talk signals (currently used in ATLAS simulation code Section 5.2). Physics cross-talk is estimated by averaging the contributions from all cells in the calorimeter. Both average magnitudes are estimated for all possible short-distance contributions. The RMS accounts for the cross-talk ratios dispersion around the central value. Calibration cross-talk values for middle-to-strip and back-to-middle contributions are respectively equated to the strip-to-middle and middle-to-back values, given that it is the procedure followed in ATLAS simulation code. For second neighbours contribution estimated using calibration runs, the magnitude between parentheses represents the contributions magnitude at $|\eta| > 1.1825$. 132

5.3 Cross-talk mean values in the LAr barrel using physics cross-talk signals using 5 samples in the OF step. Physics cross-talk is estimated by averaging the contributions from all cells in the calorimeter. Both average magnitudes are estimated for all possible short-distance contributions. The RMS accounts for the cross-talk ratios dispersion around the central value. Physics contributions are compared to calibration cross-talk signals. Calibration cross-talk values for middle-to-strip and back-to-middle contributions are respectively equated to the strip-to-middle and middle-to-back values. For second neighbours contribution estimated using calibration runs, the magnitude between parentheses represents the contributions magnitude at $|\eta| > 1.1825$. 138

5.4 Long distance contributions in the LAr barrel using 4 samples. The uncertainties values correspond to the RMS of their corresponding ratios distribution. 140

6.1 Identification efficiency of the Higgs boson production vertex using the hardest vertex or the diphoton vertex. 159

6.2 Mean of the $E_{\mathrm{T}}^{\mathrm{miss}}$ distribution for the different Higgs production modes. Values are compared between diphoton vertex TST or hardest vertex TST. Both mean values are significantly different within their error intervals. 162

6.3 RMS of the $E_{\mathrm{T}}^{\mathrm{miss}}$ distribution for the different Higgs production modes. Values are compared between diphoton vertex TST or hardest vertex TST. Both mean values are significantly different within their error intervals. 163

6.4 Slope of the $E_{\mathrm{T}}^{\mathrm{miss}}$ resolution vs the average interaction versus the bunch crossing ($< \mu >$) for different Higgs production modes. Values are compared between diphoton vertex TST or hardest vertex TST. 163

7.1 Best significance for few benchmark samples of Z'-2HDM and Z'_B models. Values in parentheses correspond to best significance vetoing leptons in the event. 181

7.2 Optimized criteria used in the categorization. Each category excludes events that are in the upper categories. 188

7.3 The analytical functions used to model the non-resonant $m_{\gamma\gamma}$ distribution, the uncertainty on the signal due to the spurious signal (Spur. signal). The variable x is defined as $m_{\gamma\gamma}/\sqrt{s}$ while a and b are parameters of the background functions. For the Rest category, the fitting function is a Bernstein polynomial of order 3, where C_3^j are binomial coefficients and $b_{j,3}$ are Bernstein polynomial coefficients [37]. The relative magnitude of the spurious signal is also presented with regard to the expected number of the background events (N_{back}) and signal events (N_{signal}) in the range $120\ \mathrm{GeV} < m_{\gamma\gamma} < 130\ \mathrm{GeV}$. N_{signal} represents the expected yield of the Z'_B model sample for $m_{Z'_B} = 200$ GeV and $m_\chi = 1$ GeV in the Mono-Higgs category. For the other categories, it represents the expected signal yield of the heavy-scalar sample with $m_{\mathrm{H}} = 275$ GeV and $m_\chi = 60$ GeV. 196

7.4 The MC yields and uncertainty in the in 122 to 128 GeV$m_{\gamma\gamma}$ window. Here no pile up reweighing is applied. 197

7.5 Relative factorization and renormalization scale uncertainty for SM Higgs boson samples. 199

7.6 Relative PDF+α_s uncertainty on SM Higgs boson samples. 199

7.7 Breakdown of the dominant systematic uncertainties in the range of 105 GeV $< m_{\gamma\gamma} <$ 160 GeV [3]. The uncertainties in the yield of signals, the background from SM Higgs-boson processes, and non-resonant background are shown. All production modes of the SM Higgs boson are considered together. Values for the impact on all categories are shown, unless one of the systematic uncertainties is not applicable to the sample, in which case the value is substituted by a "-". If a given source has a different impact on the various categories, the given range corresponds to the smallest and largest impacts among categories or among the different signal models used in the analysis. In addition, the potential bias coming from non-resonant background mismodeling is shown relative to the background. 202
7.8 Event yields in the range of 120 GeV $< m_{\gamma\gamma} <$ 130 GeV for data, signal models, the SM Higgs-boson background and non-resonant background in each analysis category, for an integrated luminosity of 36.1 fb^{-1} [3]. The signal samples shown correspond to a heavy-scalar sample with $m_{\mathrm{H}} = 275$ GeV and $m_{\chi} = 60$ GeV, a Z'_B signal with $m_{Z'_B} = 200$ GeV and $m_{\chi} = 1$ GeV and a Z'-2HDM signal with $m_{Z'} = 1000$ GeV, $m_{A^0} = 200$ GeV, $m_{H^{0,\pm}} = 300$ GeV and $m_{\chi} = 100$ GeV. For each benchmark signal model, the selection efficiency times acceptance denoted as "$\mathcal{A} \times \epsilon$" is also shown. The yields for non-resonant background are obtained from a fit to data while SM Higgs-boson events are estimated from the simulation. The uncertainties correspond to the quadrature sum of the statistical and systematic uncertainties. 206
7.9 Observed and expected upper limits (at 95% CL) on the visible cross-section for BSM physics processes producing missing transverse momentum and a SM Higgs boson decaying into two photons [3]. Limits are presented for the five different categories. The $\pm 1\sigma$ exclusion from expected limits are also given. For all the simulated signal points, the lowest and largest values of the acceptance times efficiency ($\mathcal{A} \times \epsilon$) for all three models are presented as a range. For the Z'_B model, signals with DM mass m_{χ} between 1 and 1000 GeV and mediator mass $m_{Z'_B}$ between 1 and 2000 GeV are taken into consideration. The samples with the mediator mass $m_{Z'} = 400$–1400 GeV and pseudoscalar boson mass $m_{A^0} = 200$–450 GeV are added for the Z'-2HDM model. For the heavy-scalar model, the values are taken from the signals points with m_{H} = 260 to 350 GeV and $m_{\chi} = 60$ GeV. . . 206
7.10 Observed and expected 95% CL upper limits (in fb) on $\sigma(pp \to h\chi\bar{\chi}) \times \mathcal{B}(h \to \gamma\gamma)$ and associated expected $\pm 1\sigma$ upper limits for the Z'_B benchmark model for different $m_{Z'_B}$ and for a fixed mass $m_{\chi} = 1$ GeV [3]. 209
7.11 Observed and expected 95% CL upper limits (in fb) on $\sigma(pp \to h\chi\bar{\chi}) \times \mathcal{B}(h \to \gamma\gamma)$ and the associated expected $\pm 1\sigma$ upper limits for the Z'-2HDM benchmark model for different m_{A^0} and $m_{Z'} = 1000$ GeV, $m_{\chi} = 100$ GeV [3]. 210
7.12 Observed and expected 95% CL upper limits (in fb) on the $\sigma(pp \to H) \times \mathcal{B}(H \to \gamma\gamma\chi\chi)$, where a 100% branching fraction is assumed for $H \to h\chi\chi$, and the associated expected $\pm 1\sigma$ upper limits for the heavy-scalar model for different mediator masses and $m_{\chi} = 60$ GeV [3]. 215
7.13 Categorization of the diphoton events inside the CMS collaboration [62]. 219

C.1 Cross-section values for the Z'_B model fixing different values of the g_q parameter. Values in parentheses correspond to the ratio between the given cross-section and the reference cross-section, fixed to be $\sigma_{g_q=1/3}$. Other parameters are fixed to their proposed values in [1] ($sin\theta = 0.3$, $g_{chi} = 1$ and $g_{hZ'Z'} = m_{Z'}$). 248
C.2 Cross-section values for Z'-2HDM model mass points using ATLAS ($m_{H^{\pm}} = m_{H^0} = 300$ GeV) and CMS ($m_{H^{\pm}} = m_{H^0} = m_{A^0}$) configurations. Other parameters are fixed to the values presented in DM Forum [1] ($\tan\beta = 1$, $g_{Z'} = 0.8$ and $m_{\mathrm{dm}} = 100$ GeV). 248